Planar Laser Polarisation Spectroscopy Imaging in Combustion

Julie-Ann Reppel
Schools of Chemical and Mechanical Engineering
University of Adelaide
Date of submission: 27 November 2003

julie_reppel@hotmail.com

Planar Laser Polarisation Spectroscopy Imaging in Combustion

Julie-Ann Reppel
Schools of Chemical and Mechanical Engineering
University of Adelaide
Date of submission: 27 November 2003

This work contains no material which has been accepted for the award of any other degree or diploma in any university or other tertiary institution and, to the best of my knowledge and belief, contains no material previously published or written by another person, except where due reference has been made in the text.

I give consent to this copy of my thesis, when deposited in the University Library, being available for loan and photocopying. **Note that colour coding has been used throughout this thesis. Photocopies should be in colour for the text and figures to be understood.**

Signed:

Julie-Ann Reppel
27 November 2003

Dedication:

To
Erica Jane Beresford

Acknowledgements

I acknowledge the support of my supervisors, Z.T. Alwahabi, K.D. King and G.J. Nathan, and especially K.D. King for the use of his laser laboratory and equipment therein. The workshop staff have been wonderful, especially Brian Mulcahy, Peter Kay and Jason Peak. Finally an end to the frustrating electronics of THAT lab, thanks, Derek Franklin. And many thanks to Sanh Tran for fixing that lab computer every time it froze.

Thanks, Zeyad, for talking me out of quitting, and for teaching me how to see problems clearly.

Special thanks to William G. Tong for discussions and the idea of polariser pair extinction ratios of less than 10^{-12}. Also to Dr Evonne Stokes for clarifying the method of calculating inner products of complex vectors. Many thanks to Bassam Dally for the equilibrium CHEMKIN calculations of OH number density and temperature. And to Dr John Close for a discussion of Clebsch-Gordon coefficients.

This thesis would not have been possible without all the security guys and girls who drove me home at three in the morning when I was too tired to think. Thanks for all your help.

Abstract

This thesis presents two new theories of the geometrical dependence of laser polarisation spectroscopy (LPS) signal, specifically the dependence on the pump and probe beam polarisations and the beam intersection angle; for the cases of (1) linearly and (2) circularly polarised pump beams.

Two predictions arising from these theories are confirmed experimentally. Both linearly and circularly polarised pump beam theories predict non-zero signal for orthogonal pump/probe beam intersection for clearly specified pump and probe beam polarisation geometries. The first (to the best of our knowledge) Planar Laser Polarisation Spectroscopy (PLPS) images to experimentally verify the prediction of non-zero signal for orthogonal beam intersection for both linearly and circularly polarised pump beams are presented. The images represent instantaneous and average hydroxyl radical (OH) distributions in a premixed, laminar natural gas/O_2 flame for an orthogonal pump/probe beam geometry.

The theoretical description of polarisation spectroscopy for the case of a circularly polarised pump beam predicts that the orthogonal LPS signal will be dominated by an induced linear, rather than an induced circular, dichroism. Non-zero images collected in the case of a circularly polarised pump beam and orthogonal pump/probe beam intersection for the A $^2\Sigma$-X $^2\Pi$(0-0) $Q_2(8)$ transition of the hydroxyl radical (and non-detection of signal for the A $^2\Sigma$-X $^2\Pi$(0-0) $R_2(8)$ and $P_2(8)$ transitions) support the predicted spectroscopic behaviour.

Two applications of polarisation spectroscopy are investigated. In the first, PLPS imaging of the hydroxyl radical in a premixed natural gas/O_2 flame is undertaken for 15° and 30° pump/probe beam intersection angles and a horizontally polarised pump beam. The images demonstrate the effect of thermal gradient beam steering on image quality. Correction for thermal gradient beam steering using an average probe beam background is shown to be successful for laminar flames. Equivalent correction for turbulent flames would require near-simultaneous collection of the probe beam profile with the LPS signal. A configuration to simultaneously image the probe profile and the PLPS signal is conceptually described.

The second application compares the signal due to the Planar Laser Induced Fluorescence (PLIF) and PLPS techniques. Simultaneous PLIF and PLPS images of the OH distribution in a premixed natural gas/O_2 flame from a modified glass-blowing torch are presented for a 13.6° pump/probe beam intersection angle. The PLIF images are collected in the near-linear regime of optical

pumping. The PLPS images are collected in the highly saturated regime. The images show significant differences in the apparent OH distribution detected by each technique near the tip of the modified glass-blowing torch. In a subsequent quantitative investigation, simultaneous OH linear regime LIF and saturated LPS single point signal collected for a natural gas/air flame from a rectangular mixing burner are compared (after correction to represent the number density contributing to the signal for each technique) with the predictions of the (numerical modelling) equilibrium module of the CHEMKIN library as a function of fuel equivalence ratio. The LIF signal is corrected for the fluorescence due to the probe beam. The LPS signal is corrected for the probe beam background and the square root of the resulting signal taken. The pump beam is circularly polarised and tuned to the A $^2\Sigma$-X $^2\Pi$ (0-0) $P_2(8)$ transition of OH. A linear relationship is demonstrated between the square root of the (probe background corrected) saturated regime LPS and the linear regime LIF signals representing OH number density in the natural gas/air flame.

Standard Jones matrix descriptions of the geometrical dependence of the induced dichroism and birefringence derived in this thesis are presented. Matrix descriptions are developed for both linearly and circularly polarised pump beams. The Jones matrix formalism is used to calculate easily applicable, general Jones matrices representative of the most common experimental configurations.

Table of Contents: Volume I

Table of Contents: Volume II

Appendices

List of Figures

Chapter I:

Chapter II:

Chapter III:

Chapter VII:

Appendices

List of Tables

Chapter I:

Appendices

List of References

[1] Teets, R.E., Kowalski, F.V., Hill, W., Carlson, N., and Hansch, T.W., *"Laser Polarisation Spectroscopy"*, Proc. Soc. Photo-Optical Instrumentation Engineers, **Vol. 113**, Advances in Laser Spectroscopy I, Ed. A. H. Zewail, 80-87, 1977.

[2] Wieman, C. and Hansch, T.W., *"Doppler-Free Laser Polarisation Spectroscopy"*, Phys. Rev. Letts, **36** (20), 1170-1173, 1976.

[3] Nyholm, K., Fritzon, R. and Alden, M., *"Two-dimensional imaging of OH in flames by use of polarization spectroscopy"*, Optics Letters, **18** (19). 1672-1674, 1993.

[4] Schefer, R.W., Namazian, M. and Kelly, J., *"CH, OH and CH_4 Concentration Measurements in a Lifted Turbulent-Jet Flame"*, Twenty-Third Symposium (International) on Combustion, Pittsburgh: The Combustion Institute, 669-676, 1990.

[5] Lavrinenko, A.V. and Gancheryonok, I.I., *"Angular Dependence of a Signal in Two-Wave Nonlinear Polarization Spectroscopy"*, Optics and Spectroscopy, **86** (6), 889-892, 1999, translated from Optika i Spektroskopiya, **86** (6), 990-993, 1999.

[6] Rumyantseva, N.K., Smirnov, V.S. and Tumaikin, A.M., *"Anisotropy of gaseous media in a strong electromagnetic field"*, Opt. Spektrosc. (USSR), **48** (1), 76-79, 1979.

[7] Ritze, H.-H., Stert, V. and Meisel, E., *"High Resolution Polarization Spectroscopy in the Strong Saturation Regime"*, Optics Commun., **29** (1), 51-56, 1979.

[8] Stert, V. and Fischer, R., *"Doppler-Free Polarization Spectroscopy Using Linear Polarised Light"*, Appl. Phys. **17**, 151-154, 1978.

[9] Gianfrani, L., Sasso, A. and Tino, G.M., *"Polarization Spectroscopy of Atomic Oxygen by Dye and Semiconductor Diode Lasers"*, Il, Nuovo Cimento, **13** (10), 1221-1234, 1991.

[10] Hertzler, Ch. and Foth, H.-J., *"Sub-Doppler Polarization Spectra of He, N_2 and Ar^+ recorded in discharges"*, Chem. Phys. Letts, **166** (5,6), 551-559, 1990.

[11] Raab, M., Horning, G., Castell, R. and Demtroder., W., *"Doppler-free Polarization Spectroscopy of the Cs_2 molecule at λ = 6270 A"*, Chem. Phys. Letts, **66** (2), 307-312, 1979.

[12] Nyholm, K., Maier, R., Aminoff, C.G. and Kaivola, M., *"Detection of OH in flames using polarization spectroscopy"*, Applied Optics, **32** (6), 919-924, 1993.

[13] Nyholm, K., Fritzon, R. and Alden, M., *"Single-pulse two-dimensional temperature imaging in flames by degenerate four-wave mixing and polarization spectroscopy"*, Applied Phys. B, **59**, 37-43, 1994.

[14] Nyholm, K., Kaivola, M. and Aminoff, C.G., *"Polarization spectroscopy applied to C_2 detection in a flame"*, Applied Phys. B, **60**, 5-10 (1995).

[15] Lofstedt, B. and Alden, M., *"Simultaneous detection of OH and NO in a flame using polarization spectroscopy"*, Optics Commun., **124**, 251-257, 1996.

[16] Spano, F.C. and Lehmann, K.K., *"Pulsed polarization spectroscopy with strong fields and an optically thick sample"*, Phys. Rev. A, **45**, 7997-8004, 1992.

[17] Lange, W. and Mylnek, J., *"Quantum Beats in Time-Resolved Polarization Spectroscopy"*, Phys. Rev. Letts., **40** (21), 1373-1375, 1978.

[18] Suvernev, A.A., Tadday, R. and Dreier, T., *"Measurement and theoretical modelling of quantum beats in picosecond time-resolved degenerate four-wave mixing and polarization spectroscopy of OH in atmospheric flames"*, Phys. Rev. A, **58** (5), 4102-4115, 1998.

[19] Tadday, R., Suvernev, A.A., Dreier, T. and Wolfrum, J., *"Quantum beat spectroscopy of OH radicals in atmospheric pressure flames"*, Chem. Phys. Letts, **268**, 117-124, 1997.

[20] Dreizler, A., Tadday, R., Suvernev, A.A., Himmelhaus, M., Dreier, T. and Foggi, P., *"Measurement of orientational relaxation times of OH in a flame using picosecond time-resolved polarization spectroscopy"*, Chem. Phys. Letts, **240**, 315-323, 1995.

[21] Reichardt,T.A. and Lucht, R.P., *"Theoretical calculation of lineshapes and saturation effects in polarization spectroscopy"*, J. Chem. Phys., **109** (14), 5830-5843, 1998.

[22] Collett, E., *"Polarised Light. Fundamentals and Applications"*, 443 - 456, Marcel Dekker, Inc., New York, Basel, Hong Kong, 1993, ISBN 0-8247-8729-3.

[23] Reppel, J. and Alwahabi, Z.A., *"A Uniaxial Gas Model of the Geometrical Dependence of Polarisation Spectroscopy"*, Journal of Physics D: Applied Physics, **34**, 2670-2678, 2001.

[24] Dieke, G.H. and Crosswhite, H.M., *"The Ultraviolet Bands of OH"*, J. Quant. Spectrosc. Radiat. Transfer, **2**, 97-199, 1962.

[25] *"Lambda Physik Dye Laser Scanmate Instruction Manual"*, Lambda Physik, 1993.

[26] Conversion calculation methods for the 1/2" and 1/4" flow rates are found in the *"Variable Area Flowmeter Handbook, Vol. 1, Basic Rotameter Principles"*, Fischer and Porter, Catalogue 10A1021 and *"Handbook. Tri-flat Variable-Area Flowmeters, Low flow rate indicators, Data on sizing and calibration prediction"*, Fischer and Porter, Handbook 10A9010 respectively.

[27] Zizak, G., Lanauze, J. and Winefordner, J.D., *"Cross-beam polarization in flames with a pulsed dye laser"*, Applied Optics, **25** (18), 3242-3246, 1986.

[28] Eckbreth, A.C., *"Laser Diagnostics for Combustion Temperature and Species"*, Abacus Press, Tunbridge Wells, Kent, UK, Eqn 7.36, p 326, 1988.

[29] Amiot, C., *"The infrared emissions spectrum of NO: Analysis of the $\Delta v = 3$ sequence up to $v = 22$"*, J. Mol. Spec., **94**, 150 (1982), *via* J.Luque and D.R. Crosley, *"LIFBASE: Database and Spectral Simulation Program (Version 1.5)"*, SRI International Report MP 99-009 (1999).

[30] Lofstedt, B., Fritzon, R. and Alden, M., *"Investigation of NO detection in flames by the use of polarization spectroscopy"*, Applied Optics, **35** (12), 2140-2146, 1996.

[31] Reppel, J. and Alwahabi, Z.A., *"Orthogonal Planar Laser Polarization Spectroscopy"*, Applied Optics, **41** (21), 4267-4272, 2002.

[32] Nyholm, K., *"Measurements of OH rotational temperatures in flames by using polarization spectroscopy"*, Optics Commun., **111**, 66-70, 1994.

[33] Ernst, W.E. and Torring, T., *"High Resolution Studies of Unstable Diatomics by Microwave-Optical Polarization Spectroscopy and Doppler Free Laser Polarization Spectroscopy"*, Appl. Phys. B, **28** (2-3), 222, 1982. (XIIth International Quantum Electronics Conference, 1982).

[34] Ernst, W.E., *"Doppler-free Polarization Spectroscopy of Diatomic Molecules in Flame Reactions"*, Optics. Commun., **44** (3), 159-164, 1983.

[35] Tong, W.G. and Yeung, E.S., *"Polarization Spectroscopy for Elemental Analysis at Trace Concentrations"*, Anal. Chem., **57**, 70-73, 1985.

[36] Lanauze, J.A. and Winefordner, J.D., *"Application of a Pulsed Dye Laser to Polarisation Spectroscopy for Elemental Analysis"*, Applied Spectroscopy, **40** (5), 709-711 1986.

[37] Demtroder, W., *"Laser Spectroscopy"*, Springer-Verlag, New York, 2nd Ed., p 508, 1982.

[38] Zizak, G., Lanauze, J. and Winefordner, J.D., *"Cross-beam polarization in flames with a pulsed dye laser"*, Applied Optics, **25** (18), 3242-3246, 1986.

[39] Kychakoff, G., Howe, R.D. and Hanson, R.K., *"Spatially Resolved Combustion Measurements using Cross-Beam Saturated Absorption Spectroscopy"*, Appl. Opt., **23**, 1303, 1984.

[40] K. Nyholm, R. Maier, C.G. Aminoff and M. Kaivola, *"Detection of OH in flames using polarization spectroscopy"*, Applied Optics, **32** (6), 919-924, 1993.

[41] Nyholm, K., Fritzon, R. and Alden, M.,*"Single-pulse two-dimensional temperature imaging in flames by degenerate four-wave mixing and polarization spectroscopy"*, Applied Phys. B, **59**, 37- 43, 1994.

[42] Survenev, A.A., Dreizler, A., Dreier, T. and Wolfrum, J., *"Polarisation-spectroscopic measurement and spectral simulation of OH ($A^2\Sigma$-$X^2\Pi$) and NH ($A^3\Pi$-$X^3\Sigma$) transitions in atmospheric pressure flames"*, Applied Physics B, **61**, 421-427, 1995.

[43] Nyholm, K., Fritzon, R., Georgiev, N. and Alden, M., *"Two-photon induced polarization spectroscopy applied to the detection of NH_3 and CO molecules in cold flows and flames."*, Optics Commun., **114**, 76-82, 1995.

[44] Nyholm, K., Kaivola, M. and Aminoff, C.G., *"Polarization spectroscopy applied to C_2 detection in a flame"*, Applied Phys. B, **60**, 5-10 (1995).

[45] Aminoff, C.G., Kaivola, M. and Nyholm, K., First Europ. Conf. on Quantum Electronics. Hanover, Germany, Digest of Technical Papers (University Hanover, Hanover, 1988), Paper MoCD4.

[46] Kaminski, C.F., Lofstedt, B., Fritzon, R. and Alden, M., *"Two-photon polarization spectroscopy and (2+3)-photon laser induced fluorescence of N_2"*, Optics Commun., **129**, 38-43, 1996.

[47] Lofstedt, B. and Alden, M., *"Simultaneous detection of OH and NO in a flame using polarization spectroscopy"*, Optics Commun., **124**, 251-257, 1996.

[48] Reichardt, T.A., Giancola, W.C. and Lucht, R.P., *"Experimental Investigation of saturated polarization spectroscopy for quantitative concentration measurements"*, Applied Optics, **39** (12), 2002-2008, 2000.

[49] Reichardt, T.A., Di Teodoro, F. and Farrow, R.L., *"Collisional dependence of polarization spectroscopy with a picosecond laser"*, J. Chem. Physics., **113** (6), 2263-2269, 2000.

[50] Kirby, B.J. and Hanson, R.K., *"Linear excitation schemes for IR PLIF imaging of CO and CO2."*, Applied Optics, **41**, 1190-1201, 2002.

[51] Kirby, B.J. and Hanson, R.K., *"Planar laser-induced fluorescence imaging of carbon monoxide using vibrational (infrared) transitions"*, Applied Physics B, **69** (5/6), 505-507, 1999.

[52] Roy, S., Lucht, R.P. and McIlroy, A., *"Mid-infrared polarization spectroscopy of carbon dioxide"*, Applied Physics B, Lasers and Optics, **75**, 875-882, 2002.

[53] Settersten, T.B., Farrow, R. L. and Gray, J.A., *"Coherent infra-red-ultraviolet double-resonance spectroscopy of CH_3"*, Chemical Physics Letters, **370**, 204-210, 2003.

[54] Settersten, T.B., Farrow, R. L. and Gray, J.A., *"Infra-red-ultraviolet double-resonance spectroscopy of OH in a flame"*, Chemical Physics Letters, **369**, 584-590, 2003.

[55] Bergano, N.S., Jaanimagi, P.A., Salour, M.M. and Bechtel, J.H., *"Picosecond Laser-Spectroscopy Measurement of Hydroxyl Fluorescence Lifetime in Flames"*, Optics Letters, **8**, 443-445, 1983.

[56] Tobai, J., Dreier, T. and Daily, J.W., *"Rotational level dependence of ground state recovery rates for OH $X^2\Pi$ (v" = 0) in atmospheric pressure flames using the picosecond saturating-pump degenerate four-wave mixing probe technique"*, J. Chem. Phys., **116** (10), 4030-4038, 2002.

[57] Daily, J.W. and Rothe, E.W., Applied Phys. B: Lasers Opt., **36**, 6129 (1997).

[58] Beaud, P., Radi, P.P., Franzke, D., Frey, H.-M., Mischler, B., Tzannis, A.-P. and Gerber, T., Appl. Opt., **37**, 3354 (1998).

Rahmann, U., Kreutner, W. and Kohse-Hoinghaus, K., Appl. Phys. B.: Lasers Opt., **69**, 61, 1999.

Lengel, R.K. and Crosley, D.R., J. Chem. Phys., **68**, 5309, 1978

[59] Roy, S., Lucht, R.P. and Reichardt, T.A., *"Polarisation spectroscopy using short-pulse laser: Theoretical analysis"*, J. Chem. Phys, **116** (2), 571-580, 2002.

[60] Clark Jones, R., *"A New Calculus for the Treatment of Optical Systems. I. Description and Discussion of the Calculus"*, J.O.S.A., **31**, 488-493, July 1941.

Hurwitz, Jr., H. and Clark Jones, R., *"A New Calculus for the Treatment of Optical Systems. II. Proof of Three General Equivalence Theorems"*, J.O.S.A., **31**, 493-499, July 1941.

Clark Jones, R., *"A New Calculus for the Treatment of Optical Systems. III. The Sohncke Theory of Optical Activity"*, J.O.S.A., **31**, 500-503, July 1941.

Clark Jones, R., *"A New Calculus for the Treatment of Optical Systems. IV."*, J.O.S.A., **32**, 486-493, August 1942.

Clark Jones, R., *"A New Calculus for the Treatment of Optical Systems. V. A more General Formulation, and Description of Another Calculus"*, J.O.S.A., **37** (2), 107-110, February 1947.

Clark Jones, R., *"A New Calculus for the Treatment of Optical Systems. VI. Experimental Determination of the Matrix"*, J.O.S.A., **37** (2), 110-112, February 1947.

Clark Jones, R., *"A New Calculus for the Treatment of Optical Systems. VI. Properties of the N-Matrices"*, J.O.S.A., **38** (8), 671-685, August 1948.

Clark Jones, R., Chapter 24: *"A Comedy of Errors"*, "*Polarized Light: Benchmark Papers in Optics /1*", Dowden, Hutchinson and Ross, Inc., distributed by Halsted Press, A division of John Wiley and Sons, Inc., pp 240-241, 1975.

[61] Oriel Corporation, *"Optics and Filters (Catalog). Vol. III"*, p. 12-5, Oriel Corporation, 1990, Stratford, CT, U.S.A.

Additional References from the Appendices

A1 Zare, R.N., *"Angular Momentum. Understanding Spatial Aspects in Chemistry and Physics."*, John Wiley and Sons, Inc., New York, 1st Ed., 1998.

A2 Cassels, J.M., *"Basic Quantum Mechanics"*, (p 58 and following). McGraw-Hill, London. New York. Sydney. Toronto. Mexico. Johannesburg. Panama. Singapore. 1970.

Chapter I: Introduction to Laser Polarisation Spectroscopy.

This chapter is a summary of the rate equation theory of Teets, Kowalski, Hill, Carlson and Hansch[1] which is the basis of the theories developed in later chapters of this thesis. This chapter is presented as an introduction to those not familiar with laser polarisation spectroscopy (LPS), for reference as to the basic theoretical method and as a source for tabulated results referred to in later sections. A minor correction to Teets *et al.* 's theory is included for the case of shared pump and probe beam transitions. The signal dependence on rotational quantum number is expressed in terms of a single $Z_{J,J',J''}$ function to simplify interpretation.

Polarisation spectroscopy is based on detection of polarisation changes in a linearly polarised probe laser beam due to the dichroism[a] and birefringence[b] induced by a strong, polarised pump beam. It is a coherent spectroscopic technique, with information on the target species in the pump/probe intersection volume being carried in the polarisation state of the probe beam.

The polarisation change in the probe beam is due to its passage through a region of induced dichroism and birefringence. In polarisation spectroscopy, a strong, polarised pump beam is used to induce dichroism and birefringence in a target volume. The polarisation changes in the linearly polarised probe beam are small, but detection is enhanced by placing crossed polarisers, enclosing the birefringent and dichroic region, in the probe beam path to remove the large fraction of the beam with undisturbed polarisation. The collected signal is the residual probe beam intensity which

[a] Dichroism: Selective absorption of one of two orthogonal polarisation components of incident electromagnetic radiation. If the characteristic modes of polarisation of propagation in the medium are linearly polarised, selective absorption of one linearly polarised state is termed is linear dichroism. Similarly, for characteristic propagation of orthogonal circularly polarised states, the required term is circular dichroism.

[b] Birefringence: A substance is birefringent if it exhibits different refractive indices for two orthogonal polarisation components of incident radiation. As for dichroism, the birefringence may be linear or circular for the cases of linearly or circularly polarised characteristic modes of propagation in the medium respectively.

is then a function of the number density of the target species in that region and the pump and probe beam intensities.

This spectroscopic method was first presented by Wieman and Hansch in 1976[2]. A linearly polarised probe beam is passed through an absorbing gas. Nearly crossed polarisers in the probe beam path enclose the gas volume. A counterpropagating monochromatic pump beam induces dichroism and birefringence in the absorbing gas, in turn producing a small ellipticity in the polarisation of the linearly polarised probe beam simultaneously transmitted through the gas. The optical anisotropy of the gas medium is detected as a function of the change in polarisation state of the probe beam. Doppler-free spectra are produced by a counter-propagating beam geometry, due to the requirement that both beams interact with the same velocity subset of the target species; those with near zero velocity parallel to the pump/probe axis of propagation. As a spectroscopic technique, polarisation spectroscopy is advantageous in two respects: a sub-Doppler line width for counter-propagating pump/probe beam geometries and improved identification of P, Q and R transitions via strongly P-Q-R selective transition probabilities which are selectable via the pump beam polarisation.

For spectroscopic experiments, the pump and probe beams are focussed into a single point intersection volume. Polarisation spectroscopy was first applied to two-dimensional imaging by Nyholm, Fritzon and Alden[3] in 1993. As the experimental priority was not spectroscopic, Nyholm used a co-propagating pump/probe geometry. The beams intersected at angles of 15° and 30°. The pump beam was formed into a thin sheet, while the probe beam was maintained with a circular beam profile. The intersection volume of the planar pump beam and cylindrical probe beam is elliptical in cross-section, with thickness corresponding to that of the pump sheet. Information on the distribution of the target species within the intersection volume can be inferred from polarisation changes in the circular cross-section of the probe beam. Figure 1 below shows a plane view of the horizontal intersection of a pump beam and a probe beam. The relationship between the collected image and the intersection volume can be understood from the figure. The red shaded region in the intersection volume of pump and probe beams represents the a region of concentration of the target species. The equivalent region of detected signal in the collected image is also shown.

Nyholm, Fritzon and Alden[3] were motivated by a desire to image intermediate combustion species, specifically the hydroxyl radical (OH) which indicates the hot flame zone[4]. Planar Laser Induced Fluorescence (PLIF), where the fluorescence induced by absorption from a thin laser sheet tuned to a transition of the target species is collected is collected by an intensified imaging system orthogonal to the laser sheet, is the predominant spectroscopic method for imaging intermediate flame species. The technique is species specific with relatively strong signal. However, both the signal and the flame emissions reduce as the square of the distance from the flame, making it

difficult to increase the signal to background ratio it temporal and spectroscopic filtering is not sufficient.

Coherent laser spectroscopic techniques where the signal is carried on a coherent laser beam have the advantage in this regime of allowing a strong flame emission background to be minimised by detecting the signal at a large distance from the flame. The signal-to-noise ratio then increases as the square of the distance from the flame. The limitation on the signal-to-noise ratio is defined by the maximum signal level and the detection limit of the equipment. It is, therefore, appropriate to favour technique regimes with high signal.

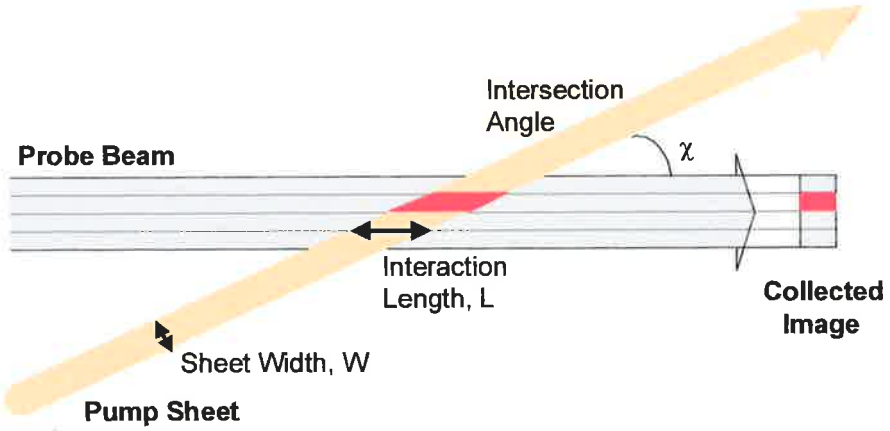

Figure 1: A plane view of the horizontal intersection of a pump beam and a probe beam at the angle, χ.

Nyholm, Fritzon and Alden noted experimentally a $\cot^2(\chi)$ dependence of signal on the pump/probe beam intersection angle, χ, in the case of perfectly crossed polarisers with a pump beam polarisation lying in the plane of intersection of the two beams. This angular dependence was attributed to *"changes in the probe volume and the projection of the pump beam polarization on the probe beam polarization"* [3]. The rapid $\cot^2(\chi)$ reduction in signal with increasing beam intersection angle to zero signal for orthogonal beam intersection implied that polarisation spectroscopy was best implemented at small beam intersection angles to maximise signal. However, imaging at small beam intersection angles results in reduced image resolution and is potentially susceptible to strong beam-steering effects in combustion due to thermal refractive index gradients.

Spatial resolution is maximal for orthogonal beam intersection. However, the experimental results of Nyholm, Fritzon and Alden suggested that the orthogonal signal was zero. The theory of Lavrinenko, Gancheryonok and Dreier[5] first suggested non-zero signal could be obtained in an

orthogonal beam intersection geometry, allowing a maximum spatial resolution favourable to imaging applications. The signal is typically much less than in near-collinear geometries. However, for strong signal, the maximal spatial resolution available for near-orthogonal beam intersection is preferable for imaging applications.

A new theory presented (and supported by experimental results) in this thesis (Chapters II to V) describes the polarisation geometries which allow non-zero signal for orthogonal beam intersection and extend the range of geometries suitable for application of polarisation spectroscopy. Thus, the first part of this thesis (Chapters I to V) concentrates on the geometrical dependence of LPS to support its application as an imaging technique. Chapters VI and VII focus on the application of LPS to imaging of combustion intermediate species, specifically of the OH radical. In conclusion, Chapters VIII and IX summarise the geometric dependence of LPS derived in earlier chapters in a Jones matrix formalism applicable to modelling of realistic combustion experiments in the case of imperfect optical elements.

Teets, Kowalski, Hill, Carlson and Hansch described the LPS signal by a relatively simple rate equation theory based on a low pressure, collision-free environment and either a linear or saturated regime of optical pumping for both linearly and circularly polarised pump beams. This theoretical description is a comprehensive extension of the third-order perturbation theory of Wieman and Hansch. Despite the assumption of a collision-free environment, the theory of Teets, Kowalski, Hill, Carlson and Hansch together with the geometrical factor noted by Nyholm, Fritzon and Alden, is a strong base for development of more complex descriptions of polarisation spectroscopy and is repeated as an introduction to the theories developed in this thesis. One correction to the theory of Teets *et al.* for the case of shared pump and probe beams in the linear regime of optical pumping is included. The correction is indicated throughout by blue text. Additional terms defined to combine the J-dependence terms in the signal strength and to clearly define vibrational and electronic transition probabilities as distinct from rotational transition probabilities for pump and probe beam transitions are also shown in blue. Blue lines on graphs **do not** indicate corrections.

The theory of polarisation spectroscopy consists of two independent sections.

(i) The optics of the system may be modelled geometrically[1 2 5 6 7 8], assuming a region of pump induced dichroism, $\Delta\alpha$, and birefringence, Δn.

(ii) The second section involves modelling of the target species Zeeman state populations in order to calculate the induced birefringence and dichroism. Many publications, both spectroscopic[9 10 11] and those investigating LPS as a combustion diagnostic technique[3 12 13 14 15] are based on the rate equation theory of Teets *et al.* Recently, quantum mechanical approaches[16 17] have been applied in the literature to model the Zeeman state populations. Relatively few papers consider complex combustion systems in modelling of the target species[18 19 20], however, Reichardt and Lucht[21] should be noted especially for considering realistic regimes of collision processes in combustion in a density matrix calculation of saturation and lineshape.

The level of complexity required of the population models is dependent on the proposed experimental conditions. Pulsed, low pressure cell experiments where collision rates are negligible require the least complex population descriptions. At high pressures and for cw pumping, the effects of collisions become increasingly more important to realistic modelling. Population modelling is highly dependent on experimental conditions and is not considered in this thesis. The theme of this thesis is polarisation spectroscopy imaging in combustion. Modelling has been directed towards understanding the geometric dependence of LPS due to its relevance to imaging resolution and signal strength.

This chapter summarises the basic theory of Teets, Kowalski, Hill, Carlson and Hansch with respect to both the geometrical optics and rate equation population model to demonstrate the separability of the two theoretical components.

The Theory of Teets, Kowalski, Hill, Carlson and Hansch

Teets, Kowalski, Hill, Carlson and Hansch use a rate equation model, assuming pumping in the linear saturation regime, to derive expressions for the time dependence of the Zeeman state populations of the target species. The induced dichroism is calculated as the sum of the dichroism due to each pair of Zeeman states linked by the pump beam transition. The major assumption is that the collision rates are small enough that the populations of each pair of states may be considered independently. This effectively limits the application of this model to low collision rate experiments. However, the logic of the theory is applicable to more complex modelling of the target populations which include strong collisional effects.

Teets, Kowalski, Hill, Carlson and Hansch follow the basic geometrical method of Wieman and Hansch. In derivation, Teets *et al.* assume that the population saturation due to the pump beam is weak and may be described in the linear approximation regime. The probe beam is assumed to not perturb the Zeeman state populations significantly in comparison to the pump beam. The theory of Teets *et al.* based on these assumptions is discussed in the remainder of this chapter.

Teets, Kowalski, Hill, Carlson and Hansch described the fractional transmission of the probe beam electric field through crossed polarisers in terms of the small, optically induced birefringence, Δn, and dichroism, $\Delta\alpha$. For a circularly polarised pump beam, the induced dichroism and birefringence relate to orthogonal circularly polarised components. For a linearly polarised pump beam, the anisotropic optical behaviour relates to orthogonal linearly polarised components. In each case, one of the orthogonal probe beam states corresponds to the polarisation state of the pump beam. The other is termed the orthogonal polarisation component.

The unperturbed refractive index and absorption coefficients are denoted by n and α respectively. The induced dichroism, $\Delta\alpha_{circ}$, experienced by the probe beam for a circularly polarised pump beam, is defined as

$$\Delta\alpha_{circ} = \alpha^{+} - \alpha^{-} \qquad \text{Equation 1}$$

where α^{+} and α^{-} are the absorption coefficients for right and left circularly polarised components respectively. The corresponding birefringence, Δn_{circ}, for a circularly polarised pump beam, is

$$\Delta n_{circ} = n^{+} - n^{-} \qquad \text{Equation 2}$$

where n^{+} and n^{-} are similarly the refractive indices for right and left circularly polarised probe beam components.

For a linearly polarised pump beam, the induced dichroism, $\Delta\alpha_{lin}$, and birefringence, Δn_{lin}, are given by

$$\Delta\alpha_{lin} = \alpha_z - \alpha_x \qquad \text{Equation 3}$$

and

$$\Delta n_{lin} = n_z - n_x \qquad \text{Equation 4}$$

where α_z and α_x are the absorption coefficients for linearly polarised probe beam components parallel and perpendicular to the Z-aligned pump polarisation. In Teets *et al.*'s derivation, the counter-propagating pump and probe beams travel parallel to the Y-axis. The equivalent refractive index components are n_z and n_x.

For a small angle of deviation, θ, from perfectly crossed probe beam polarisers[c], Teets, Kowalski, Hill, Carlson and Hansch describe the electric field strength of the probe beam transmitted through the probe beam analyser as

$$E_{\substack{probe\_transmitted \\ circ\_pump}} = E_0 \cdot (\theta + ib + \Delta n_{circ} \cdot \frac{\omega L}{2c} + i\Delta\alpha_{circ} \frac{L}{4}) \qquad \text{Equation 5}$$

for a circularly polarised pump beam and

$$E_{\substack{probe\_transmitted \\ linear\_pump}} = E_0 \cdot (\theta + ib + \Delta\alpha_{lin} \cdot \frac{L}{4} - i\Delta n_{lin} \frac{\omega L}{2c}) \qquad \text{Equation 6}$$

for a linearly polarised pump beam, where

E_0 is the probe beam electric field strength incident on the input polariser,

$E_{\substack{probe\_transmitted \\ circ\_pump}}$ and $E_{\substack{probe\_transmitted \\ linear\_pump}}$ are the probe beam electric field strengths transmitted through the nearly crossed polarisers for circularly and linearly polarised probe beams respectively,

θ is the uncrossing angle of the probe beam polarisers (the angle of deviation from perfect crossing of the polarisers),

b represents the birefringence of optical elements between the probe beam polarisers,

L is the interaction length of pump and probe beams measured along the probe beam path,

ω is the angular frequency of the probe beam, and

c is the speed of light.

Teets *et al.* assume that the uncrossing angle, θ, the optical birefringent term, b, the induced dichroism multiplied by the interaction distance, $\Delta\alpha L$, and the induced birefringence multiplied by the interaction distance, ΔnL, are of the same order of magnitude and very much less than unity.

The induced dichroism and birefringence are related according to the Kramers-Kronig dispersion relations. Defining the relative detuning, x, of the probe beam frequency, ω, from linecentre, ω_0, for the probe beam transition from the lower state (J,M) to an upper state (J",M") as

$$x = \frac{\omega - \omega_0}{\gamma} \qquad \text{Equation 7}$$

where

x is the relative detuning of the probe beam from linecentre for the transition (J,M) to (J",M"),

γ is the linewidth of a Lorentzian dichroism, $\Delta\alpha$,

ω is the angular frequency of the probe beam, and

ω_0 is the linecentre angular frequency,

[c] Teets *et al* use the direction convention that the angle between primary probe beam polariser and analyser is $\pi/2 - \theta$.

Teets, Kowalski, Hill, Carlson and Hansch introduce a Lorentzian induced dichroism dependence

$$\Delta\alpha = \frac{\Delta\alpha_0}{1+x^2} \qquad \text{Equation 8}$$

where $\Delta\alpha$ is the induced dichroism at the probe beam angular frequency and $\Delta\alpha_0$ is the linecentre induced dichroism for the probe beam.

The Kramers-Kronig relations then allow the induced birefringence, Δn, at detuning, x, experienced by the probe beam to be defined in terms of the linecentre dichroism, $\Delta\alpha_0$, as

$$\Delta n = -\frac{1}{2}\cdot\Delta\alpha_0\cdot\frac{c}{\omega_0}\cdot\frac{x}{1+x^2} \qquad \text{Equation 9}$$

where

Δn is the induced birefringence at the probe beam frequency, and

c is the speed of light.

The intensity of the transmitted probe beam is obtained by substitution of equations [8] and [9] into equations [5] and [6] for the transmitted electric field strength. Teets, Kowalski, Hill, Carlson and Hansch follow Wieman and Hansch to introduce the additional term, ξ, to represent the finite extinction ratio of the probe beam polarisers. The intensity of the transmitted probe beam is given by

$$I_{\substack{probe\_transmitted\\circ\_pump}} = I_0\left[\xi+\theta^2+b^2-\frac{1}{2}\theta\cdot\Delta\alpha_{0\_circ}L\cdot\frac{x}{1+x^2}+\frac{1}{2}b\cdot\Delta\alpha_{0\_circ}L\cdot\frac{1}{1+x^2}+\frac{1}{16}\left(\Delta\alpha_{0\_circ}L\right)^2\cdot\frac{1}{1+x^2}\right]$$

Equation 10

for a circularly polarised pump beam and

$$I_{\substack{probe\_transmitted\\linear\_pump}} = I_0\left[\xi+\theta^2+b^2+\frac{1}{2}\theta\cdot\Delta\alpha_{0\_lin}L\cdot\frac{1}{1+x^2}+\frac{1}{2}b\cdot\Delta\alpha_{0\_lin}L\cdot\frac{x}{1+x^2}+\frac{1}{16}\left(\Delta\alpha_{0\_lin}L\right)^2\cdot\frac{1}{1+x^2}\right]$$

Equation 11

for a linearly polarised pump beam, where

ξ represents the finite extinction ratio of the probe beam polarisers,

I_0 is the probe beam intensity incident on the input polariser, and

$I_{\substack{probe\_transmitted\\circ\_pump}}$ and $I_{\substack{probe\_transmitted\\linear\_pump}}$ are the probe beam intensities transmitted through the nearly crossed polarisers for circularly and linearly polarised pump beams respectively.

Equations [10] and [11] contain Lorentzian and dispersive functions of x (the relative detuning from linecentre) superimposed onto a constant background. The Lorentzian,

$$L(x) = \frac{1}{1+x^2}$$ Equation 12

and dispersive

$$D(x) = \frac{x}{1+x^2}$$ Equation 13

lineshapes are plotted in Figure 2 and are of order unity. Both the extinction background, ξ, and the coefficients of the detuning terms in equations [10] and [11] are assumed to be small and of the same order of magnitude in order to be adequately described by a first order expansion in each term.

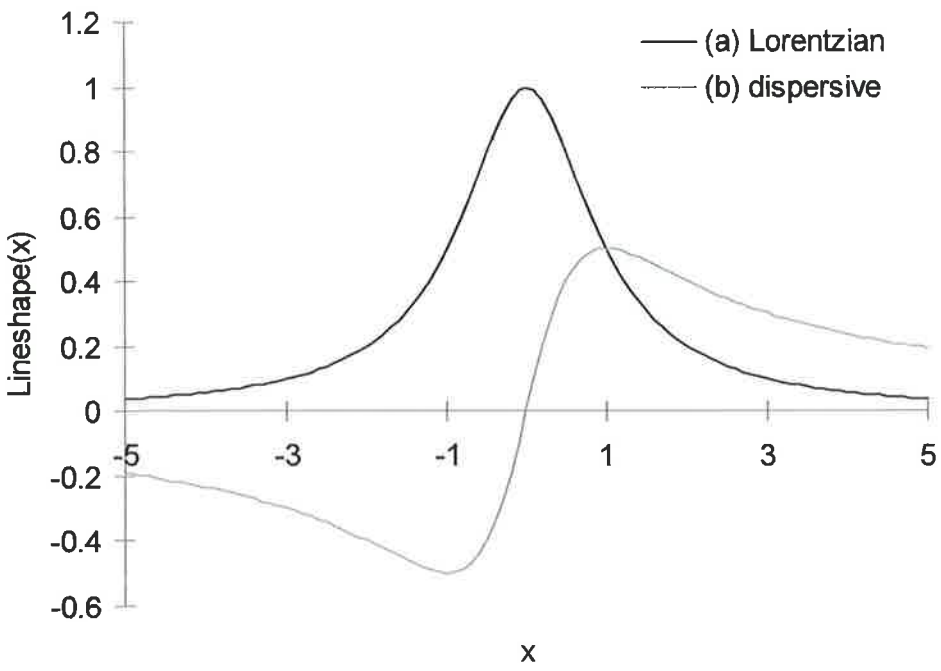

Figure 2: Lorentzian and dispersive lineshapes plotted against the relative detuning, x.

The equations describing the transmitted intensity may be simplified by choosing an experimental configuration which eliminates one of the following coefficients; the non-zero polariser uncrossing angle, θ, the interpolariser birefringent optics term, b, or the detuning, x, by pumping at angular frequency linecentre, ω_0.

For perfectly crossed polarisers, the polarisation signal strength equations reduce to

$$I_{\substack{probe\_transmitted \\ circ\_pump \\ crossed\_polarisers}} = I_0\left[\xi + b^2 + \frac{1}{2}b\cdot\Delta\alpha_{0\_circ}L\cdot\frac{1}{1+x^2} + \frac{1}{16}\left(\Delta\alpha_{0\_circ}L\right)^2\cdot\frac{1}{1+x^2}\right] \qquad \text{Equation 14}$$

for a circularly polarised pump beam and

$$I_{\substack{probe\_transmitted \\ linear\_pump \\ crossed\_polarisers}} = I_0\left[\xi + b^2 + \frac{1}{2}b\cdot\Delta\alpha_{0\_lin}L\cdot\frac{x}{1+x^2} + \frac{1}{16}\left(\Delta\alpha_{0\_lin}L\right)^2\cdot\frac{1}{1+x^2}\right] \qquad \text{Equation 15}$$

for a linearly polarised pump beam.

In the case of unconfined combustion, there is no requirement for windows or other optical elements between the crossed probe beam polarisers. In this case, the birefringent terms in equations [14] and [15] become zero and the polarisation signal for either of the two pump polarisations is given by the following equation.

$$I_{\substack{probe\_transmitted \\ circ/linear\_pump \\ crossed\_polarisers \\ unconfined\_combustion}} = I_0\left[\xi + \frac{1}{16}\left(\Delta\alpha_0 L\right)^2\cdot\frac{1}{1+x^2}\right] \qquad \text{Equation 16}$$

where once again $\Delta\alpha_0$ represents the linecentre induced dichroism. The transmitted probe beam intensity fraction takes the form of a Lorentzian lineshape multiplied by a term proportional to the square of the linecentre induced dichroism, $\Delta\alpha_0$, superimposed onto a background due to the finite extinction ratio of the probe beam polarisers, ξ.

The derivation of equations [10], [11] and [14]-[16] above is based on the optical parameters of dichroism and birefringence and is independent of the population descriptions of the pumped and probe transitions. Teets, Kowalski, Hill, Carlson and Hansch's derivation continues by describing the induced dichroism as a function of the Zeeman state populations of the probed transitions, which may be modelled independently of the above optical parameter dependence. Teets *et al.* derived expressions for the LPS signal applicable to a primarily collision-free environment. Recently, Reichardt and Lucht[21] have described density matrix modelling of more complex environments where collisional effects are important. However the complexity of the modelling required to match experimental conditions supports the inclusion below of the simpler theory of Teets *et al.* as a general indicator of the behaviour of polarisation spectroscopy.

The absorption coefficient, $\alpha^{i_{probe}}_{J,J'',M,M''}$, due to the *probed transition* from the *lower Zeeman state*, (J, M), to the *upper Zeeman state*, (J", M"), is given as the product of the number density of the population of the lower state and the cross-section of the probe beam transition according to equation [17]. The absorption coefficient is dependent on the polarisation state of the probe beam, i_{probe}. In equation [17], $C_{J,J''}$ is the non-rotational (e.g. electronic/vibrational) component of the absorption cross-section for the probe transition (J,M) to (J",M"), stated here explicitly for later convenience.

$$\alpha^{i_{probe}}_{J,J'',M,M''} = N_{J,M} \cdot \sigma^{i_{probe}}_{J,J'',M,M''} \cdot C_{JJ''} \qquad \text{Equation 17}$$

where

$\alpha^{i_{probe}}_{J,J'',M,M''}$ is the absorption coefficient for the probe transition (J,M) to (J",M"),

N_{JM} is the number density of the lower state (J,M),

$\sigma^{i_{probe}}_{J,J'',M,M''}$ is the rotational/Zeeman component of the absorption cross-section for the probe transition (J,M) to (J",M"),

$C_{J,J''}$ is the non-rotational (e.g. electronic/vibrational) component of the absorption cross-section for the probe transition (J,M) to (J",M"), and

i_{probe} represents the polarisation state of the probe beam.

The total absorption coefficient, $\alpha^{i_{probe}}_{J,J''}$, for the probed transition from the lower state, J, to the upper state, J", is obtained by summation over the absorption coefficients for each of the Zeeman states (J,M) of the lower level.

$$\alpha^{i_{probe}}_{J,J''} = \sum_{M} \left(N_{J,M} \cdot \sigma^{i_{probe}}_{J,J'',M,M''} \cdot C_{JJ''} \right) \qquad \text{Equation 18}$$

The corresponding induced dichroism, $\Delta\alpha^{i,i'}_{J,J''}$, for the probed transition is defined as the difference in absorption coefficients for the two orthogonal polarisation states, i and i', of the probe beam and is written

$$\Delta\alpha^{i,i'}_{J,J''} = \sum_{M} \left(N_{J,M} \cdot (\sigma^{i}_{J,J'',M,M''} - \sigma^{i'}_{J,J'',M,M''}) \cdot C_{JJ''} \right) \qquad \text{Equation 19}$$

Note that unless the factor, $N_{J,M}$, in equation [19] is dependent on the M quantum number, the induced dichroism, $\Delta\alpha^{i,i'}_{J,J''}$, will be zero.

Teets, Kowalski, Hill, Carlson and Hansch assume a target species population optically pumped in the linear regime with an initially unpopulated probe transition upper state. The pump and probe

transitions share a common lower state. Collisional effects are assumed to be negligible. The pumped population, $N_{J,M}$, in the lower Zeeman state, (J,M), is then a linear function of the pump beam intensity, I_0 and, for a pulsed laser system, may be written as

$$N_{J,M} = \frac{N_J}{2J+1} \cdot (1 - \frac{\sigma^{i_{pump}}_{J,J',M,M'} \cdot C_{J,J'}}{\hbar\omega_{pump}} I_{pump} t) \qquad \text{Equation 20}$$

where

N_M is the pumped population of the lower state, (J,M),

$N_J / (2J+1)$ is the equilibrium Boltzmann population of each of the Zeeman states (J,M),

$\sigma^{i_{pump}}_{J,J',M,M'}$ is the rotational/Zeeman component of the absorption cross-section for the *pump* beam transition from the *lower* state,(J,M), to the *upper* state, (J',M'),

$C_{J,J'}$ is the non-rotational component of the absorption cross-section for the pump transition (J,M) to (J',M'),

$\hbar$ is Planck's constant divided by 2π,

ω_{pump} is the angular frequency of the pump radiation,

i_{pump} is the polarisation state of the pump beam, and

t is the laser pulse length.

Substitution of equation [20] into equation [19] for the induced dichroism leads to Teets, Kowalski, Hill, Carlson and Hansch 's expression

$$\Delta\alpha^{i,i'}_{J,J''} = -N_J \cdot \sigma_{J,J'} \cdot \sigma_{J,J''} \cdot \frac{I_{pump} t}{\hbar\omega_{pump}} \cdot \zeta_{J,J',J''} \qquad \text{Equation 21}$$

where Teets *et al.* have defined the factors, $\sigma_{J,J'}$ and $\sigma_{J,J''}$, as total absorption cross-sections for the rotational pump and probe transitions respectively divided by the factor 2J +1, i.e.

$$\sigma_{J,J'} = \frac{1}{2J+1} \sum_M \sigma^{i_{pump}}_{J,J',M,M'} \cdot C_{J,J'} \qquad \text{Equation 22}$$

and

$$\sigma_{J,J''} = \frac{1}{2J+1} \sum_M \sigma^{i_{probe}}_{J,J'',M,M''} \cdot C_{J,J''} \qquad \text{Equation 23}$$

The $\sigma_{J,J'}$ and $\sigma_{J,J''}$ factors, which are summarised in Table 1, are independent of the polarisation state either pump or probe beam and also of the Zeeman quantum numbers, while retaining their electronic and vibrational components. The J dependent component of the summations represents

the ratio of the degeneracies of the upper and lower states divided by the factor 3 and quickly approaches the constant value of $^1/_3$ as J becomes large (Figure 3). Teets, Kowalski, Hill, Carlson and Hansch note that the inverse of the cross-section summation, $\sigma_{J,J'}$, is a measure of the ease of saturation of the pump beam transition for the linear approximation of optical pumping considered above. The J dependence of this factor is shown in Figure 4. Once again assuming pumping the in the linear regime, Q transitions demonstrate a constant level of saturability for different J states. R transitions are more easily saturated at low J.

$\Delta J = 1$ R transition	$\sigma_{J,J+1} = \frac{1}{3} \cdot \frac{2J+3}{2J+1} \cdot C_{J,J+1}$	
$\Delta J = 0$ Q transition	$\sigma_{J,J} = \frac{1}{3} \cdot C_{J,J}$ $= 0$	if $J > 0$ if $J = 0$
$\Delta J = -1$ P transition	$\sigma_{J,J-1} = \frac{1}{3} \cdot \frac{2J-1}{2J+1} \cdot C_{J,J-1}$ $= 0$	if $J > \frac{1}{2}$ if $J = 0, \frac{1}{2}$

Table 1: Absorption cross-section summations[d] over the Zeeman sub-levels of the lower state, J.

[d] The equations defined in this chapter are subject to the condition that the proposed transition is allowed. The rotational cross-sections for a transition are given by the squares of associated Clebsch-Gordon coefficients. The Clebsch-Gordon coefficients are defined to be zero if the vector condition on the sum, j, of two component angular momenta, j_1 and j_2,

$$|j_1 + j_2| > j > |j_1 - j_2| \qquad \text{Equation a.1}$$

is not met. In the case of absorption or emission of a photon, where $j_2 = 1$, this requires that the Clebsch-Gordon coefficients for P ($\Delta J = -1$) and Q ($\Delta J = 0$) transitions are zero for $J = 0$, and P ($\Delta J = -1$) transitions for $J = ½$. This condition governs all equations in this chapter. The tabulated and graphical representations which follow explicitly show the conditional requirement on the rotational transitions.

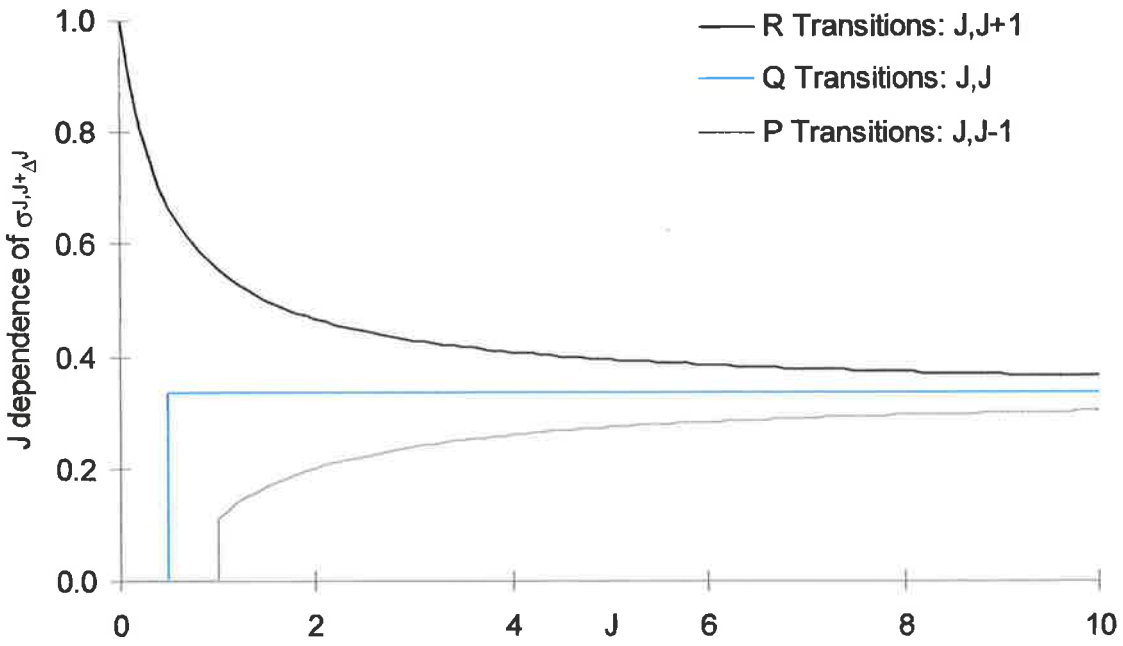

Figure 3: J dependence of the absorption cross-section summations, $\sigma_{J,J+\Delta J}$. The sudden drop to zero values at low J indicates disallowed transitions.

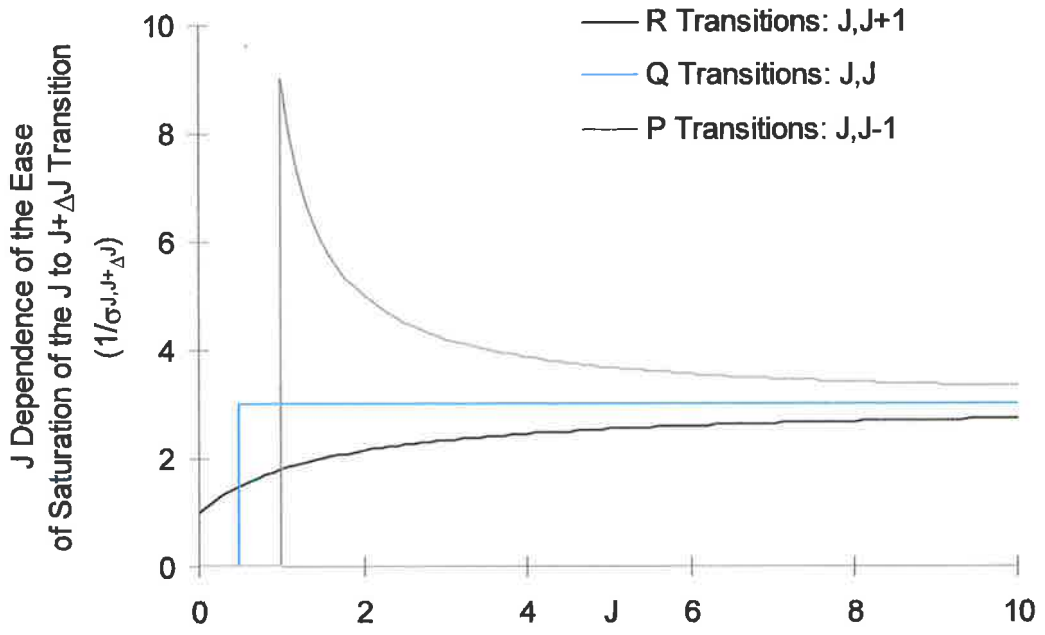

Figure 4: J dependence of the ease of saturation of the J to J + ΔJ transitions ($1/\sigma_{J,J+\Delta J}$). The sudden drop to zero values at low J indicates disallowed transitions.

The factor, $\zeta_{J,J',J''}$, of equation [21] is given by the expression

$$\zeta_{J,J',J''} = \frac{\frac{1}{2J+1} \cdot \sum_{M} \sigma^{i_{pump}}_{J,J',M,M'} \cdot C_{JJ'} \cdot (\sigma^{i}_{J,J'',M,M''} - \sigma^{i'}_{J,J'',M,M''}) \cdot C_{JJ''}}{\sigma_{J,J'} \cdot \sigma_{J,J''}}$$

Equation 24

The fractional representation of this factor allows cancellation of electronic and vibrational components of the absorption cross-section, $C_{JJ'}$ and $C_{JJ''}$, given the definitions of the $\sigma_{J,J'}$ and $\sigma_{J,J''}$ factors in equations [22] and [23]. The factor, $\zeta_{J,J',J''}$, is then a function of only the rotational quantum numbers for the pump and probe transitions.

$$\zeta_{J,J',J''} = (2J+1) \cdot \frac{\sum_{M} \sigma^{i_{pump}}_{J,J',M,M'} \cdot (\sigma^{i}_{J,J'',M,M''} - \sigma^{i'}_{J,J'',M,M''})}{\sum_{M} \sigma^{i_{pump}}_{J,J',M,M'} \cdot \sum_{M} \sigma^{i_{probe}}_{J,J'',M,M''}}$$

Equation 25

The derivation above follows the derivation of Teets, Kowalski, Hill, Carlson and Hansch in the linear pumping regime with the exception (included here for completeness and application to combustion diagnostics) of the explicit statement of the electronic and vibrational components of the absorption cross-section.

The $\zeta_{J,J',J''}$ factors were determined analytically by Teets, Kowalski, Hill, Carlson and Hansch. For reference, Tables 2 and 3 tabulate the J dependence of the $\zeta_{J,J',J''}$ factors for circularly and linearly polarised pump beams in the linear regime of optical pumping respectively. Tables 4 and 5 represent the limiting values of the $\zeta_{J,J',J''}$ factors at large J. Due to their similarity to factors required in subsequent chapters, the derivation of these factors is included in Appendix I. Figures 5 and 6 show the J dependence of the $\zeta_{J,J',J''}$ factors for a circularly polarised pump beam, and for a linearly polarised pump beam respectively. In each case, the three graphs present the $\zeta_{J,J',J''}$ factors for the (a) R, (b) Q and (c) P pump beam transitions.

	J" = J +1	J" = J	J" = J -1
J' = J +1	$= \frac{3J}{2(J+1)}$ $\forall J$	$= -\frac{3}{2(J+1)}$ if $J > 0$ $= 0$ if $J = 0$	$= -\frac{3}{2}$ if $J > ½$ $= 0$ if $J = 0, ½$
J' = J	$= -\frac{3}{2(J+1)}$ if $J > 0$ $= 0$ if $J = 0$	$= \frac{3}{2J(J+1)}$ if $J > 0$ $= 0$ if $J = 0$	$= \frac{3}{2J}$ if $J > ½$ $= 0$ if $J = 0, ½$
J' = J-1	$= -\frac{3}{2}$ if $J > ½$ $= 0$ if $J = 0, ½$	$= \frac{3}{2J}$ if $J > ½$ $= 0$ if $J = 0, ½$	$= \frac{3(J+1)}{2J}$ if $J > ½$ $= 0$ if $J = 0, ½$

Table 2: $\zeta_{J,J',J''}$ factors for a circularly polarised pump beam in the linear regime of optical pumping.

	J" = J +1	J" = J	J" = J -1
J' = J+1	$= \frac{3J(2J-1)}{10(J+1)(2J+3)}$ $\forall J$	$= -\frac{3(2J-1)}{10(J+1)}$ if $J > 0$ $= 0$ if $J = 0$	$= \frac{3}{10}$ if $J > ½$ $= 0$ if $J = 0, ½$
J' = J	$= -\frac{3(2J-1)}{10(J+1)}$ if $J > 0$ $= 0$ if $J = 0$	$= \frac{3(2J+3)(2J-1)}{10J(J+1)}$ if $J > 0$ $= 0$ if $J = 0$	$= -\frac{3(2J+3)}{10J}$ if $J > ½$ $= 0$ if $J = 0, ½$
J' = J-1	$= \frac{3}{10}$ if $J > ½$ $= 0$ if $J = 0, ½$	$= -\frac{3(2J+3)}{10J}$ if $J > ½$ $= 0$ if $J = 0, ½$	$= \frac{3(J+1)(2J+3)}{10J(2J-1)}$ if $J > ½$ $= 0$ if $J = 0, ½$

Table 3: $\zeta_{J,J',J''}$ factors for a linearly polarised pump beam in the linear regime of optical pumping.

	J" = J +1	J" = J	J" = J -1
J' = J +1	⅗	0	−⅗
J' = J	0	0	0
J' = J-1	−⅗	0	⅗

Table 4: Limiting values of the $\zeta_{J,J',J''}$ factors in the linear regime of optical pumping for a circularly polarised pump beam as $J \to \infty$.

	J" = J +1	J" = J	J" = J -1
J' = J +1	3/10	−6/10	3/10
J' = J	−6/10	12/10	−6/10
J' = J-1	3/10	−6/10	3/10

Table 5: Limiting values of the $\zeta_{J,J',J''}$ factors in the linear regime of optical pumping for a linearly polarised pump beam as $J \to \infty$.

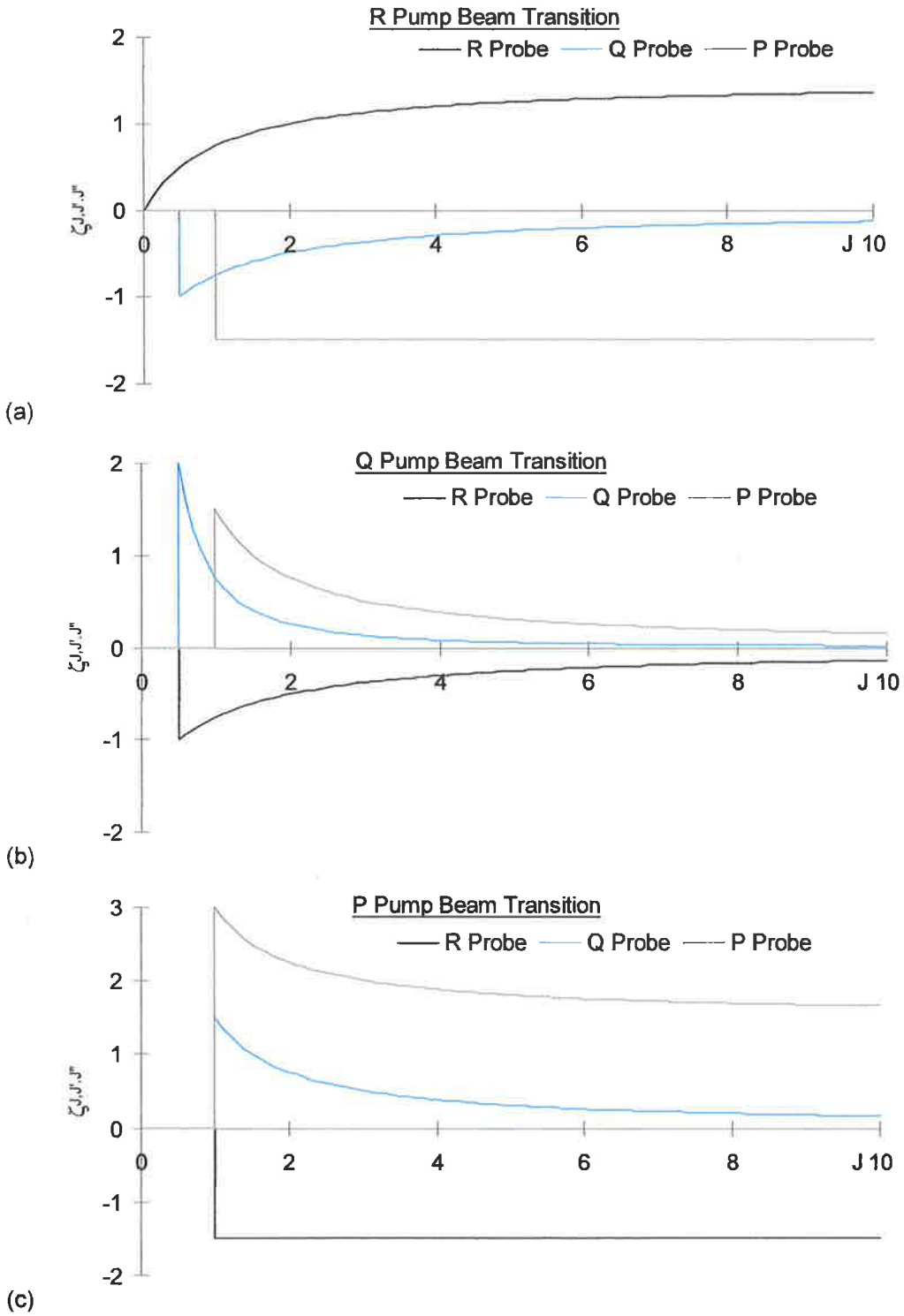

Figure 5: J dependence of the $\zeta_{J,J',J''}$ factors in the linear regime of optical pumping for a circularly polarised pump beam. The three graphs present the $\zeta_{J,J',J''}$ factors for the (a) R, (b) Q and (c) P pump beam transitions. The probe beam transitions are indicated on each graph.

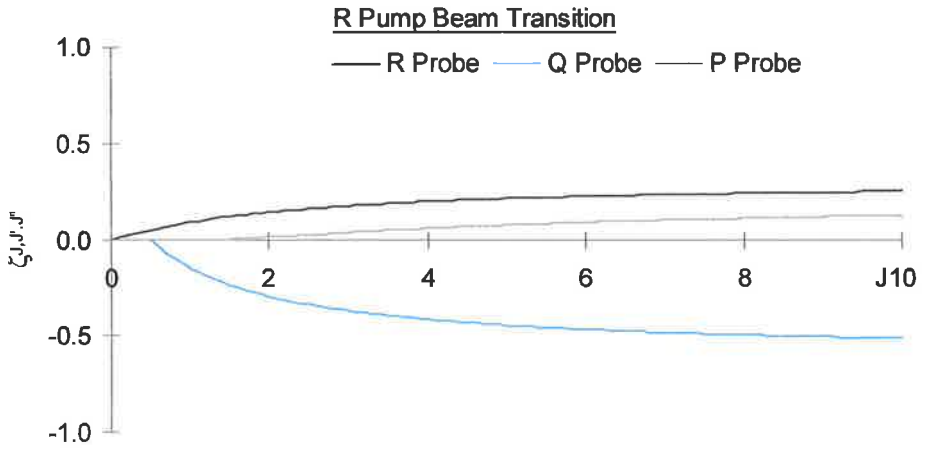

(a)

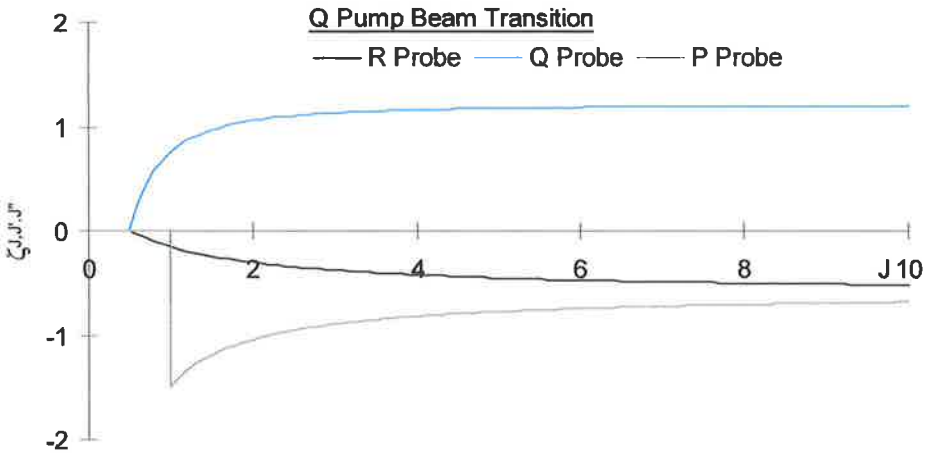

(b)

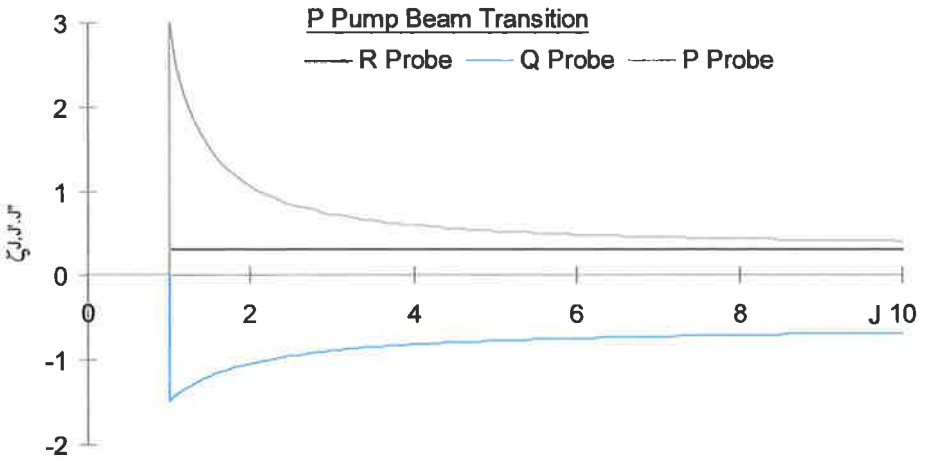

(c)

Figure 6: J dependence of the $\zeta_{J,J',J''}$ factors in the linear regime of optical pumping for a linearly polarised pump beam. The three graphs present the $\zeta_{J,J',J''}$ factors for the (a) R, (b) Q and (c) P pump beam transitions. The probe beam transitions are indicated on each graph.

The calculation of the induced dichroism as a function of the $\zeta_{J,J',J''}$ factors has assumed that the populations of each transition-coupled pair of Zeeman upper and lower states are independently described by the linear regime of an isolated two-level rate equation system. The upper state in each case is assumed to be initially unpopulated. Collisional transitions between the Zeeman states are not considered. It is assumed that no other energy states of the target species are available for population transfer. Collisional energy transfer with molecules of the target or other species are ignored, as is spontaneous emission. It is also assumed that the pump beam is equally divided between polarisation components parallel and orthogonal to the pump beam polarisation direction.

These assumptions are valid for pulsed laser, low pressure spectroscopic applications where the timescale is very much less than the characteristic timescale of collision and provided the populations do not approach saturation. At higher pressures, for saturated populations or for cw pumping, the application of polarisation spectroscopy requires more accurate depiction of the collisional transfer rates. Identification of the significant collisional processes on the timescale of a proposed experiment allows for realistic modelling of the number densities and hence the induced dichroism. Note that in ultra-fast experiments it is more likely that the populations will be modelled using density matrix rather than rate equation methods.

The calculated expressions of Teets, Kowalski, Hill, Carlson and Hansch are tabulated in a more general format than those listed in Tables 2 to 5, which is stated to be applicable to both pulsed and cw applications. These expressions were obtained by extending the theory derived in the pulsed, linear regime to a steady-state or saturated description, requiring that the pulsed saturation parameter denoting the ease of saturation of the pump transition in the two-level system,

$$S_{pulsed} \equiv \frac{\hbar\omega_{pump}}{\sigma_{J,J'}t} \qquad \text{Equation 26}$$

is replaced with a cw saturation analogue,

$$S_{cw} \equiv \frac{\hbar\omega_{pump}}{\sigma_{J,J'}} \cdot \left(\frac{1}{\gamma} + \frac{1}{\gamma'}\right) \qquad \text{Equation 27}$$

in expressions for the induced dichroism . The terms, γ and γ', are described as the lifetimes of the lower, J, and upper, J', states of the pump transition respectively. The resultant $\zeta_{J,J',J''\_general}$ factors tabulated by Teets et. al. are included as Tables 6 and 7 below for the cases of circularly and linearly polarised pump beams respectively. The limiting vales of the $\zeta_{J,J',J''\_general}$ factors as $J \rightarrow \infty$ are the same as the limiting values of the $\zeta_{J,J',J''}$ factors.

The general expressions remain unchanged from those in Tables 2 to 5 for all pump/probe beam combinations with the exception of the P-pump/P-probe and R-pump/R-probe $\zeta_{J,J',J''\_general}$ factors. In these expressions, a relaxation ratio, $r_{Teets\ et\ al.}$, defined as

$$r_{Teets\_et.\_al.} = \frac{\gamma - \gamma'}{\gamma + \gamma'} \qquad \text{Equation 28}$$

and ranging in value between -1 and 1, has been introduced *"to account for the contribution of the upper state population anisotropy to the induced dichroism in the case of equivalent pump and probe transitions"* [1]. Note that the relaxation factor does not occur in the Q pump/Q probe transition which is also subject to the shared pump/probe beam upper state anisotropy.

The general $\zeta_{J,J',J''\_general}$ factors are stated to be applicable to most pulsed or cw experimental situations by selection of the appropriate relaxation factor, $r_{Teets\ et\ al.}$. A value of r = -1 is said to correspond to the linear regime of pumping where population contributions due to terms involving the inverse of the lifetime of the upper state, $\gamma_1^{-1} = 0$, are insignificant. The J dependence of Teets, Kowalski, Hill, Carlson and Hansch's $\zeta_{J,J',J''\_general}$ factors is shown in Figures 7 and 8 for the P-pump/P-probe and R-pump/R-probe pump/probe transition combinations in which the relaxation factor occurs, for circularly and linearly polarised pump beams respectively. In each case, the range of the relaxation ratio, $-1 < r_{Teets\ et\ al.} < 1$, is indicated by the range of curves on the graph.

	J" = J +1	J" = J	J" = J -1
J' = J +1	$= \frac{3(2J^2+J(4+r)+(1+r))}{2(J+1)(2J+3)}$ $\forall J$	$= -\frac{3}{2(J+1)}$ if $J>0$ $= 0$ if $J=0$	$= -\frac{3}{2}$ if $J>½$ $= 0$ if $J=0,½$
J' = J	$= -\frac{3}{2(J+1)}$ if $J>0$ $= 0$ if $J=0$	$= \frac{3}{2J(J+1)}$ if $J>0$ $= 0$ if $J=0$	$= \frac{3}{2J}$ if $J>½$ $= 0$ if $J=0,½$
J' = J-1	$= -\frac{3}{2}$ if $J>½$ $= 0$ if $J=0,½$	$= \frac{3}{2J}$ if $J>½$ $= 0$ if $J=0,½$	$= \frac{3(2J^2-rJ-1)}{2J(2J-1)}$ if $J>½$ $= 0$ if $J=0,½$

Table 6: Teets, Kowalski, Hill, Carlson and Hansch's general $\zeta_{J,J',J''\_general}$ factors for a circularly polarised pump beam.

	J" = J +1	J" = J	J" = J -1
J' = J +1	$= \frac{3(2J^2+J(4+5r)+(5+5r))}{10(J+1)(2J+3)}$ $\forall J$	$= -\frac{3(2J-1)}{10(J+1)}$ if $J>0$ $= 0$ if $J=0$	$= \frac{3}{10}$ if $J>½$ $= 0$ if $J=0,½$
J' = J	$= -\frac{3(2J-1)}{10(J+1)}$ if $J>0$ $= 0$ if $J=0$	$= \frac{3(2J+3)(2J-1)}{10J(J+1)}$ if $J>0$ $= 0$ if $J=0$	$= -\frac{3(2J+3)}{10J}$ if $J>½$ $= 0$ if $J=0,½$
J' = J-1	$= \frac{3}{10}$ if $J>½$ $= 0$ if $J=0,½$	$= -\frac{3(2J+3)}{10J}$ if $J>½$ $= 0$ if $J=0,½$	$= \frac{3(2J^2-5rJ+3)}{10J(2J-1)}$ if $J>½$ $= 0$ if $J=0,½$

Table 7: Teets, Kowalski, Hill, Carlson and Hansch's general $\zeta_{J,J',J''\_general}$ factors for a linearly polarised pump beam.

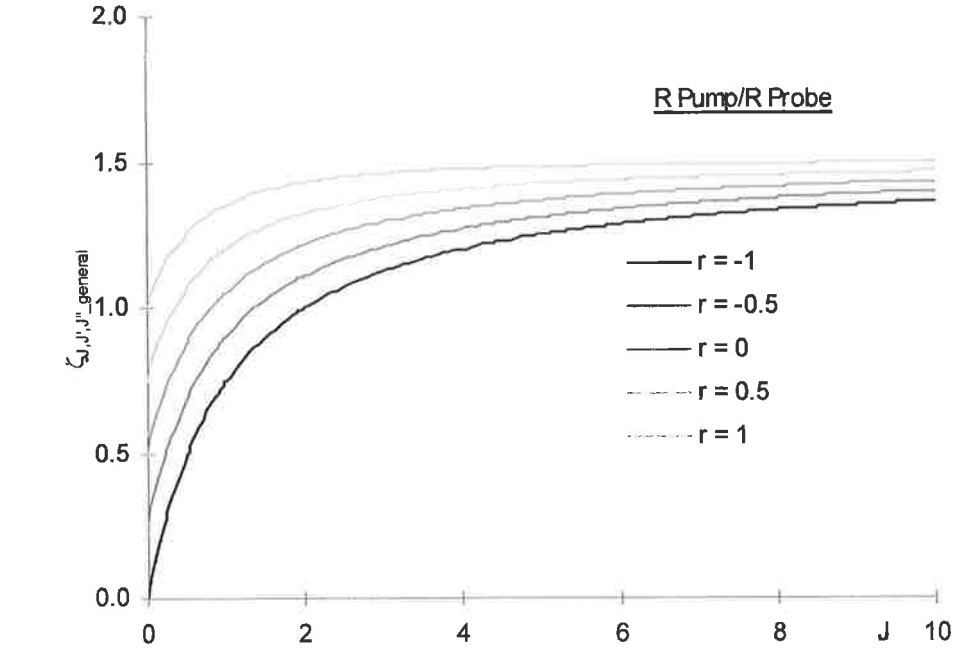

(a)

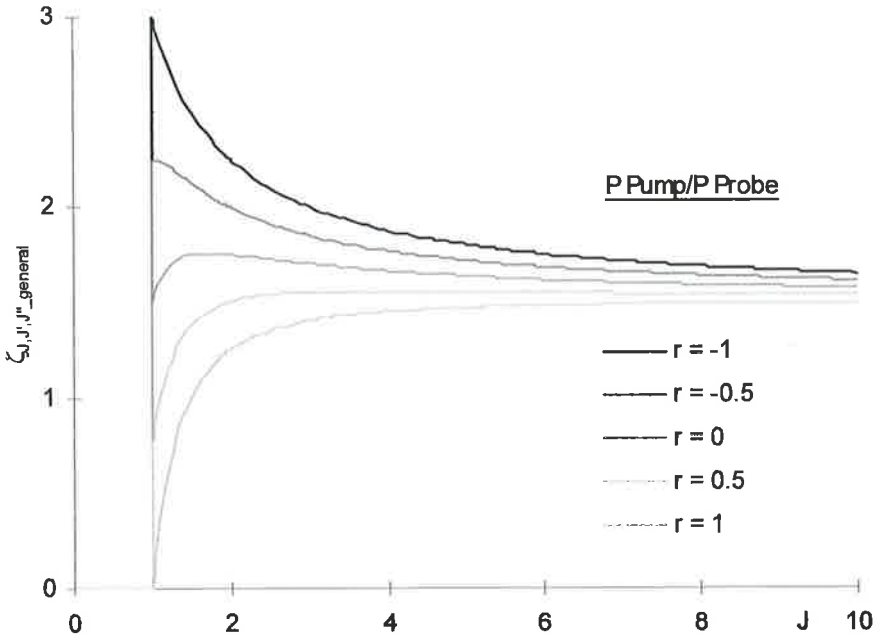

(b)

Figure 7: J dependence of Teets, Kowalski, Hill, Carlson and Hansch's general $\zeta_{J,J',J"\_general}$ factors for (a) R-pump/ R-probe transitions and (b) P-pump/P-probe transitions for a circularly polarised pump beam. The range of the ratio, $r_{Teets\ et.\ al.}$, from $-1 < r_{Teets\ et\ al.} < 1$ is indicated by the range of curves on the graph.

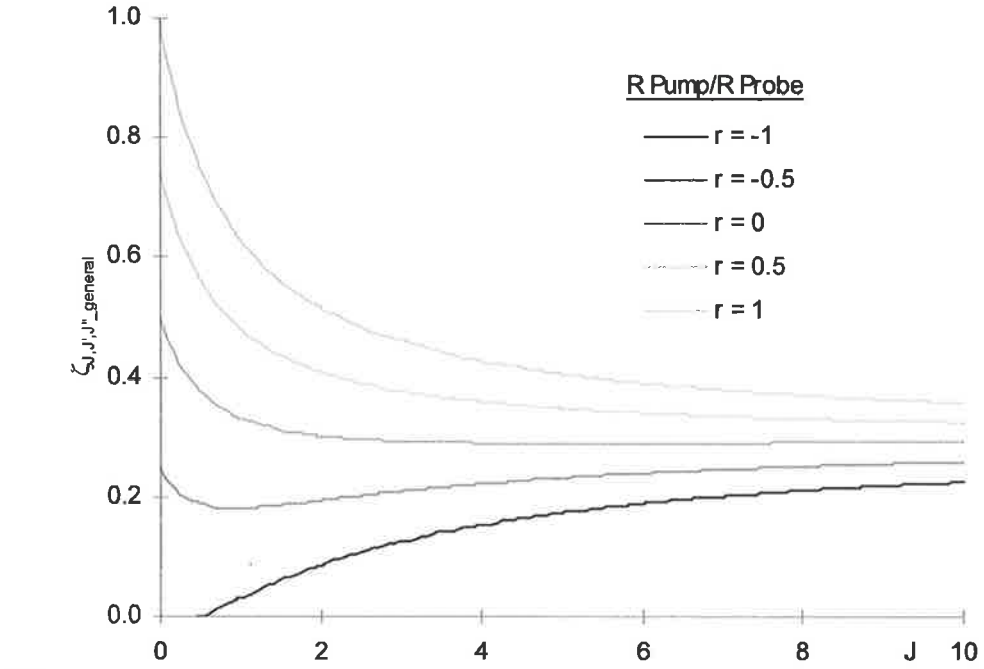

(a)

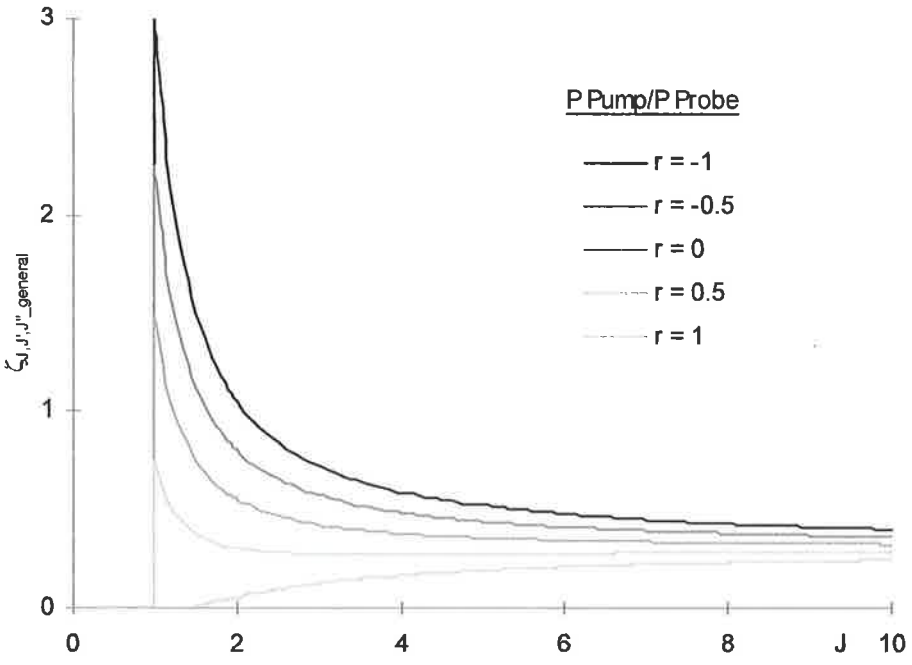

(b)

Figure 8: J dependence of Teets, Kowalski, Hill, Carlson and Hansch's general $\zeta_{J,J',J''\_general}$ factors for (a) R-pump/ R-probe transitions and (b) P-pump/P-probe transitions for a linearly polarised pump beam. The range of the ratio, $r_{Teets\ et.\ al.}$, from $-1 < r_{Teets\ et\ al.} < 1$ is indicated by the range of curves on the graph.

There is one correction to be made to the $\zeta_{J,J',J''}$ factors in the linear regime of optical pumping. Teets, Kowalski, Hill, Carlson and Hansch assumed the upper state of the pumped and probed transitions are initially unpopulated and accounted for the population of the upper state for the case of shared pump and probe transitions using the factor, r, in the general $\zeta_{J,J',J''\_general}$ factors above. However, this term disappears in the linear pumping regime. The upper state population for shared pump/probe transitions is accounted for more accurately in this regime by rewriting equations [17] (and following) to include the contribution of the population difference between the lower and upper states to the induced dichroism, rather than assuming the upper state is unpopulated, i.e. the absorption coefficient becomes

$$\alpha^{i_{probe}}_{J,J'',M,M''} = \left(N_{J,M} - N_{J',M'}\right) N_{J,M} \cdot \sigma^{i_{probe}}_{J,J'',M,M''} \cdot C_{JJ''} \qquad \text{Equation 29}$$

where the upper and lower state population difference for the pump transition has been included explicitly, and the induced dichroism, $\Delta\alpha^{i,i'}_{J,J''}$, is rewritten as

$$\Delta\alpha^{i,i'}_{J,J''} = \sum_{M}\left(\left(N_{J,M} - N_{J',M'}\right)\cdot\left(\sigma^{i}_{J,J'',M,M''} - \sigma^{i'}_{J,J'',M,M''}\right)\cdot C_{JJ''}\right) \qquad \text{Equation 30}$$

If collisional population transfer and spontaneous emission rates are insignificant in the linear regime, Appendix II shows that the population difference may be written as

$$N_{J,M\_lower} - N_{J,M\_upper} = \frac{N_J}{2J+1}\cdot\left(1 - 2\cdot\frac{\sigma^{i_{pump}}_{J,J',M,M'}\cdot C_{JJ'}}{\hbar\omega_{pump}} I_{pump}\, t\right) \qquad \text{Equation 31}$$

leading to a factor of two introduced into the $\zeta_{J,J',J''}$ factors for P-pump/P-probe, Q-pump/Q -robe and R-pump/R-probe transitions, and a resulting factor of four in the signal in these cases for perfectly crossed polarisers and no interpolariser birefringent elements in the probe beam path. This factor of four is significant in selection of strong transitions for combustion imaging. For reference, the corrected ζ_{J,J',J''_corr} factors (including the relevant factor of two) valid in the linear regime are listed in Tables 8 and 9 for circularly and linearly polarised pump beams respectively. Tables 10 and 11 quote the limiting values of the ζ_{J,J',J''_corr} factors at large J. The J dependence of the ζ_{J,J',J''_corr} factors for a circularly polarised pump beam, and for a linearly polarised pump beam is shown in Figures 9 and 10 respectively. In each case, the three graphs present the ζ_{J,J',J''_corr} factors for the (a) R, (b) Q and (c) P pump beam transitions.

	J" = J +1	J" = J	J" = J -1
J' = J +1	$=\frac{3J}{(J+1)}$ ∀J	$=-\frac{3}{2(J+1)}$ if $J>0$ $=0$ if $J=0$	$=-\frac{3}{2}$ if $J>½$ $=0$ if $J=0,½$
J' = J	$=-\frac{3}{2(J+1)}$ if $J>0$ $=0$ if $J=0$	$=\frac{3}{J(J+1)}$ if $J>0$ $=0$ if $J=0$	$=\frac{3}{2J}$ if $J>½$ $=0$ if $J=0,½$
J' = J-1	$=-\frac{3}{2}$ if $J>½$ $=0$ if $J=0,½$	$=\frac{3}{2J}$ if $J>½$ $=0$ if $J=0,½$	$=\frac{3(J+1)}{J}$ if $J>½$ $=0$ if $J=0,½$

Table 8: Corrected ζ_{J,J',J''_corr} factors valid in the linear regime of optical pumping for a circularly polarised pump beam.

	J" = J +1	J" = J	J" = J -1
J'=J+1	$=\frac{3J(2J-1)}{5(J+1)(2J+3)}$ ∀J	$=-\frac{3(2J-1)}{10(J+1)}$ if $J>0$ $=0$ if $J=0$	$=\frac{3}{10}$ if $J>½$ $=0$ if $J=0,½$
J'=J	$=-\frac{3(2J-1)}{10(J+1)}$ if $J>0$ $=0$ if $J=0$	$=\frac{3(2J+3)(2J-1)}{5J(J+1)}$ if $J>0$ $=0$ if $J=0$	$=-\frac{3(2J+3)}{10J}$ if $J>½$ $=0$ if $J=0,½$
J'=J-1	$=\frac{3}{10}$ if $J>½$ $=0$ if $J=0,½$	$=-\frac{3(2J+3)}{10J}$ if $J>½$ $=0$ if $J=0,½$	$=\frac{3(J+1)(2J+3)}{5J(2J-1)}$ if $J>½$ $=0$ if $J=0,½$

Table 9: Corrected ζ_{J,J',J''_corr} factors valid in the linear regime of optical pumping for a linearly polarised pump beam.

	J" = J +1	J" = J	J" = J -1
J' = J +1	3	0	$-3/2$
J' = J	0	0	0
J' = J-1	$-3/2$	0	3

Table 10: Limiting values of the corrected ζ_{J,J',J''_corr} factors valid in the linear regime of optical pumping for a circularly polarised pump beam as $J\to\infty$.

	J" = J +1	J" = J	J" = J -1
J' = J +1	$6/10$	$-6/10$	$3/10$
J' = J	$-6/10$	$24/10$	$-6/10$
J' = J-1	$3/10$	$-6/10$	$6/10$

Table 11: Limiting values of the corrected ζ_{J,J',J''_corr} factors valid in the linear regime of optical pumping for a linearly polarised pump beam as $J\to\infty$.

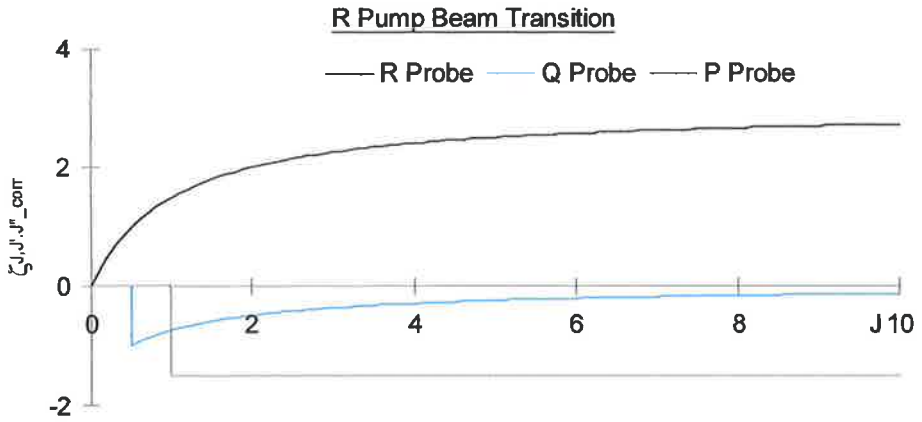

(a)

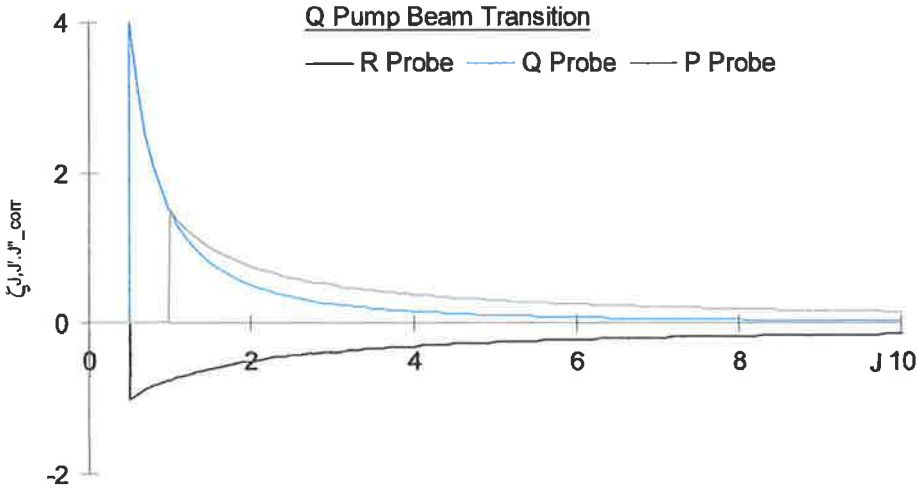

(b)

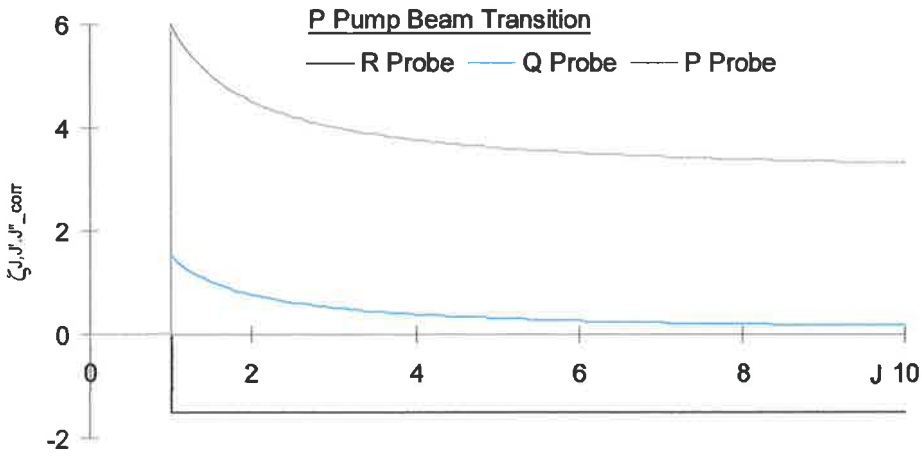

(c)

Figure 9: J dependence of the corrected ζ_{J,J',J''_corr} factors for a circularly polarised pump beam valid in the linear regime of optical pumping. The three graphs present the corrected ζ_{J,J',J''_corr} factors for the (a) R, (b) Q and (c) P pump beam transitions. The probe beam transitions are indicated on each graph. Note the increased Y-axis scale of the P pump beam graph, (c).

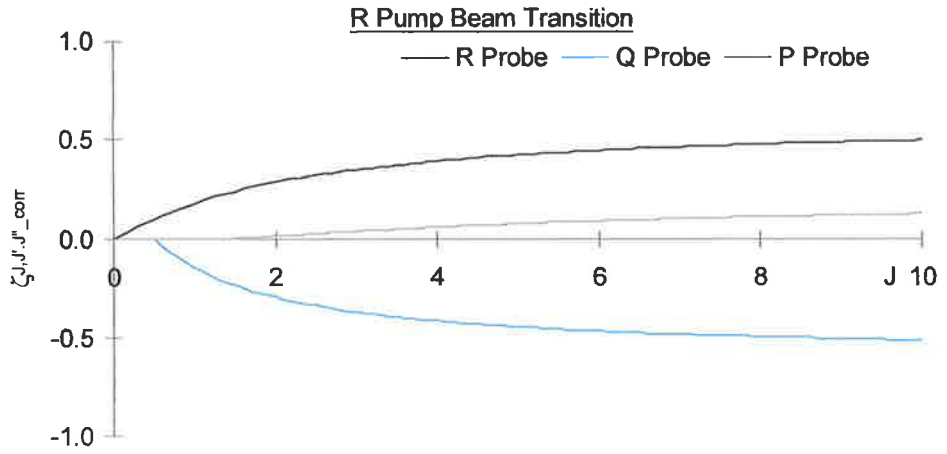

(a)

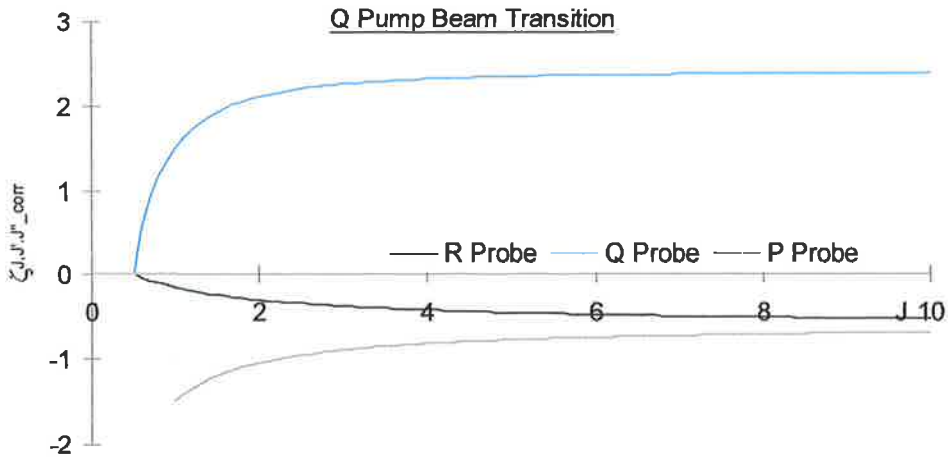

(b)

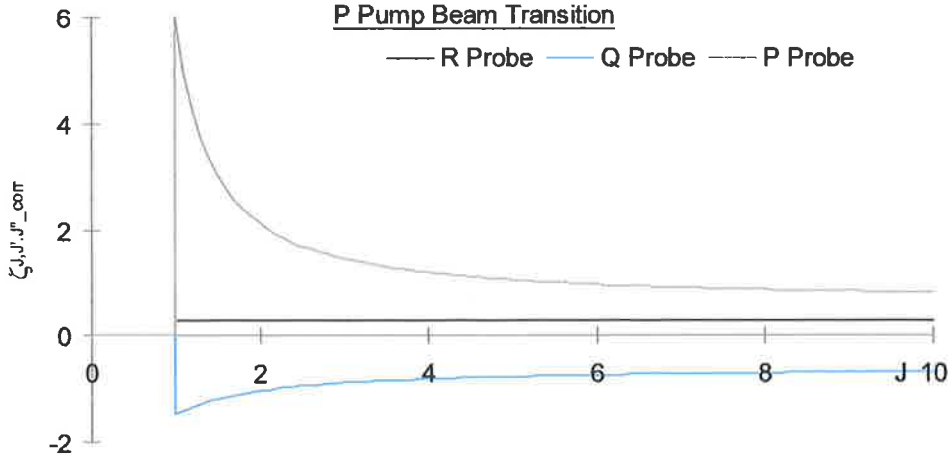

(c)

Figure 10: J dependence of the corrected $\zeta_{J,J',J"\_corr}$ factors for a linearly polarised pump beam valid in the linear regime of optical pumping. The three graphs present the corrected $\zeta_{J,J',J"\_corr}$ factors for the (a) R, (b) Q and (c) P pump beam transitions. The probe beam transitions are indicated on each graph.

It is sometimes more convenient to combine the J dependent terms of equation [21] describing the induced dichroism in the linear regime of optical pumping by isolating the J-dependence from the vibrational and electronic transition probabilities into the purely J-dependent factor, $Z_{J,J',J''}$, defined as

$$\Delta\alpha^{i,i'}_{J,J''} = -N_J \cdot \frac{I_{pump} t}{\hbar\omega_{pump}} \cdot Z_{J,J',J''} \cdot C_{J,J'} \cdot C_{J,J''} \qquad \text{Equation 32}$$

where the coefficients, $C_{J,J'}$ and $C_{J,J''}$, represent the non-rotational components of the absorption cross-sections, so that

$$Z_{J,J',J''} = \frac{\sigma_{J,J'} \cdot \sigma_{J,J''} \cdot \zeta_{J,J',J''}}{C_{J,J'} \cdot C_{J,J''}} \qquad \text{Equation 33}$$

The non-rotational elements cancel in equation [33] and what remains is a purely rotationally dependent function, $Z_{J,J',J''}$. The $Z_{J,J',J''}$ factors related to the corrected ζ_{J,J',J''_corr} factors are termed corrected Z_{J,J',J''_corr} factors. The corrected $Z_{J,J',J''}$ factors are tabulated in Tables 12 and 13, with the limiting values as $J \rightarrow \infty$ tabulated in Tables 14 and 15. Figures 11 and 12 show the J dependence of the corrected $Z_{J,J',J''}$ factors.

For no birefringent optical elements between perfectly crossed probe beam polarisers, the LPS signal (in the linear regime of optical pumping), ignoring the extinction ratio background, is proportional to the square of the corrected $Z_{J,J',J''}$ factors. Figures 13 and 14 indicate the J-dependence of the squares of the corrected $Z_{J,J',J''}$ factors in this regime for circularly and linearly polarised pump beams respectively. Note that the previously mentioned factor of 2 due to contributions of the population of the upper state in the case of a shared pump/probe transition now becomes a factor of 4 in relative signal. Figure 13 indicates that the R-transition pump/R transition probe combination is favoured for a circularly polarised pump beam for intermediate J. The Q-transition pump/Q-transition probe transition of Figure 14 is by far the strongest pump/probe transition combination for a linearly polarised pump beam, while remaining approximately 2 times weaker in signal at intermediate J than the strong R-transition pump/R transition probe combination for a circularly polarised pump beam. However, as $J \rightarrow \infty$, the Q-transition pump/Q-transition probe transition (linearly polarised pump beam), the R-transition pump/R-transition probe transition (circularly polarised pump beam) and P-transition pump/P-transition probe transition (circularly polarised pump beam) signal strengths approach the same order of magnitude.

	J" = J +1	J" = J	J" = J -1
J' = J +1	$= \frac{1}{3}\cdot\frac{J\cdot(2J+3)^2}{(J+1)(2J+1)^2}$ $\forall J$	$= -\frac{1}{6}\cdot\frac{(2J+3)}{(J+1)(2J+1)}$ if $J>0$ $= 0$ if $J=0$	$= -\frac{1}{6}\cdot\frac{(2J-1)\cdot(2J+3)}{(2J+1)^2}$ if $J>½$ $= 0$ if $J=0,½$
J' = J	$= -\frac{1}{6}\cdot\frac{(2J+3)}{(J+1)(2J+1)}$ if $J>0$ $= 0$ if $J=0$	$= \frac{1}{3}\cdot\frac{1}{J\cdot(J+1)}$ if $J>0$ $= 0$ if $J=0$	$= \frac{1}{6}\cdot\frac{(2J-1)}{J\cdot(2J+1)}$ if $J>½$ $= 0$ if $J=0,½$
J' = J-1	$= -\frac{1}{6}\cdot\frac{(2J-1)\cdot(2J+3)}{(2J+1)^2}$ if $J>½$ $= 0$ if $J=0,½$	$= \frac{1}{6}\cdot\frac{(2J-1)}{J\cdot(2J+1)}$ if $J>½$ $= 0$ if $J=0,½$	$= \frac{1}{3}\cdot\frac{(J+1)(2J-1)^2}{J\cdot(2J+1)^2}$ if $J>½$ $= 0$ if $J=0,½$

Table 12: Corrected Z_{J,J',J''_corr} factors valid in the linear regime of optical pumping for a circularly polarised pump beam.

	J" = J +1	J" = J	J" = J -1
J' = J +1	$= \frac{1}{15}\cdot\frac{J\cdot(2J-1)(2J+3)}{(J+1)(2J+1)^2}$ $\forall J$	$= -\frac{1}{30}\cdot\frac{(2J-1)(2J+3)}{(J+1)(2J+1)}$ if $J>0$ $= 0$ if $J=0$	$= \frac{1}{30}\cdot\frac{(2J-1)(2J+3)}{(2J+1)^2}$ if $J>½$ $= 0$ if $J=0,½$
J' = J	$= -\frac{1}{30}\cdot\frac{(2J-1)(2J+3)}{(J+1)(2J+1)}$ if $J>0$ $= 0$ if $J=0$	$= \frac{1}{15}\cdot\frac{(2J-1)(2J+3)}{J\cdot(J+1)}$ if $J>0$ $= 0$ if $J=0$	$= -\frac{1}{30}\cdot\frac{(2J-1)(2J+3)}{J\cdot(2J+1)}$ if $J>½$ $= 0$ if $J=0,½$
J' = J-1	$= \frac{1}{30}\cdot\frac{(2J-1)(2J+3)}{(2J+1)^2}$ if $J>½$ $= 0$ if $J=0,½$	$= -\frac{1}{30}\cdot\frac{(2J-1)(2J+3)}{J\cdot(2J+1)}$ if $J>½$ $= 0$ if $J=0,½$	$= \frac{1}{15}\cdot\frac{(J+1)(2J-1)(2J+3)}{J\cdot(2J+1)^2}$ if $J>½$ $= 0$ if $J=0,½$

Table 13: Corrected Z_{J,J',J''_corr} factors valid in the linear regime of optical pumping for a linearly polarised pump beam.

	J" = J +1	J" = J	J" = J -1
J' = J +1	⅓	0	−⅙
J' = J	0	0	0
J' = J-1	−⅙	0	⅓

Table 14: Limiting values of the corrected Z_{J,J',J''_corr} factors valid in the linear regime of optical pumping for a circularly polarised pump beam as $J\to\infty$.

	J" = J +1	J" = J	J" = J -1
J' = J +1	1/15	−1/15	1/30
J' = J	−1/15	4/15	−1/15
J' = J-1	1/30	−1/15	1/15

Table 15: Limiting values of the corrected Z_{J,J',J''_corr} factors valid in the linear regime of optical pumping for a linearly polarised pump beam as $J\to\infty$.

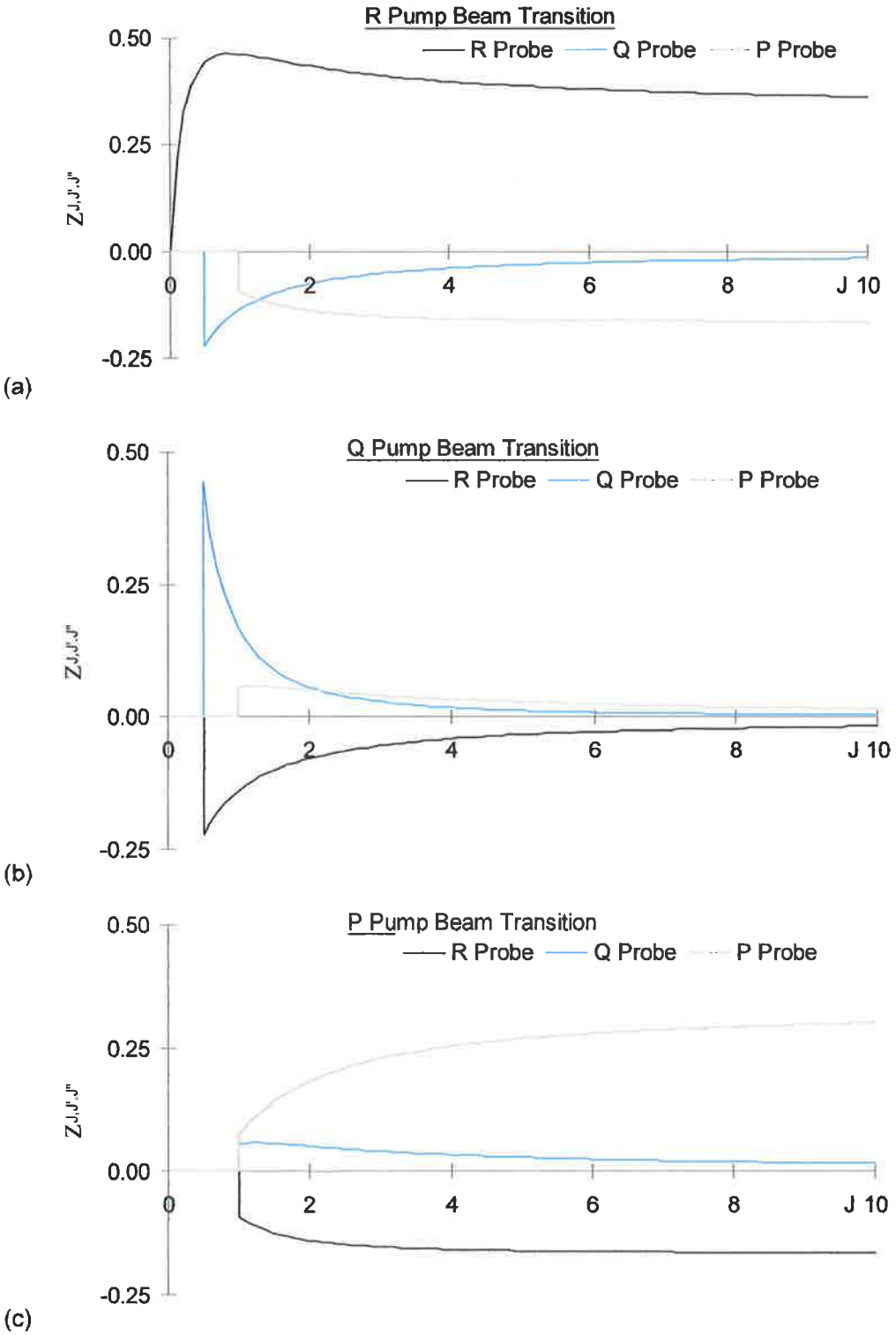

Figure 11: J dependence of the corrected Z_{J,J',J''_corr} factors valid in the linear regime of optical pumping for a circularly polarised pump beam. The three graphs present the corrected Z_{J,J',J''_corr} factors for the (a) R, (b) Q and (c) P pump beam transitions. The probe beam transitions are indicated on each graph.

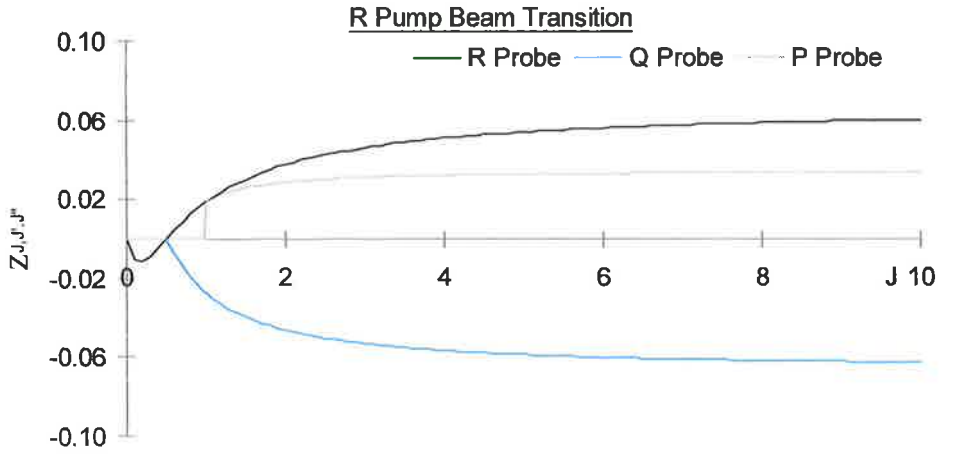

(a)

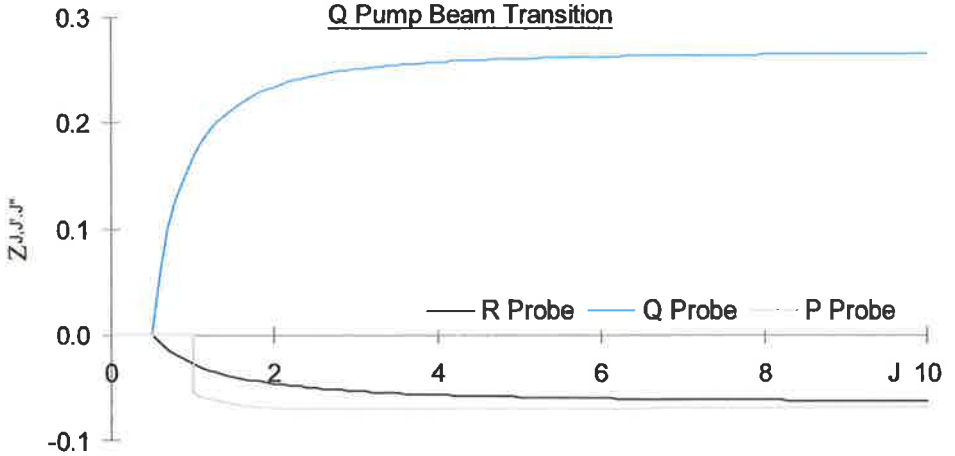

(b)

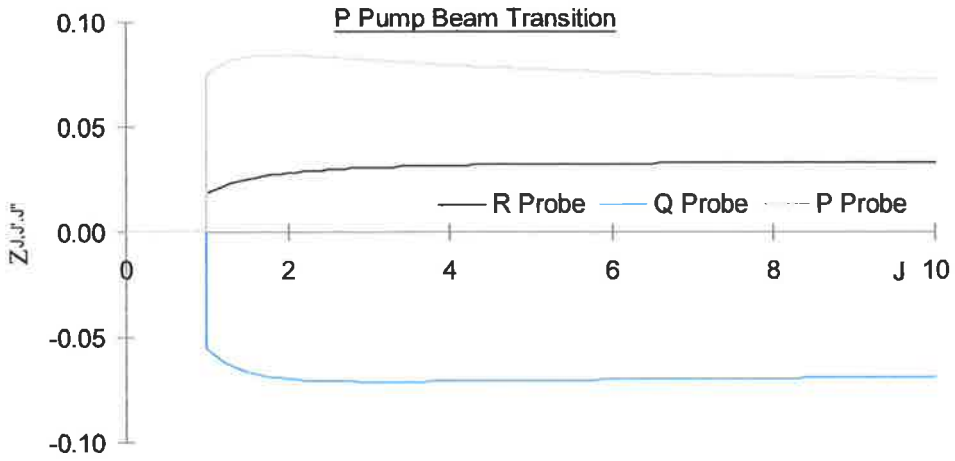

(c)

Figure 12: J dependence of the corrected $Z_{J,J',J"\_corr}$ factors valid in the linear regime of optical pumping for a linearly polarised pump beam. The three graphs present the corrected $Z_{J,J',J"\_corr}$ factors for the (a) R, (b) Q and (c) P pump beam transitions. The probe beam transitions are indicated on each graph.

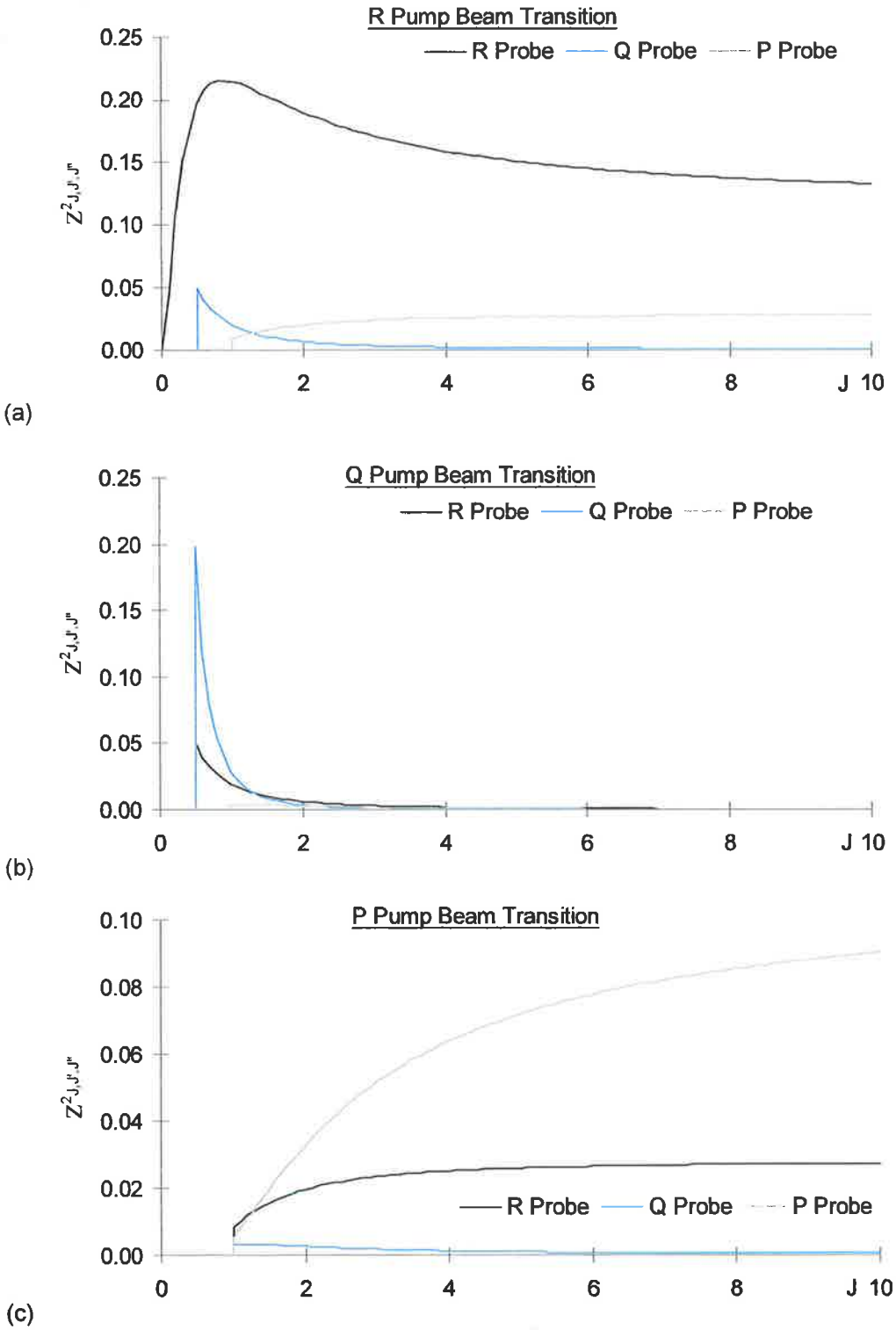

Figure 13: J dependence of the squares of the corrected Z_{J,J',J''_corr} factors valid in the linear regime of optical pumping for a circularly polarised pump beam. The three graphs present the corrected squared Z_{J,J',J''_corr} factors for the (a) R, (b) Q and (c) P pump beam transitions. The probe beam transitions are indicated on each graph.

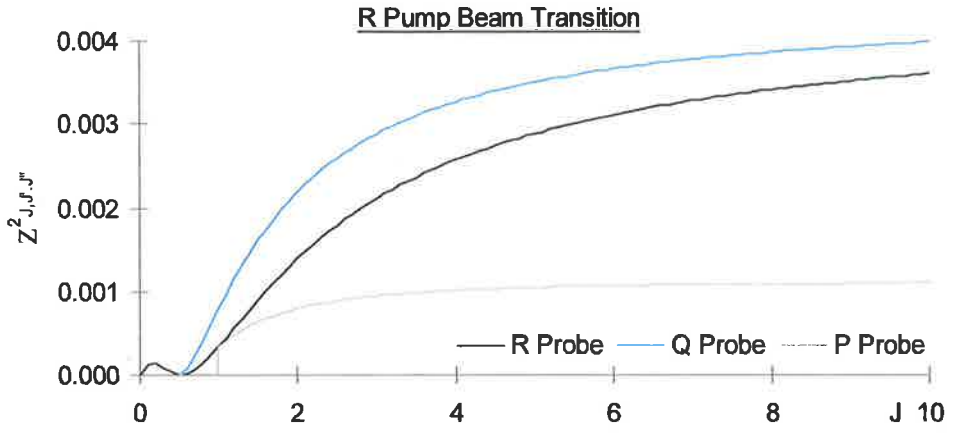

(a)

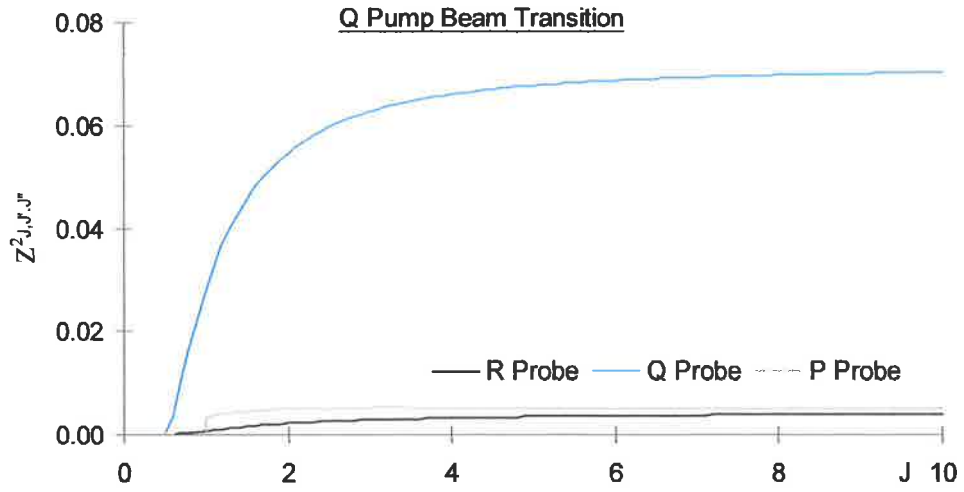

(b)

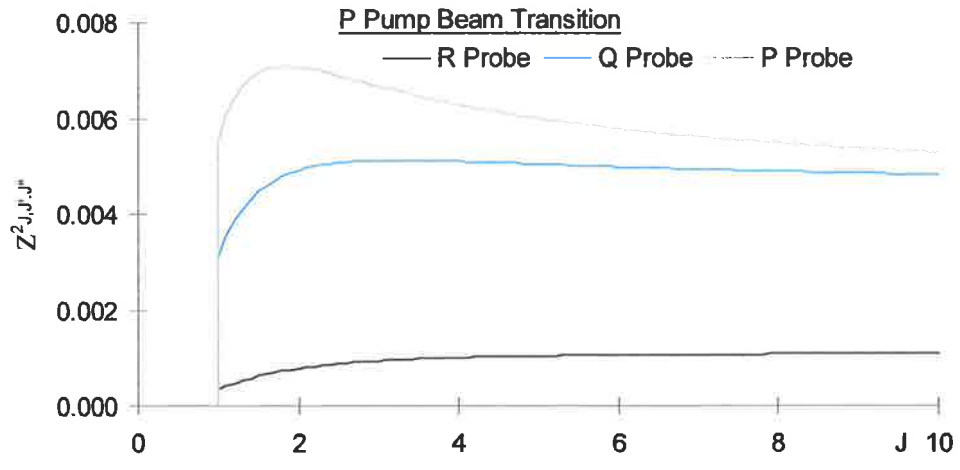

(c)

Figure 14: J dependence of the squares of the corrected Z_{J,J',J''_corr} factors valid in the linear regime of optical pumping for a linearly polarised pump beam. The three graphs present the corrected squared Z_{J,J',J''_corr} factors for the (a) R, (b) Q and (c) P pump beam transitions. The probe beam transitions are indicated on each graph.

Equivalent general $Z_{J,J',J''\_general}$ factors may be defined with respect to the general $\zeta_{J,J'',J''\_general}$ factors. These expressions do not contain the factor of 2 previously mentioned to allow for the population of the upper state in the case of a shared pump/probe transition in the linear regime of optical pumping. Tables 16 and 17 list the general $Z_{J,J',J''\_general}$ factors for circularly and linearly polarised pump beams respectively. The limiting values of the general $Z_{J,J',J''\_general}$ factors as $J \to \infty$ are listed in Tables 20 and 21.

The J dependence of the R-pump/R-probe and P-pump/P-probe transition general $Z_{J,J',J''\_general}$ factors is shown in Figure 15 for a circularly polarised pump beam. Similar curves are shown in Figure 16 for a linearly polarised pump beam. For reference, Figures 17 and 18 show the J dependence of the squares of the general $Z_{J,J',J''\_general}$ factors for circularly and linearly polarised pump beams respectively. The range of the ratio, $r_{Teets\ et.\ al.}$, from $-1 < r_{Teets\ et\ al.} < 1$ is indicated by the range of curves on the graph.

	J'' = J +1	J'' = J	J'' = J -1
J' = J +1	$= \dfrac{\begin{pmatrix} 2J^2 \\ +J(4+r) \\ +(1+r) \end{pmatrix}(2J+3)}{6(J+1)(2J+1)^2}$ $\forall J$	$= -\dfrac{1}{6}\cdot\dfrac{(2J+3)}{(J+1)(2J+1)}$ if $J>0$ $= 0$ if $J=0$	$= -\dfrac{1}{6}\cdot\dfrac{(2J-1)\cdot(2J+3)}{(2J+1)^2}$ if $J>½$ $= 0$ if $J=0,½$
J' = J	$= -\dfrac{1}{6}\cdot\dfrac{(2J+3)}{(J+1)(2J+1)}$ if $J>0$ $= 0$ if $J=0$	$= \dfrac{1}{6J(J+1)}$ if $J>0$ $= 0$ if $J=0$	$= \dfrac{1}{6}\cdot\dfrac{(2J-1)}{J\cdot(2J+1)}$ if $J>½$ $= 0$ if $J=0,½$
J' = J-1	$= -\dfrac{1}{6}\cdot\dfrac{(2J-1)\cdot(2J+3)}{(2J+1)^2}$ if $J>½$ $= 0$ if $J=0,½$	$= \dfrac{1}{6}\cdot\dfrac{(2J-1)}{J\cdot(2J+1)}$ if $J>½$ $= 0$ if $J=0,½$	$= \dfrac{\begin{pmatrix} 2J^2-1 \\ -rJ \end{pmatrix}(2J-1)}{6J(2J+1)^2}$ if $J>½$ $= 0$ if $J=0,½$

Table 16: General $Z_{J,J',J''\_general}$ factors for a circularly polarised pump beam.

	J" = J +1	J" = J	J" = J -1
J' = J +1	$= \dfrac{\begin{pmatrix}2J^2\\+J(4+5r)\\+(5+5r)\end{pmatrix}(2J+3)}{30(J+1)(2J+1)^2}$ $\forall J$	$= -\dfrac{1}{30}\cdot\dfrac{(2J-1)(2J+3)}{(J+1)(2J+1)}$ if $J>0$ $= 0$ if $J=0$	$= \dfrac{1}{30}\cdot\dfrac{(2J-1)(2J+3)}{(2J+1)^2}$ if $J>½$ $= 0$ if $J=0,½$
J' = J	$= -\dfrac{1}{30}\cdot\dfrac{(2J-1)(2J+3)}{(J+1)(2J+1)}$ if $J>0$ $= 0$ if $J=0$	$= \dfrac{1}{30}\cdot\dfrac{(2J-1)(2J+3)}{J\cdot(J+1)}$ if $J>0$ $= 0$ if $J=0$	$= -\dfrac{1}{30}\cdot\dfrac{(2J-1)(2J+3)}{J\cdot(2J+1)}$ if $J>½$ $= 0$ if $J=0,½$
J' = J-1	$= \dfrac{1}{30}\cdot\dfrac{(2J-1)(2J+3)}{(2J+1)^2}$ if $J>½$ $= 0$ if $J=0,½$	$= -\dfrac{1}{30}\cdot\dfrac{(2J-1)(2J+3)}{J\cdot(2J+1)}$ if $J>½$ $= 0$ if $J=0,½$	$= \dfrac{\begin{pmatrix}2J^2+3\\-5rJ\end{pmatrix}(2J-1)}{30J(2J+1)^2}$ if $J>½$ $= 0$ if $J=0,½$

Table 17: General $Z_{J,J',J''\_general}$ factors for a linearly polarised pump beam.

	J" = J +1	J" = J	J" = J -1
J' = J +1	⅙	0	−⅙
J' = J	0	0	0
J' = J-1	−⅙	0	⅙

Table 18: Limiting values of the general $Z_{J,J',J''\_general}$ factors for a circularly polarised pump beam as $J \to \infty$.

	J" = J +1	J" = J	J" = J -1
J' = J +1	1/30	−2/30	1/30
J' = J	−2/30	4/30	−2/30
J' = J-1	1/30	−2/30	1/30

Table 19: Limiting values of the general $Z_{J,J',J''\_general}$ factors for a linearly polarised pump beam as $J \to \infty$.

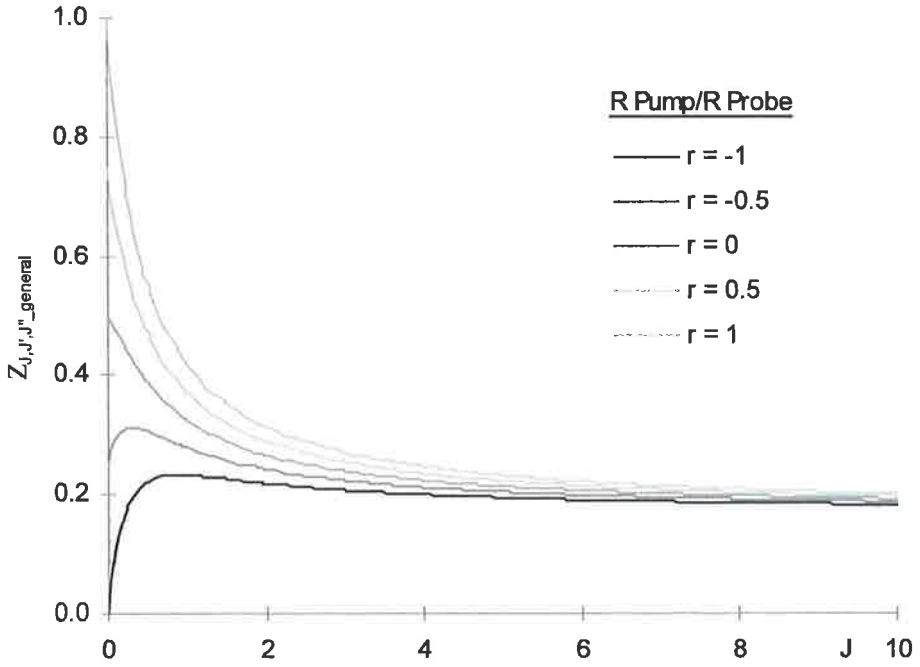

(a)

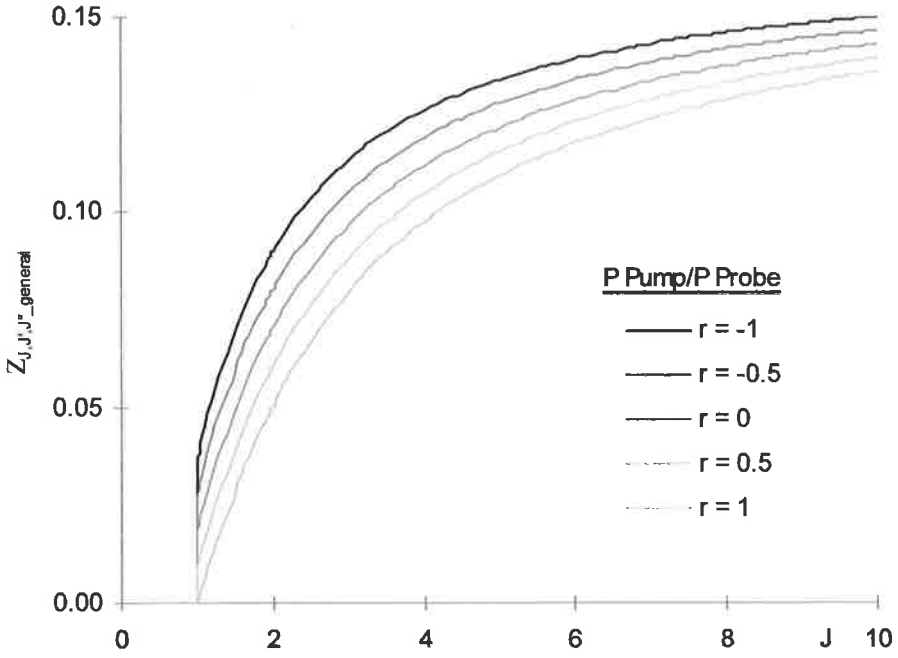

(b)

Figure 15: J dependence of the general $Z_{J,J',J''\_general}$ factors for (a) R-pump/ R-probe transitions and (b) P-pump/P-probe transitions for a circularly polarised pump beam. The range of the ratio, $r_{Teets\ et.\ al.}$, from $-1 < r_{Teets\ et\ al.} < 1$ is indicated by the range of curves on the graph. Note the difference in Y-axis scale between the two graphs.

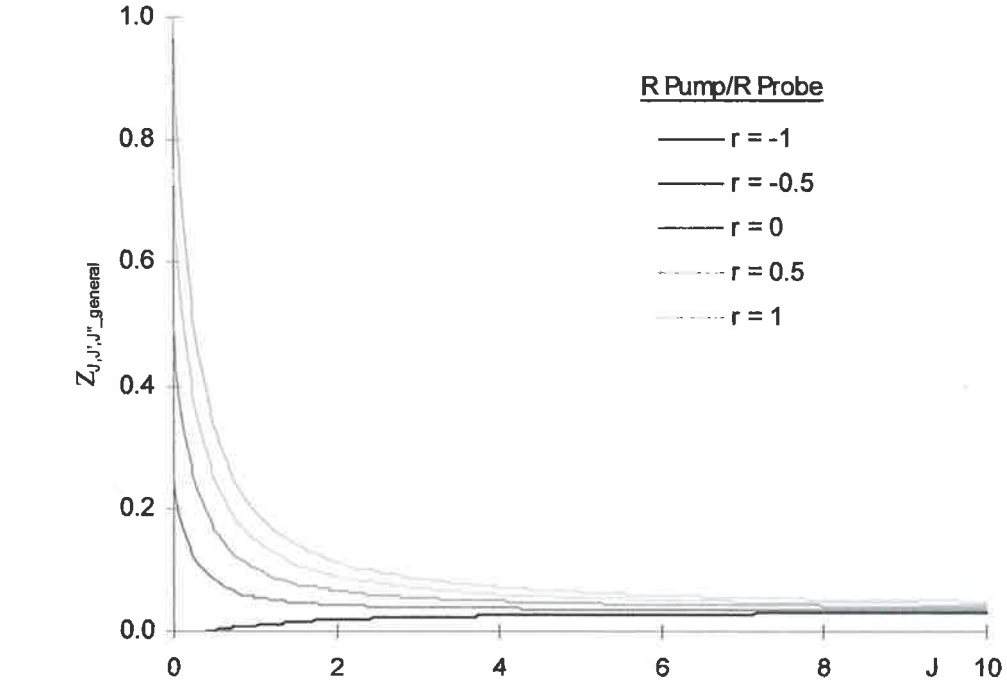

(a)

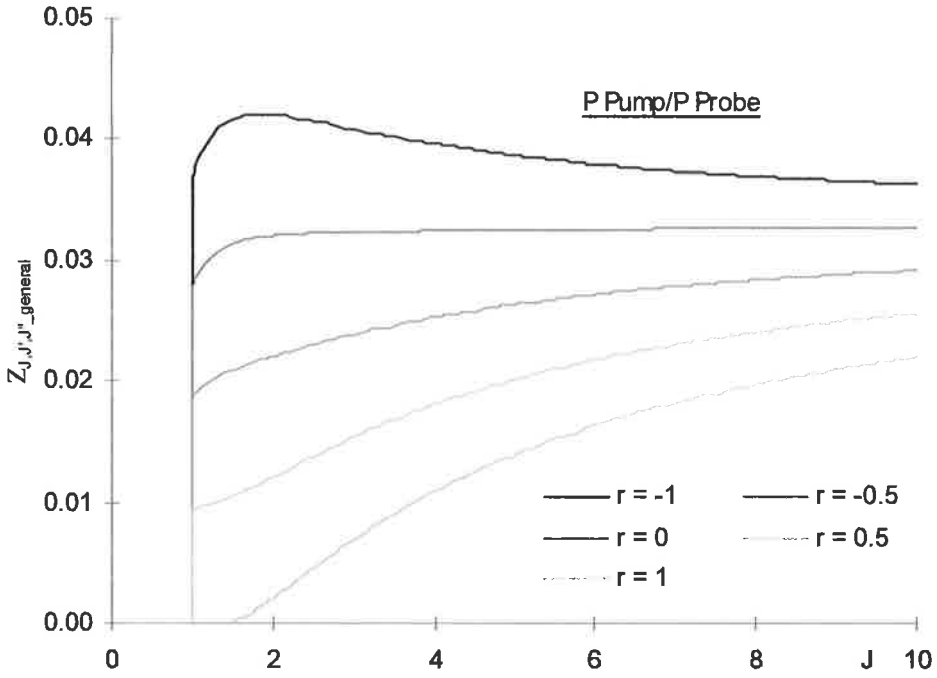

(b)

Figure 16: J dependence of the general $Z_{J,J',J''\_general}$ factors for (a) R-pump/ R-probe transitions and (b) P-pump/P-probe transitions for a linearly polarised pump beam. The range of the ratio, $r_{Teets\ et.\ al.}$, from $-1 < r_{Teets\ et\ al.} < 1$ is indicated by the range of curves on the graph. Note the difference in Y-axis scale between the two graphs.

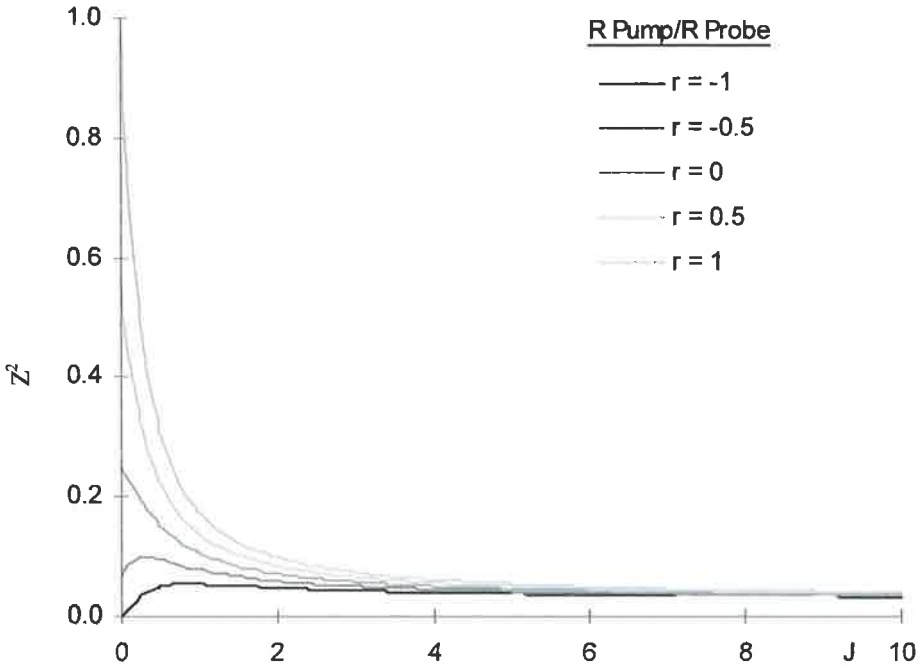

(a)

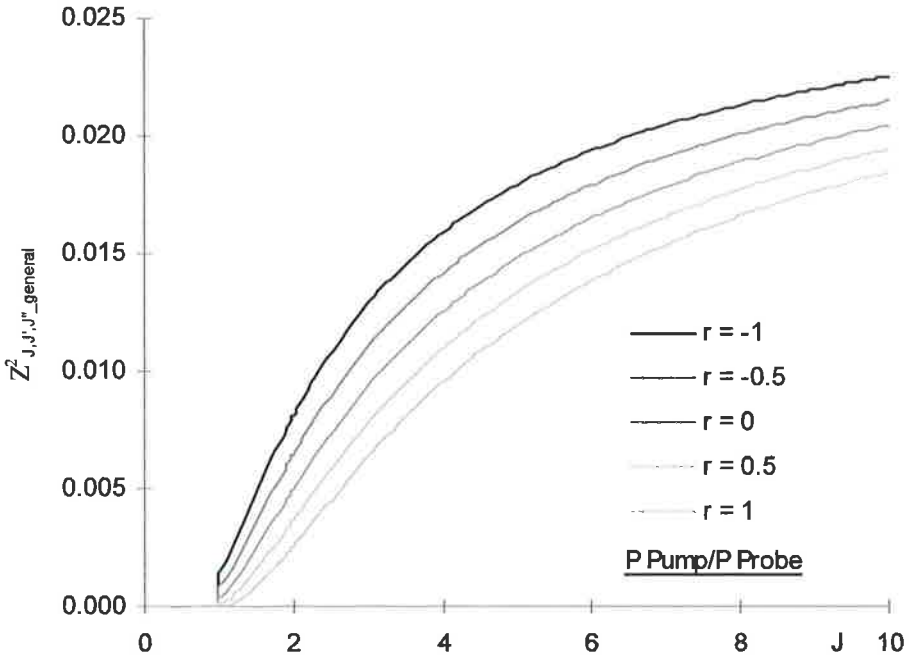

(b)

Figure 17: J dependence of the squares of the general $Z_{J,J',J''\_general}$ factors for (a) R-pump/ R-probe transitions and (b) P-pump/P-probe transitions for a circularly polarised pump beam. The range of the ratio, $r_{Teets\ et.\ al.}$, from $-1 < r_{Teets\ et\ al.} < 1$ is indicated by the range of curves on the graph. Note the difference in Y-axis scale between the two graphs.

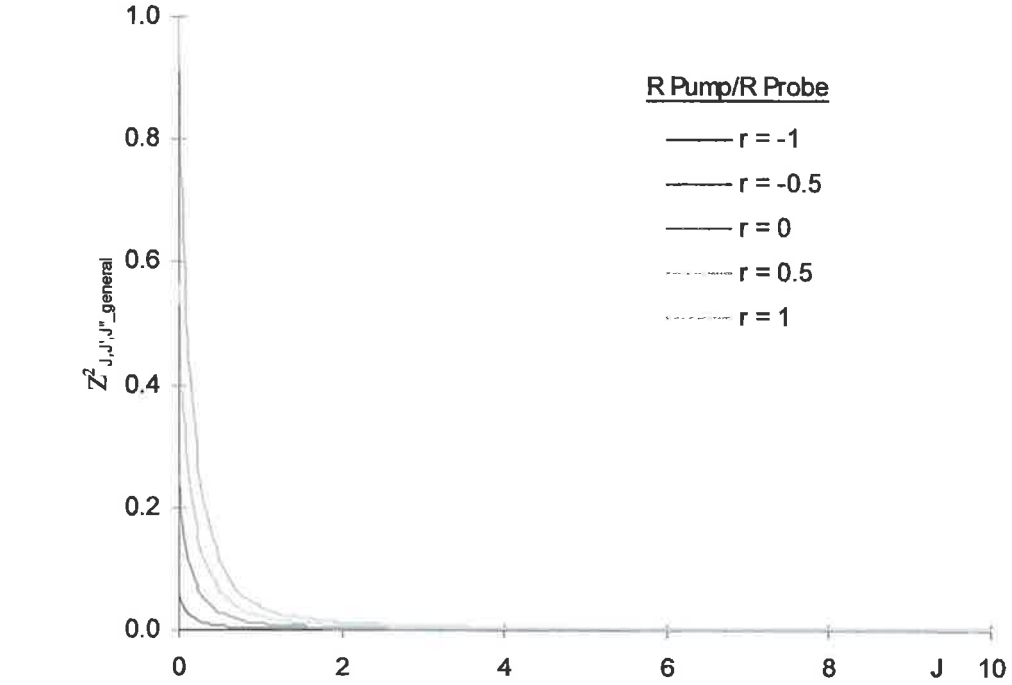

(a)

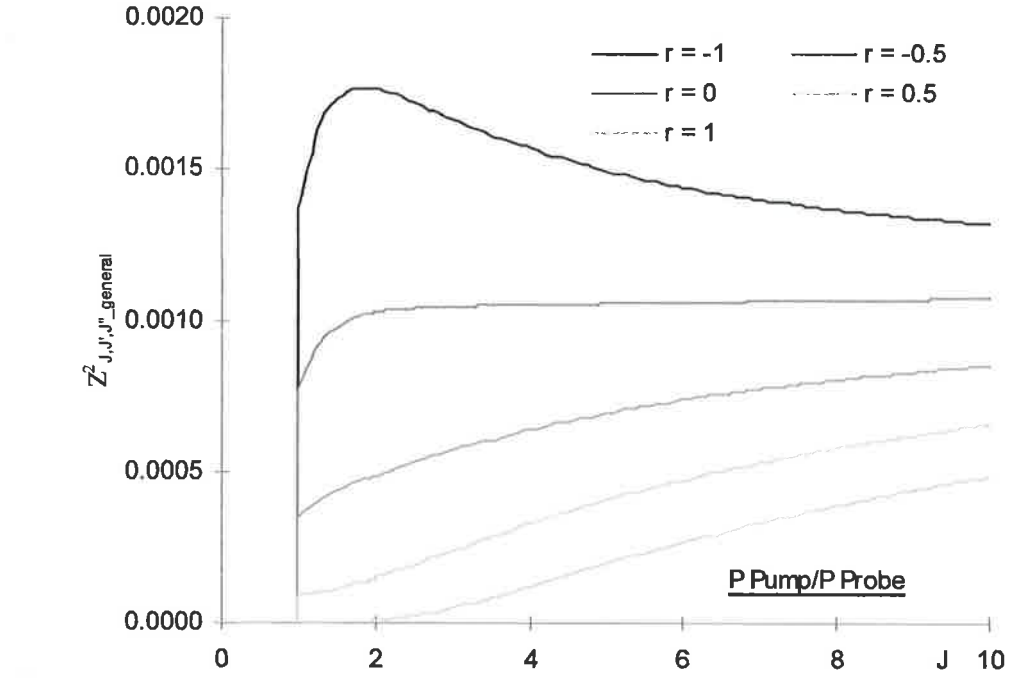

(b)

Figure 18: J dependence of the squares of the general $Z_{J,J',J''\_general}$ factors for (a) R-pump/ R-probe transitions and (b) P-pump/P-probe transitions for a linearly polarised pump beam. The range of the ratio, $r_{Teets\ et.\ al.}$, from $-1 < r_{Teets\ et\ al.} < 1$ is indicated by the range of curves on the graph. Note the difference in Y-axis scale between the two graphs.

The theory of Teets, Kowalski, Hill, Carlson and Hansch was based on the assumption of a pulsed laser system leading to a description of the pumped populations by an isolated two-level model in the linear regime of optical pumping. It is also assumed that there are no significant collisional processes on the timescale of the experiment, and that spontaneous emission rates are also insignificant on this timescale. The derivation summarised in this chapter provide a model of the polarisation signal strength valid for the imposed assumptions and applicable to combustion experiments in which the assumptions hold.

A more complex model is required to describe cw or saturated experiments where collisional processes and spontaneous emission become significant. The two level model above assumes the populations of any pair of optically coupled Zeeman states, (J,M) and (J',M') for the pumped transition or (J,M) and (J",M") for the probed transition, may be described independently. For significant collisional population transfer rates, all upper and lower Zeeman state populations are linked to each other and to the available quantum states of the molecule. As the two-level model is no longer applicable, it is unlikely that the expressions of Teets, Kowalski, Kill, Carlson and Hansch provide an accurate depiction of the dependence of cw or saturated polarisation spectroscopy on collisional processes.

However, the theory of Teets, Kowalski, Hill, Carlson and Hansch provides a strong theoretical method for description of polarisation spectroscopy. There is room for both extension of the geometrical limits of application beyond purely collinear pump/probe configurations and improvement of the two-level rate equation description of the pump and probe transition populations. Numerical models, both rate equation and density matrix approaches, may be added to the theory. However, this thesis does not attempt to model the Zeeman state populations, which will be highly dependent on the experimental conditions, focussing instead on the independent geometrical parameters of polarisation spectroscopy.

In Chapters II and IV of this thesis, a geometrical/optical parameter model is developed to describe the most general geometry of pump and probe beam intersection angles and their respective polarisation directions. The model is developed based on the theory of an uniaxial gas in the case of a linearly polarised pump beam and in terms of an optically active uniaxial gas in the case of a circularly polarised pump beam. Chapters III and V present experimental verification, via imaging of the hydroxyl radical in a premixed natural gas/O_2 flame, of the predicted non-zero signal strength at orthogonal pump/probe beam intersection for polarisation configurations specified in Chapters II and IV.

Due to the ease with which the population description and the geometrical/optical parameter modelling of the propagation of the probe beam can be separated in Teets, Kowalski, Hill, Carlson and Hansch's theory as shown in this chapter, the geometrical model developed in the following chapters can be considered independently of the population model and can be combined, as required, with comprehensive population descriptions matching experimental conditions.

Chapter II: Uniaxial Gas Model of Polarisation Spectroscopy: Linearly Polarised Pump Beam

The polarisation spectroscopy descriptions of Wieman and Hansch[2] and Teets, Kowalski, Hill, Carlson and Hansch[1] are applicable to co- or counter-propagating pump/probe beam geometries. For each of these cases, the probe beam is assumed to be equally composed of polarisation components parallel and perpendicular to the pump beam polarisation direction. In the case of a linearly polarised pump beam, the polarisation direction is orthogonal to the direction of propagation and the probe beam polarisation components are also linearly polarised. The probe beam components are subject to the pump induced birefringence and dichroism and recombine, after passing through the pumped region, into a slightly different polarisation state to that of the original probe beam. Crossed polarisers placed in the probe beam path enclosing the pumped region are used to detect the small polarisation change.

In the non-collinear geometry required for polarisation spectroscopy imaging, the polarisation of the pump beam introduces a directional anisotropy, which will be reflected in the induced dichroism and birefringence. **It is an obvious extension to the existing theory to describe the behaviour of the region of induced birefringence and dichroism as analogous to that of a uniaxial crystal or fluid.** The induced dichroism is then obtained from the induced birefringence via the Kramers-Kronig relations.

Two significant descriptions of the geometrical dependence of the LPS signal for a linearly polarised pump beam appear in the literature. Nyholm, Fritzon and Alden[3] experimentally determined a $\cot^2(\chi)$ dependence of signal on the intersection angle, χ, of pump and probe beams. The geometrical dependence was attributed to *"geometrical effects, i.e., the changes in the probe volume and in the projection of the pump beam polarization on the probe beam polarization"*[3]. The experimental configuration in this case involved a horizontally polarised pump beam and a probe beam polarised at $\pi/4$ to the pump polarisation. The two beams intersected in the horizontal plane. Experimental measurements were taken to a maximum beam intersection angle of 55°.

A large factor in the geometrical dependence of PLPS signal strength is the change in the probe volume due to the very short pump/probe interaction length (as measured along the probe beam path). The LPS signal for perfectly crossed probe beam polarisers and no inter-polariser birefringent elements, defined in equation [16] of Chapter I, is quadratically dependent on the interaction length, L, between pump and probe beams as measured along the probe beam path. The interaction length, $L(\chi)$, represents the probe beam path length in the region of induced dichroism and birefringence. For collinear pump/probe beam geometries in spectroscopic applications, the interaction length may be quite long. However for imaging applications, the thickness of the pump sheet defines interaction length and hence the resultant spatial resolution. Figure 1 shows the interaction length is given by

$$L(\chi) = \frac{W}{|\sin(\chi)|} \qquad \text{Equation 1}$$

where

χ is the pump/probe beam angle of intersection measured from the direction of travel of the probe beam as shown in Figure 2.

W is the width of the pump beam, and

$|\sin(\chi)|$ is the magnitude of the required sine function.

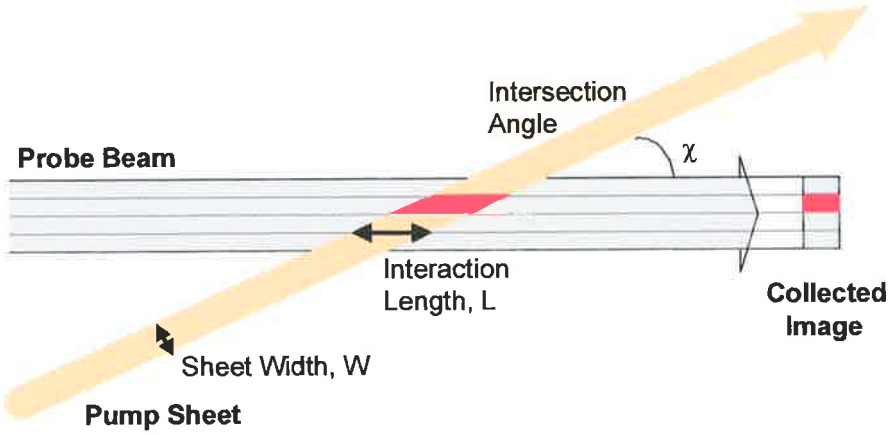

Figure 1: Interaction length, L, as a function of the pump/probe beam-crossing angle, χ.

The factor, $L(\chi)$, approaches infinity for near zero pump/probe beam intersection angles, leading to large signal due to the relatively large pump/probe interaction length. Nyholm's $\cot^2(\chi)$ dependence of signal strength implied that a orthogonal pump/probe geometry would give zero signal, and the dramatic falloff in detected signal with increasing beam intersection angle would limit the practical application of polarisation spectroscopy imaging to small beam intersection angles, with a resulting low image resolution (proportional to the factor, $\sin(\chi)$) in the direction parallel to the beam intersection plane.

However, Lavrinenko and Gancheryonok[5], recently proposed a more general solution to the geometrical dependence. Their theory developed expressions for the signal dependence on the pump/probe beam intersection angle, χ, and the polarisation directions of each beam in terms of the dielectric tensor and the projection and normal of the probe beam polarisation axis onto the pump beam polarisation axis assuming quasi-monochromatic waves. Their expression for the geometric dependence is given below in terms of the polarisation and propagation angles defined in Figure 2.

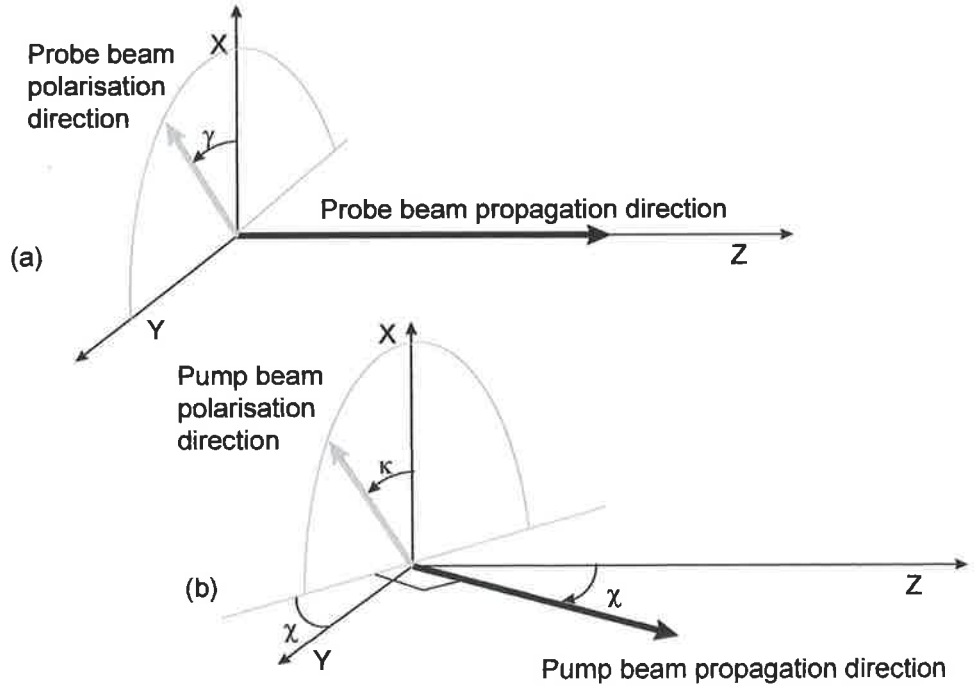

Figure 2: (a) Probe and (b) pump beam axis systems. The pump/probe beam intersection angle is, χ, the angle of the probe beam polarisation from the normal to the pump/probe beam intersection plane, γ, and the angle of the pump beam polarisation axis from the normal to the pump/probe beam intersection plane, κ.

The expression for the signal strength derived by Lavrinenko and Gancheryonok rewritten in terms of the angles, χ, γ and κ, defined above is

$$I_{L\&G} = K \; I^2 \; \frac{(C_1 + C_2)^2}{4} \cdot \left(\sin(2\gamma) \cdot \frac{(\sin^2(\kappa) \cdot \cos^2(\chi) - \cos^2(\kappa))}{\sin(\chi)} + \sin(2\kappa) \cdot \cos(2\gamma) \cdot \cot(\chi) \right)^2$$

Equation 2

where

$$K = \frac{9}{16} \left(\frac{\omega_{probe}}{c \cdot n_{probe}} \right)^2 |\chi_{1221}|^2 |E_{probe}|^2 |E_{pump}|^4$$

$$C_1 = \frac{\chi_{1122}}{\chi_{1221}}$$

$$C_2 = \frac{\chi_{1212}}{\chi_{1221}}$$

I is the width of the pumping beam,

n_{probe} is the refractive index of the medium at the probe frequency, ω_{probe}, and

χ_{ijkl} are the elements of the third-order tensor of non-linear susceptibility.

This equation predicts a $\cot^2(\chi)\cos^2(\chi)$ dependence of signal strength for the experimental configuration of Nyholm, Fritzon and Alden. The deviation between Lavrinenko and Gancheryonok's $\cot^2(\chi)\cos^2(\chi)$ dependence and Nyholm's $\cot^2(\chi)$ fit to experimental data is small and Lavrinenko and Gancheryonok suggested that the difference may be due to experimental error. Lavrinenko and Gancheryonok noted that the absence of error bars on Nyholm's data precluded a definite conclusion on the correctness of the theory although the data points showed very little deviation from the fitted $\cot^2(\chi)$ curve.

Note also that Lavrinenko and Gancheryonok's signal strength predicts a $\mathrm{cosec}^2(\chi)$ dependence for a pump beam polarised normal to the plane of intersection (with probe beam polarised at $\pi/4$ to the pump beam polarisation direction). This was the first prediction of non-zero signal for orthogonal beam intersection, raising the possibility of polarisation spectroscopy imaging for all beam intersection angles.

The derivation in this chapter and that in Chapter IV for a circularly polarised pump beam are similar to that of Lavrinenko and Gancheryonok although developed independently. However, in this model, great care is taken in defining the characteristic modes of propagation for the uniaxial gas in terms of the induced optic axis defined by the pump beam polarisation. The major differences between the two models lie in the specific statement of the geometric dependence of the induced birefringence on the direction of propagation of the probe beam with respect to the optic axis and in the identification the orthogonal vectors representing the characteristic modes of propagation through the medium.

These geometric dependence of the LPS signal may be separated into two factors[a];

- the previously described cosec(χ) dependence of the pump/probe interaction length, L(χ), and
- the pump induced ellipticity in the probe beam due to its passage through the region of induced birefringence and dichroism.

We now proceed to derive expressions for the geometric dependence of the birefringence and dichroism induced ellipticity in the probe beam by applying an analogue of the uniaxial crystal model of birefringence and dichroism, which in combination with the cosec(χ) dependence of the pump/probe interaction length, L(χ), gives the full geometric dependence of the LPS signal.

Uniaxial Description of the Induced Birefringence and Dichroism: Linearly Polarised Pump Beam

Polarisation spectroscopy relies on an optically induced birefringence and dichroism to create an environment which is anisotropic to the two polarisation components that comprise the probe beam.

Consider first the case of a co- or counter-propagating geometry. The polarisation probe beam may be envisioned as two orthogonal components polarised parallel and perpendicular to the pump beam polarisation. The magnitude of the component, $\underline{P}_{\parallel}(\chi,\gamma,\kappa)$, of the probe beam electric field which is parallel to the pump beam polarisation is given by the inner product of the electric vector of the probe beam, $\underline{E}_{probe}$, and the unit electric vector of the pump beam, $\hat{\underline{E}}_{pump}$. In notation, an underline has been used to represent a vector and an overscore a unit vector.

$$\underline{P}_{\parallel} = \left(\underline{E}_{probe} \cdot \hat{\underline{E}}_{pump}\right) \cdot \hat{\underline{E}}_{pump} \qquad \text{Equation 3}$$

Similarly, the magnitude of the perpendicular component of the probe beam electric field $\underline{Q}_{\perp}(\chi,\gamma,\kappa)$, is given by the inner product of the probe beam electric vector, $\underline{E}_{probe}$, and the unit pump vector in the electric field plane of the pump beam and perpendicular to the pump beam electric vector which we denote as $\hat{\underline{E}}_{pump\_\perp}$.

$$\underline{Q}_{\perp} = \left(\underline{E}_{probe} \cdot \hat{\underline{E}}_{pump\_\perp}\right) \cdot \hat{\underline{E}}_{pump\_\perp} \qquad \text{Equation 4}$$

[a] The geometric dependence of polarisation spectroscopy's selectivity of velocity population subsets for laser systems with linewidths narrower than the Doppler width is not considered in this chapter, but is discussed in Addendum 1.

The probe beam electric field transmitted through the primary probe beam polariser may then be written as

$$\underline{E}_{probe} = \underline{P}_{\parallel} + \underline{Q}_{\perp} \qquad \text{Equation 5}$$

Both parallel and perpendicular components may be complex if the polarisation of the pump beam is represented by a complex vector[b] as in the case of a circularly polarised pump beam.

Each component is subject to the action of polarisation-dependent absorption and dispersion over the interaction length, $\Lambda(\chi)$, of the probe beam path and the region of induced anisotropy. The transmitted electric field is then given by

$$\underline{E}_{\substack{probe \\ transmitted}}(\Lambda) = \underline{P}_{\parallel}(\chi,\gamma,\kappa)\cdot e^{-\frac{\alpha_{\parallel}\cdot\Lambda}{2}}\cdot e^{-i\cdot k_{\parallel}\cdot\Lambda} + \underline{Q}_{\parallel}(\chi,\gamma,\kappa)\cdot e^{-\frac{\alpha_{\perp}\cdot\Lambda}{2}}\cdot e^{-i\cdot k_{\perp}\cdot\Lambda} \qquad \text{Equation 6}$$

giving rise to the induced ellipticity in the electric field of the originally linearly polarised probe beam described in equation [4]. Here, $\alpha_{\parallel}$ and $\alpha_{\perp}$ are the absorption coefficients for the probe beam components polarised parallel and perpendicular to the pump beam polarisation respectively. The terms, $k_{\parallel}$ and $k_{\perp}$, represent the magnitudes of the equivalent wavevectors for the two probe beam components.

The methodology above is suitable for a collinear pump/probe geometry. However, non-collinear geometries require a more complex description. The simplest model to account for the induced

[b] Note that care must be taken in the calculation of inner products of complex vectors as the operation is not multiplicatively commutative, i.e. the order of the two vectors is not interchangeable (See Appendix III). The convention used in this thesis is that the inner product of two complex vectors,

$\underline{c} = \begin{pmatrix} c_1 \\ c_2 \\ c_3 \end{pmatrix}$ and $\underline{d} = \begin{pmatrix} d_1 \\ d_2 \\ d_3 \end{pmatrix}$, is given by

$$\underline{c}.\underline{d} = c_1\cdot(d_1)^* + c_2\cdot(d_2)^* + c_3\cdot(d_3)^* \qquad \text{Equation b.1}$$

In addition, to decompose a vector, $\underline{k} = \begin{pmatrix} k_1 \\ k_2 \\ k_3 \end{pmatrix}$, into components parallel to a basis set of orthogonal unit vectors, $\hat{g}, \hat{h}, \ldots$, the order sensitive equation is used

$$\underline{k} = (\hat{g}.\underline{k})\hat{g} + (\hat{h}.\underline{k})\hat{h} + \ldots \qquad \text{Equation b.2}$$

birefringence and dichroism in the case of a linearly polarised pump beam is that of a uniaxial gas. The collinear solution above becomes a special case of the uniaxial gas model for propagation normal to the pump beam induced optic axis[c].

We assume that the polarisation axis of the pump beam defines an optic axis. A weak probe beam will then propagate within the birefringent and dichroic medium via two polarisation modes defined by the direction of propagation of the probe beam with respect to the optic axis. Collett[22] provides a good introduction to the theory of uniaxial crystals which may be equivalently applied to a uniaxial gas or fluid. Collett's derivation of the behaviour of a (non-optically active[d]) uniaxial crystal will be applied below to a uniaxial gas and is repeated here for those not familiar with the theory. The model below is a direct application of Collett's uniaxial crystal model applied to the geometry defined by the polarisation states of the pump and probe beams and their intersection angle where the polarisation direction of the pump beam is assumed to define the optic axis of the uniaxial gas.

The propagation of light in a uniaxial gas or crystal is defined by Maxwell's equations.

$$\nabla X \underline{H} = \frac{4\pi}{c}\underline{j} + \frac{1}{c}\frac{\partial \underline{D}}{\partial t} \qquad \text{Equation 7}$$

$$\nabla X \underline{E} = -\frac{1}{c}\frac{\partial \underline{B}}{\partial t} \qquad \text{Equation 8}$$

$$\nabla . \underline{D} = 4\pi\rho \qquad \text{Equation 9}$$

$$\nabla . \underline{B} = 0 \qquad \text{Equation 10}$$

where H is the magnetic field strength, B is the magnetic flux density, D is the magnitude of the displacement vector, E is the electric field strength, j is the current density, and ρ is the charge density.

In the absence of currents or free charges, these reduce to

[c] As the angle dependence of the velocity selectivity of Doppler population subsets (which must be considered for narrow linewidth experiments) has not been considered in this chapter, the pump beam polarisation direction defines the optic axis, and the propagation direction of the pump beam with respect to the probe beam is ignored.

[d] Optical activity: A crystal is optically active if it acts to rotate the plane of polarisation of a linearly polarised beam on transmission through the crystal. The angle of rotation is proportional to the distance travelled through the crystal. The optical activity is based on a circular birefringence to the two characteristic circularly polarised modes of propagation within the crystal.

$$\nabla X\underline{H} = \frac{1}{c}\frac{\partial \underline{D}}{\partial t} \qquad \text{Equation 11}$$

$$\nabla X\underline{E} = -\frac{1}{c}\frac{\partial \underline{B}}{\partial t} \qquad \text{Equation 12}$$

$$\nabla.\underline{D} = 0 \qquad \text{Equation 13}$$

$$\nabla.\underline{B} = 0 \qquad \text{Equation 14}$$

For plane wave solutions of the form, $e^{i(\underline{k}.\underline{r}-\omega t)}$, the operators, ∇ and $\partial/\partial t$, may be replaced by the terms, $i\underline{k}$ and $i\omega$, respectively. equations [10] to [13] become

$$\underline{k}X\underline{H} = \frac{\omega}{c}\underline{D} \qquad \text{Equation 15}$$

$$\underline{k}X\underline{E} = -\frac{\omega}{c}\underline{B} \qquad \text{Equation 16}$$

$$\underline{k}.\underline{D} = 0 \qquad \text{Equation 17}$$

$$\underline{k}.\underline{B} = 0 \qquad \text{Equation 18}$$

We operate from the left on equation [15] by $\underline{k}$ X to obtain

$$\underline{k}X(\underline{k}X\underline{E}) = -\frac{\omega}{c}(\underline{k}X\underline{B}) = -\frac{\omega}{c}(\frac{\underline{k}X\underline{H}}{\mu}) = -\left(\frac{\omega}{c}\right)^2\frac{\underline{D}}{\mu} = -\frac{k_0^2}{\mu}\underline{D} \qquad \text{Equation 19}$$

This equation may be expanded using the vector identity,

$$\underline{a}X(\underline{b}X\underline{c}) = \underline{b}(\underline{a}.\underline{c}) - \underline{c}(\underline{a}.\underline{b}) \qquad \text{Equation 20}$$

to become

$$k^2\underline{E} - \underline{k}(\underline{k}.\underline{E}) = -\frac{k_0^2}{\mu}\underline{D} \qquad \text{Equation 21}$$

The electric vector is related to the displacement vector by the susceptibility tensor, ε, according to the equation

$$\begin{pmatrix} D_x \\ D_y \\ D_z \end{pmatrix} = \begin{pmatrix} \varepsilon_{11} & \varepsilon_{12} & \varepsilon_{13} \\ \varepsilon_{21} & \varepsilon_{22} & \varepsilon_{23} \\ \varepsilon_{31} & \varepsilon_{32} & \varepsilon_{33} \end{pmatrix}\begin{pmatrix} E_x \\ E_y \\ E_z \end{pmatrix} \qquad \text{Equation 22}$$

For a non-optically active gas (or crystal), the matrix may be diagonalised for a selected system of axes so that the off-diagonal elements are zero, and the diagonal elements are real and related to the principal dielectric constants of the medium.

$$\begin{pmatrix} D_x \\ D_y \\ D_z \end{pmatrix} = \begin{pmatrix} \varepsilon_x & 0 & 0 \\ 0 & \varepsilon_y & 0 \\ 0 & 0 & \varepsilon_z \end{pmatrix} \begin{pmatrix} E_x \\ E_y \\ E_z \end{pmatrix} = \begin{pmatrix} n_x^2 & 0 & 0 \\ 0 & n_y^2 & 0 \\ 0 & 0 & n_z^2 \end{pmatrix} \begin{pmatrix} E_x \\ E_y \\ E_z \end{pmatrix} \qquad \text{Equation 23}$$

The set of axes that satisfy this equation is called the principal axis system of the gas. In a uniaxial gas, the properties of light propagation are symmetric around the optic axis. Propagation parallel to the optic axis is independent of the polarisation state.

If we arbitrarily choose the Z' principal axis as the optic axis, we may rename the principal dielectric constants as

$$\begin{aligned} n_x &= n_y = n_o \\ n_z &= n_e \neq n_o \end{aligned} \qquad \text{Equation 24}$$

where the subscripts, o and e, represent the terms, ordinary and extraordinary and equation [23] may be written as

$$\begin{pmatrix} D_x \\ D_y \\ D_z \end{pmatrix} = \begin{pmatrix} n_o^2 & 0 & 0 \\ 0 & n_o^2 & 0 \\ 0 & 0 & n_e^2 \end{pmatrix} \begin{pmatrix} E_x \\ E_y \\ E_z \end{pmatrix} \qquad \text{Equation 25}$$

We are now in a position to solve equation [21]. By choosing a propagation direction in the X'Z' plane with respect to the principal axes of the uniaxial gas, at an angle, φ, to the optic axis, the wavevector, $\underline{k}$, may be written as

$$\underline{k} = \begin{pmatrix} k \cdot \sin(\varphi) \\ 0 \\ k \cdot \cos(\varphi) \end{pmatrix} \qquad \text{Equation 26}$$

Substitution of equations [25] and [26] into equation [21] produces three simultaneous equations with variables, the three components of the electric vector.

$$\begin{pmatrix} k^2 \cdot \cos^2(\varphi) + \dfrac{k_0^2 \cdot n_o^2}{\mu} & 0 & -k^2 \cdot \sin(\varphi)\cos(\varphi) \\ 0 & k^2 + \dfrac{k_0^2 \cdot n_o^2}{\mu} & 0 \\ -k^2 \cdot \sin(\varphi)\cos(\varphi) & 0 & k^2 \cdot \sin^2(\varphi) + \dfrac{k_0^2 \cdot n_e^2}{\mu} \end{pmatrix} \cdot \begin{pmatrix} E_x \\ E_y \\ E_z \end{pmatrix} = 0 \qquad \text{Equation 27}$$

A non-trivial solution to the modes of propagation characteristic of the uniaxial gas requires the determinant of the matrix on the left-hand side of equation [27 above] to be zero, giving the condition

$$\left(k^2 - \frac{k_0^2}{\mu}\cdot n_o^2\right)\cdot\left(k^2\cdot\sin^2(\varphi)\cdot n_o^2 + k^2\cdot\cos^2(\varphi)\cdot n_e^2 - \frac{k_0^2}{\mu}\cdot n_o^2\cdot n_e^2\right) = 0 \qquad \text{Equation 28}$$

This equation describes two solutions. Taking μ as unity, the ordinary solution

$$k^2 = k_0^2\cdot n_o^2 \qquad \text{Equation 29}$$

propagates as a spherical wave subject to the ordinary refractive index, n_o. The second, termed the extraordinary solution,

$$k^2 = k_0^2\cdot\frac{1}{\left(\frac{\sin^2(\varphi)}{n_e^2} + \frac{\cos^2(\varphi)}{n_o^2}\right)} = \frac{k_0^2}{\mu}\cdot\frac{n_o^2\cdot n_e^2}{n_o^2\sin^2(\varphi) + n_e^2\cos^2(\varphi)} \qquad \text{Equation 30}$$

propagates as an ellipsoidal wave, with wavevector, and hence velocity, a function of the direction of propagation. For propagation along the optic axis, $\varphi = 0$, the extraordinary ray travels at the same velocity as the ordinary ray. For propagation normal to the optic axis, $\varphi = \pi/2$, the extraordinary ray is governed purely by the extraordinary refractive index, n_e, while the ordinary ray is governed by the ordinary refractive index, n_o.

The birefringence, or difference in refractive indices, for propagation at the angle, φ, to the optic axis, ranges between 0 for propagation along the optic axis to a maximum of $n_e - n_o$ for propagation normal to the optic axis. It can be seen from equation [30] that the extraordinary ray refractive index, $n_e(\varphi)$, is described by

$$n_e^2(\varphi) = \frac{n_o^2\cdot n_e^2}{n_o^2\sin^2(\varphi) + n_e^2\cos^2(\varphi)} \qquad \text{Equation 31}$$

We can then define the angular dependence of the birefringence as

$$n_e(\varphi) - n_o = \left(\sqrt{\frac{n_e^2}{n_o^2\sin^2(\varphi) + n_e^2\cos^2(\varphi)}} - 1\right)\cdot n_o \qquad \text{Equation 32}$$

The equations above represent the standard theory of light propagation in a uniaxial crystal as described by Collett, here applied to a gas with an induced optic axis defined as the polarisation axis of the pump beam. From the basis of this description, we proceed to apply the uniaxial model to polarisation spectroscopy. The methodology is to identify the small induced birefringence and the

ordinary and extraordinary polarisation axes in the frame describing the experiment, before applying absorptive and dispersive terms to the orthogonal probe beam components in the usual way.

If we assume that the induced dichroism and birefringence is small, so that we may write

$$n_e = n_{av} + \frac{\Delta n}{2} \qquad \text{Equation 33}$$

and

$$n_o = n_{av} - \frac{\Delta n}{2} \qquad \text{Equation 34}$$

Equation [32] , describing the induced linear birefringence may be approximated to first order (See Appendix IV) as

$$n_e(\varphi) - n_o = \sin^2(\varphi)\cdot(n_e - n_o) \qquad \text{Equation 35}$$

The ordinary ray and the extraordinary ray are distinguished by polarisation state. Substitution of the ordinary solution of equation [29] into the matrix equation [27] produces the (standard theory) ordinary polarisation vector

$$\underline{E}_{ordinary} = \begin{pmatrix} 0 \\ 1 \\ 0 \end{pmatrix} \qquad \text{Equation 36}$$

in the principal axes frame, while the (standard theory) extraordinary polarisation vector is similarly obtained;

$$\underline{E}_{extraordinary} = \begin{pmatrix} n_e^2 \cdot k_z \\ 0 \\ -n_o^2 \cdot k_x \end{pmatrix} = \begin{pmatrix} n_e^2 \cdot k \cdot \cos(\varphi) \\ 0 \\ -n_o^2 \cdot k \cdot \sin(\varphi) \end{pmatrix} \qquad \text{Equation 37}$$

For a small induced birefringence, $n_e \sim n_o$, equation [37] approximates an electric field lying in the X'Z' principal plane and normal to the direction of propagation defined in equation [26], i.e.

$$\hat{\underline{E}}_{extraordinary\_approx} = \begin{pmatrix} \cos(\varphi) \\ 0 \\ -\sin(\varphi) \end{pmatrix} \qquad \text{Equation 38}$$

The ordinary and extraordinary polarisation directions may then be described by vectors normal to the direction of propagation of the probe beam, so that a probe beam propagating at the angle, φ, to the optic axis be decomposed into

(i) an ordinary component polarised parallel to the Y' principal axis, $\underline{P}_{ordinary}$,

(ii) and an extraordinary component, $\underline{Q}_{extraordinary}$ lying in the X'Z' principal plane.

Equation [5], representing the electric field of the probe beam transmitted through the primary probe beam polariser, may then be re-expressed as

$$\underline{E}_{probe} = \underline{P}_{ordinary} + \underline{Q}_{extraordinary} \qquad \text{Equation 39}$$

where

$$\underline{P}_{ordinary} = \left(\underline{E}_{probe} \cdot \hat{\underline{E}}_{ordinary}\right) \cdot \hat{\underline{E}}_{ordinary} \qquad \text{Equation 40}$$

and

$$\underline{Q}_{ordinary} = \left(\underline{E}_{probe} \cdot \hat{\underline{E}}_{extraordinary}\right) \cdot \hat{\underline{E}}_{extraordinary} \qquad \text{Equation 41}$$

After passing a distance, Λ, through the region of birefringence and dichroism, the electric field is

$$\underline{E}_{probe_{transmitted}}(\Lambda) = \underline{P}_{ordinary} \cdot e^{-\frac{\alpha_o}{2}\Lambda} \cdot e^{ik_o\Lambda} + \underline{Q}_{extraordinary} \cdot e^{-\frac{\alpha_e}{2}\Lambda} \cdot e^{ik_e\Lambda} \qquad \text{Equation 42}$$

The transmitted probe beam electric field transmitted after passing through an (assumed perfect) analysing polariser aligned with transmission axis, $\hat{\underline{R}}_{analyser}$, orthogonal to the transmission axis of the primary probe beam polariser, is then given by

$$\underline{E}_{probe_{transmitted\_through\_analyser}}(\Lambda) = \begin{pmatrix} \underline{P}_{ordinary} \cdot \hat{\underline{R}}_{analyser} \cdot e^{-\frac{\alpha_o}{2}\Lambda} \cdot e^{ik_o\Lambda} \\ +\underline{Q}_{extraordinary} \cdot \hat{\underline{R}}_{analyser} \cdot e^{-\frac{\alpha_e}{2}\Lambda} \cdot e^{ik_e\Lambda} \end{pmatrix} \qquad \text{Equation 43}$$

or

$$\underline{E}_{probe_{transmitted\_through\_analyser}}(\Lambda) = \begin{pmatrix} \left(\underline{E}_{probe} \cdot \hat{\underline{E}}_{ordinary}\right) \cdot \left(\hat{\underline{E}}_{ordinary} \cdot \hat{\underline{R}}_{analyser}\right) \cdot e^{-\frac{\alpha_o}{2}\Lambda} \cdot e^{ik_o\Lambda} \\ +\left(\underline{E}_{probe} \cdot \hat{\underline{E}}_{extraordinary}\right) \cdot \left(\hat{\underline{E}}_{extraordinary} \cdot \hat{\underline{R}}_{analyser}\right) \cdot e^{-\frac{\alpha_e}{2}\Lambda} \cdot e^{ik_e\Lambda} \end{pmatrix}$$

Equation 44

where the absorption coefficients and dispersive terms in equations [42] to [44] are those experienced by the probe beam propagating at the angle, φ, with respect to the induced optic axis.

Writing

$$\alpha_o = \alpha_{av} + \frac{\Delta\alpha}{2} \qquad \text{Equation 45}$$

$$\alpha_e = \alpha_{av} - \frac{\Delta\alpha}{2} \qquad \text{Equation 46}$$

and

$$k_o = k_{av} + \frac{\Delta k}{2} \qquad \text{Equation 47}$$

$$k_e = k_{av} - \frac{\Delta k}{2} \qquad \text{Equation 48}$$

and introducing the terms

$$f = \left(\hat{\underline{E}}_{probe} \cdot \hat{\underline{E}}_{ordinary}\right) \cdot \left(\hat{\underline{E}}_{ordinary} \cdot \hat{\underline{R}}_{analyser}\right) \qquad \text{Equation 49}$$

and

$$g = \left(\hat{\underline{E}}_{probe} \cdot \hat{\underline{E}}_{extraordinary}\right) \cdot \left(\hat{\underline{E}}_{extraordinary} \cdot \hat{\underline{R}}_{analyser}\right) \qquad \text{Equation 50}$$

equation [44] becomes

$$\frac{\underline{E}_{probe\_transmitted\_through\_analyser}(\Lambda)}{E_{probe\_0}} = \left(f \cdot e^{-i\frac{\Delta\alpha}{4}\Lambda} \cdot e^{i\frac{\Delta k}{2}\Lambda} + g \cdot e^{i\frac{\Delta\alpha}{4}\Lambda} \cdot e^{-i\frac{\Delta k}{2}\Lambda}\right) \cdot e^{-i\frac{\alpha_{av}}{2}\Lambda} \cdot e^{ik_{av}\Lambda} \qquad \text{Equation 51}$$

where E_{probe_0} is the magnitude of the electric field of the probe beam incident on the primary polariser. The transmitted electric field may be calculated from equation [51] once the geometry of the principal axes of the uniaxial gas are defined in the co-ordinate system of the probe beam.

We define a set of system axes based on the probe beam path as shown in Figure 2. The Z axis corresponds to the direction of propagation of the probe beam. The X axis is vertical. The pump and probe beams intersect in the horizontal YZ plane. We define the probe beam polarisation direction to lie at an angle, γ, to the vertical X axis in the usual sense with respect to the XYZ axes.

The electric field of the probe beam is

$$\underline{E}_{probe} = E_{probe\_0} \cdot \begin{pmatrix} \cos(\gamma) \\ \sin(\gamma) \\ 0 \end{pmatrix} \qquad \text{Equation 52}$$

The linearly polarised pump beam propagates at an angle, χ, from the Z axis, with the sense of the rotation towards the positive Y axis. The polarisation direction lies at the angle, κ, to the vertical X axis in the usual sense of rotation for a right-handed set of axes defined as X' = the vertical X axis,

Y' = the Y axis component of the polarisation direction and Z' is the direction of propagation of the pump beam. The pump beam electric field, which represents the induced optic axis of the uniaxial medium, is parallel to the unit vector,

$$\hat{\underline{E}}_{optic\_axis} = \begin{pmatrix} \cos(\kappa) \\ \sin(\kappa)\cdot\cos(\chi) \\ -\sin(\kappa)\cdot\sin(\chi) \end{pmatrix} \qquad \text{Equation 53}$$

Projecting an elliptical cross-section, with the optic axis defined in equation [53] as major axis, through the origin to visualise the principal section, it can be seen that the ordinary ray polarisation which lies normal to the principal section lies perpendicular to

$$\hat{\underline{E}}_{extraordinary} = \frac{\begin{pmatrix} \cos(\kappa) \\ \sin(\kappa)\cdot\cos(\chi) \\ 0 \end{pmatrix}}{\sqrt{\cos^2(\kappa)+\sin^2(\kappa)\cdot\cos^2(\chi)}} \qquad \text{Equation 54}$$

and must lie in the electric field plane of the probe beam, giving

$$\hat{\underline{E}}_{ordinary} = \frac{\begin{pmatrix} -\sin(\kappa)\cdot\cos(\chi) \\ \cos(\kappa) \\ 0 \end{pmatrix}}{\sqrt{\cos^2(\kappa)+\sin^2(\kappa)\cdot\cos^2(\chi)}} \qquad \text{Equation 55}$$

Assuming the probe beam is initially parallel to the transmission axis of the primary polariser, and the case of perfectly crossed polarisers, the transmission axis of the analyser lies parallel to the unit vector

$$\hat{\underline{R}}_{analyser} = \begin{pmatrix} -\sin(\gamma) \\ \cos(\gamma) \\ 0 \end{pmatrix} \qquad \text{Equation 56}$$

We may now calculate the terms, f and g, defined in equations [49] and [50] as

$$f = -g = \frac{1}{2} \cdot \frac{\sin(2\gamma)\cdot\left(\cos^2(\kappa) - \sin^2(\kappa)\cdot\cos^2(\chi)\right) - \cos(2\gamma)\cdot\sin(2\kappa)\cdot\cos(\chi)}{\cos^2(\kappa) + \sin^2(\kappa)\cdot\cos^2(\chi)} \qquad \text{Equation 57}$$

or, rewriting this in terms that will easily be cancelled in later calculations,

$$f = -g = \frac{1}{2} \cdot \frac{\sin(2\gamma)\cdot\left(\cos^2(\kappa) - \sin^2(\kappa)\cdot\cos^2(\chi)\right) - \cos(2\gamma)\cdot\sin(2\kappa)\cdot\cos(\chi)}{1 - \sin^2(\kappa)\cdot\sin^2(\chi)} \qquad \text{Equation 58}$$

The transmitted probe beam electric field is then

$$\frac{E_{\substack{probe \\ transmitted\_through\_analyser}}(\Lambda)}{E_{probe\_0}} = f \cdot \left(e^{-\frac{\Delta\alpha}{4}\Lambda} \cdot e^{i\frac{\Delta k}{2}\Lambda} - e^{\frac{\Delta\alpha}{4}\Lambda} \cdot e^{-i\frac{\Delta k}{2}\Lambda} \right) \cdot e^{-\frac{\alpha_{av}}{2}\cdot\Lambda} \cdot e^{ik_{av}\Lambda} \qquad \text{Equation 59}$$

which may be rewritten as

$$\frac{E_{\substack{probe \\ transmitted\_through\_analyser}}(\Lambda)}{E_{probe\_0}} = f \cdot \left(e^{i(\frac{\Delta k}{2} + i\frac{\Delta\alpha}{4})\cdot\Lambda} - e^{-i(\frac{\Delta k}{2} + i\frac{\Delta\alpha}{4})\Lambda} \right) \cdot e^{-\frac{\alpha_{av}}{2}\Lambda} \cdot e^{ik_{av}\Lambda} \qquad \text{Equation 60}$$

or

$$\frac{E_{\substack{probe \\ transmitted\_through\_analyser}}(\Lambda)}{E_{probe\_0}} = 2\cdot i\cdot f\cdot \sin\left(\frac{\Delta k}{2}\cdot\Lambda + i\cdot\frac{\Delta\alpha}{4}\cdot\Lambda\right)\cdot e^{-\frac{\alpha_{av}}{2}\Lambda}\cdot e^{ik_{av}\Lambda} \qquad \text{Equation 61}$$

with transmitted probe beam intensity given by

$$\frac{I_{\substack{probe \\ transmitted\_through\_analyser}}(\Lambda)}{I_{probe\_0}} = (2\cdot f)^2 \cdot \sin^2\left(\frac{\Delta k}{2}\cdot\Lambda + i\cdot\frac{\Delta\alpha}{4}\cdot\Lambda\right)\cdot e^{-\alpha_{av}\cdot\Lambda} \qquad \text{Equation 62}$$

Remembering that the induced dichroism and birefringence in this expression are those experienced by the probe beam propagating at the angle, φ, to the induced optic axis, this should be more accurately written as

$$\frac{I_{\substack{probe \\ transmitted\_through\_analyser}}(\Lambda)}{I_{probe\_0}} = (2\cdot f)^2 \cdot \sin^2\left(\frac{\Delta k(\varphi)}{2}\cdot\Lambda + i\cdot\frac{\Delta\alpha(\varphi)}{4}\cdot\Lambda\right)\cdot e^{-\alpha_{av}\cdot\Lambda} \qquad \text{Equation 63}$$

For small induced dichroism and birefringence (and remembering that we have assumed perfectly crossed polarisers and no interpolariser birefringent optical elements in the probe beam path in the above derivation), this expression for the transmitted probe beam intensity may be approximated to second order by

$$\frac{I_{\substack{probe \\ transmitted\_through\_analyser}}(\Lambda)}{I_{probe\_0}} = (2\cdot f)^2 \cdot \left(\left(\frac{\Delta k(\varphi)}{2}\cdot\Lambda\right)^2 + \left(\frac{\Delta\alpha(\varphi)}{4}\cdot\Lambda\right)^2 \right)\cdot e^{-\alpha_{av}\cdot\Lambda} \qquad \text{Equation 64}$$

or, since

$$\Delta k = \Delta n \cdot \frac{\omega_0}{c} \qquad \text{Equation 65}$$

by

$$\frac{I_{probe\ transmitted\_through\_analyser}(\Lambda)}{I_{probe\_0}} = (2\cdot f)^2 \cdot \left(\left(\frac{\Delta n(\varphi)}{2} \cdot \frac{\omega_0}{c} \cdot \Lambda \right)^2 + \left(\frac{\Delta\alpha(\varphi)}{4} \cdot \Lambda \right)^2 \right) \cdot e^{-\alpha_{av}\cdot\Lambda} \qquad \text{Equation 66}$$

Remembering the Lorentzian dependence of the dichroism

$$\Delta\alpha = \Delta\alpha_0 \cdot \frac{1}{1+x^2} \qquad \text{Equation 67}$$

and the dispersive dependence of the birefringence, defined by the Kramers-Kronig relations in equation [9] of Chapter I,

$$\Delta n = -\frac{1}{2}\cdot\Delta\alpha_0 \cdot \frac{c}{\omega_0}\cdot\frac{x}{1+x^2} = -\Delta n_0 \cdot \frac{x}{1+x^2} \qquad \text{Equation 68}$$

equation [66] becomes

$$\frac{I_{probe\ transmitted\_through\_analyser}(\Lambda)}{I_{probe\_0}} = (2\cdot f)^2 \cdot \left(\left(-\frac{\Delta\alpha_0(\varphi)}{4} \cdot \frac{x}{1+x^2} \cdot \Lambda \right)^2 + \left(\frac{\Delta\alpha_0(\varphi)}{4} \cdot \frac{1}{1+x^2} \cdot \Lambda \right)^2 \right) \cdot e^{-\alpha_{av}\cdot\Lambda}$$

$$\frac{I_{probe\ transmitted\_through\_analyser}(\Lambda)}{I_{probe\_0}} = (2\cdot f)^2 \cdot \left(\left(\frac{\Delta\alpha_0(\varphi)}{4} \cdot \Lambda \right)^2 \cdot \left(\frac{1}{1+x^2} \right) \right) \cdot e^{-\alpha_{av}\cdot\Lambda} \qquad \text{Equation 69}$$

or, in terms of the linecentre induced birefringence as defined in equation [65],

$$\frac{I_{probe\ transmitted\_through\_analyser}(\Lambda)}{I_{probe\_0}} = (2\cdot f)^2 \cdot \left(\left(\frac{\Delta n_0(\varphi)}{2} \cdot \frac{\omega_0}{c} \cdot \Lambda \right)^2 \cdot \left(\frac{1}{1+x^2} \right) \right) \cdot e^{-\alpha_{av}\cdot\Lambda} \qquad \text{Equation 70}$$

For small induced birefringence in an optically thin gas, the refraction of the ordinary and extraordinary rays is insignificant, and the term, Λ, may be represented by the factor, $L(\chi)$, which is defined in equation [1]. We require only an expression for the sine of the angle, φ, between the optic axis and the direction of probe beam propagation to determine the geometric dependence of the transmitted probe beam intensity.

The cosine of the angle, φ, is obtained from the dot product

$$\cos(\varphi) = \hat{k}_{probe} \cdot \hat{E}_{optic\_axis} = \begin{pmatrix} 0 \\ 0 \\ 1 \end{pmatrix} \cdot \begin{pmatrix} \cos(\kappa) \\ \sin(\kappa)\cdot\cos(\chi) \\ -\sin(\kappa)\cdot\sin(\chi) \end{pmatrix} = -\sin(\kappa)\cdot\sin(\chi) \qquad \text{Equation 71}$$

so that equation [35] becomes

$$n_e(\chi) - n_o = (1-\sin^2(\kappa)\cdot\sin^2(\chi))\cdot(n_e - n_o) = G_{lin}(\kappa,\chi)\cdot(n_e - n_o) \qquad \text{Equation 72}$$

where the term, $G_{lin}\kappa,\chi)$, has been introduced to represent the geometric dependence of the induced birefringence.

Substitution of the derived expressions of equations [1], [58] and [72] into equation [70] gives the geometric dependence of the transmitted probe beam intensity for a linearly polarised pump beam.

$$\frac{I_{probe\ transmitted\_through\_analyser}^{(\Lambda)}}{I_{probe\_0}} = F_{lin}(\gamma,\kappa,\chi)\cdot G_{lin}(\kappa,\chi)^2 \cdot \left(\frac{(n_e - n_o)\cdot\omega_0\cdot L}{2\cdot c}\right)^2 \frac{1}{1+x^2}\cdot e^{-\alpha_{av}\cdot\Lambda} \qquad \text{Equation 73}$$

where the geometric dependence (aside from that implicit in the induced birefringence) has been consolidated into the factor, $F_{lin}(\gamma,\kappa,\chi)$[e],

$$F_{lin}(\gamma,\kappa,\chi) = \frac{\left(\sin(2\gamma)\cdot\left(\cos^2(\kappa)-\sin^2(\kappa)\cdot\cos^2(\chi)\right)-\cos(2\gamma)\cdot\sin(2\kappa)\cdot\cos(\chi)\right)^2}{\sin^2(\chi)\cdot(1-\sin^2(\kappa)\cdot\sin^2(\chi))^2} \qquad \text{Equation 74}$$

Combining the two geometric factors, $F_{lin}(\gamma,\kappa,\chi)$ and $G_{lin}(\kappa,\chi)^2$, leads to the following expression, $H_{lin}(\gamma,\kappa,\chi)$, for the combined geometric dependence.

$$H_{lin}(\gamma,\kappa,\chi) = F_{lin}(\gamma,\kappa,\chi)\cdot G_{lin}(\kappa,\chi)^2 = \frac{\left(\sin(2\gamma)\cdot\left(\cos^2(\kappa)-\sin^2(\kappa)\cdot\cos^2(\chi)\right)-\cos(2\gamma)\cdot\sin(2\kappa)\cdot\cos(\chi)\right)^2}{\sin^2(\chi)\cdot(1-\sin^2(\kappa)\cdot\sin^2(\chi))} \qquad \text{Equation 75}$$

We can now consider several common experimental configurations as described by the geometrical function derived above.

For co-propagating beams, $\chi = 0$, the factor, $H_{lin}(\gamma,\kappa,\chi)$, reduces to

$$H_{lin}(\gamma,\kappa,0) = \left(\frac{\sin(2\gamma)\cdot\cos(2\kappa)-\cos(2\gamma)\cdot\sin(2\kappa)}{\sin(\chi)}\right)^2 = \left(\frac{\sin(2(\gamma-\kappa))}{\sin(\chi)}\right)^2 \qquad \text{Equation 76}$$

which, ignoring the infinity due to the zero denominator in the co-propagating geometry as the interaction length of pump and probe beams must have a finite limit, has maxima for probe beam polarisations at $\pi/4$ to the linear pump beam polarisation.

The same results are obtained for counterpropagating beams, $\chi = \pi$, where

[e] Note that the second term in the denominator does not lead to an infinite factor, $F_{lin}(\gamma,\kappa,\chi)$, as the conditions for the second term to be zero ($\sin(\kappa) = \sin(\chi) = 1$), is the same condition for the numerator to be zero. The infinity due to the $\sin^2(\chi)$ factor in the denominator occurs for collinear geometries and is usually ignored as it represents an effectively infinite pump/probe beam intersection length.

$$H_{lin}(\gamma,\kappa,\pi)=\left(\frac{\sin(2\gamma)\cdot\cos(2\kappa)+\cos(2\gamma)\cdot\sin(2\kappa)}{\sin(\chi)}\right)^2=\left(\frac{\sin(2\cdot(\gamma+\kappa))}{\sin(\chi)}\right)^2 \qquad \text{Equation 77}$$

The dependence of the $H_{lin}(\gamma, \kappa, \chi)$ function on the intersection angle of pump and probe beams is emphasised if we consider three pump beam polarisations.

Case 1: For a vertically polarised pump beam, $\kappa = 0$, the geometric dependence reduces to

$$H_{lin}(\gamma,0,\chi)=\sin^2(2\gamma)\cdot\mathrm{cosec}^2(\chi) \qquad \text{Equation 78}$$

Case 2: For a pump beam polarised at $\pi/4$ to the vertical, the dependence becomes

$$H_{lin}(\gamma,\frac{\pi}{4},\chi)=\frac{\left(\sin(2\gamma)\cdot\frac{\sin(\chi)}{2}-\cos(2\gamma)\cdot\cot(\chi)\right)^2}{(1-\frac{\sin^2(\chi)}{2})} \qquad \text{Equation 79}$$

which for a probe beam polarised at $\pm\,{}^{\pi}/_{4}$ to the pump polarisation, $\gamma = 0$ or $\pi/2$, reduces to

$$H_{lin}(0 \text{ or } \frac{\pi}{2},\frac{\pi}{4},\chi)=\frac{\cot^2(\chi)}{(1-\frac{\sin^2(\chi)}{2})} \qquad \text{Equation 80}$$

Case 3: For a horizontally polarised pump beam, $\kappa = \pi/2$, the geometrical dependence is given by

$$H_{lin}(\gamma,\frac{\pi}{2},\chi)=\sin^2(2\gamma)\cdot\cot^2(\chi) \qquad \text{Equation 81}$$

Figure 3 shows the dependence of the $H_{lin}(\gamma, \kappa, \chi)$ function on pump/probe intersection angle, χ, assuming a probe beam polarised at $\pm\,{}^{\pi}/_{4}$ to the pump polarisation for pump beam polarisation angles of (a) 0, (b) ${}^{\pi}/_{6}$, (c) ${}^{\pi}/_{3}$ and (d) ${}^{\pi}/_{2}$.

The LPS signal is maximised if the probe beam is equally composed of ordinary and extraordinary components. For collinear beam geometries, this corresponds to a probe beam polarised at $\pi/4$ to the pump beam polarisation. However, this rule becomes more complex for non-collinear beam geometries.

Equations [54] and [55] above can be used to show that the optimal probe beam polarisation direction lies at $\pi/4$ from the ordinary axis direction which lies at the angle, η, from the normal to the beam intersection plane, defined as

$$\tan(\eta) = \tan(\kappa)\cdot\cos(\chi)$$ Equation 82

For collinear beam geometries, χ = 0, the ordinary axis can be identified with the pump beam polarisation direction, and the optimal probe beam polarisation direction lies at $\kappa + \pi/4$ from the normal to the beam intersection plane.

For orthogonal beam geometries, $\chi = \pi/2$, the ordinary axis is normal to the beam intersection plane for all pump beam polarisations, and the optimal probe beam polarisation direction lies at $\pi/4$ from the normal to the beam intersection plane.

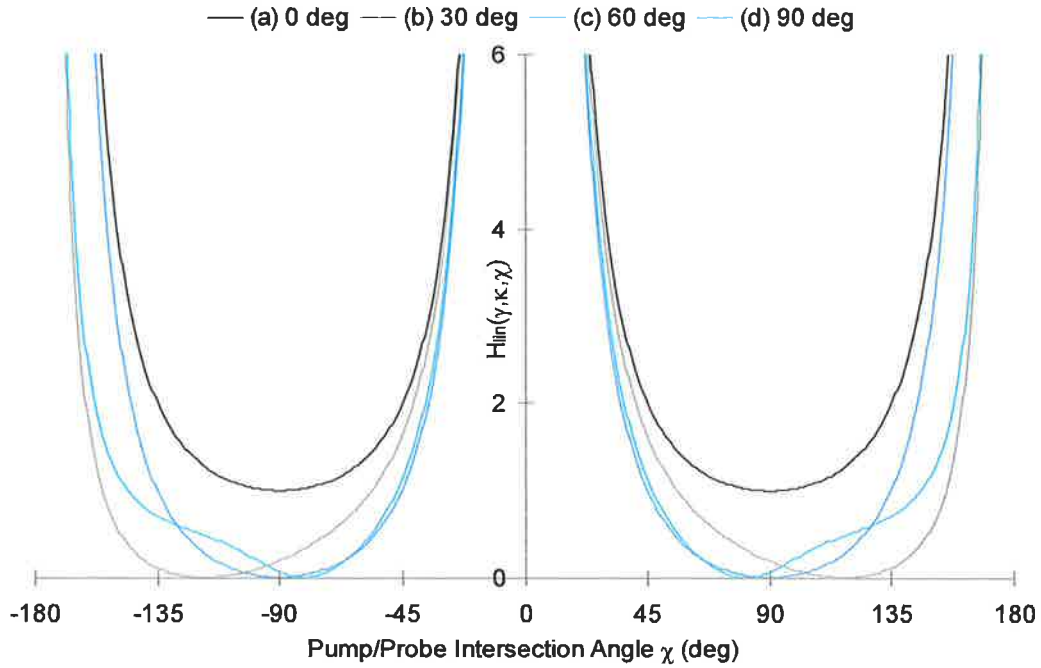

Figure 3: Geometric dependence of the transmitted probe beam intensity on the pump/probe beam intersection angle for a linearly polarised pump beam and perfectly crossed probe beam polarisers. The pump beam polarisation angle lies at κ = (a) 0, (b) $\pi/6$, (c) $\pi/3$ and (d) $\pi/2$ to the vertical. The probe beam is polarised at $\pm\pi/4$ to the pump beam polarisation.

For intermediate beam intersection angles, the cos(χ) factor in equation [82] tends to bias the ordinary axis from the direction of the pump beam polarisation toward the axis normal to the beam intersection plane, with the extreme of this behaviour for orthogonal beam intersection when the ordinary axis is normal to the beam intersection plane for all χ.

In addition, for a pump beam polarised normal to the beam intersection plane, κ = 0, the optimal probe beam polarisation lies at π/4 from the normal to the beam intersection plane for all beam intersection angles.

To avoid difficulties in identifying the optimal probe beam polarisation direction, two simple pump beam polarisation directions are suggested (and shown in Figure 3);

(i) for a pump beam polarised normal to the beam intersection plane, $\kappa = 0$,

(ii) and for a pump beam polarised in the beam intersection plane, $\kappa = \pi/2$.

For the first case, the optimal probe beam polarisation is at π/4 from the normal to the beam intersection plane for all beam intersection angles. The infinities which prevent equation [82] from identifying the optimal probe beam polarisation direction for the second case can be avoided by using equations [54] directly. This equation identifies the ordinary axis as the Y axis, and once again, the optimal probe beam polarisation lies at π/4 from the normal to the beam intersection plane for all beam intersection angles.

Assuming this probe beam polarisation direction, the geometrical dependencies of the function, $H_{lin}(\gamma, \kappa, \chi)$, on the pump/probe beam intersection angle, χ, for these two cases are

Case 4: For a vertically polarised pump beam, $\kappa = 0$, and a probe beam polarised at $\gamma = \kappa \pm \pi/4$,

$$H_{lin}(\pm\pi/4, 0, \chi) = \operatorname{cosec}^2(\chi) \qquad \text{Equation 83}$$

Case 5: For a horizontally polarised pump beam, $\kappa = \pi/2$, and a probe beam polarised at $\gamma = \kappa \pm \pi/4$,

$$H_{lin}\left(\frac{\pi}{2} \pm \frac{\pi}{4}, \frac{\pi}{2}, \chi\right) = \cot^2(\chi) \qquad \text{Equation 84}$$

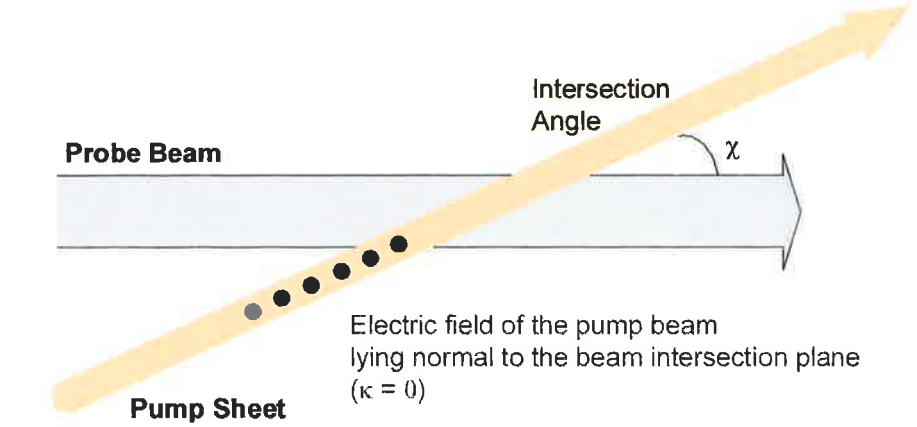

(a)

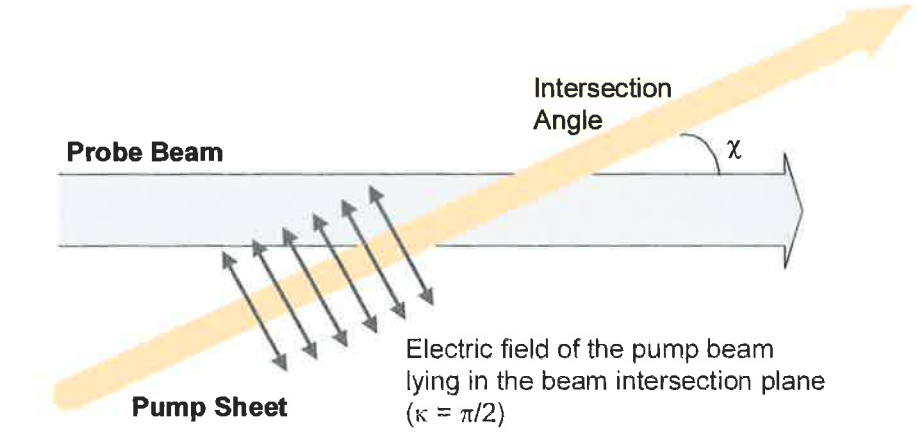

(b)

Figure 4: Pump beam polarisation directions leading to simple identification of the optimal probe beam polarisation direction for all beam intersection angles; (a) a pump beam polarised normal to the beam intersection plane ($\kappa = 0$) and (b) a pump beam polarised in the beam intersection plane ($\kappa = \pi/2$). Configuration (b) leads to non-zero signal for orthogonal beam intersection.

These geometric dependencies are symmetric with respect to the pump/probe beam intersection angle, χ, and are shown in Figure 5 for (a) a pump beam polarised normal to the beam intersection plane and (b) a pump beam polarised in the beam intersection plane.

Equation [84] above matches the $\cot^2(\chi)$ experimental result of Nyholm, Fritzon and Alden[3] for the same configuration of a pump beam polarised in the beam intersection plane and a probe beam polarised at $\pi/4$ to the normal to the beam intersection plane. The $\cot^2(\chi)\cos^2(\chi)$ dependence of Lavrinenko and Gancheryonok differs from that derived in this chapter which matches the experimental $\cot^2(\chi)$ dependence.

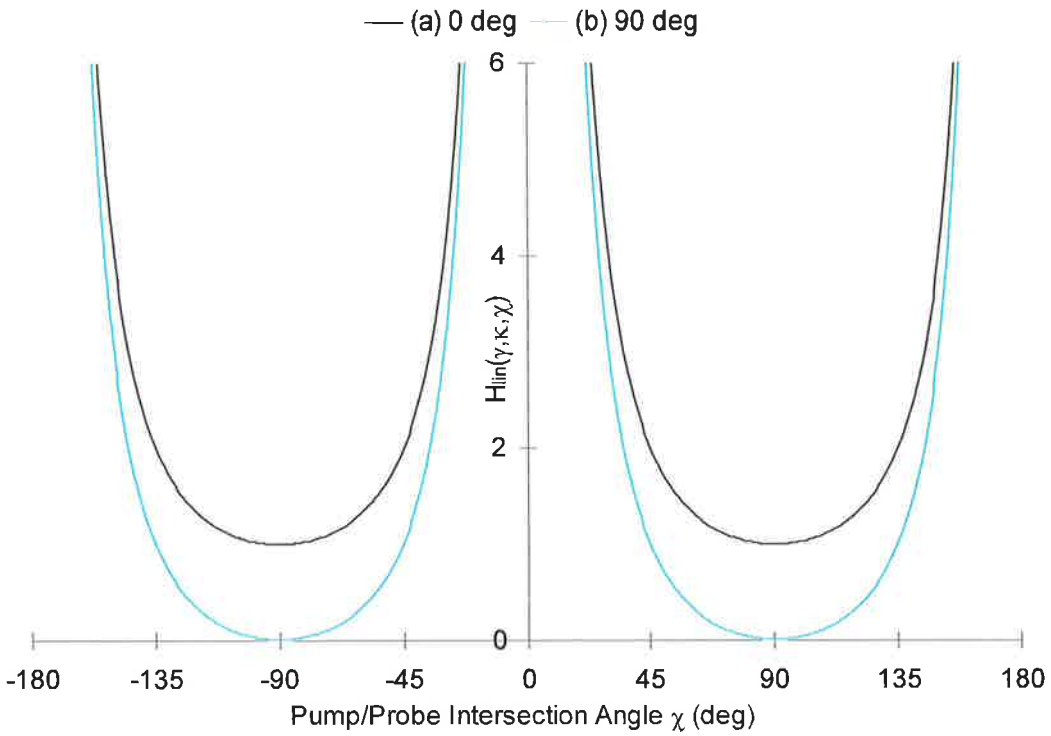

Figure 5: Geometric dependence of the transmitted probe beam intensity on the pump/probe beam intersection angle for (a) a vertically polarised pump beam and (b) a horizontally polarised pump beam for a linearly polarised pump beam and perfectly crossed probe beam polarisers. The pump and probe beams intersect in the horizontal plane. The probe beam is polarised at $\pm \pi/4$ to the normal to the beam intersection plane.

The difference between the model of Lavrinenko and Gancheryonok and that discussed above lies primarily in the explicit statement of the geometrical dependence of the induced birefringence on the beam intersection angle, χ, and the polarisation direction of the pump beam, κ, defined in equation [72]. The theory of Lavrinenko and Gancheryonok in the case of a linearly polarised pump beam appears to represent calculation of the transmission and recombination of the probe beam polarisation components EXCLUDING the angular dependence of the induced birefringence. Lavrinenko and Gancheryonok also do not emphasise identification of the characteristic modes of propagation in the pump medium before multiplication by the terms containing the absorption and refractive index coefficients for each of the modes. In the case of a linearly polarised pump beam, the characteristic modes of propagation are linearly polarised and appear to match those of Lavrinenko and Gancheryonok.

It should be noted, however, that the difference between the $\cot^2(\chi)\cos^2(\chi)$ dependence of Lavrinenko and Gancheryonok and the $\cot^2(\chi)$ dependence of this chapter and the experimentally

determined signal of Nyholm, Fritzon and Alden is small (see Figure 6), and in the absence of error bars on the experimental result could be considered as a possible solution.

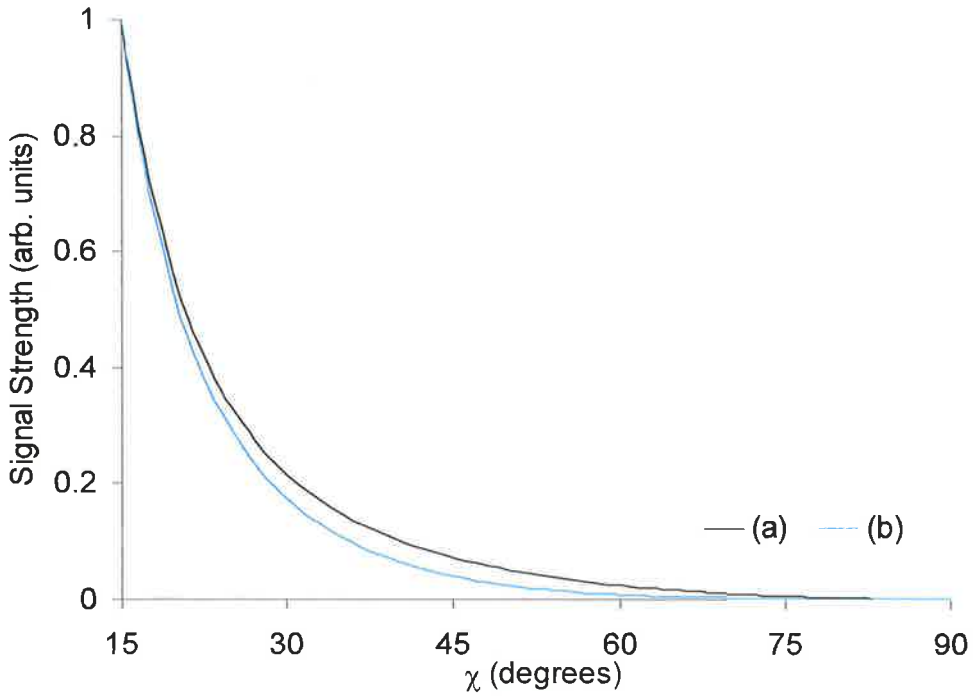

Figure 6: (b) $\cot^2(\chi)\cos^2(\chi)$ curve comparison with a (a) $\cot^2(\chi)$ curve.

Nyholm, Fritzon and Alden show a graph of signal strength for the range 15° to 60°. The data points lie closely on the $\cot^2(\chi)$ theoretical curve. To address the concern that the data (on which experimental error bars are not shown) could equally fit on a $\cot^2(\chi)\cos^2(\chi)$ curve, Figure 5 shows the two theoretical curves for the same range as that of the experimental data with both curves normalised to their values at 15° to minimise the relative difference between the two. It is clear that the two curves are close. However, the fit of Nyholm *et al.*'s data to a $\cot^2(\chi)$ curve (see K. Nyholm, R. Fritzon and M. Alden, *"Two-dimensional imaging of OH in flames by use of polarization spectroscopy"*, Optics Letters, **18** (19), 1672-1674, 1993) is much better than the approach of the two theoretical curves to each other in Figure 6. For reference a plot of the difference of the (*15° normalised*) $\cot^2(\chi)\cos^2(\chi)$ curve from the (*15° normalised*) $\cot^2(\chi)$ curve as a percentage of the normalised signal at 15° is shown in Figure 7. This graph indicates that the experimental error on the data of Nyholm *et al.* would have to be of the order of <2-5 % of the maximum signal at 15° over the range of experimental beam intersection angles to fit the $\cot^2(\chi)\cos^2(\chi)$ curve as well as the data points appear to fit the $\cot^2(\chi)$ curve. For most of the experimental range of beam intersection angles, it can be seen from Figure 6 that this would represent a significant fraction of the collected signal. The quality of the fit of Nyholm, Fritzon and Nyholm data points to a $\cot^2(\chi)$ curve suggests

that the theory developed in this chapter provides a better fit to the experimental data in the theory of Lavrinenko and Gancheryonok.

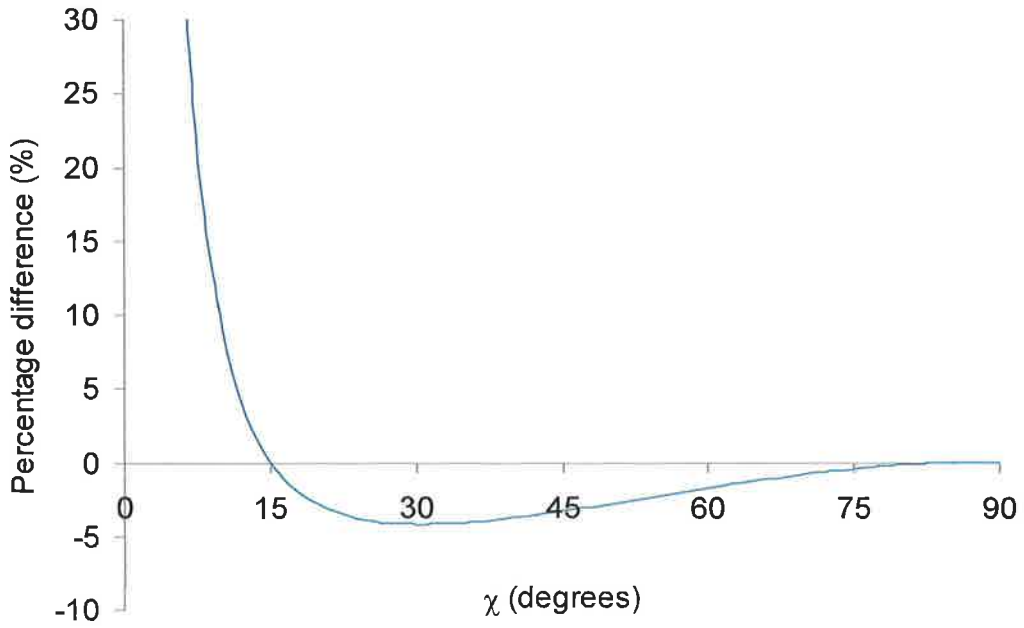

Figure 7: Percentage difference of the (*15° normalised*) $\cot^2(\chi)\cos^2(\chi)$ curve from the (*15° normalised*) $\cot^2(\chi)$ curve as a fraction of the maximum signal in the experimental range of Nyholm, Fritzon and Alden at $\chi = 15^\circ$.

The theory developed in this chapter supports the $\cot^2(\chi)$ dependence of LPS signal of beam intersection angle, χ, found by Nyholm, Fritzon and Alden[3] for a pump beam polarised in the beam intersection plane and a probe beam polarised at $\pi/4$ to the normal to that plane. This theory, and that of Lavrinenko and Gancheryonok[5], predict that for a pump beam polarised normal to the beam intersection plane, and a probe beam polarised at $\pi/4$ to the normal to the intersection plane, the signal is non-zero for all beam intersection angles. This prediction dramatically increases the range of beam geometries available for polarisation spectroscopy imaging and in the resultant image resolution.

This prediction is tested experimentally in the next chapter, which presents the first (to the best of our knowledge) polarisation spectroscopy imaging for orthogonal beam intersection for a pump beam polarised normal to and a probe beam polarised at $\pi/4$ to the beam intersection plane. The experiment imaged the LPS signal due to the hydroxyl radical in the premixed natural gas/O_2 flame from a modified glass-blowing torch. The same flame was used to confirm the

zero signal level for orthogonal beam intersection for a pump beam polarised in the plane of intersection.

The model derived in this chapter can be extended to consider the case of a circularly polarised pump beam. Chapter IV uses an analogue of an optically active uniaxial crystal to derive expressions for the geometrical dependence of the LPS signal in the case of a circularly polarised pump beam. This model leads to an interesting prediction of spectroscopic behaviour which is not noted in the case of a linearly polarised pump beam. The predictions of the theory developed for a circularly polarised pump beam are tested in Chapter V, confirming a similar non-zero signal strength for all beam intersection angles for a specified probe beam polarisation direction.

Chapter III: Orthogonal Imaging for a Linearly Polarised Pump Beam.

In this chapter,

- **the first (to the best of our knowledge) orthogonal pump/probe beam intersection LPS signal detection, and**
- **the first (to the best of our knowledge) Orthogonal Polarisation Laser Spectroscopy imaging (OPLPS)**

for a linearly polarised pump beam is demonstrated.

Conventionally, polarisation spectroscopy is implemented in a counterpropagating, Doppler-free[2] pump and probe beam geometry to maximise signal strength and minimise linewidth. However, polarisation spectroscopy imaging requires a finite beam intersection angle to obtain reasonable spatial resolution in the collected image. Nyholm, Fritzon and Alden[3] first demonstrated polarisation spectroscopic imaging (of the hydroxyl radical in a premixed natural gas/O_2 flame for pump/probe beam intersection angles of 15° and 30°) in 1993. In their experimental geometry, the linearly polarised probe beam intersected a horizontally polarised pump laser sheet with the probe beam polarised at $\pi/4$ to the vertical. The signal was shown experimentally to follow a $\cot^2(\chi)$ dependence on the intersection angle of pump and probe beams, χ. The dependence was explained in terms of the combined effects of the change in the interaction volume between pump and probe beams and the projection of the pump beam polarisation onto that of the probe beam.

The reported $\cot^2(\chi)$ falloff in signal with increasing intersection angle leads to a zero signal for a pump/probe beam intersection angle of $\pi/2$. This decreasing signal strength dependence has implied a limitation on the application of polarisation spectroscopy imaging to relatively small pump/probe beam intersection angles. Chapter II described a model developed by Reppel and Alwahabi[23] which predicted this $\cot^2(\chi)$ falloff in signal with beam intersection angle, χ, for the experimental geometry of Nyholm, Fritzon and Alden (for a pump beam polarised in the beam intersection plane and a probe beam polarised at $\pi/4$ to the normal to that plane). The same theory predicts a signal strength dependence on beam intersection angle for a pump beam polarised normal to the beam intersection plane (and a probe beam polarised at $\pi/4$ to the normal to that plane) described by the equation

$$H_{lin}(\frac{\pi}{4},0,\chi) \propto \mathrm{cosec}^2(\chi)$$ Equation 1

For this polarisation configuration, the signal is NON-ZERO for all beam intersection angles.

The $\cot^2(\chi)$ and $\mathrm{cosec}^2(\chi)$ functions are plotted in Figure 1. The $\cot^2(\chi)$function drops to zero signal for $\pi/2$ intersection of pump and probe beams, while the $\mathrm{cosec}^2(\chi)$ function predicts non-zero signal for $\pi/2$ pump/probe intersection. This prediction allows an orthogonal pump/probe beam intersection geometry to be considered for polarisation spectroscopy imaging. Additionally, the range of beam intersection angles associated with reasonable LPS signal strength increases for a pump beam polarised normal to the beam intersection plane of intersection in comparison with the case of a pump beam polarised in the beam intersection plane.

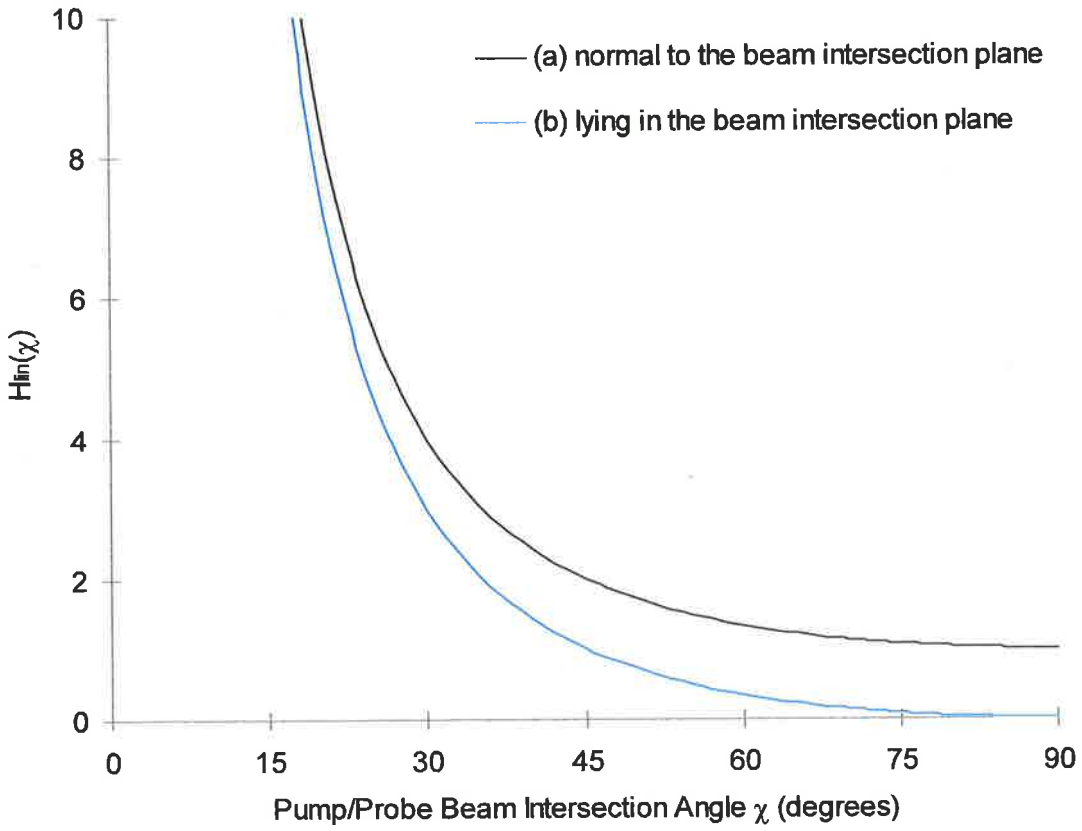

Figure 1: Dependence of LPS signal on pump/probe beam intersection angle, χ, for a pump beam polarised (a) in the horizontal beam intersection plane ($\pi/2$ from the vertical axis) and (b) normal to the horizontal beam intersection plane (parallel to the vertical axis).

The $\mathrm{cosec}^2(\chi)$ signal decreases rapidly with increasing intersection angle. However, for the purposes of imaging, intersection of pump and probe beams at large angles is desirable in terms of

increased image resolution. The gain in spatial resolution with increasing beam intersection angle must be weighed against the corresponding decrease in signal described in equation [1].

Assuming a minimum intersection angle of 10° for effective imaging and a pump beam polarised normal to the beam intersection plane, the ratio of possible signal strengths predicted by the theory at 10° and 90° is 29.3:1. (For comparison, the equivalent signal strength ratio in the case of a pump beam polarised in the beam intersection plane is infinite as the orthogonal signal is zero). A beam intersection angle of 30° would normally be considered a reasonable angle for application of polarisation spectroscopy imaging. The signal strength for a pump beam polarised normal to the beam intersection plane only drops by the relatively small factor of 4:1 between the pump/probe intersection angles of 30° and 90°. This would indicate that if sufficient signal is obtained for 30° imaging, 90° beam intersection angle imaging is clearly within the experimental range. Note also that the signal for a pump beam polarised in the beam intersection plane at a beam intersection angle of 30° is only 3 times that of the orthogonal PLPS signal for a pump beam polarised normal to the beam intersection plane. The signal increases rapidly between the beam intersection angles of 30° and 15°. The signals for the cases of pump beams polarised in and normal to the beam intersection plane at 15° beam intersection are, respectively, 13.9 and 14.9 times the orthogonal PLPS signal in the case of a vertically polarised pump beam.

The experiments in this chapter aim to confirm the prediction of non-zero signal for orthogonal pump/probe beam intersection based on the theory of Chapter II. The existence of significant signal for near-orthogonal beam intersection has vast implications for the range of spatial resolution available to polarisation spectroscopy imaging. In order the confirm the possibility of non-zero signal for orthogonal beam intersection, this chapter contains the following three experiments;

(1) confirmation (within the range of experimental error) of zero signal for orthogonal pump/probe beam intersection in the case of a pump beam polarised *in the beam intersection plane* (as previously demonstrated by Nyholm, Fritzon and Alden[3]),

(2) the first (to the best of our knowledge) experimental confirmation of non-zero signal LPS strength for orthogonal pump/probe beam intersection for a pump beam polarised *normal to the beam intersection plane*, and the first (to the best of our knowledge) OPLPS images obtained for the orthogonal pump/probe beam geometry.

(3) the first (to the best of our knowledge) imaging of the PLPS signal due to the OH radical in a premixed natural gas/O_2 flame. The images are obtained for a pump beam polarised *normal to the beam intersection plane*. The images set is used to investigate the accuracy of correction for the probe beam background.

The experiments detected the LPS signal of the hydroxyl (OH) radical in a premixed natural gas/O_2 flame from a modified glass-blowing torch. The laser system was tuned to probe the $A^2\Sigma$–$X^2\Pi$ (0-0)

$Q_2(8)$ transition of OH at 309.7727 nm[24]. Approximately 3 mm of the base of the flame near the tip of the burner was imaged using an ICCD. In the absence of a PMT detection system, all measurements were taken with the ICCD imaging system. The OH radical indicates the hot flame zone[4], and should be distributed throughout the base of the small laminar flame. For a stoichiometric CH_4/O_2 flame, the adiabatic flame temperature is 3054 K and the expected OH concentration ~ 2.28 x 10^{17} cm^{-3} [a].

Before describing the experiment and results, the method of image interpretation used for the PLPS images collected for this thesis is presented.

Image Interpretation

The PLPS experiments described throughout this thesis were based on

- perfectly crossed polarisers, (or crossed to the $\pm 0.003^{\circ}$ accuracy of the analyser rotator),
- no interpolariser birefringent optical elements in the probe beam path, and
- line-centre pumping.

In these cases, for both linearly and circularly polarised pump beams, the detected probe beam intensity was defined in equation [16] of Chapter I as

$$I_{\substack{probe\_transmitted \\ circ/linear\_pump \\ crossed\_polarisers \\ unconfined\_combustion}}(x) = I_0\left[\xi + \frac{1}{16}(\Delta\alpha_0 L)^2 \cdot \frac{1}{1+x^2}\right] \qquad \text{Equation 2}$$

where the induced dichroism, $\Delta\alpha_0$, is identified in equation [32] of Chapter I as

$$\Delta\alpha^{i,i'}_{J,J''} = -N_J \cdot \frac{I_{pump}\, t}{\hbar\omega_{pump}} \cdot Z_{J,J',J''} \cdot C_{J,J'} \cdot C_{J,J''} \qquad \text{Equation 3}$$

The pump transition is from the shared lower rotational state, J, to the upper rotational state, J'. The upper rotational state of the probe beam transition is J". The terms, i and i', refer to the orthogonal polarisation states of the two probe beam components which experience the induced dichroism.

To realistically model the experiment, equation [2] must be rewritten to include some experimental factors which have been omitted:

$$\frac{I_{\substack{probe\_detected \\ circ/linear\_pump \\ crossed\_polarisers \\ unconfined\_combustion}}(x)}{I_0 \cdot f_{detector} \cdot T_{polariser} \cdot T_{analyser}} = e^{-\alpha_{av} \cdot L} \cdot e^{-\int_H \alpha_{unperturbed}\, dl} \cdot \left[\xi + \frac{1}{16}(\Delta\alpha_0 L)^2 \cdot \frac{1}{1+x^2}\right] \qquad \text{Equation 4}$$

[a] Calculated by *"Gaseq: Chemical equilibria for perfect gases"*, Version 0.63, Chris Morley, c.orley@ukgateway.net.

where

I_0 is the probe beam intensity incident on the primary probe beam polariser,

$f_{detector}$ is the collection efficiency of the detection system,

$T_{polariser}$ and $T_{analyser}$ are the transmission axis transmittivities of the probe beam primary polariser and analyser respectively,

ξ represents the finite extinction ratio of the probe beam polarisers,

$\Delta\alpha_0$ is the line-centre induced dichroism defined by the pumped populations and the experimental geometry,

L is the interaction length of the pump and probe beams as measured along the probe beam path and, in imaging, is related to the pump sheet thickness, W, and the intersection angle of pump and probe beams, χ, via

$$L = \frac{W}{|\sin(\chi)|} \qquad \text{Equation 5}$$

α_{av} is the average induced absorption coefficient for the two probe beam polarisation modes of propagation in the pump/probe beam interaction region,

$\alpha_{unperturbed}$ is the absorption coefficient for the probe beam within the combustion region, but outside the interaction volume of pump and probe beams,

H is the probe beam path length through the combustion region excluding the interaction volume of pump and probe beams, and

x is the detuning of the probe beam transition from line-centre.

Aside from the efficiency of the detection system and the transmittivities of the probe beam polarisers (which can themselves lead to a large reduction in the detected signal), this equation identifies the dependence of polarisation spectroscopy on absorption factors for both probe beam and pump beam (via the appearance of the pump beam intensity in the expression for the induced dichroism in equation [3]).

Even with crossed polarisers with extinction ratios of the order of 10^{-5}–10^{-6}, the transmitted fraction of the probe beam associated with the extinction ratio, ξ, of the polariser can be significant with respect to the magnitude of the collected signal. In a scanned spectroscopic experiment, it is possible to determine the non-resonant background if the spectroscopic transitions are well separated. In an imaging experiment, usually undertaken with the laser system tuned to linecentre, either the extinction background (due to residual transmission of the probe beam through the analyser) must be minimised or pre-determined to allow the signal to be identified from the background in the collected image.

The first option, to reduce the magnitude of the probe beam extinction background, is limited by the availability of high quality polarisers. The second option is to premeasure the probe beam

background. For this method to be reliable, the conditions of the probe beam path through the flame must be nearly identical for both collection of the probe extinction background and for the signal (including the extinction background component) images. If this is not the case, the differing absorption terms in equation [4] may lead to misestimation of the required signal correction.

Ideally, the line-centre induced dichroism, $\Delta\alpha_0$, and hence the target species number density, would be determined from near-simultaneous (on the timescale of the flame evolution) measurement of the signal from two probe pulses, one with pump beam blocked so that the Lorentzian term in equation [4] is zero and the intensity represents the background term, B, of the signal, and one with the pump unblocked with intensity representing the sum of the signal term, S, and the background term, B. In the case of such near-simultaneous timing, the absorption terms will be largely (see below) equivalent and the ratio of the two pulse intensities, R_{signal}, will isolate the signal and the background factors according to the equation

$$R_{signal} = \frac{I_{probe}}{I_{probe\_blocked\_pump}} = \frac{B + S}{B} = 1 + \frac{S}{B} \qquad \text{Equation 6}$$

The induced dichroism which appears to second order in the signal factor, S, in the case of perfectly crossed polarisers may be obtained from the image ratio, R_{signal}, via the following equation.

$$\frac{S}{B} = R_{signal} - 1 = \frac{\frac{1}{16}(\Delta\alpha_0 L)^2 \cdot \frac{1}{1+x^2}}{\xi} \qquad \text{Equation 7}$$

The simple form of this equation is due to the cancellation of the absorption terms. The ratio technique above relies on the assumption that the average induced absorption term due to the thickness of the laser sheet, $e^{-\alpha_{av} \cdot L}$, is approximately unity due to the short interaction distance, L, of pump and probe beams, and is equivalent to its unpumped equivalent. All other absorption terms cancel if the background and combined signal/background images are taken near-simultaneously on the timescale of the flame. Note that unless the polariser extinction ratio is known, the induced dichroism will not be not known absolutely unless calibrated against a known standard. It is assumed that the detuning, x, is determined experimentally.

The strong point of a near-simultaneous double probe pulse technique for PLPS signal interpretation is the ease with which the probe beam absorption terms may be eliminated. In the absence of near-simultaneous measurement of the probe beam extinction background, care must be taken to determine the effects of absorption on both pump and probe beams and correct for the pulse-to-pulse laser energy fluctuation. Practically, the near-simultaneous double probe pulse

technique is achievable with a single pulse by monitoring the rejected output of a Glan-laser polariser used as probe beam analyser. The rejected component represents the background probe beam profile subject to the absorption terms, but many orders of magnitude higher in intensity. The effect of the pump beam on the intensity profile of the rejected component of the probe beam will be negligible. High attenuation and careful alignment would allow both the signal beam and the rejected component to be imaged on the same CCD, or alternatively with a double CCD system. Distortion of the profile due to reflection from the internal surface of the analyser may be corrected geometrically. The signal strength of the two images could be normalised by blocking the pump beam and directly comparing the intensities of the signal and the rejected component. Note that this method allows direct correction of the signal image without simultaneous measurement of the pump beam energy. Alternatively if the flame and laser profile are steady, an average probe extinction background may be taken to correct instantaneous and average signal images due to the linearity of the probe extinction background with probe beam intensity.

The signal term, S, is, however, quadratic in the pump beam intensity (for the linear regime of optical pumping) which, when combined with the linear dependence on the probe beam intensity, produces a total cubic dependence on laser energy for a single laser system. It is difficult to collect an instantaneous pump beam profile which accounts accurately for the effects of absorption.

A method for obtaining either a near-simultaneous or average probe beam extinction background to correct the collected images with respect to the probe beam profile has been described above. In the case of near-simultaneous probe background collection, the absorptive terms in equation [7] cancel, aside from those due to the pump beam intensity dependence of the induced dichroism. It is not possible to automatically correct for the absorptive terms due to the passage of the pump beam through the flame. Care must be taken in quantitative imaging to either select a pump transition for which the flame appears optically thin or to carefully model the effects of absorption of the pump beam on transmission through the flame.

Image Correction

Unless otherwise noted as instantaneous images, the PLPS images below are unweighted averages of 50 shots and are shown in two modes.

- Mode 1 represents the image (corrected for the non-zero background of the ICCD alone), and represents a largely uncorrected image.
- Mode 2 represents the ratio, S/B, of the pure signal, S, (free of probe beam extinction components) to the background (with flame), B. The ratio is proportional to the square of the induced dichroism as described in equation [7] above.

Average images were taken after determining that the pulse-to-pulse intensity of the doubled output of the laser system had a standard deviation of 4.6%. This small variation was used to justify collection of average images for a technique that is cubic in laser energy without correction for shot-to-shot intensity. A second justification for the collection of average images is given in Chapter VI, where it is shown that the images in Chapters III, V and VI were collected in the saturated regime of optical pumping (to maximise signal) where the LPS signal is linear with the laser energy.

All grey-scale images in this chapter (with the exception of two early reverse greyscale images) are plotted on a linear grey-scale normalised to a 5 to 95% scale of the signal strength in each image. Instantaneous images are only shown in Mode 1 format to demonstrate the quality of the single-shot images collected in comparison with the Mode 1 average images.

Experimental Equipment and Arrangement

A schematic of the orthogonal PLPS experiment for a vertically polarised pump beam is shown in Figure 2[b]. The output of a Nd:YAG (Continuum Surelite II) pumped dye laser (Lambda Physik Scanmate) operating with Rhodamine 101 was directed to a Lambda Physik frequency doubling unit to produce the required UV beam at ~310 nm to probe the $A^2\Sigma$–$X^2\Pi$ (0-0) transition of OH. The UV linewidth and pulse length were estimated to be 0.4 cm^{-1} and 3 ns respectively. The dye laser output is specified[25] to have linewidth 0.2 cm^{-1} and pulselength 5 ns.

The UV beam emerged horizontally polarised from the doubling system. A UV telescope/spatial filter (magnification 4:1,f_1 = 50 mm, f_2 = 200 mm, pinhole diameter = 200 μm) expanded and cleaned the beam cross-section. The importance of a uniform, interference and diffraction free probe beam cross-section is described in detail below. The front face reflection from an uncoated fused silica wedge was used as the weak probe beam. The transmitted the pump beam was redirected by a fused silica 90° prism (in a reverse orientation to allow the internal reflection from the hypotenuse surface to produce a net redirection of the pump beam through a small angles) to pass through a through a fused silica ½-wave double Fresnel Rhomb (Halbo Optics: 10 mm x 10 mm input plane dimension) which rotated the plane of polarisation to the vertical for the experiment involving a pump beam polarisation normal to the horizontal plane beam intersection plane. The rhomb was removed for the case of a pump beam polarised in the plane of intersection.

The pump beam passed through a vertically (or horizontally depending on the required pump beam polarisation) aligned Glan-Taylor polariser. A cylindrical lens (f_3 = 340 mm) placed after the pump beam polariser produced the thin sheet which passed through the flame and intersected the weak probe beam, which was itself expanded by a additional spherical telescope (magnification 2:1, f_4 = 75 mm, f_5 = 150 mm (2")) after being redirected by an aluminium UV mirror. Measurements of the polarisation state of the pump beam before and after the cylindrical lens indicated that the lens produced negligible change in pump beam polarisation state. The probe beam passed through the flame to intersect the pump beam at 90°.

Glan-Taylor calcite polarisers (Karl Lambrecht) were used for the combustion experiments. An A grade polariser (quoted extinction ratio < $5x10^{-5}$) was used for the pump beam. Two E grade polarisers were crossed in the probe beam path (quoted extinction ratio < $5x10^{-6}$). The clear aperture of the polarisers was 20 mm. A high resolution polariser rotator (Oriel) allowed rotation of

[b] More detailed descriptions of the equipment specifications than those given in this Chapter are given in Appendix V.

the analyser to ± 0.003° or 5.2×10^{-5} radians. An inhouse designed[c] Allen key adjustment controlled the vertical and horizontal alignment of the analyser to the probe beam direction. After passing through the analyser, the probe beam was redirected by a second aluminium mirror and passed through the combination of two spherical lenses and an iris to be detected by an ICCD-576E (576x384 pixel array) Princeton Instruments camera gated at 200 ns and operating with the lens removed.

The UV pump and probe beam pulse energies were estimated as 4 mJ and 0.16 mJ respectively before passing through the system optics. The pump sheet height was 25 mm and the sheet thickness was ~< 0.6 mm (for a pump beam energy density of 26.7 mJ/cm^2 or power density of 8.9 MW/cm^2). The probe beam was expanded to an area of 35 mm x 10 mm (a probe beam energy density of 0.046 mJ/cm^2 or power density of 15.2 kW/cm^2). In polarisation spectroscopy, the probe beam intensity is assumed to be very much less than that of the pump beam. In the imaging experiments described in this chapter and in Chapters IV, V and VI, no attempt was made to collect signal in the linear regime. Every effort was made to maximise signal strength, both to confirm non-zero signal for orthogonal pump/probe beam intersection in the case of a pump beam polarised normal to the beam intersection plane, and to demonstrate that in the case of a pump beam polarised in the beam intersection plane, non-detectable signal within the limits of the experiment.

The experiment timing was dominated by the requirement to operate the Nd:YAG flashlamp at 10 Hz to maximise laser energy and optimise temperature stabilisation while allowing for the minimum ICCD image acquisition rate, which was approximately 1 frame per 0.8 seconds. The camera and laser system were triggered with a 1 Hz external signal, while a supplementary pulse train generator[d] was connected between the pulse input to the flashlamp and the flashlamp itself (Figure 3). The pulse train generator triggered the flashlamp at 0.1 second intervals by generating nine equally spaced pulses between each external trigger input. The flashlamp was thus maintained at the optimum pulsing rate, 10 Hz, although the Nd:YAG Q-switch and ICCD were only triggered once a second.

The OH radical distribution in a premixed natural gas/O_2 welding torch type flame was imaged using PLPS. A small modified glass-blowing torch producing a laminar flame (Re ~ 95) was used in the imaging experiments. The fuel and oxidiser mixture was chosen to maximise the strength of the OH LPS signal.

[c] Designed by Jason Peak.

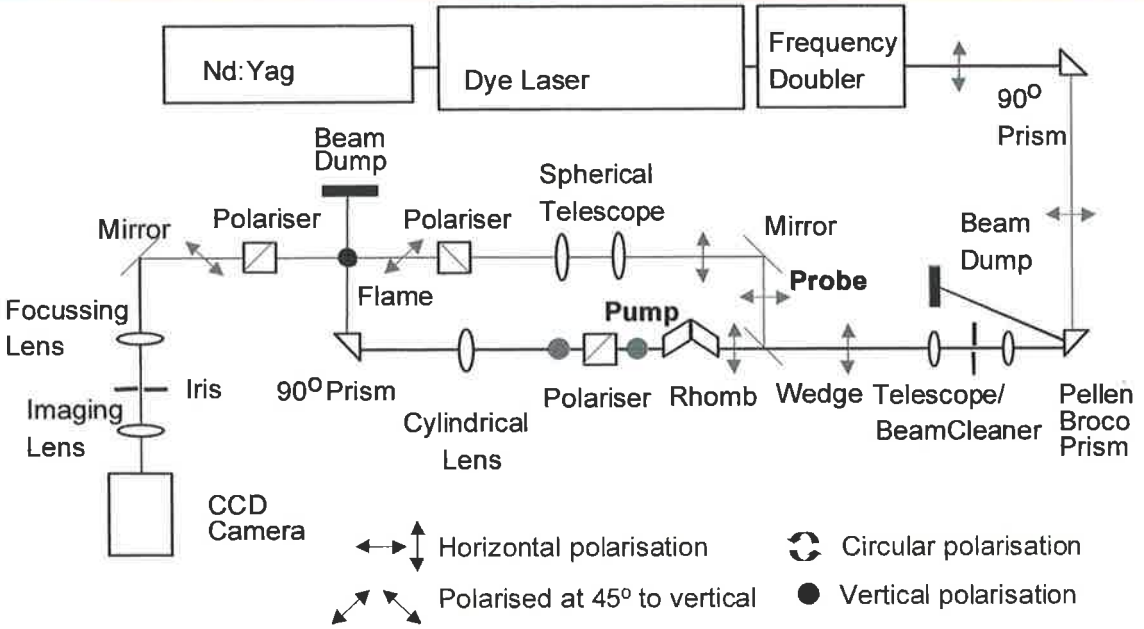

Figure 2: Schematic diagram of the orthogonal PLPS experiment for a pump beam polarised in the horizontal beam intersection plane. The ½-wave rhomb in the pump beam path rotates the plane of polarisation of the frequency doubled beam to vertical. The probe beam is polarised at $\pi/4$ to the vertical.

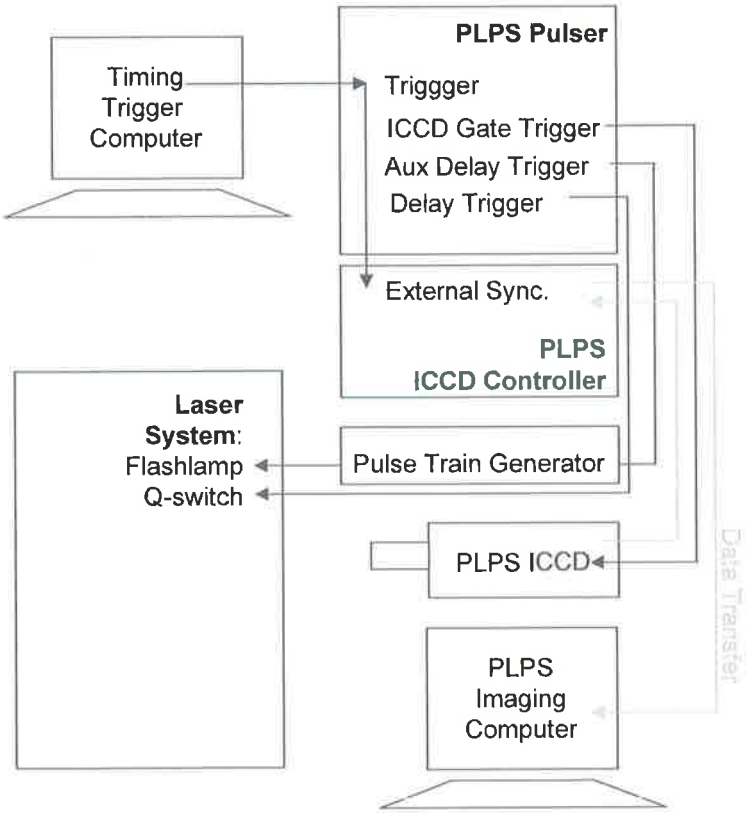

Figure 3: Timing system for single ICCD camera mode operation.

[d] Designed and built by Derek Franklin.

The tip of the glass-blowing torch used in the imaging experiments is shown in Figure 4. The tip of the torch has a diameter of 6.2 mm and the exit orifice has a diameter of 1.2 mm. A secondary ring of small orifices surrounds the central orifice and is connected to the same gas supply. The modifications to the torch involved removing the standard fuel/oxidiser controls on the handle of the torch and attaching the nozzle to the output of a externally controlled premixed natural gas/O_2 supply. For the OH PLPS flame images in this and the following chapters, the fuel lean laminar flame had a Reynolds number of ~ 95. The flame was extremely steady and allowed average images to be taken to enhance images in conditions of low signal.

Figure 4: Tip of the modified glass-blowing burner used in the PLPS and PLIF imaging experiments. The tip of the torch has diameter 6.2 mm and the exit orifice has diameter 1.2 mm.

The flowrates[26] of the fuel and oxidiser lines were monitored via Fischer and Porter 1/2" and 1/4" flowmeters. Pressure gauges were attached to each flowmeter to determine the operating pressure. The temperature of the fuel flow was assumed to be ambient. The fuel and oxidiser were high pressure compressed natural gas (BORAL Gas) and oxygen (BOC Gases: Industrial grade, 020G). For safety, a flashback arrester was attached to the burner inlet port of either the fuel line or the premixed fuel/oxidiser line. Safety blowoff values were also attached to the high pressure cylinders to prevent the line pressure from exceeding safe operation levels for the glass flowmeter tubes .

Diffraction, Interference and Thermal Gradient Effects on the Probe Beam Profile

Considerable care was taken to produce a uniform probe beam profile and eliminate diffraction and interference effects. The primary beam expander was used to clean the doubled output of the Lambda-Physik dye laser and to increase the cross-sectional area of the beam to avoid damage to mirrors and optical elements. The pinhole in the focal plane also eliminated stray radiation not quite collinear with the beam path. Irises were used to align both pump and probe beams throughout the system, but were opened during the experiment to eliminate diffraction effects. Care was taken to separate the front and back-face reflections from the beamsplitter to produce the probe beam. Even a slight non-separation of the reflected components of the probe beam resulted in detectable interference fringes across the probe beam profile.

The probe beam profile was very sensitive to dust particles, interference and edge diffraction effects as shown in Figures 5 and 6. Figure 5 shows interference fringes in the probe beam due to incomplete separation of the front and back face reflections from a quartz plate (non-wedged) beamsplitter. Dust particles on the probe beam optics produced the diffraction patterns across the probe beam profile in Figure 6. The image is typical of the optical system before careful cleaning of the system and optimisation of the probe beam profile. The interference and diffraction effects were not noticeable in single-shot images due to the low signal level, and only became apparent in average images. The images in Figures 5 to 8 are 50 shot averages.

The tip of the glass-blowing burner is shown in silhouette at the base of the image in Figure 6. Small edge diffraction fringes are visible, but it is noticeable how little polarisation change in the probe beam is induced by glancing reflection from the burner edges. However ND filters should be used in the detecting system during the setup of the experiment to determine the extent of transmission of such glancing reflections through the analyser before exposing the ICCD to the full magnitude of the signal. This is especially the case in beam geometries where the pump beam, whose polarisation axis is such that it may be easily transmitted through the analysing polariser, is incident on the burner on the same side as the probe beam imaging optics. It is interesting to note that in simultaneous PLIF/PLPS experiments described later in this thesis, the PLIF camera had to be very carefully shielded from probe and pump beam scattering from the burner tip in all cases to prevent saturating the CCD, while the PLPS experiment was relatively immune (the experiments were primarily in the collinear rather than counterpropagating geometries) to these effects.

Note that the non-zero background of the PLPS ICCD (~ 55 counts) was corrected in all images presented in this thesis by taking a 50 image background average after one hour's temperature stabilisation at the start of each day's experiment. The background was automatically subtracted

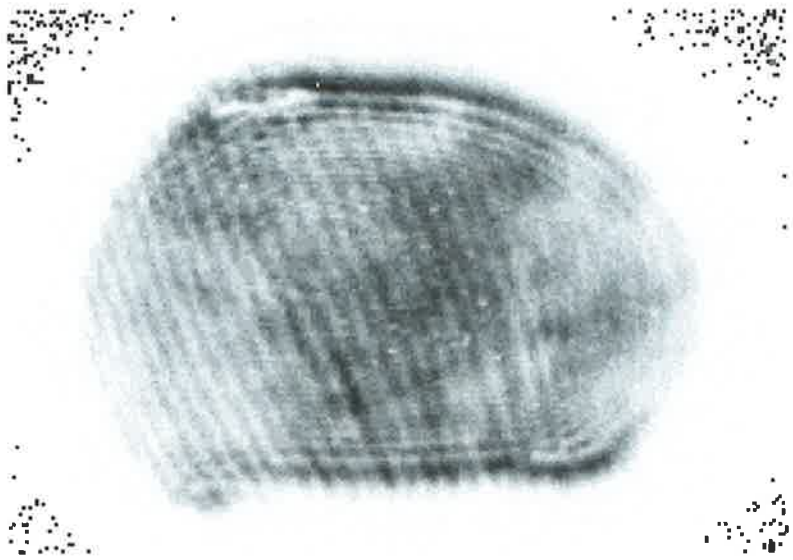

Figure 5: Interference fringes in the probe beam profile due to slight non-separation of front and back face reflections from a non-wedged beamsplitter. This early image is presented in an inverse greyscale. The silhouette of the 6.2 mm glass-blowing burner tip is at the base of the image. Note also the diffraction around the edge of the probe beam due to the presence of an iris in the probe beam path. The pixelation of the image is primarily due the storage format of this image, rather than limitations of the image collection system.

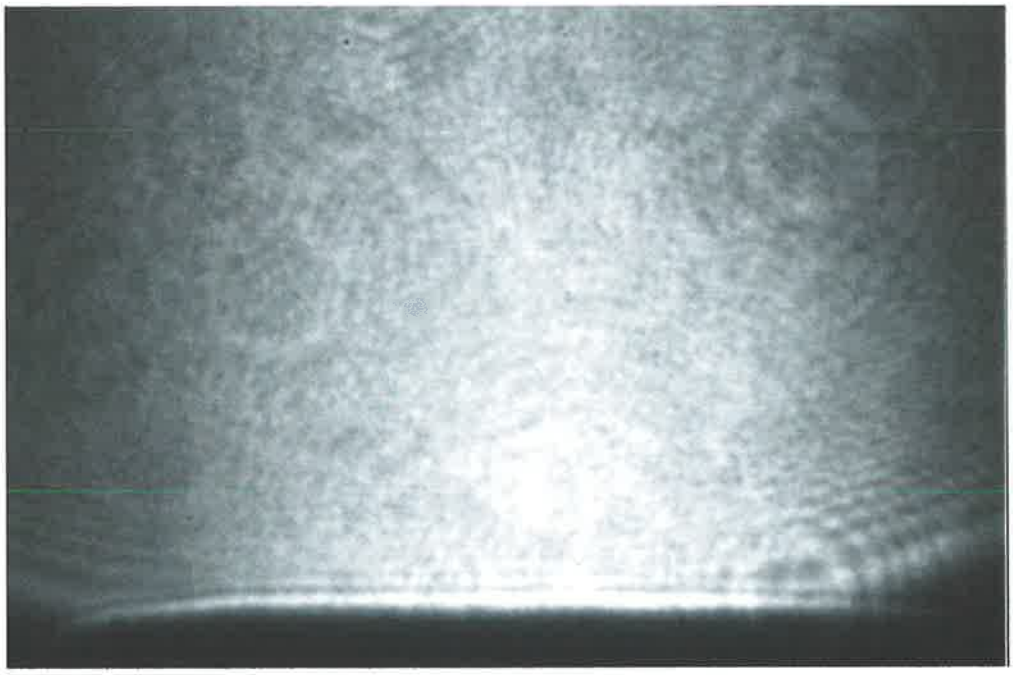

Figure 6: Diffraction effects in the probe beam profile due to dust on the probe beam optics (before cleaning). Note also the edge diffraction from the 6.2 mm tip of the modified glass-blowing torch at the base of the image. These diffraction structures were only detectable in averaged, rather than instantaneous, images.

Figure 7: Flame edge thermal gradient features imposed on a probe beam profile. The shadow of the tip of the glass-blowing torch may just be seen at the base of the image. The thermal gradient features at the edge of the image appear to correspond in position to the hot edge of the bulbous flame. This early image is shown in inverse greyscale.

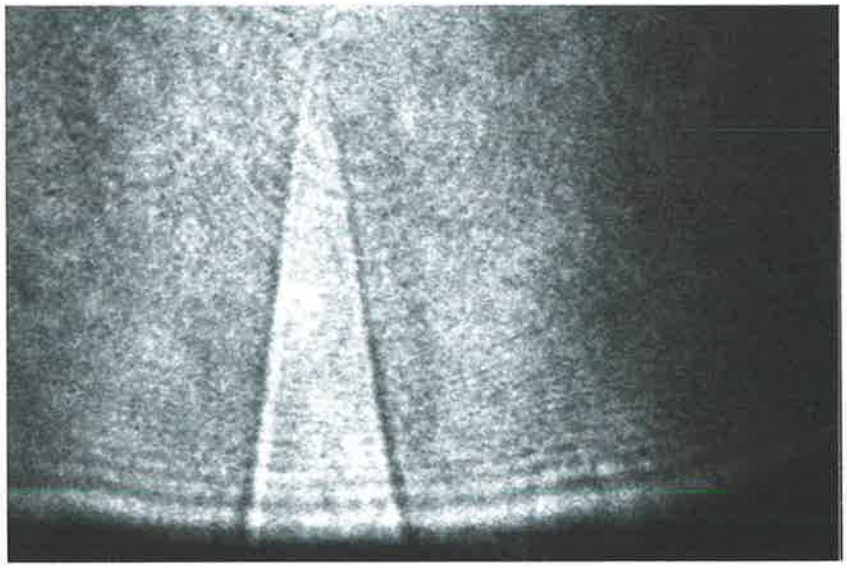

Figure 8: Central cone thermal gradient features imposed on a probe beam profile with additional small burner edge and dust diffraction patterns. The tip of the glass-blowing torch is at the base of the image. It should also be noted that the thermal gradient features are due to the integrated path of the probe beam through the flame, while the PLPS signal in the images that follow are representative of the elliptical interaction region of pump and probe beams.

from the remainder of the day's images. The average background varied by less than ±1 count over the 576 x 384 pixel array and, after the initial stabilisation period, was constant over the course of the day.

The effects of passage through a fuel-lean premixed flame on the probe beam profile was to introduce polarisation changes due to beamsteering at large refractive index/thermal density change boundaries. These effects were not present in the images collected for diffusion flames but were extremely noticeable for premixed, fuel-lean flames, especially if a deep blue central cone structure was visible at the base of the flame. Figure 7 shows an early probe beam profile (i.e. probe beam extinction background) taken with a large probe beam cross-section in comparison with the size of the flame. The tip of the burner may just be seen in silhouette at the base of the image. The flame in this case consisted of a central deep blue cone anchored to the exit orifice of the burner. The surrounding flame bulb was a pale blue in colour and extended out from the tip of the burner. The change in probe beam profile due to passage through the flame is primarily in the appearance of strong thermal gradient features near the base of the central cone region and the hot edge of the flame bulb. The thermal gradient features attributed to the hot flame edge corresponded to a region approximately three to five times larger than the visible extent of the flame itself. Figure 8 shows a similar image collected in a later experiment imaging a smaller fraction of the probe beam cross-section concentrating on the central cone region. The strong central cone shaped polarisation feature noted in Figure 8 and later images is common to most of the premixed fuel-lean flames examined in this thesis.

The relative strength of the probe beam profile structures due to refractive index/thermal density boundaries with respect to the probe beam extinction background can be minimised with the use of an iris, or alternatively a large pinhole, in the focal plane of the post-analyser beam cleaner. Two pinholes, ~ 70 μm and 200 μm, were trialled in this experiment, but both removed too much information from the transmitted probe beam, resulting in a blurred and incomplete image. A 1 mm iris gave the best result, as shown in Figure 6, but experimentation with pinholes in the range 0.3-0.8 mm may show further removal of the thermal gradient structures without loss of image integrity.

Note that it would be premature to attribute the thermal gradient structures to changes in the probe beam polarisation state due to transmission through thermal density variations in the flame. Visually similar features occurred in the probe beam profile for uncrossed probe beam polarisers if no iris or pinhole was used in the beam path and are probably due to largely to thermal beam steering, which acts to slightly redirect the probe beam path. In a similar way to the conservation of probe beam polarisation for glancing reflection from the burner tip, passage through the flame does not appear to significantly change the polarisation state of the probe beam. Consequently, the rejected Glan-Laser probe beam component, which would also contain these features, could potentially be used

for correction of the probe beam background thermal gradient structures. The extent to which the signal beam and rejected polariser component probe beam profile structures are linearly related has not yet been determined.

(1) Orthogonal Zero Signal Confirmation Experiment

A preliminary experiment was undertaken with no Fresnel rhomb to confirm that the LPS signal is zero (within the detection limits of the equipment) for orthogonal pump/probe beam intersection and a horizontally polarised pump beam (with probe beam polarised at $\pi/4$ to the beam intersection plane) as predicted by Nyholm, Fritzon and Alden. The images for this experiment were collected as an unweighted average of 50 shots to confirm the zero signal level in a regime where weak or zero signal was expected.

Linecentre wavelength for the strong OH $A^2\Sigma$–$X^2\Pi$ (0-0) $Q_2(8)$ transition (see Appendix V) was determined by previous alignment of the experiment for a pump/probe beam intersection angle of 30° and confirmed in the following experiment for a pump beam polarised normal to the plane of incidence and orthogonal intersection of pump and probe beam. In addition, the laser system was scanned through the transition to ensure a zero signal level existed over the transition linewidth. The premixed, fuel-lean natural gas/O_2 flame condition leading to maximal OH PLPS signal was selected in the previous 30° beam intersection experiment.

Figure 9 shows the raw Mode 1 (50 shot average) image collected for this geometry, and Figure 10 the Mode 2 (50 shot average) corrected image representing the signal (without probe extinction background), S, to background (with flame), B, ratio, S/B.

The Mode 1 image of Figure 9 appeared to be identical to the probe beam extinction background with the pump beam blocked before intersecting the probe beam. The average signal level of the probe beam extinction background was 15 counts at a gain of 9. It was necessary to correct the Mode 1 image for the probe beam extinction background to identify the signal to background ratio, S/B, as described in equation [7]. **The average corrected signal to background ratio in the flame region of the resultant Mode 2 image of Figure 10 is 0.02 ± 0.11 counts. Consequently, the orthogonal signal component to background ratio is zero or below the level of detection of this system for orthogonal beam intersection for a linearly polarised pump beam polarised in and a probe beam polarised at $\pi/4$ to the beam intersection plane as found previously by Nyholm, Fritzon and Alden[3].**

The level of correction for the probe beam background in the Mode 2 image of Figure 10 is remarkable for a 50 shot average image since the (zero) signal and background were taken in successive image sets. However, given the steadiness of the flame and the laser system (and since

the signal term which would be cubic with laser pulse energy in the linear regime of optical pumping is zero for this experiment), the non-simultaneous method of collecting the average image appears to be valid. A faint edge of the central flame cone is evident in the corrected image, but this is more a polarisation structure (as discussed above) and represents the slight variation in the steady flame cone structure for the two data sets collected, rather than traces of signal. This image emphasises the need for near-simultaneous collection of a probe beam extinction background with each PLPS image for correctable imaging in turbulent flames.

The uniformity of the corrected image in Figure 10 is good. The image ratio method is successful in correcting for non-uniform probe beam background. However, every effort should be taken to produce a reasonably defect free beam cross-section as it may be difficult to completely eliminate strong thermal gradient structures due to passage of the probe beam through the flame from the probe beam defects if there are significant levels of beam steering.

Figures 9 and 10 demonstrate that within the limits of our system, the signal strength in the case of orthogonal intersection of a pump beam polarised in the beam intersection plane (and probe beam polarised at $\pi/4$ to that plane) is zero.

(2) Orthogonal Non-Zero Signal Confirmation Experiment

The Fresnel rhomb was returned to the pump beam path to produce a vertically polarised pump beam. The pump beam polariser was rotated by 90° so that the transmission axis was vertical. The experiment was otherwise unchanged.

Figure 11 is a (50 shot average) raw OH image obtained for this vertically polarised pump beam and an orthogonal pump/probe beam geometry. The flame is the premixed laminar fuel-lean natural gas/O_2 flame previously described. **For orthogonal intersection of a pump beam polarised normal to the beam intersection plane (and a probe beam polarised at $\pi/4$ to that plane) the signal is clearly non-zero in comparison with Figure 9**. The signal overwhelms the probe extinction background which is still present in the image with maximum (spatially) averaged count levels of ~ 180 in the flame region for a ICCD gain of 9. The probe beam average background level due to the polariser extinction ratio is ~ 15 counts. The experiment was largely unchanged from (and conducted in the same experimental session as) that of the previous orthogonal zero signal confirmation experiment, emphasising the zero and non-zero signal dependency on pump polarisation alone.

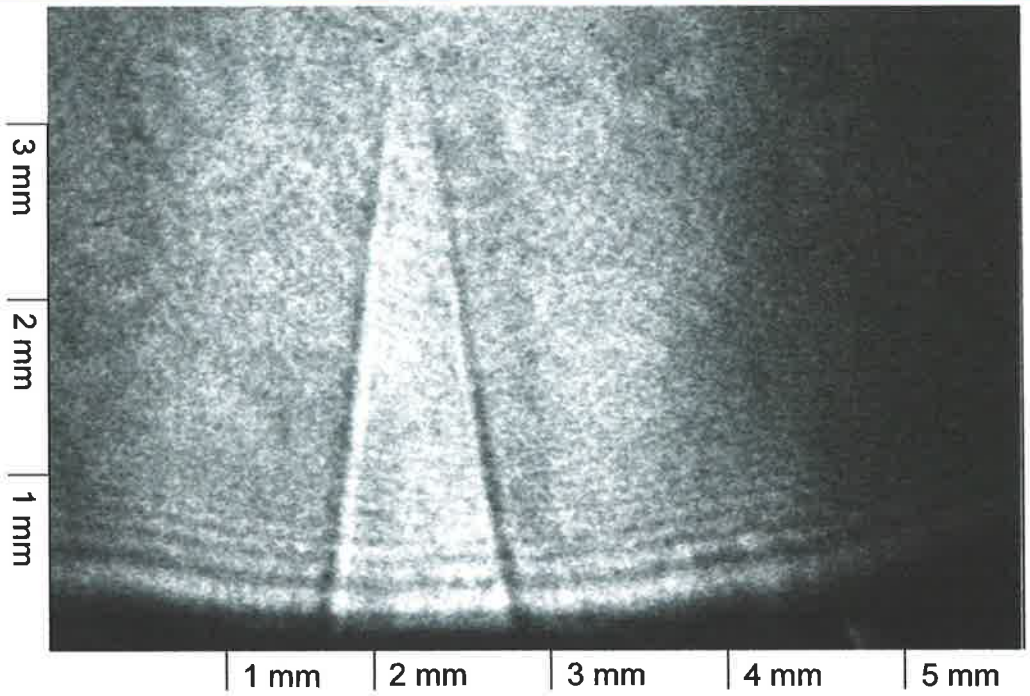

Figure 9: Raw Mode 1 (50 shot average) OH PLPS image for a premixed, fuel-lean natural gas/O_2 flame (OH $A^2\Sigma$–$X^2\Pi$ (0-0) $Q_2(8)$ transition) for an orthogonal pump/probe beam geometry and a pump beam polarised in (and probe beam polarised at $\pi/4$ to) the beam intersection plane. The average count level is 15 at gain 9.

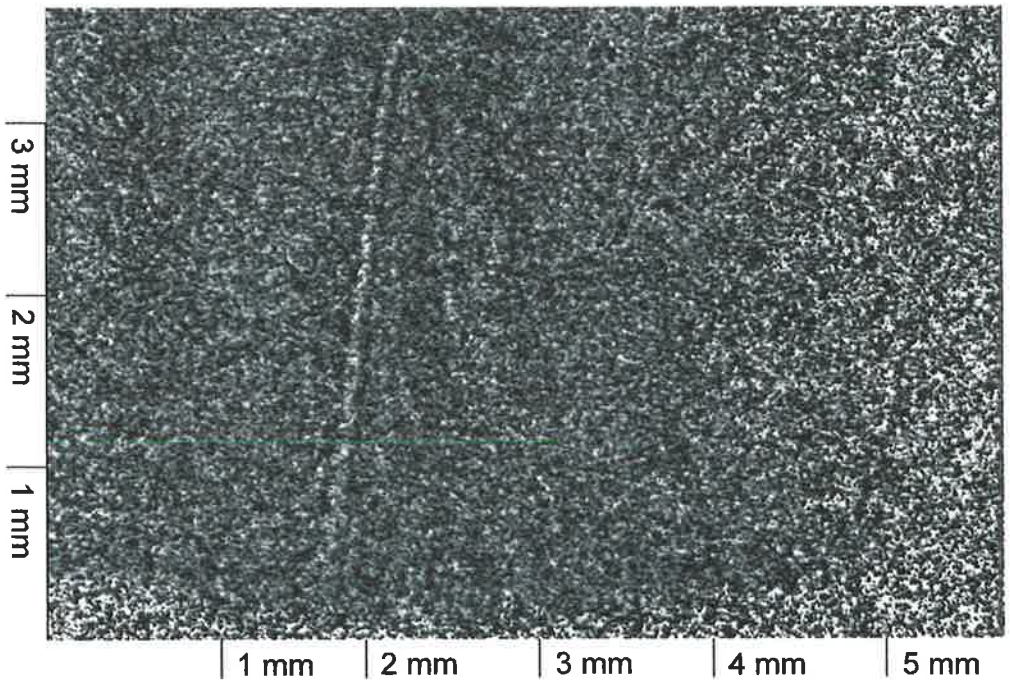

Figure 10: Mode 2 corrected PLPS image (50 shot average) based on Figure 9 above. The average corrected signal to background level in the flame region is 0.02 ± 0.11 counts.

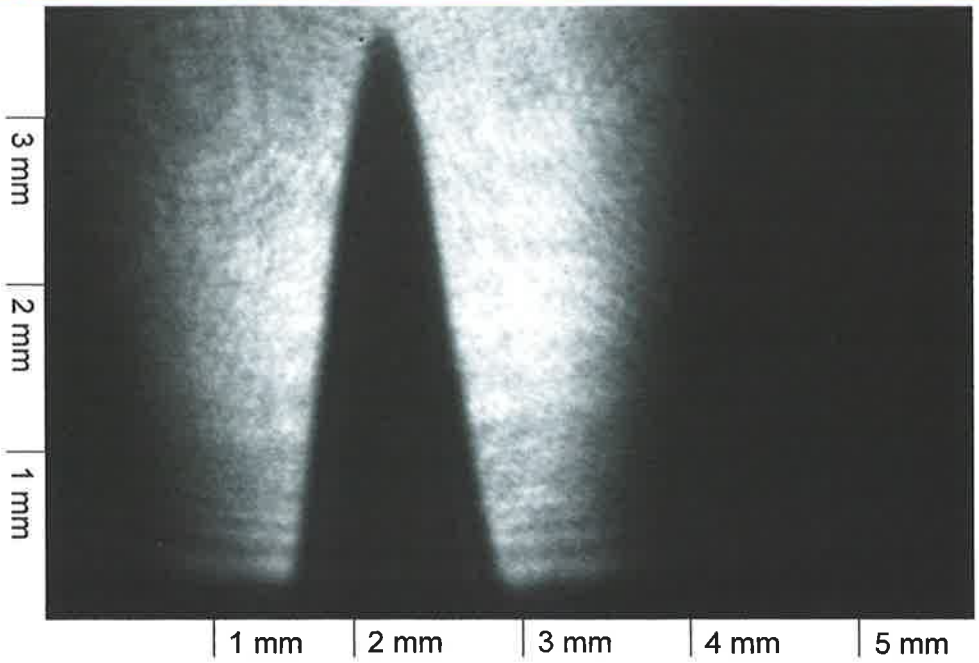

Figure 11: Raw Mode 1 (50 shot average) OH PLPS image for a premixed, fuel-lean natural gas/O_2 flame (OH $A^2\Sigma$–$X^2\Pi$ (0-0) $Q_2(8)$ transition) for an orthogonal pump/probe beam geometry and a pump beam polarised normal (and probe beam polarised at $\pi/4$) to the beam intersection plane. The maximum count level is ~ 180 at gain 9.

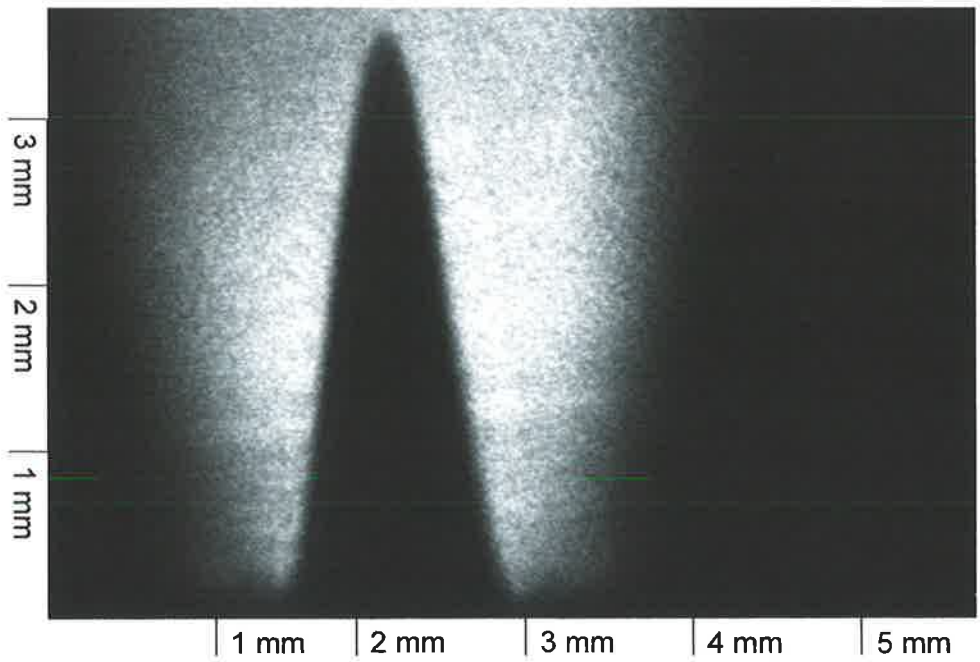

Figure 12: Mode 2 corrected PLPS image (50 shot average) based on Figure 11 above. The maximum signal to background (S/B) level in the flame region is ~ 10-11. The average signal to background level at the edge of the image is 0.05 ± 0.10, while the interior of the central flame cone has an average signal to background level of 0.11 ± 0.09.

The Mode 2 corrected (50 shot average) image based on the (50 shot average) image in Figure 11 is shown in Figure 12. The Mode 2 signal to background level in the flame region is typically ~ 10-11. The average Mode 2 signal to background level at the flame-free edge of the image is 0.05 ± 0.10, while the central (assumed OH free) flame cone region has an average Mode 2 signal to background level of 0.11 ± 0.09, resulting in a maximum (corrected) signal to noise ratio of ~ 200:1. This is in contrast to the signal to probe extinction background ratio in the Mode 1 image of ~ 9:1. Figures 11 and 12 represent 50 shot averaged images. It is clear that correction for the probe extinction background is necessary to obtain high signal to noise ratios in PLPS imaging. In this steady flame is was sufficient to take an averaged background image for correction. However, in flows and flames that are not steady in time, the probe beam extinction background should be taken nearly simultaneously with the signal image on the timescale of the flame or flow.

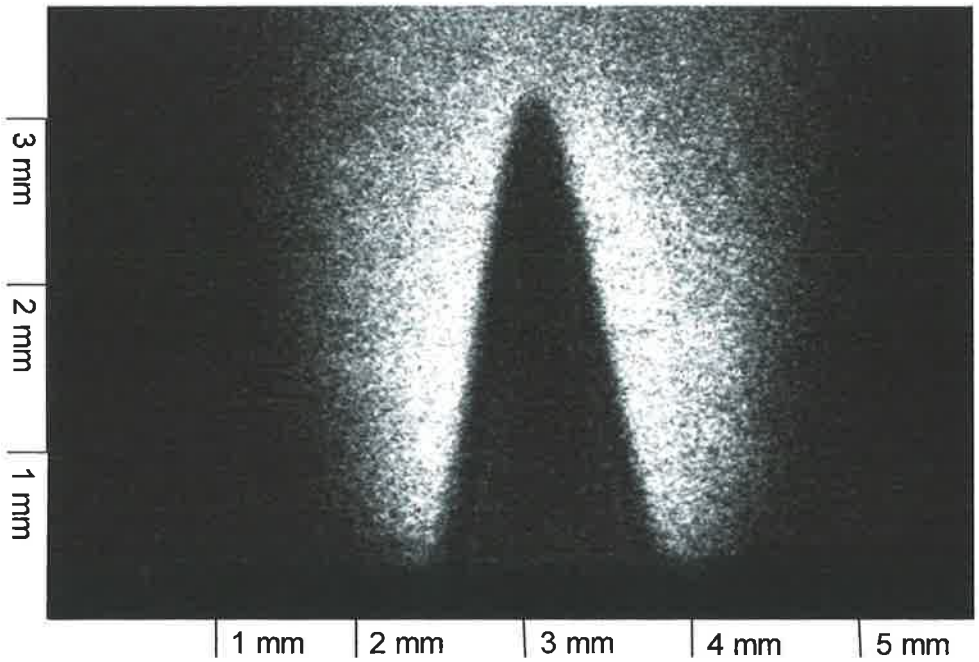

Figure 13: Mode 1 instantaneous image for a premixed, fuel-lean natural gas/O_2 flame (OH $A^2\Sigma$–$X^2\Pi$ (0-0) $Q_2(8)$ transition) for an orthogonal pump/probe beam geometry and a pump beam polarised normal to the beam intersection plane. The probe beam is polarised at $\pi/4$ to the beam intersection plane. The maximum count level in the flame region is ~ 300 ± 50. The average count level at the edge of the image is 11 ± 10, while the interior of the central flame cone has an average count level of 24 ± 14 counts. The silhouette of the modified glass-blowing burner may be seen at the base of the image.

The smoothness of the Mode 2 corrected image when compared with the Mode 1 image is also of interest. The linearity of the LPS signal and background with probe beam intensity leads to extremely good elimination of diffraction, interference and non-uniform probe profiles if the image

ratio method defined to calculate the Mode 2 images is used. Once again, the technique depends on signal image and probe background being collected near-simultaneously on the timescale of the flame.

A representative uncorrected (Mode 1) instantaneous OH PLPS image is shown in Figure 13 to demonstrate the similarity between average and instantaneous images for this flame condition. The steadiness of the flame leads to little variation between the average and instantaneous OH structures in the PLPS images of Figures 11 and 13. The tip of the central cone region varied in height by less than 0.3 mm over a timescale of minutes. In comparison with the average images, average count levels of 150 to 420 in the regions of maximum signal were noted for the instantaneous images. Due to the low absolute level of signal and background collected by the ICCD, diffraction and interference structures are not noticeable in instantaneous images. Note that the instantaneous image in Figure 13 was taken in a different dataset than the average image of Figure 11, accounting for the difference in flame position.

Figures 11 and 12 demonstrate clearly that the LPS signal is non-zero for orthogonal intersection and a pump beam polarised normal to the beam intersection plane (and probe beam polarised at $\pi/4$ to that plane). It follows that polarisation spectroscopy imaging is applicable to all beam intersection angles if the signal strength is sufficiently high to allow for the reduction in signal strength with beam intersection angle according to the $\mathrm{cosec}^2(\chi)$ dependence for the above polarisation configuration.

Significance of Orthogonal Imaging with Respect to Spatial Resolution

The imaged area in Figures 11 and 12 is 3.7 mm x 5.5 mm with resolution of 9.5 μm per pixel. For a beam intersection angle of 30°, the equivalent spatial resolution of the elliptical pump/probe interaction region measured along the axis lying in the beam intersection plane would be half this, 19 μm per pixel. The thickness of the laser sheet and hence of the elliptical interaction region for this set of average images was estimated to be 700 μm. The thickness of the laser sheet as measured along the probe beam path is the ultimate limitation on the volume resolution of the polarisation spectroscopy planar imaging technique.

The collected PLPS image is carried on the circular cross-section of the probe beam and represents the elliptical intersection region of pump and probe beams. Figure 14 shows the relevant intersection volume contributing to each pixel in the collected image of the probe beam cross-section for nonorthogonal beam intersection. The collected image is foreshortened along an axis lying in the beam intersection plane. While it is tempting to stretch the collected image along this axis, the stretched image is representative of the distribution of the target species in the elliptical

interaction region as viewed from an angle of incidence of $\pi/2 - \chi$, and not as viewed from normal incidence (see Figure 15).

The stretched image is representative of the elliptical interaction region as viewed from normal incidence if the rhomboid shaded region in the elliptical interaction region contributing to a single pixel in the collected image in Figure 15 may be approximated by the equivalent rectangular volume in the stretched image. This is the case if the distance, d, (shown in Figure 15) which represents *the increase in the distance measured along the axis lying in the beam intersection plane in the elliptical beam intersection volume which is imaged by each pixel*, and defined as

$$d = \frac{W}{|\tan(\chi)|} \qquad \text{Equation 8}$$

is of the order of magnitude of or smaller than the pixel resolution of the stretched image, p, with respect to the axis lying in the beam intersection plane. Ignoring any magnification factors due to imaging systems placed after the probe beam analyser, the pixel resolution, p, is defined as

$$p = \frac{p_{90°}}{|\sin(\chi)|} \qquad \text{Equation 9}$$

where $p_{90°}$ is the pixel resolution in an orthogonal geometry. This condition requires that the orthogonal pixel resolution satisfy the equation

$$p_{90°} \sim W \cdot |\cos(\chi)| \qquad \text{Equation 10}$$

PLPS may be used to easily image regions on the scale of 10 μm per pixel. Given a typical pump beam thickness of W ~300 μm in the UV, the distance, d, is of the order of or smaller than a pixel image dimension of 10 μm only for beam intersection angles greater than 88°. **For a beam intersection angle of 30°, the distance, d, under the same conditions is ~ 52 times the pixel image dimension. The distribution of the target species obtained from the stretched image will clearly deviate significantly from that which would be inferred from viewing the elliptical interaction region from a position orthogonal to the pump sheet plane**.

The pixel resolution in the collected PLPS image of the elliptical beam interaction region (along the axis lying in the beam intersection plane) was described in equation [9] above. Maximum pixel resolution is obtained for orthogonal imaging geometries. The pixel resolution decreases only by a factor of 2 for a beam intersection angle of 30° and by a factor of 3.86 for a beam intersection angle of 15°. This is acceptable given the rapid increase in signal strength for small beam intersection angles. However, the collected image will compressed in the dimension of the intersection plane and, even when stretched, the inferred species distribution will represent the elliptical pump/probe interaction region as viewed from a 60° or 75° angle of incidence (for 30° and 15° beam intersection angles respectively).

The major limit of spatial resolution is due to the finite thickness of the pump beam. The effective thickness of the pump beam measured along the direction of propagation of the probe beam leads to a sheet thickness resolution of

$$q = \frac{W}{|\sin(\chi)|}$$ Equation 11

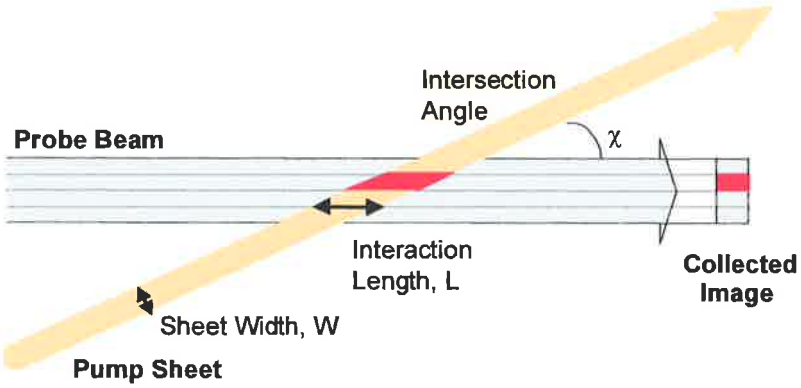

Figure 14: Intersection of pump and probe beams leading to a 1/sin(χ) dependence of interaction length measured along the probe beam path.

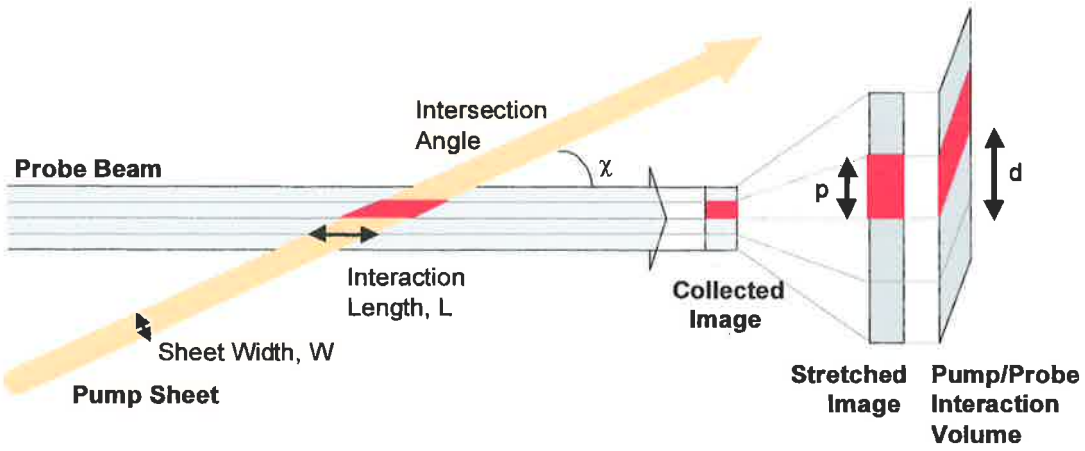

Figure 15: Difference between the stretched image and the elliptical interaction volume with respect to representation of the target species distribution. For large beam intersection angles, the thickness of the laser sheet defines the number of pixels over which the signal from a single target species region will be distributed.

Once again, this corresponds to a decrease of a factor of 2 for a beam intersection angle of 30° and by a factor of 3.86 for a beam intersection angle of 15°. For a pump sheet thickness of 300 μm,

this corresponds to a resolution along the probe beam path of 600 μm for an intersection angle of 30° and a resolution of 1.16 mm for a beam intersection angle of 15°.

This lack of resolution due to the thickness of the pump sheet is shared by common imaging techniques such as PLIF as well as polarisation spectroscopy imaging. The increase in signal strength at small angles of beam intersection is offset by the decrease in both pixel and beam thickness resolution in the collected image. Note that there is no loss of pixel resolution in the direction normal to the beam intersection plane. One dimensional imaging in this direction would allow high signal strength and no loss of spatial resolution other than that due to the thickness of the pump sheet. Such a technique would be eminently suitable for validation of numerical flame models of species concentration normal to the surface of standard flat flame burners.

The identification of non-zero LPS signal for orthogonal pump/probe beam intersection (and hence - based on the theory in Chapter II- for all beam intersection angles between 0 and π) has vastly increased the spatial resolution available to polarisation spectroscopy imaging.

(3) Orthogonal OH PLPS Imaging for a Linearly Polarised Pump Beam

All images shown so far in this chapter correspond to symmetrical flames with the pump sheet aligned to the central axis of the flame. For orthogonal imaging, this geometry allows for coincidental overlap of the central cone probe beam polarisation feature (which is due to the path-integrated effect of the probe beam transmission through the flame), and the shape of the region of OH signal (which originates from the region of interaction of pump and probe beams). The overlap of these two structures in the flame simplifies the corrected images and incorrectly represents the degree of correction achieved for the probe extinction background.

The set of images presented in Figures 16 and 17 investigates the adequacy of correction for thermal gradient features in the probe extinction background for images in which the pump sheet does not pass through the axis of the flame. The following set of images are for orthogonal beam intersection (within reasonable accuracy) for a pump beam polarised in the beam intersection plane. The images are compared with equivalent images for pump beam intersection angles of 15° and 30° in following chapters.

Figures 16 and 17 show a set of images obtained by scanning the pump beam across the flame tip using a screw control on the deflecting 90° prism in the pump beam path. Figure 16 shows the (50 shot average) Mode 1 images as the pump beam is scanned across the flame, while Figure 17 shows the equivalent (50 shot average) Mode 2 images. The raw (Mode 1) and corrected (Mode 2) images for the same pump beam position are shown on the same page to clearly indicate the level of correction achieved in each case.

Note that, due to the use of a screw control to rotate rather than purely translate the deflecting prism, the pump/probe beam intersection angle varied slightly from 90° for this set of images. The maximum deviation of pump/probe intersection angle from normal incidence was estimated to be 2.8°, so there is some small distortion of the images and the geometry is not purely orthogonal. However, the signal to noise and signal to background ratios from Figures 11 and 12 have already demonstrated that the LPS signal is non-zero for an orthogonal geometry and a pump beam polarised normal to the beam intersection plane (with probe beam polarised at $\pi/4$ to the same plane).

The image set of Figures 16 and 17 clearly demonstrates the effects of thermal density variation induced probe beam features in the probe extinction background on both (50 shot average) Mode 1 (uncorrected) and Mode 2 (corrected) images. It is apparent that the clarity of images in Figures 11 and 12 is due to the coincidence of the edges of the central depolarisation cone feature and the OH signal in the same region. This coincidence disappears for images where the pump beam does not pass accurately through the central plane of the axisymmetric flame.

Figure 16 shows that the uncorrected images are clear in the regions where no thermal gradient features occur. The OH signal is distorted in regions where strong thermal gradient features occur. However, it is apparent that the corrected images shown in Figure 17 based on a premeasured average probe beam extinction background minimise the effects of the thermal gradient features surprisingly well. The Mode 2 correction method is remarkably successful in reducing or eliminating even strong, sharp thermal gradient features on the probe beam extinction background. Where the central cone edge structure in the grey-scale 2-D images remains residually in the Mode 2 images, the strength of the structure is due largely to pattern recognition. The edges of the (corrected) structure are unnoticeable in 1-D signal cross-section plots and correspond to less than half a (corrected) Mode 2 count or about 5% of the maximum Mode 2 (corrected) count level. However, the evidence of the these images reinforces the requirement for accurate probe beam background correction in any flame or flow which introduces any significant perturbation of the probe beam intensity or profile.

As stated at the beginning of the chapter, the experimental results above support the theoretical models of both Reppel and Alwahabi[23] and those of Lavrinenko and Gancheryonok but do not differentiate between the two models. However, the experimental results in this chapter stand in indicating that polarisation spectroscopy may be applied in ALL beam geometries in the case of a linearly polarised pump beam if the pump beam polarisation direction is aligned normal to the beam intersection plane. The theory developed in Chapter II shows that maximum signal in the case of a linearly polarised pump beam will be obtained for a probe beam polarised at 45° to the normally

polarised pump beam. Such a polarisation configuration allows significant signal strength for all beam intersection angles with respect to the signal which would be obtained for the reasonably small beam intersection angle of 30°. This extends the range of application of polarisation spectroscopy imaging extensively, considering that combustion experiments are often undertaken in locations which severely limit laser diagnostic input and detection angles.

In this chapter, the first (to the best of our knowledge) planar laser polarisation spectroscopy imaging for orthogonal intersection of pump beam probe beams has been demonstrated. The pump beam was polarised normal to the beam intersection plane and the probe beam at $\pi/4$ to that plane. This result supports the prediction (based on the theory developed in Chapter II) that LPS signal may be obtained for all beam intersection angles for specified pump and probe beam polarisation configurations. This result allows the development of polarisation spectroscopy imaging (PLPS) for all pump/probe beam geometries, resulting in a large improvement in the spatial resolution available in the collected images.

A zero LPS signal strength for the case of a pump beam polarised in the plane of intersection of pump and probe beams for orthogonal beam intersection as reported by Nyholm, Fritzon and Alden[3] has been confirmed (to the limits of the experimental apparatus).

In Chapter III, a similar theoretical description of polarisation spectroscopy to that derived in Chapter II for a linearly polarised pump beam is derived in the case of a circularly polarised pump beam. The theory is based on the optical behaviour of an optically active uniaxial gas.

The predictions of this theory are supported by experimental results in Chapter IV. The first (to the best of our knowledge) LPS signal and the first (to the best of our knowledge) polarisation spectroscopy images achieved in the case of a circularly polarised pump beam for orthogonal pump/probe beam intersection are presented.

Figures 16 and 17: Set of (50 shot average) OH PLPS images of the premixed, fuel/lean natural gas/O_2 flame for a pump beam polarised in the beam intersection plane (with probe beam polarised at $\pi/4$ to that plane) and an orthogonal pump/probe beam geometry. The image set was obtained by scanning the pump sheet across the tip of glass-blowing torch. The two images on each pages represent corresponding raw (Figure 16: top image) Mode 1 and corrected (Figure 17: base image) Mode 2 images. The images are plotted on a grey scale based on the 5 to 95% signal strength of each image with black representing the lowest signal.

(a) (Figures 16 and 17)

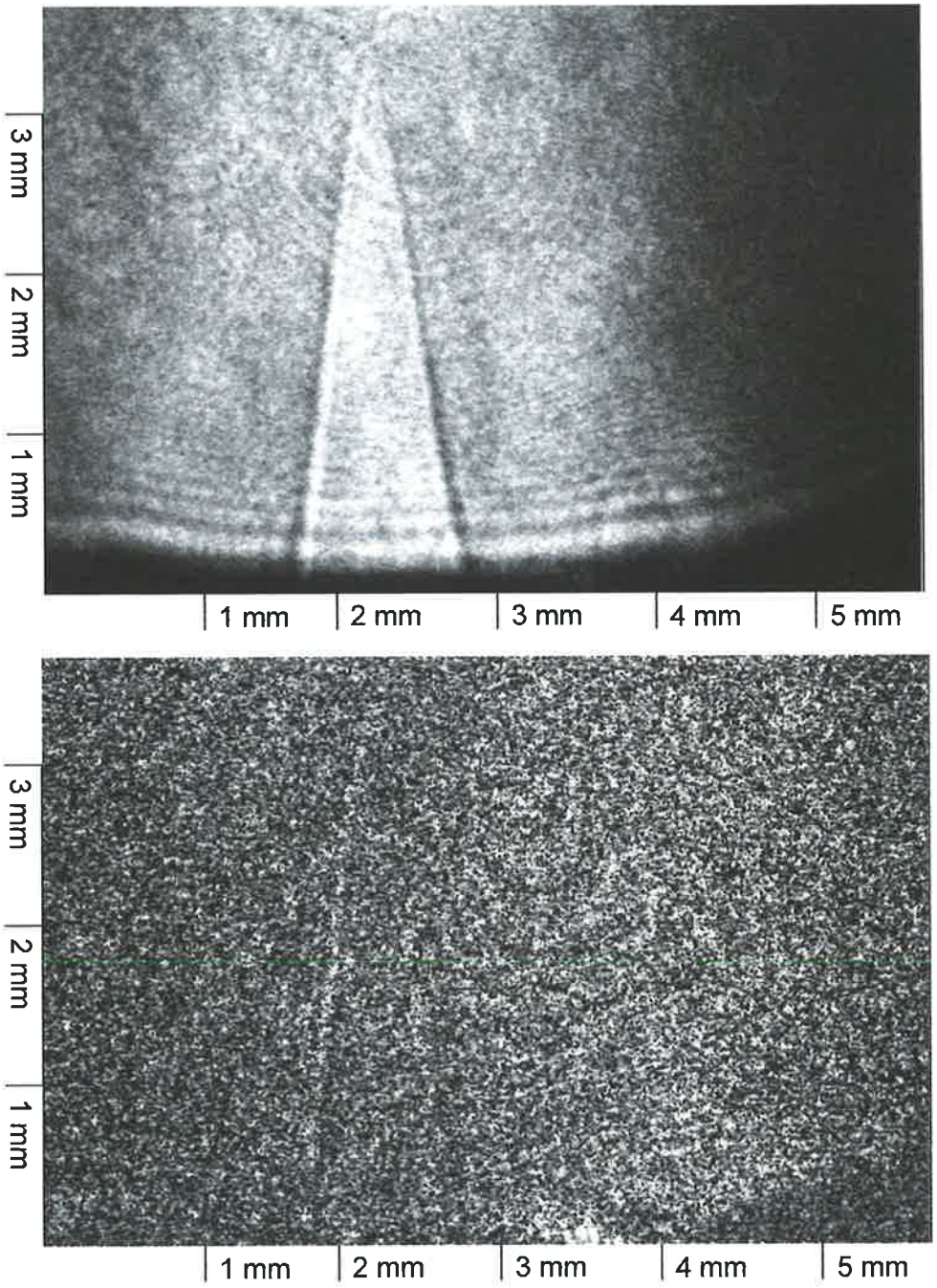

(b) (Figures 16 and 17)

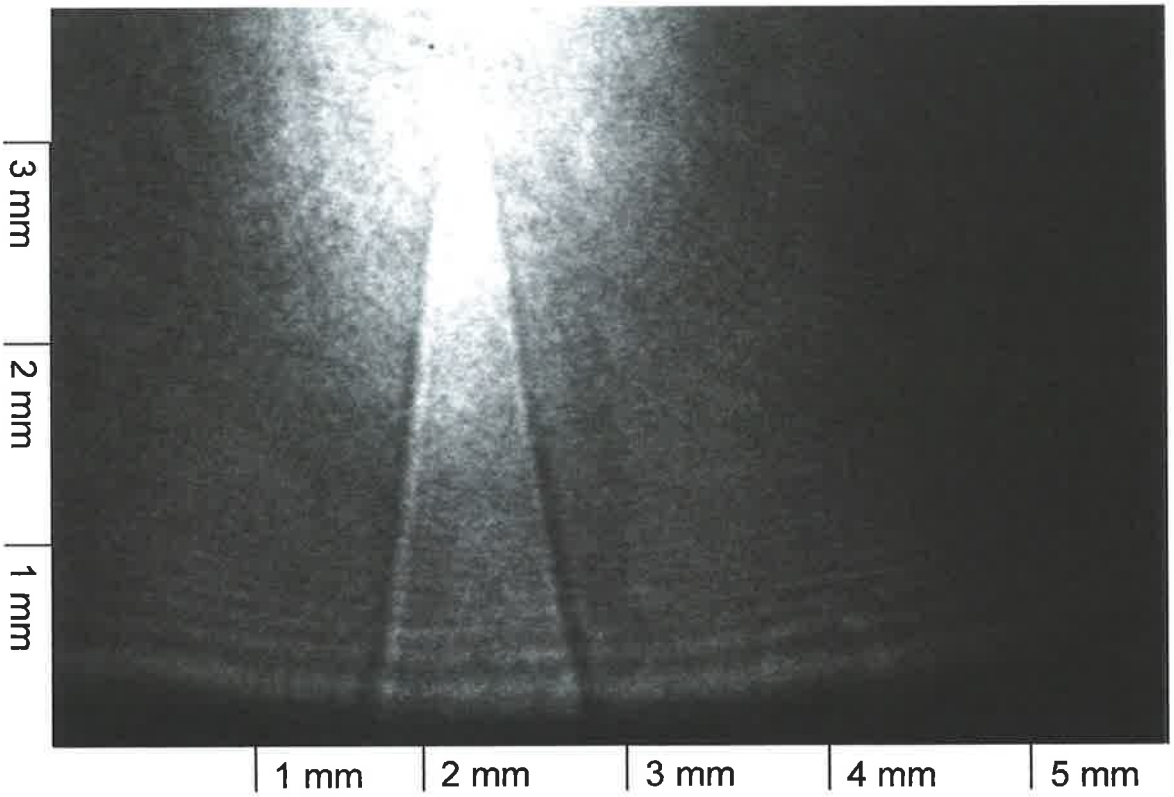

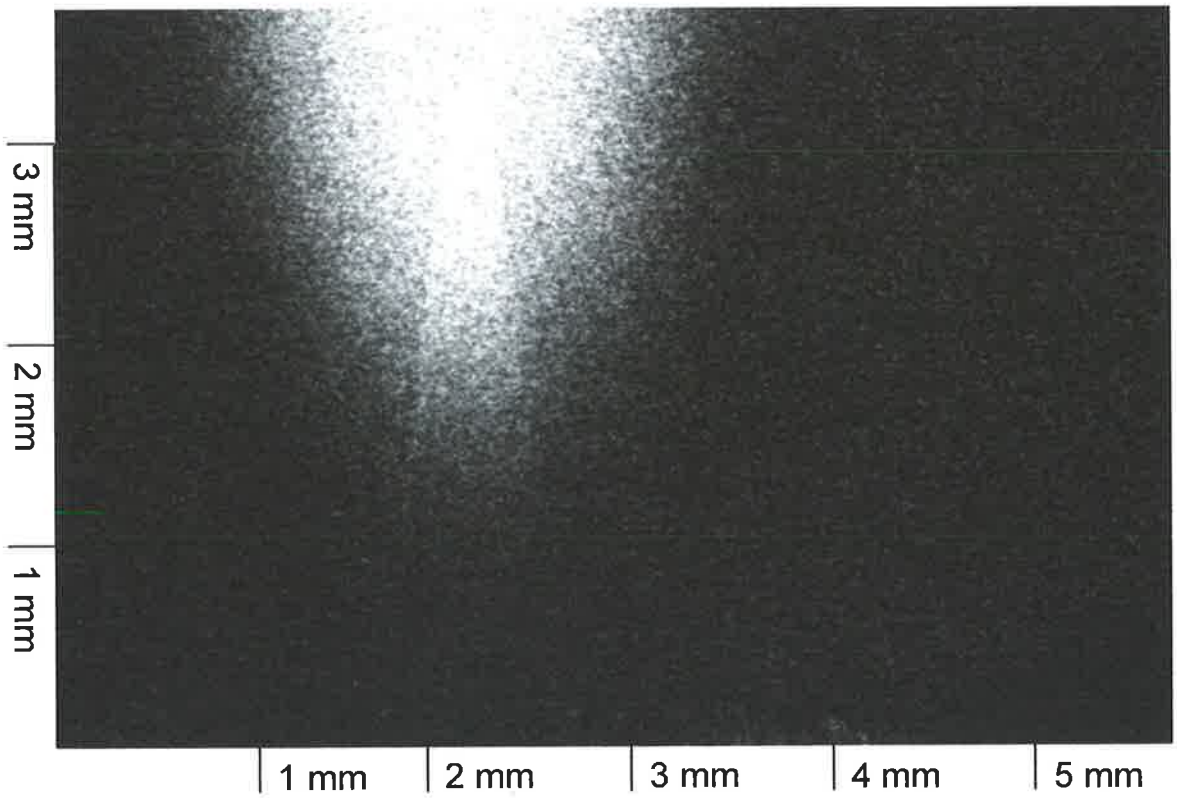

(c) (Figures 16 and 17)

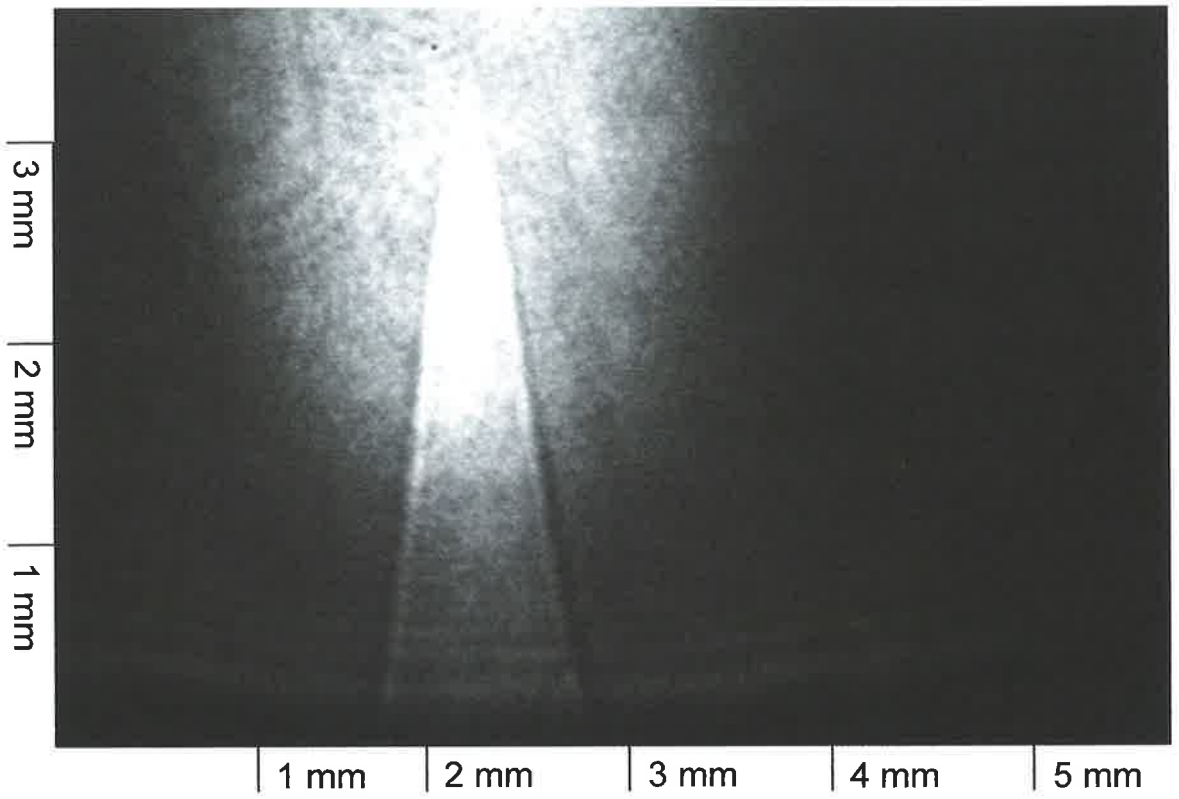

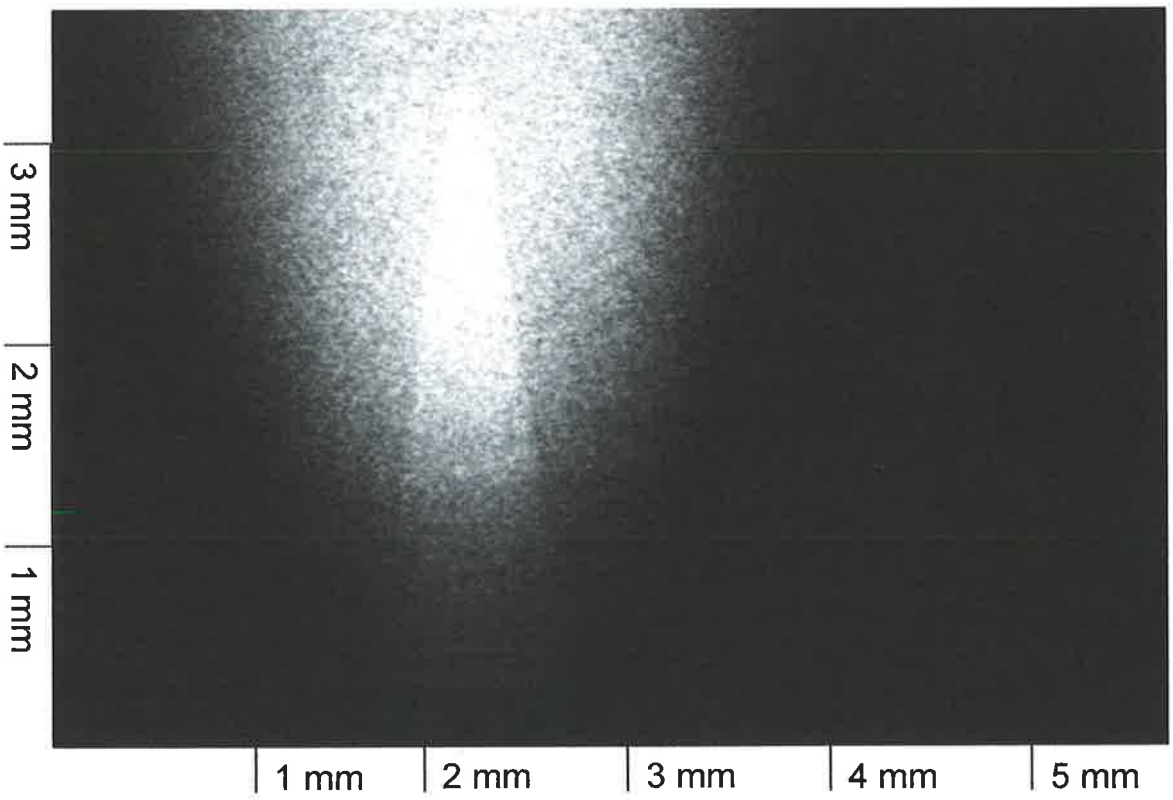

(d) (Figures 16 and 17)

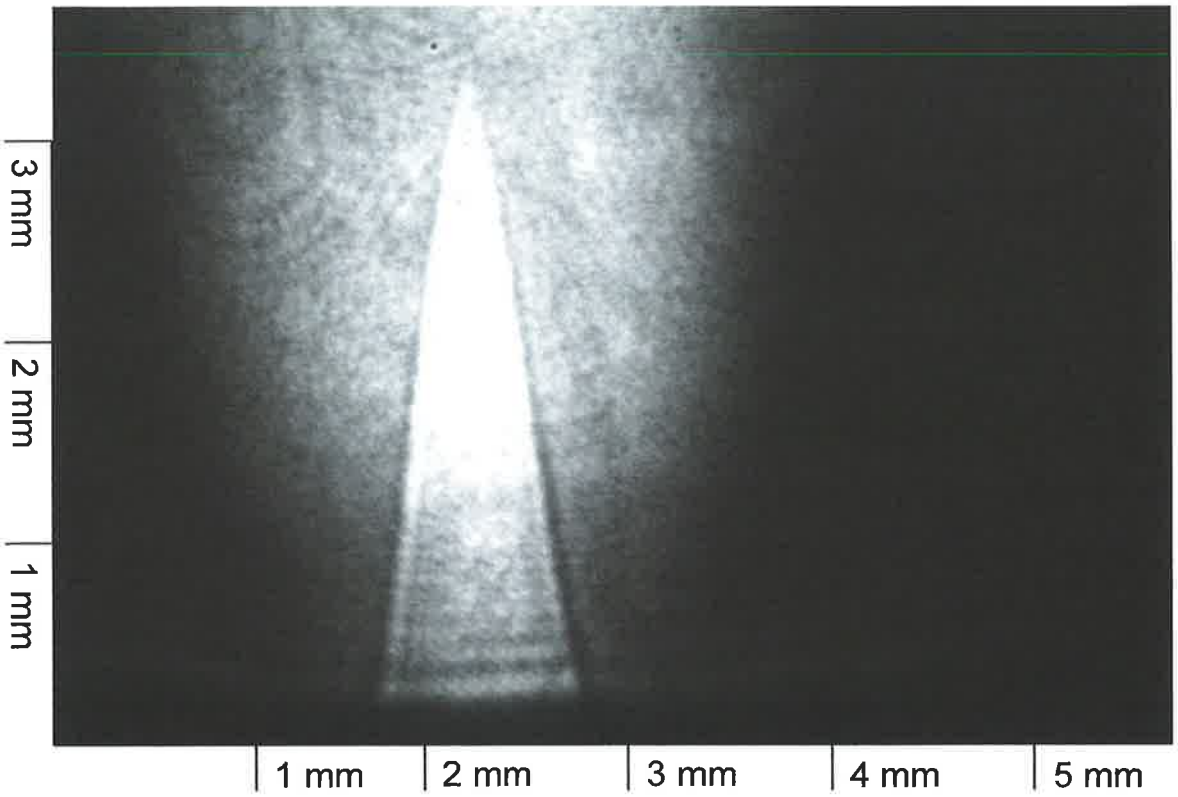

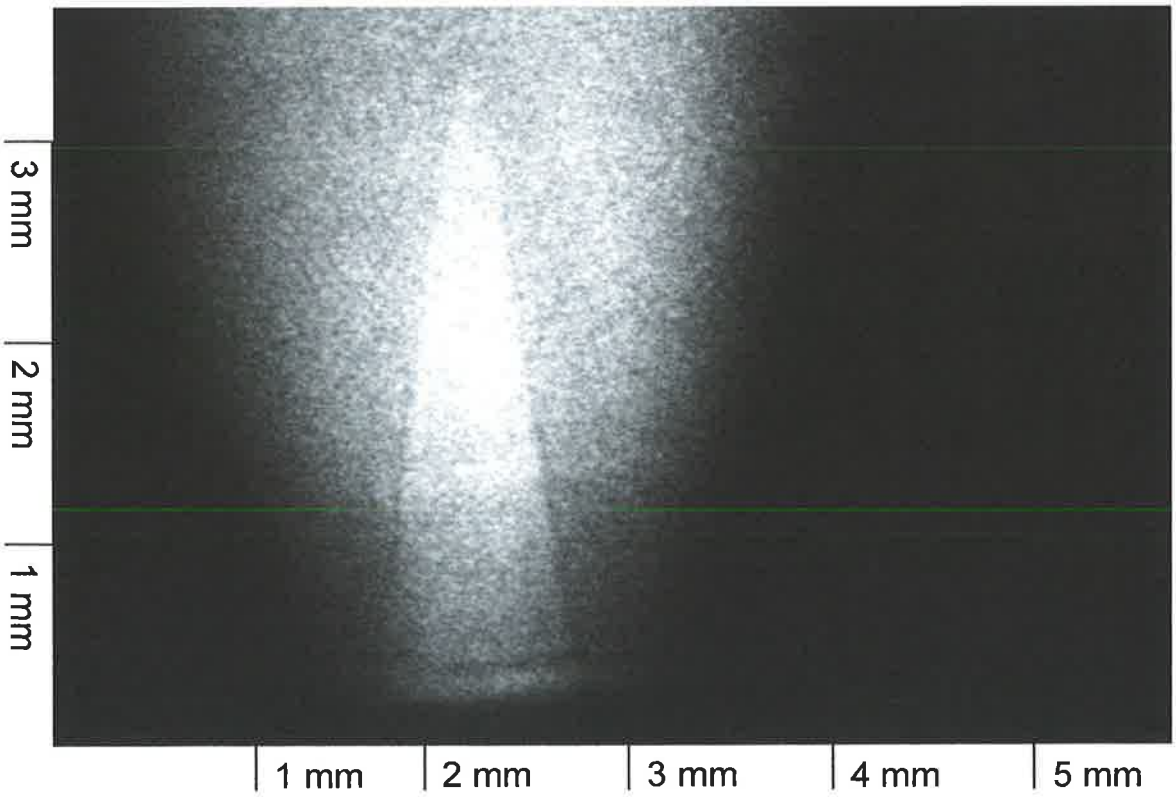

(e) (Figures 16 and 17)

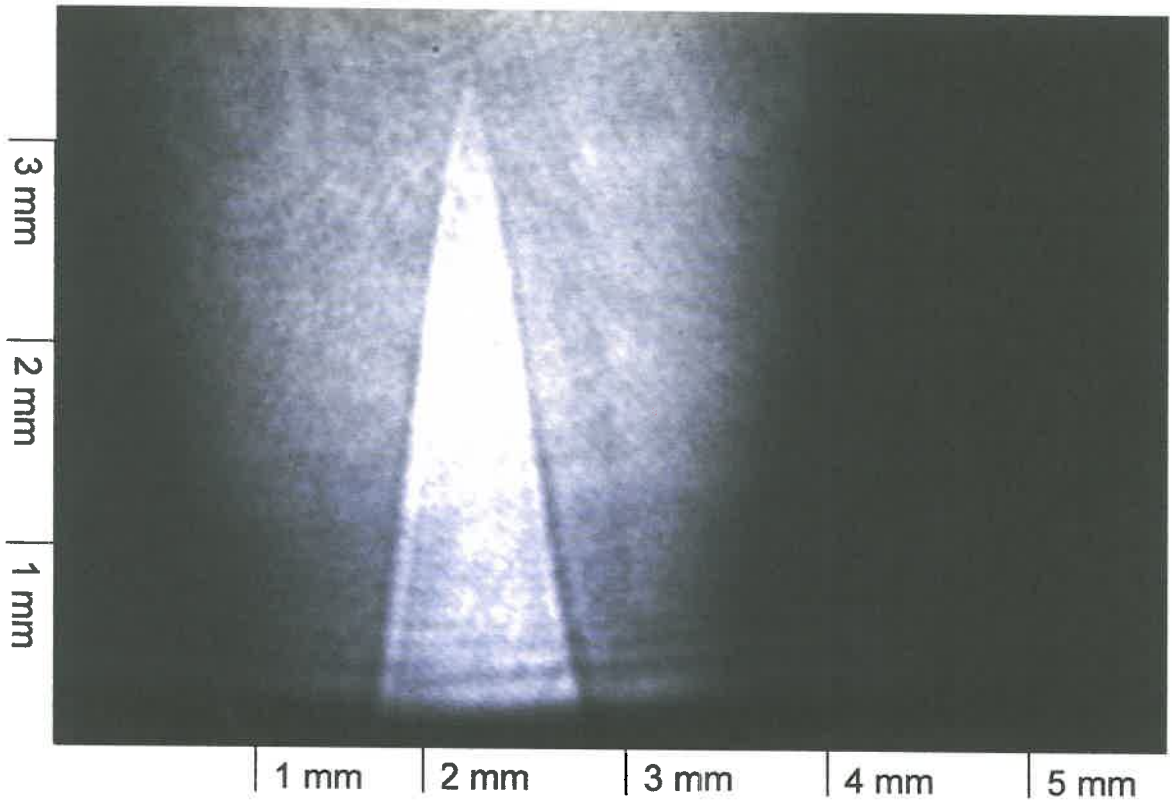

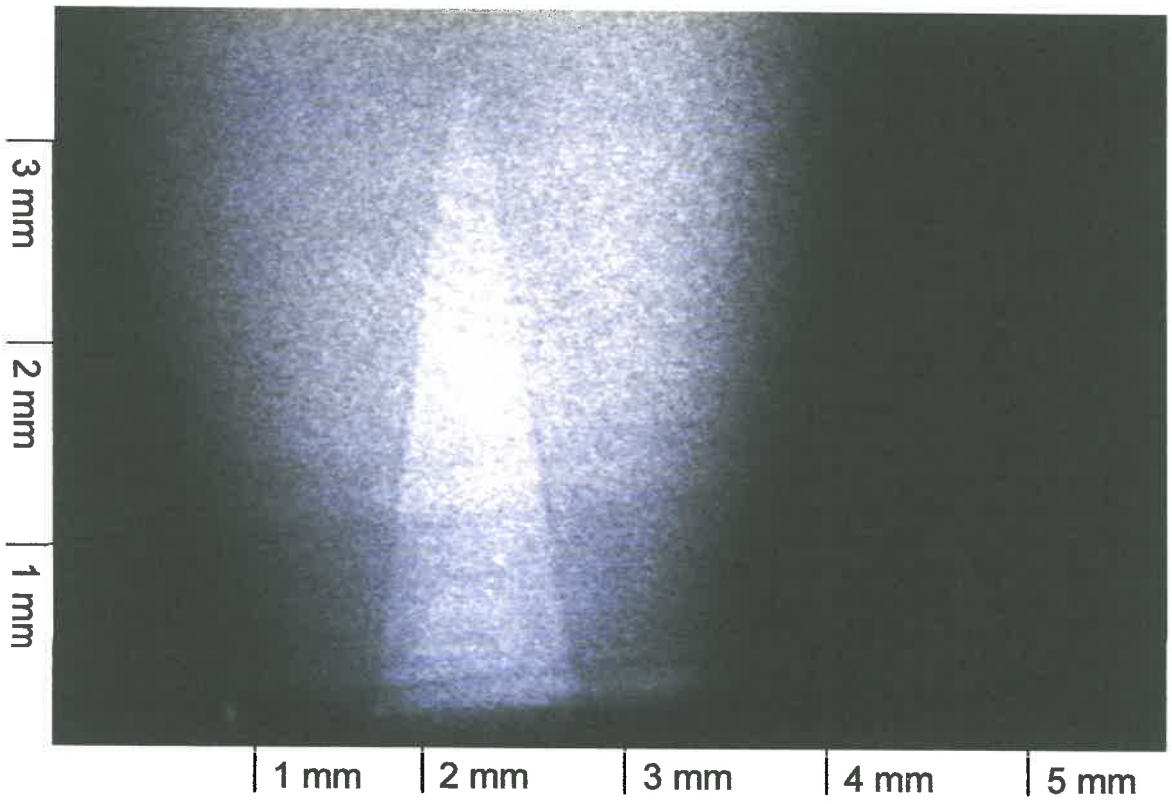

(f)

(Figures 16 and 17)

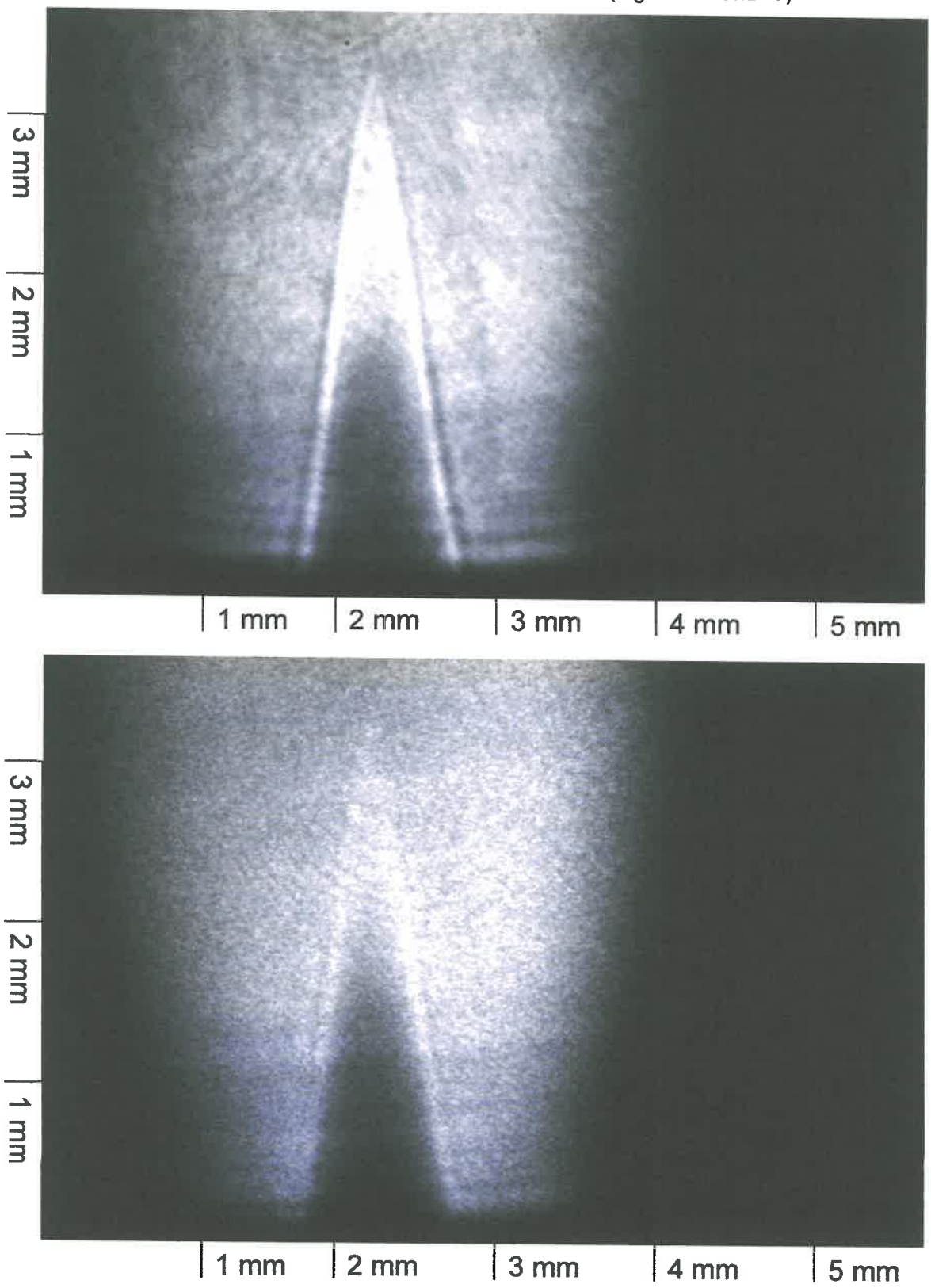

(g) (Figures 16 and 17)

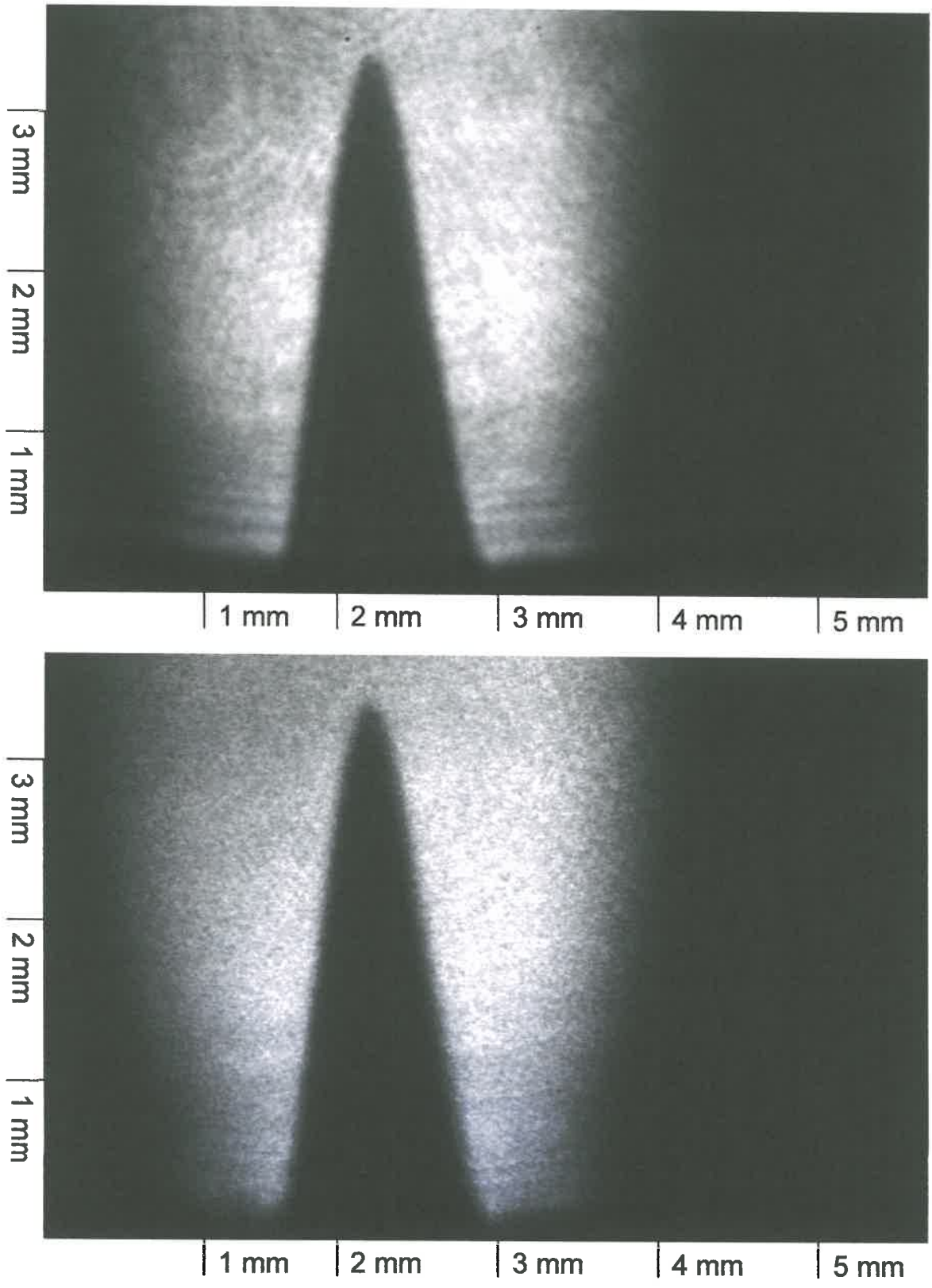

(h)

(Figures 16 and 17)

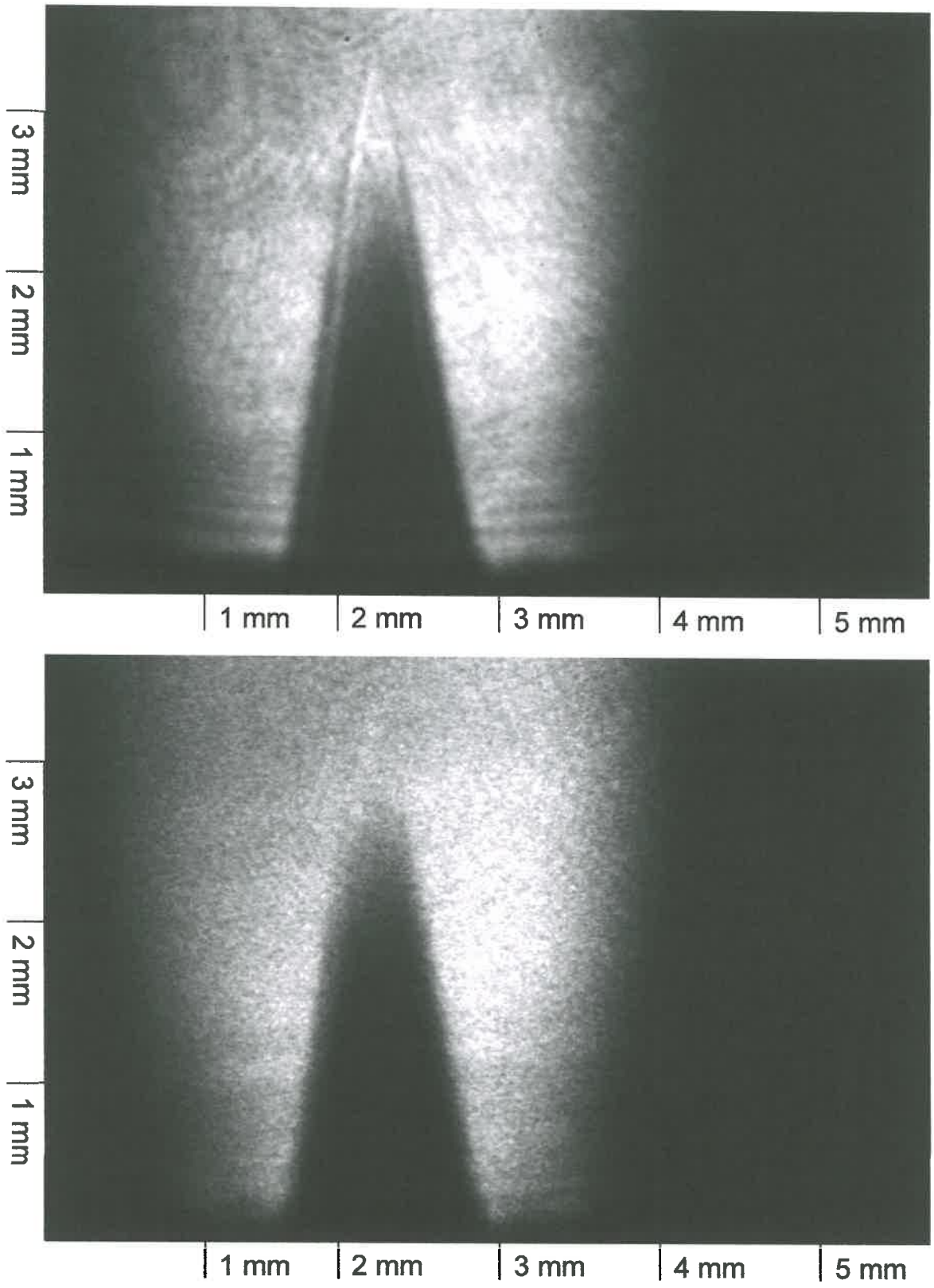

(i) (Figures 16 and 17)

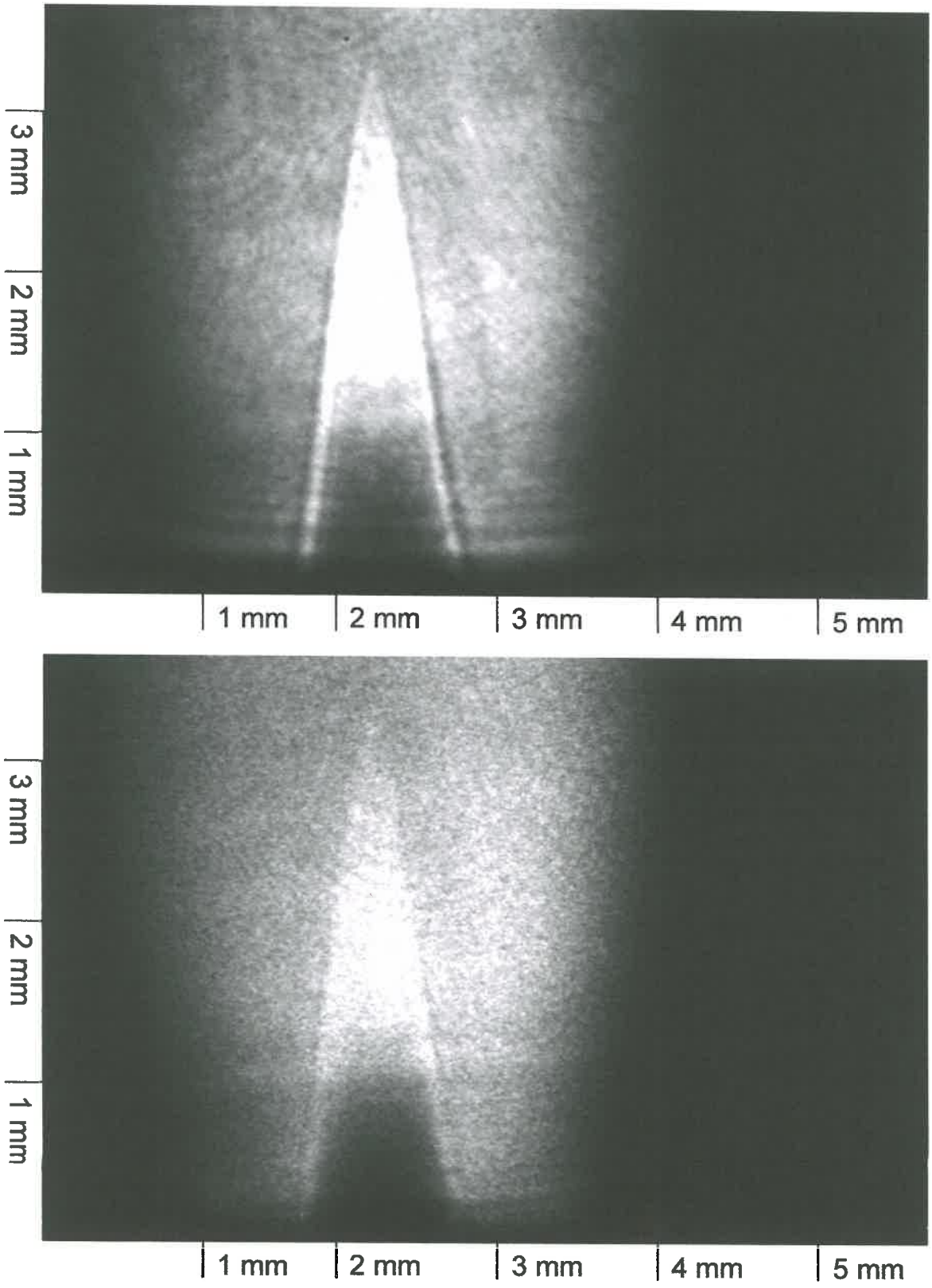

(j)

(Figures 16 and 17)

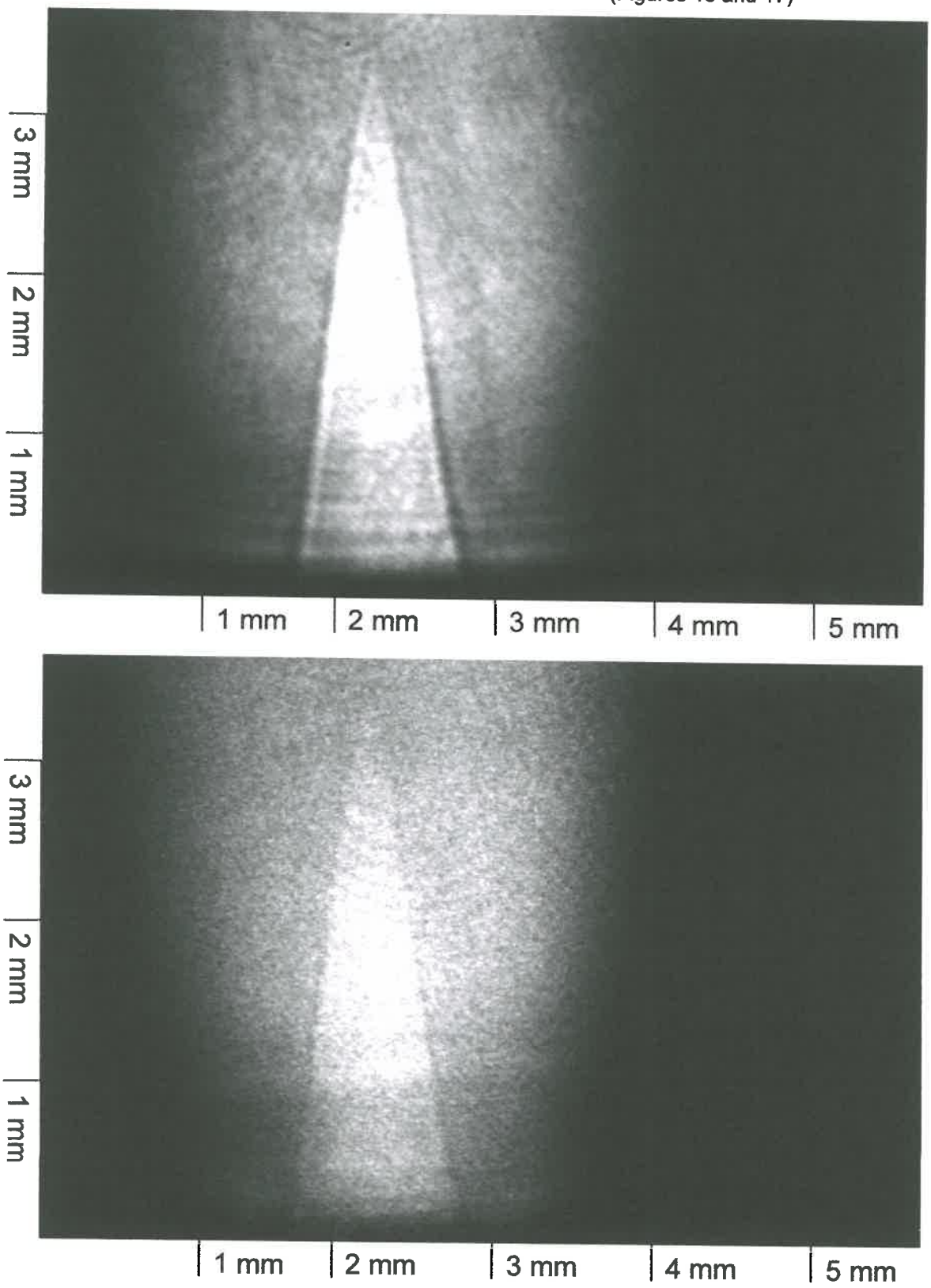

(k)

(Figures 16 and 17)

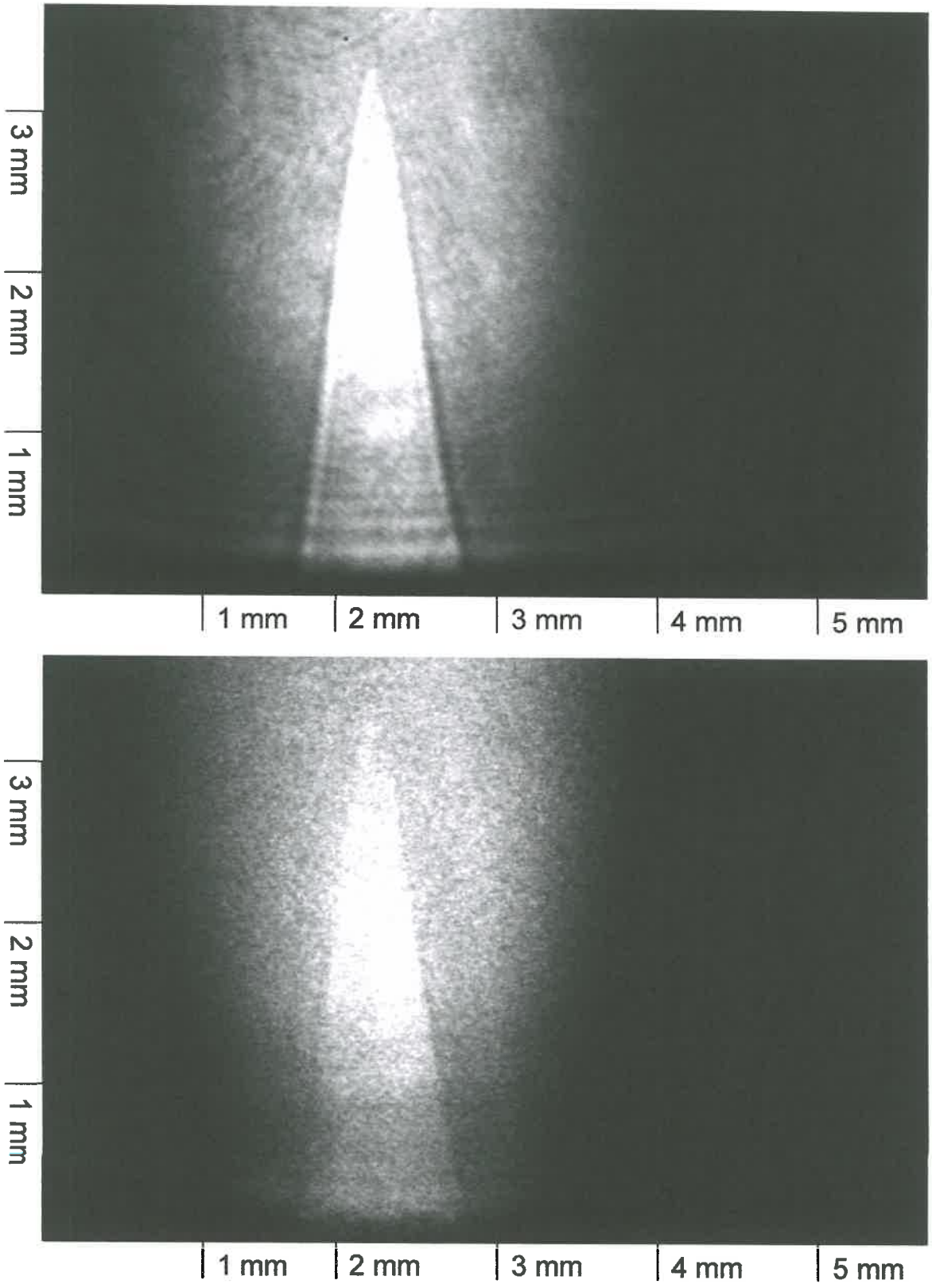

(I) (Figures 16 and 17)

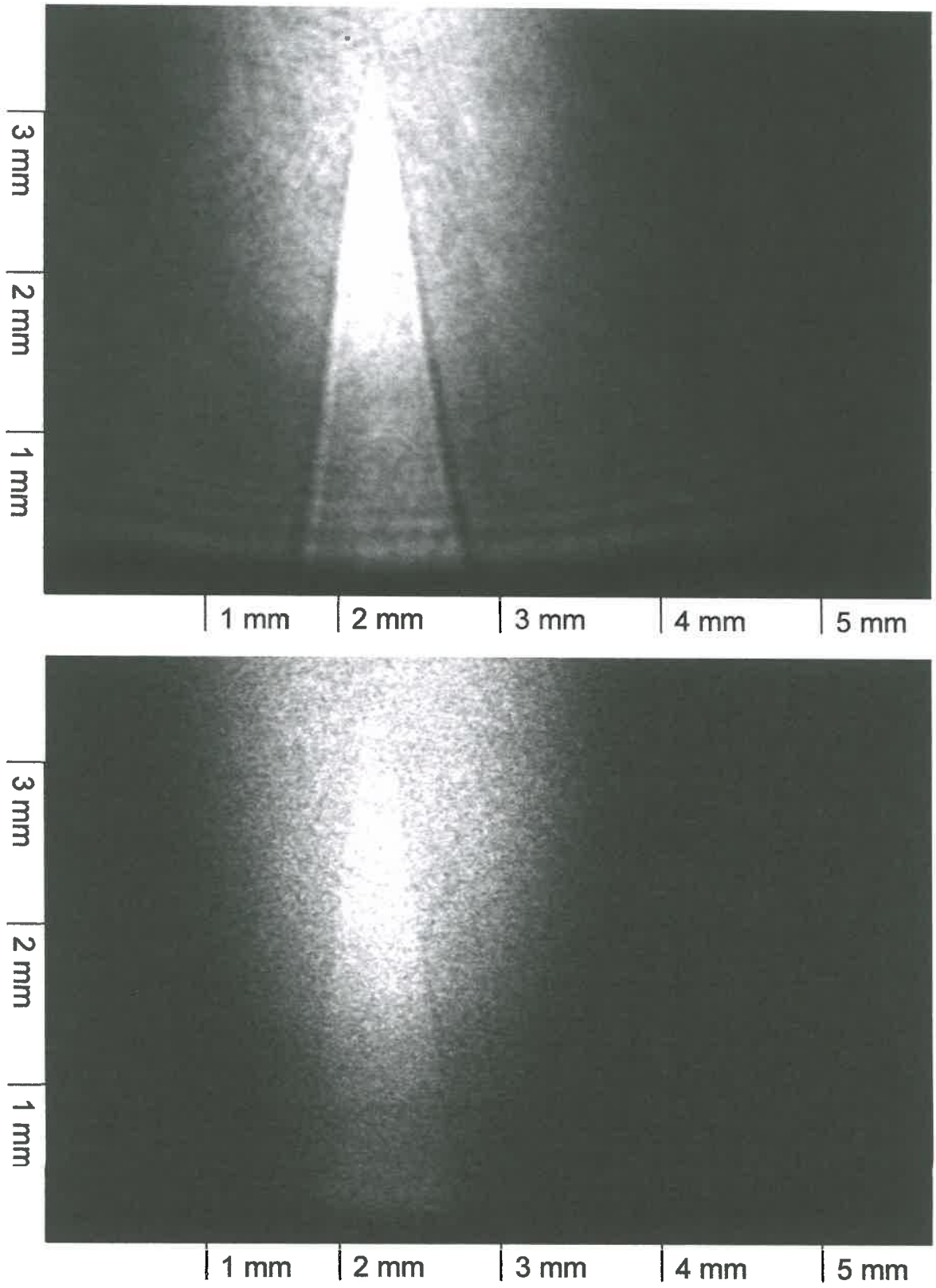

(m)

(Figures 16 and 17)

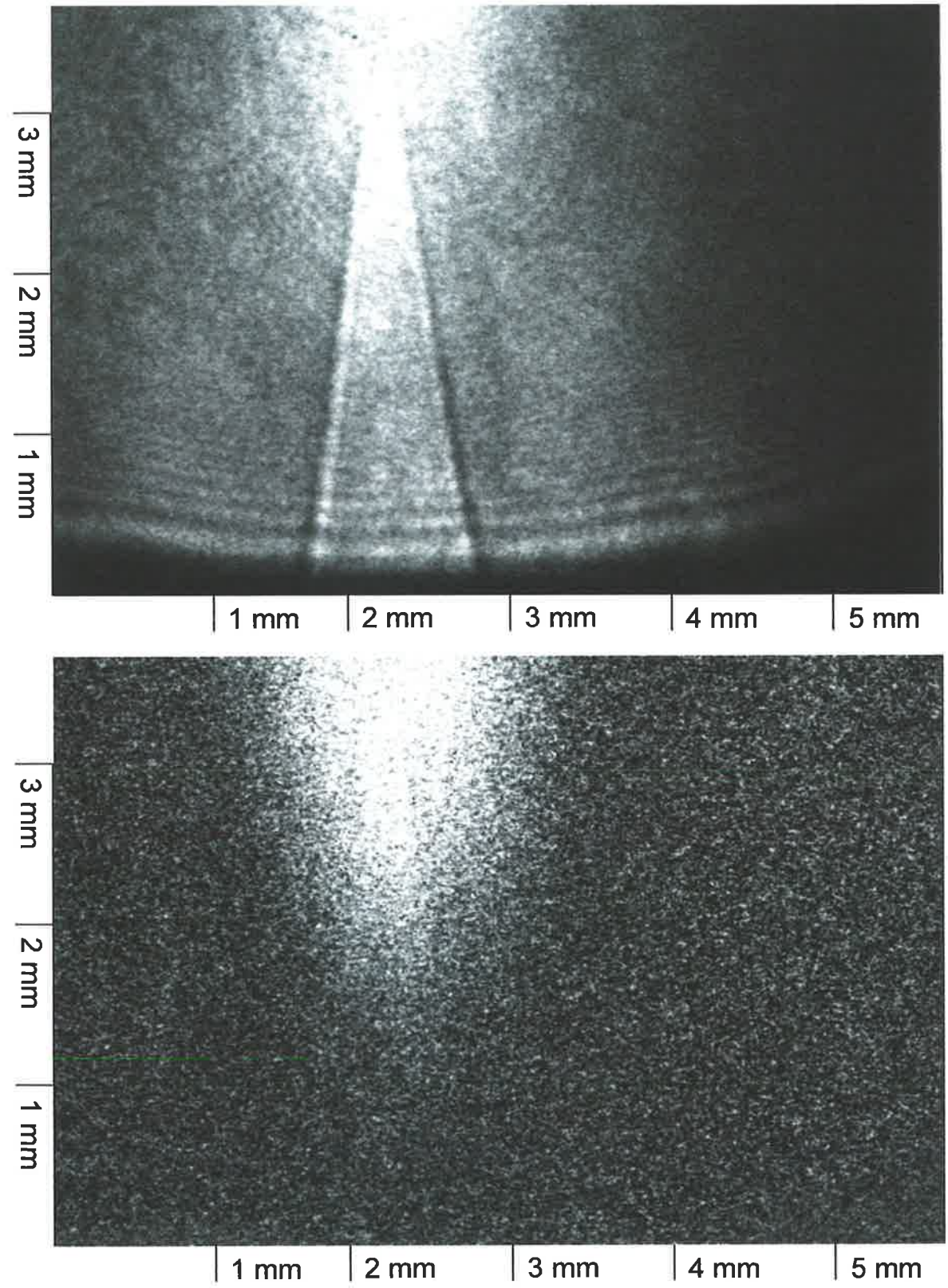

(n) (Figures 16 and 17)

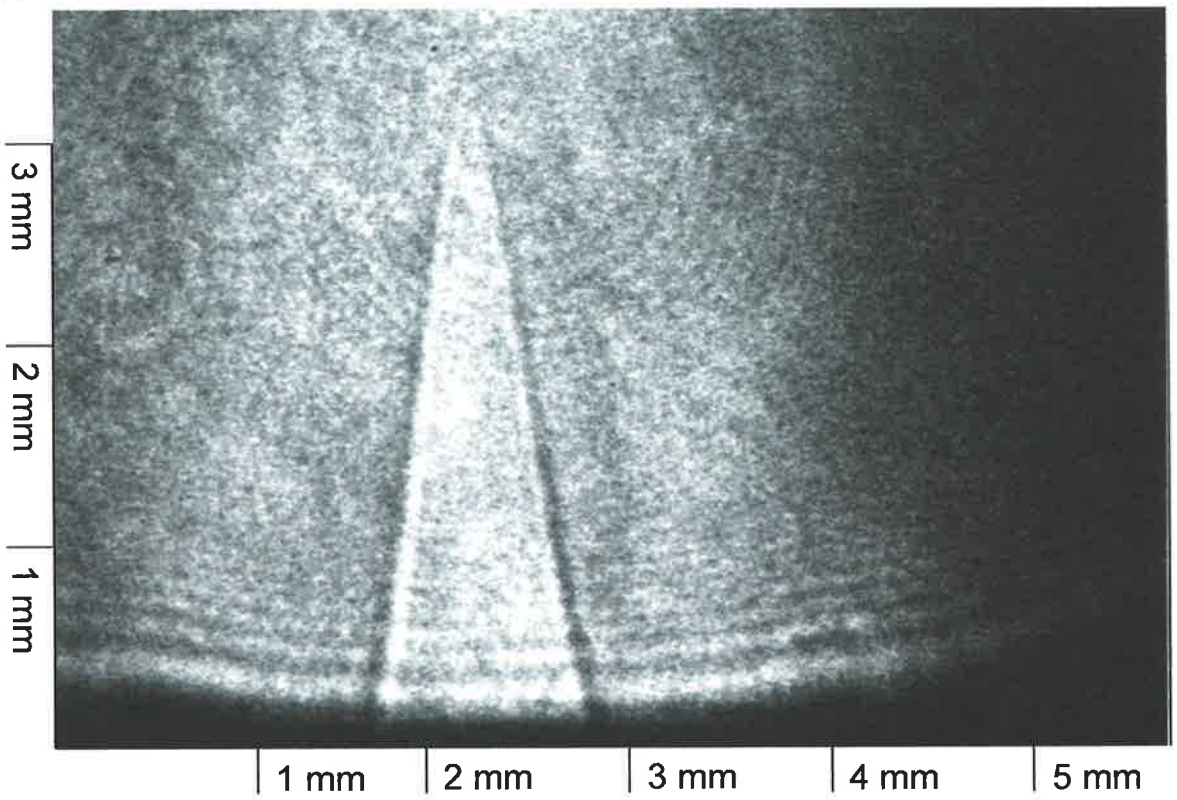

There is no corrected image presented in this case due to the low (barely detectable) signal level. The mode 1 image above is included to illustrate the typical probe beam (flame present) extinction background for this image set. The polarisation features are clearly present on the probe extinction background.

Chapter IV: Uniaxial Gas Model of Polarisation Spectroscopy: Circularly Polarised Pump Beam.

For convenience in the following chapter, the angles defined in Chapter II are used to describe the pump and probe beam propagation and polarisation directions: with pump/probe beam intersection angle, χ, and the angle of the probe beam polarisation from the normal to the pump/probe beam intersection plane, γ.

Chapter II presented an uniaxial model of induced birefringence and dichroism due to a linearly polarised pump beam. The theory was compared with that of Lavrinenko and Gancheryonok[5] for the case of a linearly polarised pump beam. In addition, Lavrinenko and Gancheryonok[5] developed a theory to represent the geometrical dependence of the LPS signal for the case of a circularly polarised pump beam.

This chapter compares Lavrinenko and Gancheryonok's model for a circularly polarised pump beam with that developed by Reppel and Alwahabi[23] (and described in detail in this chapter). In Chapter II, the differences between the theories of Lavrinenko and Gancheryonok[5] and Reppel and Alwahabi[23] were discussed for a linearly polarised pump beam. The present chapter points out the differences between the two models in the case of a circularly polarised pump beam. Experimental confirmation of the non-zero signal predicted by both theories in an orthogonal geometry for a probe beam polarised at $\pi/4$ to the beam intersection plane is described in Chapter V.

Lavrinenko and Gancheryonok appear to have applied the derivation method used in the case of the linearly polarised pump beam to produce expressions for the transmitted probe beam intensity for a circularly polarised pump beam. Their expression for the detected probe beam intensity, $I_{L\&G}$, is quoted below

$$I_{L\&G} = KI^2\left(\sin^2(2\cdot\gamma)\sin^2(\chi)(C_1+C_2)^2+\cot^2(\chi)(C_1-C_2)^2\right) \qquad \text{Equation 1}$$

where

$$K = \frac{9}{16}\left(\frac{\omega_{probe}}{cn_{probe}}\right)^2 |\chi_{1221}|^2 |E_{probe}|^2 |E_{pump}|^4,$$

$$C_1 = \frac{\chi_{1122}}{\chi_{1221}}$$

$$C_2 = \frac{\chi_{1212}}{\chi_{1221}}$$

l is the width of the pumping beam,

n_{probe} is the refractive index of the medium at the probe frequency, ω_{probe}, and

χ_{ijkl} are the elements of the third-order tensor of nonlinear susceptibility.

Lavrinenko and Gancheryonok were unable to compare this dependence conclusively with that obtained experimentally by Zizak, Lanauze and Winefordner[27] who previously demonstrated experimentally a $\cot^2(\chi)$ LPS signal dependence on beam crossing angle. Zizak *et al.* used a circularly polarised pump beam. However, the polarisation direction of the probe beam was not specified. The experimental result would match the theoretical description of Lavrinenko and Gancheryonok if the probe beam was polarised normal to, or in, the beam intersection plane ($\gamma = 0$ or $\pi/2$ respectively). The LPS signal was obtained by pumping (seeded) Na in a premixed air-acetylene flame. Dependence on beam intersection angle was investigated for angles up to 30°. Above this angle, the signal was too weak to be detected.

Zizak, Lanauze and Winefordner noted the signal dependence on beam intersection angle *"could be explained by taking into account geometrical considerations relating the interaction length between the beams and component of the pump intensity along the probe beam"*[27]. Lavrinenko and Gancheryonok raised an objection to this description noting that, for a circularly polarised pump beam, the scalar product of the pump beam polarisation vector and the transmission axis of the primary probe beam polariser is complex and understanding of the projection of the pump beam polarisation vector onto that of the probe beam *"loses its clearness"*[5].

The present chapter presents an alternative model of the geometrical dependence of polarisation spectroscopy to that of Lavrinenko and Gancheryonok. Clear identification of the characteristic polarisation modes of propagation of the probe beam in the pumped medium is the basis of the theory. The theory is similar to that described in Chapter II which proposed an analogy between the optical behaviour of the pumped populations and the behaviour of a uniaxial gas or crystal.

However, the susceptibility tensor, ε, now includes components which represent the optical activity[a] of the uniaxial medium. The derivation notes that the characteristic modes of propagation in such a medium are typically elliptically polarised (ranging from purely circular polarisation modes for propagation parallel to the induced optic axis, through increasingly elliptically polarised modes to near-linear polarisation modes for propagation normal to the optic axis) and care has been taken to decompose the probe beam polarisation as a linear combination of the two propagation modes. Once again, this model has similarities and differences to the theory of Lavrinenko and Gancheryonok. The major differences lie in the specific statement of the geometric dependence of the induced birefringence and the care taken in identifying the characteristic polarisation modes of propagation in the pumped medium before applying the appropriate refractive index and absorption coefficients to each.

Optically Active Uniaxial Description of the Induced Birefringence and Dichroism: Circularly Polarised Pump Beam

The derivation in Chapter II is modified in the case of a uniaxial medium displaying optical activity. Maxwell's equations for the non-optically active medium were solved in the previous section in terms of two linearly polarised modes of propagation. For a uniaxial, optically active medium, the polarisation state of the two solutions is a function of the angle of propagation with respect to the optic axis. The polarisation mode solutions approach linear polarisation for propagation normal to the optic axis, and are purely circularly polarised for propagation along the optic axis. For propagation at other angles, φ, to the optic axis, the polarisation states are elliptical.

Once again, the derivation follows the Collett's[22] methodology by solving Maxwell's equations in terms of the refractive indices associated with a particular direction of propagation and identifying the characteristic polarisation modes of propagation. The induced optic axis may be associated with the vector lying parallel or anti-parallel to the direction of propagation of the pump beam depending on the handedness of the circularly polarised light. The model below is then derived from the basic theory by considering the geometrical factors defined by the geometry of the polarisation spectroscopy experiment.

Following Collett's suggestion, the behaviour of the optically active uniaxial crystal or gas is modelled by introducing complex off-diagonal elements, δ, in the electric susceptibility tensor to represent the optical activity.

[a] Optical activity is defined as the rotation of the plane of polarisation with distance propagated through a medium due to circular birefringence, the difference in refractive index for the two orthogonal circular polarisation states.

$$\underline{D} = \varepsilon \underline{E} + i(\underline{\delta} X \underline{E})$$ Equation 2

If we consider a circularly polarised pump beam and assume that the optical activity will be directed along the optic axis parallel (or anti-parallel) to the polarisation axis of the circularly polarised pump beam, the Z axis in the principal section, we may write

$$\underline{\delta} = \begin{pmatrix} 0 \\ 0 \\ \delta \end{pmatrix}$$ Equation 3

Assuming the diagonalised uniaxial geometry of the previous derivation, the displacement vector is then related to the electric field vector via

$$\begin{pmatrix} D_x \\ D_y \\ D_z \end{pmatrix} = \begin{pmatrix} n_o^2 & -i\delta & 0 \\ i\delta & n_o^2 & 0 \\ 0 & 0 & n_e^2 \end{pmatrix} \begin{pmatrix} E_x \\ E_y \\ E_z \end{pmatrix}$$ Equation 4

This equation may be substituted into equation [2] to give the matrix equation

$$\begin{pmatrix} k^2 \cdot \cos^2(\varphi) + \frac{k_0^2 \cdot n_o^2}{\mu} & i\delta \cdot k_0^2 & -k^2 \cdot \sin(\varphi)\cos(\varphi) \\ -i\delta \cdot k_0^2 & k^2 + \frac{k_0^2 \cdot n_o^2}{\mu} & 0 \\ -k^2 \cdot \sin(\varphi)\cos(\varphi) & 0 & k^2 \cdot \sin^2(\varphi) + \frac{k_0^2 \cdot n_e^2}{\mu} \end{pmatrix} \begin{pmatrix} E_x \\ E_y \\ E_z \end{pmatrix} = 0$$ Equation 5

If we divide through by k_0^2, and take μ as unity, this simplifies to

$$\begin{pmatrix} n^2 \cdot \cos^2(\varphi) + n_o^2 & i\delta & -n^2 \cdot \sin(\varphi)\cos(\varphi) \\ -i\delta & k^2 + n_o^2 & 0 \\ -n^2 \cdot \sin(\varphi)\cos(\varphi) & 0 & n^2 \cdot \sin^2(\varphi) + n_e^2 \end{pmatrix} \begin{pmatrix} E_x \\ E_y \\ E_z \end{pmatrix} = 0$$ Equation 6

The non-trivial solutions are obtained by setting the determinant of the left-hand matrix to zero in the usual manner as shown in Appendix VI. Writing

$$n_e^2 = n_o^2 \cdot (1 + \Delta)$$ Equation 7

and

$$\sigma = \frac{\delta}{n_0^2}$$ Equation 8

and assuming both δ and σ are small, the two refractive index solutions may be written as

$$\left(\left(\frac{n_\alpha}{n_o}\right)^2\right)_{approx} = \left(1 + \left(\frac{\Delta - \sigma^2}{2}\right) \cdot \sin^2(\varphi)\right) \cdot \left(1 + \sqrt{\sin^4(\varphi) \cdot \left(\frac{\Delta + \sigma^2}{2}\right)^2 + \cos^2(\varphi) \cdot \sigma^2}\right)$$

Equation 9

and

$$\left(\left(\frac{n_\beta}{n_o}\right)^2\right)_{approx} = \left(1+\left(\frac{\Delta-\sigma^2}{2}\right)\cdot\sin^2(\varphi)\right)\cdot\left(1-\sqrt{\sin^4(\varphi)\cdot\left(\frac{\Delta+\sigma^2}{2}\right)^2+\cos^2(\varphi)\cdot\sigma^2}\right)$$

Equation 10

where the subscripts, α and β, represent the two polarisation solutions.

If we further take only first order terms in the expansion, indicating this by the subscript, 0_approx, equations [9] and [10] may be approximated by

$$\left(\left(\frac{n_\alpha}{n_o}\right)^2\right)_{0\_approx} = 1+\left(\frac{\Delta-\sigma^2}{2}\right)\cdot\sin^2(\varphi)+\sqrt{\sin^4(\varphi)\cdot\left(\frac{\Delta+\sigma^2}{2}\right)^2+\cos^2(\varphi)\cdot\sigma^2}$$

Equation 11

and

$$\left(\left(\frac{n_\beta}{n_o}\right)^2\right)_{0\_approx} = 1+\left(\frac{\Delta-\sigma^2}{2}\right)\cdot\sin^2(\varphi)-\sqrt{\sin^4(\varphi)\cdot\left(\frac{\Delta+\sigma^2}{2}\right)^2+\cos^2(\varphi)\cdot\sigma^2}$$

Equation 12

with approximate birefringence

$$\left(\frac{n_\alpha-n_\beta}{n_o}\right)_{0\_approx} = \sqrt{\sin^4(\varphi)\cdot\left(\frac{\Delta+\sigma^2}{2}\right)^2+\cos^2(\varphi)\cdot\sigma^2}$$

Equation 13

Note that this reduces to

$$\left(\frac{n_\alpha-n_\beta}{n_o}\right)_{\substack{0\_approx\\ \varphi\approx 0}} \approx \cos(\varphi)\cdot\sigma$$

Equation 14

for probe beam propagation close to the optic axis, where $\varphi \sim 0$, and to

$$\left(\frac{n_\alpha-n_\beta}{n_o}\right)_{\substack{0\_approx\\ \varphi\approx \frac{\pi}{2}}} \approx \sin^2(\varphi)\cdot\frac{(\Delta+\sigma^2)}{2}$$

Equation 15

for probe beam propagation nearly normal to the optic axis, where $\varphi \sim {}^{\pi}/_{2}$.

Note that the induced circular birefringence, via the term, σ, controls the spectroscopic behaviour for probe beam propagation close to the optic axis, while both linear and circular induced birefringence contribute to the signal strength for probe beam propagation normal to the optic axis.

The term, σ, is of second order in equation [15], while the linear birefringence term, Δ, is first order in the equation [14]. For small Δ and σ, this suggests that the linear birefringence controls the behaviour of the signal strength for propagation of the probe beam normal to the optic axis induced by the circularly polarised pump beam. If the induced terms, Δ and σ, are of the same order of magnitude, equation [93] may be further approximated as

$$\left(\frac{n_\alpha - n_\beta}{n_0}\right)_{\substack{0\_approx \\ small\_induced\_dichroism \\ \varphi \approx \frac{\pi}{2}}} \approx \sin^2(\varphi)\cdot\frac{\Delta}{2} \qquad \text{Equation 16}$$

Equation [14] allows us to identify the term, σ, as the maximum induced *fractional* circular birefringence for collinear pump and probe beams, $\Delta n_{circ}/n_o$. Remembering the assumption of small induced linear birefringence, equation [7] may be approximated by

$$n_e = n_o\cdot\left(1+\frac{\Delta}{2}\right) \qquad \text{Equation 17}$$

so that the term, $\Delta/2$, may be identified in equation [16] as the maximum induced *fractional* linear birefringence, $\Delta n_{lin}/n_o$.

Summarising these refractive index expressions for a circularly polarised pump beam (which assume small induced dichroism and birefringence, i.e. Δn_{lin}, Δn_{circ} <<1), **we have**

$$\Delta n_{lin} = \frac{\Delta}{2}\cdot n_o \qquad \text{Equation 18}$$

and

$$\Delta n_{circ} = \sigma\cdot n_o \qquad \text{Equation 19}$$

so that

$$\left(n_\alpha - n_\beta\right)_{\substack{0\_approx \\ \varphi \approx 0}} \approx \cos(\varphi)\cdot\Delta n_{circ} \qquad \text{Equation 20}$$

and

$$\left(n_\alpha - n_\beta\right)_{\substack{0\_approx \\ small\_induced\_dichroism \\ \varphi \approx \frac{\pi}{2}}} \approx \sin^2(\varphi)\cdot\Delta n_{lin} \qquad \text{Equation 21}$$

We proceed to redefine the polarisation spectroscopy geometry applied in Chapter II of a circularly polarised pump beam propagating at the angle, χ, to the Z axis and probe beam propagating along the Z axis. We start from the assumption that the direction of propagation of the circularly polarised pump beam defines the optic axis, so that the angle of probe beam propagation, φ, with respect to the optic axis is

$$\varphi = \chi \qquad \text{Equation 22}$$

We now assume a variation on the polarisation spectroscopy axis system as described in Chapter II for the reminder of this derivation. For convenience, we derive expressions for the polarisation modes of propagation for the optically active medium in the frame of the pump beam, defining the optic axis as the Z axis and considering the probe beam as propagating at the angle, χ, to the optic axis. The pump and probe beams intersect in the YZ plane. The X axis is vertical as usual. It then remains to determine the characteristic modes of propagation and to determine the geometrical dependence of the LPS signal strength for a circularly polarised pump beam in terms of the induced birefringence defined above.[b]

For probe beam propagation at an angle, χ, to the induced optic axis, the electric field modes are of the form

$$\left(\underline{E}_{0\_approx}\right)_{\iota} = \begin{pmatrix} i\cdot\sigma\cdot\left(\cos^2(\chi)-(s_{\iota}-\Delta)\right) \\ \left(\cos^2(\chi)-(s_{\iota}-\Delta)\right)\cdot s \\ -\sin(\chi)\cdot\cos(\chi)\cdot s_{\iota} \end{pmatrix} \qquad \iota = \alpha, \beta \qquad \text{Equation 23}$$

where the term, s_i, is given by

$$\left(\frac{n_{\iota}}{n_o}\right)^2 = 1 + s_{\iota} \qquad \iota = \alpha, \beta \qquad \text{Equation 24}$$

Remember that the electric field plane of the probe beam has electric field defined as

$$\underline{E}_{plane\_of\_polarisation} = \begin{pmatrix} a \\ b\cdot\cos(\chi) \\ -b\cdot\sin(\chi) \end{pmatrix} \qquad \iota = \alpha, \beta \qquad \text{Equation 25}$$

where a and b are constants and may be complex. It can be seen that the electric field modes of equation [23] lie in an electric field plane normal to the direction of propagation of the probe beam for $\cos^2(\chi) >> s_{\iota} - \Delta$. For larger angles, where $\cos^2(\chi) << s_{\iota} - \Delta$, refraction results in the electric field of the β probe beam component lying slightly outside the unrefracted (i.e. normal to the direction of

[b] The majority of the derivation is included in Appendix VI, and the important steps repeated in this chapter.

propagation) electric field plane of the probe beam. As a result, the propagation of the probe beam through the optically active medium is treated in two sections: for $\cos^2(\chi) >> s_\iota - \Delta$ and for $\cos^2(\chi) << s_\iota - \Delta$.

We consider the first case where the two characteristic polarisation modes lie in the electric field plane of the incident probe beam ($\cos^2(\varphi) >> s_\iota - \Delta$). The unnormalised electric field vectors are of the form

$$\left(\underline{E}_{0\_approx}\right)_\iota = \begin{pmatrix} i\cdot\sigma\cdot\cos^2(\chi) \\ \cos^2(\chi)\cdot s_\iota \\ -\sin(\chi)\cdot\cos(\chi)\cdot s_\iota \end{pmatrix} = \cos(\chi)\cdot\begin{pmatrix} i\cdot\sigma\cdot\cos(\chi) \\ \cos(\chi)\cdot s_\iota \\ -\sin(\chi)\cdot s_\iota \end{pmatrix} \qquad \iota = \alpha, \beta \qquad \text{Equation 26}$$

Ignoring the shared $\cos(\chi)$ factor, the unnormalised electric field vectors are written

$$\underline{E}_{\alpha\_0\_approx} = \begin{pmatrix} i\cdot\frac{\sigma}{s_\alpha}\cdot\cos(\chi) \\ \cos(\chi) \\ -\sin(\chi) \end{pmatrix} \qquad \text{Equation 27}$$

and

$$\underline{E}_{\beta\_0\_approx} = \begin{pmatrix} i\cdot\frac{\sigma}{s_\beta}\cdot\cos(\chi) \\ \cos(\chi) \\ -\sin(\chi) \end{pmatrix} \qquad \text{Equation 28}$$

The probe beam electric field is expressed in terms of the unnormalised polarisation modes, α and β, as

$$\frac{\underline{E}_{probe}}{E_{probe\_0}} = f\,\underline{E}_{\alpha\_0\_approx} + g\,\underline{E}_{\beta\_0\_approx} \qquad \text{Equation 29}$$

where E_{probe_0} is the magnitude of the probe beam electric field incident on the (assumed perfect) primary probe beam polariser.

The electric field of the probe beam transmitted through a distance, Λ, of the birefringent and dichroic medium is obtained by applying the α and β absorption and dispersion factors to each of the terms in equation [29].

$$\frac{\underline{E}_{probe}(\Lambda)}{E_{probe\_0}} = f\,\underline{E}_{\alpha\_0\_approx} e^{-\frac{\alpha_\alpha}{2}\Lambda} e^{ik_\alpha \Lambda} + g\,\underline{E}_{\beta\_0\_approx} e^{-\frac{\alpha_\beta}{2}\Lambda} e^{ik_\beta \Lambda} \qquad \text{Equation 30}$$

The probe beam electric field transmitted through the analysing polariser aligned parallel to the unit vector, $\underline{\hat{R}}_{analyser}$, is then given by

$$\frac{\underline{E}_{\substack{probe \\ transmitted\_through\_analyser}}(\Lambda)}{E_{probe\_0}} = \begin{pmatrix} f\,(\underline{E}_{\alpha\_0\_approx} \cdot \underline{\hat{R}}_{analyser}) e^{-\frac{\alpha_\alpha}{2}\Lambda} e^{ik_\alpha \Lambda} \\ +g\,(\underline{E}_{\beta\_0\_approx} \cdot \underline{\hat{R}}_{analyser}) e^{-\frac{\alpha_\beta}{2}\Lambda} e^{ik_\beta \Lambda} \end{pmatrix} \qquad \text{Equation 31}$$

The transmitted intensity is related in the usual way to the electric field via

$$I_{\substack{probe \\ transmitted\_through\_analyser}}(\Lambda) = \left| \underline{E}_{\substack{probe \\ transmitted\_through\_analyser}}(\Lambda) \right|^2 \qquad \text{Equation 32}$$

and, following the same reasoning as for the linearly polarised pump beam, is finally written as (see Appendix VI for details)

$$\frac{I_{\substack{probe \\ transmitted\_through\_analyser}}(\Lambda)}{I_{probe\_0}} = F_{circ}(\gamma,\chi)_{0\_approx} \cdot \left(\frac{(n_\alpha(\chi) - n_\beta(\chi)) \cdot \omega_0 \cdot L}{2 \cdot c} \right)^2 \frac{1}{1+x^2} \cdot e^{-\alpha_{av} \cdot \Lambda} \qquad \text{Equation 33}$$

where the geometric dependence, aside from that implicit in the induced birefringence, has been consolidated into the factor, $F_{circ}(\gamma,\chi)_{0\_approx}$. If we consolidate the geometrical dependence of birefringence with that of the factor, $F_{circ}(\gamma,\chi)_{0\_approx}$, we can write

$$\frac{I_{\substack{probe \\ transmitted\_through\_analyser}}(\Lambda)}{I_{probe\_0}} = J_{circ}(\gamma,\chi)_{0\_approx} \cdot \left(\frac{n_0 \cdot \omega_0 \cdot L}{2 \cdot c} \right)^2 \frac{1}{1+x^2} \cdot e^{-\alpha_{av} \cdot \Lambda} \qquad \text{Equation 34}$$

where

$$J_{circ}(\gamma,\chi)_{0\_approx} = \frac{\left(\left(\cos^2(\gamma) \cdot \sin^4(\chi) \cdot \Delta + \cos^2(\chi) \right) \cdot \sigma \right)^2 + \left(\cos(\chi) \cdot \sin^2(\chi) \cdot \cos(\gamma) \cdot \sin(\gamma) \cdot (\Delta - \sigma^2) \right)^2}{(\cos(\chi) \cdot \sin(\chi))^2} \qquad \text{Equation 35}$$

Consider the dependence of this function on the intersection angle of pump and probe beams, χ,

for three experimental configurations of probe beam polarisation angle from the vertical, γ.

Case 1: $\gamma = 0$

$$J_{circ}(0,\chi)_{0\_approx} = \frac{\left(\sin^4(\chi)\cdot\Delta+\cos^2(\chi)\right)^2}{\left(\cos(\chi)\cdot\sin(\chi)\right)^2}\cdot\sigma^2 = \left(\sin^2(\chi)\tan(\chi)\cdot\Delta+\cot(\chi)\right)^2\cdot\sigma^2 \quad \text{Equation 36}$$

Case 2: $\gamma = {}^{\pi}/_{4}$

$$J_{circ}\left(\frac{\pi}{2},\chi\right)_{0\_approx} = \frac{1}{4}\cdot\frac{\left(\left(\sin^4(\chi)\cdot\Delta+2\cdot\cos^2(\chi)\right)\cdot\sigma\right)^2+\left(\cos(\chi)\cdot\sin^2(\chi)\cdot\left(\Delta-\sigma^2\right)\right)^2}{\left(\cos(\chi)\cdot\sin(\chi)\right)^2} \quad \text{Equation 37}$$

$$= \frac{1}{4}\cdot\left(\sin^2(\chi)\tan(\chi)\cdot\Delta+2\cdot\cot(\chi)\right)^2\cdot\sigma^2+\sin^2(\chi)\cdot\left(\Delta-\sigma^2\right)^2$$

Case 3: $\gamma = {}^{\pi}/_{2}$

$$J_{circ}\left(\frac{\pi}{2},\chi\right)_{0\_approx} = \cot^2(\chi)\cdot\sigma^2 \quad \text{Equation 38}$$

These expressions are valid for $\cos^2(\chi) >> \sigma^2, \Delta$.

Figure 1 shows the dependence of the LPS signal strength defined in equations [33] to [35] for a circularly polarised pump beam for probe beam polarisation angles of $\gamma = 0$, ${}^{\pi}/_{4}$ and ${}^{\pi}/_{2}$. Values of $\Delta = 0.1$ and $\sigma = 0.05$ were assumed for the calculation. The plotted dependencies are valid according to the condition above for $\chi < 71.6°$. The divergence of the solution for beam intersection angles outside this range ($\chi > 71.6°$, i.e. $\cos^2(\chi) << \sigma^2, \Delta$) is clear.

We now consider the second range of pump/probe intersection angle, χ, such that $\cos^2(\chi) << \sigma^2, \Delta$, where the polarisation modes do not lie exactly in the electric field plane of the incident probe beam.

The α and β polarisation modes for $\cos^2(\chi) << \sigma^2, \Delta$ are of the form

$$\underline{E}_{0\_approx} = s\cdot\begin{pmatrix} i\cdot\sigma\cdot\dfrac{\cos^2(\chi)-(s-\Delta)}{s} \\ \cos^2(\chi)-(s-\Delta) \\ -\sin(\chi)\cdot\cos(\chi) \end{pmatrix} \quad \text{Equation 39}$$

where, from equations [11] and [12] and the definition of the term, s, in equation [24], we can see that, for $\cos(\chi) \sim 0$,

$$s_{\alpha\_0\_approx} = \Delta \cdot \sin^2(\chi)$$ Equation 40

and

$$s_{\beta\_0\_approx} = -\sigma^2 \cdot \sin^2(\chi)$$ Equation 41

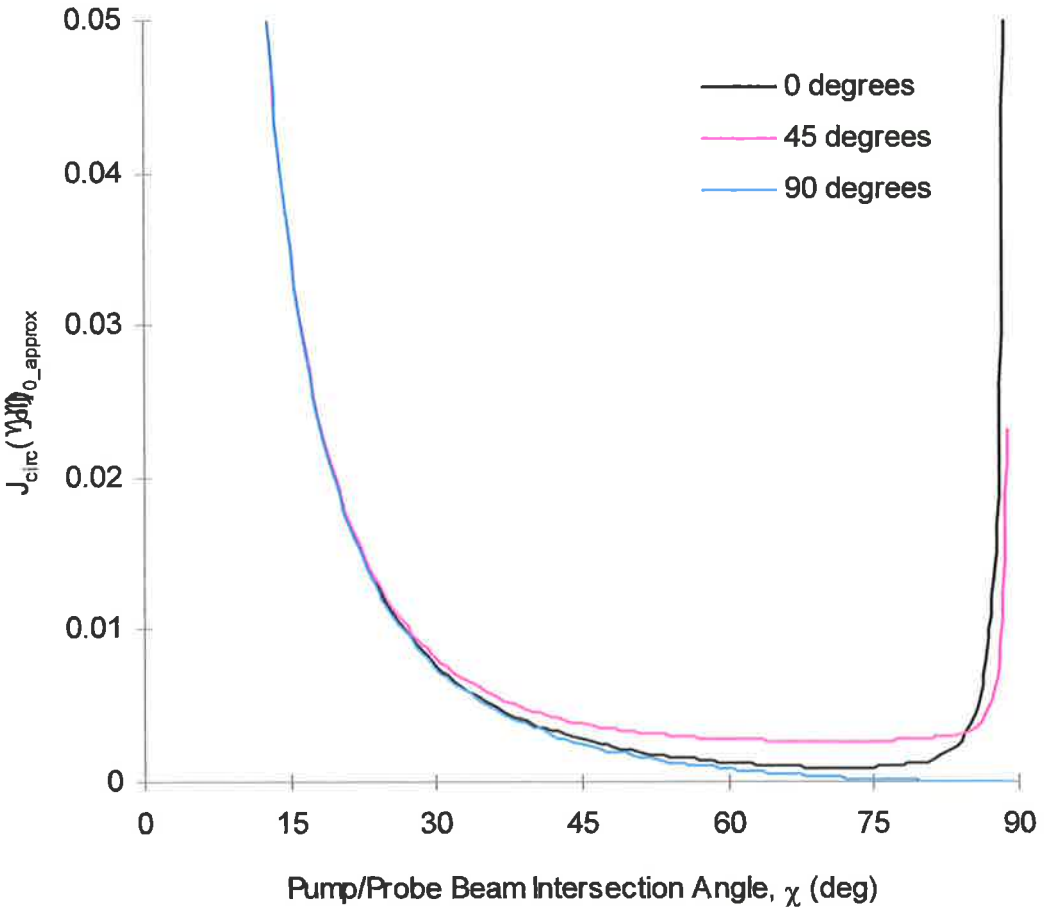

Figure 1: Calculated dependence of the LPS signal strength, $J_{circ}(\gamma,\chi)_{0\_approx}$, for a circularly polarised pump beam for probe beam polarisation angles of γ = 0 (black line), $\pi/4$ (pink) and $\pi/2$ (blue). Values of Δ = 0.1 and σ = 0.05 were assumed for the calculation. The resultant plotted dependencies are valid for $\cos^2(\chi) >> \sigma^2, \Delta$, i.e. for pump/probe intersection angles, $\chi < 71.6°$.

The α and β electric field vectors are then given by

$$\underline{E}_{\alpha\_0\_approx} = \Delta \cdot \sin^2(\chi) \cdot \cos(\chi) \cdot \begin{pmatrix} i \cdot \left(\frac{\sigma}{\Delta}\right) \cdot \frac{\cos(\chi) \cdot (1+\Delta)}{\sin^2(\chi)} \\ \cos(\chi) \cdot (1+\Delta) \\ -\sin(\chi) \end{pmatrix} \qquad \text{Equation 42}$$

or, more approximately, (since for small induced birefringence, $1+\Delta \approx 1$)

$$\underline{E}_{\alpha\_0\_approx} \approx \Delta \cdot \sin^3(\chi) \cdot \cos(\chi) \cdot \begin{pmatrix} i \cdot \left(\frac{\sigma}{\Delta}\right) \cdot \frac{\cos(\chi)}{\sin^3(\chi)} \\ \frac{\cos(\chi)}{\sin(\chi)} \\ -1 \end{pmatrix} \qquad \text{Equation 43}$$

and

$$\underline{E}_{\beta\_0\_approx} = -\sigma \cdot \sin^2(\chi) \cdot \begin{pmatrix} i \cdot \frac{(\sigma^2 \cdot \sin^2(\chi) + \Delta)}{\sin^2(\chi)} \\ (\sigma^2 \cdot \sin^2(\chi) + \Delta) \cdot \sigma \\ -\sin(\chi) \cdot \cos(\chi) \cdot \sigma \end{pmatrix} \qquad \text{Equation 44}$$

which, continuing with the approximation, (since $\sigma^2 \cdot \sin^2(\chi) + \Delta \approx \sigma^2 + \Delta$ for $\cos(\chi) \sim 0$)

$$\underline{E}_{\beta\_0\_approx} = -i \cdot \sigma \cdot (\sigma^2 + \Delta) \cdot \begin{pmatrix} 1 \\ -i \cdot \sin^2(\chi) \cdot \sigma \\ i \cdot \sin^3(\chi) \cdot \cos(\chi) \cdot \frac{\sigma}{(\sigma^2 + \Delta)} \end{pmatrix} \qquad \text{Equation 45}$$

These expressions, for $\chi = {}^{\pi}/_{2}$, reduce to

$$\left(\underline{E}_{\alpha\_0\_approx}\right)_{\chi=\frac{\pi}{2}} = \Delta \cdot \sin^3(\chi) \cdot \cos(\chi) \cdot \begin{pmatrix} 0 \\ 0 \\ -1 \end{pmatrix} \qquad \text{Equation 46}$$

and

$$\left(\underline{E}_{\beta\_0\_approx}\right)_{\chi=\frac{\pi}{2}} = -i \cdot \sigma \cdot (\sigma^2 + \Delta) \cdot \begin{pmatrix} 1 \\ -i \cdot \sigma \\ 0 \end{pmatrix} \qquad \text{Equation 47}$$

Note that we are only interested in the vector component of the electric vectors, as the final polarisation modes may be normalised to unity.

For $\chi = {}^{\pi}/_{2}$, the α polarisation mode lies along the Z axis of the experimental geometry, while the β polarisation mode lies very close to the vertical X axis, with a small Y component due to the induced circular birefringence. We may approximate a first solution to the transmitted probe beam electric field in the limit of $\cos^2(\chi) << \sigma^2, \Delta$ by normalising the vectors to a maximum component value of unity along the X and Z axes when $\chi = {}^{\pi}/_{2}$ and setting the complex electric field components to zero. The transmitted probe beam electric field is then described as the propagation of purely linearly polarised probe beam components under the action of the optically active induced birefringence.

The linear approximations to the polarisation modes of propagation are obtained by normalising the vector to a maximum value of unity for the most significant field component and setting the complex terms of equations [40] and [42] to zero to give

$$\underline{E}_{\alpha\_linear\_approx} = \begin{pmatrix} 0 \\ \dfrac{\cos(\chi)}{\sin(\chi)} \\ -1 \end{pmatrix} \qquad \text{Equation 48}$$

and

$$\underline{E}_{\beta\_0\_linear\_approx} = \begin{pmatrix} 1 \\ 0 \\ 0 \end{pmatrix} \qquad \text{Equation 49}$$

Note that the magnitude of the Y component of the α polarisation mode goes to zero as the intersection angle, χ, approaches $\pi/2$.

The probe beam electric field may be written as a sum of the linear approximation electric field components as shown below.

$$\underline{E}_{probe} = \begin{pmatrix} \cos(\gamma) \\ \sin(\gamma)\cdot\cos(\chi) \\ -\sin(\gamma)\cdot\sin(\chi) \end{pmatrix} = \sin(\gamma)\cdot\sin(\chi)\cdot\begin{pmatrix} 0 \\ \dfrac{\cos(\chi)}{\sin(\chi)} \\ -1 \end{pmatrix} + \cos(\gamma)\cdot\begin{pmatrix} 1 \\ 0 \\ 0 \end{pmatrix} \qquad \text{Equation 50}$$

For $\cos^2(\chi) << \sigma^2, \Delta$, and assuming that the induced dichroism and birefringence are small, we assume (in the linear approximation) that the X axis components of the probe beam are equivalent to the β polarisation mode while the Z and small Y probe beam components represent the α polarisation mode. The probe beam is then written as

$$\underline{E}_{probe} = \begin{pmatrix} \cos(\gamma) \\ \sin(\gamma)\cdot\cos(\chi) \\ -\sin(\gamma)\cdot\sin(\chi) \end{pmatrix} = \begin{pmatrix} 0 \\ \sin(\gamma)\cdot\cos(\chi) \\ -\sin(\gamma)\cdot\sin(\chi) \end{pmatrix} + \begin{pmatrix} \cos(\gamma) \\ 0 \\ 0 \end{pmatrix} \qquad \text{Equation 51}$$

and the usual refractive index and dispersion terms applied to the α and β components to describe

the electric field component transmitted a distance, Λ, through the dichroic and birefringent medium.

$$\underline{E}_{probe}(\Lambda) = \begin{pmatrix} 0 \\ \sin(\gamma)\cdot\cos(\chi) \\ -\sin(\gamma)\cdot\sin(\chi) \end{pmatrix} \cdot e^{-\frac{\alpha_\alpha}{2}\Lambda} \cdot e^{ik_\alpha\Lambda} + \begin{pmatrix} \cos(\gamma) \\ 0 \\ 0 \end{pmatrix} \cdot e^{-\frac{\alpha_\beta}{2}\Lambda} \cdot e^{ik_\beta\Lambda} \qquad \text{Equation 52}$$

The derivation in Appendix VI shows that the resultant intensity of the probe beam transmitted through an analyser perfectly crossed with the primary polariser is given by

$$\frac{I_{probe\_transmitted\_through\_analyser}(\Lambda)}{I_{probe\_0}} = F_{circ}(\gamma,\chi)_{linear\_approx} \cdot \left(\frac{(n_\alpha(\chi)-n_\beta(\chi))\cdot\omega_0\cdot L}{2\cdot c}\right)^2 \frac{1}{1+x^2} \cdot e^{-\alpha_{av}\cdot\Lambda} \qquad \text{Equation 53}$$

The geometric dependence of the $F_{circ}(\gamma,\chi)_{linear\_approx}$ factor and the induced birefringence in the equation above may be consolidated in the factor, $J_{circ}(\gamma,\chi)_{linear\_approx}$, defined by the equation

$$\frac{I_{probe\_transmitted\_through\_analyser}(\Lambda)}{I_{probe\_0}} = J_{circ}(\gamma,\chi)_{linear\_approx} \cdot \left(\frac{n_0\cdot\omega_0\cdot L}{2\cdot c}\right)^2 \frac{1}{1+x^2} \cdot e^{-\alpha_{av}\cdot\Lambda} \qquad \text{Equation 54}$$

where

$$J_{circ}(\gamma,\chi)_{linear\_approx} = \sin^2(2\cdot\gamma)\cdot\sin^2(\chi)\cdot\left(\frac{\Delta+\sigma^2}{2}\right)^2 \qquad \text{Equation 55}$$

Consider the same experimental cases as calculated for $\cos^2(\varphi) >> \sigma^2, \Delta$.

Case 1: $\gamma = 0$

$$J_{circ}(0,\chi)_{linear\_approx} = 0 \qquad \text{Equation 56}$$

Case 2: $\gamma = \pi/4$

$$J_{circ}\left(\frac{\pi}{4},\chi\right)_{linear\_approx} = \sin^2(\chi)\cdot\left(\frac{\Delta+\sigma^2}{2}\right)^2 \qquad \text{Equation 57}$$

or, for Δ, $\sigma << 1$ and of the same order of magnitude,

$$J_{circ}\left(\frac{\pi}{4},\chi\right)_{linear\_approx} = \sin^2(\chi)\cdot\left(\frac{\Delta}{2}\right)^2 \qquad \text{Equation 58}$$

Case 3: $\gamma = \pi/2$

$$J_{circ}\left(\frac{\pi}{2},\chi\right)_{linear\_approx} = 0 \qquad \text{Equation 59}$$

These expressions are valid for $\cos^2(\chi) << \sigma^2, \Delta$.

Equations [52] to [55] predict that the polarisation signal strength for a circularly polarised pump beam is typically non-zero for normal incidence of pump and probe beams, unless the probe beam is polarised normal to, or in, the plane of intersection of the pump and probe beams. The equations also predict that the near-orthogonal beam intersection ($\chi \sim \pi/2$) signal strength for a circularly polarised pump beam (and probe beam not polarised in or normal to the beam intersection plane) is dependent on both the induced circular birefringence and an induced linear birefringence.

The derivation above has approximated two regimes for the polarisation modes of propagation, for $\cos^2(\chi) >> \sigma^2, \Delta$ and for $\cos^2(\chi) << \sigma^2, \Delta$. The geometric dependence of the LPS signal strength on the pump/probe beam intersection angle, χ, must consider both regimes within their respective ranges of approximation. The accuracy of the derived expressions depends on the quality of the approximation $\Delta, \sigma^2 << 1$. The smaller the induced dichroism and birefringence, the closer the predicted two curves asymptote to each other over the region of non-definition, $\cos^2(\chi) \approx \sigma^2, \Delta$.

The model above describes the geometric dependence of the LPS signal strength in terms of a factor, $J(\gamma,\chi)$, defined as

$$\frac{I_{probe\ transmitted\_through\_analyser}(\Lambda)}{I_{probe\_0}} = J_{circ}(\gamma,\chi)\cdot\left(\frac{(n_\alpha - n_\beta)\cdot\omega_0\cdot L}{2\cdot c}\right)^2 \frac{1}{1+x^2}\cdot e^{-\alpha_{av}\cdot\Lambda} \qquad \text{Equation 60}$$

Combining the results obtained for the two ranges of approximation of the model, the geometrical dependence of the detected signal (ignoring factors due to imperfect optical elements such as the probe beam extinction background), $J_{circ}(\gamma,\chi)$, in the case of perfectly crossed polarisers and no birefringent interpolariser optical elements in the probe beam path may be written as

For $\cos^2(\chi) >> \sigma^2, \Delta$:

(collinear and intermediate (non-orthogonal) beam intersection angles)

$$J_{circ}(\gamma,\chi)_{0\_approx} = \frac{\left(\left(\cos^2(\gamma)\cdot\sin^4(\chi)\cdot\Delta+\cos^2(\chi)\right)\cdot\sigma\right)^2 + \left(\cos(\chi)\cdot\sin^2(\chi)\cdot\cos(\gamma)\cdot\sin(\gamma)\cdot\left(\Delta-\sigma^2\right)\right)^2}{\left(\cos(\chi)\cdot\sin(\chi)\right)^2}$$ Equation 61

For $\cos^2(\chi) << \sigma^2, \Delta$:

(near-orthogonal imaging)

$$J_{circ}(\gamma,\chi)_{linear\_approx} = \sin^2(2\cdot\gamma)\cdot\sin^2(\chi)\cdot\left(\frac{\Delta+\sigma^2}{2}\right)^2$$ Equation 62

These equations may be simplified for three common experimental configurations based on the angle of the probe beam polarisation, γ, from the normal to the pump/probe beam intersection plane:

Case 1: $\gamma = 0$

For $\cos^2(\chi) >> \sigma^2, \Delta$:

$$J_{circ}(0,\chi)_{0\_approx} = \left(\sin^2(\chi)\tan(\chi)\cdot\Delta+\cot(\chi)\right)^2\cdot\sigma^2$$ Equation 63

For $\cos^2(\chi) << \sigma^2, \Delta$:

$$J_{circ}(0,\chi)_{linear\_approx} = 0$$ Equation 64

Case 2: $\gamma = \pi/4$

For $\cos^2(\chi) >> \sigma^2, \Delta$:

$$J_{circ}\left(\frac{\pi}{4},\chi\right)_{0\_approx} = \frac{1}{4}\cdot\left(\sin^2(\chi)\tan(\chi)\cdot\Delta+2\cdot\cot(\chi)\right)^2\cdot\sigma^2+\sin^2(\chi)\cdot\left(\Delta-\sigma^2\right)^2$$ Equation 65

For $\cos^2(\chi) << \sigma^2, \Delta$:

$$J_{circ}\left(\frac{\pi}{4},\chi\right)_{linear\_approx} = \sin^2(\chi)\cdot\left(\frac{\Delta+\sigma^2}{2}\right)^2$$ Equation 66

Case 3: $\gamma = \pi/2$

For $\cos^2(\chi) >> \sigma^2, \Delta$:

$$J_{circ}\left(\frac{\pi}{2},\chi\right)_{0\_approx} = \cot^2(\chi)\cdot\sigma^2$$ Equation 67

For $\cos^2(\chi) << \sigma^2, \Delta$:

$$J_{circ}\left(\frac{\pi}{2},\chi\right)_{linear\_approx} = 0$$ Equation 68

It is clear that, although probe beam polarisations normal to, and lying in, the pump/probe beam intersection plane lead to zero signal at a beam intersection angle of $\pi/2$, all other probe beam polarisations lead to non-zero signal for an orthogonal geometry. The signal is maximised for all beam intersection angles if the pump beam is polarised at $\pi/4$ to the pump/probe beam intersection plane (Case 2 above).

Figures 2 and 3 each show two curves representing the signal strength solutions for the two regimes for a probe beam polarisation angle of $^{\pi}/_{4}$. In Figure 2, the induced constants are set to Δ = 0.1 and σ = 0.05, while in Figure 3, the induced dichroism and birefringence are assumed to be much smaller and the constants are set to the values of Δ = 0.02 and σ = 0.01. The two curves approach well in the non-defined region for the induced constants Δ = 0.1 and σ = 0.05 in Figure 2. However, the fit of the two curves is more exact for the case of smaller induced dichroism and birefringence (Δ = 0.1 and σ = 0.05) in Figure 3.

Remembering that the geometric dependence of the detected probe beam intensity in the theory of Lavrinenko and Gancheryonok[5] is given by the following expression

$$I_{L\&G} = KI^2\left(\sin^2(2\cdot\gamma)\sin^2(\chi)(C_1+C_2)^2+\cot^2(\chi)(C_1-C_2)^2\right) \qquad \text{Equation 69}$$

where the terms C_1 and C_2 refer to ratios of elements of the third-order tensor of nonlinear susceptibility. This expression gives the following results in the three probe beam polarisation cases considered above.

Case 1: $\gamma = 0$: $I_{L\&G} = KI^2\cdot\cot^2(\chi)(C_1-C_2)^2$ Equation 70

Case 2: $\gamma = {}^{\pi}/_{4}$: $I_{L\&G} = KI^2\left(\cot^2(\chi)(C_1-C_2)^2+\sin^2(\chi)(C_1+C_2)^2\right)$ Equation 71

Case 3: $\gamma = {}^{\pi}/_{2}$: $I_{L\&G} = KI^2\cdot\cot^2(\chi)(C_1-C_2)^2$ Equation 72

Case 3 is obviously the same for both models if the term $(C_1 - C_2)^2$ is assumed proportional to the term, σ^2; following a $\cot^2(\chi)$ dependence on beam intersection angle.

The expression derived in this chapter for Case 1 reduces to that of Lavrinenko and Gancheryonok if the term representing the circularly polarised pump beam induced linear birefringence, Δ, is deleted, to produce once again a $\cot^2(\chi)$ dependence. The term is an order of magnitude smaller than the $\cot^2(\chi)$ contribution for small beam intersection angles and may be discarded in such cases. In regimes where the term is large (for large beam intersection angles), the condition for the approximations made in the derivation to be valid may not apply and the

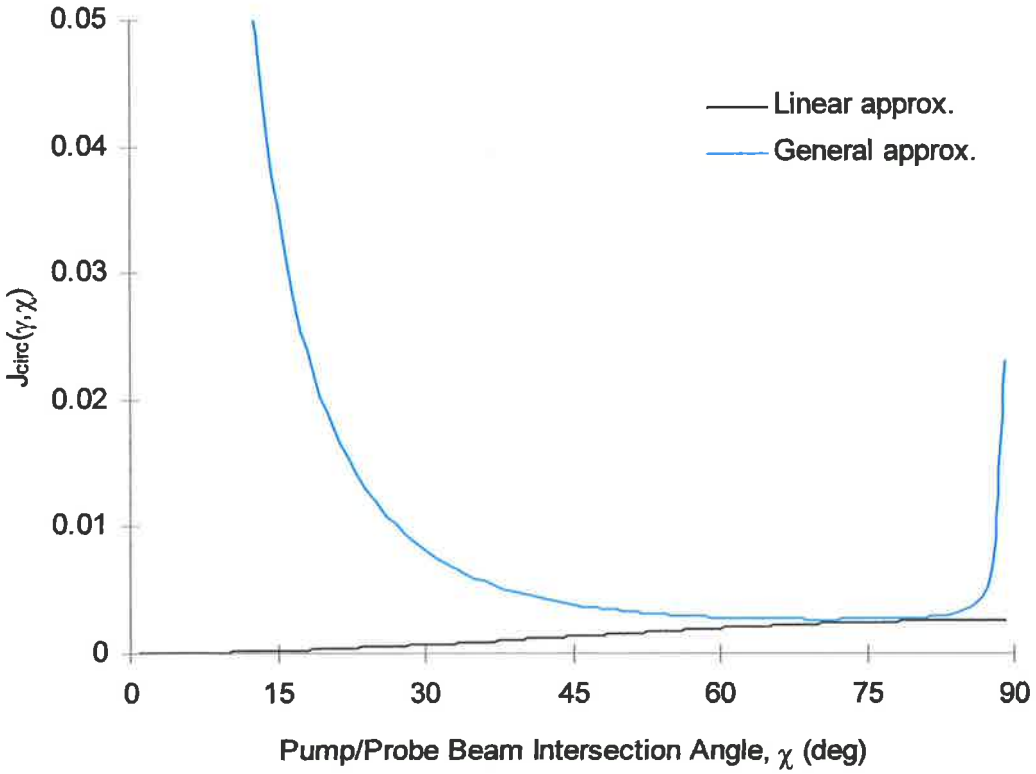

Figure 2: Calculated dependence of the two approximations representing the LPS signal for a circularly polarised pump beam for a probe beam polarisation angle of $\gamma = {}^{\pi}/_{4}$. Values of $\Delta = 0.1$ and $\sigma = 0.05$ were assumed for the calculation. The resultant grey line plotted dependence, $J_{circ}({}^{\pi}/_{4},\chi)_{0\_approx}$, is valid for the approximation regime, $\cos^2(\chi) >> \sigma^2, \Delta$, i.e. for pump/probe intersection angles, $\chi < 71.6°$, while the linear approximation, $J_{circ}({}^{\pi}/_{4},\chi)_{linear\_approx}$, represented by the black line, is valid for , $\chi > 71.6°$.

solution asymptotes to a zero signal for orthogonal intersection. It would be valid to consider the linear birefringent term proportional to the factor, Δ, in Case 1 to be a small higher order approximation contribution.

The expressions obtained by Lavrinenko and Gancheryonok and Reppel and Alwahabi for Case 3 are equivalent if the small linear birefringent term discussed for Case 2 is ignored and the term $(C_1 + C_2)^2$ is assumed proportional to the term, $((\Delta + \sigma^2)/2)^2$ (having previously also assumed the term, $(C_1 - C_2)^2$, to be proportional to the term, σ^2).

Summarising these results, the two theories match for the case of a circularly polarised pump beam if

- $(C_1 - C_2)^2 \propto \sigma^2$,

- $(C_1 + C_2)^2 \propto ((\Delta + \sigma^2)/2)^2$,
- and it is assumed that the contribution of the first term, which is proportional to the induced linear dichroism, Δ, in equation [61], contributes negligibly to the signal.

In this respect, it can be considered that the theory of Reppel and Alwahabi is a solution with a higher order of approximation than that of Lavrinenko and Gancheryonok which. However, the theory in this chapter states the geometric dependence of the induced birefringence explicitly and the care taken in defining the characteristic probe beam polarisation modes has provided a clear understanding of the nature of the complex projection referred to by Lavrinenko and Gancheryonok[5].

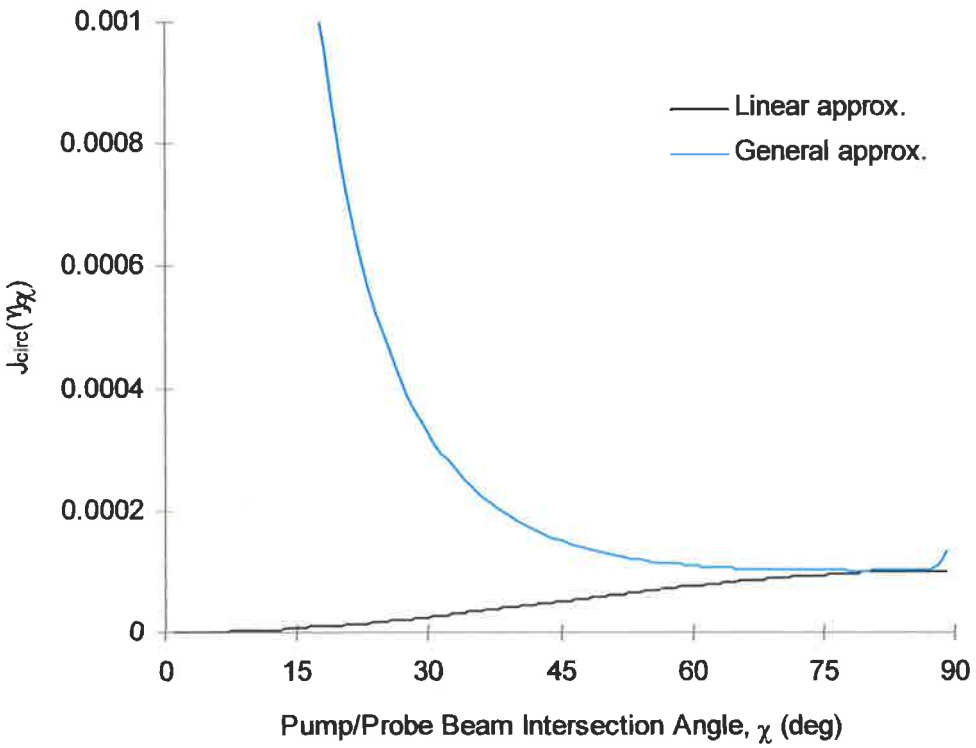

Figure 3: Calculated dependence of the two approximations representing the LPS signal for a circularly polarised pump beam for a probe beam polarisation angle of $\gamma = {}^{\pi}/_{4}$. Values of $\Delta = 0.02$ and $\sigma = 0.01$ were assumed for the calculation. The resultant grey line plotted dependence, $J_{circ}({}^{\pi}/_{4},\chi)_{0\_approx}$, is valid for the approximation regime, $\cos^2(\chi) >> \sigma^2, \Delta$, i.e. for pump/probe intersection angles, $\chi < 81.9°$, while the linear approximation, $J_{circ}({}^{\pi}/_{4},\chi)_{linear\_approx}$, represented by the black line, is valid for , $\chi > 81.9°$.

The form of the expressions obtained by Lavrinenko and Gancheryonok and Reppel and Alwahabi is based on a rapid falloff in detected signal via a $\cot^2(\chi)$ dependence on beam intersection

angle, proportional to the induced circular dichroism due to a circularly polarised pump beam. An additional $\sin^2(\chi)$ dependent term produces the signal for orthogonal beam intersection. The additional term is proportional to the factor, $(\Delta + \sigma^2)^2$, in the case of the approximation assuming characteristically linear polarisation modes for the probe beam for near-orthogonal beam intersection. Polarisation signal may be obtained for orthogonal beam intersection as long as the probe beam is not polarised normal to, or in, the plane of intersection. Maximum signal is obtained for orthogonal beam intersection for a probe beam polarised at $\pi/4$ to the beam intersection plane.

Earlier in the chapter, the term, σ, was identified as the maximum induced *fractional* circular birefringence induced by a circularly polarised pump beam (for collinear pump and probe beams), $\Delta n_{circ}/n_o$. The term, $\Delta/2$, was identified as the maximum induced *fractional* linear birefringence, $\Delta n_{lin}/n_o$, due to a circularly polarised pump beam.

$$\Delta n_{lin} = \frac{\Delta}{2} \cdot n_o \qquad \text{Equation 73}$$

and

$$\Delta n_{circ} = \sigma \cdot n_o \qquad \text{Equation 74}$$

In Chapter I, the J dependence of the induced dichroism (and hence birefringence) was derived as a summation of a function of the squares of the Clebsch-Gordon coefficients over the contributing Zeeman states[c]. The expression contains squares of the Clebsch-Gordon coefficients representing both pump and probe beam polarisation components. In this way, Teets, Kowalski, Hill, Carlson and Hansch[1] derived expressions for the J dependence of

- the *linear* dichroism induced by a *linearly* polarised pump beam, and
- the *circular* dichroism induced by a *circularly* polarised pump beam.

To complete the set of dichroism calculations suggested by the model in this chapter, the equivalent J dependence of the

- the *linear* dichroism induced by a *circularly* polarised pump beam, and
- the *circular* dichroism induced by a *linearly* polarised pump beam

must be calculated.

Teets, Kowalski, Hill, Carlson and Hansch's[1] J dependence of the induced dichroism in the linear regime of optical pumping and assuming no significant collisional population transfer was shown in equation [21] of Chapter I to be proportional to the function, $\zeta_{J,J',J''}$, defined in equation [25] of Chapter I as

[c] The populations of each pair of Zeeman states linked by the selected transition are assumed to be independent and it is assumed that no collisional redistribution of the population occurs.

$$\zeta_{J,J',J''} = (2J+1)\cdot\frac{\sum_{M}\sigma^{i_{pump}}_{J,J',M,M'}\cdot(\sigma^{i}_{J,J'',M,M''}-\sigma^{i'}_{J,J'',M,M''})}{\sum_{M}\sigma^{i_{pump}}_{J,J',M,M'}\cdot\sum_{M}\sigma^{i_{probe}}_{J,J'',M,M''}}$$ Equation 75

according the equation

$$\Delta\alpha^{i,i'}_{J,J''} = -N_J\cdot\sigma_{J,J'}\cdot\sigma_{J,J''}\cdot\frac{I_{pump}t}{\hbar\omega_{pump}}\cdot\zeta_{J,J',J''}$$ Equation 76

Calculation of the additional $\zeta_{J,J',J''}$ functions is easily achieved by substituting squares of the Clebsch-Gordon coefficients for the required pump beam polarisation, $\sigma^{i_{pump}}_{J,J',M,M'}$, into equation [75] and retaining the squares of the Clebsch-Gordon coefficients for the probe beam transition in the term, $\sigma^{i}_{J,J'',M,M''}-\sigma^{i'}_{J,J'',M,M''}$, for the polarisation type (circular or linear) of the induced dichroism. The calculations are included in Appendix VII and produce an interesting result.

- The J dependence of the induced circular dichroism due to a linearly polarised pump beam is zero for all pump/probe beam transitions.
- The J dependence of the induced linear dichroism due to a circularly polarised pump beam is of opposite sign and exactly half the magnitude of *the linear dichroism due to a linearly polarised pump beam.*

The additional $\zeta_{J,J',J''}$ functions for the case of an induced linear dichroism due to a circularly polarised pump beam are tabulated in Table 1. Table 2 shows the limiting values of the expressions in Table 1 as $J \rightarrow \infty$.

For the assumption of the linear regime of optical pumping and no significant collisional population transfer processes, the additional $\zeta_{J,J',J''}$ functions indicate that **a linearly polarised pump beam will induce only a linear dichroism. However, a circularly polarised pump beam may induce both linear and circular dichroism**, which contribute to the LPS signal strength as a function of beam intersection angle according to equations [61] and [62].

The J dependence of the signal strength due to the $\zeta_{J,J',J''}$ functions and $\sigma_{J,J'}/\sigma_{J,J''}$ may be consolidated into the $Z_{J,J',J''}$ function defined in equation [32] of Chapter I

$$\Delta\alpha^{i,i'}_{J,J''} = -N_J\cdot\frac{I_{pump}t}{\hbar\omega_{pump}}\cdot Z_{J,J',J''}\cdot C_{J,J'}\cdot C_{J,J''}$$ Equation 77

where

$$Z_{J,J',J''} = \frac{\sigma_{J,J'}\cdot\sigma_{J,J''}\cdot\zeta_{J,J',J''}}{C_{J,J'}\cdot C_{J,J''}}$$ Equation 78

	J" = J +1	J" = J	J" = J -1
J' = J +1	$\frac{-3}{20}\cdot\frac{(2\cdot J-1)}{(2\cdot J+3)}\cdot\frac{J}{(J+1)}$ $\forall$ J	$\frac{3}{20}\cdot\frac{(2\cdot J-1)}{(J+1)}$ if J > 0	$\frac{-3}{20}$ if J > ½
J' = J	$\frac{3}{20}\cdot\frac{(2\cdot J-1)}{(J+1)}$ if J > 0	$\frac{-3}{20}\cdot\frac{\left(4\cdot J^2+4\cdot J-3\right)}{(J\cdot(J+1))}$ if J > 0	$\frac{3}{20}\cdot\frac{(2\cdot J+3)}{J}$ if J > ½
J' = J-1	$\frac{-3}{20}$ if J > ½	$\frac{3}{20}\cdot\frac{(2\cdot J+3)}{J}$ if J > ½	$\frac{-3}{20}\cdot\frac{(2\cdot J+3)\cdot(J+1)}{(2\cdot J-1)\cdot J}$ if J > ½

Table 1: $\zeta_{J,J',J''}$ factors related to the linear dichroism induced by a circularly polarised pump beam in the linear regime of optical pumping.

	J" = J +1	J" = J	J" = J -1
J' = J +1	-3/20	3/10	-3/10
J' = J	3/10	-3/5	3/10
J' = J-1	-3/10	3/10	-3/20

Table 2: Limiting values of the $\zeta_{J,J',J''}$ factors in the linear regime of optical pumping related to the linear dichroism induced by a circularly polarised pump beam as $J \to \infty$.

	J" = J +1	J" = J	J" = J -1
J' = J +1	$\frac{-1}{60}\cdot\frac{(2\cdot J+3)\cdot(2\cdot J-1)\cdot J}{(2\cdot J+1)^2\cdot(J+1)}$ $\forall$ J	$\frac{1}{60}\cdot\frac{(2\cdot J+3)}{(2\cdot J+1)}\cdot\frac{(2\cdot J-1)}{(J+1)}$ if J > 0	$\frac{-1}{60}\cdot\frac{(2\cdot J+3)\cdot(2\cdot J-1)}{(2\cdot J+1)^2}$ if J > ½
J' = J	$\frac{1}{60}\cdot\frac{(2\cdot J+3)}{(2\cdot J+1)}\cdot\frac{(2\cdot J-1)}{(J+1)}$ if J > 0	$\frac{-1}{60}\cdot\frac{\left(4\cdot J^2+4\cdot J-3\right)}{(J\cdot(J+1))}$ if J > 0	$\frac{1}{60}\cdot\frac{(2\cdot J-1)\cdot(2\cdot J+3)}{(2\cdot J+1)\cdot J}$ if J > ½
J' = J-1	$\frac{-1}{60}\cdot\frac{(2\cdot J-1)\cdot(2\cdot J+3)}{(2\cdot J+1)^2}$ if J > ½	$\frac{1}{60}\cdot\frac{(2\cdot J-1)\cdot(2\cdot J+3)}{(2\cdot J+1)\cdot J}$ if J > ½	$\frac{-1}{60}\cdot\frac{(2\cdot J-1)\cdot(2\cdot J+3)\cdot(J+1)}{(2\cdot J+1)^2\cdot J}$ if J > ½

Table 3: $Z_{J,J',J''}$ factors related to the linear dichroism induced by a circularly polarised pump beam in the linear regime of optical pumping.

	J" = J +1	J" = J	J" = J -1
J' = J +1	-1/60	1/30	-1/60
J' = J	1/30	-1/15	1/30
J' = J-1	-1/60	1/30	-1/60

Table 4: Limiting values of the $Z_{J,J',J''}$ factors in the linear regime of optical pumping related to the linear dichroism induced by a circularly polarised pump beam as $J \to \infty$.

	J" = J +1	J" = J	J" = J -1
J' = J +1	$\frac{-3}{10}\cdot\frac{(2\cdot J-1)\cdot J}{(2\cdot J+3)\cdot(J+1)}$ $\forall$ J	$\frac{3}{20}\cdot\frac{(2\cdot J-1)}{(J+1)}$ if J > 0	$\frac{-3}{20}$ if J > ½
J' = J	$\frac{3}{20}\cdot\frac{(2\cdot J-1)}{(J+1)}$ if J > 0	$\frac{-3}{10}\cdot\frac{(4\cdot J^2+4\cdot J-3)}{(J+1)\cdot J}$ if J > 0	$\frac{3}{20}\cdot\frac{(2\cdot J+3)}{J}$ if J > ½
J' = J-1	$\frac{-3}{20}$ if J > ½	$\frac{3}{20}\cdot\frac{(2\cdot J+3)}{J}$ if J > ½	$\frac{-3}{10}\cdot\frac{(2\cdot J+3)\cdot(J+1)}{(2\cdot J-1)\cdot J}$ if J > ½

Table 5: Corrected ζ_{J,J',J''_corr} factors related to the linear dichroism induced by a circularly polarised pump beam in the linear regime of optical pumping.

	J" = J +1	J" = J	J" = J -1
J' = J +1	-3/10	3/10	-3/10
J' = J	3/10	-6/5	3/10
J' = J-1	-3/10	3/10	-3/10

Table 6: Limiting values of the corrected ζ_{J,J',J''_corr} factors in the linear regime of optical pumping related to the linear dichroism induced by a circularly polarised pump beam as $J \to \infty$.

	J" = J +1	J" = J	J" = J -1
J' = J +1	$\frac{-1}{30}\cdot\frac{(2\cdot J+3)\cdot(2\cdot J-1)\cdot J}{(2\cdot J+1)^2\cdot(J+1)}$ $\forall$ J	$\frac{1}{60}\cdot\frac{(2\cdot J+3)}{(2\cdot J+1)}\cdot\frac{(2\cdot J-1)}{(J+1)}$ if J > 0	$\frac{-1}{60}\cdot\frac{(2\cdot J+3)\cdot(2\cdot J-1)}{(2\cdot J+1)^2}$ if J > ½
J' = J	$\frac{1}{60}\cdot\frac{(2\cdot J+3)}{(2\cdot J+1)}\cdot\frac{(2\cdot J-1)}{(J+1)}$ if J > 0	$\frac{-1}{30}\cdot\frac{(4\cdot J^2+4\cdot J-3)}{(J+1)\cdot J}$ if J > 0	$\frac{1}{60}\cdot\frac{(2\cdot J-1)\cdot(2\cdot J+3)}{(2\cdot J+1)\cdot J}$ if J > ½
J' = J-1	$\frac{-1}{60}\cdot\frac{(2\cdot J-1)\cdot(2\cdot J+3)}{(2\cdot J+1)^2}$ if J > ½	$\frac{1}{60}\cdot\frac{(2\cdot J-1)\cdot(2\cdot J+3)}{(2\cdot J+1)\cdot J}$ if J > ½	$\frac{-1}{30}\cdot\frac{(2\cdot J-1)\cdot(2\cdot J+3)\cdot(J+1)}{(2\cdot J+1)^2\cdot J}$ if J > ½

Table 7: Corrected Z_{J,J',J''_corr} factors related to the linear dichroism induced by a circularly polarised pump beam in the linear regime of optical pumping.

	J" = J +1	J" = J	J" = J -1
J' = J +1	-1/30	1/30	-1/60
J' = J	1/30	-2/15	1/30
J' = J-1	-1/60	1/30	-1/30

Table 8: Limiting values of the corrected Z_{J,J',J''_corr} factors in the linear regime of optical pumping related to the linear dichroism induced by a circularly polarised pump beam as $J \to \infty$.

The $Z_{J,J',J''}$ functions relating to the $\zeta_{J,J',J''}$ functions in Table 1 are listed in Table 3, with the limiting values when $J \rightarrow \infty$ in Table 4. For reference, the corrected ζ_{J,J',J''_corr} functions which account for the contribution of the population of the upper state in the linear regime of optical pumping for shared pump/probe beam transitions via a additional factor of 2 are listed in Table 5, with limiting values in Table 6. The corresponding corrected Z_{J,J',J''_corr} functions and their limits are listed in Tables 7 and 8.

The interesting optics contained in equations [61] and [62] lies in the contribution of *an induced linear birefringence* in addition to the conventionally considered *induced circular birefringence* due to a circularly polarised pump beam for all but collinear pump/probe geometries. The induced circular birefringence dominates in near co- and counterpropagating geometries, which would explain why the effect has not been noted (to the best of our knowledge) in the literature for spectroscopic applications. However, the theory above predicts that the induced linear birefringence, Δ, will dominate for orthogonal pump/probe beam intersection with the induced linear birefringence appearing to second order. The induced circular birefringence, σ^2, appearing to the fourth power in the signal strength.

This result would appear to modify the spectroscopic behaviour considered to be characteristic of polarisation spectroscopy. As can be inferred from the Figures [13] to [14] of Chapter I, a circular polarised pump beam is favoured for R-pump/R-probe and P-pump/P-probe transitions, while Q-pump/Q-probe transitions are optimised by a linearly polarised pump beam in a collinear pump/probe beam geometry. However, the results tabulated above predict that, for non-zero signal strength in an orthogonal beam geometry for a circularly polarised pump beam, while Q-pump/Q-probe transitions may be found to be generally favoured if the induced linear dichroism dominates ($\Delta > \sigma^2$), rather than R-pump/R-probe and P-pump/P-probe transitions. Note that the LPS signal for a linearly polarised pump beam is optimised for Q transitions for all beam intersection angles. It is clear that selection of optimum transitions for the case of a circularly polarised pump beam is now a function of beam intersection angle.

The LPS signal for near-collinear beam intersection for a circularly polarised pump beam is dominated by the induced circular birefringence (via the term σ). However, associating the LPS signal for near-orthogonal beam intersection purely with the induced linear birefringence (via the term $\Delta/2$) is correct only to first order. Difficulties arise with this assumption if the two induced birefringence terms appearing in equation [62] are not the same order of magnitude.

For $\cos^2(\chi) << \sigma^2, \Delta$ (near-orthogonal imaging), the geometrical dependence of the signal strength is (from equation [62]) given by

$$J_{\substack{circ \\ linear\_approx}}(\gamma,\chi) = \sin^2(2\cdot\gamma)\cdot\sin^2(\chi)\cdot\left(\frac{\Delta+\sigma^2}{2}\right)^2 \qquad \text{Equation 79}$$

Figures 4 to 6 compare the relative J dependence of the terms, σ^2 and Δ. The J dependence of the induced circular birefringence, σ, is given by the $Z_{J,J",J"\_circ\_corr}$ functions defined in Chapter I. The J dependence of the induced linear birefringence, $\Delta/2$, is given by the additional $Z_{J,J',J"\_corr}$ functions calculated in Appendix VII and tabulated in Tables 3 and 4. Figures 4 to 6 show the J dependence of the terms, σ^2 and Δ, by plotting

(a) twice the additional linear corrected $Z_{J,J',J"\_corr}$ functions (to represent Δ), and

(b) the square of the circular corrected $Z_{J,J',J"\_circ\_corr}$ functions (to represent σ^2)

for P (Figure 4), Q (Figure 5) and R (Figure 6) pump beam transitions respectively.

The three possible probe beam transitions are shown on each figure. For convenience, the corrected $Z_{J,J",J"\_corr}$ functions have been used to plot these figures. It can be seen that the induced linear birefringence, Δ, and the square of the induced circular birefringence, σ^2, are of the same order of magnitude even though the circular birefringence appears to second order in equation [79].

The orthogonal LPS signal strength is shown in equation [79] to be proportional to the square of the factor, $(\Delta + \sigma^2)$. The square of this factor is shown in Figures 7 to 9 for P, Q and R transitions respectively. Once again, the three possible probe beam transitions are shown on each figure. The dip in LPS signal strength at low J for the case of a Q-pump/Q-probe transition is due to the switchover between dominance of the signal by circular to linear dichroism as J increases.

Q-pump/Q-probe transitions are favoured for orthogonal beam intersection, although P-pump/P-probe and R-pump/R-probe transitions are also relatively strong for low J. Consequently,

- for near-collinear beams (for a circularly polarised pump beam), P-pump/P-probe and R-pump/R-probe transitions are favoured,
- for near-orthogonal beams, Q transitions are optimal for strong signal.

For intermediate beam intersection angles, the spectroscopic behaviour will be a function of both the induced linear and induced circular birefringence. Thus the dominant birefringent component for a given beam intersection angle controls the type of spectroscopic transition which is favoured.

It is clear that disparity between the linear and circular corrected $Z_{J,J',J"}$ functions for a given J will lead to conditions when either of the induced linear or induced circular birefringent terms, Δ or σ^2, dominates the behaviour for orthogonal polarisation spectroscopy for a circularly polarised pump

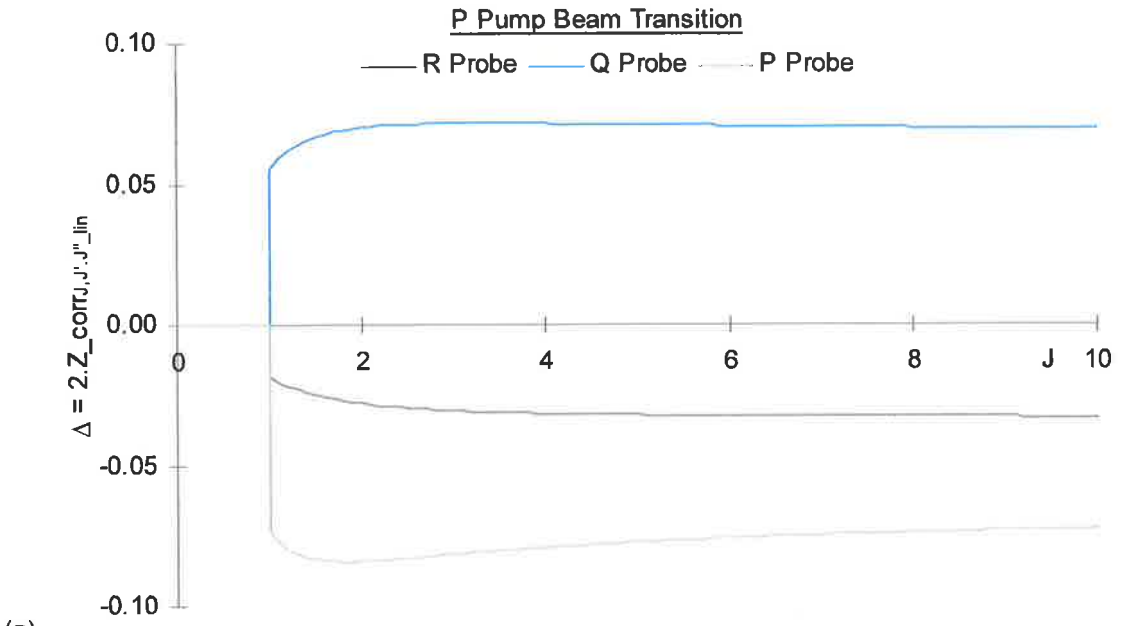

(a)

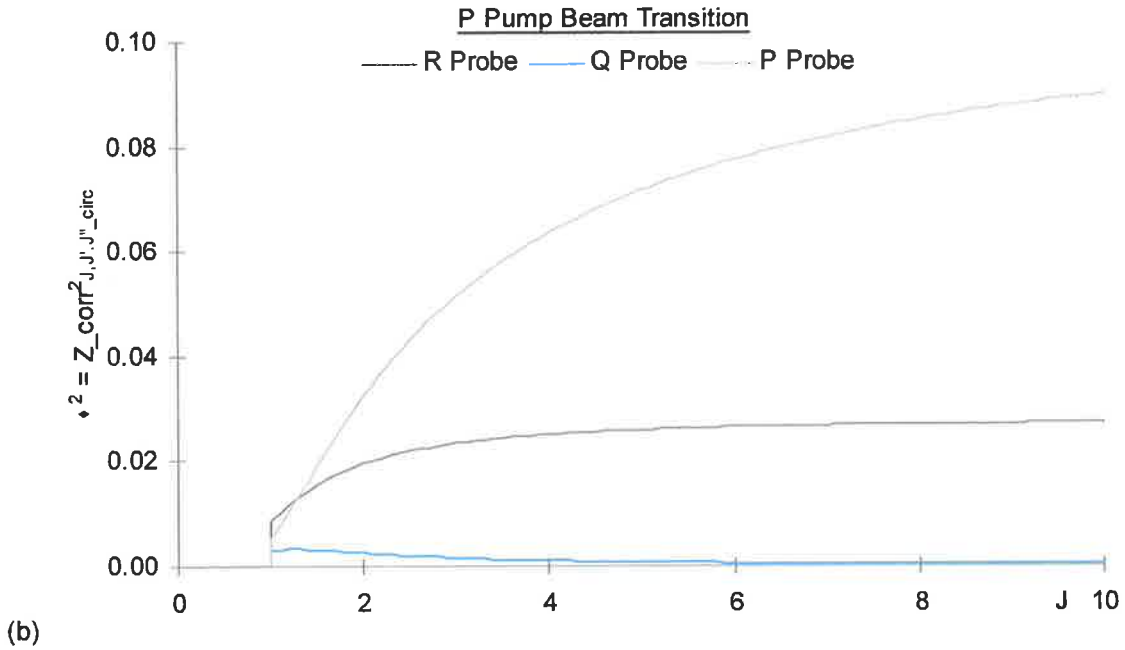

(b)

Figure 4: J dependence of the relative (a) (circularly polarised pump beam) induced linear birefringence (a first order factor) and (b) induced circular birefringence (a second order factor) contributions to the square root of the orthogonal LPS signal strength according to Equation [79] in the case of a circularly polarised pump beam (P transition) and probe beam polarised at $\pi/4$ to the beam intersection plane. The probe beam polarisation is chosen to maximise orthogonal signal. The probe beam transitions are indicated on each graph.

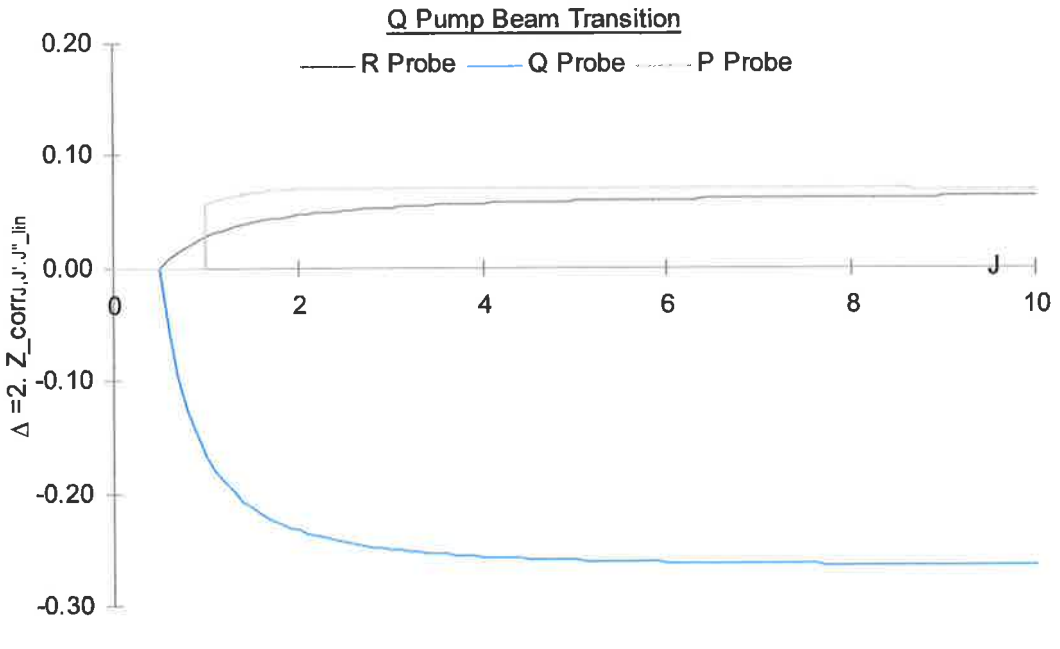

(a)

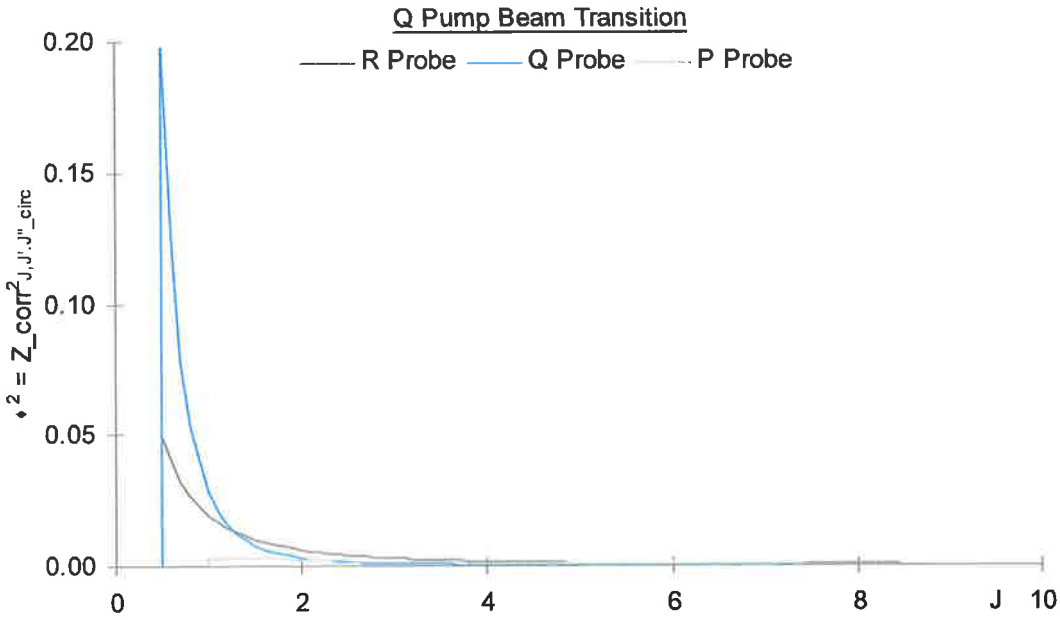

(b)

Figure 5: J dependence of the relative (a) (circularly polarised pump beam) induced linear birefringence (a first order factor) and (b) induced circular birefringence (a second order factor) contributions to the square root of the orthogonal LPS signal strength according to Equation [79] in the case of a circularly polarised pump beam (Q transition) and probe beam polarised at $\pi/4$ to the beam intersection plane. The probe beam polarisation is chosen to maximise orthogonal signal. The probe beam transitions are indicated on each graph.

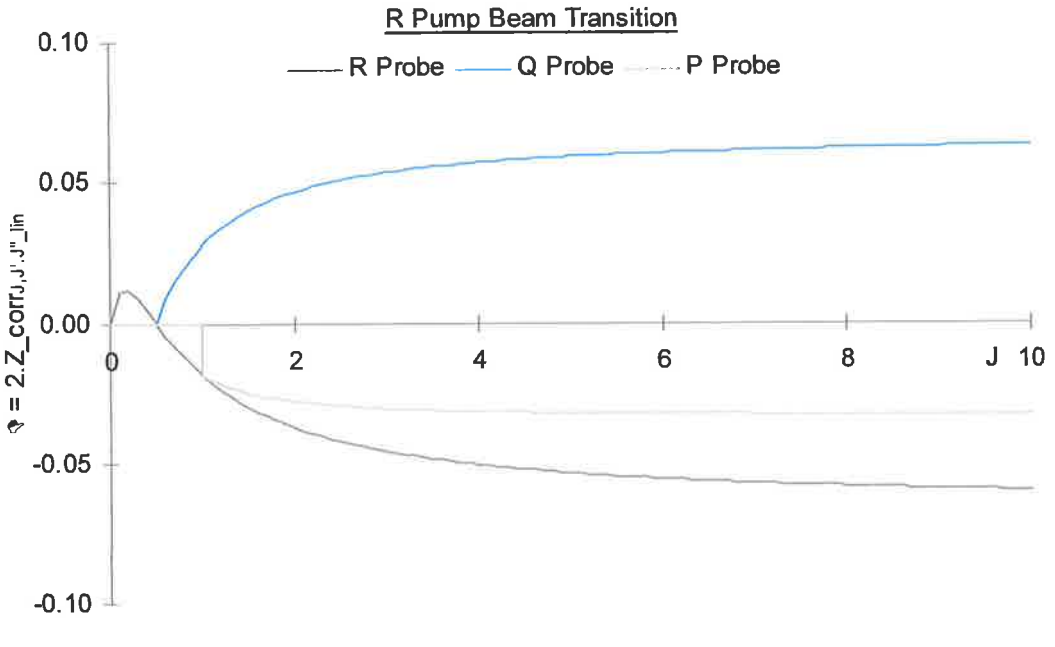

(a)

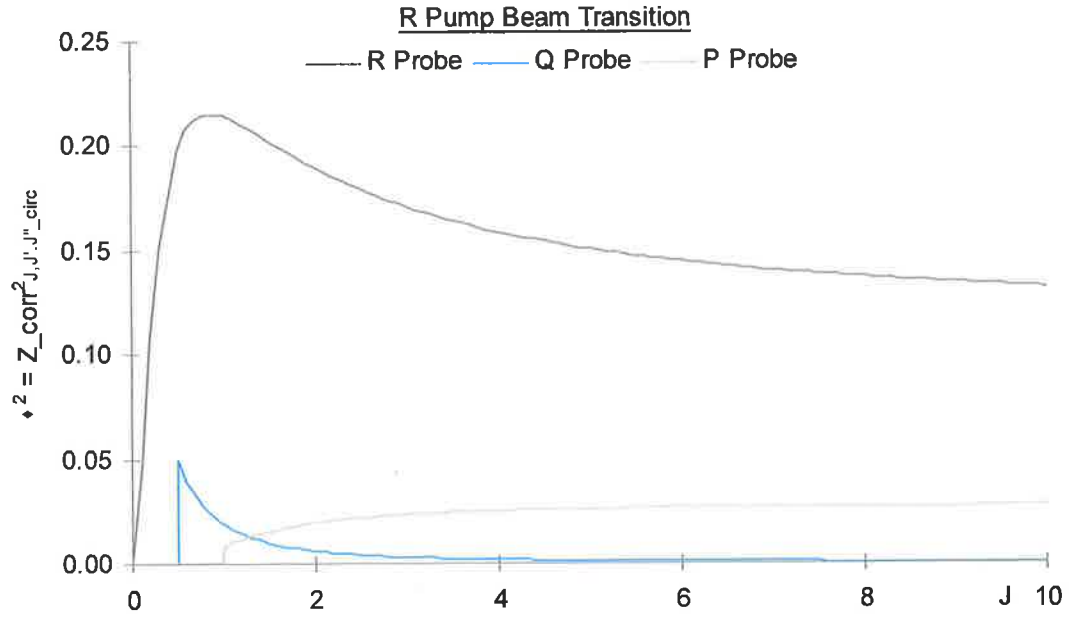

(b)

Figure 6: J dependence of the relative (a) (circularly polarised pump beam) induced linear birefringence (a first order factor) and (b) induced circular birefringence (a second order factor) to the square root of the orthogonal LPS signal strength according to equation [79] in the case of a circularly polarised pump beam (R transition) and probe beam polarised at $\pi/4$ to the beam intersection plane. The probe beam polarisation is chosen to maximise orthogonal signal. The probe beam transitions are indicated on each graph.

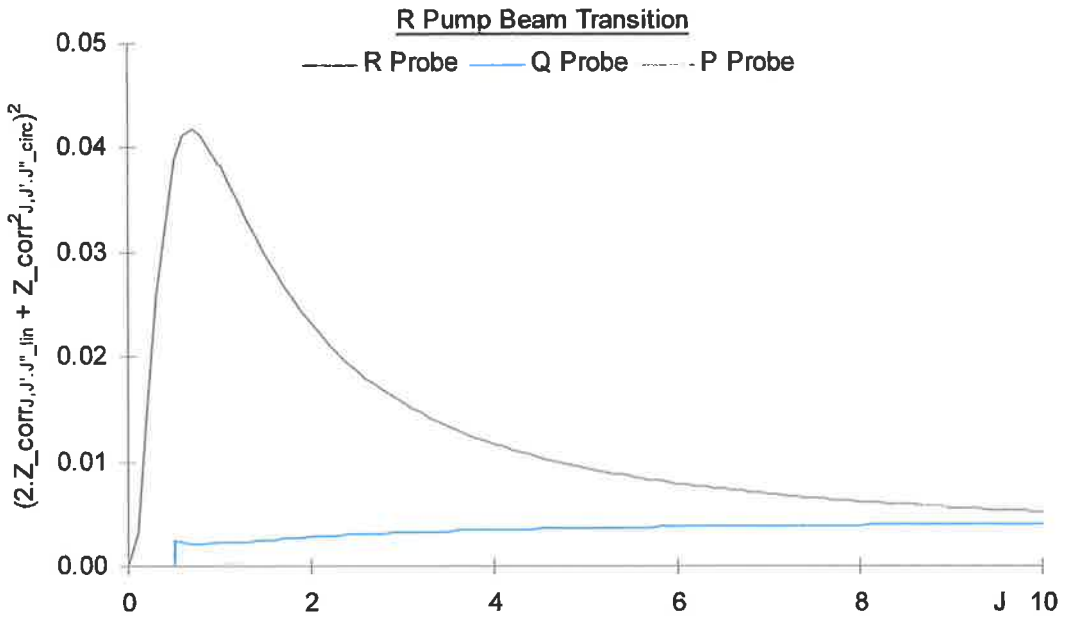

Figure 7: J dependence of the term, $(\Delta - \sigma^2)^2$, in the case of a P transition and a circularly polarised pump beam. The probe beam transitions are indicated on the figure.

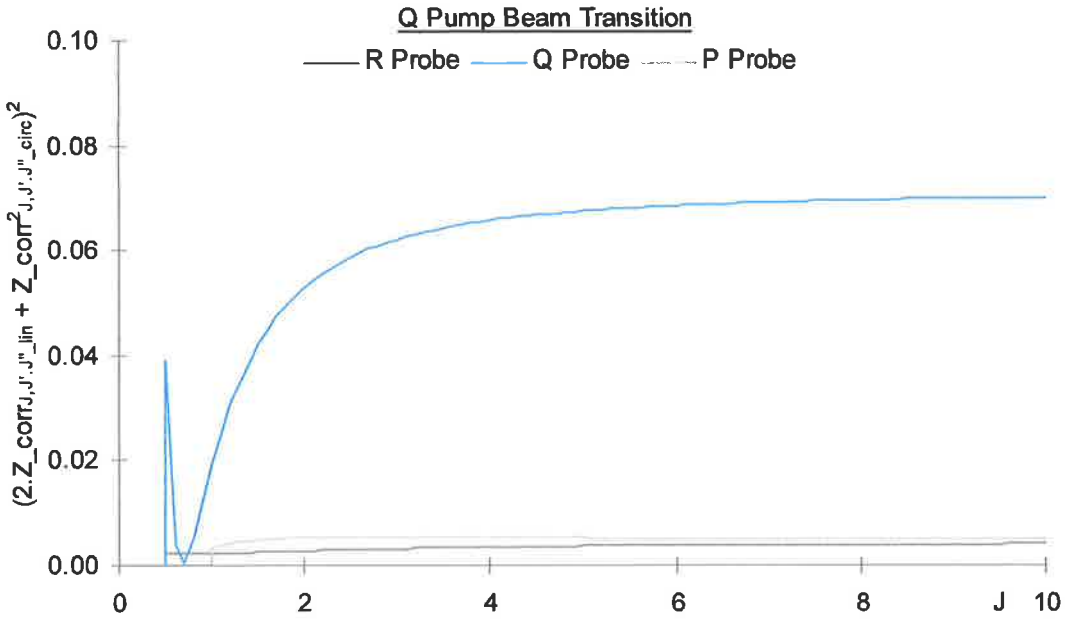

Figure 8: J dependence of the term, $(\Delta - \sigma^2)^2$, in the case of a Q transition and a circularly polarised pump beam. The probe beam transitions are indicated on the figure.

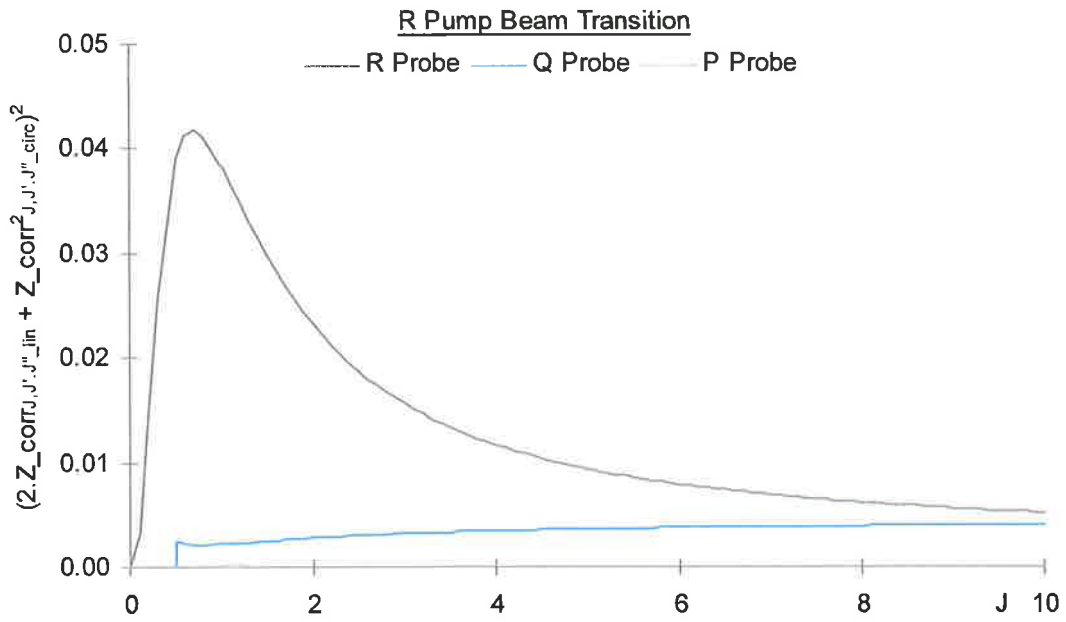

Figure 9: J dependence of the term, $(\Delta - \sigma^2)^2$, in the case of an R transition and a circularly polarised pump beam. The probe beam transitions are indicated on the figure.

beam. Typically, dominant induced linear birefringence terms lead to strong Q-pump/Q-probe beam transitions, while dominant induced circular birefringence terms lead to strong P-pump/P-probe beam and R-pump/R-probe beam transitions.

The next chapter describes an experiment designed to demonstrate non-zero orthogonal signal in the case of a circularly polarised pump beam as was demonstrated in Chapter III for a linearly polarised pump beam. The experiment validates the prediction of strong Q–pump/Q-probe transitions for orthogonal beam intersection for a circularly polarised pump beam by collecting orthogonal PLPS images for the of the $A^2\Sigma$–$X^2\Pi$ (0-0) $Q_2(8)$ line of OH. This verification of non-zero signal for orthogonal signal would allow polarisation spectroscopy imaging to be applied for all beam intersection angles.

This chapter has described a model of the behaviour of polarisation spectroscopy in the case of a circularly polarised beam. The model is very similar to that of Lavrinenko and Gancheryonok[5], but extends the approximation level to higher order terms which are especially important to the spectroscopic behaviour of polarisation spectroscopy for orthogonal imaging. Importantly, the model provides an analogy with the behaviour of an optically active uniaxial crystal, or more accurately uniaxial gas, to extend our understanding of polarisation spectroscopy in non-collinear geometries.

Chapter V: Orthogonal Imaging for a Circularly Polarised Pump Beam.

In this chapter, for the case of a circularly polarised pump beam

- **the first (to the best of my knowledge) orthogonal LPS signal is reported, and**
- **the first (to the best of my knowledge) Orthogonal Polarisation Spectroscopy Imaging (OPLPS) is demonstrated.**

Polarisation spectroscopy is conventionally implemented with near-collinear pump and probe beams. PLPS imaging require a non-zero pump/probe beam intersection angle, χ., to obtain good spatial resolution of the imaged region. Chapter III demonstrated that significant signal may be obtained for the case of a linearly polarised pump beam for all pump/probe beam intersection angles, supporting the geometrical theory of polarisation spectroscopy developed in Chapter II.

A similar geometrical theory of polarisation spectroscopy for a circularly polarised pump beam is presented in Chapter IV. This theory also predicts a non-zero signal for orthogonal pump/probe beam intersection angles for probe beam polarisations which do not lie in or normal to the plane of intersection.

A $\cot^2(\chi)$ dependence of LPS signal in the weak saturation regime was found previously in the experiment of Zizak, Lanauze and Winefordner[27] (1986) for a circularly polarised pump beam. The experiment detected seeded sodium (Na D_2 line) in a premixed air/acetylene flame. Zizak, Lanauze and Winefordner explained the geometric dependence of the signal strength as a function of the change in the interaction volume between pump and probe beams and the component of the pump beam intensity on the direction of the probe beam. The experiment was limited to intersection angles less than 30^o due to low signal strength.

Chapter IV points out the possible equivalence of two theories describing orthogonal polarisation spectroscopy for a circularly polarised pump beam: those of Laverinenko and Gancheryonok[5]and Reppel and Alwahabi[23]The two theories cannot be distinguished geometrically for orthogonal polarisation. However, the theory of Reppel and Alwahabi explicitly states that the dominant induced dichroism is linear, rather than circular, for orthogonal polarisation spectroscopy and a circularly

polarised pump beam. As a result, the favoured transitions for a single-laser system and a combusting system (where there is little species population for J < 5), are Q-pump/Q-probe rather than the conventionally assumed (for a circularly polarised pump beam) P-pump/P-probe and R-pump/R-probe transitions.

The LPS signal for a linearly polarised pump beam is proportional to the square of the induced linear dichroism and, for the polarisation described above, follows a

$$F_{lin}(\chi) = \text{cosec}^2(\chi) \qquad \text{Equation 1}$$

dependence on pump/probe beam intersection angle. (Note that for a horizontally polarised pump beam and probe beam polarised at $\pi/4$ to the vertical, the dependence on the intersection angle, χ, follows a $\cot^2(\chi)$ curve, leading to zero signal in an orthogonal geometry).

The derivation derived in Chapter IV for a circularly polarised pump beam required two regions of approximation to describe the full range of pump/probe beam geometries. For the first region, near-collinear and moderate beam intersection angles, circular and elliptical polarisation modes described the characteristic polarisation modes of propagation through the pumped region. For the second region, near-orthogonal beam intersection, linear polarisation modes were used to describe the propagation of the probe beam.

The LPS signal for perfectly crossed polarisers and no interpolariser birefringent optical elements in the probe beam path is predicted in Chapter IV to be proportional to the factor, $J_{circ}(\gamma,\chi)$. In the two regions of approximation, this factor is written as

For near-collinear/moderate beam intersection angles, $\cos^2(\chi) >> \sigma^2, \Delta$

$$J_{circ}(\gamma,\chi)_{0\_approx} = \frac{\left(\left(\cos^2(\gamma)\cdot\sin^4(\chi)\cdot\Delta+\cos^2(\chi)\right)\cdot\sigma\right)^2 + \left(\cos(\chi)\cdot\sin^2(\chi)\cdot\cos(\gamma)\cdot\sin(\gamma)\cdot\left(\Delta-\sigma^2\right)\right)^2}{\left(\cos(\chi)\cdot\sin(\chi)\right)^2} \qquad \text{Equation 2}$$

For near-orthogonal beam intersection, $\cos^2(\chi) << \sigma^2, \Delta$

$$J_{circ}(\gamma,\chi)_{linear\_approx} = \sin^2(2\cdot\gamma)\cdot\sin^2(\chi)\cdot\left(\frac{\Delta+\sigma^2}{2}\right)^2 \qquad \text{Equation 3}$$

where

γ is the angle of the probe beam polarisation direction from the normal to the beam intersection plane,

χ is the beam intersection angle, and

σ is the maximum fractional induced circular dichroism due to a circularly polarised pump beam,

$\Delta/2$ is the maximum fractional induced linear dichroism due to a circularly polarised pump beam.

Maximum signal is obtained for a probe beam polarised at $\pi/4$ to the normal to the beam intersection plane. In this case, equations [2] and [3] reduce to

For $\cos^2(\chi) >> \sigma^2, \Delta$

$$J_{circ}\left(\frac{\pi}{4},\chi\right)_{0\_approx} = \frac{1}{4}\cdot\left(\sin^2(\chi)\tan(\chi)\cdot\Delta + 2\cdot\cot(\chi)\right)^2\cdot\sigma^2 + \sin^2(\chi)\cdot\left(\Delta-\sigma^2\right)^2 \qquad \text{Equation 4}$$

For $\cos^2(\chi) << \sigma^2, \Delta$

$$J_{circ}\left(\frac{\pi}{4},\chi\right)_{linear\_approx} = \sin^2(\chi)\cdot\left(\frac{\Delta+\sigma^2}{2}\right)^2 \qquad \text{Equation 5}$$

Note that for a probe beam polarised in, or normal to, the beam intersection plane, the LPS signal reverts to a $\cot^2(\chi)$ dependence on beam intersection angle, with zero signal for orthogonal beam intersection.

The LPS signal strength is dependent on both the induced linear and induced circular dichroism due to a circularly polarised pump beam via the terms, $\Delta/2$ and σ. Assuming pumping in the linear regime and no significant collisional population transfer, the fractional induced circular dichroism due to a circularly polarised pump beam is proportional to the corrected Z_{J,J',J''_corr} factors for a circularly polarised pump beam defined in Chapter I. The corrected Z_{J,J',J''_corr} factors account for the contribution of the upper state of the pumped transition to the induced dichroism.

The induced linear dichroism due to a circularly polarised pump beam is shown in Appendix VII to be of opposite sign and half the magnitude of the linear dichroism induced by a linearly polarised pump beam. The induced linear dichroism due to a linearly polarised pump beam is proportional to the corrected Z_{J,J',J''_corr} factors for a linearly polarised pump beam defined in Chapter I. The induced linear dichroism due to a circularly polarised pump beam is proportional to the additional corrected Z_{J,J',J''_add_corr} factors for a circularly polarised pump beam defined in Chapter IV. The Z_{J,J',J''_add_corr} factors have been summarised in Table 1 assuming a likely laser diagnostic rather than spectroscopic, experiment, with pump and probe beams sharing the same transition.

The rotational quantum number, J, dependence of the LPS signal for a linearly polarised pump beam is independent of the $\mathrm{cosec}^2(\chi)$ dependence on beam intersection angle described in equation [1]. However, the J and χ signal strength dependence is predicted not to be separable in the case of a circularly polarised pump beam. Thus, the favoured transitions are a function of beam intersection angle as well as J.

The predicted J dependence of the LPS signal for a circularly polarised pump beam and probe beam polarised at $\pi/4$ to the beam intersection plane is shown in Figures 1 to 3 for the three beam intersection angles, 15°, 30°, and 90°, respectively. For small to intermediate beam intersection angles, the LPS signal follows a similar dependence on J with P and R transitions favoured over the relatively weak Q transition. However, for near-orthogonal beam intersection the LPS signal dependence on the rotational quantum number changes dramatically, with Q transitions favoured over P and R transitions. It is clear that the spectroscopic behaviour of polarisation spectroscopy changes for a circularly polarised pump beam as the pump/probe beam intersection angle approaches near-orthogonal geometries. For reference, the LPS signal for a linearly polarised pump beam is shown for the same set of beam intersection angles, 15°, 30°, and 90°, in Figure [4], [5] and [6] respectively.

The J dependence of the LPS signal is important for spectroscopic temperature diagnostic techniques as the calculation of (rotational) temperature is based on the ratios of the intensities of two or more rotational lines. Temperature determination in polarisation spectroscopy is independent of beam intersection angle for a linearly polarised pump beam. However, as described above, the competing contributions of the induced circular and linear dichroism due to a circularly polarised pump beam produce a geometric contribution to temperature determination using polarisation spectroscopy. Near-collinear and near-orthogonal pump/probe beam geometries may be chosen to limit the J dependence to approximately those of the induced circular and linear dichroism respectively. The transition angle indicating the limit of the term "near-orthogonal" is defined by the condition, $\cos^2(\chi) \sim \Delta,\ \sigma$.

For the linear dichroism induced by a linearly polarised pump beam

R-pump/R-probe transition	$\frac{1}{15}\cdot\frac{J\cdot(2J-1)(2J+3)}{(J+1)(2J+1)^2}$	$\forall J$
Q-pump/Q-probe transition	$\frac{1}{15}\cdot\frac{(2J-1)(2J+3)}{J\cdot(J+1)}$	if $J>0$
P-pump/P-probe transition	$\frac{1}{15}\cdot\frac{(J+1)(2J-1)(2J+3)}{J\cdot(2J+1)^2}$	if $J>\frac{1}{2}$

For the linear dichroism induced by a circularly polarised pump beam
(of opposite sign and half the magnitude of the linear dichroism induced by a linearly polarised pump beam)

R-pump/R-probe transition	$\frac{-1}{30}\cdot\frac{(2\cdot J+3)\cdot(2\cdot J-1)\cdot J}{(2\cdot J+1)^2\cdot(J+1)}$	$\forall J$
Q-pump/Q-probe transition	$\frac{-1}{30}\cdot\frac{\left(4\cdot J^2+4\cdot J-3\right)}{(J+1)\cdot J}$	if $J>0$
P-pump/P-probe transition	$-\frac{1}{30}\cdot\frac{(J+1)(2J-1)(2J+3)}{J\cdot(2J+1)^2}$	if $J>\frac{1}{2}$

For the circular dichroism induced by a circularly polarised pump beam

R-pump/R-probe transition	$\frac{1}{3}\cdot\frac{J\cdot(2J+3)^2}{(J+1)(2J+1)^2}$	$\forall J$
Q-pump/Q-probe transition	$\frac{1}{3}\cdot\frac{1}{J\cdot(J+1)}$	if $J>0$
P-pump/P-probe transition	$\frac{1}{3}\cdot\frac{(J+1)(2J-1)^2}{J\cdot(2J+1)^2}$	if $J>\frac{1}{2}$

Table 1: The J dependent corrected Z_{J,J',J''_corr} expressions of Teets, Kowalski, Hill, Carlson and Hansch[1] and the additional (non-zero) corrected Z_{J,J',J''_add_corr} expressions defined in Chapter IV assuming pumping in the linear regime and negligible collisional population transfer. The signal is proportional to the square of this factor for perfectly crossed polarisers and no inter-polariser birefringent optical elements in the probe beam path.

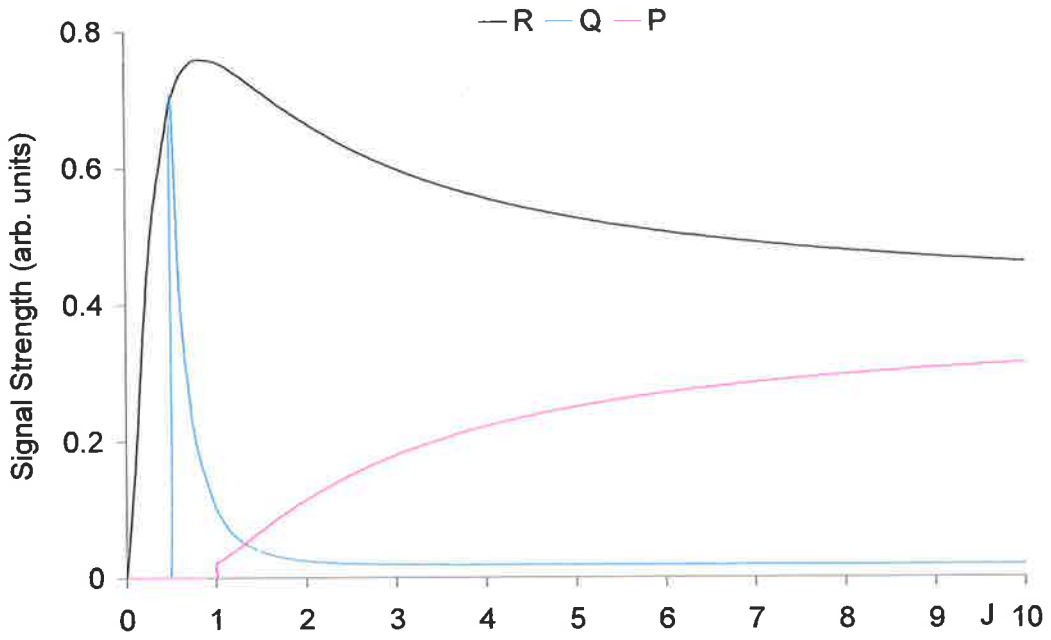

Figure 1: J dependence of the LPS signal for P, Q and R transitions for a circularly polarised pump beam and a pump/probe beam intersection angle of 15°. The probe beam is polarised at π/4 to the beam intersection plane.

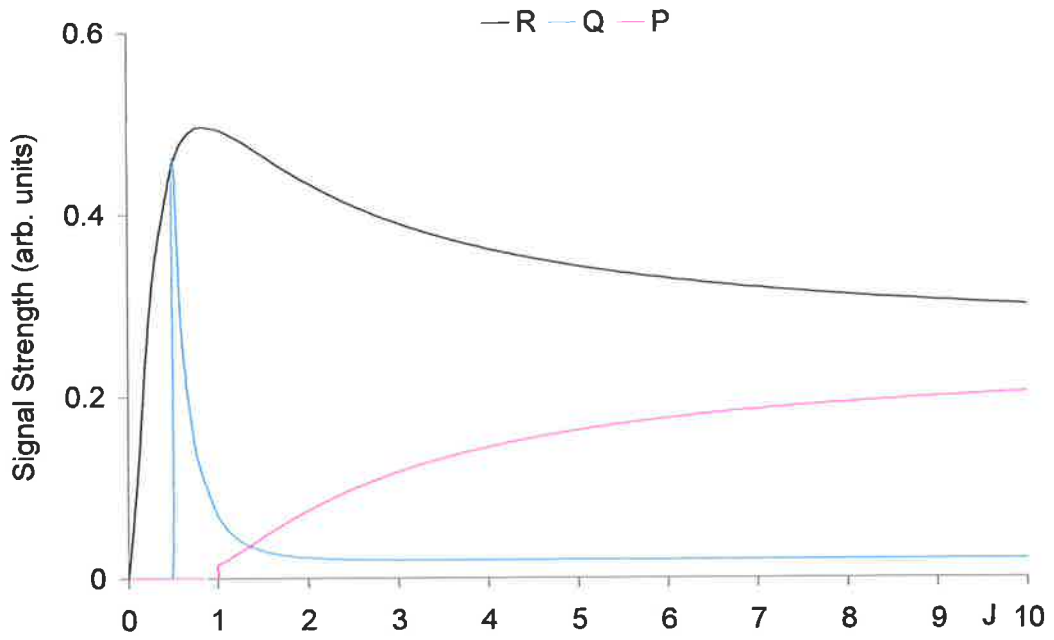

Figure 2: J dependence of the LPS signal for P, Q and R transitions for a circularly polarised pump beam and a pump/probe beam intersection angle of 30°. The probe beam is polarised at π/4 to the beam intersection plane.

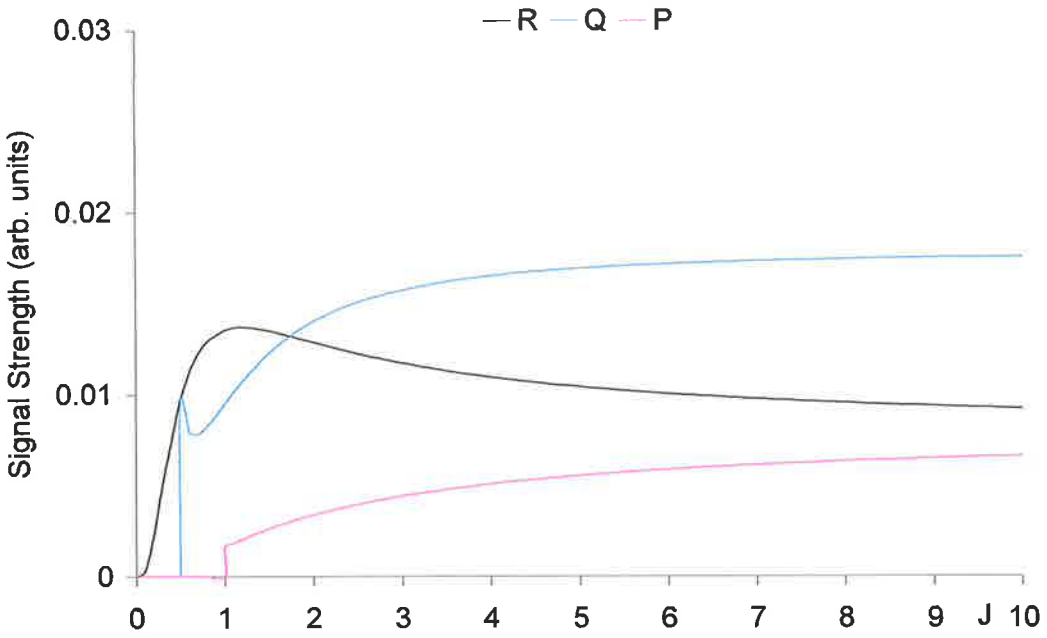

Figure 3: J dependence of the LPS signal for P, Q and R transitions for a circularly polarised pump beam and a pump/probe beam intersection angle of 90°. The probe beam is polarised at π/4 to the beam intersection plane.

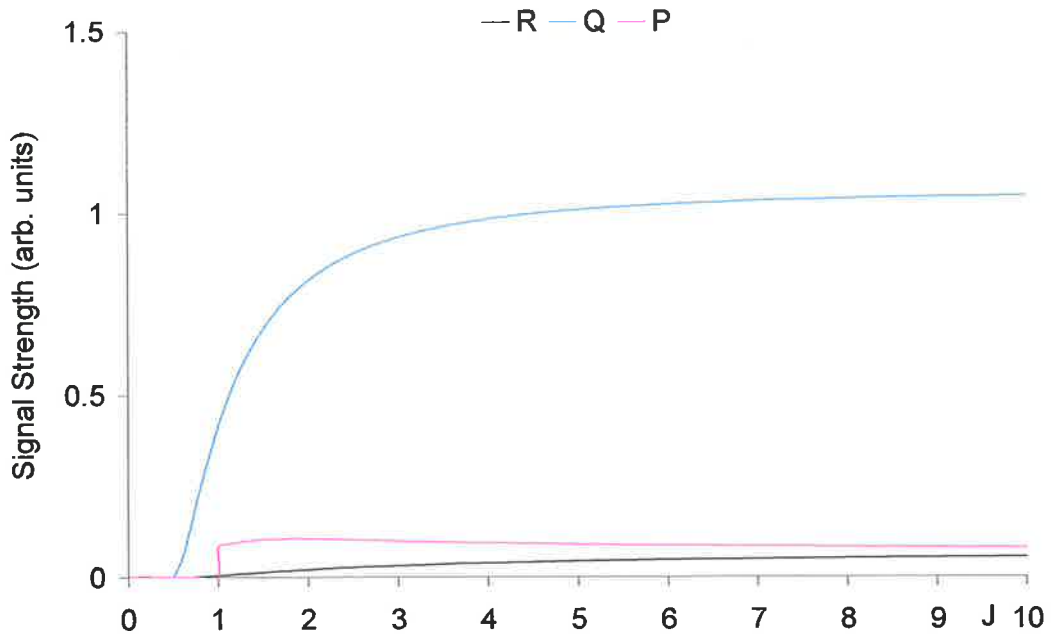

Figure 4: J dependence of the LPS signal for P, Q and R transitions for a linearly polarised pump beam and a pump/probe beam intersection angle of 15°. The pump beam is polarised normal to (and the probe beam polarised at π/4 to) the beam intersection plane.

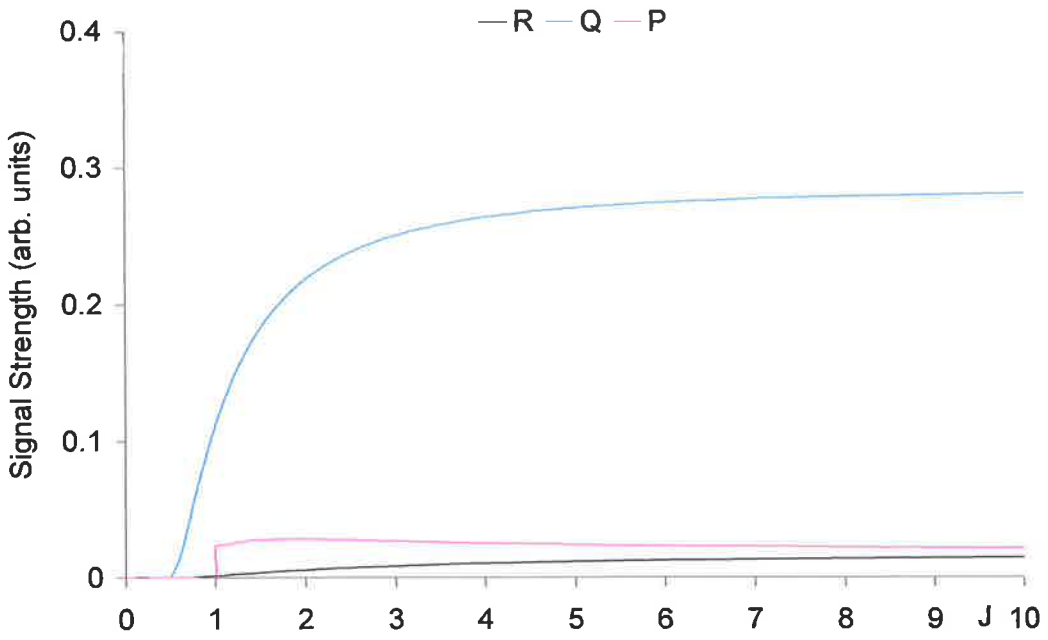

Figure 5: J dependence of the LPS signal for P, Q and R transitions for a linearly polarised pump beam and a pump/probe beam intersection angle of 30°. The pump beam is polarised normal to (and the probe beam polarised at $\pi/4$ to) the beam intersection plane.

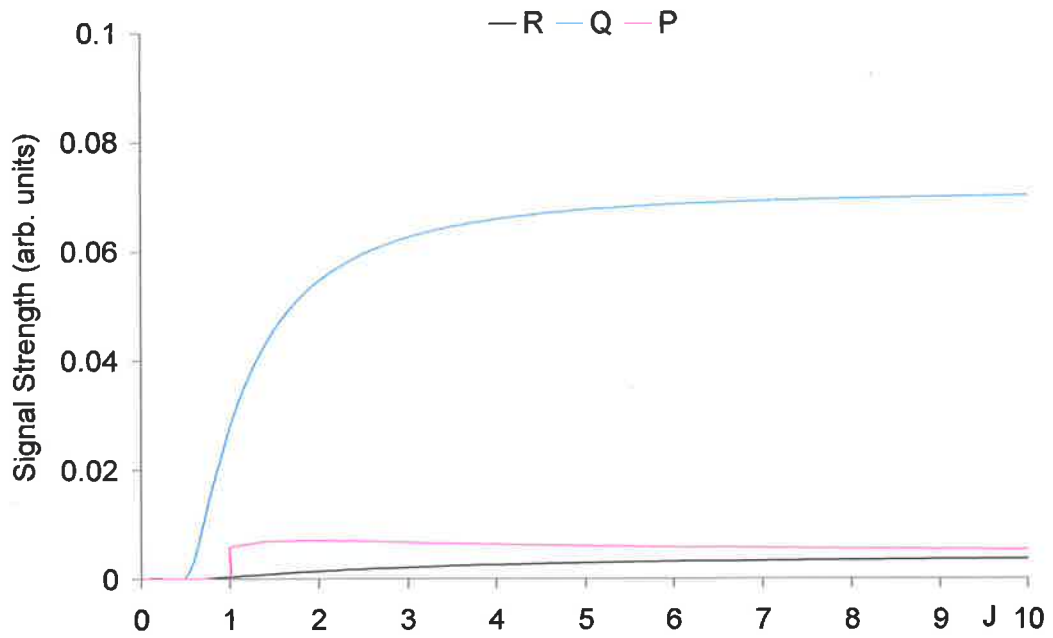

Figure 6: J dependence of the LPS signal for P, Q and R transitions for a linearly polarised pump beam and a pump/probe beam intersection angle of 90°. The pump beam is polarised normal to (and the probe beam polarised at $\pi/4$ to) the beam intersection plane.

Orthogonal Circular PLPS Experiment

The experiment reported in this chapter was designed to demonstrate that

- orthogonal PLPS for a circularly polarised pump beam and a probe beam polarised at $\pi/4$ to the intersection plane of pump and probe beams produces a non-zero signal strength, and
- the orthogonal LPS signal favours Q-pump/Q-probe rather than P-pump/P-probe and R-pump/R-probe transitions.

Both these results were predicted by the theory developed in Chapter IV. The theories of Lavrinenko and Gancheryonok and Reppel and Alwahabi both predict non-zero LPS signal for orthogonal beam intersection for a probe beam polarisation direction not aligned normal to or in the beam intersection plane. If the first prediction above is confirmed, non-zero LPS signal may be obtained for all beam intersection angles for both linearly and circularly polarised pump beams. This would allow polarisation spectroscopy imaging for any beam intersection geometry for both beam polarisations. The second result will confirm the predicted spectroscopic behaviour of polarisation spectroscopy for orthogonal imaging. The spectroscopic behaviour for non-orthogonal and non-collinear beam geometries may then be predicted from equations [61] and [62] of Chapter IV.

The experiment was a minor variation on that described in Chapter III for orthogonal imaging for a linearly polarised pump beam. The experiment was modified from the case of a linearly polarised pump beam to test for non-zero LPS signal for orthogonal imaging for a circularly polarised pump beam. However, time constraints and an ongoing experimental program limited the experiment to confirming non-zero signal for a probe beam polarised at $\pi/4$ to the vertical so as not to disturb the experimental alignment.

One half of the double ½-wave rhomb in the pump beam path before the pump beam polariser was removed and the remaining ¼-wave rhomb placed after the pump beam polariser to produce a circularly polarised pump beam as shown in Figure 7. The OH signal was imaged only for the case of a probe beam polarised at 45° to the vertical.

The pulse energies were the same as those in the case of a linearly polarised pump beam, with the UV pump and probe beam pulse energies were estimated as 4 mJ and 0.16 mJ, respectively, before passing through the optical system. The pump sheet height was 25 mm and the sheet thickness was ~< 0.6 mm (26.7 mJ/cm^2 or 8.9 MW/cm^2). The probe beam was expanded to an area of 35 mm x 10 mm (0.046 mJ/cm^2 or 15.2 kW/cm^2).

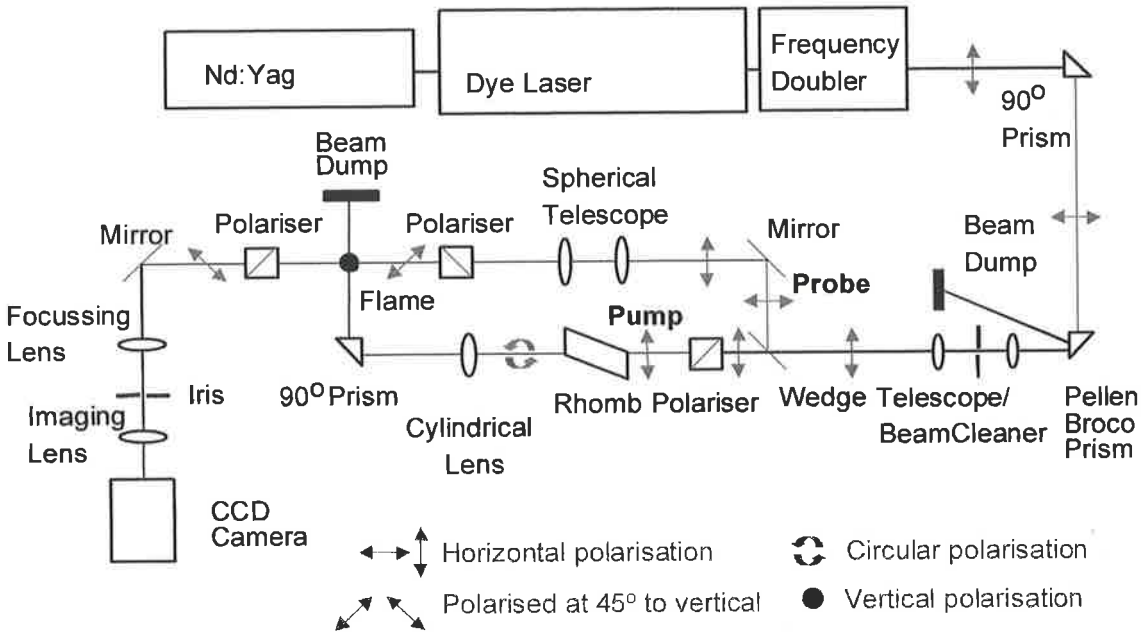

Figure 7: Schematic diagram of the orthogonal PLPS experiment for a circularly polarised pump beam. The ¼-wave rhomb in the pump beam path after the pump beam polariser with transmission axis aligned to horizontal produces a circularly polarised pump beam. The probe beam is polarised at $\pi/4$ to the vertical.

Burner/Flame System

The orthogonal OH PLPS experiments imaged the OH radical distribution in the premixed natural gas/O_2 flame from a modified glass blowing torch flame described in Chapter III. The equivalence ratio was chosen on the basis of maximum LPS signal strength. The resultant laminar flame was fuel-lean, with an OH distribution extending throughout the flame base.

Image Correction

As for Chapter III, unless otherwise noted as instantaneous images, the PLPS images below are obtained by taking an unweighted average of 50 shots and are shown in two modes. Mode 1 corresponds to an image corrected only for the non-zero background of the ICCD. Mode 2 represents the ratio, S/B, of the signal (without background), S, to the background (with flame), B, and is proportional to the square of the induced dichroism. The Mode 2 images were calculated from the image ratio term, R_{signal}, defined in Chapter III, according to the equation

$$\frac{S}{B} = R_{signal} - 1 = \frac{I_{probe}}{I_{probe\_blocked\_pump}} - 1 = \frac{B + S}{B} - 1 \qquad \text{Equation 6}$$

where R_{signal} is the ratio of the collected PLPS signal (including the probe beam extinction background), I_{probe}, to the probe beam extinction background (measured with no pump beam

present), $I_{probe\_blocked\_pump}$. The grey-scale images in this chapter are plotted on a linear grey-scale normalised to a 5 to 95% scale of the signal strength in each image.

Instantaneous images are shown in Mode 1 format as simultaneous instantaneous probe profile backgrounds could not be collected for correction.

(1) Orthogonal Non-Zero Signal Confirmation Experiment

Non-zero LPS signal was immediately detected for orthogonal beam intersection for a circularly polarised pump beam with probe beam polarised at $\pi/4$ to the beam intersection plane. The laser system was tuned to the $A^2\Sigma$–$X^2\Pi$ (0-0) $Q_2(8)$ transition of OH, a transition which would not be favoured in the conventional near-collinear theory of polarisation spectroscopy.

Figures 8 and 9 show (50-shot) average uncorrected (Mode 1) and corrected (mode2) images due to the OH distribution in the premixed flame described above. The signal is obviously non-zero and is distributed throughout the flame with the exception of the cone-shaped OH-free structure at the base of the flame. This presence of this non-zero signal supports the predictions for the case of a circularly polarised pump beam of both Laverinenko and Gancheryonok[5] and Reppel and Alwahabi[23].

The maximum (50 shot) average Mode 1 signal strength in the flame region was 56 counts at a gain of 9, with more typical average signal levels of 41.5 ± 3.2 counts in the region of high OH concentration. For comparison, the average count level at the non-flame edge of the image was ~ 8.8 ± 1.1 counts, and in the OH-free central flame cone,6.2 ± 0.9 counts.

The Mode 2 corrected image is shown in Figure 9. The Mode 2 count level in the flame region is typically ~4.8 ± 0.8 counts. The average Mode 2 count level at the edge of the image is ~ 0.14 ± 0.21, while the central OH-free flame cone has an average Mode 2 count level of –0.09 ± 0.15 counts. The maximum Mode 2 corrected signal to noise ratio is then 24: 1 for this 50 shot average orthogonal PLPS image for a circularly polarised pump beam.

Figure 3 shows an equivalent instantaneous Mode 1 OH PLPS for the same pump/probe/polarisation geometry. Maximum count levels of 275 were detected in the instantaneous images, with more typical values in the high OH concentration regions on the order of 133 counts. The instantaneous images differed only marginally from the average images due to the stability of the laminar (Re ~ 95) natural gas/O_2 flame. Signal levels primarily due to the polarisation

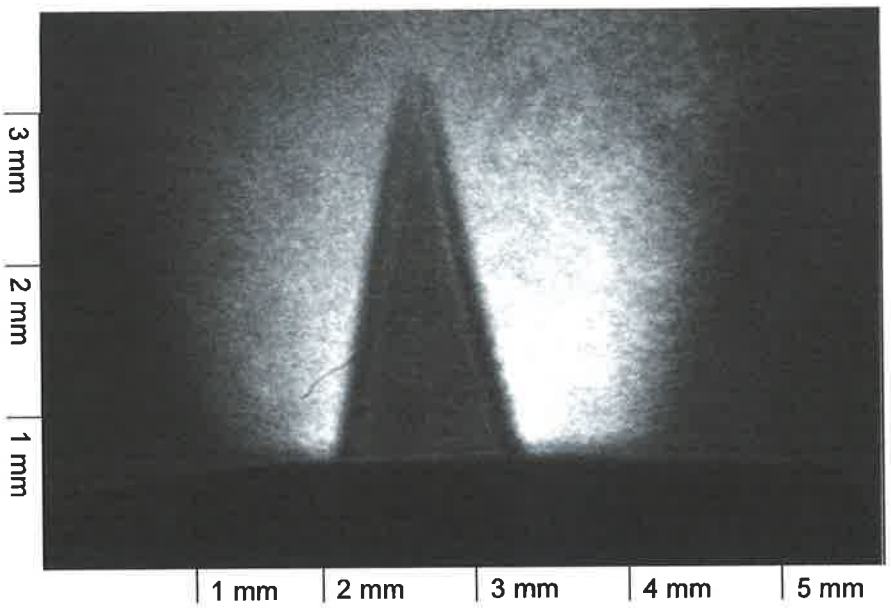

Figure 8: Average (50 shot) Mode 1 PLPS image for an orthogonal pump/probe beam geometry and a circularly polarised pump beam. The obvious OH signal is generated in a laminar premixed natural gas/O_2 flame produced by a 1.2 mm jet exit diameter burner. The maximum count level was ~ 56 counts at gain 9.

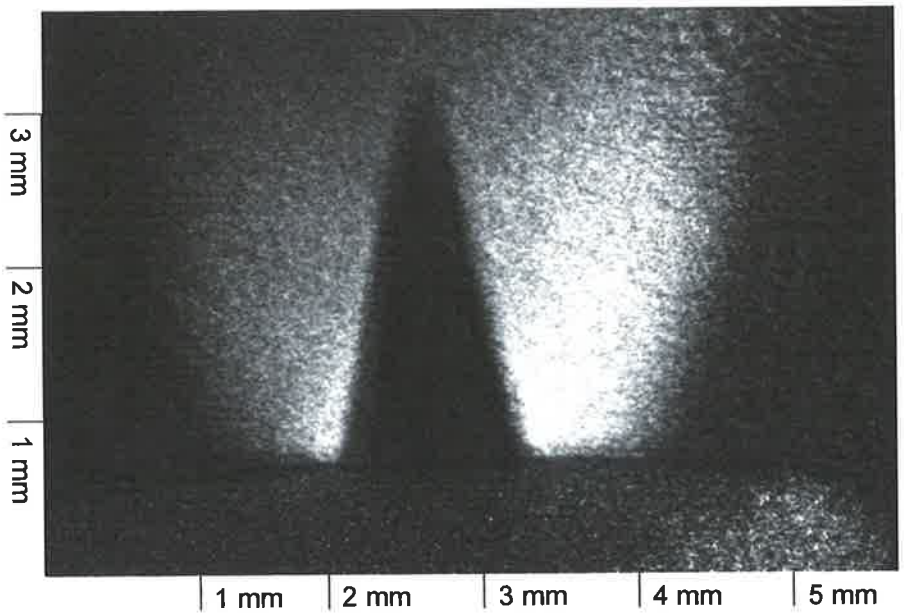

Figure 9: Mode 2 average corrected PLPS image calculated from the image above for an orthogonal pump/probe beam geometry and a circularly polarised pump beam. The Mode 2 count level in the flame region is typically ~ 4-5. The average Mode 2 count level at the edge of the image is ~ 0.14 ± 0.21, while the central flame cone has an average count level of ~ -0.09 ± 0.15 counts.

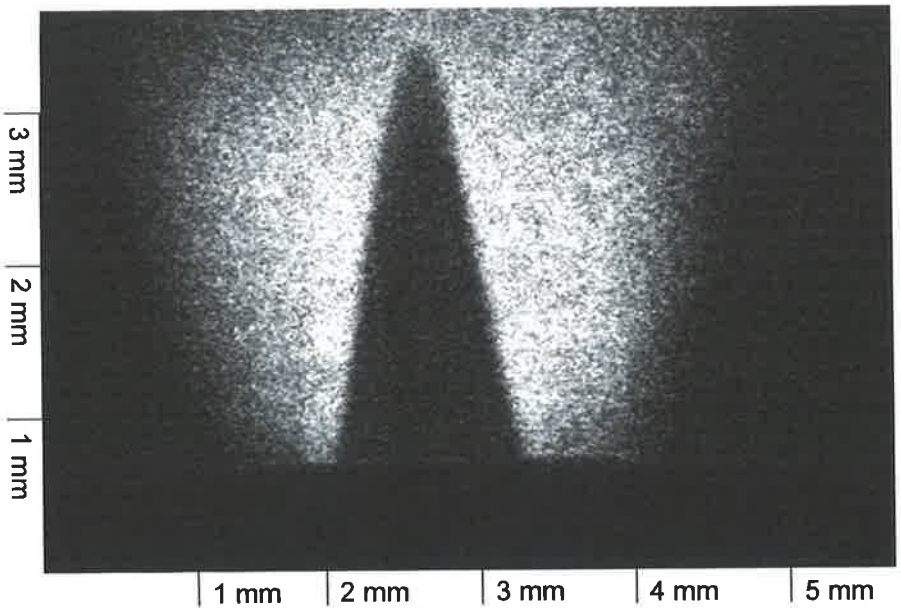

Figure 10: Mode 1 instantaneous image for a circularly polarised pump beam and an orthogonal pump/probe beam geometry. The maximum signal level is 275 with a typical value of 133 counts. The image was chosen for best signal in a set of 50 shots rather than an average count level image.

extinction background at the edge of the image show count levels of 10.3 ± 7.6 counts, and in the central OH-free cone 18.4 ± 9.8 counts.

The images do not require elongation in the horizontal direction to represent the elliptical intersection volume of pump and probe beams, as is the case for small intersection angle polarisation spectroscopy. The imaged area is 3.7 mm x 5.5 mm with resolution of 9.5 μm per pixel. The thickness of the elliptical interaction region for this set of average images was estimated to be 700 μm.

(2) Orthogonal Q-pump/Q-probe Favouring Confirmation

Figures 8 to 10 above were taken with the pump and probe beams tuned to the $A^2\Sigma$-$X^2\Pi(0\text{-}0)$ $Q_2(8)$ transition of OH. Figure 9 in Chapter I indicates that this transition should have near zero signal for a circularly polarised pump beam in a collinear geometry, while $R_2(8)$ and $P_2(8)$ pump/probe transitions are favoured. However, Figures 4 to 9 in Chapter IV indicate that an induced linear dichroism (due to a circularly polarised pump beam) would favour the $Q_2(8)$ transition for orthogonal beam intersection. For this case, the $R_2(8)$ and $P_2(8)$ pump/probe transitions are predicted to be much weaker.

Scans through the $P_2(8)$ and $R_2(8)$ pump/probe transitions for the same experiment **revealed no detectable lineshapes for the orthogonal geometry and a circularly polarised pump beam.** This result contradicts the conventional collinear dichroism theory[1] and further supports the theory of Reppel and Alwahabi.

In comparison, for a pump/probe intersection angle of 13.6° and a circularly polarised pump beam, a scan of the $Q_2(2)$ line revealed no detectable signal, while it was easy to detect the strong $R_2(8)$ and $P_2(8)$ lines. Signal was also obtained for the $R_2(2)$ and $P_2(2)$ lines. This result matches the conventional theory of the a dominant induced circular dichroism for near-collinear geometries[1] and demonstrates the angular dependence of the spectroscopic behaviour of the signal.

The spectroscopic behaviour predicted in Chapter IV has been supported by orthogonal PLPS images obtained experimentally for a circularly polarised pump beam. The laser system was tuned to the $A^2\Sigma$-$X^2\Pi$(0-0) $Q_2(8)$ transition of OH and the OH PLPS signal in a premixed natural gas/O_2 flame was imaged. The probe beam was polarised at $\pi/4$ to the beam intersection plane. It was not possible to detect orthogonal OH PLPS signal for $R_2(8)$ and $P_2(8)$ transitions for this pump beam polarisation. Despite the low signal level in this experiment, this result supports the prediction in Chapter IV of an induced linear dichroism dominating the behaviour of polarisation spectroscopy for a circularly polarised pump beam and orthogonal beam intersection.

For near-collinear geometries, a circular dichroism dominates the LPS signal strength for a circularly polarised pump beam. Consequently, P and R transitions are favoured for the intermediate to high J quantum numbers which are associated with significant species population for temperatures typically associated with combustion. In near-orthogonal pump/probe beam geometries, this chapter has demonstrated that the LPS signal is dominated by a linear dichroism induced by the circularly polarised pump beam. For orthogonal beam intersection angles and a circularly polarised pump beam, Q transition are optimal for intermediate to high J values.

Chapters II and IV predict that the orthogonal LPS signal is dominated by an induced linear dichroism for both linearly and circularly polarised pump beams. These predictions have been supported by the experimental results presented in Chapters III and V. **For intermediate to high J values, Q transitions are then favoured for all orthogonal PLPS experiments.**

Q transitions are also favoured for all beam intersection angles for a linearly polarised pump beam. However, the spectroscopic behaviour of the LPS signal is a function of beam intersection angle for a circularly polarised pump beam. The signal ranges from dominance by an induced circular dichroism for near-collinear beams to dominance by an induced linear dichroism for orthogonal

beams. This geometric dependence of LPS signal strength on J should be modelled accurately in circular PLPS temperature diagnostics.

Orthogonal PLPS imaging has been demonstrated above for a circularly polarised pump beam. As described by the theory in Chapter IV, the orthogonal PLPS signal is dependent on both the induced fractional linear birefringence, $\Delta/2$, and the induced fractional circular birefringence, σ, due to the circularly polarised pump beam. For near-collinear beams, the LPS signal is dominated by the induced circular birefringence. However, the LPS at intermediate beam intersection angles is a more complex function of the two induced birefringence terms.

The complexity of the LPS signal dependence on these two factor is increased by the J dependence of the induced linear and circular birefringence. The relative strength of Δ and σ is a strong function of the rotational quantum number. As a result, the angular dependence of the LPS signal strength is also a function of J.

Figures 11 to 20 show the dependence of the LPS signal strength for a circularly polarised pump beam on the beam intersection angle, χ, based on the theory presented in Chapter IV. A probe beam polarised at $\pi/4$ to the vertical has been assumed. The black line in each figure represents the linear approximation LPS signal valid for near-orthogonal beam geometries satisfying the condition $\cos^2(\chi) >> \sigma^2, \Delta$. The blue line in each figure represents the general approximated LPS signal valid for near-collinear and intermediate beam geometries satisfying the condition, $\cos^2(\chi) << \sigma^2$. In Figures [12] to [14] and [16], the linear approximation signal is effectively zero on the scale of the figure and lies on the χ axis.

Values for the induced linear birefringence, $\Delta_{\text{induced by a circularly polarised pump beam}}$, and the induced circular birefringence, σ, for Figures 11 to 20 were selected based on the ratio of the corrected Z_{J,J',J''_corr} factors calculated in Chapters I and IV. The corrected Z_{J,J',J''_corr} factors induced by a circularly polarised pump beam and tabulated in Chapter I were used to represent the J dependence of the induced circular dichroism. The additional corrected Z_{J,J',J''_add_corr} factors induced by a circularly polarised pump beam and tabulated in Chapter IV were used to represent the J dependence of the induced linear dichroism due to a circularly polarised pump beam. As this gives a ratio of the two birefringence terms and not absolute values, a range of constant factors were used to scale the birefringence terms for each figure.

Figures 11 and 12 show the predicted LPS signal strength as a function of beam intersection angle for P(2)-pump/P(2)-probe and P(8)-pump/P(8)-probe transitions respectively. Values of

- $\Delta_{\text{circularly polarised pump beam}} = -0.021$, and
- $\sigma = 0.045$

were assumed for J = 2, and

- $\Delta_{\text{circularly polarised pump beam}}$ = -0.0019, and
- σ = 0.073

were assumed for J = 8. Figures 13 and 14 show the equivalent curves for R-pump/R-probe transitions. The values of the birefringence terms used in the calculations are listed in the caption at the base of each figure.

The figures for P and R transitions show typical falloffs in signal strength with beam intersection angle to near-zero signal at orthogonal beam intersection. For these transitions, the contribution due to the (circular pump beam) induced linear dichroism, which is strongest for Q transitions, does not contribute significantly to the signal strength in comparison with the signal due to the induced circular dichroism. Figures 11 to 14 indicate the low signal predicted for orthogonal beam intersection for P-pump/P-probe and R-pump/R-probe transitions.

Figures 15 and 16 show the equivalent LPS signal as a function of beam intersection angle for Q(2)-pump/Q(2)-probe and Q(8)-pump/Q(8)-probe transitions respectively. The value of the constant scaling factor used to calculate the induced birefringence terms for Figures 11 to 14 was also used to calculate Figures 15 and 16. The increased strength of the induced linear dichroism (due to the circularly polarised pump beam) for Q-pump/Q-probe transitions is immediately apparent in the figures in the significant signal for orthogonal beam intersection.

Figures 17 and 18 show the signal strength for the same Q-pump/Q-probe transitions, but with double the constant scaling factor used to calculate Figures 11 to 16. Similarly, Figures 19 and 20 show the Q-pump/Q-probe transitions with three times the constant scaling factor as that assumed in Figures 11 to 16.

It is clear that the decay of LPS signal to near zero signal with increasing beam intersection angle is not always characteristic of polarisation spectroscopy for the case of a circularly polarised pump beam. Significant increase in LPS strength for intermediate and near-orthogonal beam intersection angles will occur if there is a strong (circular pump beam) induced linear birefringence. Depending on the relative values of the induced linear and circular birefringence terms, the orthogonal LPS signal may be of the order of, or even larger than, the signal at even the small beam intersection angle of 15°. It should be noted that the signal for near-collinear beam intersection angles ($\chi < 5^{\circ}$) is always strong.

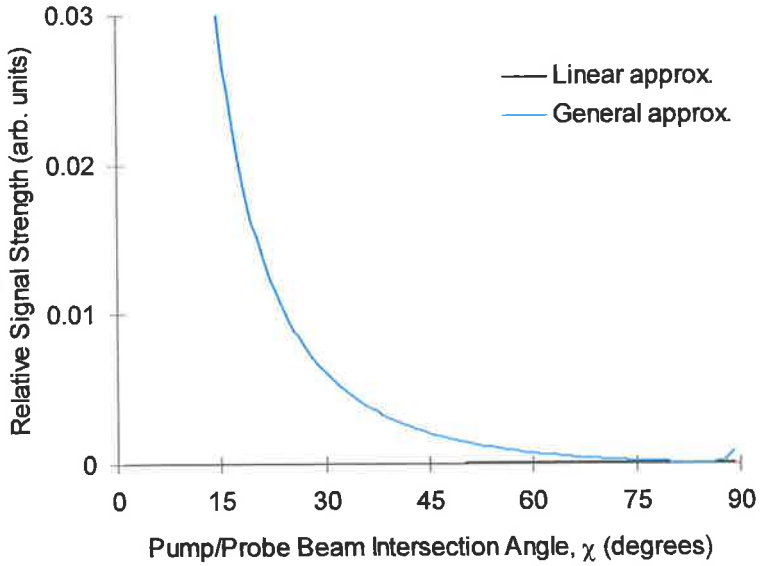

Figure 11: Calculated dependence of the two approximations representing the LPS signal for a circularly polarised pump beam (P(2)-pump/P(2)-probe transition) for a probe beam polarisation angle of $\gamma = {}^{\pi}/_{4}$. Values of $\Delta_{\text{circularly polarised pump beam}} = -0.021$ and $\sigma = 0.045$ were assumed. The demarcation angle between the two regimes is 81.7°.

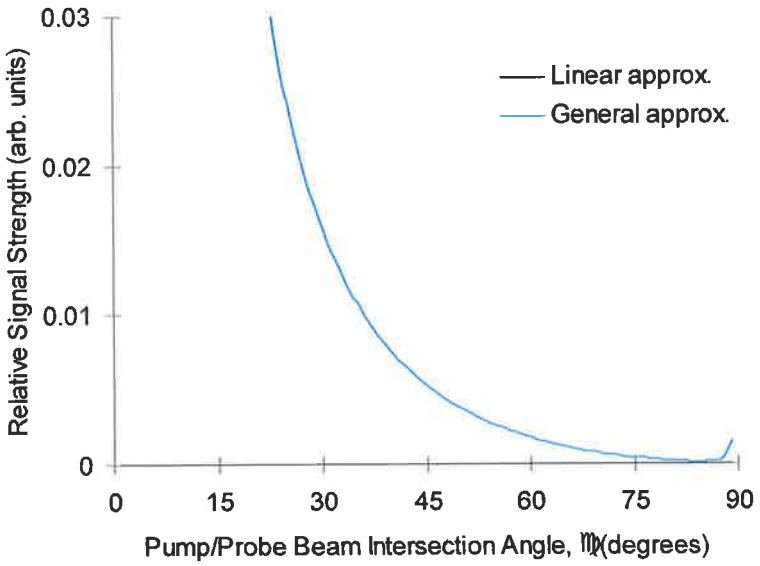

Figure 12: Calculated dependence of the two approximations representing the LPS signal for a circularly polarised pump beam (P(8)-pump/P(8)-probe transition) for a probe beam polarisation angle of $\gamma = {}^{\pi}/_{4}$. Values of $\Delta_{\text{circularly polarised pump beam}} = -0.0185$ and $\sigma = 0.0725$ were assumed. The demarcation angle between the two regimes is 82.2°.

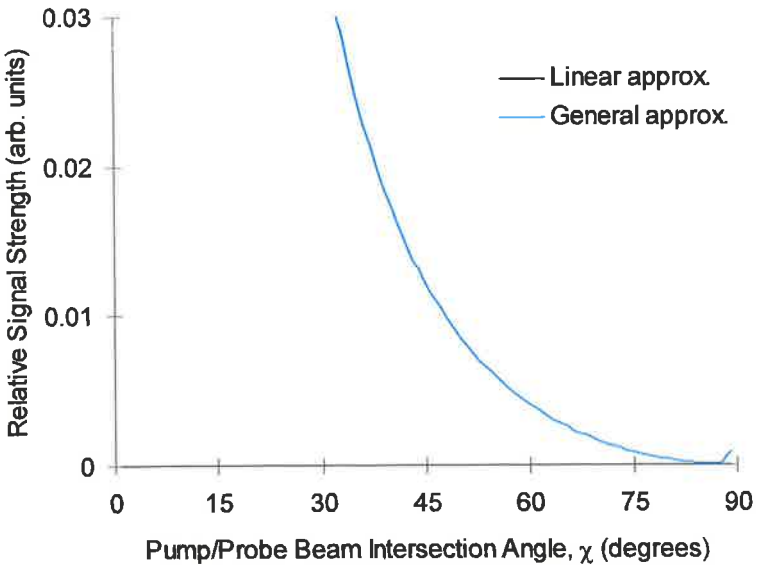

Figure 13: Calculated dependence of the two approximations representing the LPS signal for a circularly polarised pump beam (R(2)-pump/R(2)-probe transition) for a probe beam polarisation angle of $\gamma = {}^{\pi}/_{4}$. Values of $\Delta_{\text{circularly polarised pump beam}} = -0.00925$ and $\sigma = 0.11$ were assumed. The demarcation angle between the two regimes is 83.7°.

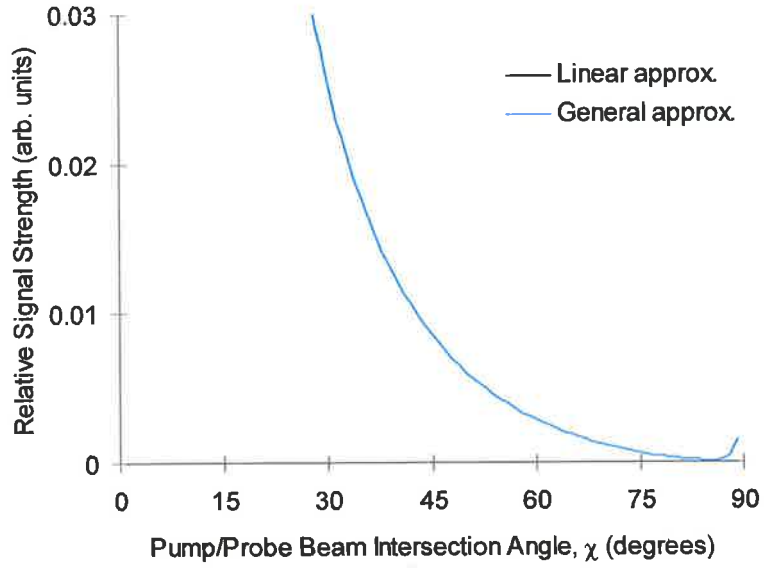

Figure 14: Calculated dependence of the two approximations representing the LPS signal for a circularly polarised pump beam (R(8)-pump/R(8)-probe transition) for a probe beam polarisation angle of $\gamma = {}^{\pi}/_{4}$. Values of $\Delta_{\text{circularly polarised pump beam}} = -0.0145$ and $\sigma = 0.0925$ were assumed. The demarcation angle between the two regimes is 83.1°.

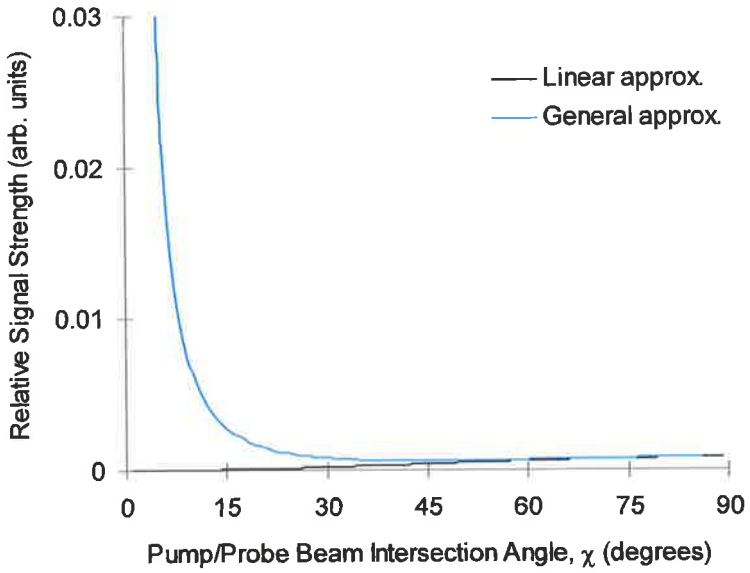

Figure 15: Calculated dependence of the two approximations representing the LPS signal for a circularly polarised pump beam (Q(2)-pump/Q(2)-probe transition) for a probe beam polarisation angle of $\gamma = {}^{\pi}/_{4}$. Values of $\Delta_{\text{circularly polarised pump beam}} = -0.0575$ and $\sigma = 0.014$ were assumed. The demarcation angle between the two regimes is 76.1°.

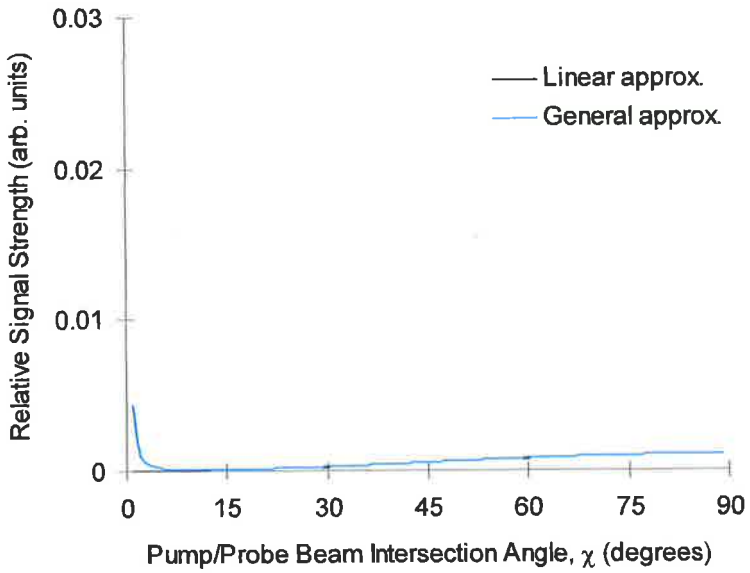

Figure 16: Calculated dependence of the two approximations representing the LPS signal for a circularly polarised pump beam (Q(8)-pump/Q(8)-probe transition) for a probe beam polarisation angle of $\gamma = {}^{\pi}/_{4}$. Values of $\Delta_{\text{circularly polarised pump beam}} = -0.065$ and $\sigma = 0.00115$ were assumed. The demarcation angle between the two regimes is 75.2°.

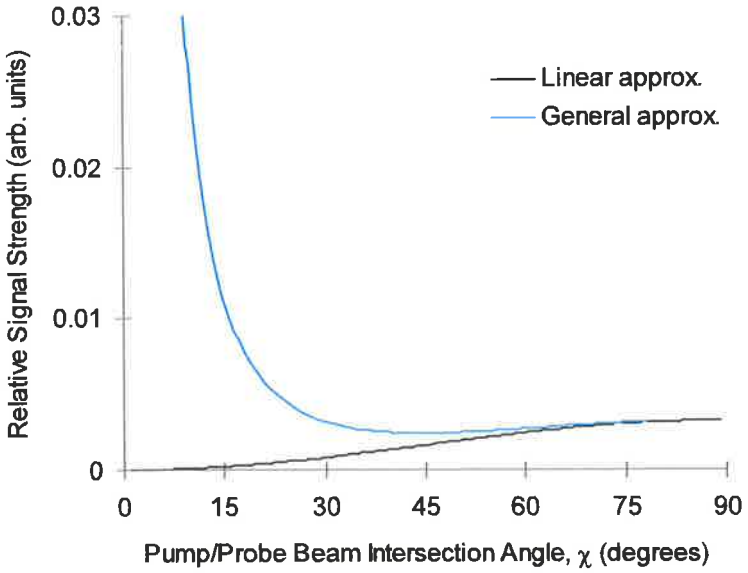

Figure 17: Calculated dependence of the two approximations representing the LPS signal for a circularly polarised pump beam (Q(2)-pump/Q(2)-probe transition) for a probe beam polarisation angle of $\gamma = {}^{\pi}/_{4}$. Values of $\Delta_{\text{circularly polarised pump}} = -0.0115$ and $\sigma = 0.028$ were assumed. The demarcation angle between the two regimes is 70.2°.

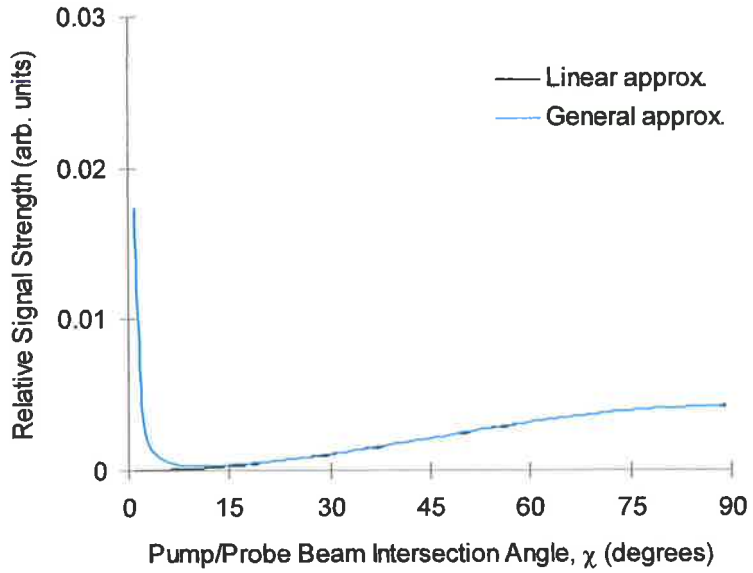

Figure 18: Calculated dependence of the two approximations representing the LPS signal for a circularly polarised pump beam (Q(8)-pump/Q(8)-probe transition) for a probe beam polarisation angle of $\gamma = {}^{\pi}/_{4}$. Values of $\Delta_{\text{circularly polarised pump beam}} = -0.13$ and $\sigma = 0.0023$ were assumed. The demarcation angle between the two regimes is 68.9°.

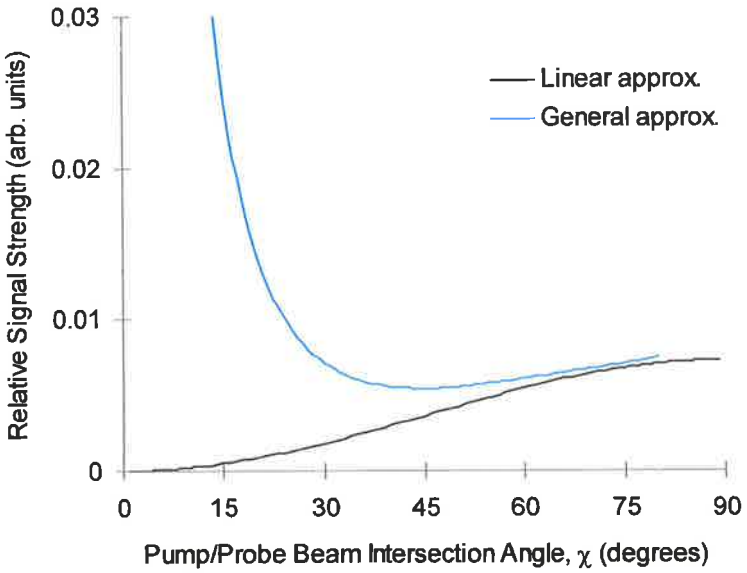

Figure 19: Calculated dependence of the two approximations representing the LPS signal for a circularly polarised pump beam (Q(2)-pump/Q(2)-probe transition) for a probe beam polarisation angle of $\gamma = {}^{\pi}/_{4}$. Values of $\Delta_{\text{circularly polarised pump}} = -0.1725$ and $\sigma = 0.042$ were assumed. The demarcation angle between the two regimes is 65.5°.

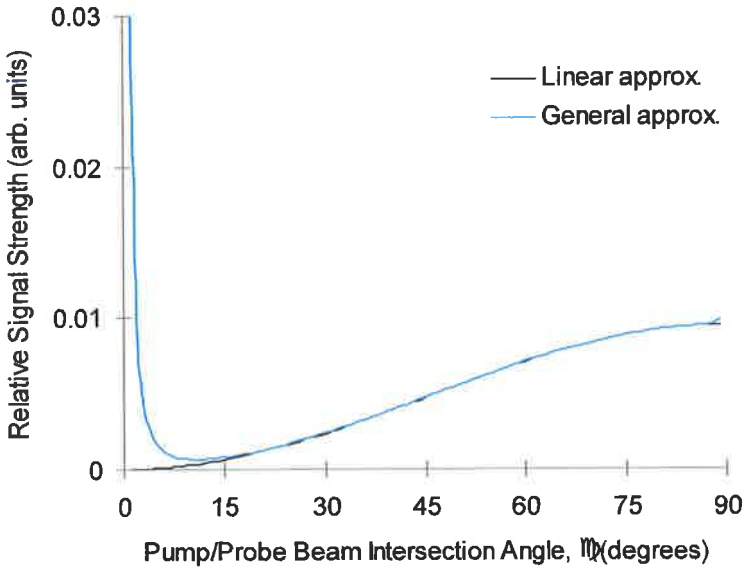

Figure 20: Calculated dependence of the two approximations representing the LPS signal for a circularly polarised pump beam (Q(8)-pump/Q(8)-probe transition) for a probe beam polarisation angle of $\gamma = {}^{\pi}/_{4}$. Values of $\Delta_{\text{circularly polarised pump beam}} = -0.195$ and $\sigma = 0.00345$ were assumed. The demarcation angle between the two regimes is 63.8°.

Strong (circular pump beam) induced linear birefringence is characteristic of Q-pump/Q-probe beam transitions, especially for large J. The dominance of the linear birefringence based contribution to the signal strength is a function of the relative strengths of the induced linear and induced circular birefringence terms for the selected transition.

Figures 22 and 23 show a series of Mode 1 and Mode 2 OH PLPS images taken for a circularly polarised pump beam for a range of beam intersection angles. Each image is a 50 shot average of the OH PLPS signal (for the $A^2\Sigma$–$X^2\Pi$ (0-0) $Q_2(8)$ transition) in a fuel/lean premixed natural gas/O_2 flame. Images for beam intersection angles of 20°, 30°, 45°, 55°, 60°, 70°, 80° and 90° are presented. In each case, the probe beam was left undisturbed and the pump beam redirected to intersect the probe beam at the required angle (See Figure 21).

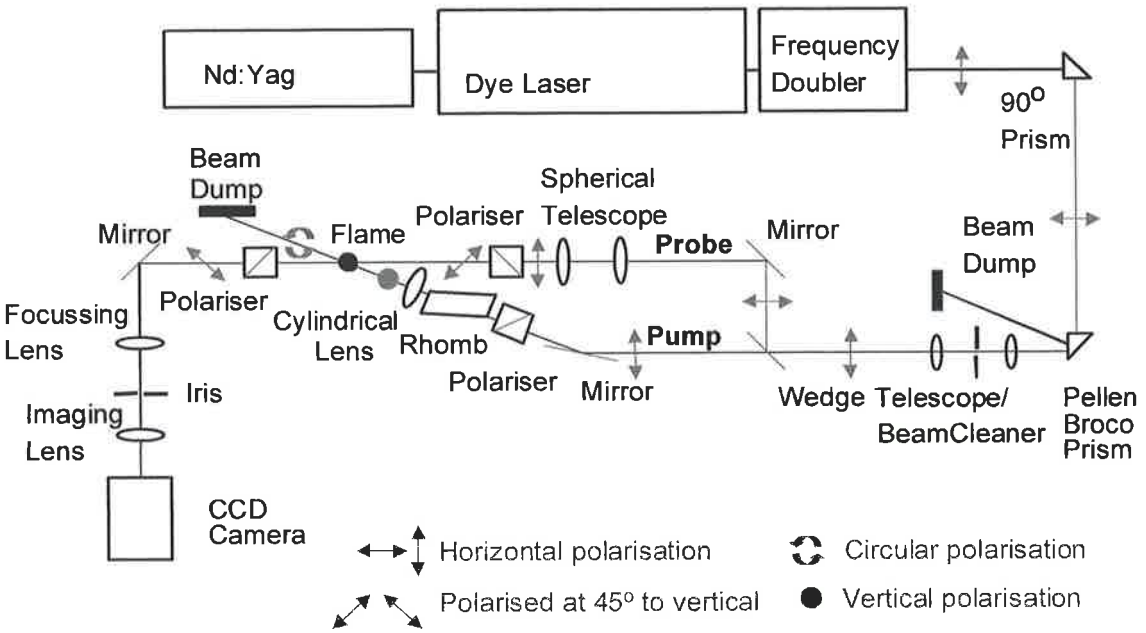

Figure 21: Experimental arrangement for polarisation spectroscopy imaging for a circularly polarised pump beam with variable beam intersection angle. The angle at which the pump beam intersects the probe beam can be varied by moving the pump beam redirection mirror (directly after the beamsplitting wedge in the pump beam path) parallel to the probe beam path and repositioning the mirror to reflect the pump beam through the flame, intersecting the probe beam. For the images in Figures 15 and 16, the pump beam was circularly polarised by a combination of a polariser (to ensure an initially polarised pump beam) and a ¼-wave Fresnel rhomb. The probe beam is polarised at $\pi/4$ to the vertical and the pump and probe beams intersect in the horizontal plane.

Figure 22 shows the Mode 1 images collected for the given beam intersection angle. Figure 23 shows the equivalent Mode 2 images. The images are interleaved so that corresponding Mode 1 (top of each page) and Mode 2 (base of each page) images are shown on the same page. This

allows the relative difficulty of probe beam correction with respect to the thermal gradient structures introduced by passage through the flame to be demonstrated for a range of beam intersection angles.

The images in Figures 22 and 23 are not stretched along the horizontal axis to represent the elliptical pump/probe beam interaction region, but are shown with the horizontal scale of the orthogonal images. This allows the effectiveness of the probe beam correction to be studied as a function of beam intersection angle. Note that any defects introduced by imperfect correction in regions of LPS signal will be emphasised in the stretched images. It is easy to note that a larger fraction of the image area where the LPS signal occurs will be influenced by overlapping thermal gradient features on the probe beam profile for small beam intersection angles. It is suggested that, when imaging with small beam intersection angles, greater care should be taken to minimise thermal gradient structures in the probe beam profile or, alternatively, to collect signal from probe beam regions where such features do not occur. The images in Figures 22 and 23 are plotted on a greyscale based on the 5 to 95% signal strength of each image with black representing the lowest signal.

The images in Figures 22 and 23 were obtained for a transition previously considered not favoured for the case of a circularly polarised pump beam. This strength of the LPS signal for the $A^2\Sigma$–$X^2\Pi$ (0-0) $Q_2(8)$ transition is due largely to an induced linear dichroism rather than the induced circular dichroism usually associated with a circularly polarised pump beam. It should be noted that the collected images are of high quality for the range of beam intersection angles investigated (20° to 90°) indicating that the induced linear dichroism, which is dominant for orthogonal beam intersection, is still significant for beam intersection angles as low as 20°.

Figures 22 and 23: (Pages following) A series of (50 shot average) OH PLPS images of the fuel-lean premixed natural gas flame for a circularly polarised pump beam for beam intersection angles of (a) 20°, (b) 30°, (c) 45°, (d) 55°, (e) 60°, (f) 70°, (g) 80° and (h) 90°. The probe beam is polarised at $\pi/4$ to the vertical. Figure 22 (top of each page) shows the Mode 1 image collected for each beam intersection angle. The corresponding Mode 2 image is shown in Figure 23 (at the base of each page) to demonstrate the relative difficulty of probe beam correction with respect to the thermal gradient structures as a function of beam intersection angle. The images are plotted on a greyscale based on the 5 to 95% signal strength of each image with black representing the lowest signal.

(Figures 22 and 23)

(a) 20° Beam Intersection Angle

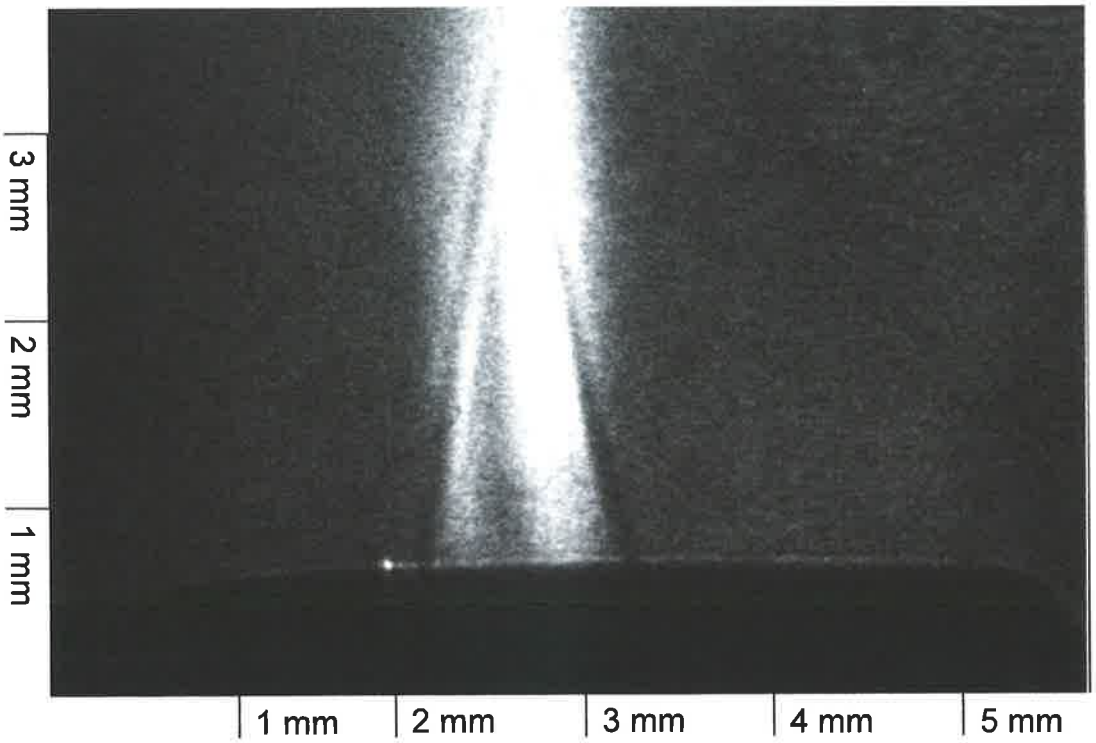

(Figure 22)

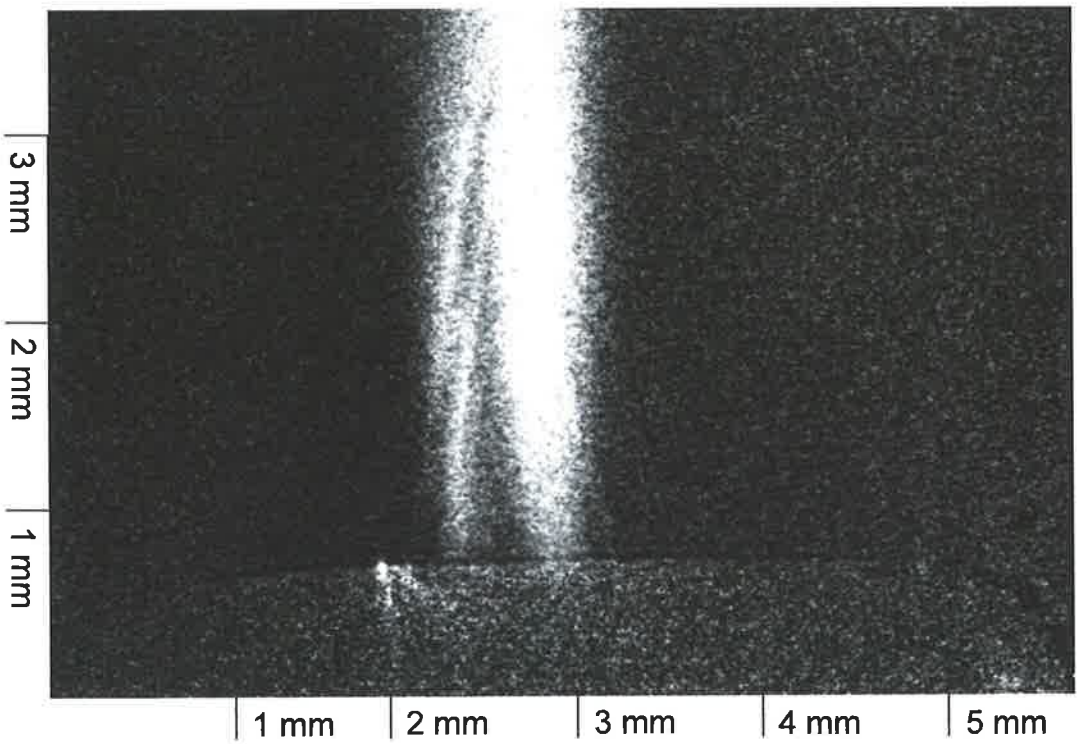

(Figure 23)

(Figures 22 and 23)

(b) 30° Beam Intersection Angle

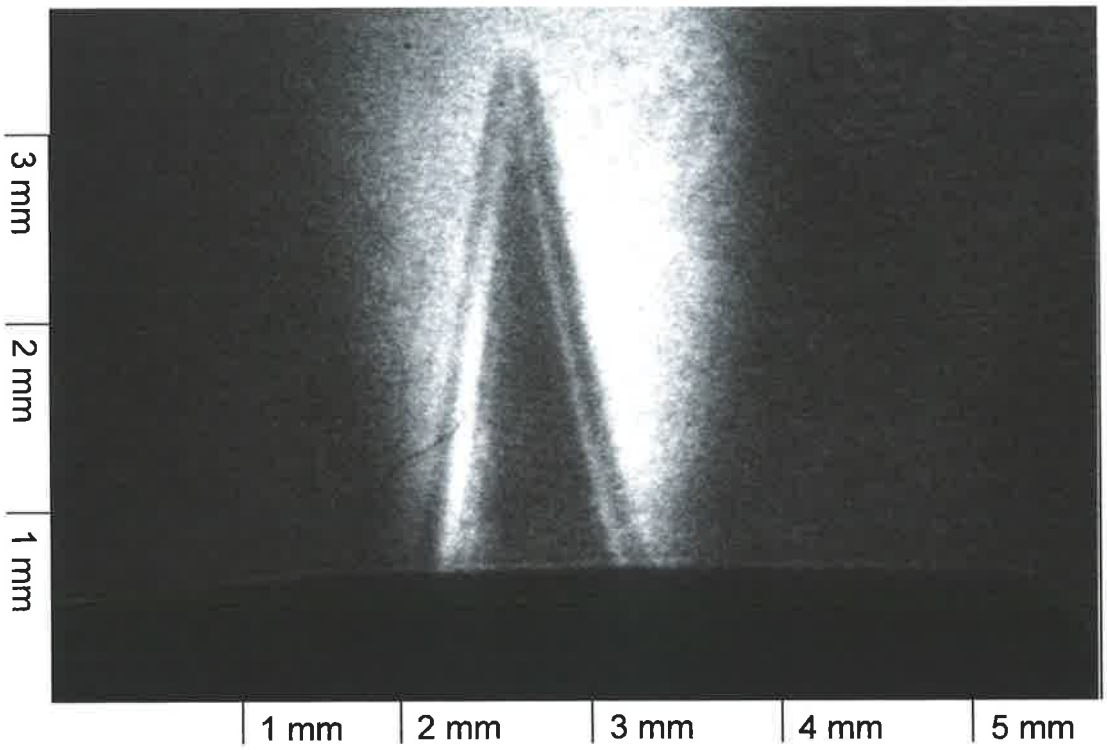

(Figure 22)

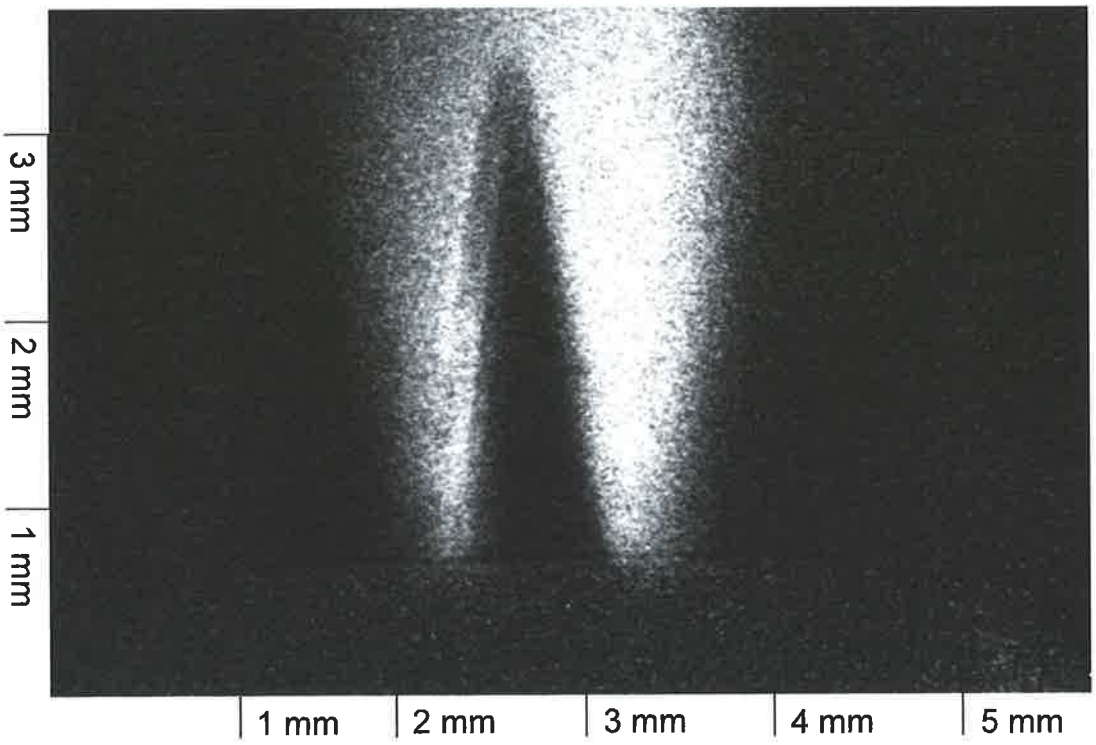

(Figure 23)

(Figures 22 and 23)

(c) 45° Beam Intersection Angle

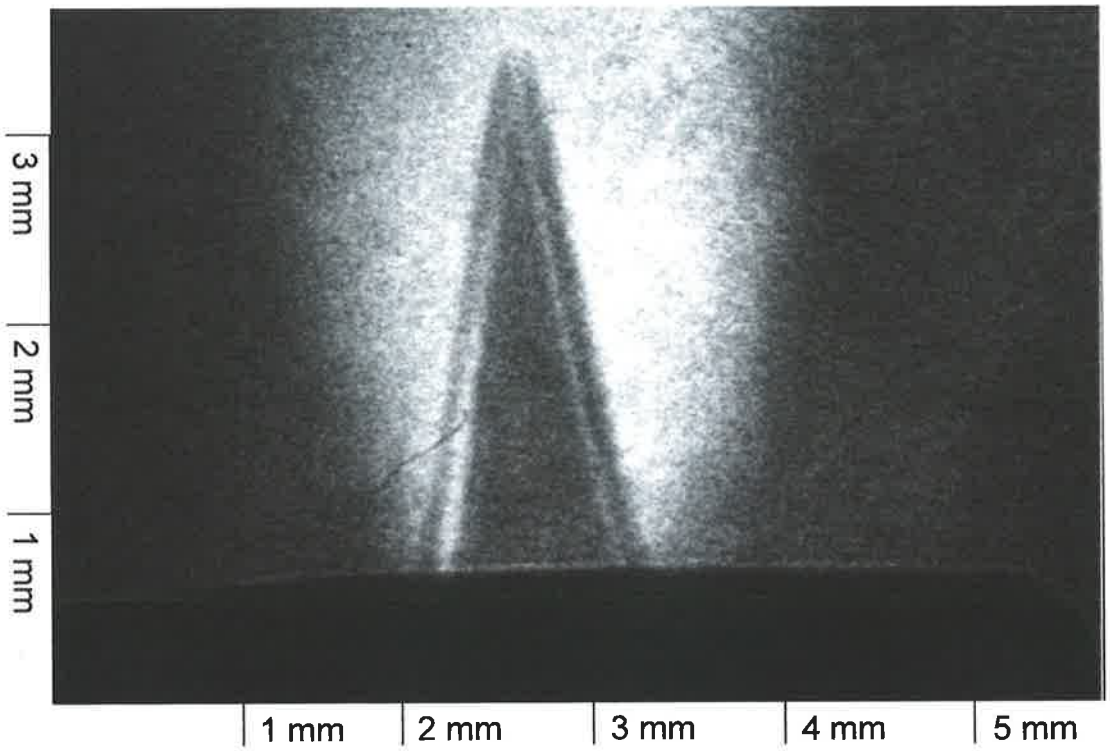

(Figure 22)

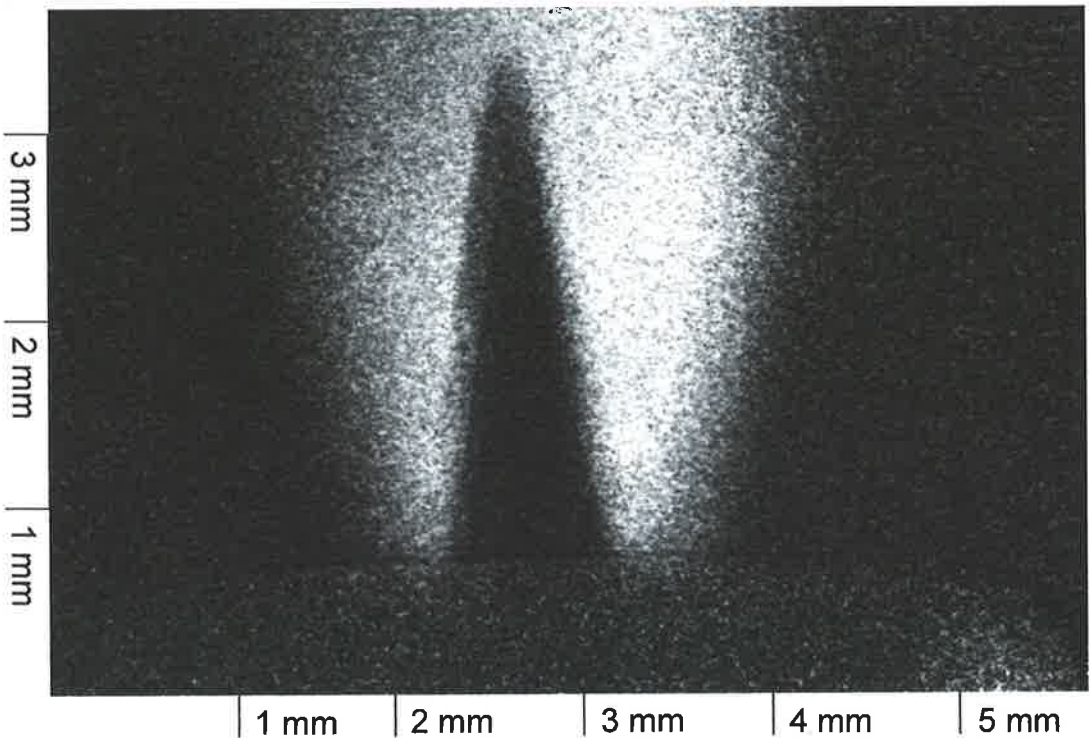

(Figure 23)

(Figures 22 and 23)

(d) 55° Beam Intersection Angle

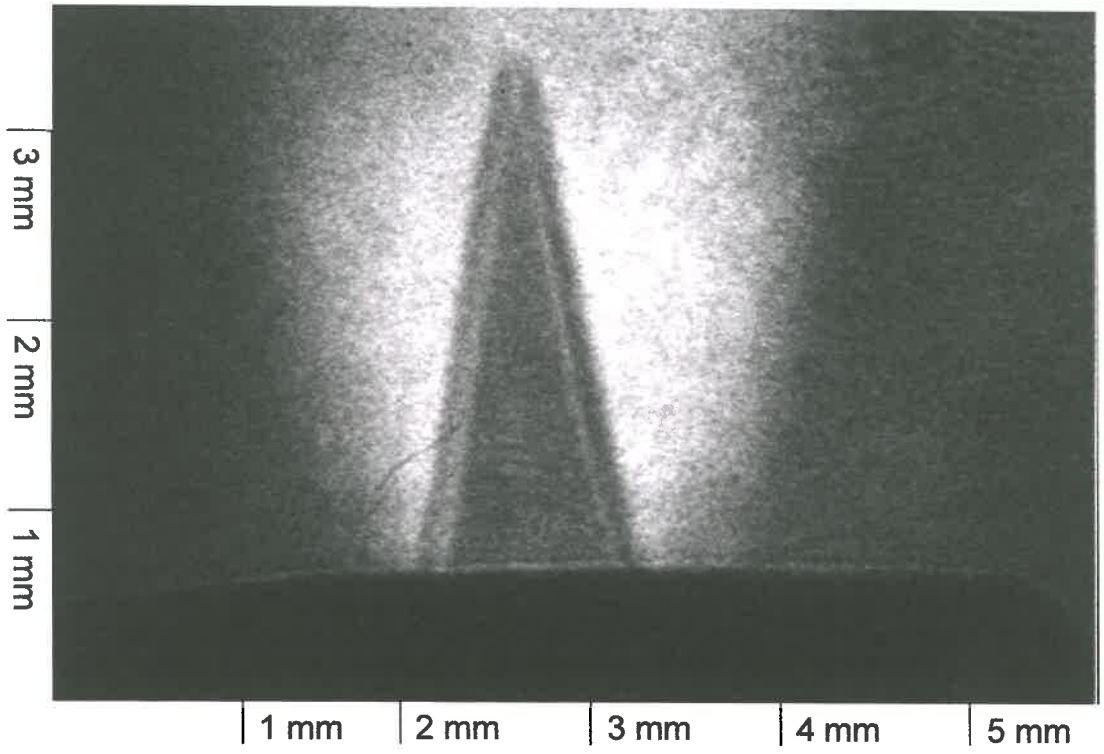

(Figure 22)

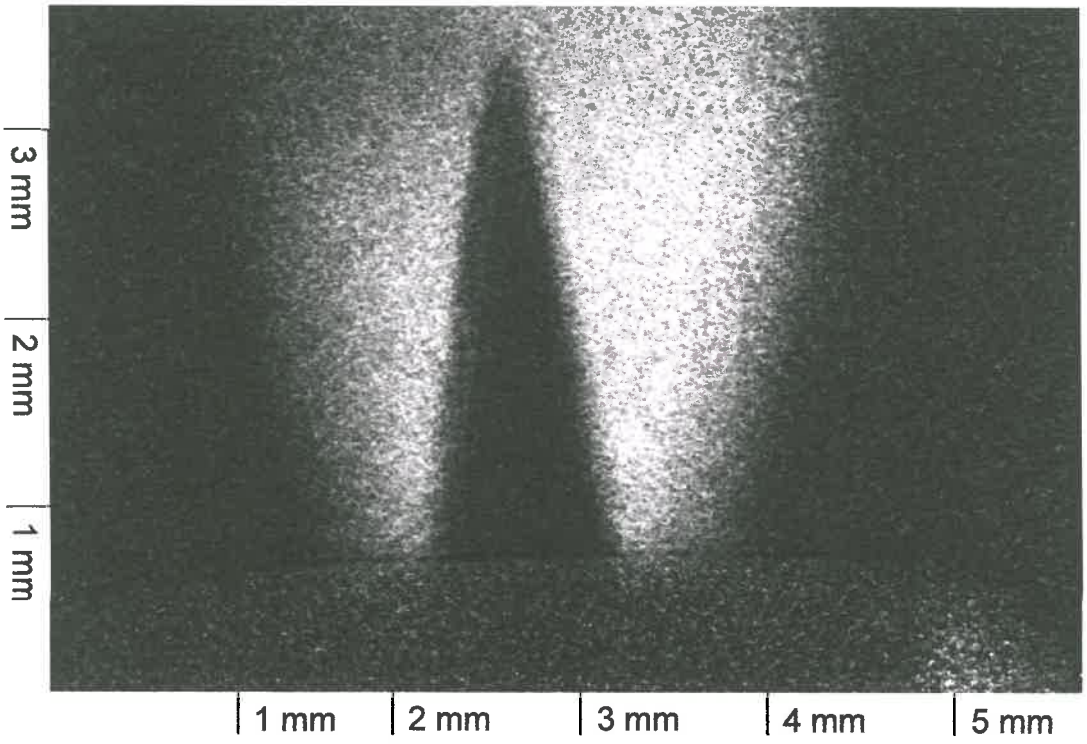

(Figure 23)

(Figures 22 and 23)

(e) 60° Beam Intersection Angle

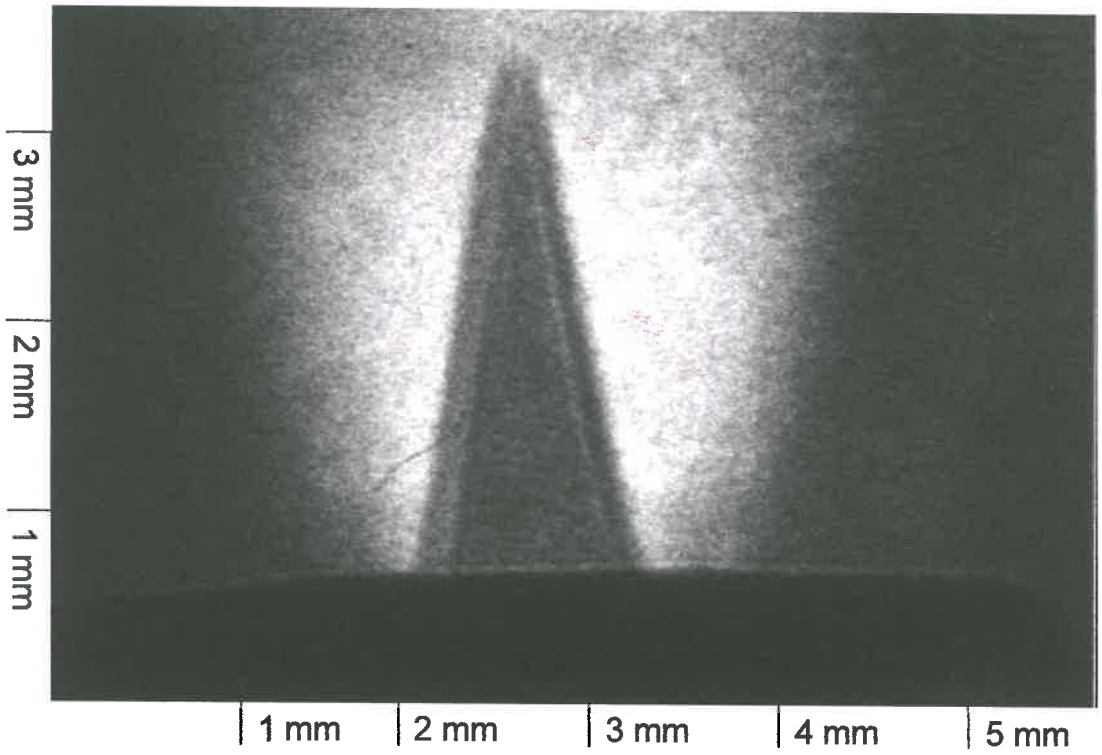

(Figure 22)

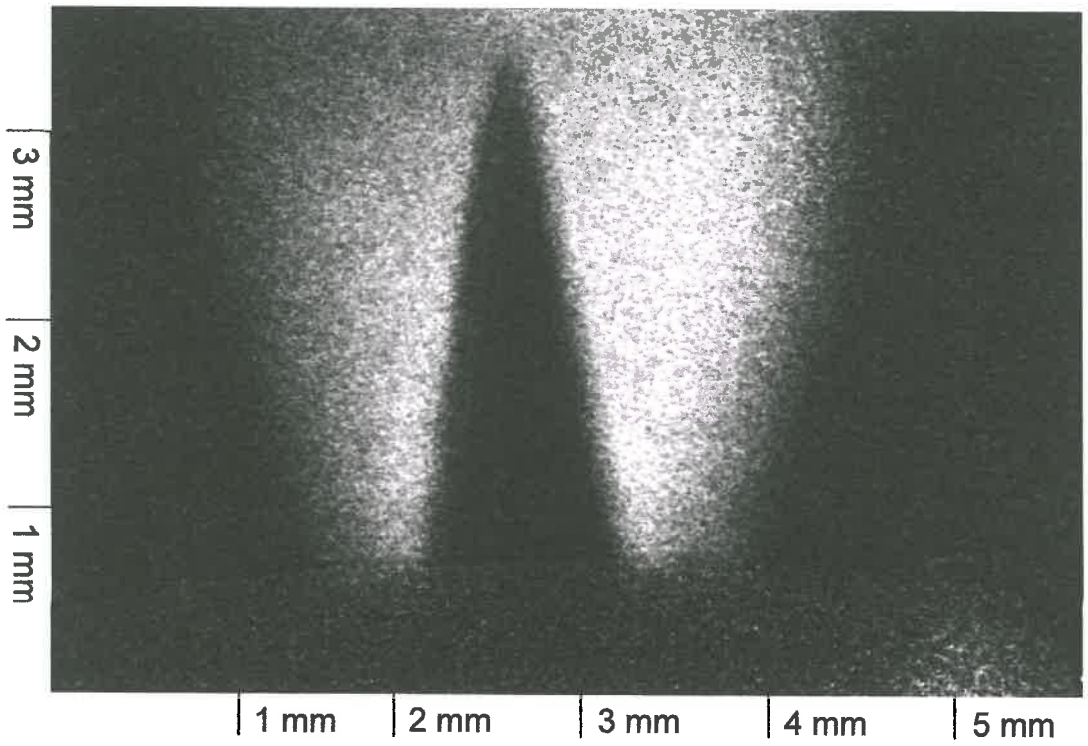

(Figure 23)

(Figures 22 and 23)

(f) 70° Beam Intersection Angle

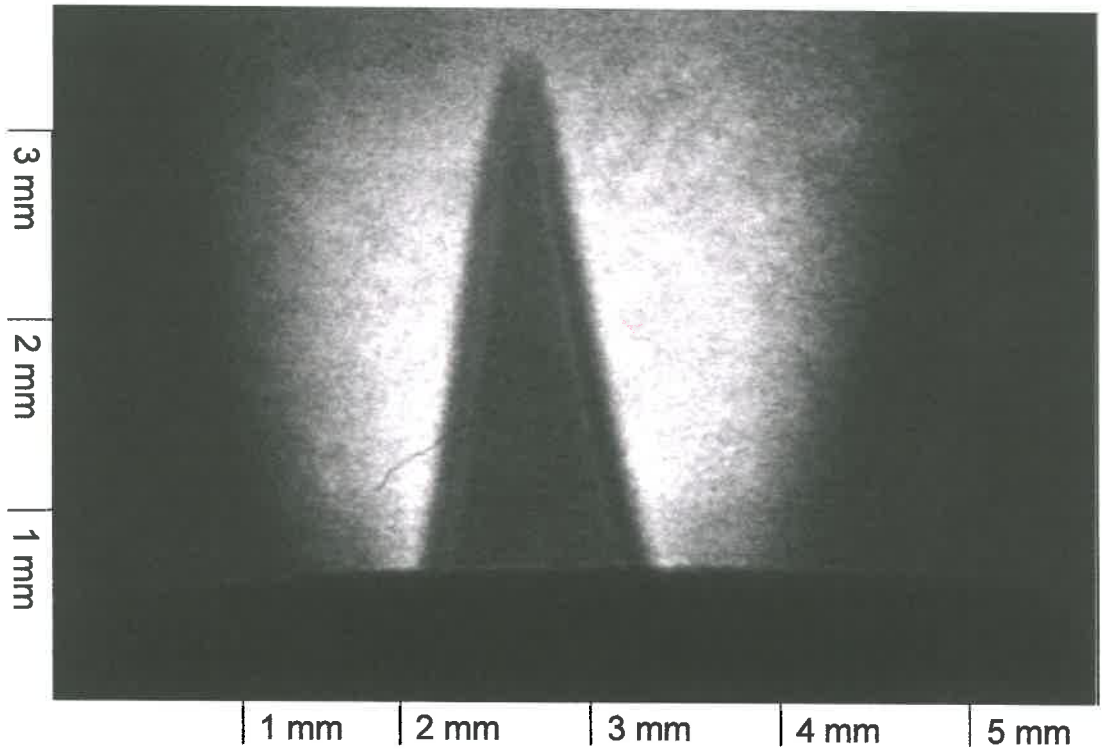

(Figure 22)

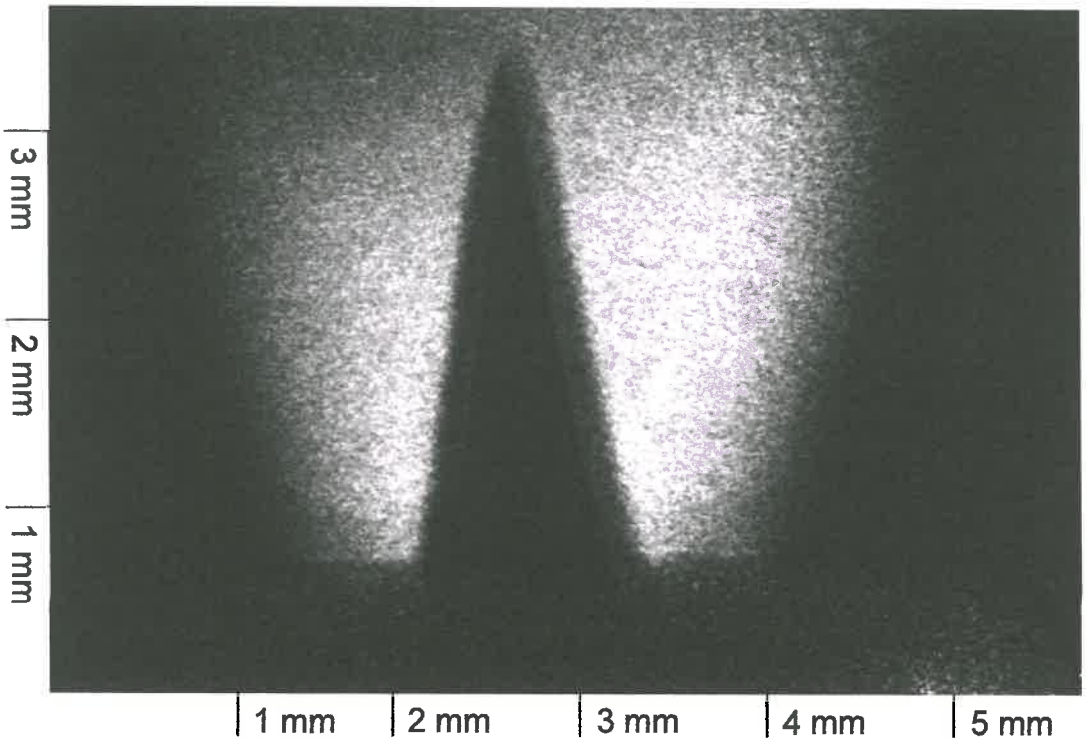

(Figure 23)

(Figures 22 and 23)

(g) 80° Beam Intersection Angle

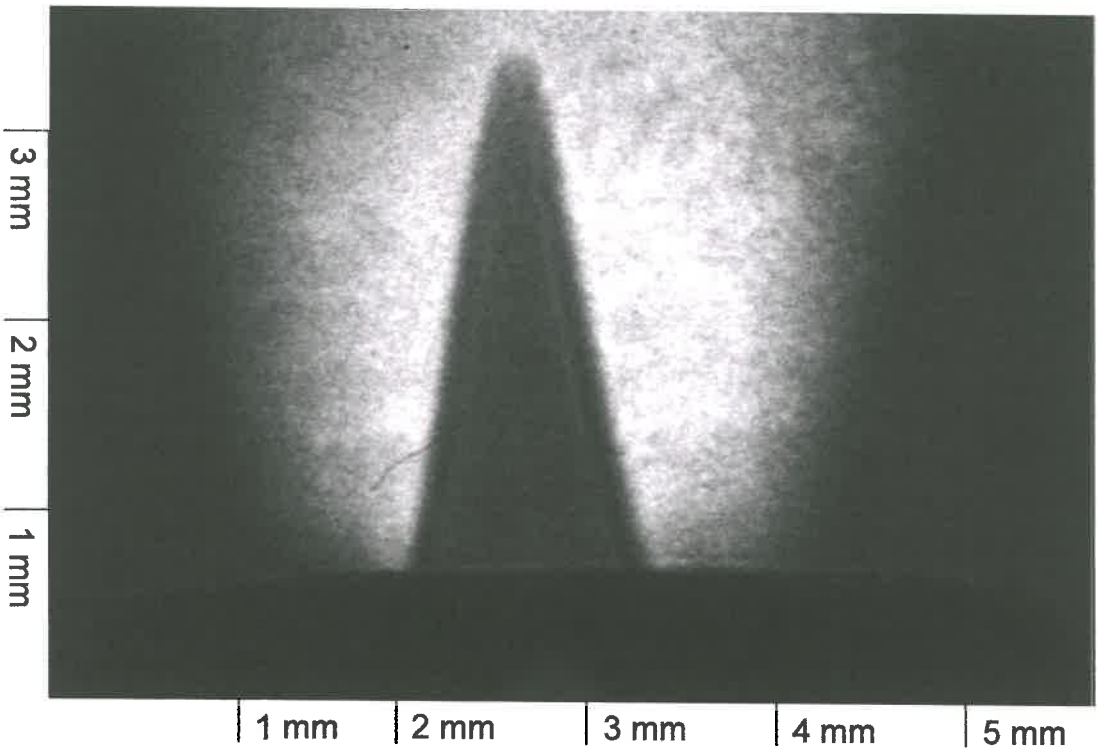

(Figure 22)

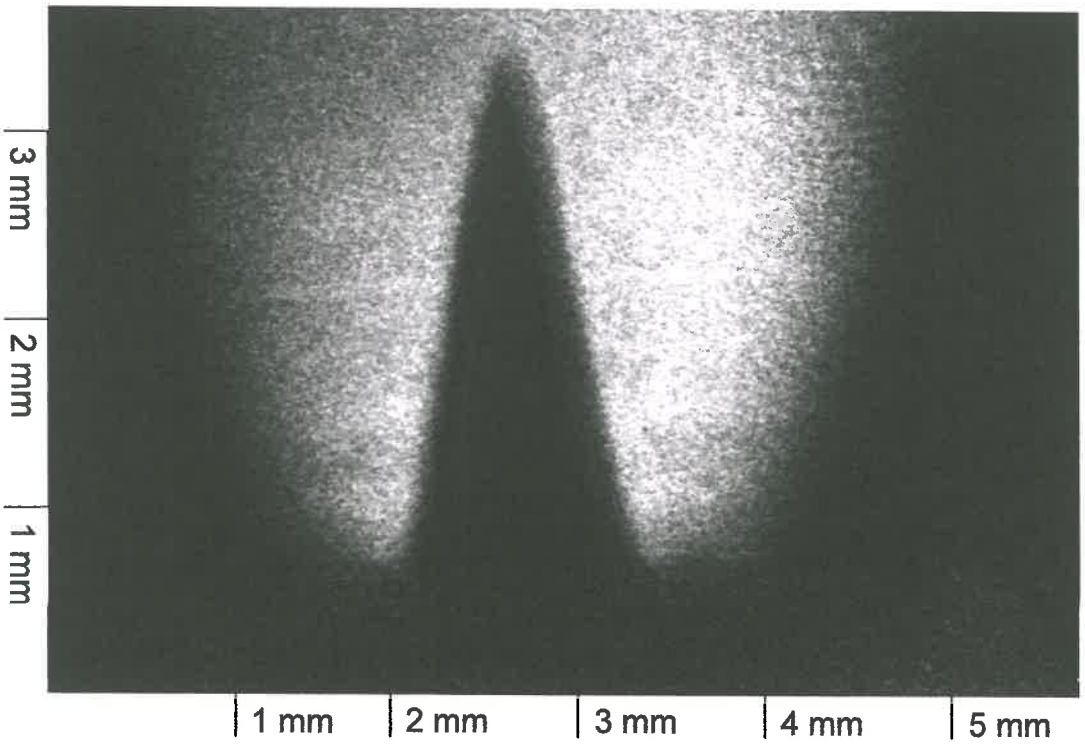

(Figure 23)

(Figures 22 and 23)

(h) 90° Beam Intersection Angle

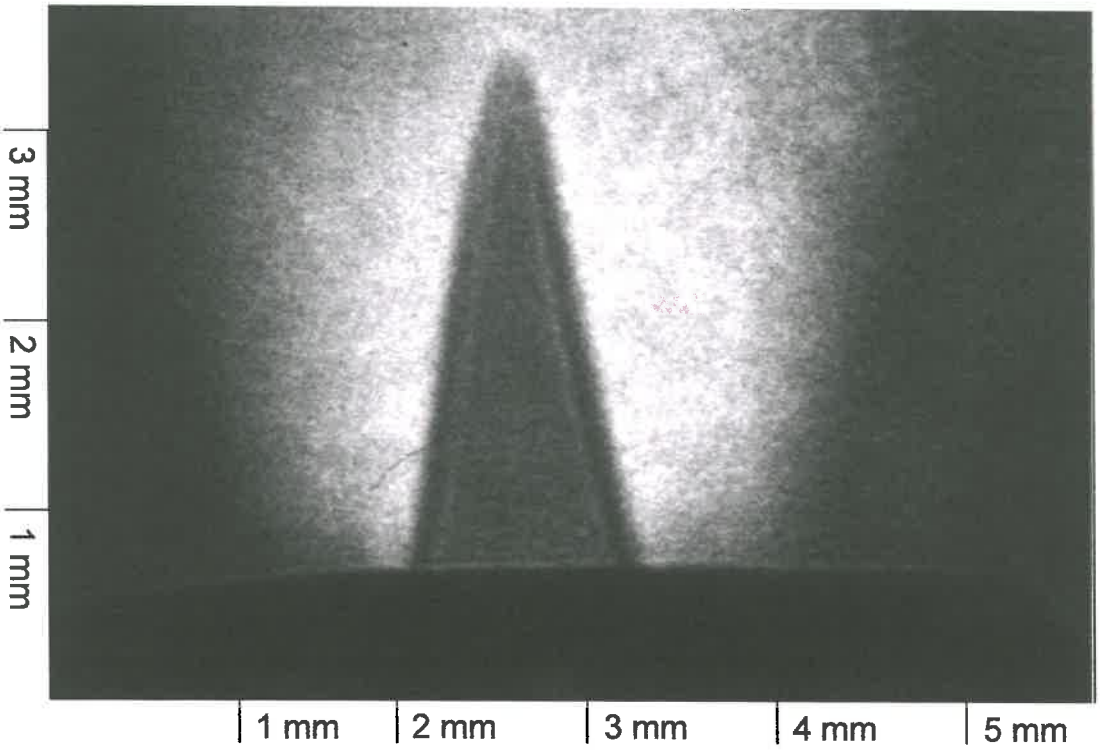

(Figure 22)

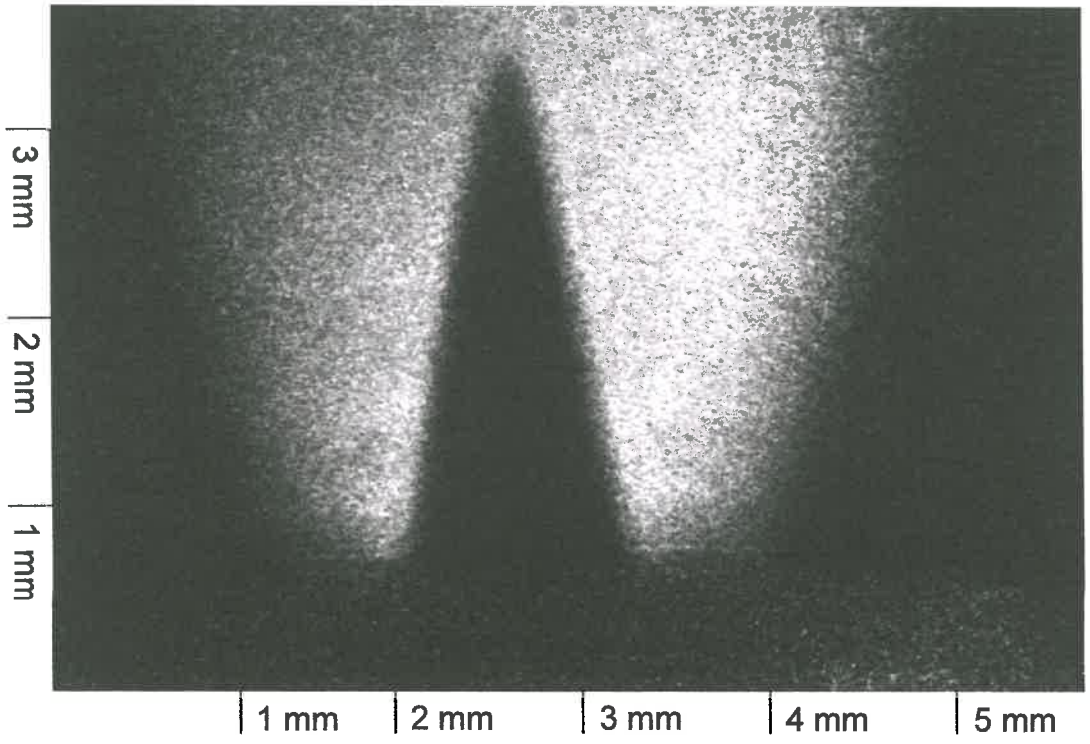

(Figure 23)

The experiment was not quantitative as the pump beam energy was not measured for each beam intersection angle, and would be expected to be a function of angle of reflection from the redirection mirror. However, the signal did not increase rapidly as the beam intersection angle decreased. The maximum OH PLPS signal was approximately 50 counts for orthogonal beam intersection and approximately 65 counts for 20° beam intersection. This suggests that the strong increase in LPS signal commonly associated with decreasing beam intersection angle does not occur for all J for a circularly polarised pump beam.

This result may be compared with the reported OH $A^2\Sigma$-$X^2\Pi$ (1,0) and NO $A^2\Sigma^+$-$X^2\Pi$ (0,0) spectra of Lofstedt and Alden[14] probing a premixed hydrogen/nitrous-oxide flame for a beam intersection angle of 10°. LPS excitation scans collected using linearly and circularly polarised pump beams showed the strong presence of non-favoured branches; NO $R_2(29.5)$ for the case of a linearly polarised pump beam and NO $Q_2(26.5)$ for the case of a circularly polarised pump beam. The authors ascribed the presence of these non-favoured transitions to the presence of minority polarisation types in the pump beam. The experiment was optimised for dual species (OH at 285 nm and NO at 226 nm) detection, requiring suboptimal alignment of the polarising[a] and lensing systems for each of the individual wavelengths. A polariser placed after a spherical lens produced the linearly polarised pump beam used to produce the spectra. The authors state that in the case of a circularly polarised pump beam, *"a single Fresnel rhomb was inserted immediately after the focussing lens"*. In this second case, it is possible that a polariser was not used to ensure the linearity of the beam polarisation entering the rhomb and the assignment of the spectroscopic behaviour to minority polarisation types may be valid. However, despite the slight wavelength dependence in the extinction behaviour of the polarisers it is unlikely that that the authors' explanation is valid in the case of the linearly polarised pump beam, where the pump beam polariser would be expected to produce a highly linearly polarised beam for both wavelengths.

The theory described in Chapter II predicts purely linearly induced dichroism induced by a linearly polarised pump beam. The standard theory of polarisation spectroscopy based on the calculation of the induced linear dichroism itself accounts the so-termed non-favoured branch in Lofstedt and Alden's spectra for the case of a linearly polarised pump beam. Table 4 in Chapter I lists the limiting values of the $\zeta_{J,J',J''}$ factors which are proportional to the induced linear birefringence as $J \rightarrow \infty$[b] for a linearly polarised pump beam. The ratio between the birefringence induced for R-pump/R-probe and Q-pump/Q-probe transitions in the linear regime and for large J is 1:4. This leads to a ratio of

[a] Lofstedt and Alden[14] noted that the extinction angle for the probe beam polarisers differed slightly between the two probed frequencies. The experiment was set with the extinction angle as a compromise between the two.

[b] Note that $\zeta_{J,J',J''}$ functions and corrected $\zeta_{J,J',J''}$ functions are largely independent of J for $J > 5$.

16 in relative signal strength for the transitions discussed. This factor does not account for the relative Boltzmann populations for the two transitions. In a hydrogen-nitrous oxide flame, temperatures are high enough to populate J levels up to 35. For Lofstedt and Alden's spectrum in the case of a linearly polarised pump beam, the NO $R_2(29.5)$ line is approximately half the intensity of the NO $Q_2(35.5)$ line. Given the quadratic dependence on species number density, the above ratio of induced birefringence and assuming pumping in the linear regime, this level of signal could be explained by a ratio of $\sqrt{8} \sim 2.8$ between the populations of the J = 29 and J = 35 states. Figure 24 shows the Boltzmann distributions[28] for the NO $X^2\Pi$ (v = 0) state assuming temperatures of 1400, 1700 and 2000 K. The ratios between the populations of the two states are 1.6, 1.5 and 1.3 respectively for each of these temperatures. Assuming no saturation in the experiment of Lofstedt and Alden and ignoring all collisional effects, the theory described in Chapter I in the limit as $J \rightarrow \infty$ in combination with the Boltzmann population fractions expected for a hydrogen/nitrous-oxide flame predicts the ratio of signal strengths for the NO $R_2(29.5)$ and $Q_2(35.5)$ lines to within a factor of four.

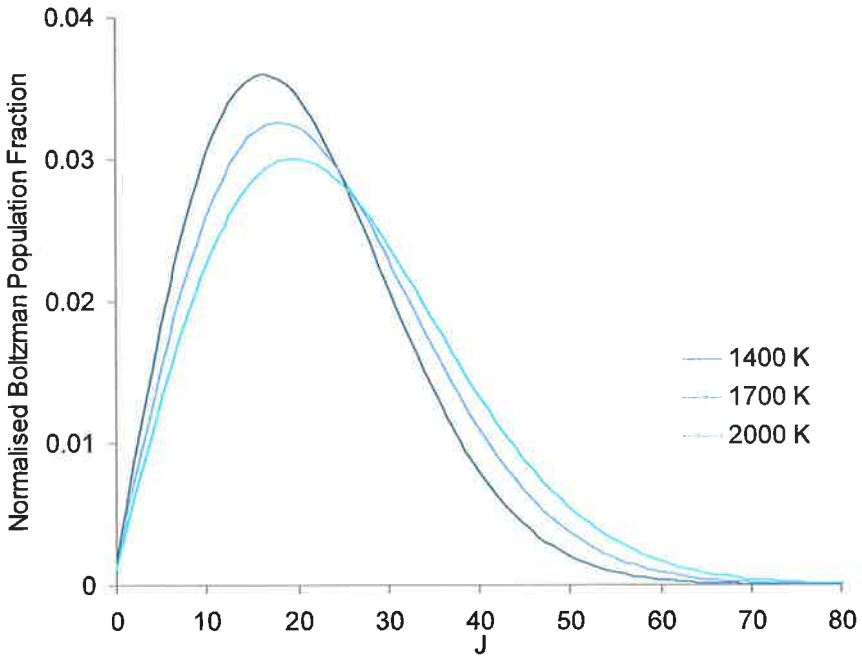

Figure 24: Boltzmann distributions of populations for the NO $X^2\Pi$ (v = 0) state assuming temperatures of 1400, 1700 and 2000 K. (B_{NO} = 1.705 cm-1[29])

However, it is more difficult to explain the non-favoured $Q_2(26.5)$ transition appearing in the LPS spectrum for a circularly polarised pump beam. The theory of Teets, Kowalski, Hill, Carlson and Hansch predicts a limit of zero LPS signal strength as $J \rightarrow \infty$ for Q-pump/Q-probe transitions in the case of a circularly polarised pump beam. Although the theory developed in Chapter II allows for an induced linear dichroism due to a circularly polarised pump beam, the contribution of this linear dichroism to the total signal is four orders of magnitude lower that that due to the induced circular

dichroism for a beam intersection angle of 10°. This implies that it is unlikely that a purely circularly polarised pump beam would produce an LPS NO spectrum with $R_2(20.5)$ and $Q_2(26.5)$ lines with signal strength ratio ~ 2:1. In this case, it must be assumed that the spectroscopic behaviour is due to a significant linearly polarised component in the pump beam due to the possible absence of a polariser before the rhomb used to create circular polarisation in the pump beam.

Chapters III and V demonstrate experimentally that planar laser polarisation spectroscopy is possible for perpendicular intersection of pump and probe beams for both linearly and circularly polarised pump beams. This supports the predictions of the theories developed in Chapters II and IV. The theory developed in Chapter IV shows that maximum orthogonal signal for a circularly polarised pump beam is obtained for a probe beam polarised at 45° to the plane of intersection of pump and probe beams.

It has also been shown in this chapter that the spectroscopic behaviour of the LPS strength for a circularly polarised pump beam is a function of beam intersection angle, dependent on dominance of either an induced linear or an induced circular dichroism due to the circularly polarised pump beam. A corollary of this is that the LPS signal dependence on beam intersection angle, χ, does not always demonstrate a rapid increase in signal strength as χ decreases from $\pi/2$. However, the LPS signal is always relatively high for near-collinear beam geometries ($\chi < 5°$).

Chapter VI: Near-Collinear Polarisation Spectroscopy Imaging in Combustion.

This chapter demonstrates the technique of near-collinear polarisation spectroscopy imaging developed by Nyholm, Fritzon and Alden[3]. The PLPS signal representing the OH distribution in a laminar premixed natural gas/O_2 flame is imaged for beam intersection angles of 30° and 15° for a horizontally polarised pump beam. The probe beam is polarised at π/4 to the vertical. The advantages and disadvantages of polarisation spectroscopy imaging in a near-collinear pump/probe beam geometry in combustion are noted in comparison with orthogonal polarisation spectroscopy imaging. The chapter includes a summary of the significant papers on polarisation spectroscopy imaging.

Planar Laser Polarisation Spectroscopy in Combustion

Laser polarisation spectroscopy was developed initially as a spectroscopic technique[1,2] due to the Doppler-free linewidth available for low-pressure experiments and counter-propagating pump and probe beams. The application of LPS to imaging, via the PLPS technique, has been limited to a relatively small number of experiments

1. Nyholm, K., Fritzon, R. and Alden, M., *"Two-dimensional imaging of OH in flames by use of polarization spectroscopy"* (1993)[3].
2. Nyholm, Fritzon, and Alden, *"Single-pulse two-dimensional temperature imaging in flames by degenerate four-wave mixing and polarisation spectroscopy"* (1994)[13].
3. Lofstedt, Fritzon and Alden, *"Investigation of NO detection in flames by the use of polarization spectroscopy"* (1996)[30].
4. Lofstedt and Alden, *"Simultaneous detection of OH and NO in a flame using polarization spectroscopy"* (1996)[15].
5. Reppel and Alwahabi, *"Orthogonal Planar Laser Polarization Spectroscopy"* (2002)[31].

Nyholm, Fritzon and Alden demonstrated the first PLPS imaging, presenting two-dimensional images of the OH radical distribution in a CH_4/O_2 flame for the (near-collinear) beam intersection angles of 15° and 30°. The output of a Nd:YAG/dye laser system was doubled to probe the $A^2\Sigma$-

$X^2\Pi$ (0-0) $Q_1(9)$ transition of OH. Images were presented for flames with fuel equivalence ratios of 0.5 and 2.0 as well as a pure diffusion flame.

After a preliminary investigation of OH LPS signal strength[12] in combustion (*"Detection of OH in flames by using polarization spectroscopy", Nyholm, Maier, Aminoff and Kaivola, 1993*[a]), Nyholm Fritzon and Alden extended the 1-D polarisation spectroscopy technique to 2-D PLPS imaging. The horizontally polarised pump laser beam was formed into a thin laser sheet using a cylindrical lens. The linearly polarised probe beam (polarised at 45° to the pump polarisation direction) was allowed to intersect the pump sheet as an unfocussed beam.

The probe beam was expanded and spatially filtered to obtain a near flat-top profile. The 0.5 mJ pump beam was focussed into a premixed CH_4/O_2 flame by a f = 600 mm cylindrical lens. The pump sheet height at the flame was 5 mm and the beam thickness was <200 μm. The laser linewidth was 0.1 cm^{-1} and the pulse length was ~ 10 ns. Based on these numbers, the pump sheet irradiance was ~ 5 x 10^6 W/cm^2. The saturation regime in which the images were taken was not stated by Nyholm *et al.*

The probe beam was imaged onto a Princeton Instruments (576S) ICCD camera by a f = 150 mm lens after passing through crossed polarisers with extinction ration < 10^{-5}. An aperture was placed at the lens focus and the beam was allowed to expand before reaching the ICCD. A UG11 coloured glass filter was used to minimise non-resonant contributions to the detected probe beam background.

Nyholm, Fritzon and Alden presented four single-pulse 2-D images of the OH polarisation spectroscopy signal for a premixed CH_4/O_2 flame with 2 mm nozzle diameter

- for an equivalence ratio of ϕ = 0.5 at a beam crossing angle of 15° (maximum signal 8000 counts)
- for a pure methane diffusion flame at a beam crossing angle of 15° (maximum signal 600 counts)
- for an equivalence ratio of ϕ = 0.5 at a beam crossing angle of 30° (maximum signal 3000 counts)
- for an equivalence ratio of ϕ ~ 2 at a beam crossing angle of 30° (maximum signal 600 counts).

[a] Saturation curves presented by Nyholm, Maier, Aminoff and Kaivola[12] indicated clear saturation of the OH LPS signal collected for an (assumed since it is not clear in the paper's text) acetylene/air flame for pump intensities of 10^5 W/cm^2 (for a UV linewidth of 0.24 cm^{-1}).

The images were uncorrected with a background count level of less than 20 counts. Allowing for the foreshortening of the images in the plane of intersection of the pump and probe beams, the images show the characteristic OH distribution for premixed (broad regions of OH indicating combustion) and diffusion flames (thin OH structures at the flame edge controlled by the diffusion rate of air into the central fuel core). The images also indicate the proportionality of the signal to the intensity of the probe beam leading to a modulation of the signal component of the image by the probe beam profile. The single-shot images show evidence of interference fringes (possibly due to the beamsplitter used to form the pump and probe beams) and a faint diffraction edge on the circular probe beam profile (possibly due to the aperture creating the flat-top probe profile). However, the OH structures are clearly defined and there is no evidence of thermal beam-steering features due to passage of the probe beam through the flame. The authors also noted that *"Experiments in sooting flames (in diffuse methane and propane flames) showed no disturbing signal from polyaromatic hydrocarbons in polarization spectroscopy in contrast to laser-induced fluorescence measurements."*[3]

Nyholm, Fritzon and Alden determined a $\cot^2(\chi)$ dependence of LPS signal strength on beam intersection angle for the case of a horizontally polarised pump beam (which was discussed in Chapter III). Based on the signal levels in the collected images, Nyholm, Fritzon and Alden then predicted signal to background ratios of greater than 1000:1 could be obtained for small beam intersection angles.

The authors noted that the rotational temperature maps could be obtained from two images taken for different rotational lines for conditions of no saturation using the theory of Teets, Kowalski, Hill, Carlson and Hansch[1]. Nyholm *et al.* calculated a temperature map for the premixed CH_4/O_2 flame from 10 shot average images for the transitions, $Q_1(2)$ and $Q_1(9)$ for a beam intersection angle of 30°. The temperature scale on the images ranges from 2000-3500K, and an average temperature for the flame was estimated to be 2950K. The adiabatic temperature for a stoichiometric CH_4/O_2 flame is 3054 K [b].

The temperature map shows an improvement in image quality due to image averaging and reduction in probe beam profile modulation as a result of taking the ratio of the two images. Interference fringes are still seen, but the temperature map is much more uniform with respect to signal continuity than the single shot images. No statement of saturation regime is made for the temperature map presented. However, the general theory of Teets *et al.* which was used to calculate the temperature map allows the same rotational number dependence for Q transitions in the saturated and linear regime of optical pumping.

[b] Calculated by *"Gaseq: Chemical equilibria for perfect gases"*, Version 0.63, Chris Morley, c.morley@ukgateway.net.

Nyholm, Fritzon and Alden suggested, in conclusion, investigation of *"pressure effects on lineshapes, on collisional relaxation, and on signal strength"*, adding, *"Preliminary spectral measurements on the $A^2\Sigma$-$X^2\Pi$ (0,0) band of OH in flames at atmospheric pressures show low rotational-number dependence of the collisional depolarization rates."*[3]

Nyholm, Fritzon and Alden increased the level of complexity of experimental arrangement in their next paper which compares the imaging capabilities of two coherent techniques, *degenerate four-wave mixing* (DFWM) and *laser polarisation spectroscopy* (LPS), in combustion.

Both techniques are based on the intersection of a thin laser sheet and a cylindrical probe beam to image the elliptical intersection region of both beams. In polarisation spectroscopy, a single pump beam intersects a probe beam, the signal being the polarisation change induced in the probe beam. In DFWM (as applied in Nyholm, Fritzon and Alden's paper), counter-propagating (and spatially overlapping) pump beams (in a phase-conjugate geometry) intersect the probe beam resulting in the generation of a fourth beam counter-propagating with respect to the probe beam.

The aim of the experiment was single-pulse 2-D temperature measurement in a premixed propane/oxygen flame produced by a burner similar to a welding torch. A Nd:YAG pumped dual-wavelength dye laser system was used to allow simultaneous collection of OH $A^2\Sigma$-$X^2\Pi$ (0-0) signal for two rotational transitions, $Q_1(2)$ and $Q_1(9)$ at 308.084 and 309.623 nm respectively. The UV wavelengths were produced by two KDP crystals in series in the beam path, each tuned to one of the dual-wavelength dye laser outputs. The resultant UV beams had pulse durations of ~ 10 ns and bandwidths of 0.1 cm^{-1}. The two UV beams followed the same beam paths throughout the experiment before separation of the two wavelength components by a diffraction grating (600 lines per mm, blaze 2.5 μm) prior to imaging. A coloured glass filter was placed in front of the CCD camera to minimise incoherent light in the collected image in the case of the polarisation spectroscopy experiment.

The arrangement of the polarisation spectroscopy experiment is shown in Figure 1. The probe beam profile was near top-hat as only the central 5 mm of the expanded beam width was used and the pulse intensities were determined from the non-signal regions of the probe beam imaged on the detector after passing through the crossed polarisers (extinction ratio quoted as 10^{-5}). The pump beam was horizontally polarised. The pump/probe beam intersection angle was not specified. The pump beam energy was ~ 1.5 mJ and the probe beam approximately ~ 4 μJ. The pump sheet was ~ 5 mm high and < 0.2 mm thick. This corresponds to a pump beam irradiance of 150 x 10^5 W/cm^2. The authors noted that the LPS images were obtained were in the unsaturated regime of optical pumping.

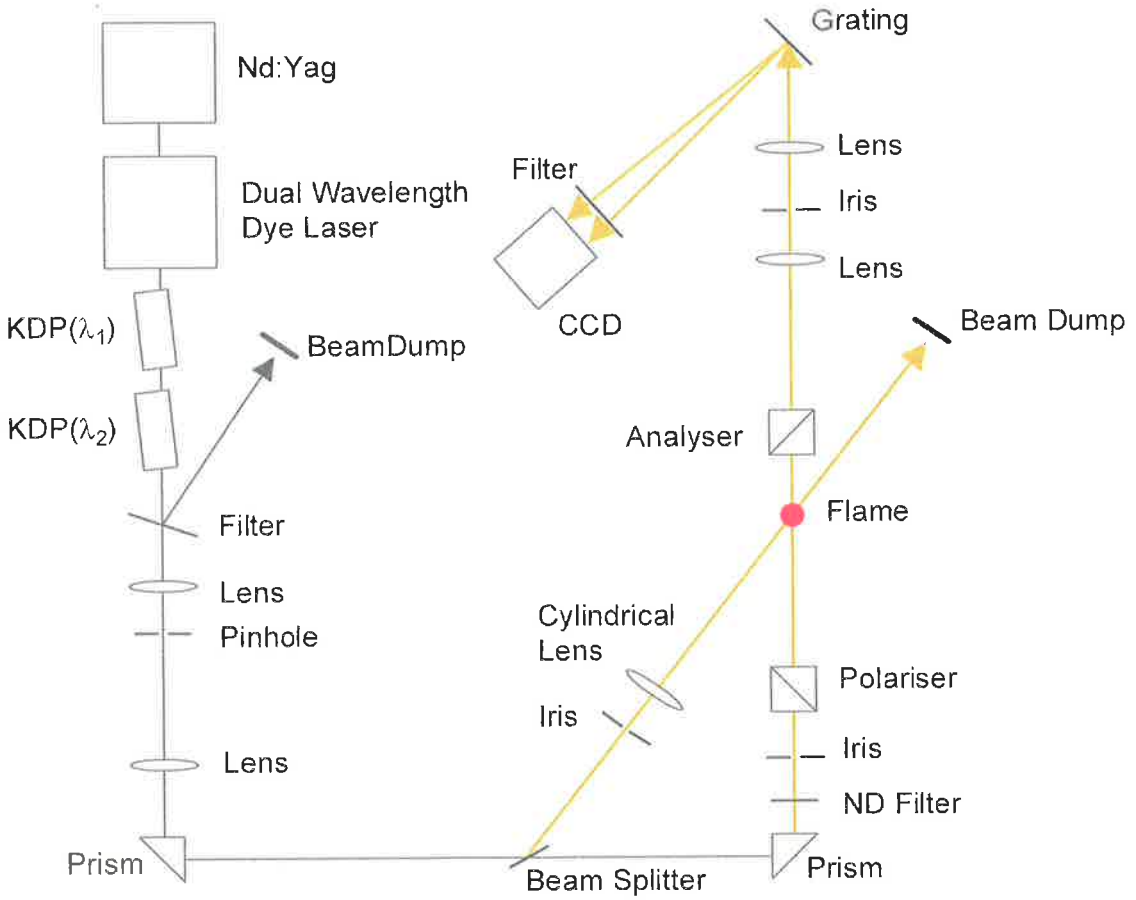

Figure 1: Experimental arrangement for the dual wavelength polarisation spectroscopy temperature mapping of Nyholm, Fritzon and Alden[13].

The DFWM experiment geometry was more complex and is shown in Figure 2. The two UV beams (~ 5 mJ) were split into pump and probe beams using a primary 50/50 beamsplitter. A secondary beamsplitter was used to further split each of the probe beams into a transmitted and a reflected component. The reflected probe beam components were directed to intersect the pump sheets at approximately a 15° angle.

Before passing through the flame, the probe beam was focussed through a 0.2 mm pinhole by a f = 500 mm spherical lens and diverged towards the flame after reflection from the secondary 50/50 beamsplitter. The counterpropagating signal beam converged back through the second beamsplitter to an iris placed at the equivalent focal plane of this beam before expanding to a second (collimating) spherical lens (f ~ 1000 mm). This lens was placed so as to image the flame directly on the CCD camera. The images due to the two rotational transitions were separated using the diffraction grating and imaged on the same CCD chip. Care was taken in collimation in order to minimise distortion of the image by the grating. [It is interesting to note that a collimating imaging

system, when trialled in the experiments reported in this thesis, demonstrated the greatest susceptibility to beam steering features in the collected image due to transmission of the probe beam through a flame.]

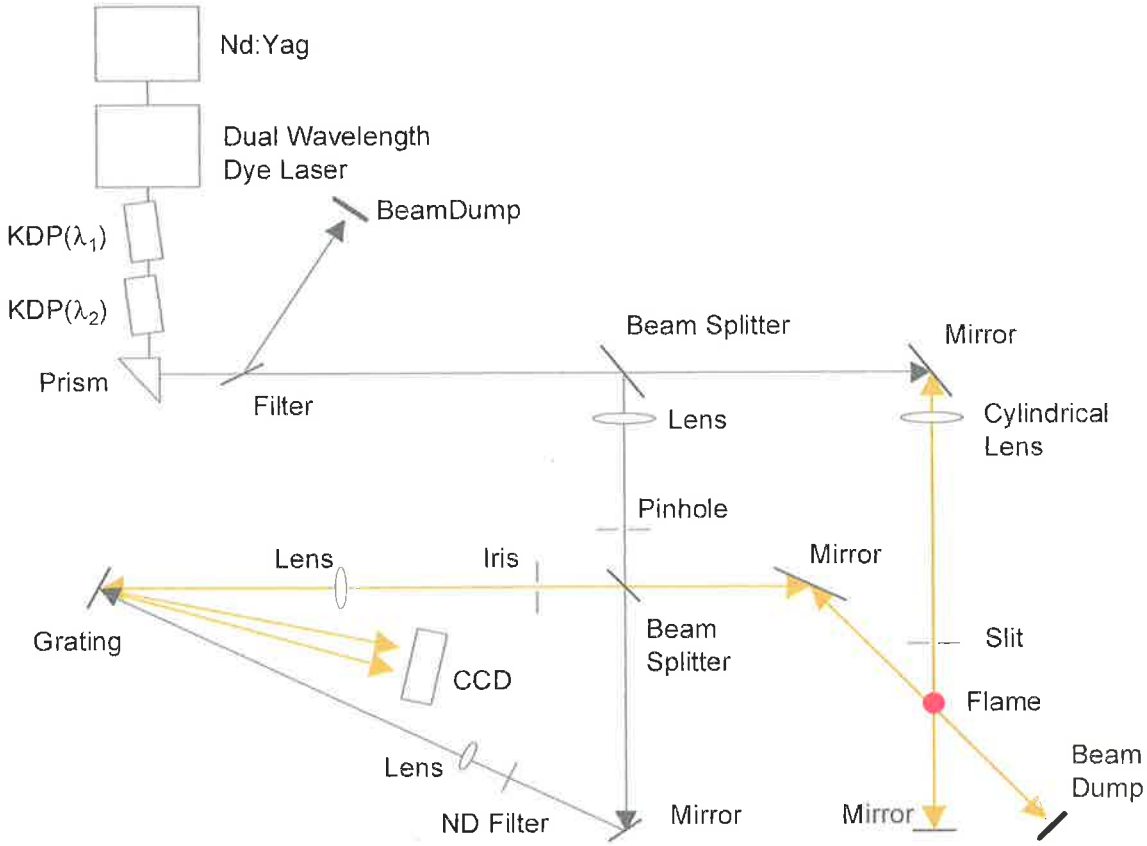

Figure 2: Experimental arrangement for the dual wavelength DFWM temperature mapping of Nyholm, Fritzon and Alden[13].

The two wavelength fractions of the probe beam which were transmitted through the secondary beamsplitter were collimated (f = 1000 mm lens) and directed to the diffraction grating and, at a different diffraction order, were imaged on the CCD chip (creating four images). This allowed shot-to-shot correction for the probe beam profile for the DFWM experiment assuming that transmission through the flame introduces no distortion of the probe beam profile.

The flame used in Nyholm, Fritzon and Alden's experiment was a very thin (~ 5 mm) lean propane/oxygen premixed flame produced by a welding torch (orifice diameter 2 mm). Oxidiser rich flames studied in this thesis produced beamsteering structures in the pre-analyser probe beam profile, an effect which reduced as the fuel/oxidiser ratio increased, however, such structures have not been reported by Nyholm, Fritzon and Alden[3,13]. The lack of these features may be due to unreported imaging strategies or the slightly larger burner orifice diameters for these papers.

However, imaging for reduction of flame transmission beamsteering features should be considered as integral to coherent combustion imaging diagnostics.

To compare the two techniques, Nyholm, Fritzon and Alden took the following simple theoretical descriptions of degenerate four wave mixing and polarisation spectroscopy signal strength. For DFWM, to first order the signal strength is given by

$$I_{DFWM} \propto \left(B_J N_{OH}(J)\right)^2 \cdot I_{pump1} \cdot I_{pump2} \cdot I_{probe} \qquad \text{Equation 1}$$

where I_{DWFM} is the intensity of the DFWM signal,

B_J is the transition probability of the transition,

$N_{OH}(J)$ is the number density of the target species in the lower state,

I_{pump1} and I_{pump2} are the intensities of the two counter-propagating pump beams, and

I_{probe} is the probe beam intensity.

For polarisation spectroscopy (assuming a low polarisation extinction background, no inter-polariser birefringent elements, perfectly crossed polarisers, negligible initial population of the upper state of the transition and in the linear regime of optical pumping), the signal strength is given by

$$I_{PLPS} \propto \left(\zeta_J B_J N_{OH}(J)\right)^2 \cdot I_{pump}{}^2 \cdot I_{probe} \qquad \text{Equation 2}$$

where

B_J is the transition probability of the transition,

$N_{OH}(J)$ is the number density of the target species in the lower state,

I_{PLPS} is the PLPS signal,

I_{probe} is the probe beam intensity,

I_{pump} is the pump beam intensity, and

ζ_J is the J dependent factor defined by Teets, Kowalski, Hill, Carlson and Hansch.

The DFWM signal is effectively quadratically dependent on the pump beam intensity and linearly dependent on the probe beam intensity. The signal is quadratically dependent on the number density of the target species in the lower state of the pumped transition. In this regard, the coherent LPS and DFWM techniques show the same dependence on beam intensity and number density. The advantage of the DFWM technique is that high quality polarisers are not required. There is a limit to the size of high quality polarisers which, when added to the restriction on birefringent optical elements between the probe beam polarisers in the probe beam path, severely limits the area which can be imaged by polarisation spectroscopy. DFWM is not subject to this restriction, and does not demonstrate the extinction background characteristic of polarisation spectroscopy. However, as shown above, the experimental arrangement and alignment procedure is much more complex. Nyholm, Fritzon and Alden compared the applicability of the two techniques in this paper.

If the signal to noise ratio achievable with DFWM is significantly larger than that for polarisation spectroscopy, it is more logical to consider DWFM in preference to LPS as an imaging diagnostic.

Nyholm, Fritzon and Alden successfully demonstrated single-pulse 2-D temperature mapping in a flame using OH DFWM and LPS based on the equations [1] and [2]. The temperature maps obtained via DFWM ranged from a minimum temperature of ~ 1500K and exhibited a maximum signal to noise ration of 50:1. In the case of polarisation spectroscopy, the maximum signal to noise ratio was ~ 75:1. Temporal and spatial PDFs of temperature for a set of ~ 50 images showed an average flame temperature of ~ 2300 ± 200 K[c] determined in the DFWM experiment. The spatial PDF of LPS signal is much broader (~ 2200 ± 300 K[c]) and the average temperature associated with the temporal LPS PDFs is lower (~ 1800 ± 200 K[c]). The adiabatic temperature for a stoichiometric propane/oxygen flame is 3095.4 K[d]. It should be noted that the flame in this experiment was fuel lean which would produce a lower flame temperature. Differences between the temperatures obtained with the two techniques are easily attributed to the technical difficulties reported for the experiment including the difficulty in tuning the dual laser system simultaneously to the maxima of the respective rotational absorption lines and the effect of spatial averaging due to the small size and temperature distribution of the experimental flame. In addition, slightly different regions were imaged in the two experiments, with the DFWM experiment imaging below the flame tip and PLPS experiment imaging a region slightly higher in the flame.

The authors noted the importance of a high quality spatial probe beam profile as both techniques are linear with the probe beam intensity, necessitating the use of a spatial filter in the beam path prior to the flame. The effect of the reduction in energy due such filtering is minimal as both DFWM and PS require low laser intensities. A technical difficulty noted by the authors is the overlapping of equivalent pixels in the two rotational images and the two respective probe beam profiles collected on the CCD for correction of the DFWM images

In conclusion, Nyholm, Fritzon and Alden note that the theoretical models used are the simplest available and do not include the effects of absorption (or absorption coefficient differences between the two transitions), which may be especially significant for the OH in such a flame. The authors suggested that an improved experimental geometry for DFWM would have the two pump beams entering the flame from opposite directions rather than being retro-reflected through the flame by a mirror to minimise the effects of absorption. The authors also note the need to investigate *"collisional relaxation effects, e.g. collisional depolarisation of the magnetic sublevels, which*

[c] Estimated from Figures 8 and 9 of Nyholm, Fritzon and Alden's paper[13].

[d] Calculated by *"Gaseq: Chemical equilibria for perfect gases"*, Version 0.63, Chris Morley, c.orley@ukgateway.net.

influences the temperature calculation from polarization spectroscopy"[13]. This statement is based on the deviation of low J predicted populations from a straight line fit to a Boltzmann population plot found by Nyholm[32] (*"Measurements of OH rotational temperatures in flames by using polarization spectroscopy"*, 1994). This would lead to an overestimation of the population of the $Q_1(2)$ state based on the collected LPS signal, an hence to an underestimation of the calculated temperature.

Nyholm, Fritzon and Alden demonstrated that both DFWM and PLPS produce similar signal to noise levels in imaging of the OH radical in a fuel-lean propane/oxygen flame. On the basis of possible size of imaged area, DFWM is preferable to PLPS. However, the DFWM experimental alignment is far more complex, requiring accurate overlapping of the two pump beams.

For a horizontally polarised pump beam, the LPS signal follows a $\cot^2(\chi)$ dependence on pump/probe beam intersection angle, χ. Nyholm, Fritzon and Alden stated that DFWM signal decreases less rapidly with increasing pump/probe beam intersection angle. This suggests good DFWM signal may be obtained for intermediate beam intersection angles allowing high spatial resolution in the collected image. Further comparisons of the two techniques are required to determine which is optimal for combustion diagnostics. However, the simplicity of alignment is a good argument for preferring polarisation spectroscopy for small scale imaging in combustion.

Lofstedt, Fritzon and Alden published the first NO PLPS image in 1996 (*"Investigation of NO detection in flames by the use of polarization spectroscopy"*)[30] as part of an investigation of detection of nitric oxide using polarisation spectroscopy. The experiment was largely unchanged from that of Nyholm, Fritzon and Alden[3] which produced the first OH PLPS image. A mixing system was added to the Nd:Yag pumped dye laser/doubling system used for the OH experiment to produce radiation near 226 nm to pump the $A^2\Sigma^+$-$X^2\Pi$ (0-0) band of NO. The pump beam was horizontally polarised and the pump and probe beams intersected at an angle of 8.5°.

The $Q_2(10.5)$ NO PLPS image for a premixed H_2/N_20 flame was an average of 200 shots and was corrected for both the (average) probe beam background and (average) flame emission background. The image shows a characteristic central distribution of NO within the flame region. The imaged area was 10 mm x 11 mm. The sheet thickness was 0.5 mm.

Lofstedt, Fritzon and Alden carefully specified the optics required to *"image the coherent signal"*[30] carried on the unfocussed probe beam. A lens with focal length, f, and an aperture are placed in front of the ICCD imaging camera. The lens is placed a distance, 2f, from the flame, and the surface of the detector a distance, 2f, after the lens. The aperture is placed half-way between the lens and the detector surface. A 230 nm interference filter and a Schott BG 24 coloured glass filter were used to minimise the detected background for the image.

The authors concluded that the PLPS technique showed great promise, especially in reduction of resonant fluorescence background due to the coherent nature of the technique. However, Lofstedt *et al.* noted a major problem was the spatial and temporal variation of the probe beam profile due largely to the combined doubling and mixing system.

In the same year, **Lofstedt and Alden** extended the preliminary investigation of the NO imaging described in their previous paper to present the fourth planar laser polarisation spectroscopy paper existing in the literature. The paper takes advantage of coincidences between the spectra of the hydroxyl and nitric oxide radicals, via the OH $A^2\Sigma$-$X^2\Pi$ (1,0) and NO $A^2\Sigma^+$-$X^2\Pi$ (0,0) bands (285 nm and 226 nm respectively). Lofstedt and Alden used both the doubled and mixed output of a Nd:YAG/dye laser system to simultaneously pump OH and NO in a premixed H_2/N_20 flame with a single laser. A single detection system captured both images after separation of the two wavelength components by a Pellen-Broca prism. A Schott UG11 filter and a standard bandpass (230 nm) filter were placed in the separated 285 nm and 225 nm beams respectively before detection on a single CCD. The imaging system consisted of a f = 500 mm lens placed at approximately 1m from the CCD. The Pellen-Broca crystal was placed between this lens and the detector (See Figure 3).

The 285nm and 226 nm beam energies were ~ 10 mJ and 5 mJ respectively. The polarisation of the two pump beams was matched by using a double Fresnel rhomb to rotate the polarisation of the 226 nm beam by 90°. For experiments with circularly polarised pump beams, a single Fresnel rhomb was placed in the beam path after the sheet forming cylindrical lens. It appears that no polariser was placed in the path of the pump beams allowing any ellipticity of the UV beams to influence the experiment. This is evident in the presence of an NO $R_2(29.5)$ line in the sample spectrum presented for a linearly polarised pump beam and a NO $Q_2(26.5)$ line in the spectrum in the case of a circularly polarised pump beam as discussed in Chapter V. The Bernard Halle probe beam polarisers were specified to have an extinction ratio of 10^{-7}. The laser linewidth was ~ 0.15 cm^{-1} at 285 nm and 0.8 cm^{-1} at 226 nm. The pulse length was ~10 ns.

Lofstedt and Alden published the first OH PLPS images and the first NO PLPS images for circularly polarised pump beams. The pump and probe beam intersected at an angle of 20°. The

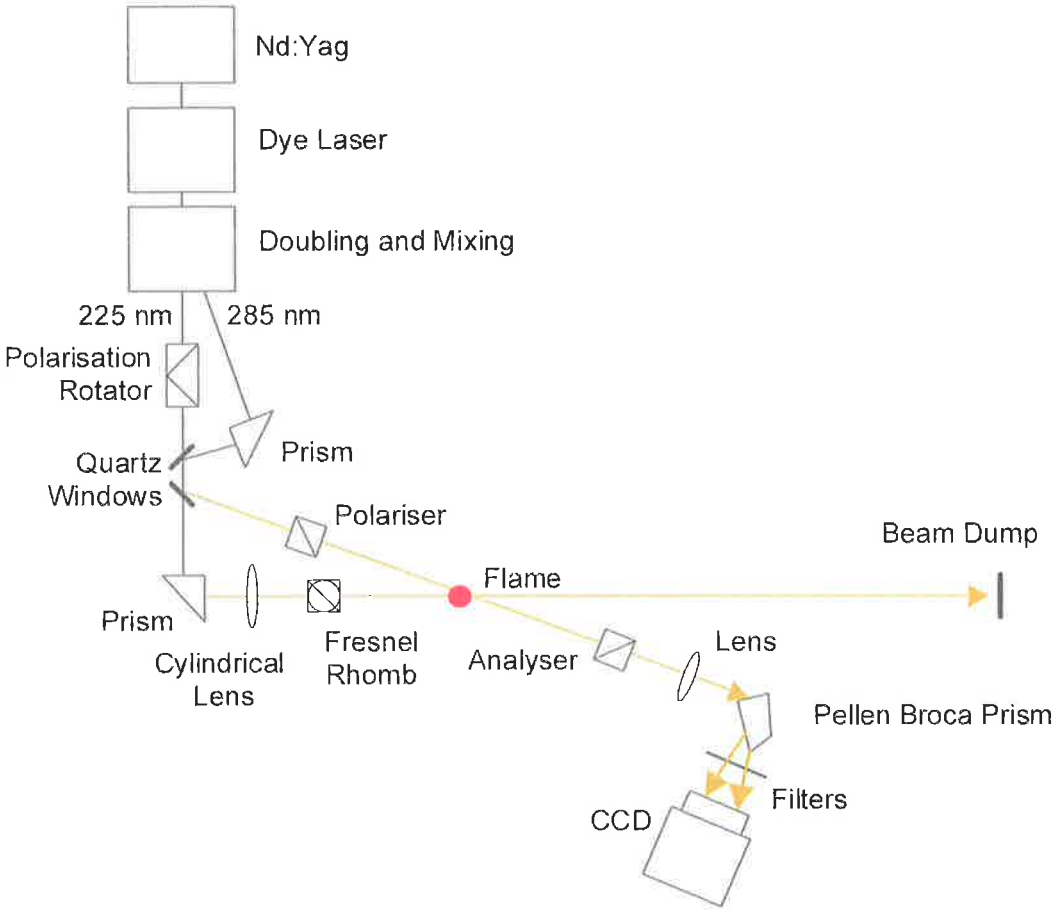

Figure 3: Experimental arrangement for the dual species PLPS imaging (OH at ~ 285 nm and NO at ~ 226 nm) of Lofstedt and Alden[15].

images, resulting from the coincidence of the OH $P_1(9.5)$ and NO $R_2(20.5)$ lines, were 100 shot averages and possibly show residual probe beam thermal beamsteering features superimposed on the signal after subtraction of the probe extinction background and correction for the probe beam intensity profile (collected with no pump beam present). The authors also collected single shot images. The imaged region was ~ 6 mm high and the maximum signal to noise ratio was ~ 15:1.

The experiment was limited by technical difficulties. The intensity of the mixed beam was controlled by rotating the mixing crystal to minimise domination of the signal by one of the two signals. The sheet forming lens was not achromatic, resulting in the two pump sheets being displaced ~0.5 mm with respect to each other, thus imaging slightly different regions in the flame. In addition, the polariser crossing angles providing minimum extinction background for the two beams differed slightly. An additional problem was that the maxima of the "coincident" NO and OH absorption lines did not match exactly, although this effect can be corrected for reasonably in a theoretical model provided the pulse-to-pulse variation of the wavelength is known. The experiment was biased

between the two optimal configurations for the OH and NO signals resulting in the relatively low signal to noise ratio. However, the experiment is a very good example of a double species imaging experiment which can be achieved with a single laser/single detection system. The quality of the probe profile correction for the images is exceptional considering the probe beams were not spatially filtered in this experiment.

The limiting factor of the dual-species detection technique with a single laser system is not technical, but the restriction on the transitions which coincide between the two species, which may correspond to low population or highly temperature dependent states in a given experiment. The coincident lines suggested in this paper are actually suitable for a large range of flame temperatures; OH $Q_1(9.5)$/NO $Q_2(20.5)$ and OH $P_1(11.5)$/NO $R_2(35.5)$[e].

Lofstedt and Alden noted that the dual species experiment could be improved greatly by the use of an achromat lens as long as the coincidence of the two pump beams does not photochemically breakdown N_20 in the flame leading to excess OH concentrations. If photochemical breakdown is expected, one of the two UV beams could be delayed by a time of the order of the pulse length and the ICCD gate increased slightly. If two additional probe beam polarisers are available, the two probe beam components could be aligned to cross the sheet plane from opposite directions but in the same sense of propagation direction with respect to the pump beams (i.e. at beam intersection angles of χ and $-\chi$ for the two wavelengths) to image the same image plane before redirection for imaging on a single CCD. This would avoid sub-optimal alignment of the probe beam polarisers and the requirement to spectrally separate the two images. Note that in this case, the path through the flame (and hence absorption) differs for the two probe beams.

Aside from the four papers described above, the only other PLPS imaging paper available at the time of writing is that of **Reppel and Alwahabi** which presented orthogonal PLPS images for both circularly and linearly polarised pump beams. Those images were collected in the saturated regime of optical pumping. Chapters V and VI of this thesis have presented additional saturated PLPS images collected for circularly and linearly polarised pump beams respectively. There has been no attempt to quantify the signal or saturation in these images. The next chapter (Chapter VII) describes an imaging experiment comparing (average) PLIF and PLPS images collected simultaneously where the saturation has been quantified. The advantage of comparing the OH distribution using the PLIF and PLPS techniques is that both signals result from the same pump sheet allowing simultaneous collection of the images due to both techniques and negating the need to overlap two pump beams accurately.

[e] The OH $Q_1(9.5)$/NO $Q_2(20.5)$ transition pair requires a linearly polarised pump beam and the OH $P_1(11.5)$/NO $R_2(35.5)$ transition pair requires a circularly polarised pump beam.

(1) Near-Collinear LPS Imaging in Combustion Experiment

This chapter describes a near-collinear PLPS experiment imaging the OH distribution in a premixed CH_4/O_2 flame from a modified glass-blowing torch for beam intersection angles of 15° and 30°. The experiment is designed for direct comparison with the imaging experiment of Nyholm, Fritzon and Alden and to highlight the degree of correction for an (average) probe beam background which may be achieved for laminar flames.

The near-collinear PLPS experimental arrangement is shown in Figure 4. The optics were largely unchanged from the orthogonal PLPS experiment. The horizontally polarised pump beam was redirected to intersect the probe beam in a near-collinear geometry (at either 15° or 30° beam intersection angle). The ¼-wave rhomb was removed from the path of the pump beam which emerged roughly horizontally polarised from the doubling system. A polariser was then used to accurately define the horizontal pump beam polarisation axis. The probe beam was polarised at $\pi/4$ to the polarisation axis of the pump beam. The probe and pump beam energies were estimated to be 160 μJ and 4 mJ respectively. The laser system was tuned to pump the $A^2\Sigma$–$X^2\Pi$ (0-0) $Q_2(8)$ transition of OH at ~ 309.772 nm. The laser linewidth was estimated to be 0.4 cm^{-1} and the pulse length ~ 3 ns.

The PLPS images in this chapter are unweighted 50 shot averages and are shown in the two modes described in Chapter III. Mode 1 represents the image minus for the non-zero background of the ICCD alone, and represents an uncorrected image as a sum of the LPS signal, S, and the probe beam extinction background, B. Mode 2 represents the ratio of the LPS signal (corrected for the probe background) to the probe extinction background and is proportional to the square of the induced dichroism.

The Mode 2 images were calculated from the image ratio term, R_{signal}, defined in Chapter III, according to the equation

$$\frac{S}{B} = R_{signal} - 1 = \frac{I_{probe}}{I_{probe\_blocked\_pump}} - 1 = \frac{B + S}{B} - 1 \qquad \text{Equation 3}$$

where R_{signal} is the ratio of the collected PLPS signal (including the probe beam extinction background), I_{probe}, to the probe beam extinction background (measured with no pump beam present), $I_{probe\_blocked\_pump}$.

The average background of the ICCD (~ 55 counts) varied by less than ±1 count over the 576 x 384 pixel array over the course of a day and was automatically subtracted (after one hour's temperature stabilisation at the start of each day's experiment) from each of the following images.

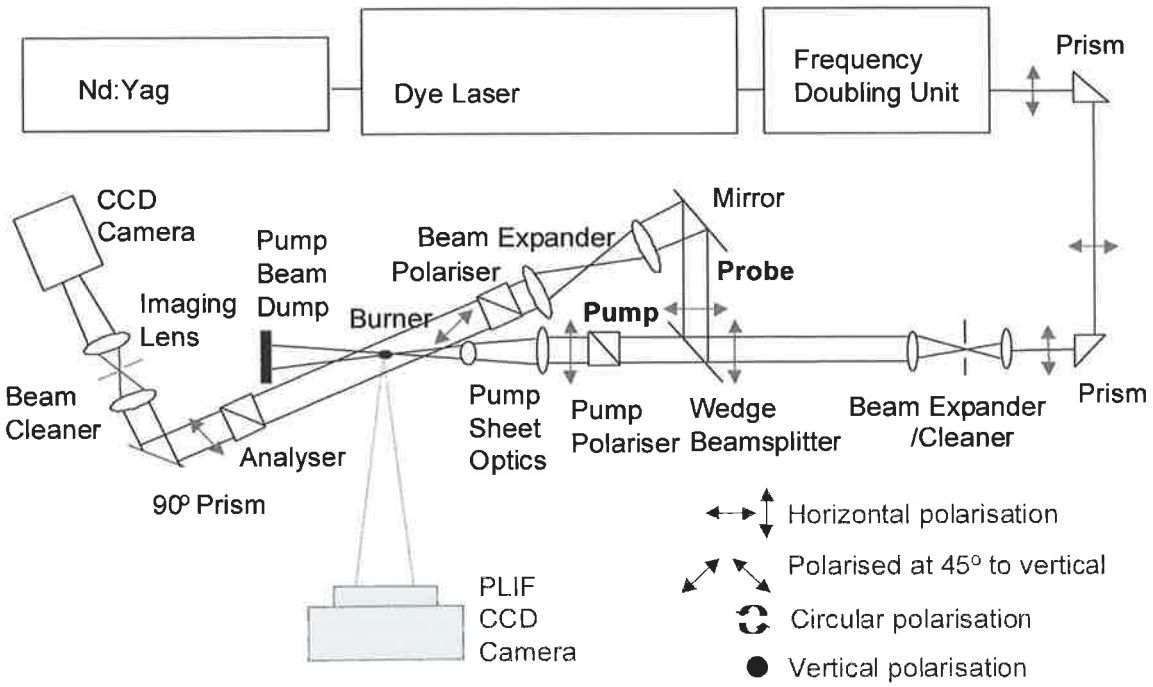

Figure 4: Experimental arrangement for near-collinear polarisation spectroscopy imaging for the case of a horizontally polarised pump beam. The probe beam is polarised at 45° to the vertical.

The validity of taking average images in the case of a nonlinear technique is always questionable (The PLPS signal is linear with the probe beam intensity and, in the linear regime, quadratic with respect to the pump beam intensity). However, the following images were taken to determine the effect of thermal gradient features on the OH PLPS images for a range of beam intersection angles and, both to maximise signal strength and to minimise the dependence on the pump beam profile, in the saturated, rather than linear, regime. Thus the PLPS technique becomes linearly dependent on the laser intensity. The relative stability of the laser system (the standard deviation of the pulse-to-pulse UV intensity was 4.6%) then supported the use of the following average images for image interpretation purposes.

The images are presented as sets of consecutive vertical cross-sections through the base of the flame obtained as the pump sheet is spatially moved across the tip of the burner. The Mode 1 and Mode 2 PLPS images for a pump/probe beam intersection angle of 30° are shown in Figures 5 and 6 respectively. The figures are presented in an interleaved form (two images to a page) to allow direct comparison of raw and corrected PLPS images. Figure 5 represents the Mode 1 images for an image set obtained by spatially scanning the pump beam across the base of the flame. The images represent consecutive cross-sections of the OH PLPS signal through the flame base. The equivalent Mode 2 images are shown in Figure 6. The top image on each page of the figure is the

relevant Mode 1 image of Figure 5, while the equivalent base image represents Figure 6. Figures 7 and 8 show a similar set of Mode 1 and 2 images for a beam intersection angle of 15°.

The position of the laser sheet with respect to the central axis of the flame determines the position of the foreshortened region of LPS signal on the circular cross-section of the probe beam. The probe beam cross-section remains circular for all beam intersection angles. However the foreshortened[f] elliptical interaction region of pump and probe beams progresses in position across the probe beam background as the pump sheet is scanned spatially across the flame. As a result, the LPS signal moves through the strong central cone-shaped thermal gradient structure on the probe beam profile as the pump beam is swept across the flame. A strongly visible probe beam extinction background in the Mode 1 images implies a relatively weaker maximum signal in the selected image. The relatively strong probe background in the Mode 1 images of Figures 5 and 7 where the pump sheet passes through the edge of the flame is due to the low OH concentration in this region. The images are individually scaled for the greyscale to include pixels in the 5 to 95% range of intensity.

The Mode 1 images for 30° and 15° beam intersection have maximum signal count levels of ~320 counts and ~550 counts at an ICCD gain of 9 respectively. The probe beam extinction background was approximately 35 counts. However, after correction for the probe beam background, the Mode 2 images of Figures 6 and 8 demonstrated an average noise level in non-flame regions of ~ 0.1 count, with maximum corrected signal levels of 16 and 25 for the for the 30° and 15° images respectively. This demonstrates the important difference between the signal to background ratio (~9:1 and ~16:1 respectively in these cases) and the much higher signal to noise ratio (~ 160:1 and ~250:1 respectively) in polarisation spectroscopy, and the necessity for accurate correction for the probe beam profile in polarisation spectroscopy imaging.

The scale in the Mode 1 and Mode 2 images of Figures 5 and 7 is 105 pixels per millimetre or 9.5 μm per pixel, creating an imaged probe beam area of 3.7 mm x 5.5 mm. One limitation in polarisation spectroscopy is the size of high quality polarisers. The increase in background due to the birefringence, b, of inter-polariser optical elements in the probe beam path (according to equations [10] and [11] of Chapter I) restricts the use of magnifying optics between the probe beam polarisers to increase the imaged area. The polarisers used in these experiments had a clear aperture of 20 mm. The smaller imaged area in the images in this chapter is due to the magnification of the post-analyser transmitted probe beam.

The circular cross-section of the probe beam carries information on the elliptical interaction region of pump and probe beams. The images must be stretched by the inverse of the sine of the angle of

[f] by the factor $\sin(\chi)$ in the ICCD detection plane.

intersection to represent the imaged area (as viewed from an incidence angle of $\pi/2 - \chi$ as discussed in Chapter III). The converse of this is that, for a flame of radius, r, the required imaging probe beam width in the horizontal plane is $r.\sin(\chi)$. The reduction in required probe beam width is significant for small pump/probe beam intersection angles, but is limited by the consequent decrease in horizontal resolution of the corrected image. Thus a wide flame expanse may be imaged on a relatively narrow ICCD area using polarisation spectroscopy if a small beam intersection angle is selected.

The decrease in resolution is evident in Figures 9 and 10, which show the stretched Mode 2 images for the case of pump/probe intersection angles of 15° and 30° respectively. The 15° signal is obviously imaged on a much smaller fraction of the probe beam profile than in the case of a 30° beam intersection angle. Stretched images for small beam intersection angles will then be more sensitive to the effects of imperfections in the probe beam profile and average background correction. In addition, the OH distribution is tilted in both sets of stretched Mode 2 images, but is more pronounced in the case of the 15° beam intersection angle. The alignment of the glass blowing torch was based on comparison with the unstretched image on the ICCD which, if the misalignment is small, underestimates the angle of vertical (normal to the beam intersection plane) misalignment of the flame by a factor of $1/\sin(\chi)$, where χ is the pump/probe beam intersection angle.

The Mode 2 images indicate that correction for, in this case average, probe beam extinction background is still highly successful for non-collinear imaging. The prominent thermal gradient structures present on the probe beam profile which modulate the OH PLPS signal in the uncorrected Mode 1 images are largely absent in the Mode 2 image ratio corrected images.

Figures 5 and 6: (Pages following) Set of OH PLPS images of the fuel/lean premixed natural gas/O_2 flame for a horizontally polarised pump beam and a 30° beam intersection angle. The probe beam was polarised at $\pi/4$ to the vertical. The image set was obtained by scanning the pump sheet across the tip of glass-blowing torch. The two images on each pages represent corresponding raw (top image) Mode 1 and corrected (base image) Mode 2 images. The images are plotted on a greyscale based on the 5 to 95% signal strength range of each image with black representing the lowest signal.

(a) (Figures 5 and 6)

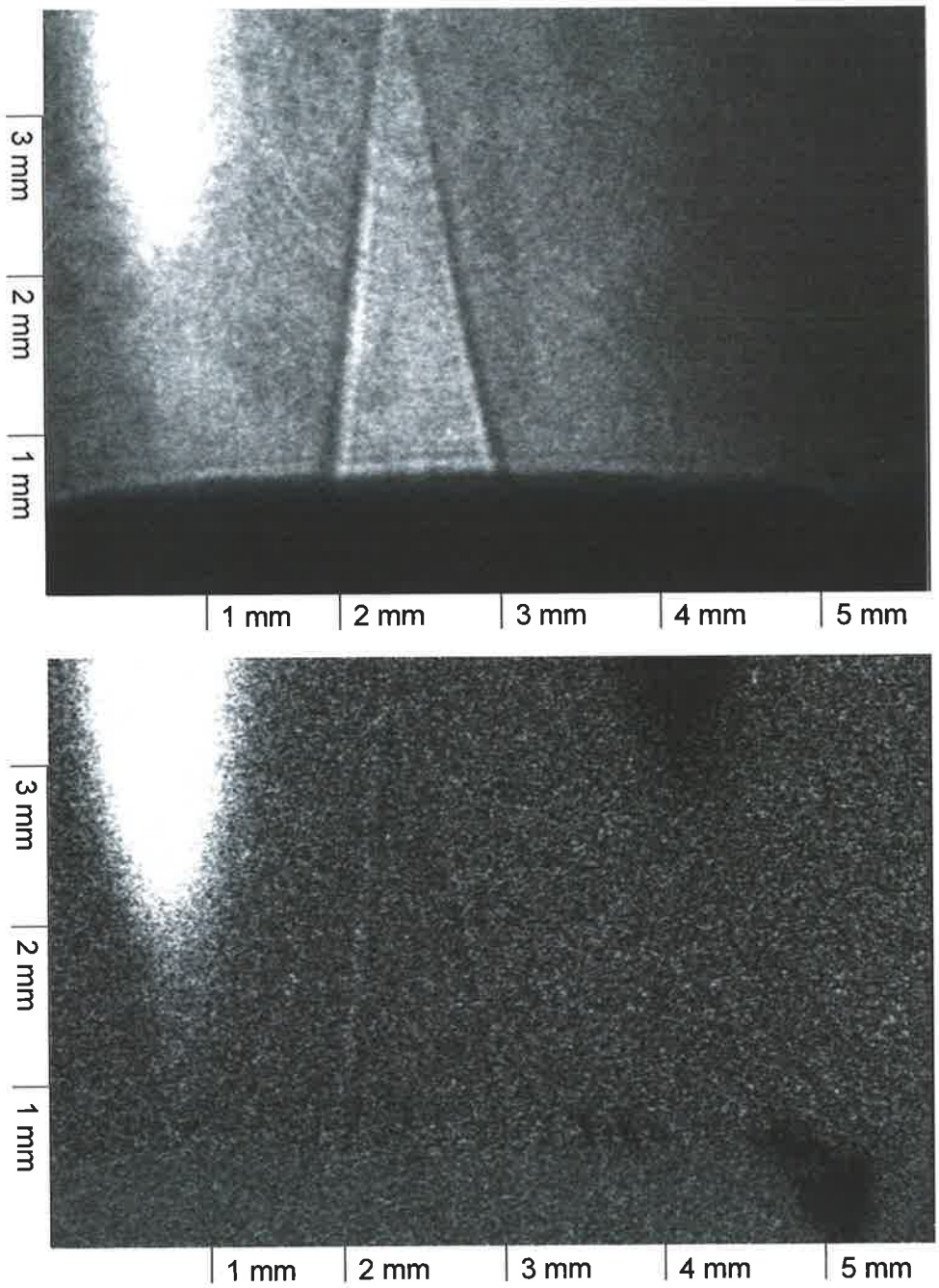

(b) (Figures 5 and 6)

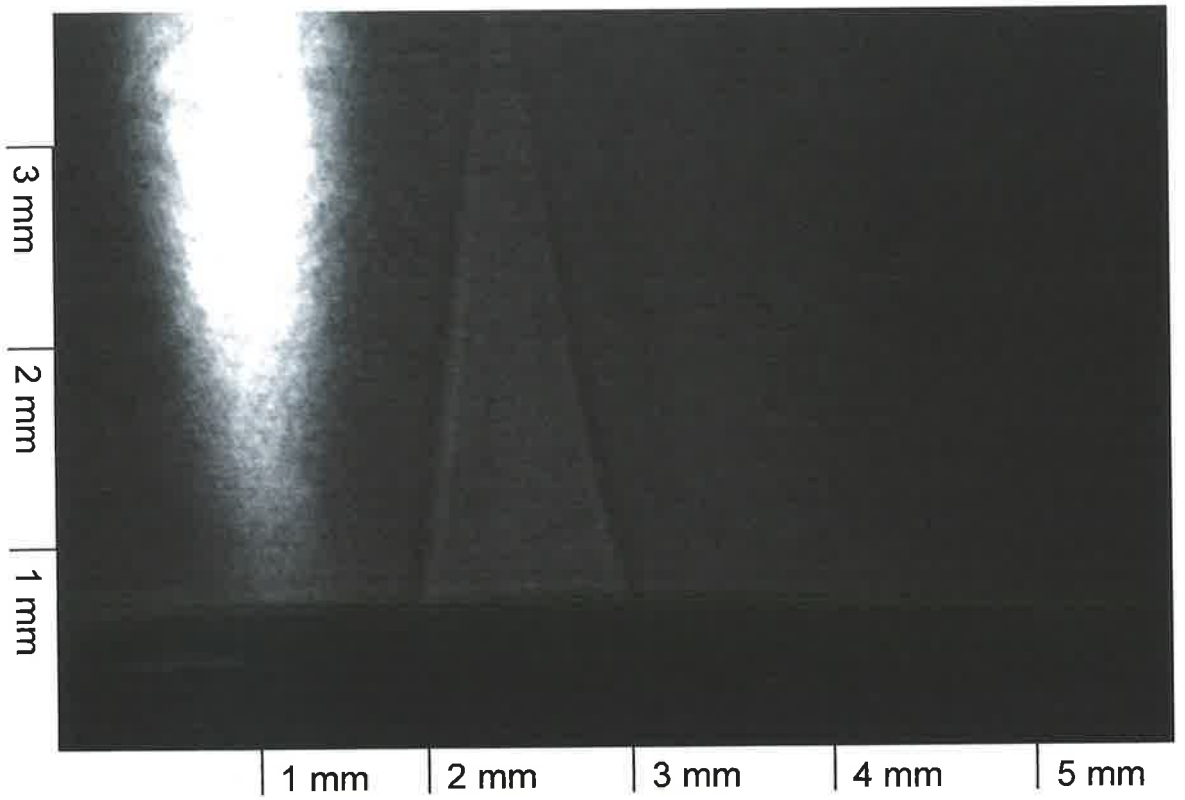

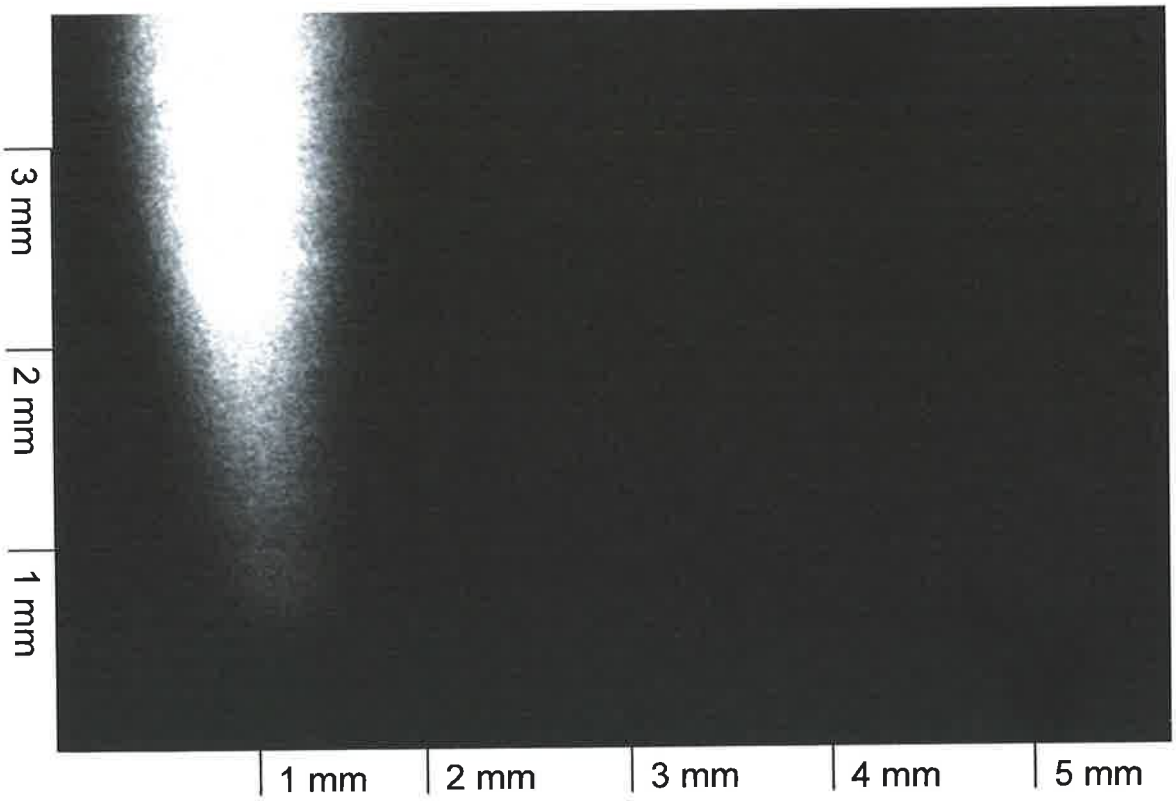

(c) (Figures 5 and 6)

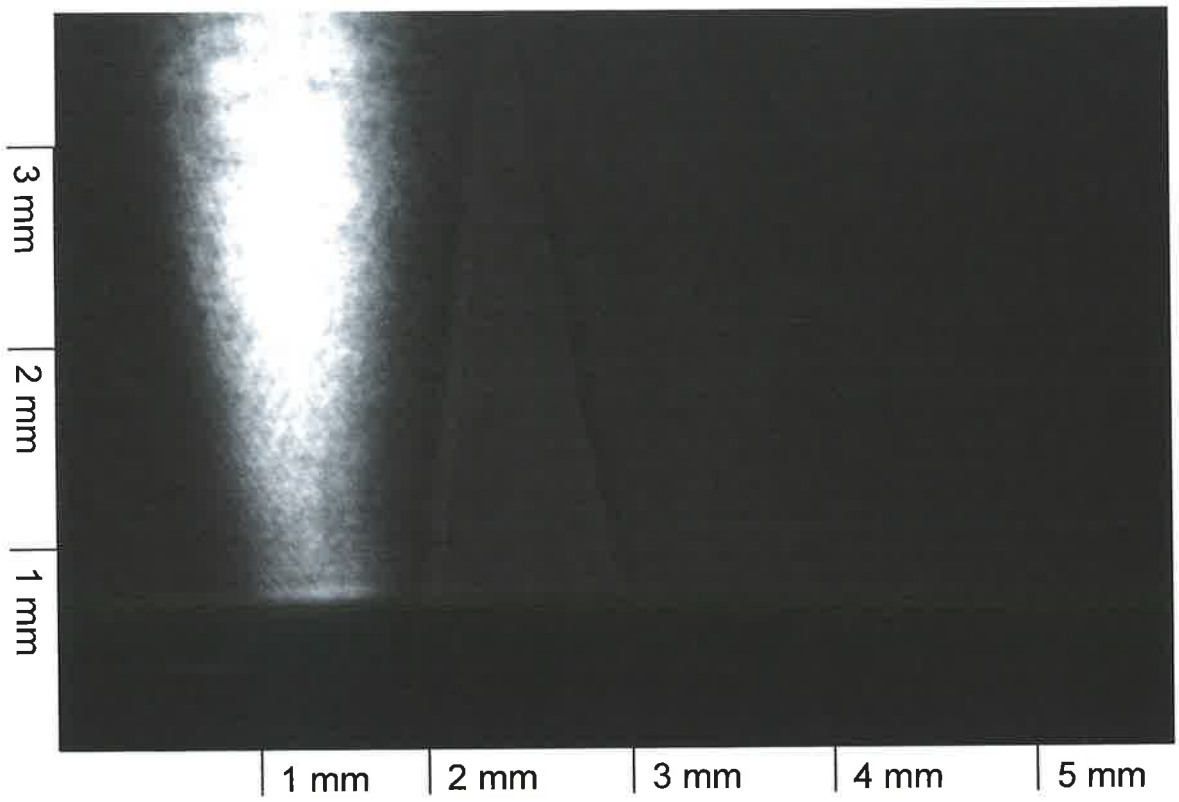

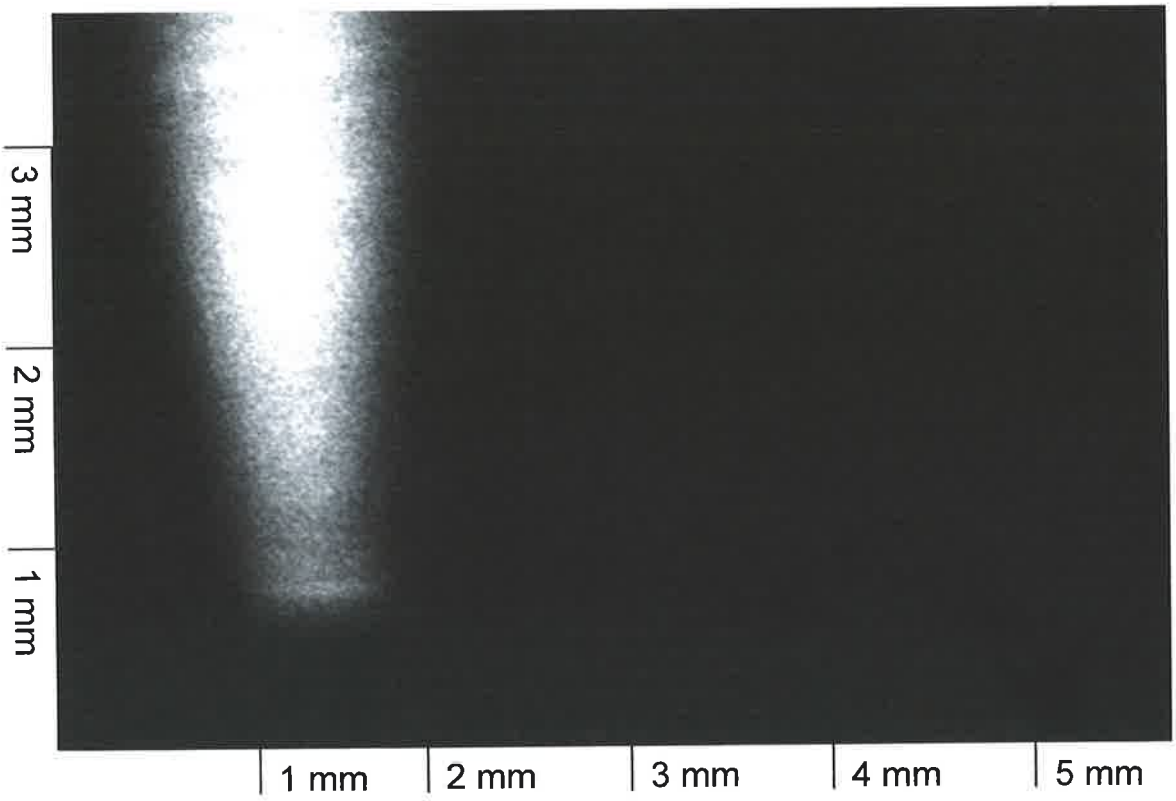

(d) (Figures 5 and 6)

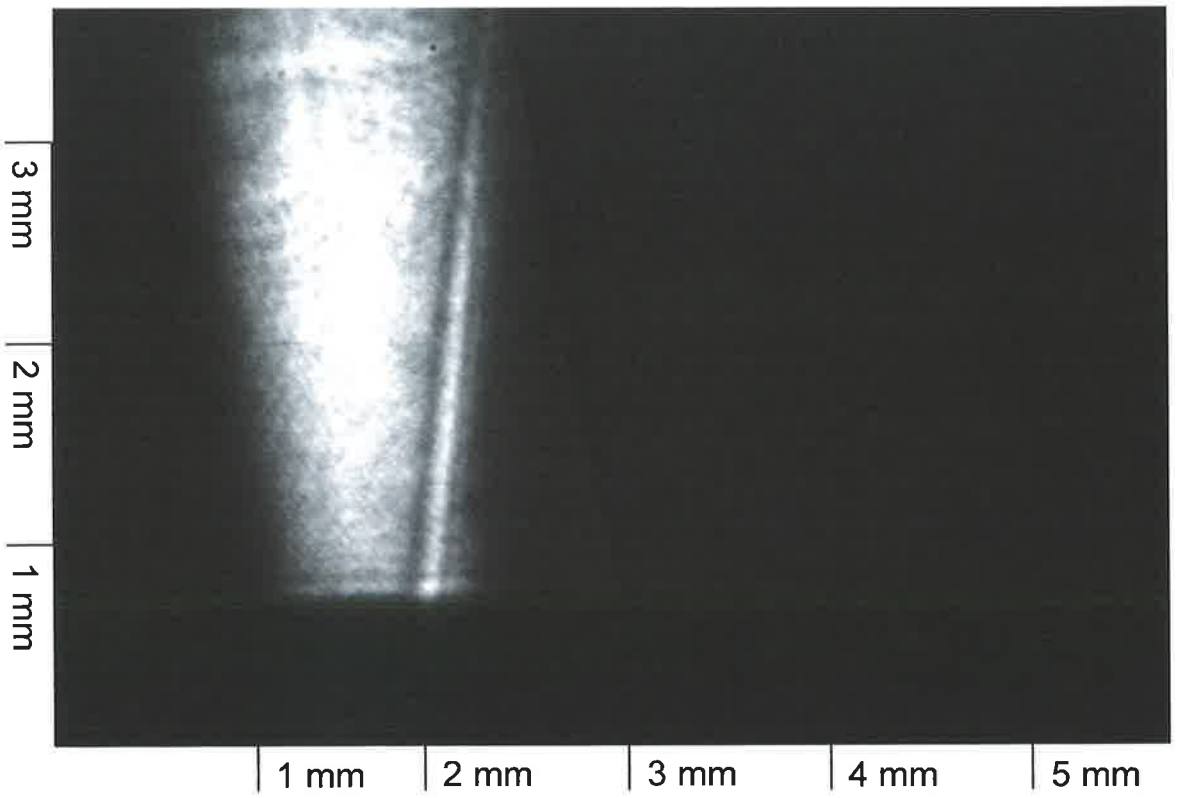

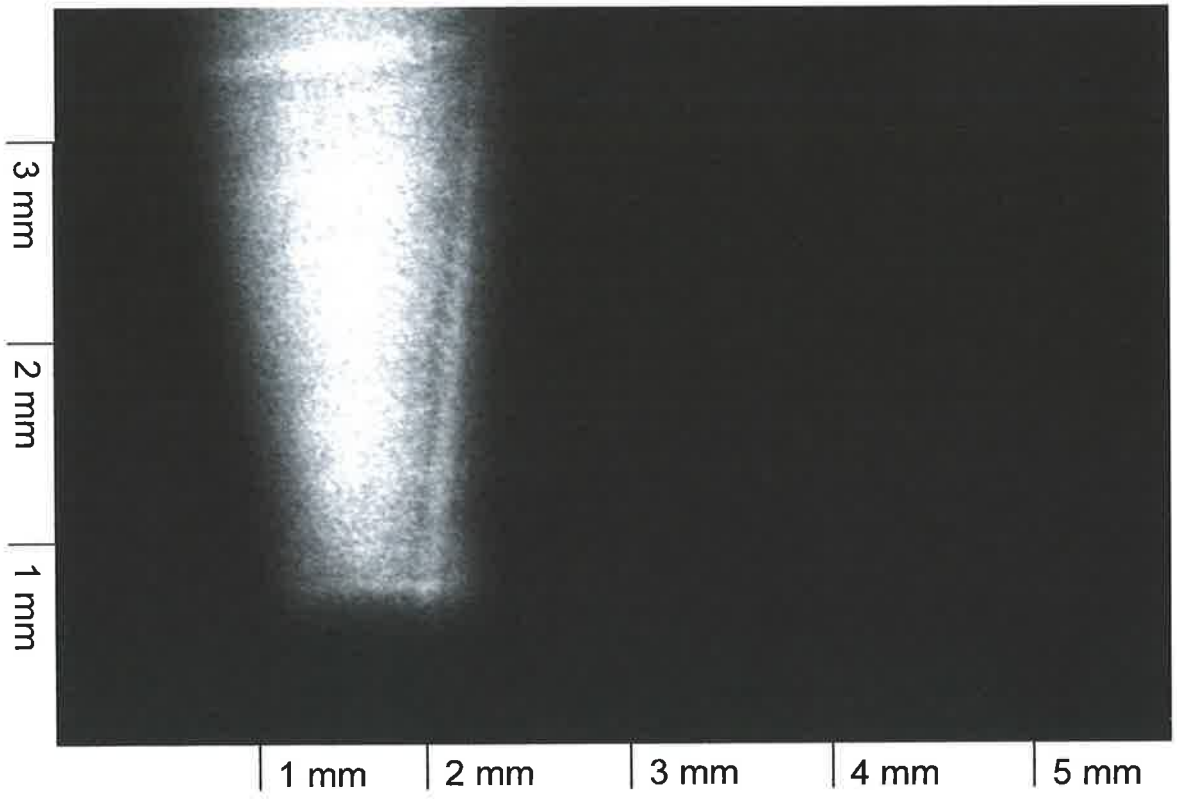

(e) (Figures 5 and 6)

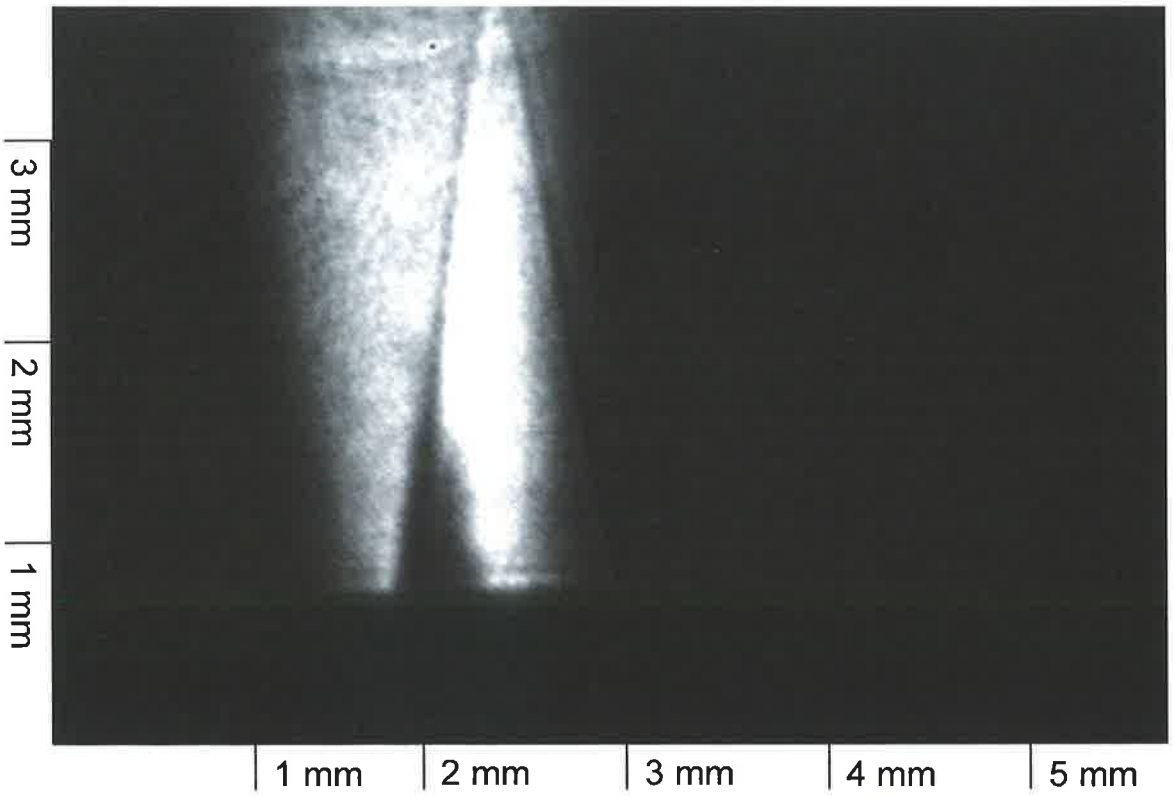

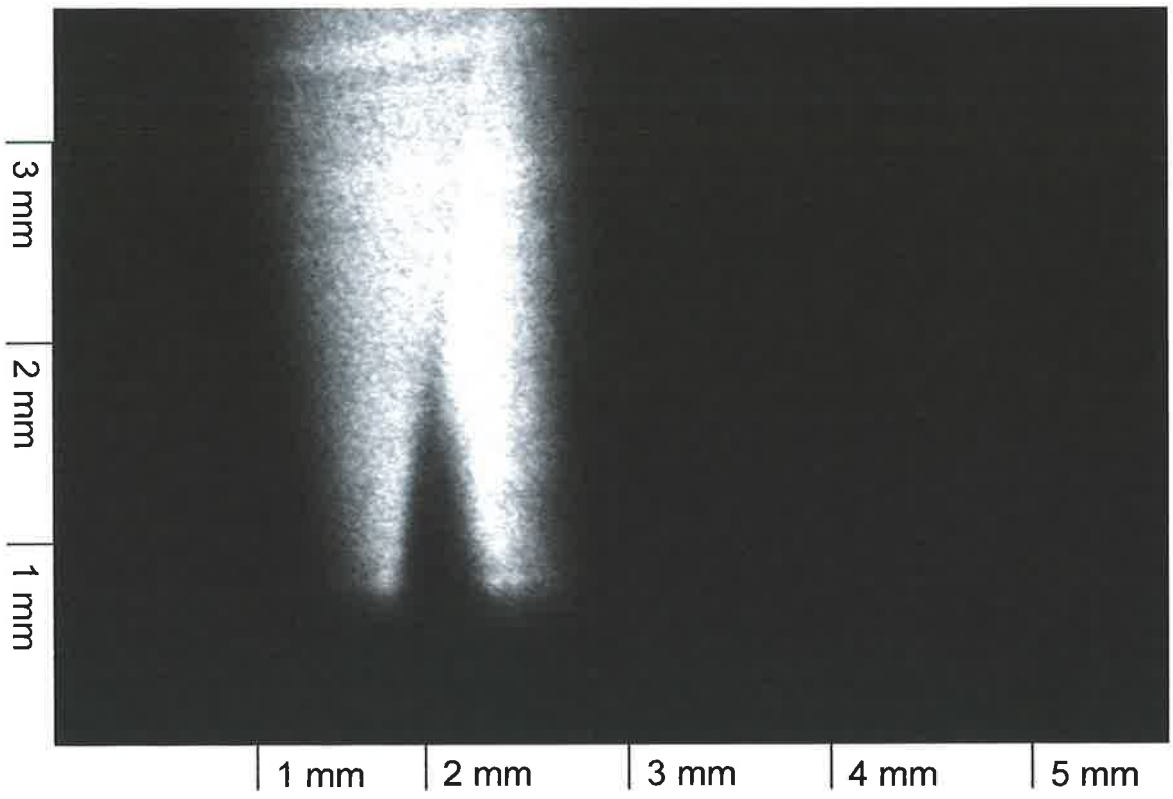

(f) (Figures 5 and 6)

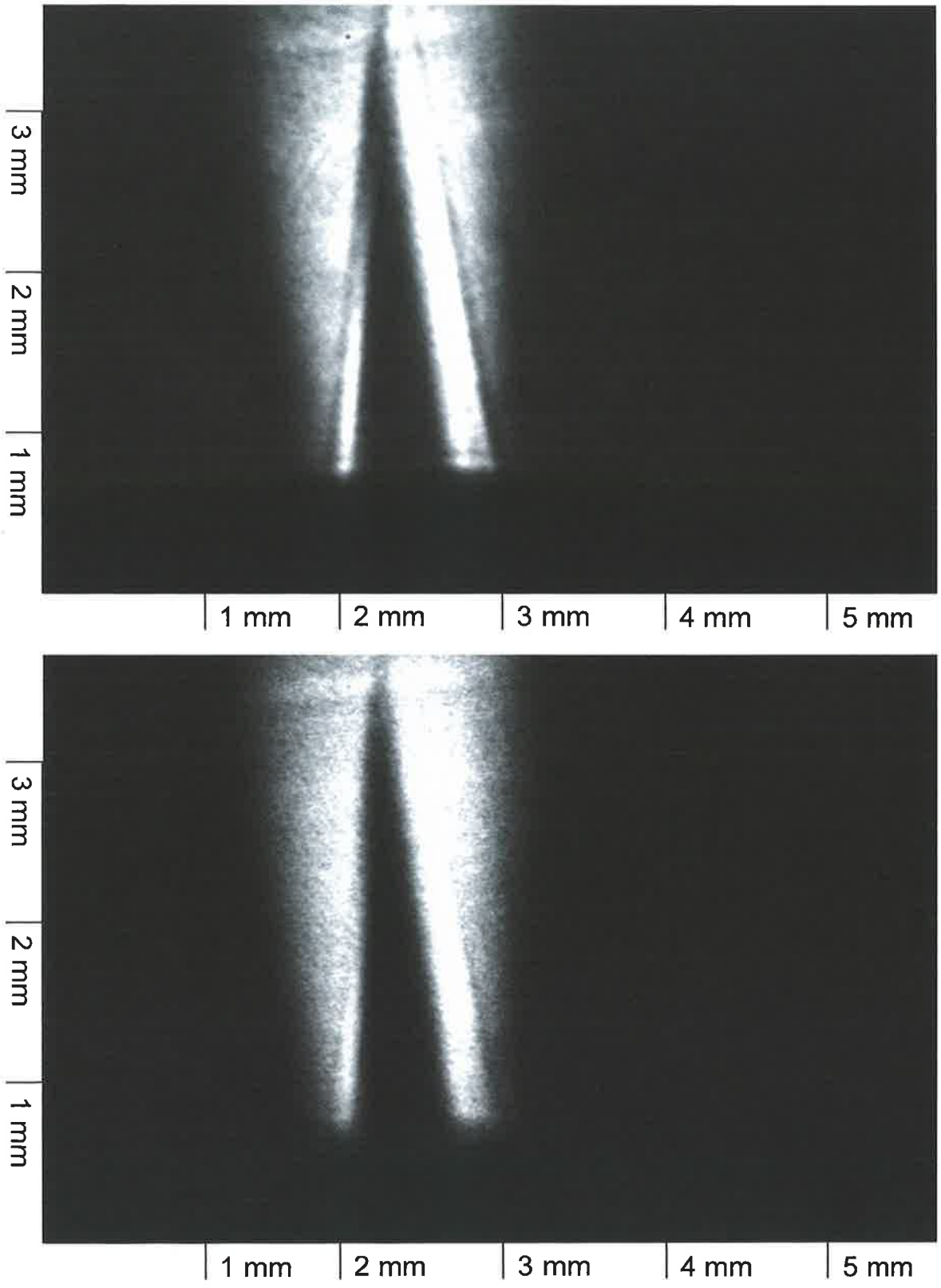

(g)

(Figures 5 and 6)

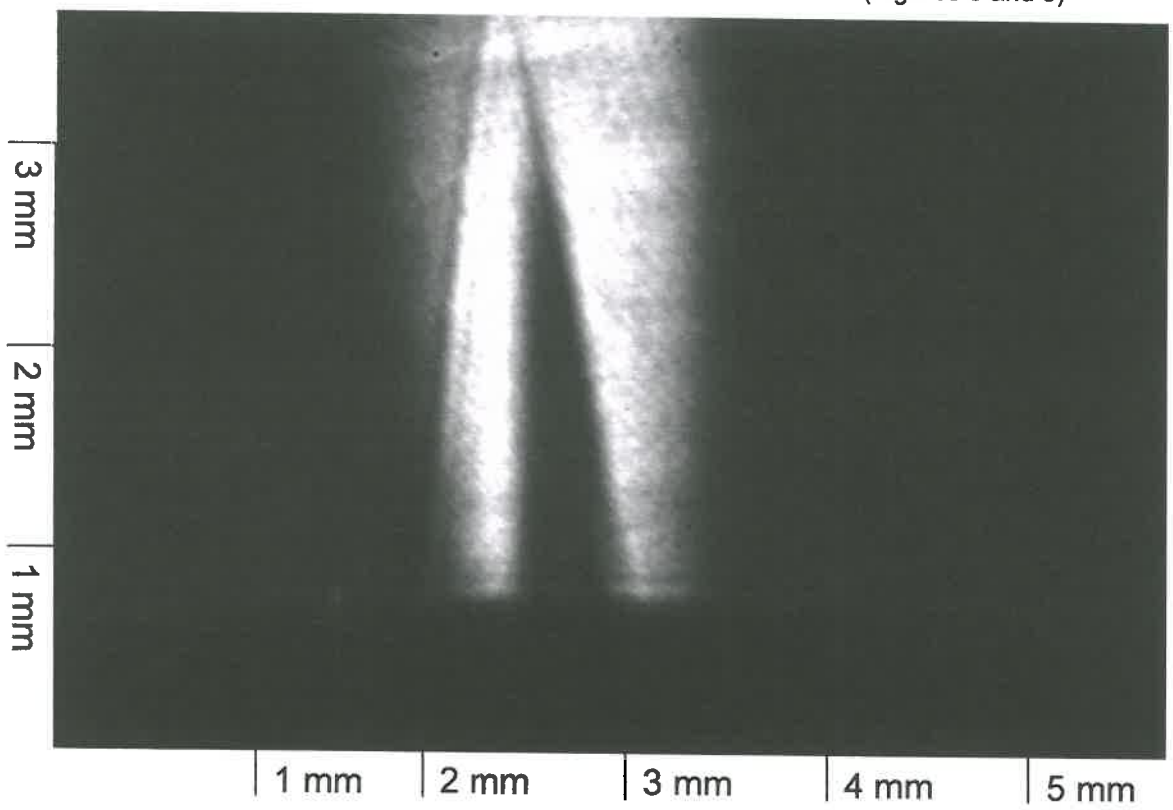

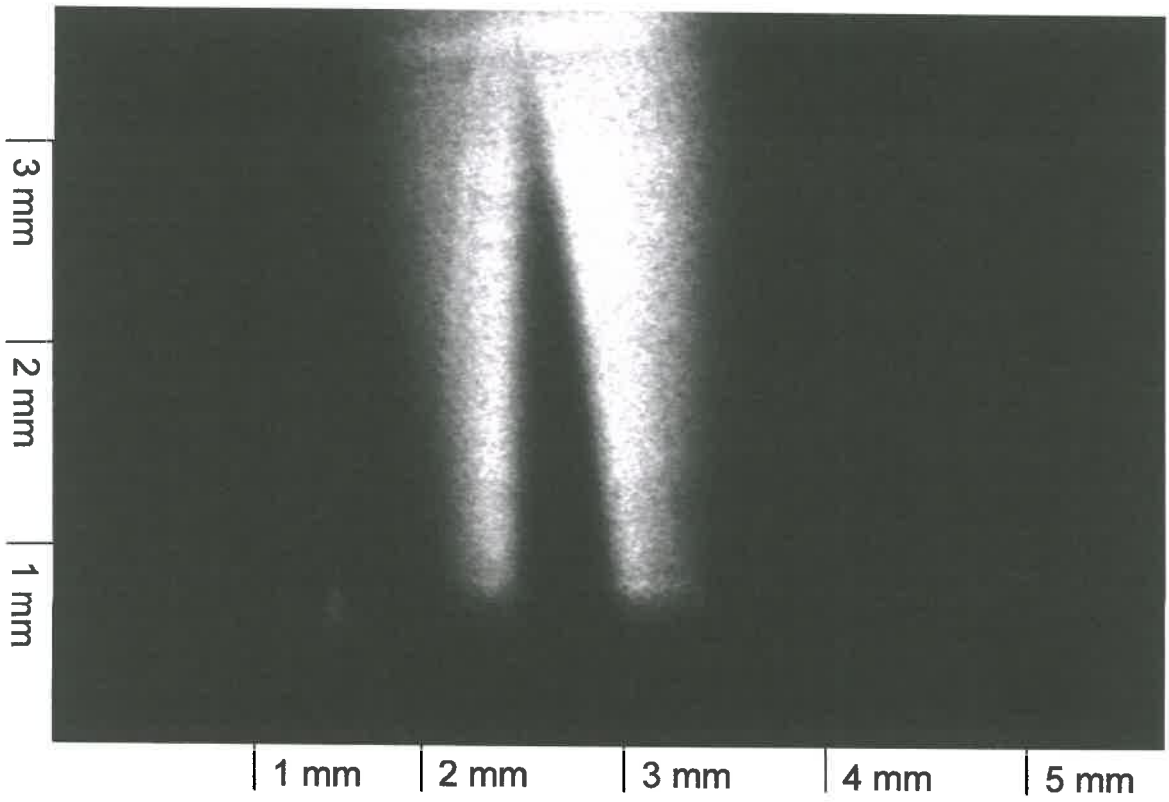

(h)

(Figures 5 and 6)

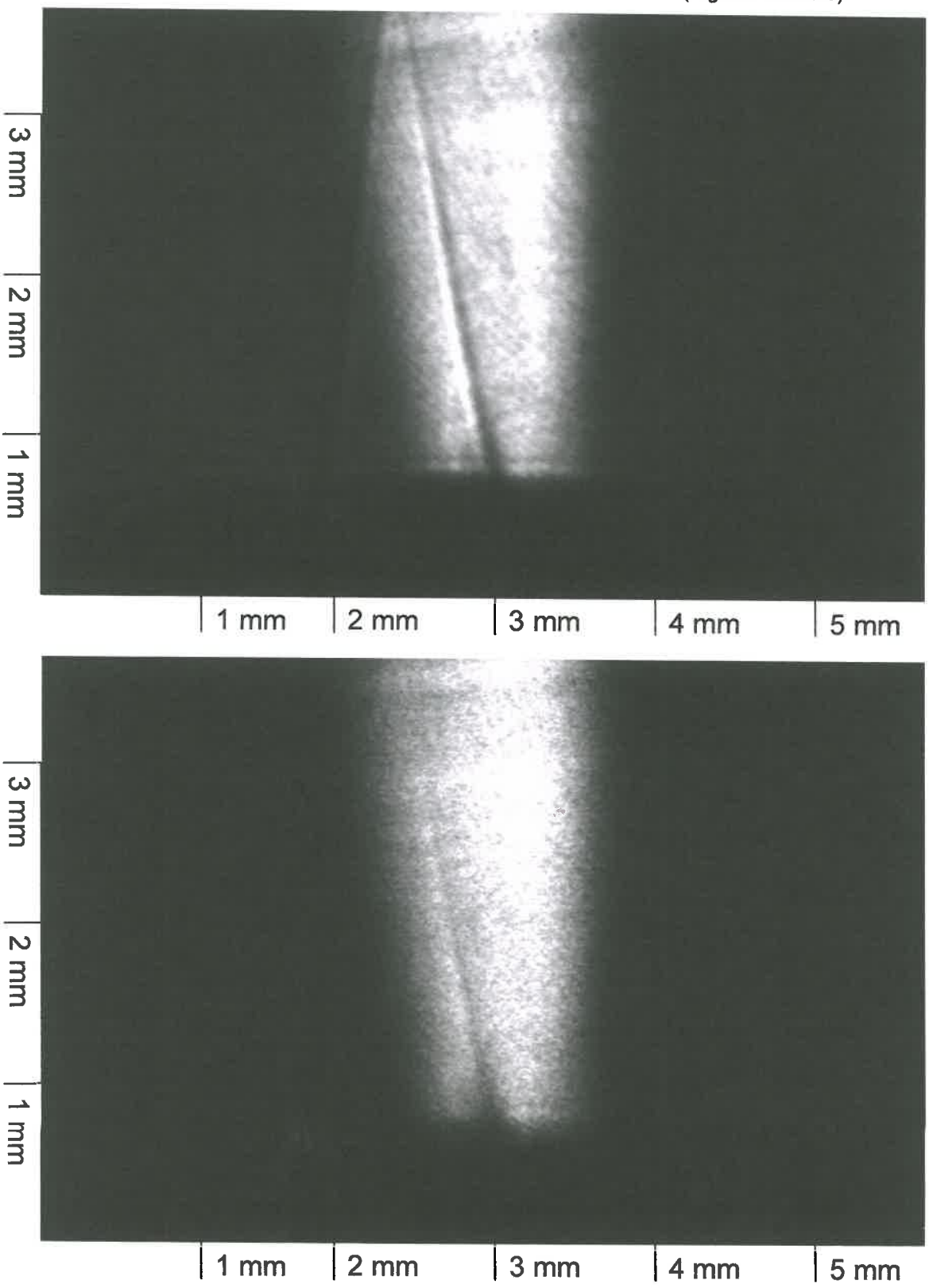

(i)

(Figures 5 and 6)

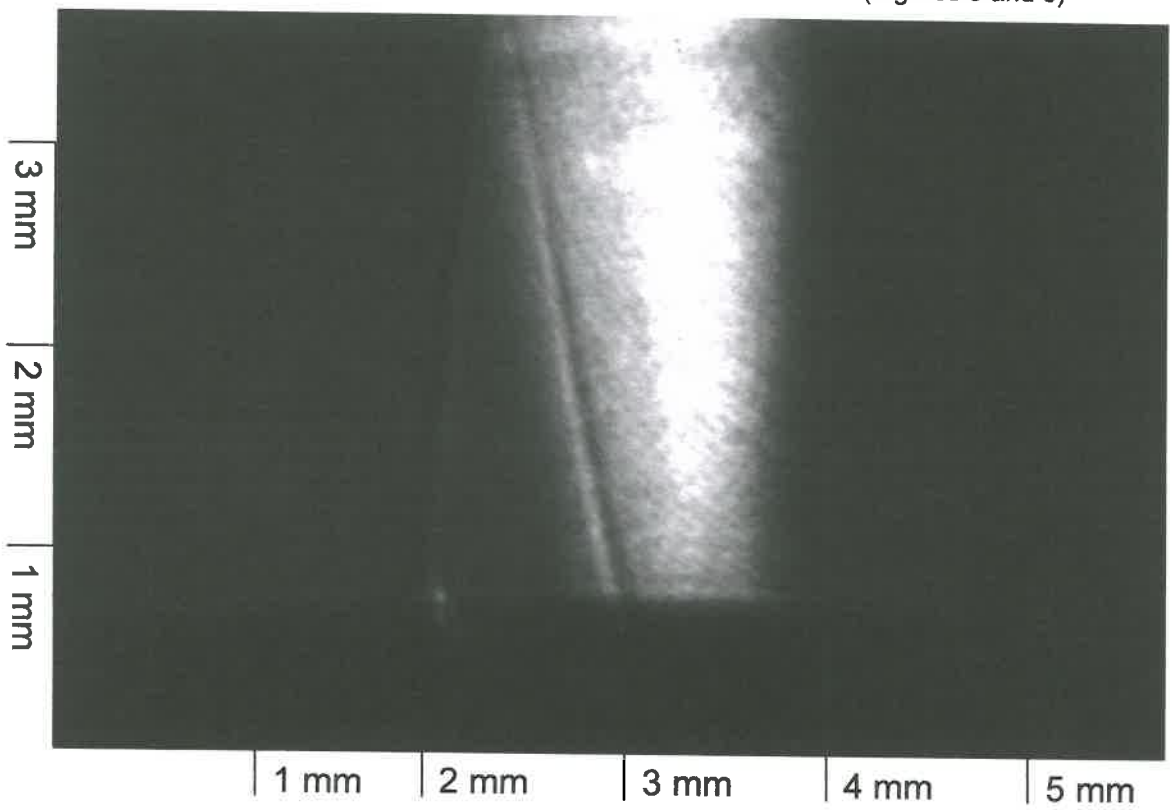

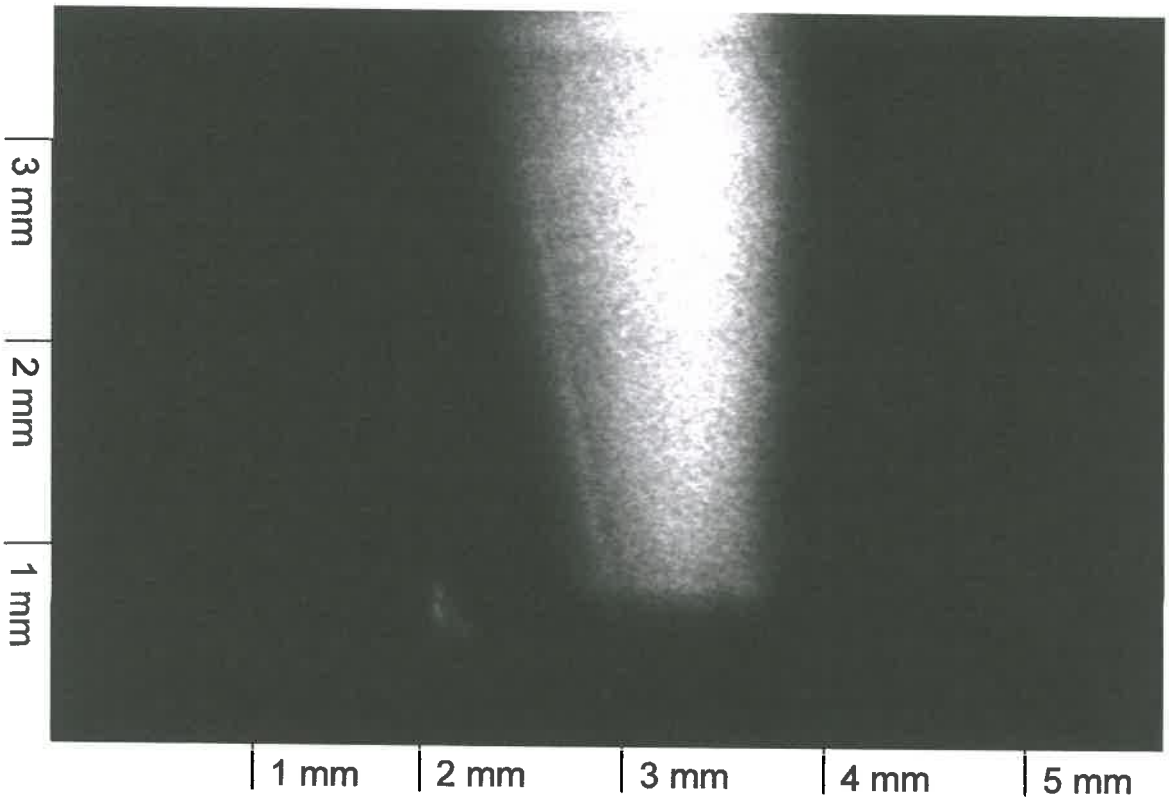

(j)

(Figures 5 and 6)

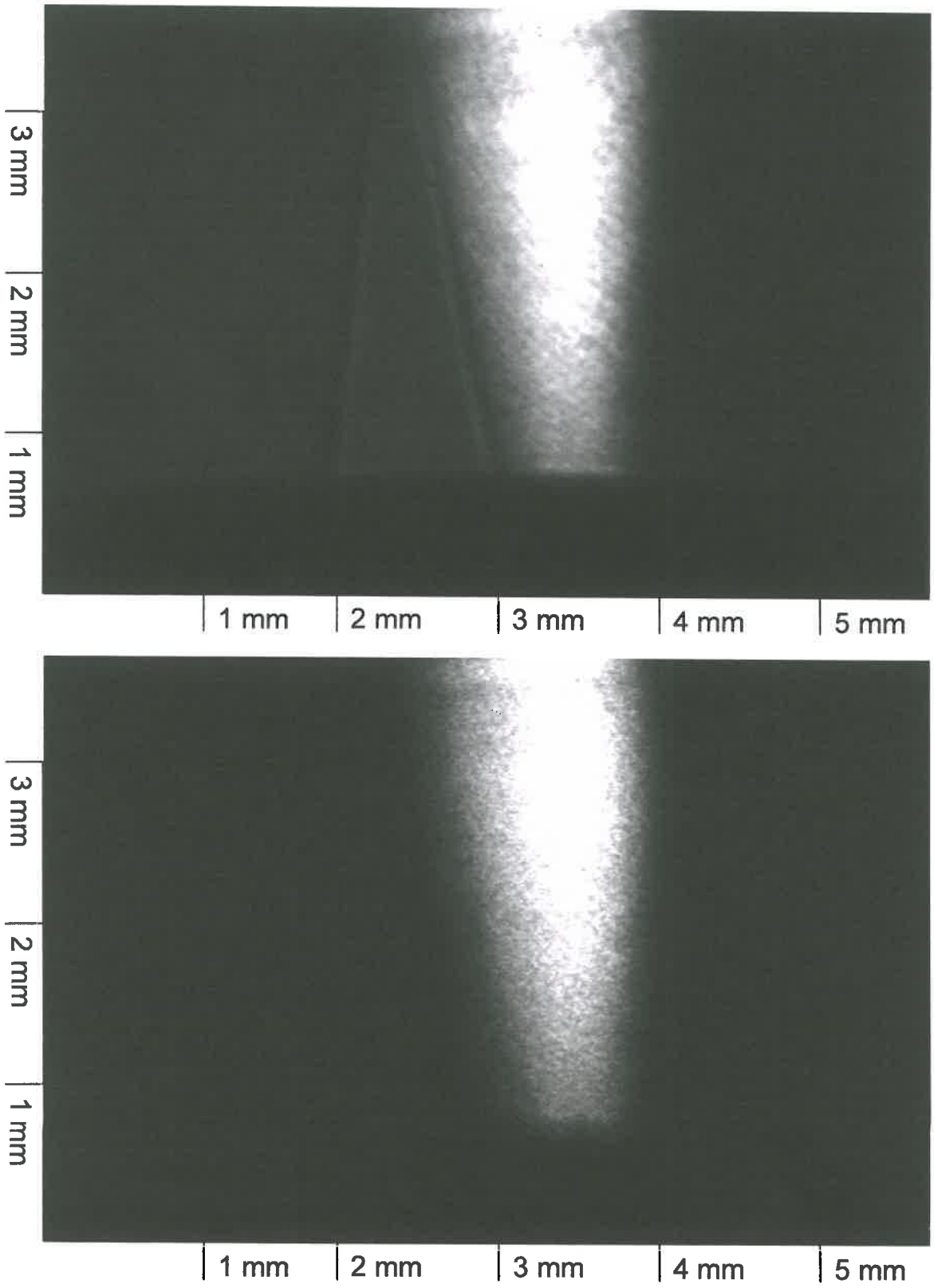

(k)

(Figures 5 and 6)

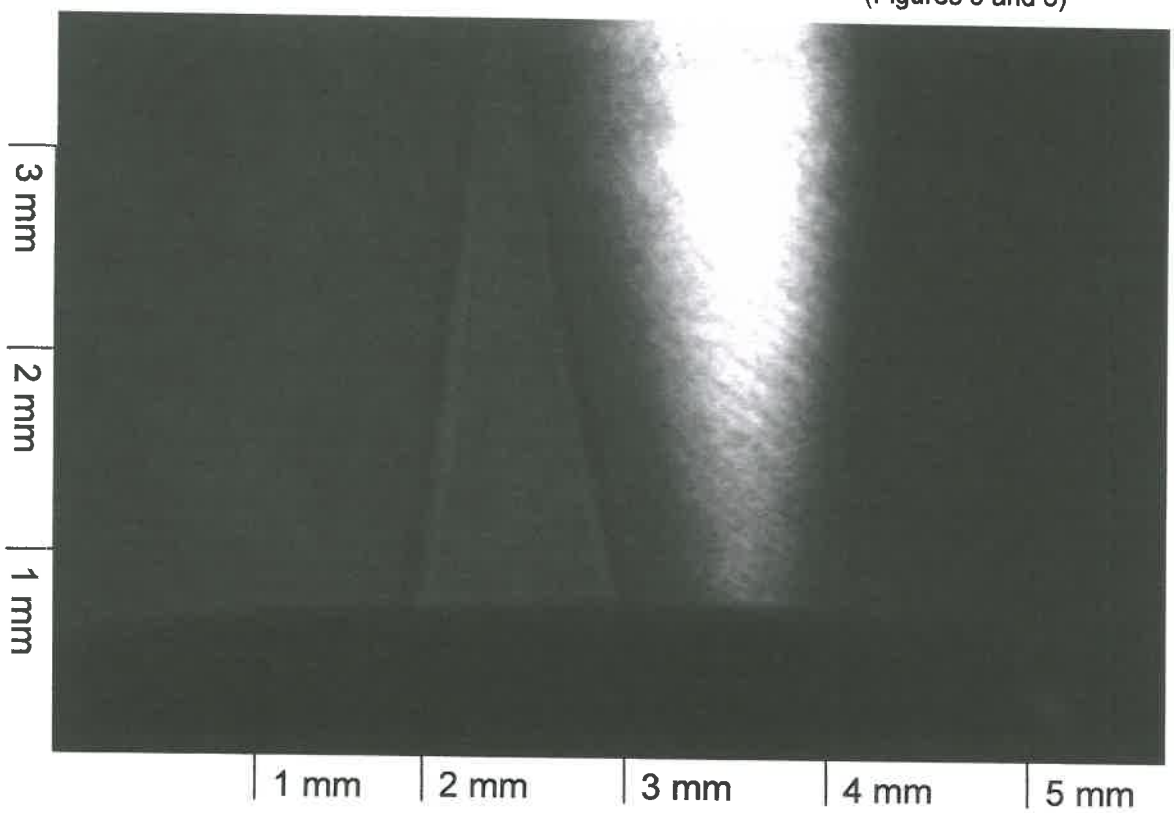

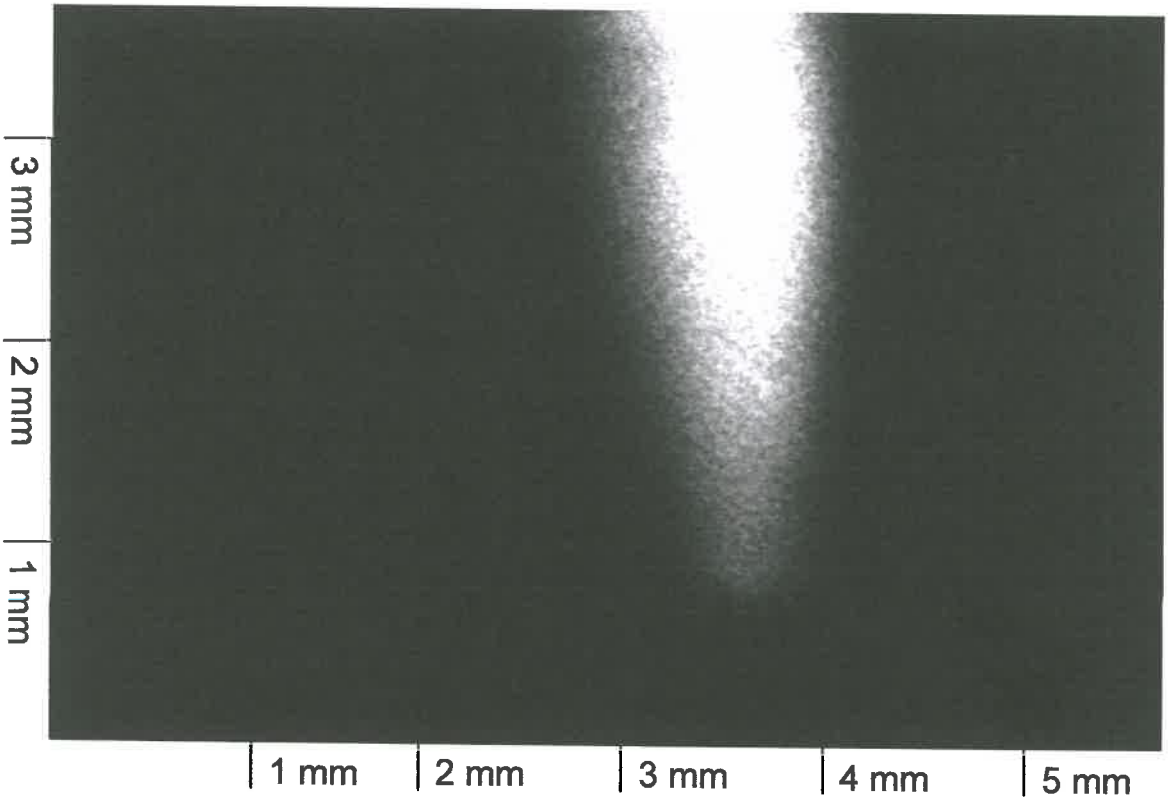

(I)

(Figures 5 and 6)

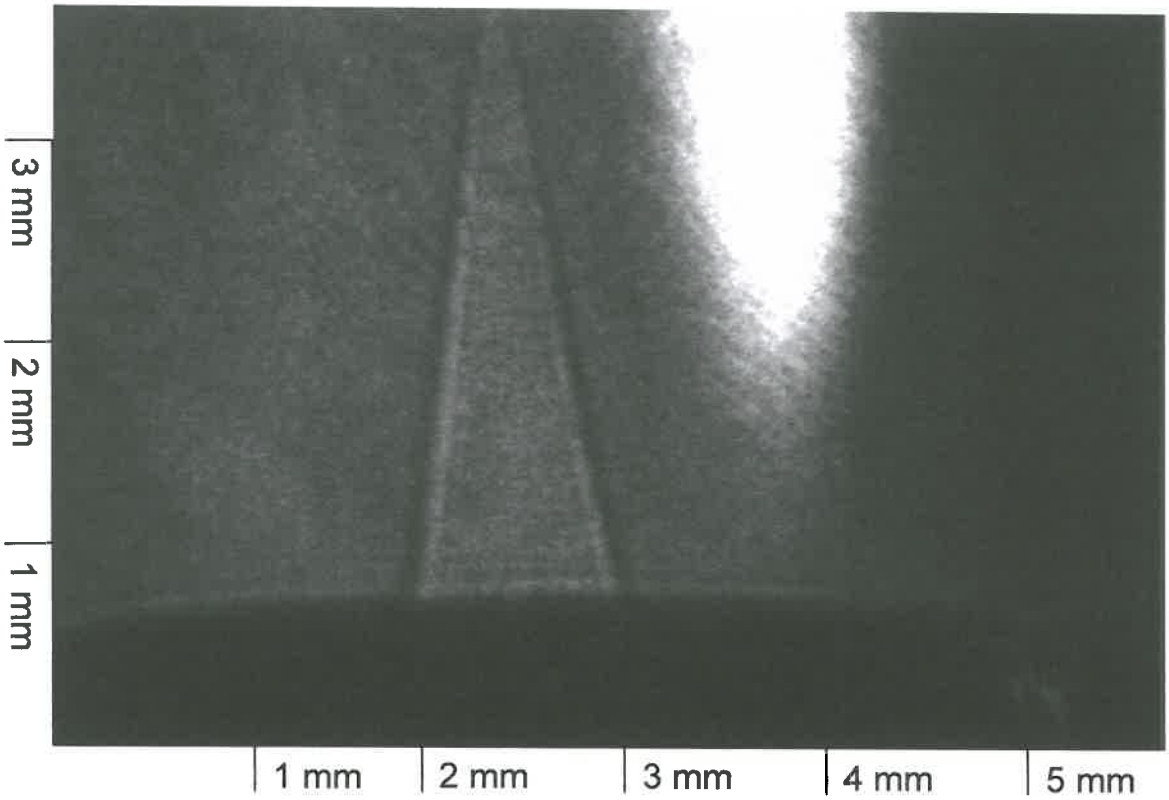

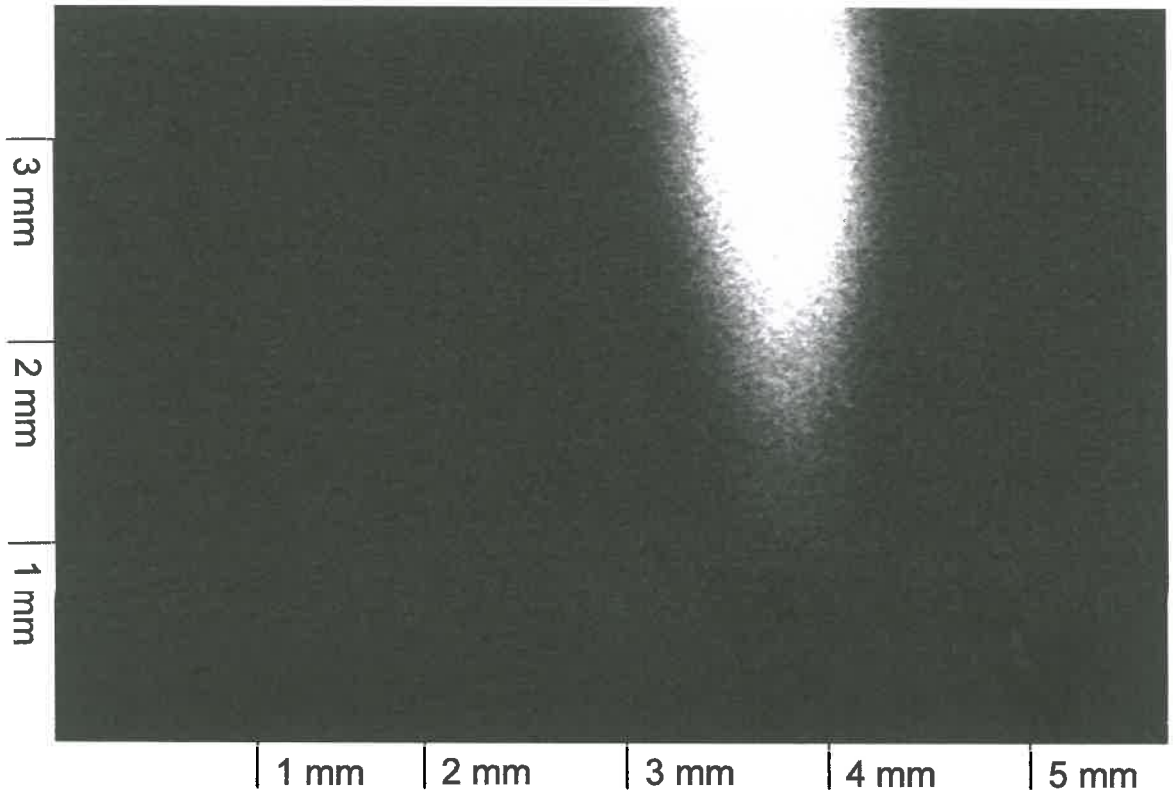

(m)

(Figures 5 and 6)

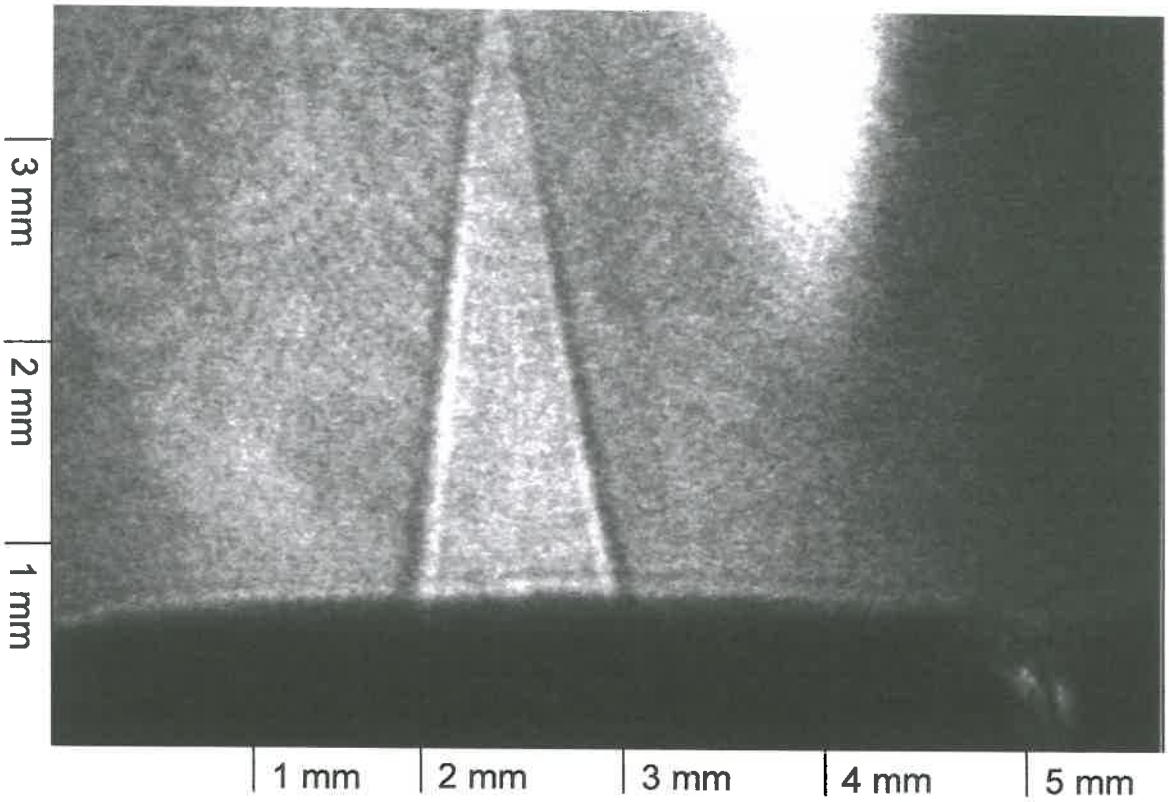

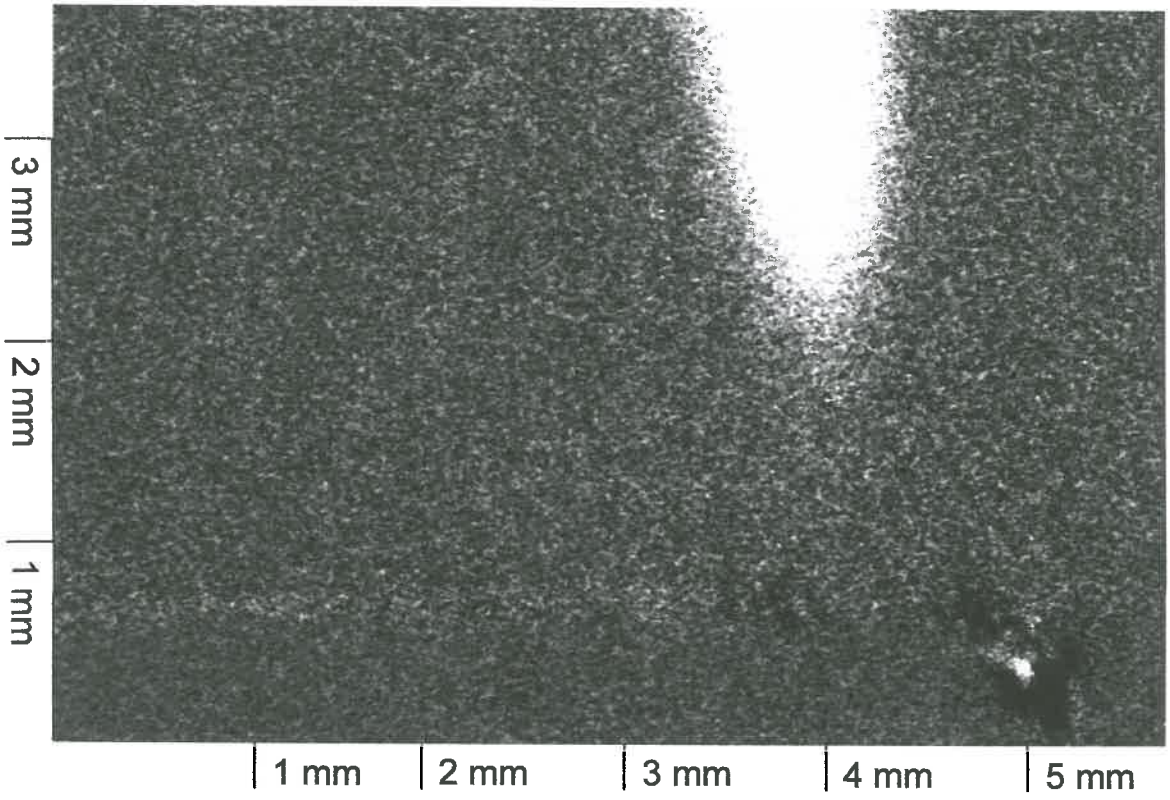

(n) (Figures 5 and 6)

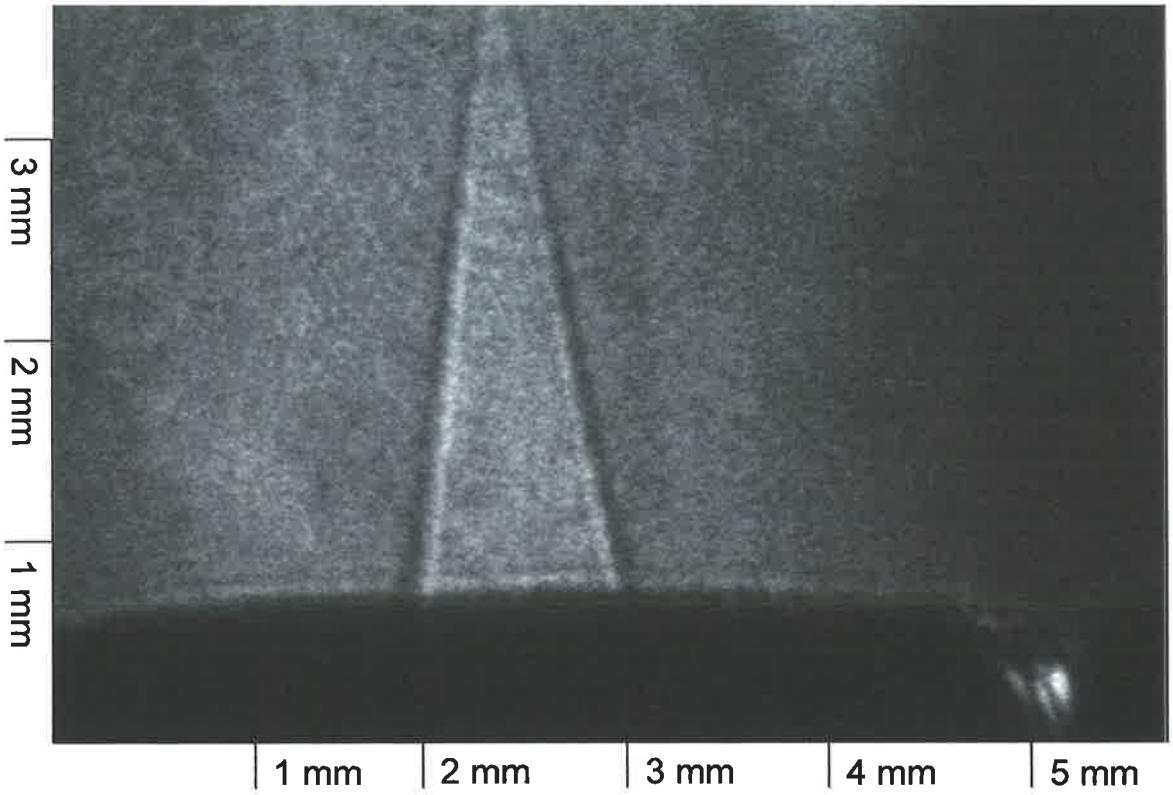

These is no corrected image in this case due to the low signal level. The image is included to illustrate the typical probe beam (flame present) background for this image set.

Figures 7 and 8: (Pages following) Set of OH PLPS images of the fuel/lean premixed natural gas/O_2 flame for a horizontally polarised pump beam and a 15° beam intersection angle. The probe beam was polarised at $\pi/4$ to the vertical. The image set was obtained by scanning the pump sheet across the tip of glass-blowing torch. The two images on each pages represent corresponding raw (top image) Mode 1 and corrected (base image) Mode 2 images. The images are plotted on a greyscale based on the 5 to 95% signal strength range of each image with black representing the lowest signal.

(a) (Figures 7 and 8)

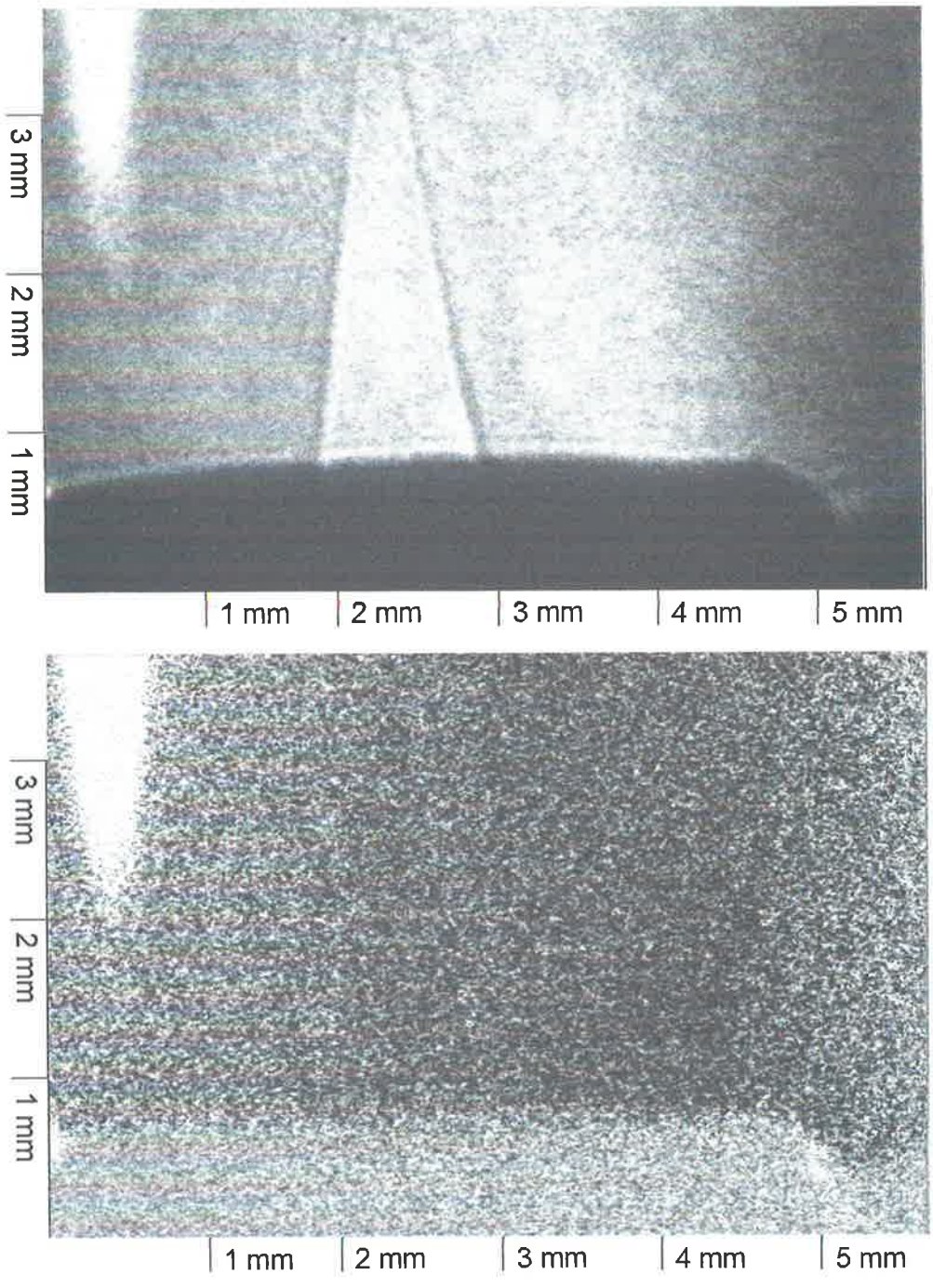

(b)

(Figures 7 and 8)

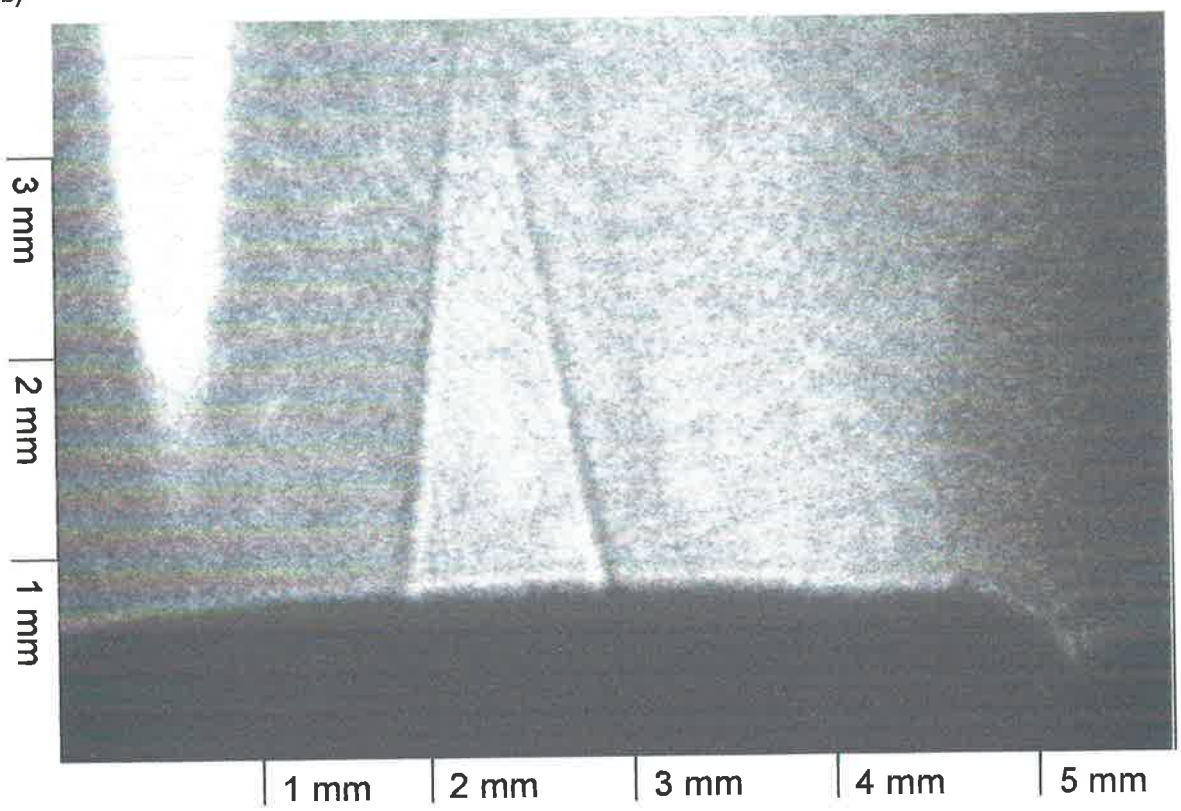

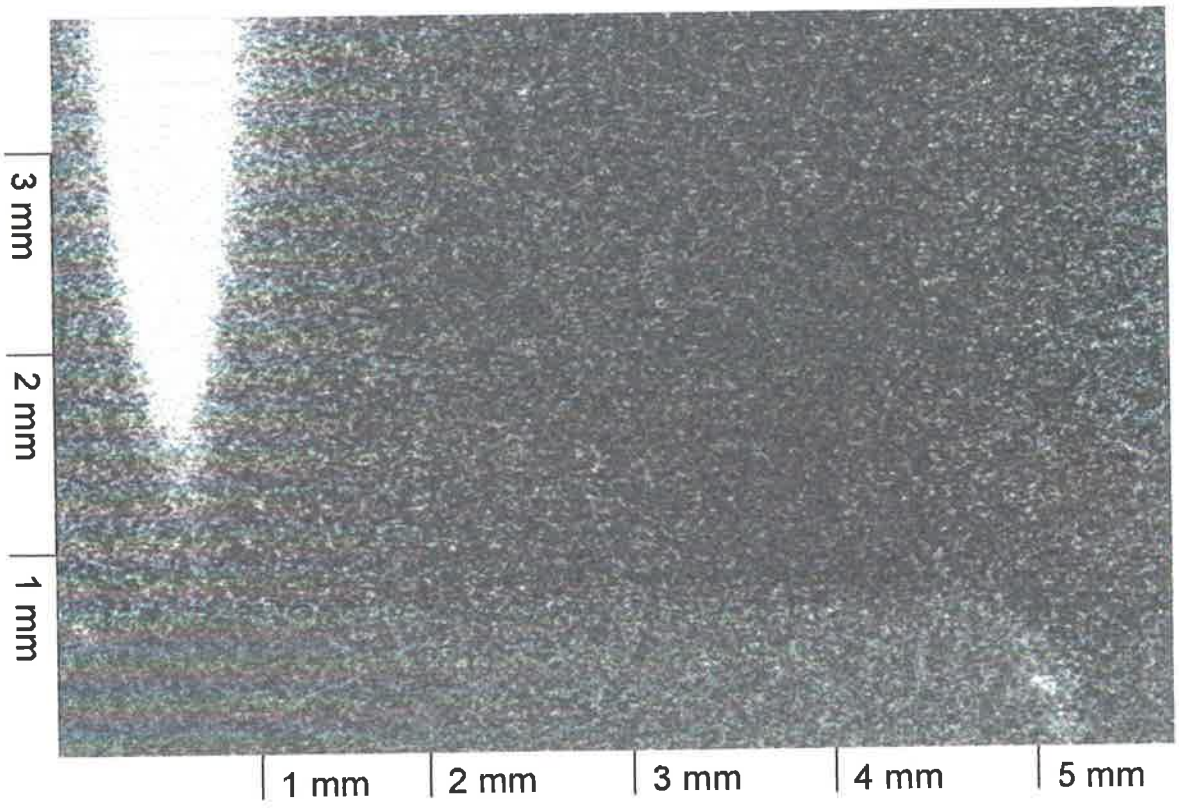

(c) (Figures 7 and 8)

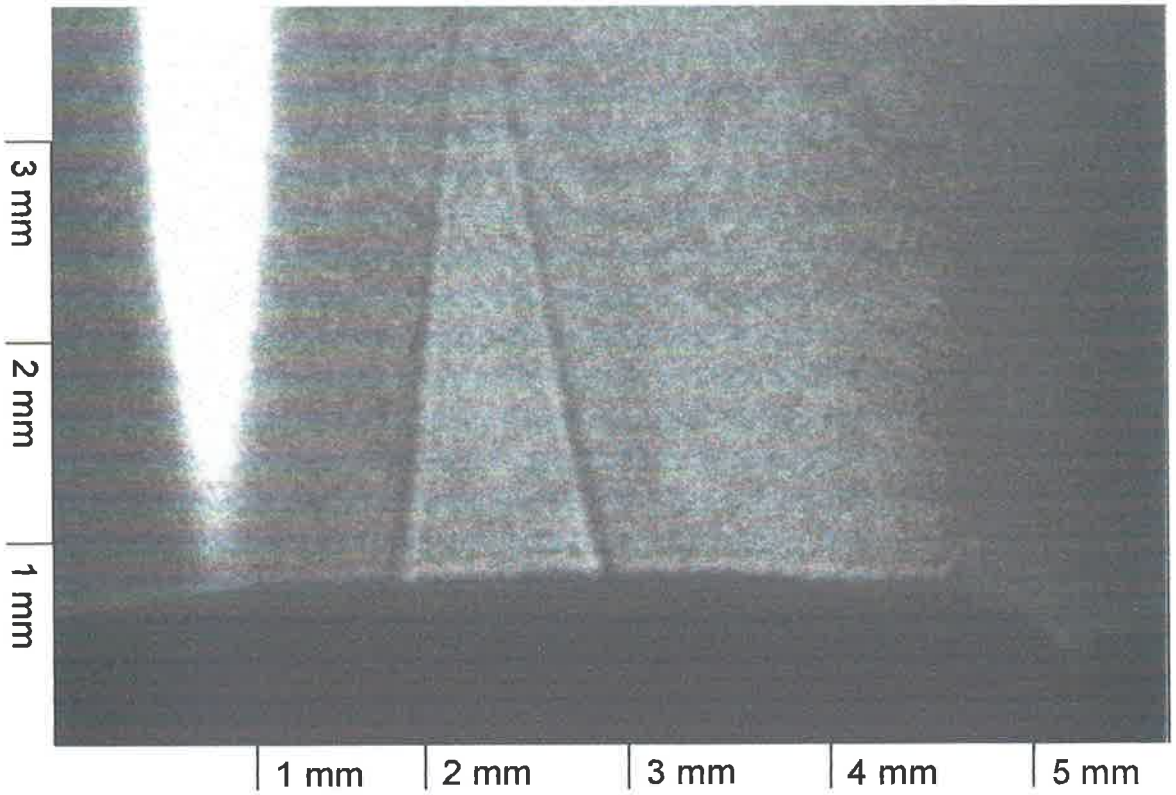

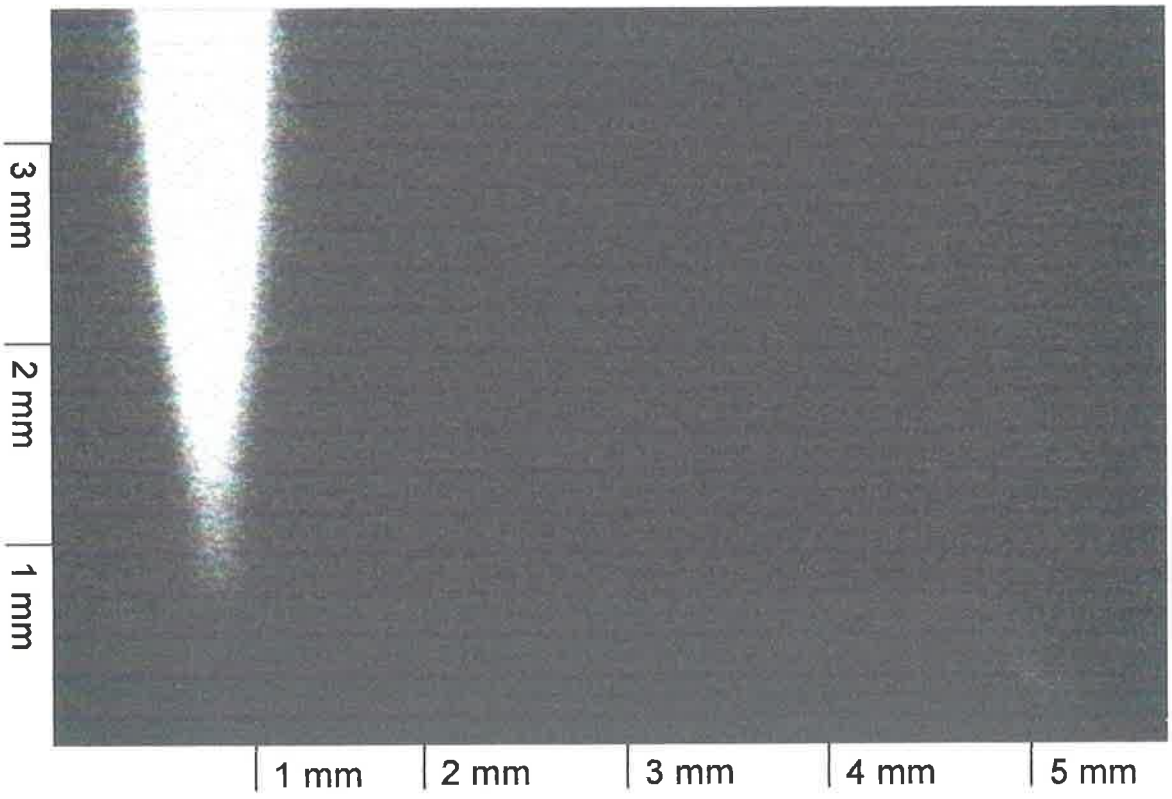

(d) (Figures 7 and 8)

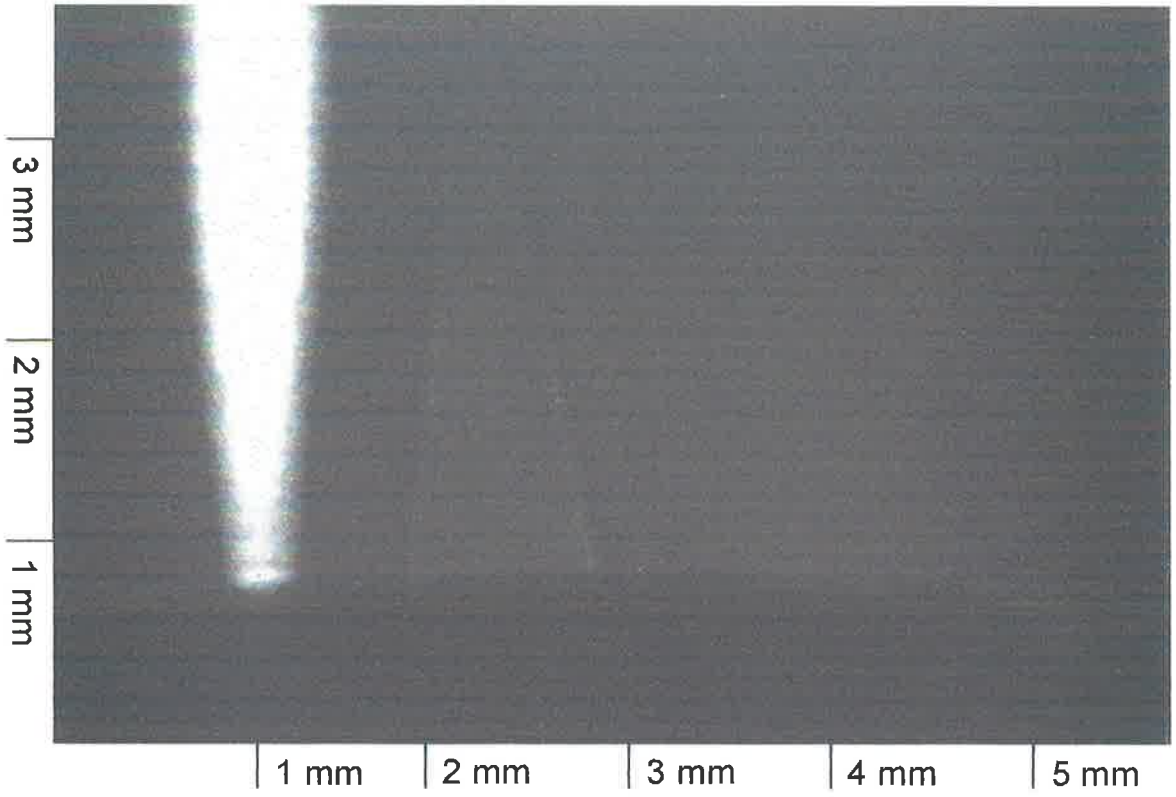

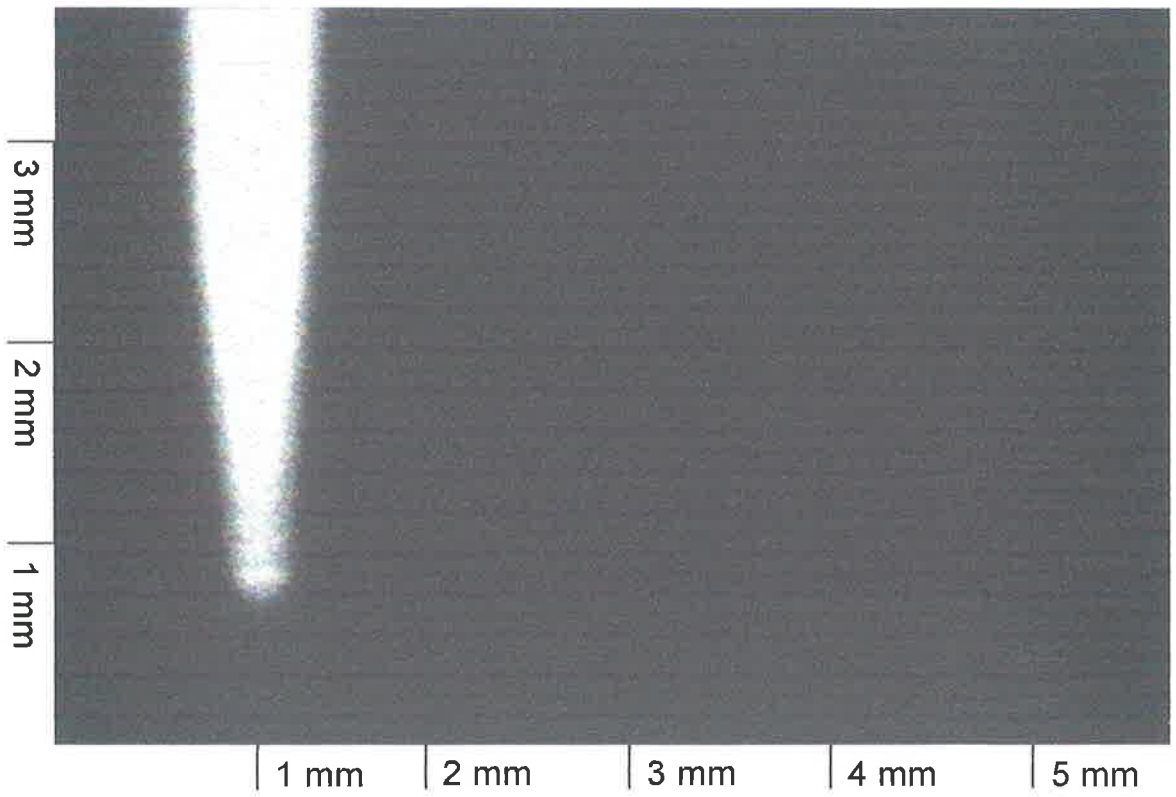

(e) (Figures 7 and 8)

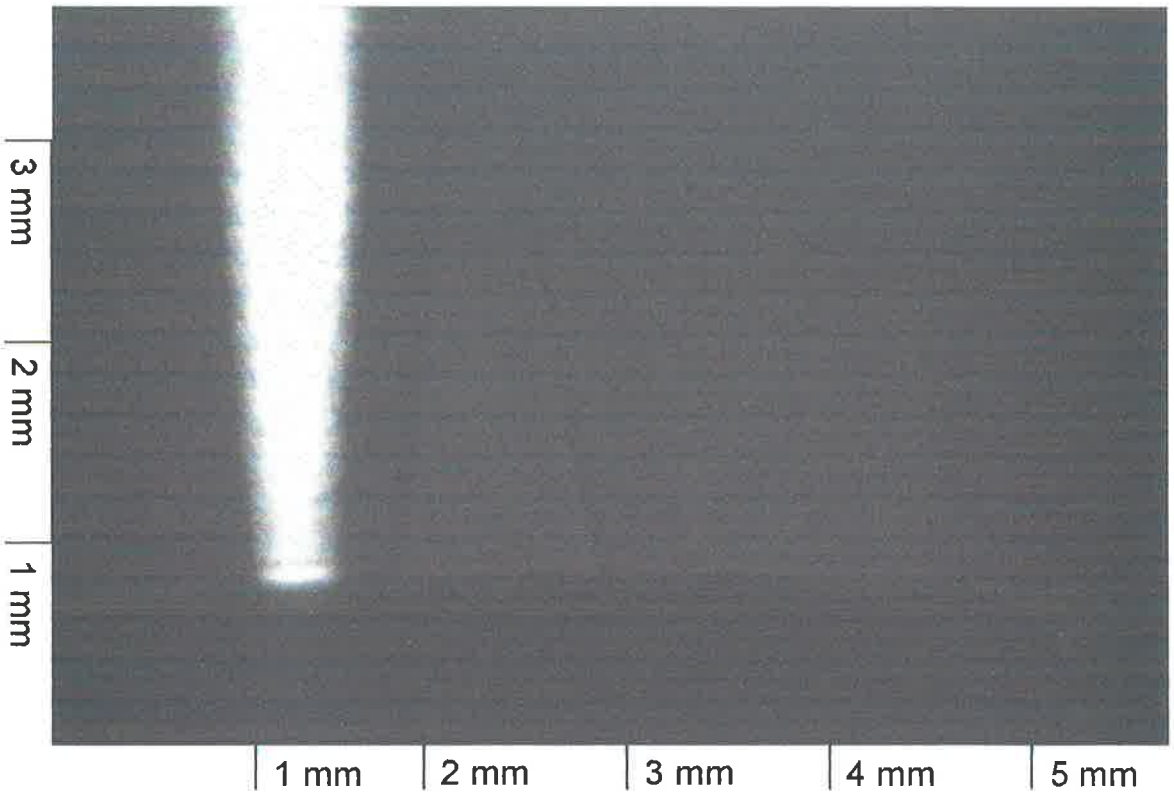

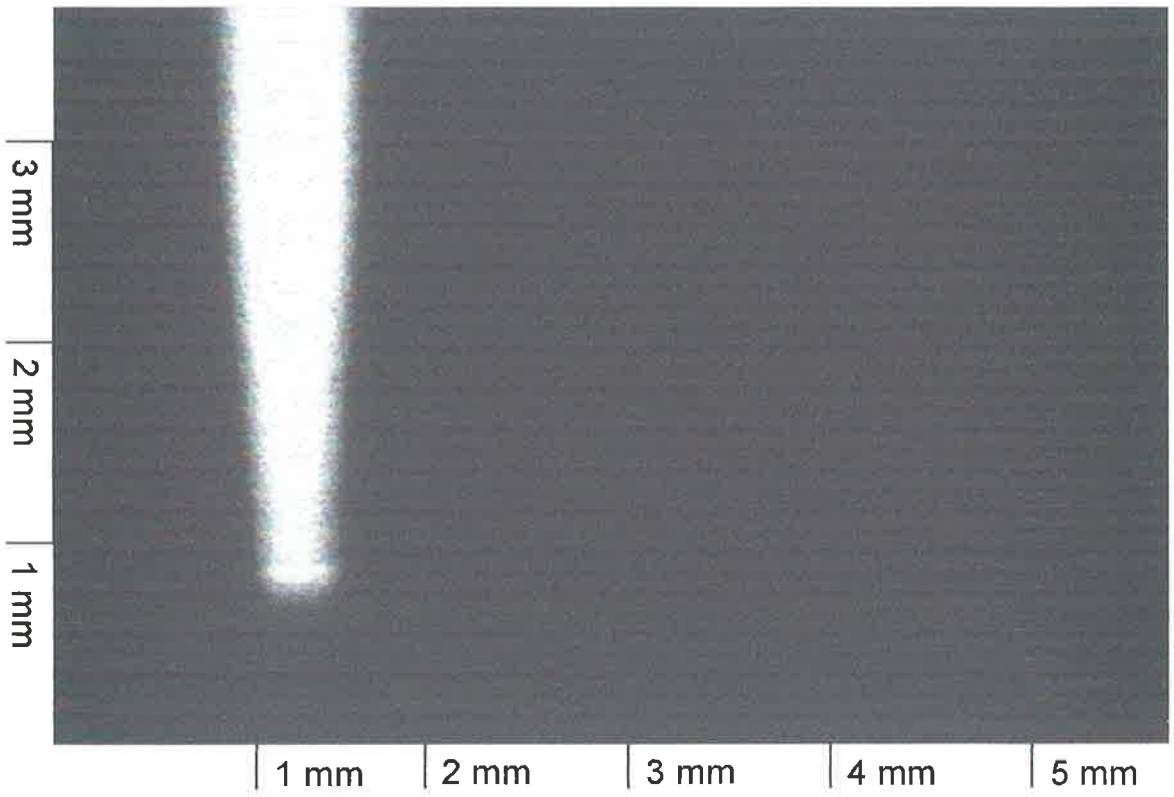

(f) (Figures 7 and 8)

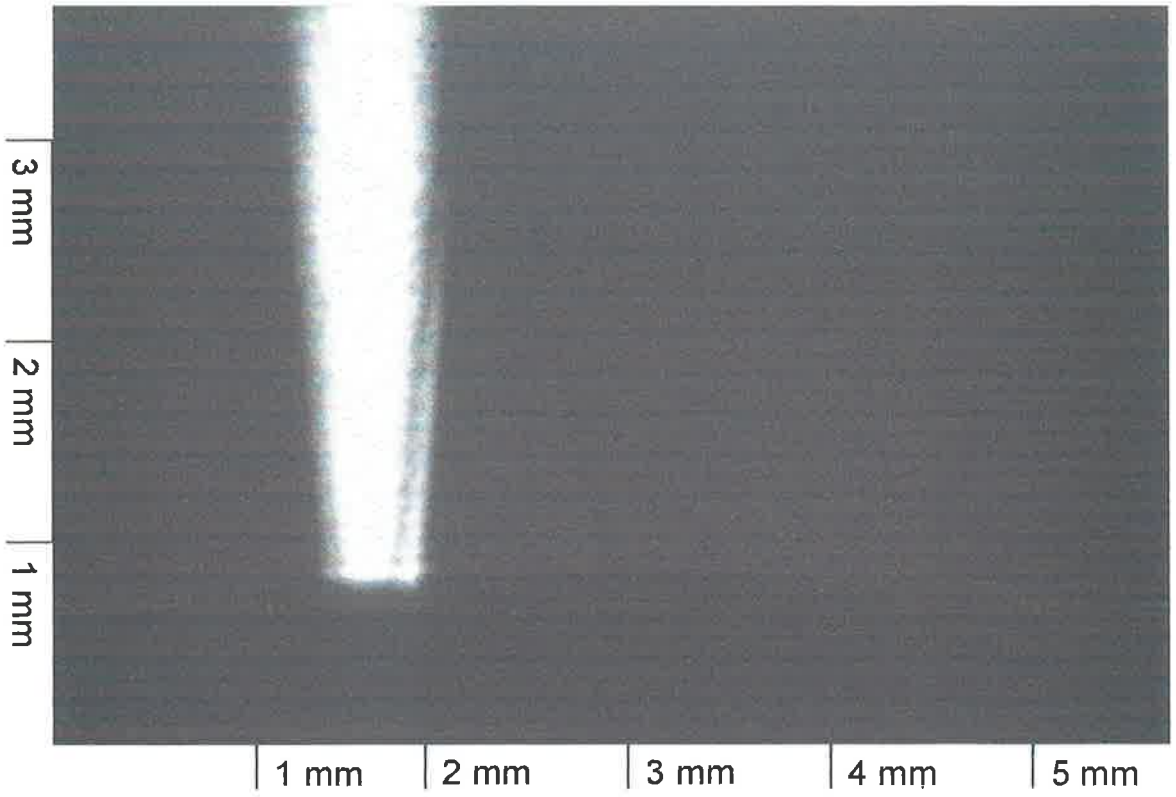

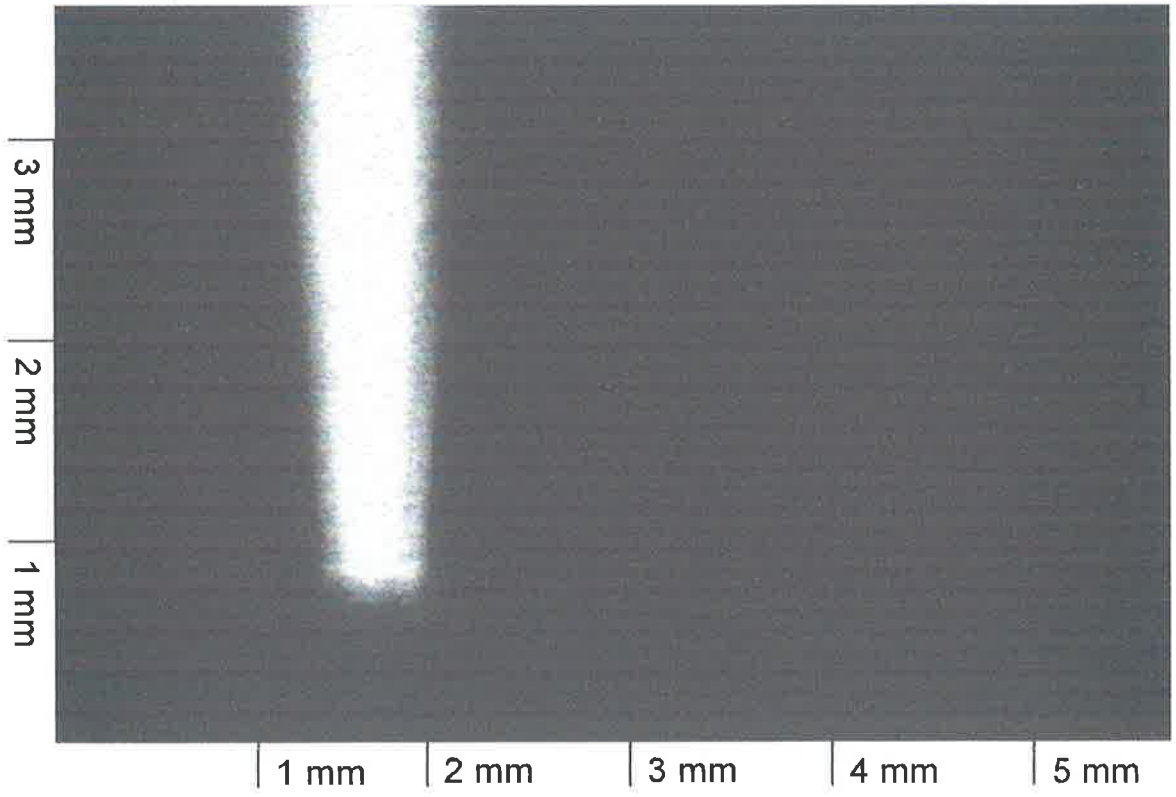

(g) (Figures 7 and 8)

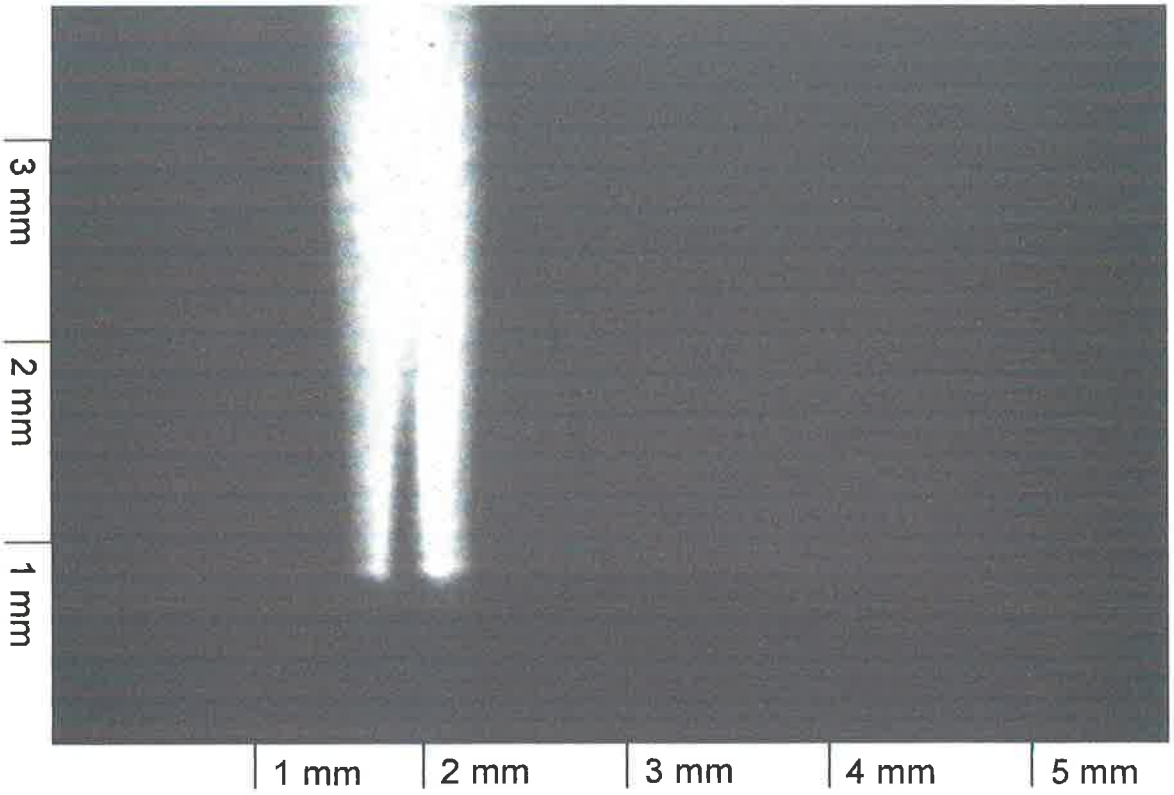

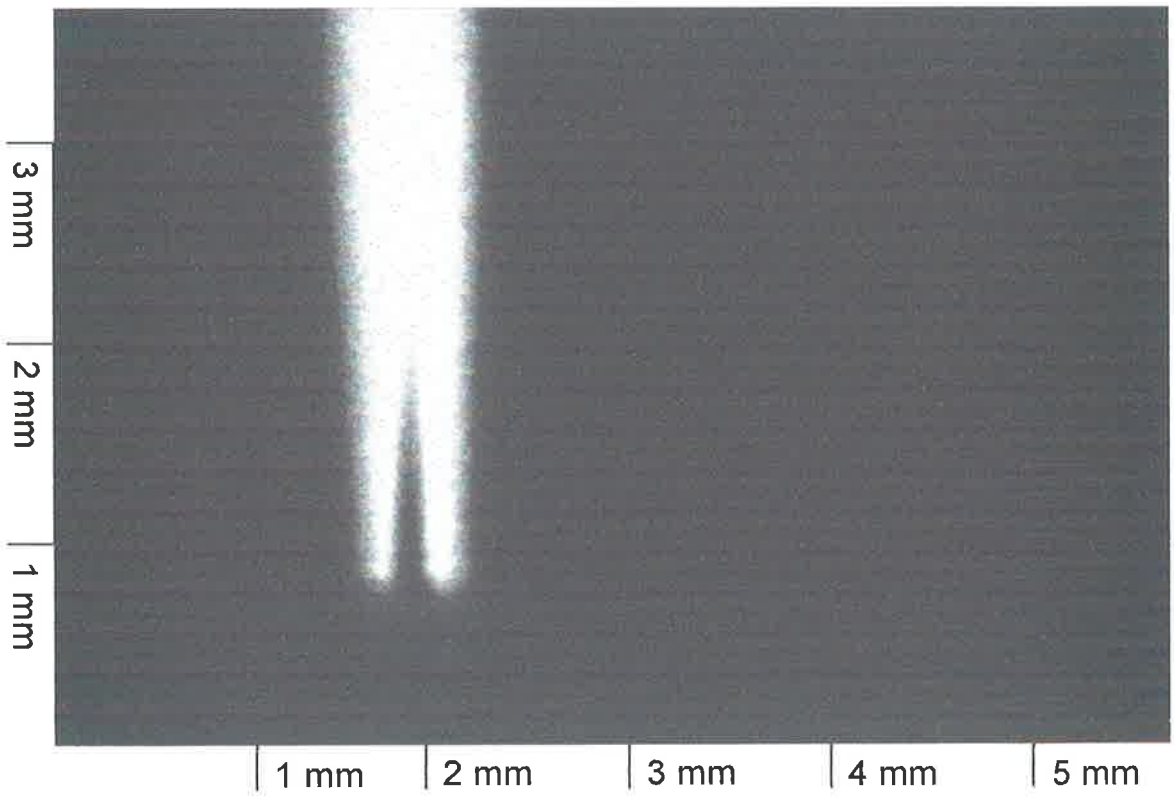

(h) (Figures 7 and 8)

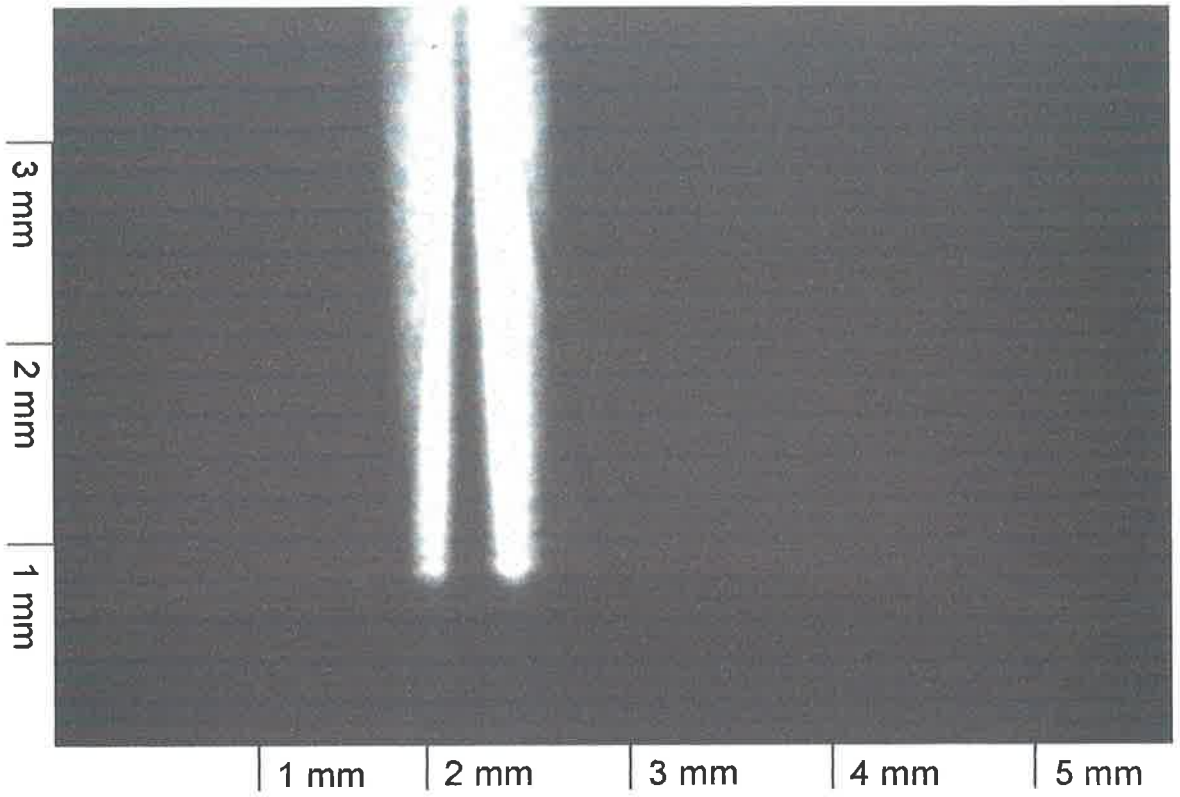

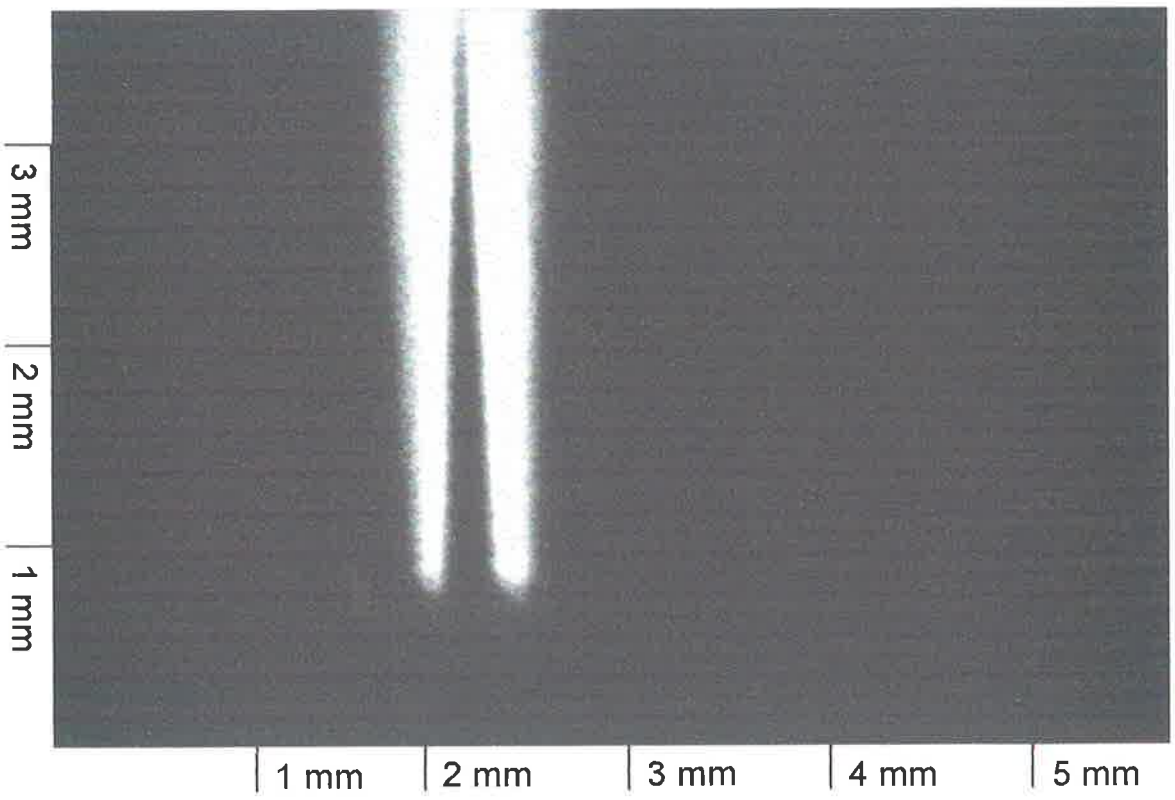

(i) (Figures 7 and 8)

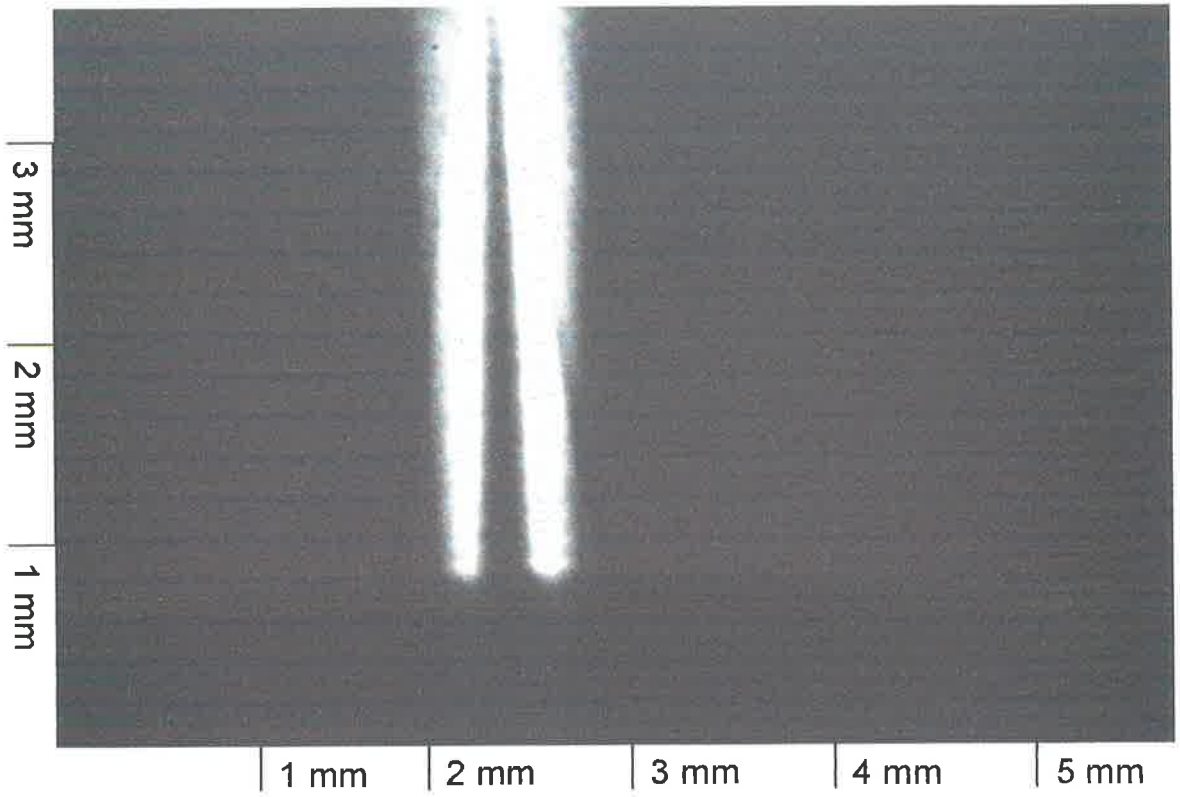

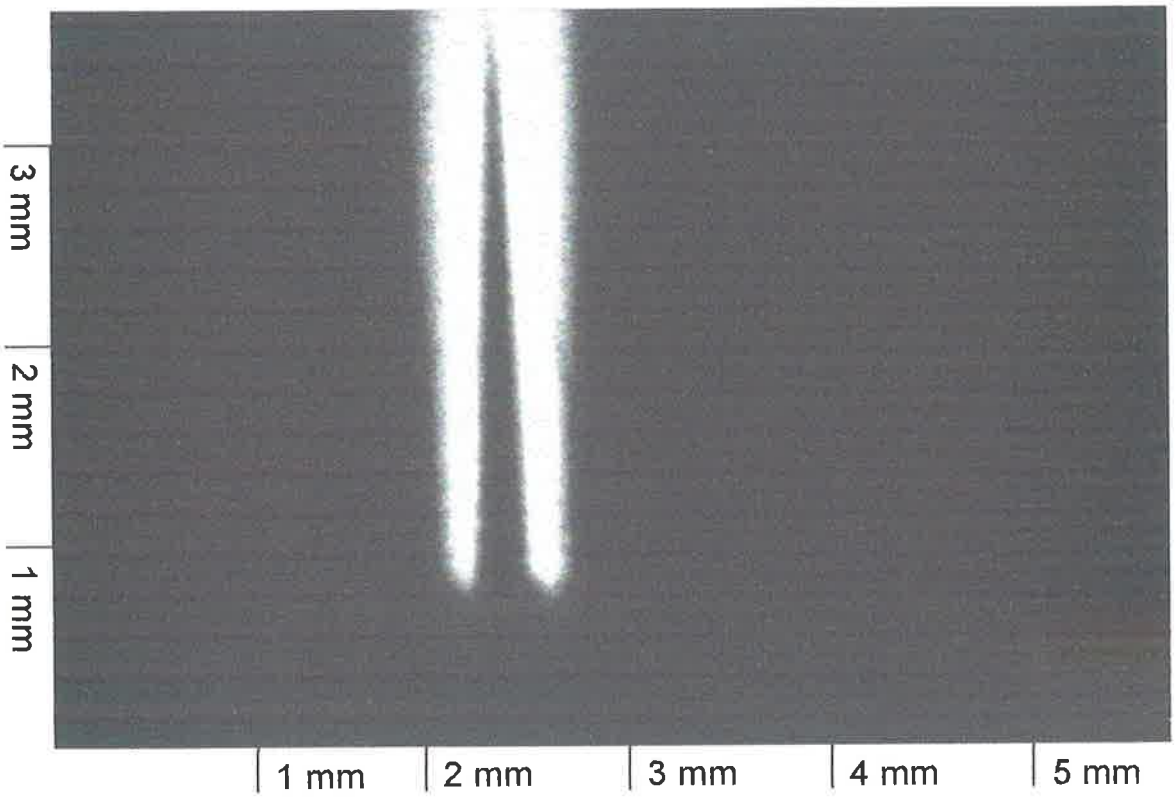

(j) (Figures 7 and 8)

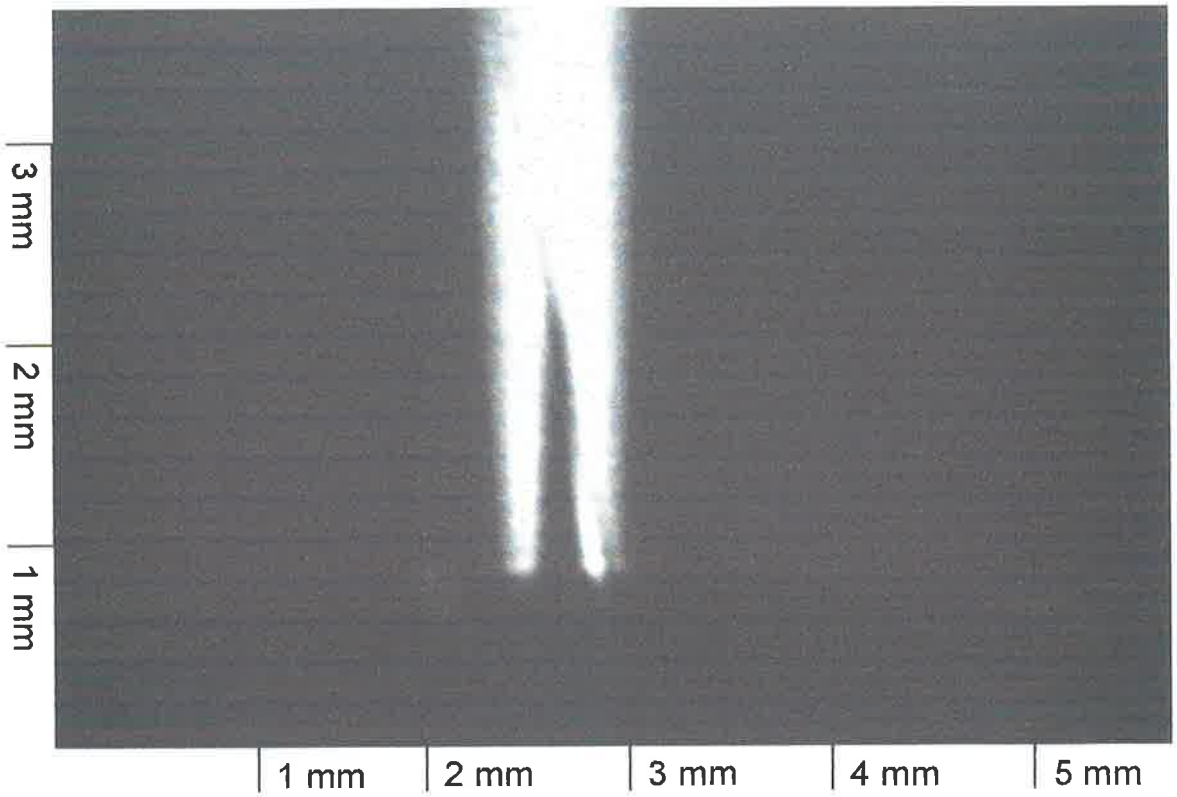

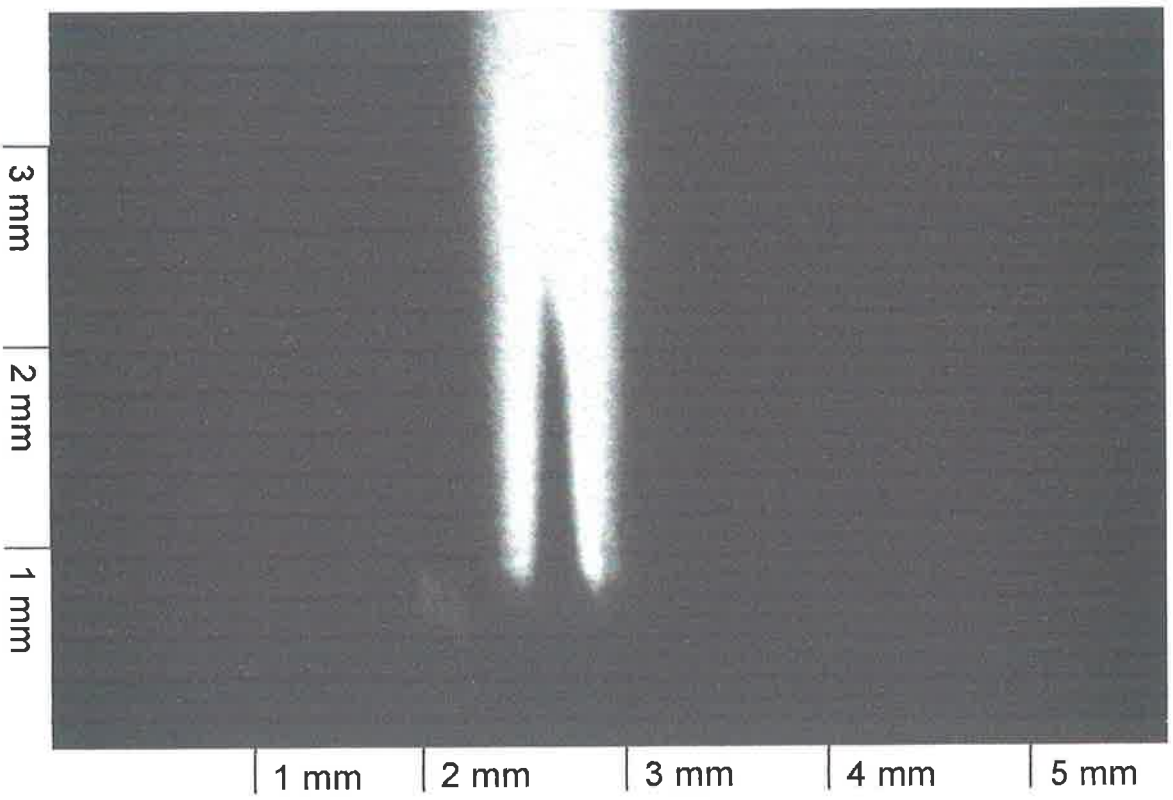

(k) (Figures 7 and 8)

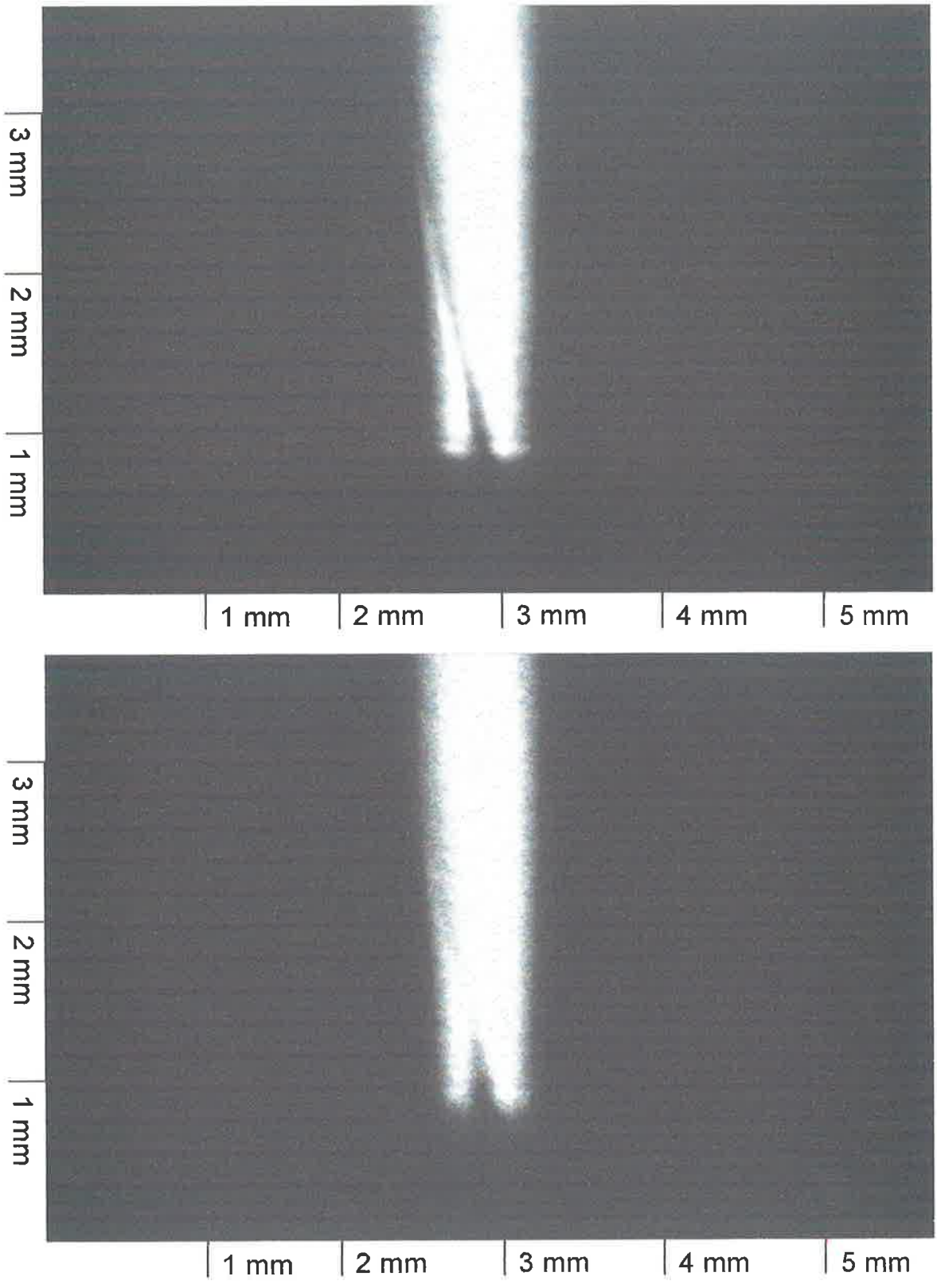

(I) (Figures 7 and 8)

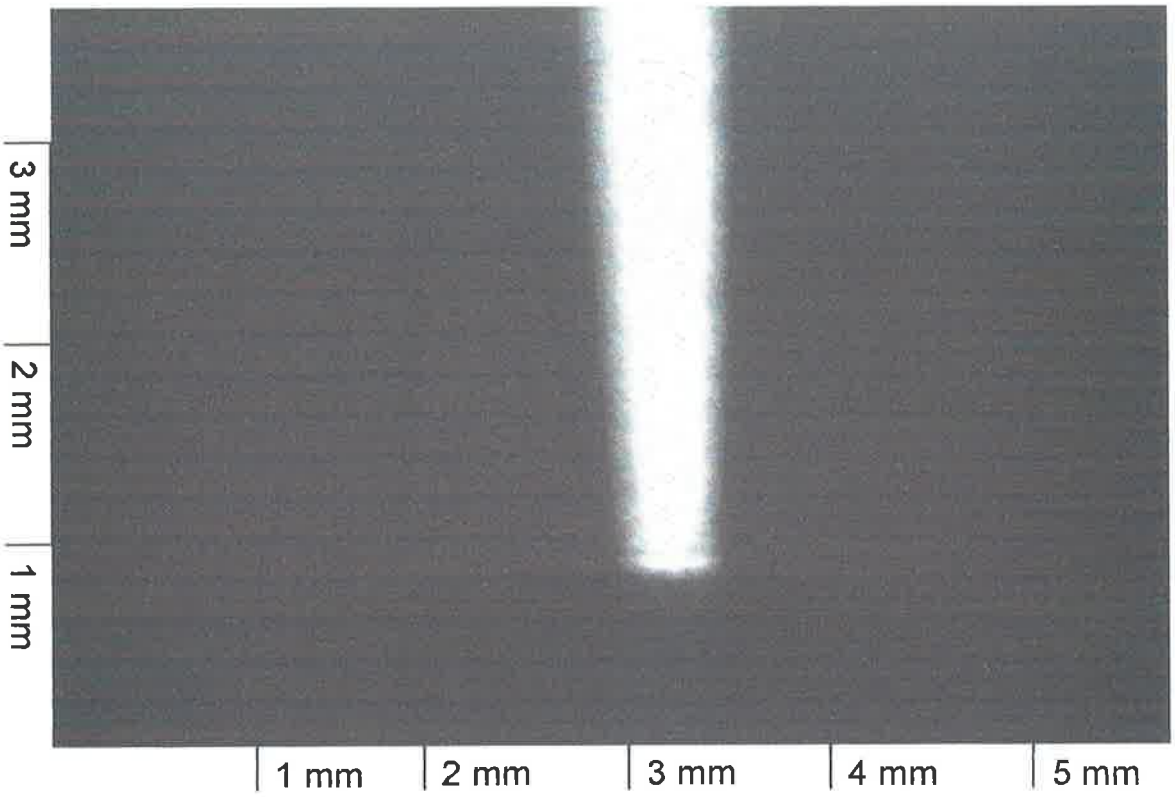

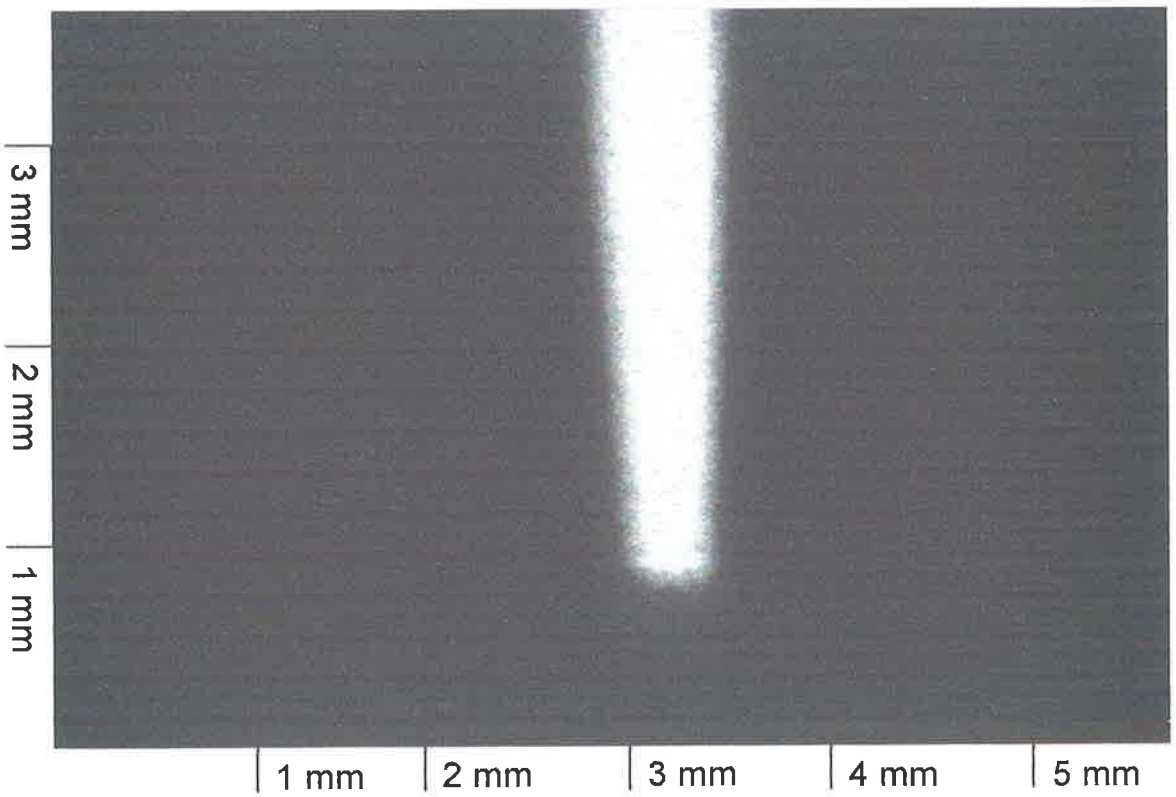

(m)

(Figures 7 and 8)

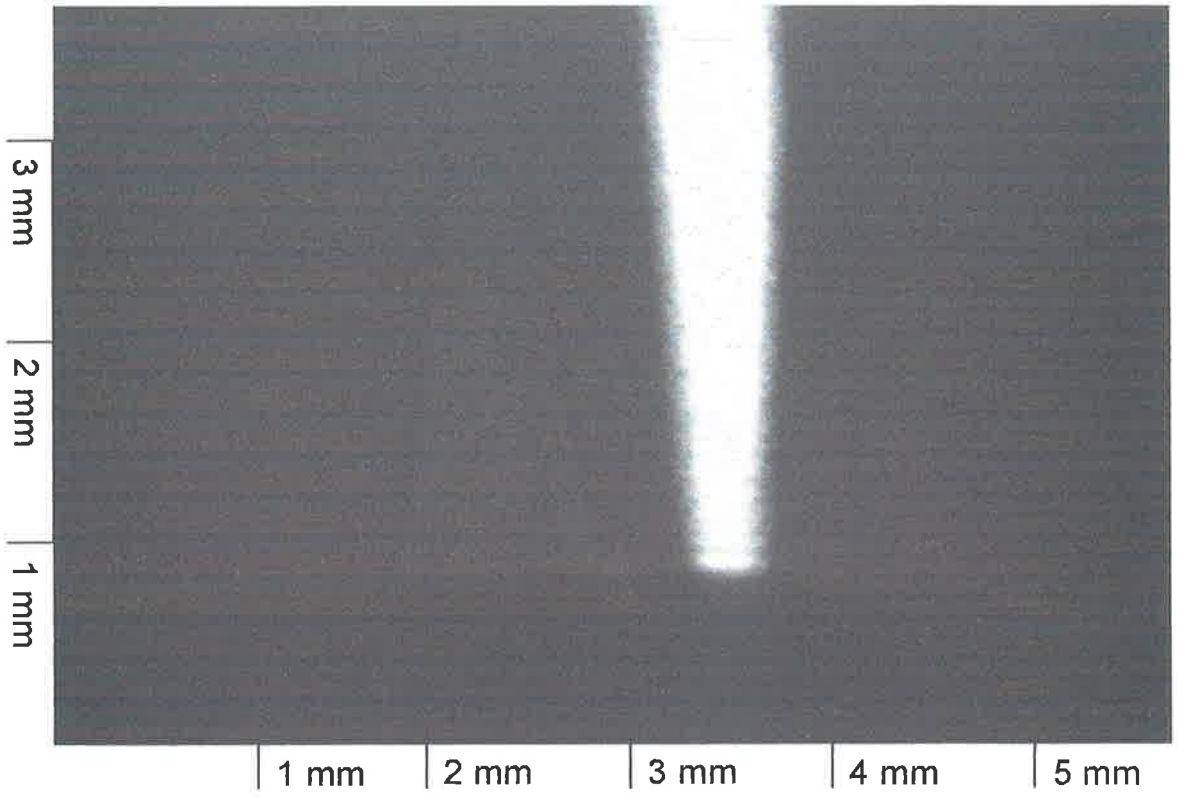

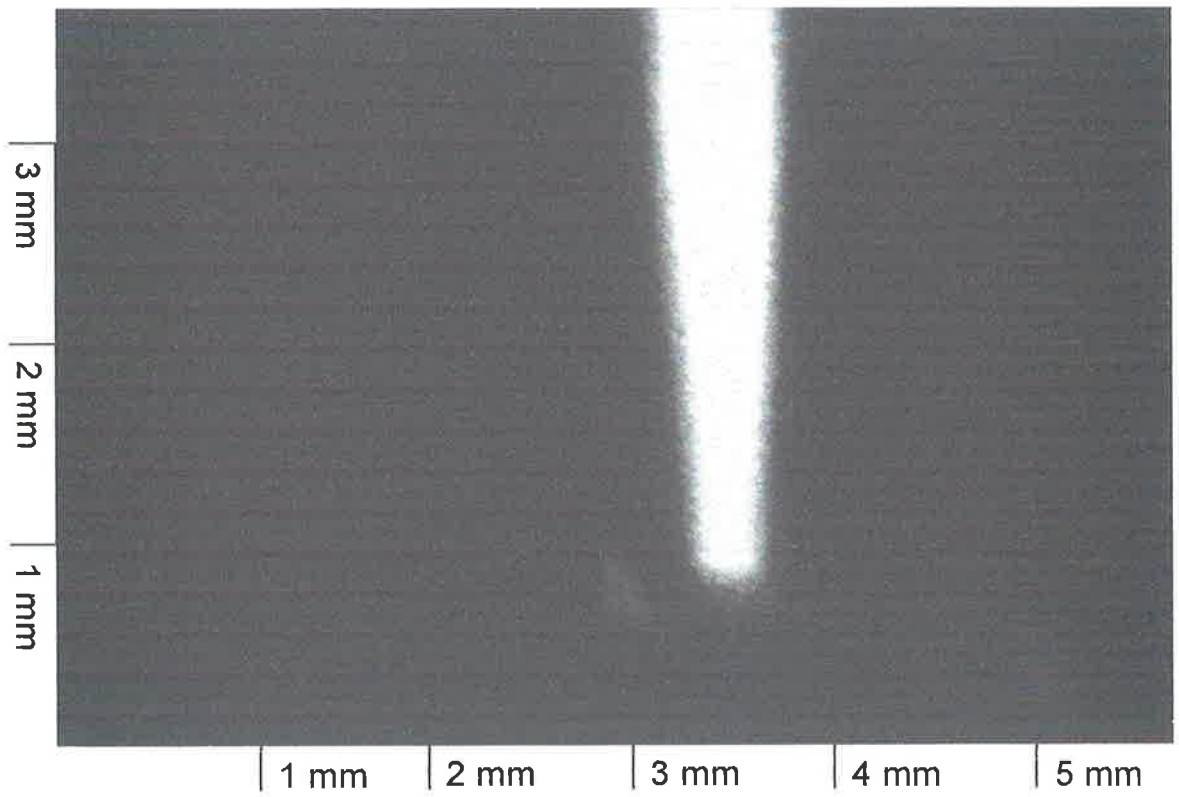

(n)

(Figures 7 and 8)

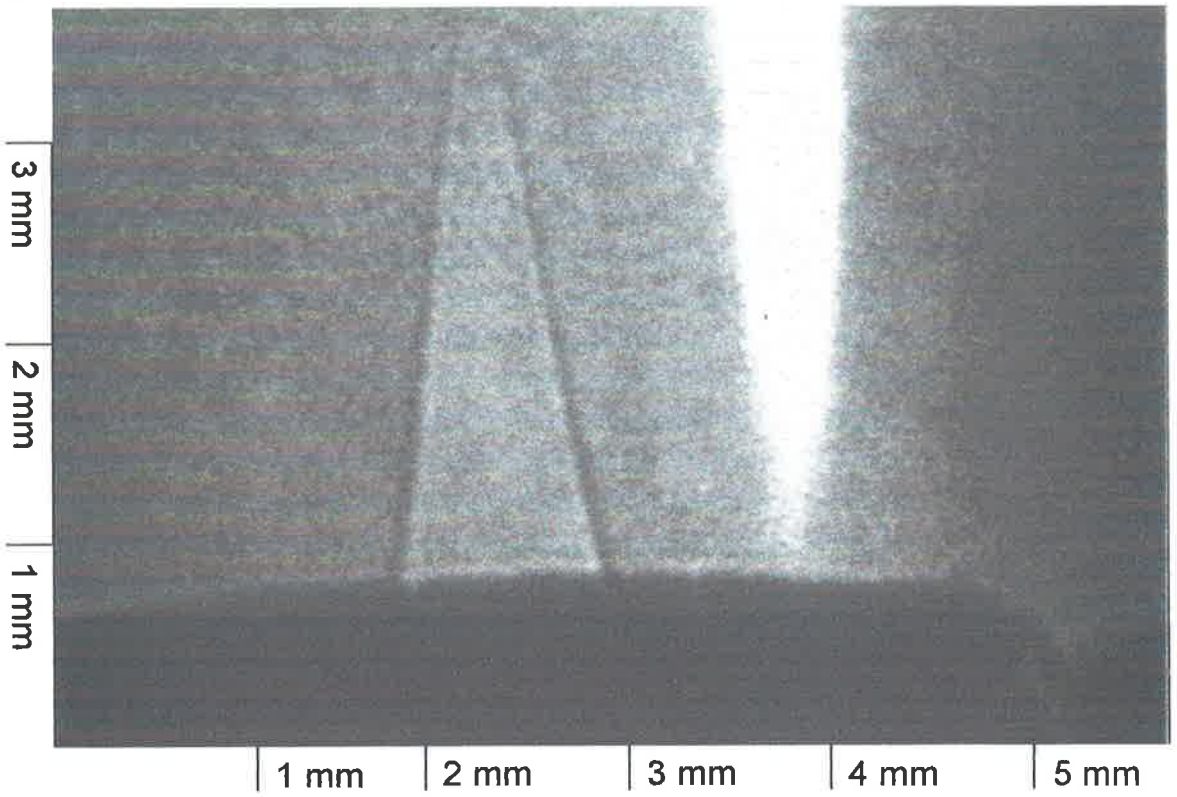

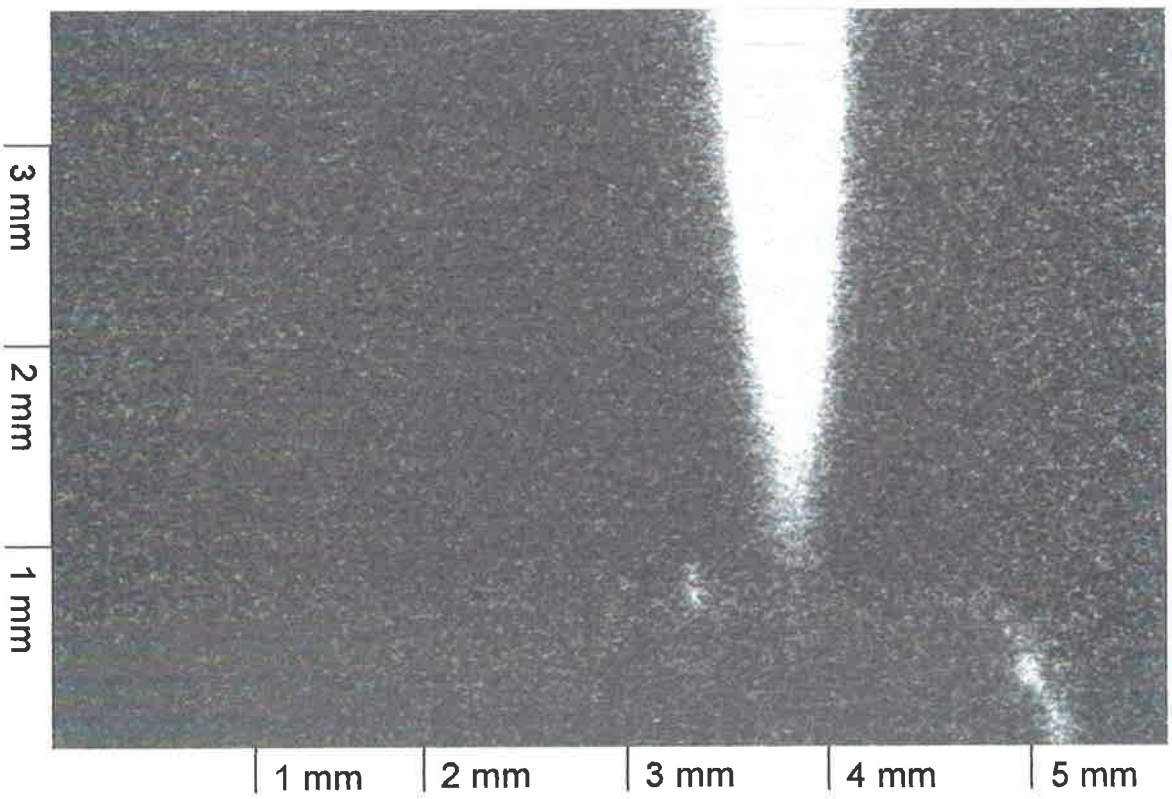

(o) (Figures 7 and 8)

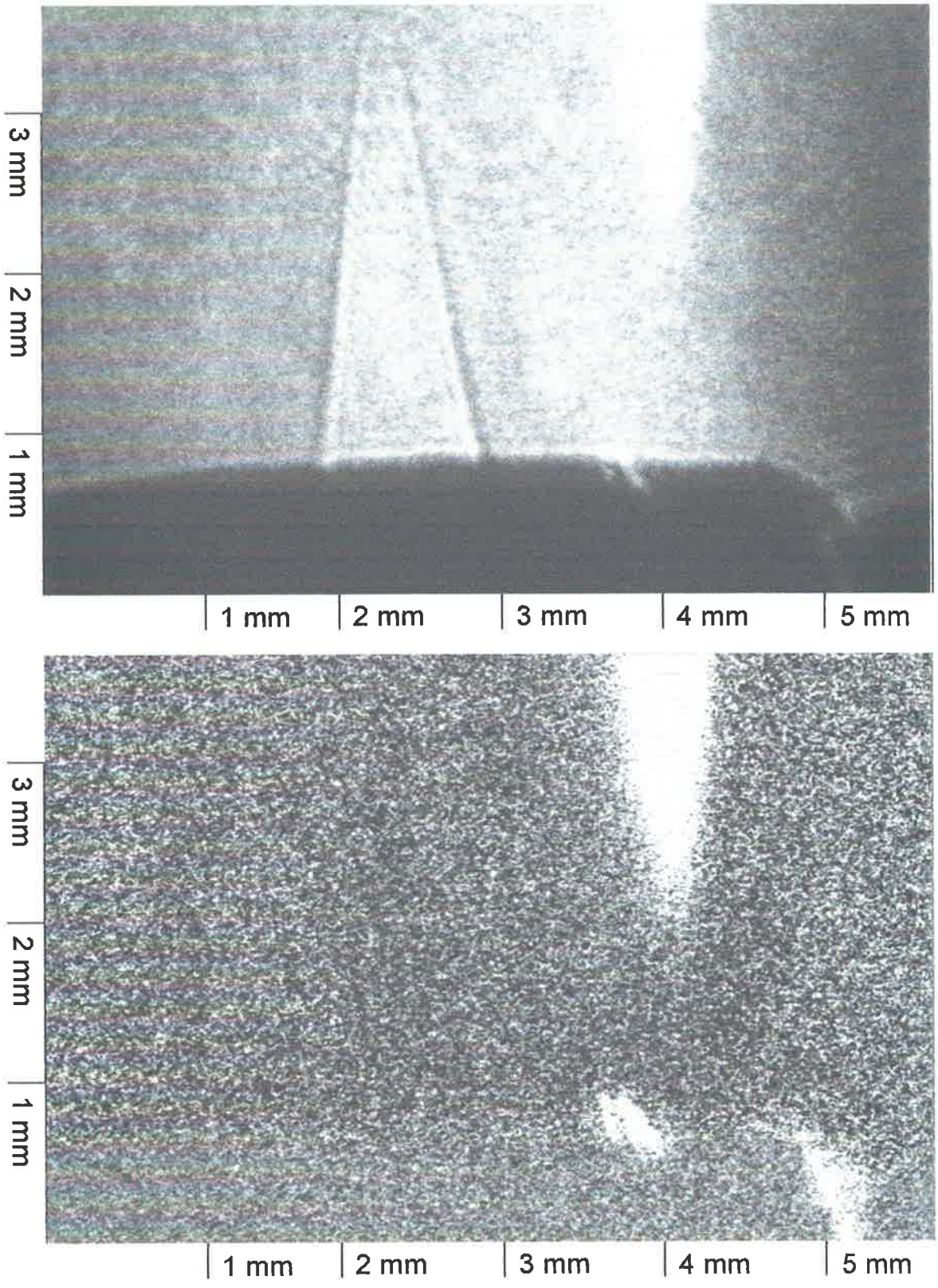

(p) (Figures 7 and 8)

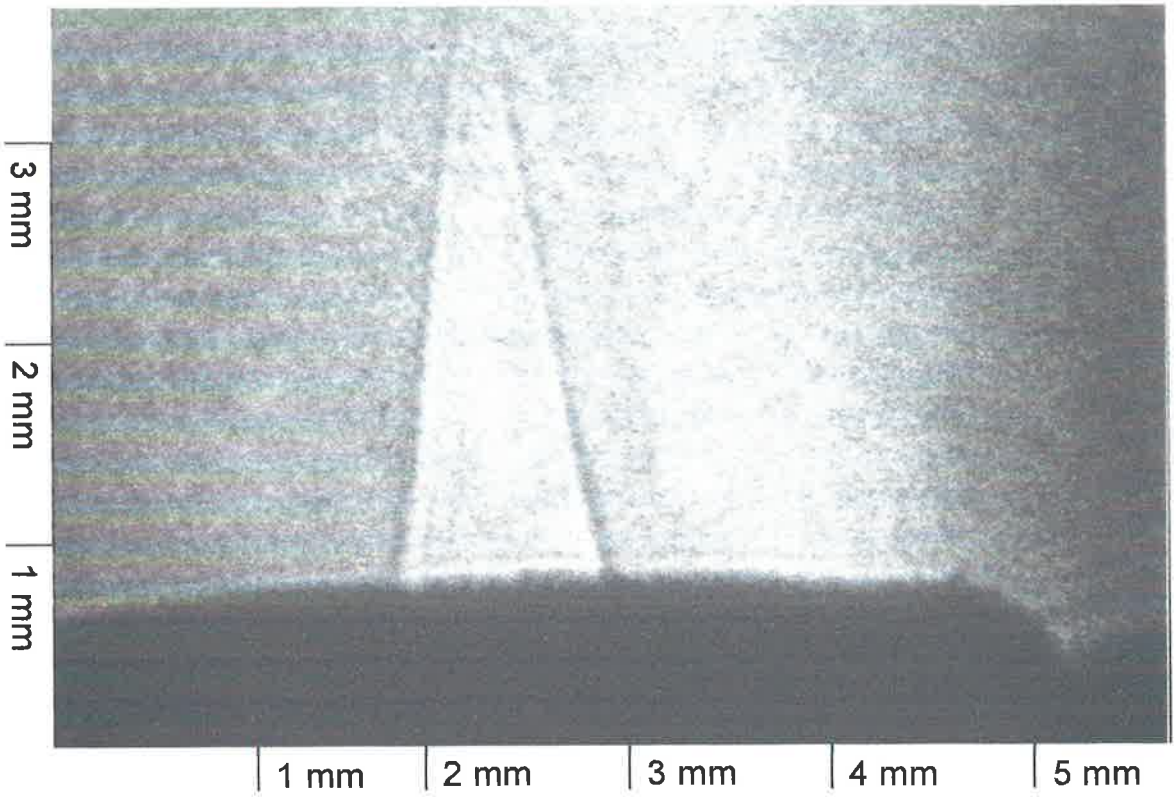

These is no corrected image in this case due to the low signal level. The image is included to illustrate the typical probe beam (flame present) background for this image set.

Figure 9: (Pages following) Set of OH PLPS images of the fuel/lean premixed natural gas/O_2 flame for a horizontally polarised pump beam and a 30° pump/probe beam intersection angle. The probe beam is polarised at $\pi/4$ to the vertical. The image set corresponds to the stretched Mode 2 image set of Figure 3 obtained by scanning the pump sheet across the tip of glass-blowing torch. The images are plotted on a greyscale based on the 5 to 95% signal strength range of each image with black representing the lowest signal.

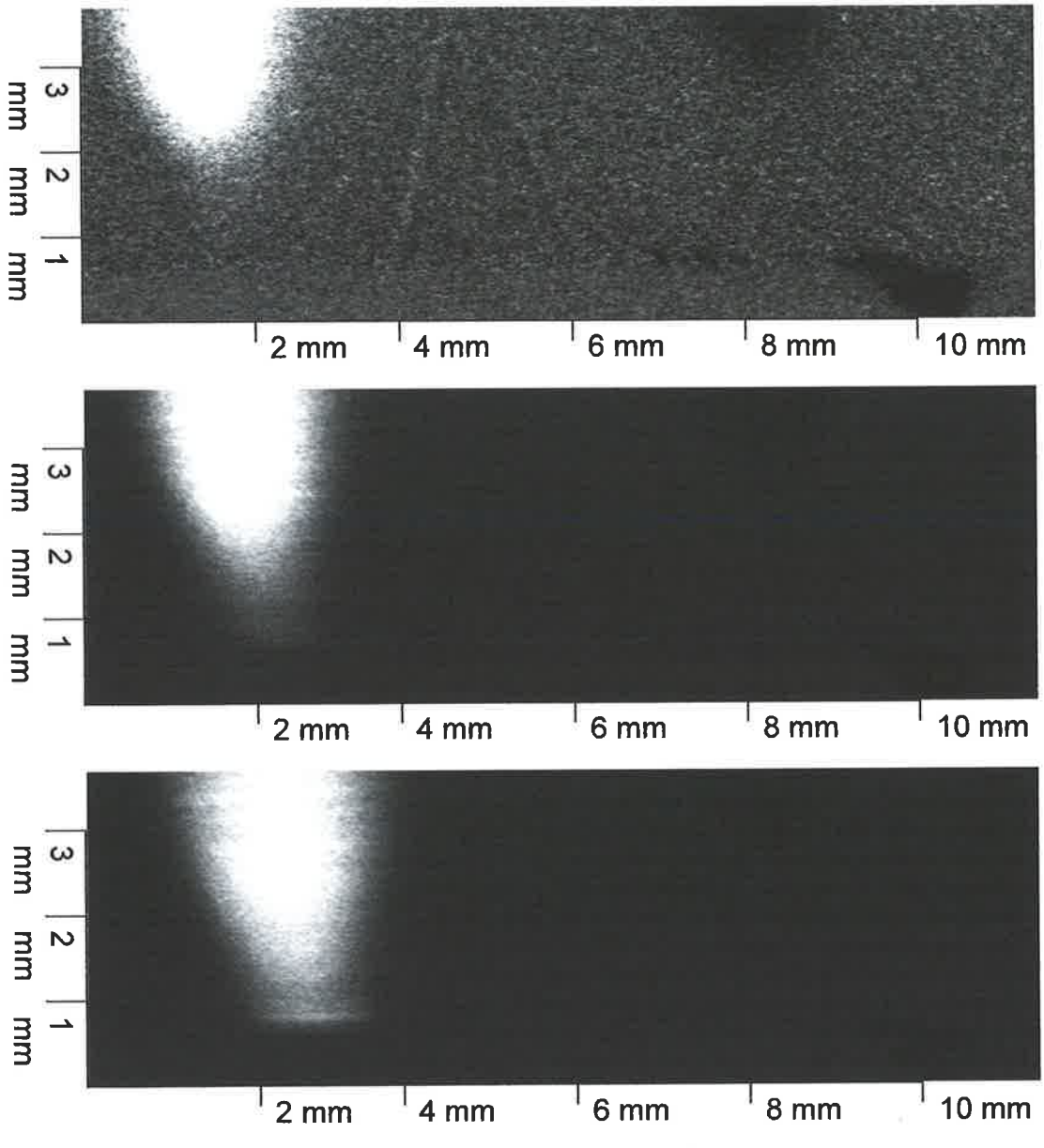

(Figure 9)

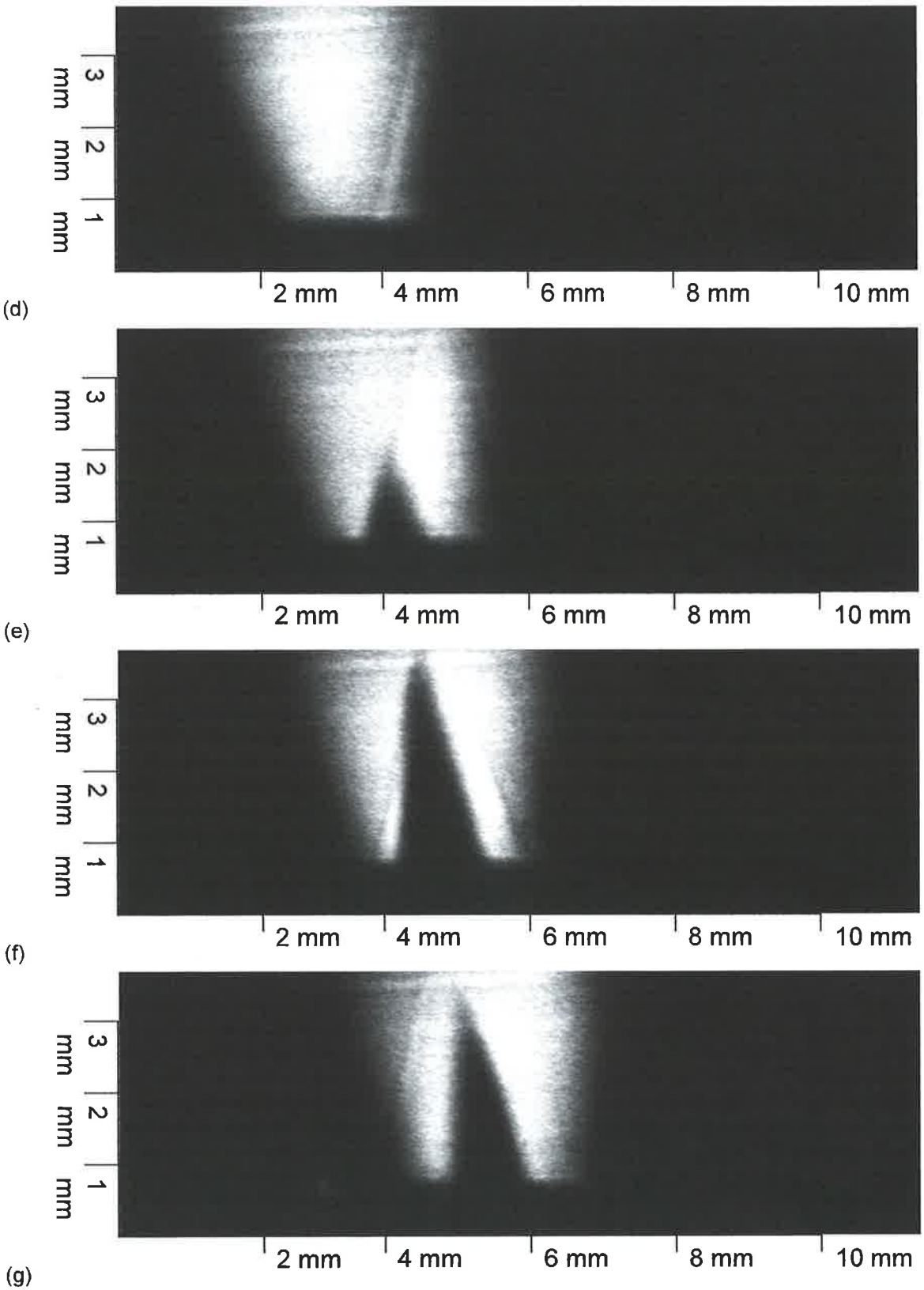
(d)
3 mm
2 mm
1 mm
2 mm
4 mm
6 mm
8 mm
10 mm
(e)
3 mm
2 mm
1 mm
2 mm
4 mm
6 mm
8 mm
10 mm
(f)
3 mm
2 mm
1 mm
2 mm
4 mm
6 mm
8 mm
10 mm
(g)
3 mm
2 mm
1 mm
2 mm
4 mm
6 mm
8 mm
10 mm

(Figure 9)

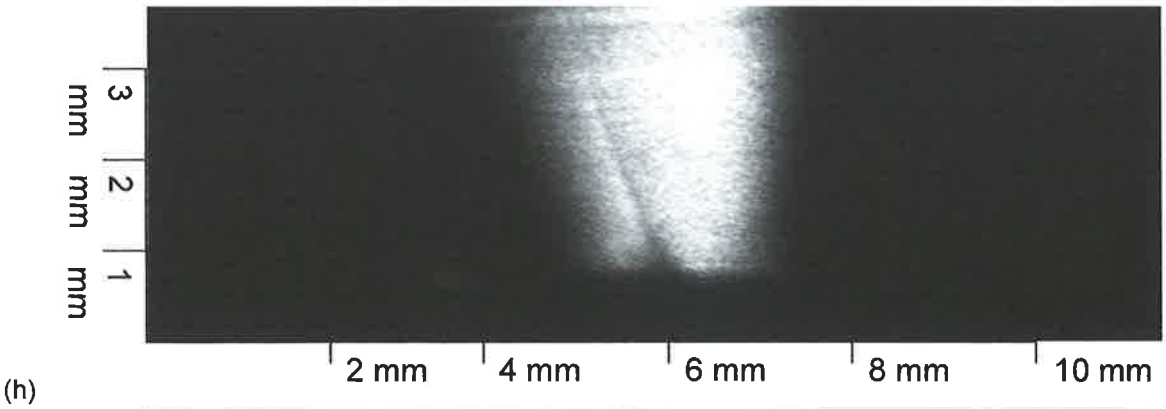

(h)

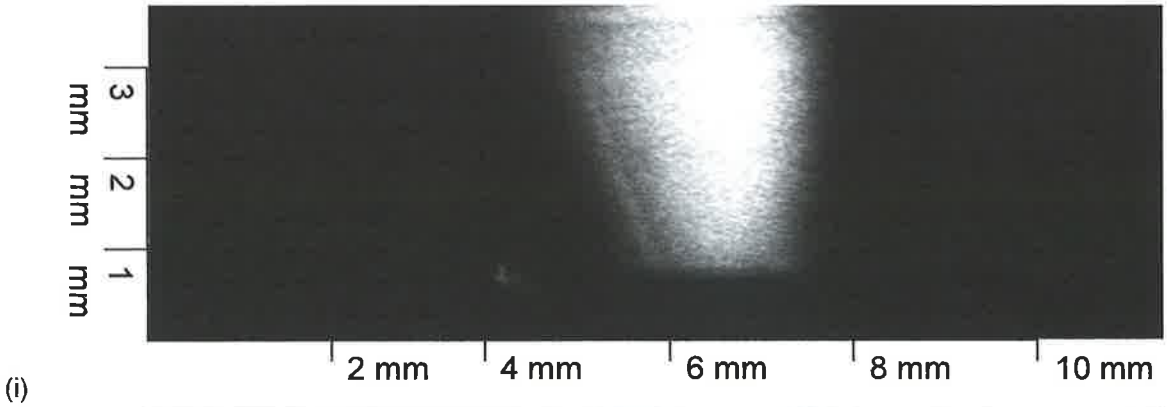

(i)

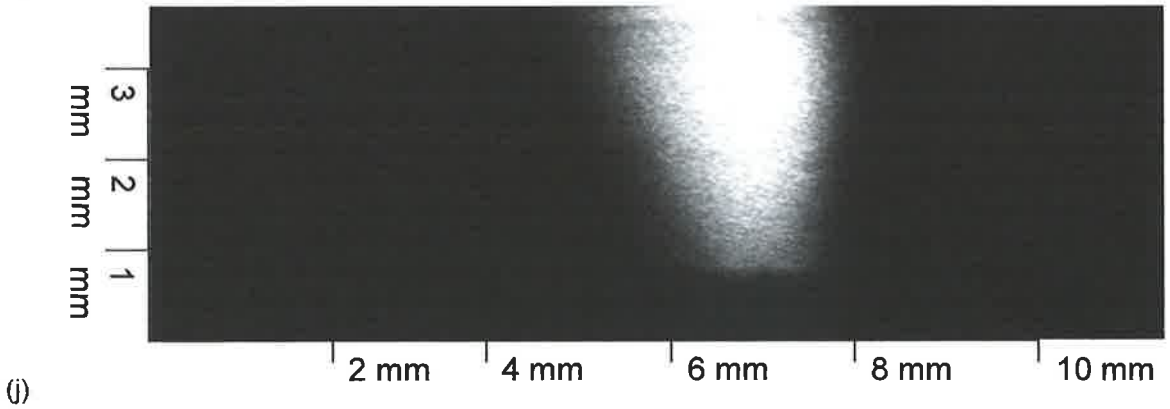

(j)

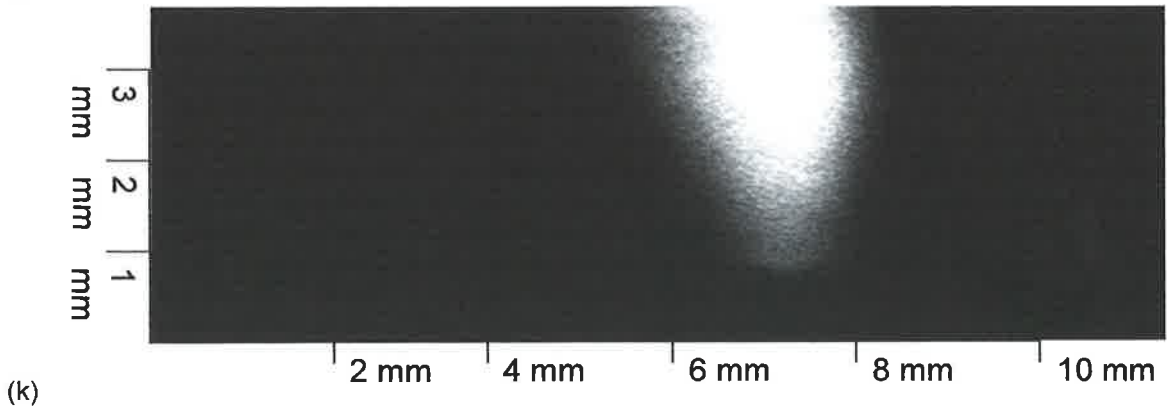

(k)

(Figure 9)

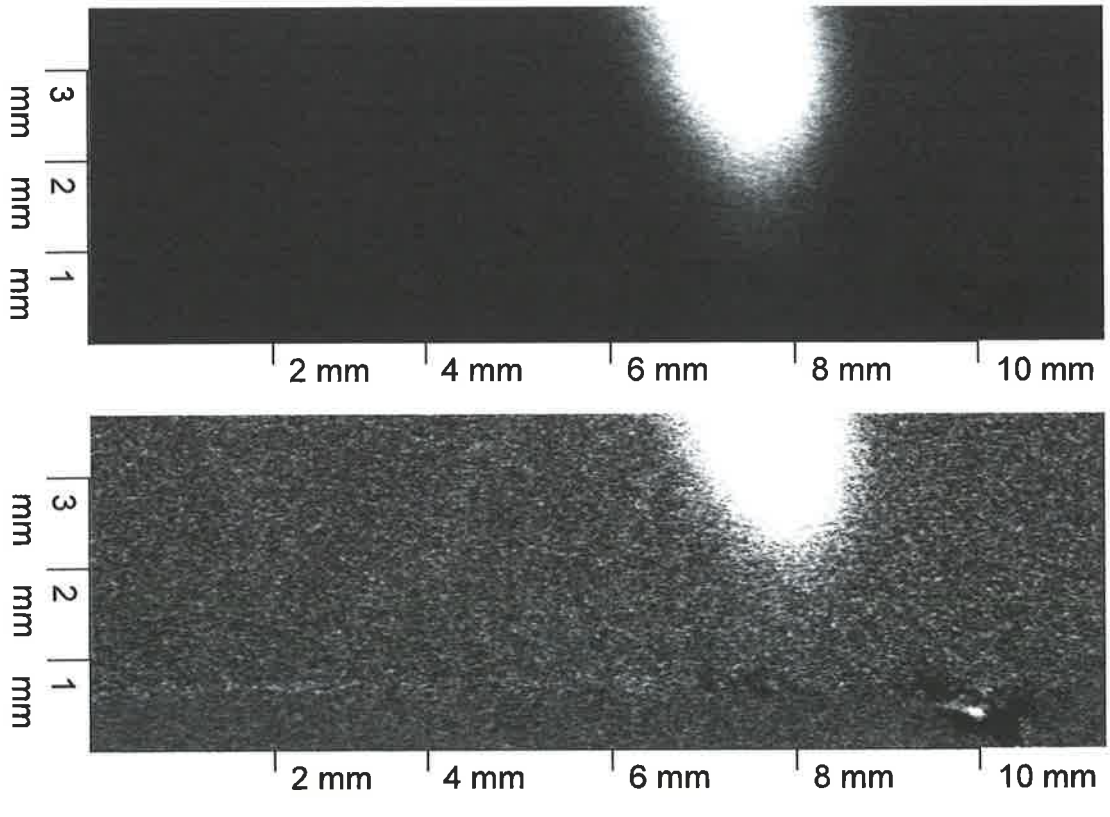
3 mm
2 mm
1 mm
2 mm
4 mm
6 mm
8 mm
10 mm

(l)

3 mm
2 mm
1 mm
2 mm
4 mm
6 mm
8 mm
10 mm

(m)

Figure 10: (Pages following) Set of OH PLPS images of the fuel/lean premixed natural gas/O_2 flame for a horizontally polarised pump beam and a 15° pump/probe beam intersection angle. The probe beam is polarised at $\pi/4$ to the vertical. The image set corresponds to the stretched Mode 2 image set of Figure 5 obtained by scanning the pump sheet across the tip of glass-blowing torch. The images are plotted on a greyscale based on the 5 to 95% signal strength range of each image with black representing the lowest signal.

(a)

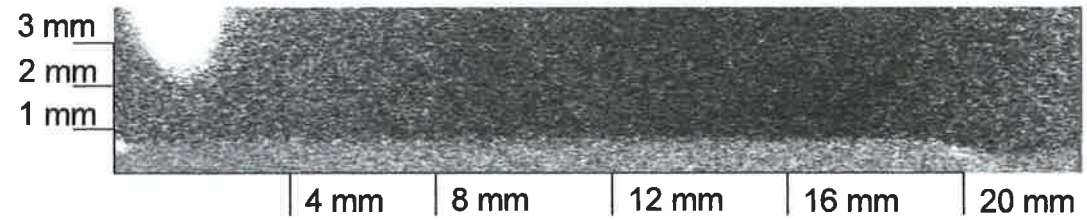

(b)

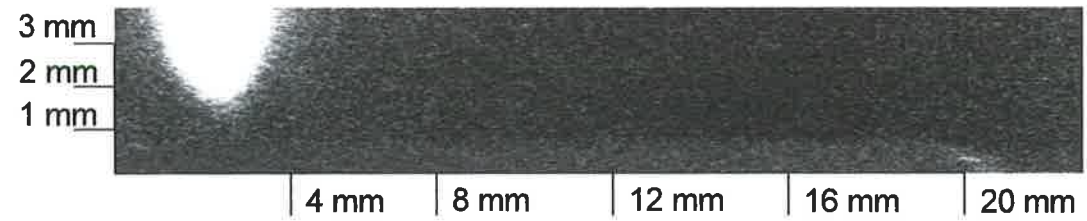

(c)

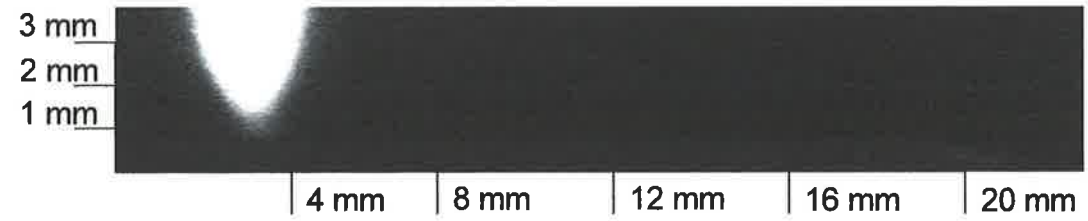

(d)

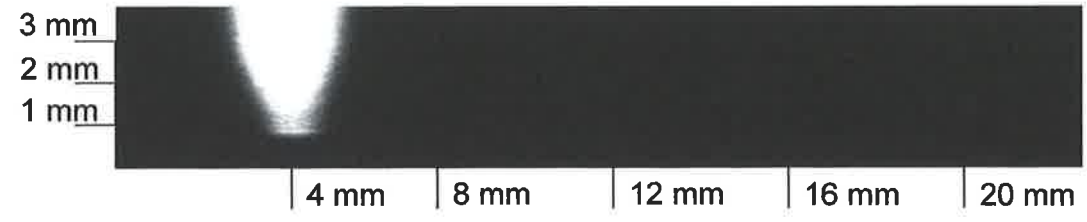

(e)

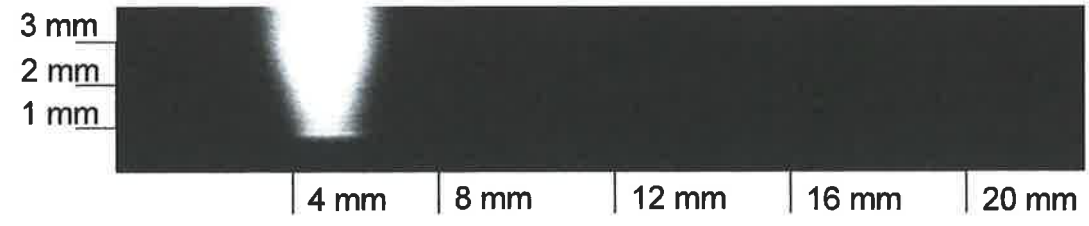

(f) (Figure 10)

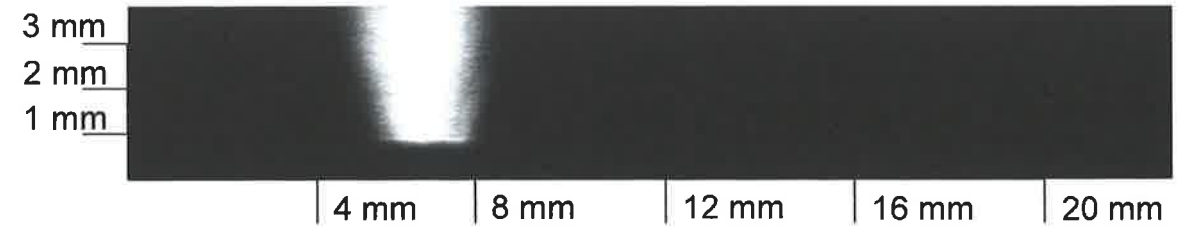

(g)

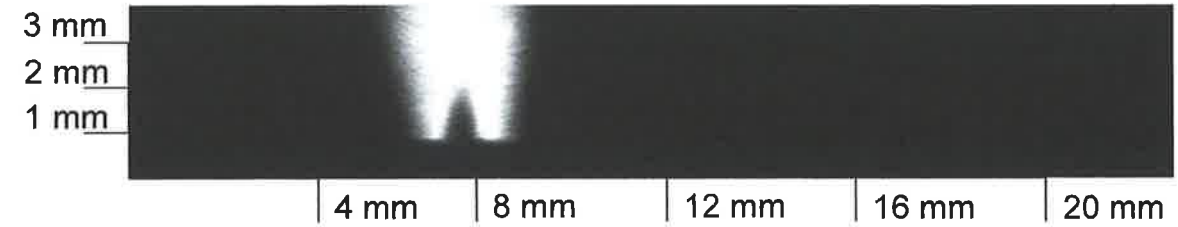

(h)

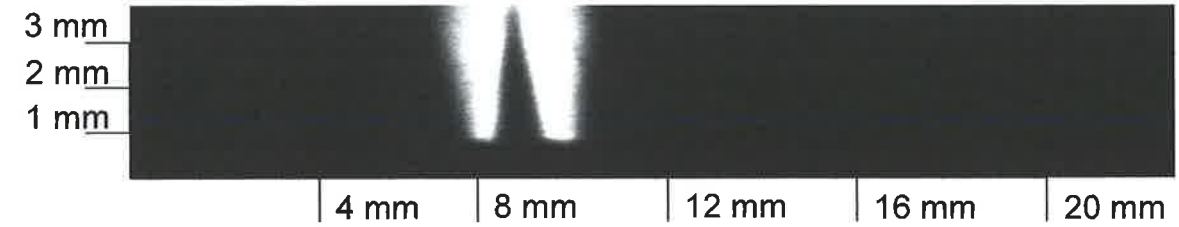

(i)

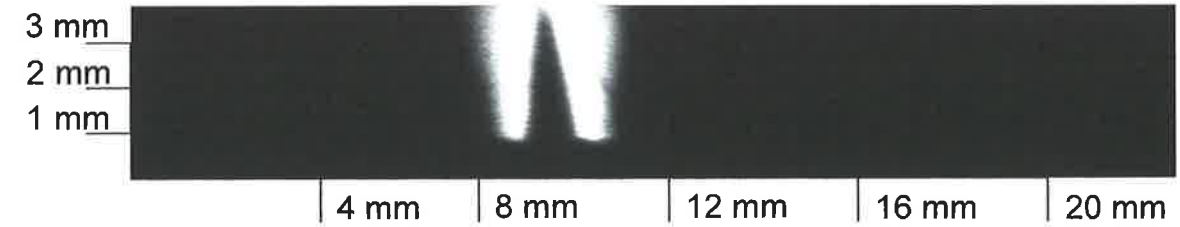

(j)

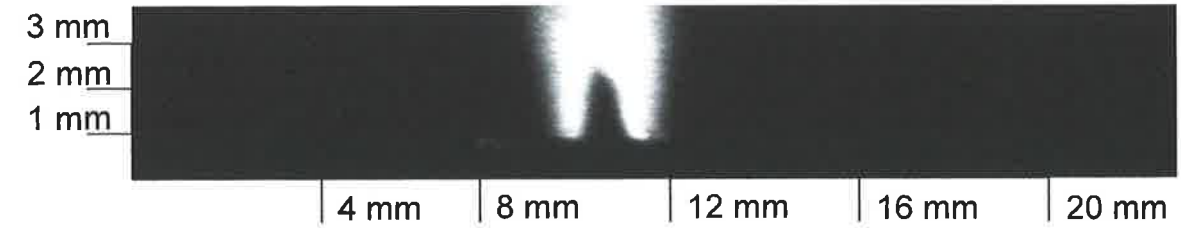

(k) (Figure 10)

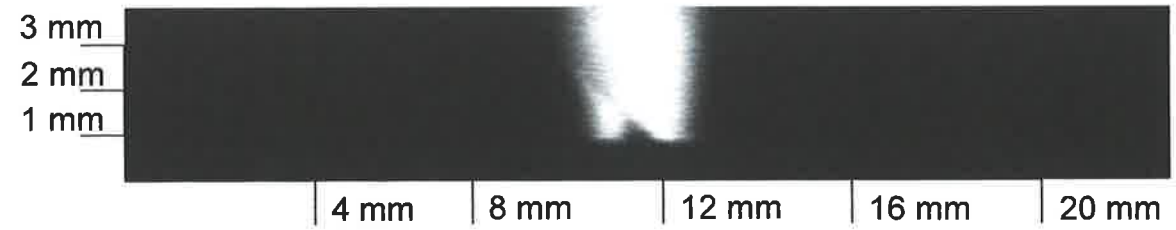

(l)

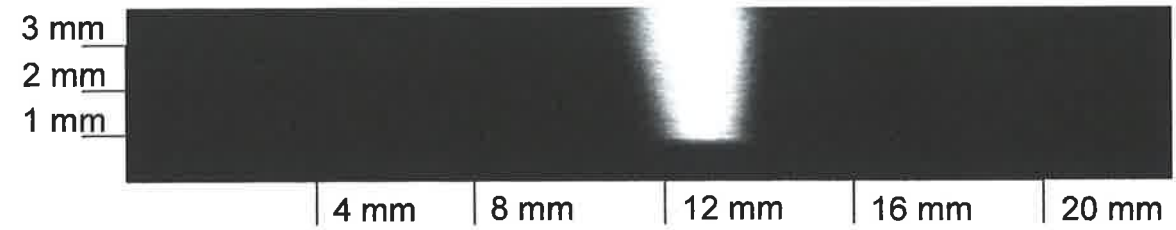

(m)

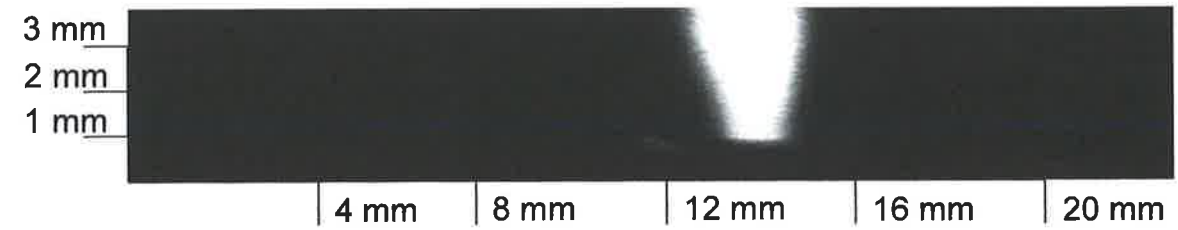

(n)

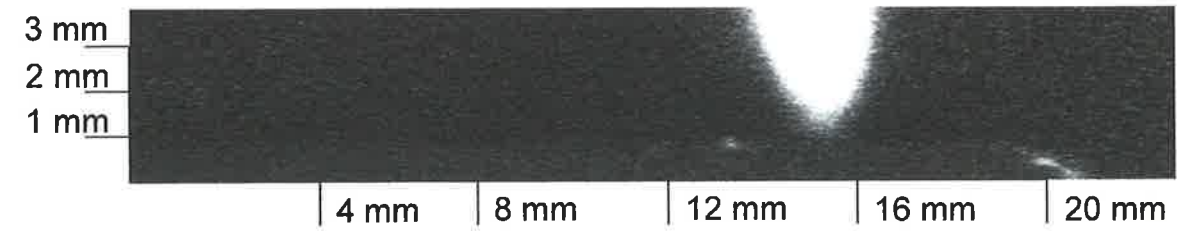

(o)

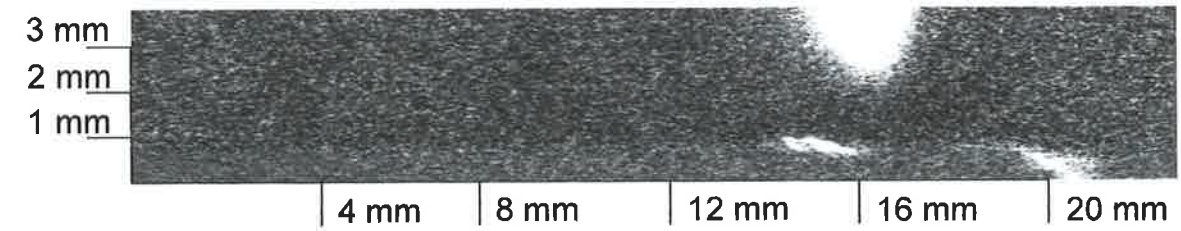

The Mode 2 images in the figures on the previous pages have not been corrected for the pump beam profile. This correction is difficult to implement on a shot-to-shot basis in polarisation spectroscopy. The pump sheet is usually focussed as it passes through the flame and diverges after leaving it. Assuming the pump sheet is collimated with respect to its height (the width of the pump beam will vary as it is focussed by a cylindrical lens into the flame), the optics shown in Figure 11 can be used to determine the pre- and post beam profiles.

A beamsplitter, placed before the primary focussing lens but after the pump beam polariser, can be used to split off a front-face reflection of the pre-flame pump beam. A second lens with the same focal length as that producing the pump sheet can be used to image the pump beam on a second camera directly (after attenuation) or indirectly via collection of the fluorescence of a dye cell. The post-flame pump profile may be collected in an similar configuration. The high intensity of the pre- and post-flame pump beams means that an intensified camera is not required. It was noted experimentally that the LPS signal is not as dependent on the purity of the polarisation state of the pump beam as that of the probe beam, so non-birefringent optics placed after the polariser in the pump beam path are acceptable.

This collection system can be calibrated by comparing the two pump sheet profiles in the absence of a flame. The system depends on accurate collimation of the pump sheet with respect to its height and also depends on there being limited distortion of the sheet due to beam steering effects as it passes through the flame.

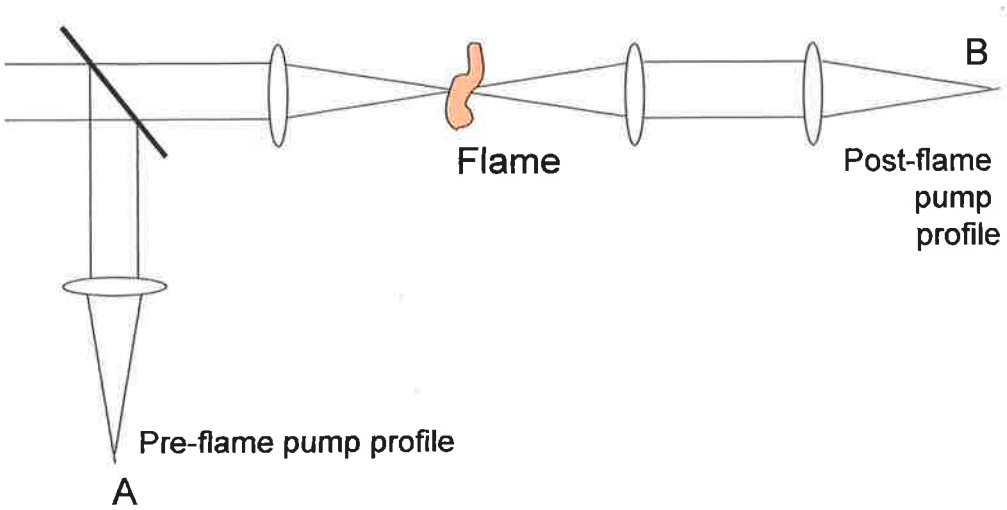

Figure 11: Configuration for pulse-to-pulse collection of pre- and post-flame pump beam profiles.

Absorption of the pump beam is a significant factor in image interpretation. The absorption of the probe beam can be cancelled from the Mode 2 images if the probe beam absorption background is collected nearly simultaneously with the signal image on the timescale of the flame. In this case, the probe beam path of the background and signal are comparable. It is assumed that the difference in the probe beam average absorption coefficient in the pump/probe interaction region due to the presence of the pump beam negligible. However, the LPS signal is quadratic with the pump beam intensity leading to a more exacting requirement on correction of absorption factors for the pump beam profile than for a linear laser diagnostic technique. The most applicable solution for quantitative application of PLPS in a flow or flame where the distribution of the target species cannot be modelled (and hence pump beam intensity cannot be approximated across the width of the flow/flame) is to choose a low absorption transition.

Beamsteering and lensing due to thermal gradients in the flame can effect both pump and probe beams. The two behaviours lead to inaccurate interpretation of the collected images. For example, if significant thermal beam steering results in "holes" in a probe beam profile, a strong signal image with negligible probe beam background may be misinterpreted as representative of the true target species distribution if the probe profile is not collected for comparison.

Beamsteering and thermal lensing features in the probe beam profile may be minimised by the appropriate imaging methods. Beamsteering effects in PLIF images are typically small due to a combination of relatively small flame dimensions and collection of a focussed image. A small flame dimension with respect to the distance to the imaging system is important in minimising the beamsteering spatial offset of the LPS signal from each point in the image. The limited depth of focus of an imaging system constrains the strongest collected signal to correspond to those fluorescence components with wavefront curvature largely unchanged by the thermal refractive index gradients. This limits density gradient effects in the collected image to primarily spatial offsets of the signal source position.

Figure 12 shows a typical arrangement for PLIF image collection. It can be seem that the spatial offset of a beamsteered component of the induced fluorescence is minimal if the distorting flame or flow dimension is small. Figure 13 shows the beamsteering offsets typical of a 310 nm UV beam passing through a laminar (Re ~ 3000, orifice diameter 3 mm) natural gas simple jet flame. The beam diameter was reduced to ~ 1 mm by an iris before passing through the flame. A set of 22 shots showed a maximum beam deflection of the centre of the 1 mm diameter beam of less than 0.0091°. For this dataset, the probe beam was detected by a CCD camera at a distance of 1.888 m from the flame without imaging optics (as shown in Figure 14) to determine the uncorrected extent of the beamsteering.

A successful imaging arrangement for minimised beamsteering in polarisation spectroscopy is shown in Figure 15. A lens system is necessary to reduce the effects of beamsteering. If no lens system is used, the probe beam position on the imaging system is fully subject to full beamsteering offsets as shown in Figure 14. A (typically) unsuccessful beamsteering reduction system is shown in Figure 16. The use of two lenses spatially separated exactly by the sum of their two focal lengths transfers the beamsteering inherent in the input probe beam to the transmitted beam. For a given beamsteering deflection angle, there will be a given distance of the detector after the second imaging lens (as shown in Figure 16) for which the beamsteering will be negligible. However for detector positions before and after this distance, there will be net beamsteering in the collected image. Given that there may be a range of beamsteering deflection angles associated with a transmission through a flame, the imaging optics shown in Figure 16 are not generally appropriate for representative imaging of the pump beam plane. It is interesting to note that the imaging configuration suggested by Lofstedt, Fritzon and Alden is similar to that in Figure 16. Lofstedt *et al.* place the surface of the detector at the position of the second lens in the figure. It can be seen that this arrangement retains purely beemsteering effects, but does discriminate against probe beam components with radii of curvature which have been changed by passage through refractive index gradients.

The most successful imaging system (Figure 17) found in the experiments undertaken in this thesis required two lenses and an iris introduced to reduce the contributions of flame emissions and induced fluorescence to the collected signal. The signal is carried on the probe beam profile and has the same radius of curvature as the probe beam. The collected image is subject to two interferences,

- beamsteering and thermal gradient lensing distortions of the probe beam profile, and
- background flame emissions and laser induced fluorescence (LIF) due to the pump laser sheet.

If there are no beamsteering effects, the probe beam, and associated LPS signal, can be imaged with any conventional beam cleaning system which would remove the thermal lensing structures and non-signal contributions with radii of curvature different from that of the probe beam.. The iris at the focal plane of the primary imaging lens cuts LIF contributions to the image background as the emissions and fluorescence focus at a larger distance from the primary lens and are largely blocked by the iris.

The background is further cut down by the usual $1/r^2$ falloff in isotropic radiation intensity with distance from the source, r. In all PLPS images presented in this thesis, the flame background was negligible with maximum average levels of less than two counts at a gain of 9.0. The iris also acts to limit detection of high intensity scattering from the pump sheet. The scattered pump sheet light

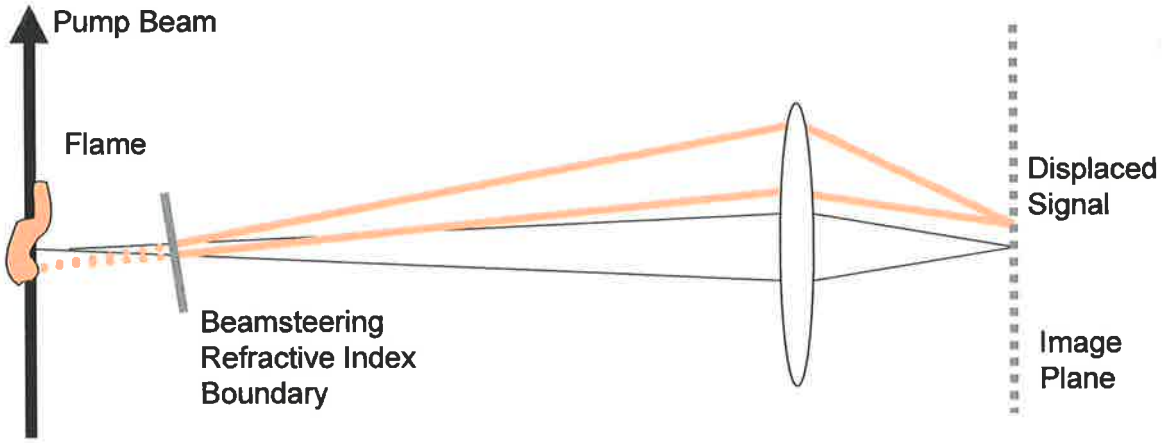

Figure 12: Beamsteering in PLIF images. If the beamsteering boundary is relatively close to the flame the displacement of the signal will be small. A large flame will produce correspondingly larger signal displacement in the collected image.

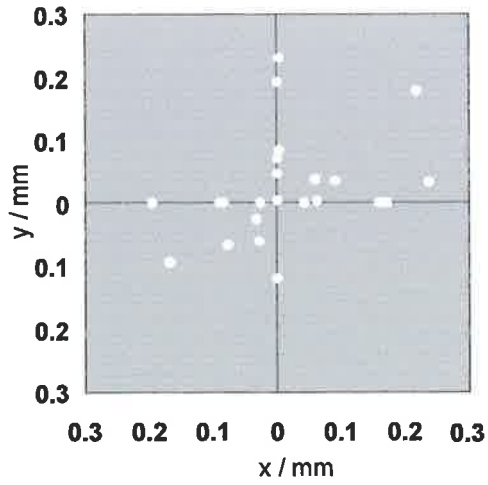

Figure 13: (22 shot) Distribution of the beamsteered probe beam position due to thermal refractive index gradients in a laminar (Re ~ 2000) natural gas flame. The probe beam was detected without imaging optics to determine the extent of beamsteering without optical correction. The maximum deflection corresponded to a beam deflection angle of 0.0091°.

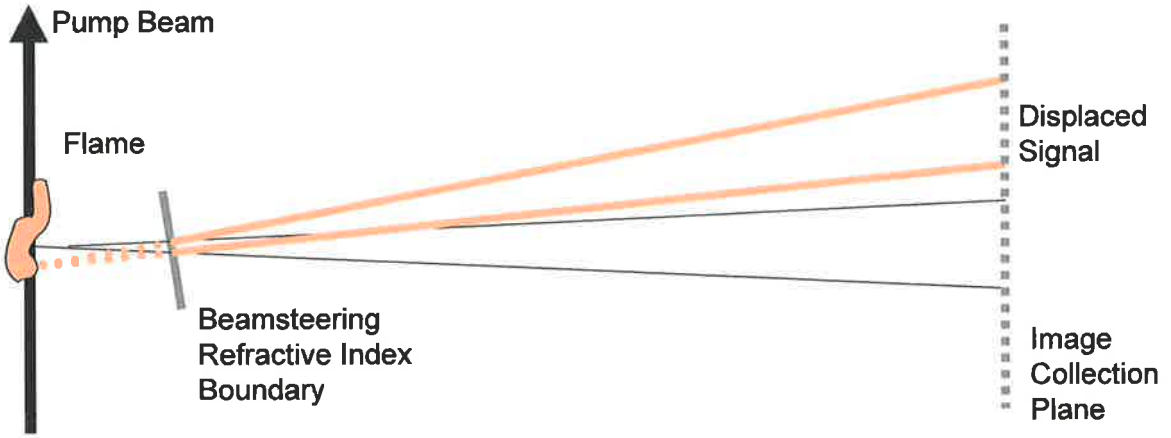

Figure 14: Detection of beemsteering using no imaging optics for image collection. The elimination of imaging optics maximises the effects of beamsteering in the collected image.

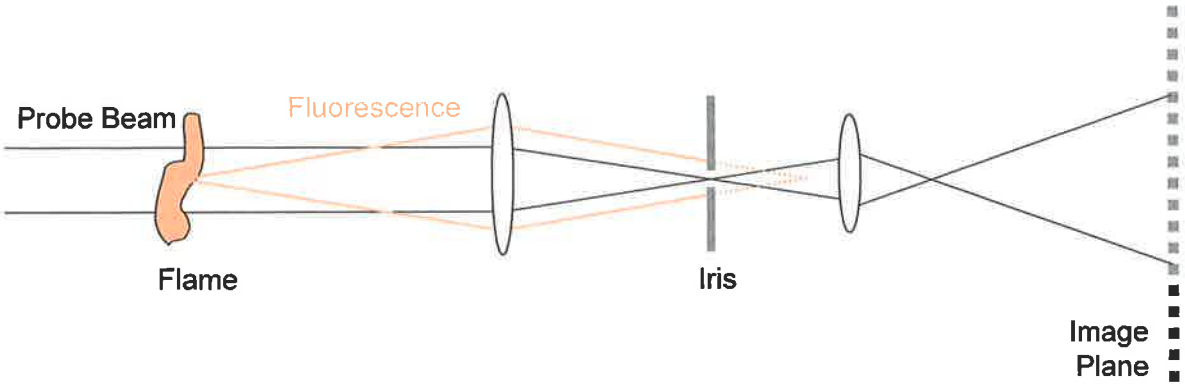

Figure 15: Optical configuration for imaging the probe beam profile and LPS signal.

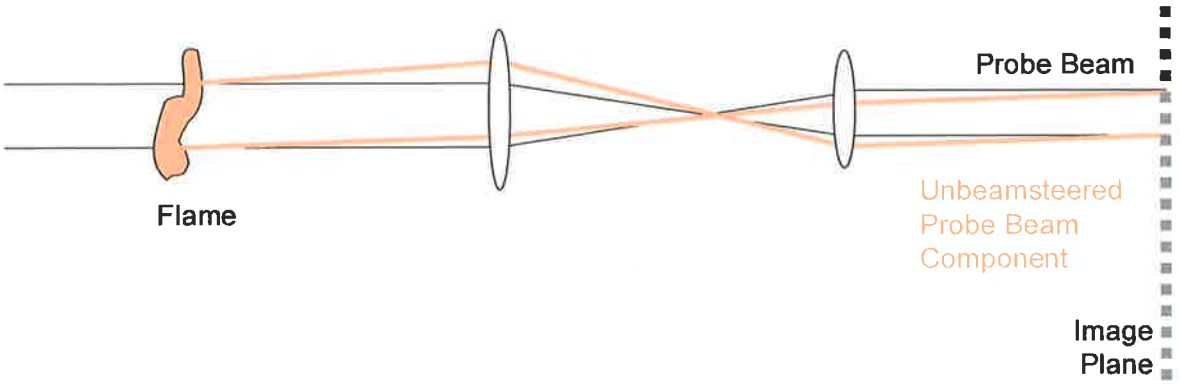

Figure 16: Imaging configuration which will retain beamsteering effects in the collected image unless the image plane is chosen to minimise the spatial offset of the probe beam image (as shown) for the range of beamsteering angles associated with the given flame.

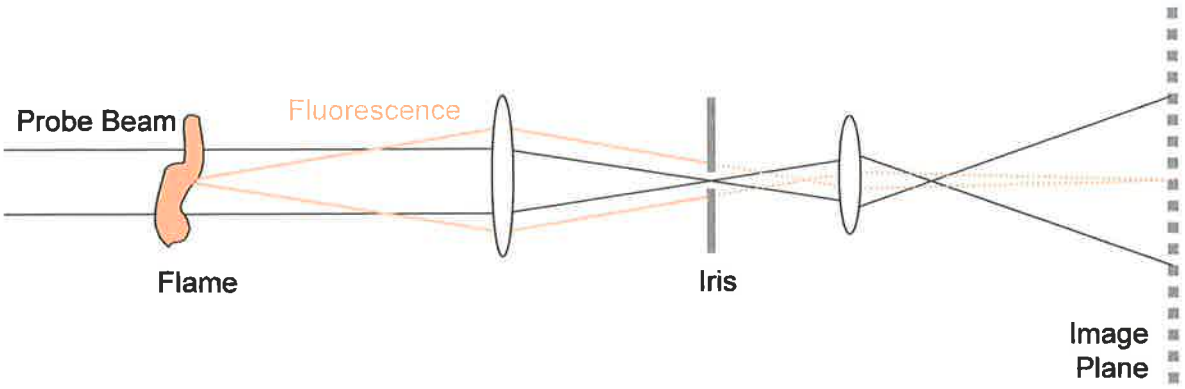

Figure 17: Optimal optical configuration for minimising beamsteering, thermal lensing and fluorescence contributions in polarisation spectroscopy images.

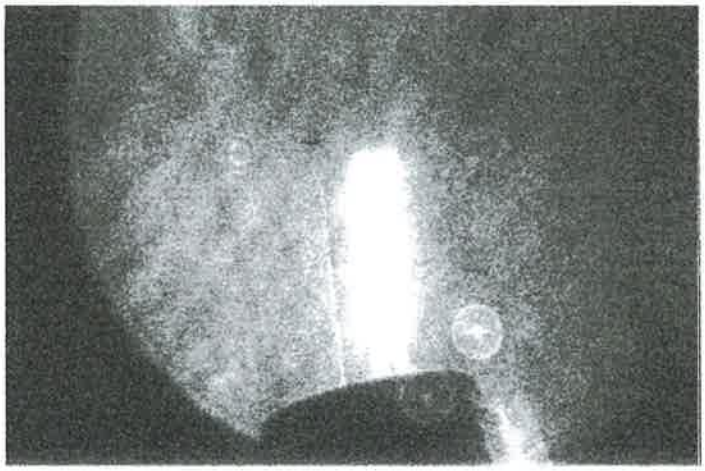

Figure 18: Scattering of the strong pump beam by small particles collected on an early uncorrected OH PLPS Mode 1 image when the pinhole in the imaging system was removed. The greyscale colour map with darkest colour representing lowest signal has been chosen to highlight the scattering and blurs the central OH PLPS signal. The silhouette of the misaligned tip of the burner can be seen at the base of the image.

focuses at the same distance from the primary lens as the flame background emissions and fluorescence. Figure 18 shows pump beam scattering collected in an early uncorrected PLPS image with the pinhole removed. Such scattering was eliminated from the collected mages when the pinhole was replaced.

Experimentally it was determined that **images least affected by beamsteering were obtained for a secondary imaging lens positioned to image the primary lens flame image plane on the surface of the ICCD detector.** With the iris open, this is an analogue of the imaging configuration to minimise beamsteering distortions in a PLIF image (Figure 12). The iris is then closed to reduce image contributions due to thermal lensing, fluorescence and scattering with any radius of curvature other than that of the probe beam. The probe beam passes through the secondary lens and, after passing through the focus, expands to fill the input aperture of the ICCD detector (acting without a lens imaging system). The required magnification of the PLPS image is achieved by moving the ICCD array and the secondary lens along the probe beam path. **As the PLPS image is carried on the cross-section of the probe beam, there is no requirement for the PLPS image to be focussed.**

Note for this optical configuration, it would simply be coincidental for the PLPS and PLIF images (obtained by opening the central iris) due to the same laser sheet to have the same magnification. It is also of interest to note that thermal gradient effects on the probe beam profile due to passage

through the small symmetrical flame used in the imaging experiments were minimal for distances less than ~10 cm from the ~10 mm diameter flame. Distortion of the probe profile (largely unchanged in spatial distribution with distance from the flame) was noted at distances from 10 cm to the largest distance investigated, ~ 2 m, after the flame. Focussing the imaging optics on source planes more than 10 cm from the flame position imaged the thermal gradient features present at that position. These structures were present even with the iris included in the imaging system and should be associated with similar radii of curvature to that of the probe beam and hence identified with beamsteering rather than thermal lensing. Consequently, it makes sense to "image" the probe beam profile at the point of minimum apparent distortion due to thermal gradient features, i.e. the central plane of the flame itself, to minimise thermal gradient structures in the PLPS image. Note however, if the flame diameter is large with respect to the distance at which thermal gradient features appear in the probe beam, this imaging technique will not be as successful as in a smaller flame.

The averaged images in this chapter for the near-collinear beam intersection angles of 15° and 30° show that correction for thermal gradient features in the probe beam profile using the Mode 2 image ratio method is valid and produces images of the same quality as for the case of orthogonal beam intersection. The relatively higher signal and higher signal to background ratios in the near-collinear geometry gives incentive for use of this configuration in experiments where the signal is weak. However, for imaging purposes, the relative increase in signal is confined to beam intersection angles less than 20°. The very high signal levels associated with beam intersection angles of the order of degrees in single point experiments are not available to imaging experiments where image resolution requires a moderate beam intersection angle. Single point experiments for small beam intersection angles are also subject, in combustion, to rapid change of signal strength due to slight beamsteering of the beam intersection angle, with a corresponding difficulty in quantitative interpretation of the results. The playoff between increased signal and decreased image resolution for the range of realistic imaging beam intersection angles is to a large extent constrained by the parameters of individual experiments.

An additional factor which clearly indicates an advantage in near-orthogonal imaging is the loss in resolution with respect to the pump sheet width with decreasing beam intersection angle. The thickness of the pump sheet as measured along the probe beam path is given by $W.\sin(\chi)$ where W is the width of the pump sheet. For a beam intersection angle of 15°, the resolution along the probe beam path decreases by a factor of 3.86 from that for orthogonal beam intersection. For a pump beam width of ~ 400 mm, the effective pumped volume thickness measured along the probe beam path increases to 1.55 mm. The resolution due to the width of the pump sheet is the ultimate limit to the volume resolution of imaging techniques such as PLIF and PLPS.

The images in this chapter demonstrate the imaging application of and difficulties associated with combustion PLPS. There has been no attempt to quantify the range of number densities of OH detectable with this technique as, to maximise signal strength, the images have been collected in the saturated regime of optical pumping, rather than the linear regime described by the theory of Teets, Kowalski, Hill, Carlson and Hansch[1].

It has been shown in this thesis that both near-collinear and orthogonal beam intersection geometries allow correction for thermal gradient structures in the probe beam profile. Note that in both cases, the ideal experiment would collect probe beam profiles nearly instantaneously with each signal image on the timescale of the flow or flame for accurate shot-to-shot correction. The increased signal in near-collinear images is justification for using small beam intersection angles. However, the loss of resolution due to the pump sheet width is a major factor in recommending the orthogonal beam intersection geometry.

Chapter VII: Simultaneous PLIF and PLPS in Combustion.

This chapter compares the LIF and LPS laser diagnostic techniques for detection of the OH radical. The laser system was tuned to the $Q_2(8)$ transition of the $A^2\Sigma$–$X^2\Pi$ (0-0) band of OH. Simultaneously collected (average) PLIF and PLPS images due to the OH distribution in a laminar premixed natural gas/O_2 flame from a glass-blowing torch are presented. The PLPS images were collected in the saturated regime of optical pumping and the PLIF images in a near-linear saturation regime and demonstrate significant differences between the predicted OH distribution for each technique.

OH LIF and LPS signal is also shown as a function of flame equivalence ratio in a premixed natural gas/air flame from a rectangular mixing burner. Once again, the LPS signal was saturated while the LIF signal was collected in the linear regime. A linear relationship between the (saturated) LPS and (linear regime) LIF signal when corrected to represent number density is demonstrated.

Comparison with OH concentrations calculated using the equilibrium module of the CHEMKIN library indicates that the predicted (relative) OH concentration for both LIF and LPS techniques closely matches the calculated results for fuel-rich flames. Based on the number density scaling factor between calculated and experimentally predicted OH concentration, the LIF and LPS signals overestimate the OH concentration for fuel-lean flames.

The previous chapters have investigated practical implications for experimental application of PLPS. The range of beam intersection angles for non-zero LPS signal has been extended to allow orthogonal beam intersection with significant implications for the spatial resolution of the collected images. Models of the dependence of the signal strength on the polarisation directions of pump and probe beam and the beam intersection angle have been developed. The effects of thermal density gradient induced structures on the probe beam profile have been discussed.

These results are important to the application of polarisation spectroscopy imaging. For quantitative use of polarisation spectroscopy as a combustion diagnostic technique, the dependence of the LPS

signal on number density of the target species in a range of combustion environments must be determined.

Polarisation Spectroscopy as a Quantitative Laser Diagnostic Technique

Laser polarisation spectroscopy was first applied as a combustion diagnostic technique to the detection of trace species seeded into or produced by chemical reaction from seeded species in flames. The use of seeded species makes the technique applicable to chemical analysis and provided the basis for the development of polarisation spectroscopy to detection of low concentration combustion species.

The first application of polarisation species to combustion was by Ernst and Torring in 1982. **Ernst and Torring** (*"High Resolution Studies of Unstable Diatomics by Microwave-Optical Polarization Spectroscopy and Doppler Free Laser Polarization Spectroscopy"*, 1982)[33] detected the unstable species CaCl produced in a flame reaction in a low pressure cell (10^{-5} Torr partial pressure, 0.05 Torr total cell pressure) using a microwave-optical polarisation spectroscopy technique (MOPS). The pump and probe beams shared a common ground state. The probe beam was tuned to an electronic transition and the (linearly polarised and counter-propagating) pump beam tuned to a microwave transition of the target species . The probe beam was polarised at 45° to the probe beam polarisation axis. In order to investigate hyperfine splitting of the ground state of CaCl, the pump laser was tuned to the N = 6←5 and N = 3←2 transitions in the $^2\Sigma$ ground state of CaCl and the probe beam to the $P_1(6)$, $P_2(6)$, $P_1(3)$ and $P_2(3)$ $B^2\Sigma \leftarrow X^2\Pi\ (0,0)$ optical transitions. Doppler-free polarisation spectroscopy of the optical probe beam transitions of the $B^2\Sigma \leftarrow X^2\Pi\ (0,0)$ band of CaCl were also investigated.

In 1983, **Ernst** (*"Doppler-free Polarization Spectroscopy of Diatomic Molecules in Flame Reactions"*)[34] suggested the **suitability of polarisation spectroscopy in flames for investigation of gas phase reactions producing radicals or molecules that are hard to evaporate**. Ernst compared the signal to noise ratios for three techniques; polarisation spectroscopy with slightly uncrossed polarisers ($\theta^2 = \xi$), saturated absorption spectroscopy and intermodulated fluorescence spectroscopy. Using the assumption that the major noise level in each technique is due to fluctuations in either the detected probe intensity (for coherent techniques) or the pump beam intensity (for the intermodulated fluorescence), Ernst suggested that polarisation spectroscopy would demonstrate the highest signal to noise ratio for the condition

$$\alpha_o L < \xi^{-1/2} \qquad \text{Equation 1}$$

where

ξ is the extinction ratio of the probe beam polarisers,

α_o is the linecentre absorption coefficient, and

L is the absorption length.

Experimentally, Ernst reported investigation of the $A^1\Sigma$-$X^1\Sigma$ (1,0) band of BaO and the $B^2\Sigma$-$X^2\Sigma$ (0,0) band of CaCl with polarisation spectroscopy using a circularly polarised pump beam (to probe the Σ-Σ P and R transitions) and a linearly polarised pump beam (to preferentially probe the Q transitions).

The basis of the experiments of Ernst and Torring[33] and Ernst[34] was spectroscopic investigation. **Tong and Yeung** (*"Polarization Spectroscopy for Elemental Analysis at Trace Concentrations"*)[35] **extended the concept of polarisation spectroscopy in combustion to the detection of trace species** rather than spectroscopic investigation in 1985.

Tong and Yeung studied the detection limits for seeded atomic species in flames using polarisation spectroscopy in comparison with other techniques. Na and Ba were seeded into a laminar acetylene/air flame produced by a 6 cm slot burner. Using a counterpropagating beam geometry and a circularly polarised pump beam, Tong and Yeung applied polarisation modulated detection (PMD) to improve the polarisation spectroscopy detection limit. For comparison, amplitude modulated detection (AMD) was also investigated.

The authors used the theory of Wieman and Hansch[2].The polarisation modulation allowed a step function modulation of the linearly polarised pump beam polarisation before it entered a ¼-wave Fresnel rhomb to become circularly polarised, periodically rotating the input plane of polarisation by 90°. The resultant pump beam polarisation oscillated between right and left-handed polarisation states. The background of the signal is unchanged with pump polarisation. However, the handedness of the pump beam controls the sign of the induced dichroism, via the term, s, in Wieman and Hansch's expression for the signal strength (repeated below) in the case of a circularly polarised pump beam.

$$\frac{I}{I_0} = \xi + \theta^2 + \frac{1}{2}\cdot\theta\cdot s\cdot\frac{x}{1+x^2} + \frac{1}{16}\cdot s^2\cdot\frac{1}{1+x^2} \qquad \text{Equation 2}$$

This does not affect the sign of the Lorentzian term (shown in red), but reverses the sign of the dispersive signal (shown in blue). Oscillation (at 800 Hz) between the two pump beam states allowed difference measurement of the dispersive term in the above equation, while eliminating the constant background and the Lorentzian term. Note that this experiment requires a non-zero polariser uncrossing angle, θ. (Note: although the paper appears to suggest that polarisation modulated polarisation spectroscopy was undertaken with perfectly crossed polarisers, this statement in fact refers to the final calculation of trace element detectability using the maximum signal to noise ratio characteristic of perfectly crossed polarisers. This interpretation of the intention

of the paper is supported by the reported dependence of the signal on laser intensity and species concentration.)

Tong and Yeung made great efforts to quantify the behaviour of the technique. The polarisation spectroscopy lineshape (normalised to the same background intensity) was investigated as a function of polariser uncrossing angle for a circularly polarised pump beam. The polarisation modulated polarisation spectroscopy lineshape for the case of a linearly polarised pump beam (with polarisation modulation leading to oscillation of the pump beam polarisation between orthogonal polarisation directions) was investigated as a function of angle from probe beam polarisation. As expected, maximum signal was obtained for a linearly polarised pump beam polarisation direction lying at 45° to the probe beam polarisation axis. A quadratic dependence on laser intensity and a linear dependence on species concentration (over 3 orders of magnitude) was found (supporting the argument above that the technique was applied with slightly uncrossed polarisers).

The PMD experiment led to detection limits (S/N = 2) of 30 ppt[a] for sodium and 37 ppb for barium, a factor of 5 improvement on the results obtained using amplitude modulated detection. The authors concluded that PMD polarisation spectroscopy leads to detection limits comparable to, or better than, atomic fluorescence spectroscopy and noted the advantage of polarisation spectroscopy with respect to detection of resonance transitions.

Lanauze and Winefordner (*"Application of a Pulsed Dye Laser to Polarization Spectroscopy for Elemental Analysis"*, 1986)[36] **noted this application of polarisation spectroscopy to high sensitivity trace species detection and**, to extend the range of experimental applicability, **proposed operation with pulsed dye lasers** rather than the frequency-stabilised (Ar-ion pumped) ring dye laser used by Tong and Yeung[35]. Using the theory described in Demtroder[37] (which summarises the results of Teets, Kowalski, Hill, Carlson and Hansch[1]), Lanauze and Winefordner applied polarisation spectroscopy with a circularly polarised pump beam and an excimer pumped Lumonics (EDP 330) tuneable dye laser to obtain detection limits (at S/N = 3) of 2 μg/L (= 2 ng/ml, c.f. Tong and Yeung 0.03 ng/ml) of Na in an air/acetylene flame from a 6 cm long slot burner, however requiring an 3000 pulse average to obtain this result. The experiment was extremely limited by an achievable polariser extinction ratio of 1/200 [b], although the probe beam Glan-

[a] The concentration limit states refers to the concentration of the seeded solution.

[b] The polariser extinction ratio may be quoted in either of the two forms, e.g. 10^{6} or 10^{-6}. This thesis sticks to the convention of using the ratio less than unity to match the extinction background term, ξ, in expressions for the polarisation spectroscopy signal strength.

Foucault polariser pair were specified with 10^{-6} extinction ratio. This is probably due to birefringence introduced by the use of a prism, four mirrors (and a front face reflection from a quartz flat and, unmarked in the experimental diagram, attenuation by 10^3 by neutral density filters) and *a lens* in the probe beam path between the probe beam primary polariser and analyser. In addition, the pump beam was limited to the ~ 500 mJ/pulse available from the laser system. If the effects of birefringence were minimised by placing the optical elements outside the region enclosed by the probe beam polarisers, it is probable that extinction ratios of the order of 10^{-6} would have been obtainable with this experiment, leading to detection limits of 0.1 ng/L (= 0.001 ng/ml, c.f. Tong and Yeung 0.03 ng/ml) for a 3000 pulse average. As it stands, this experiment demonstrates that polarisation spectroscopy can be applied with inter-polariser optical elements, however at a large loss in signal to noise ratio. The suitability of pulsed dye lasers for polarisation spectroscopy detection of trace species is also clearly demonstrated.
A power dependence of the signal strength (for a circularly polarised pump beam) on seeded solute concentration for perfectly crossed polarisers of 2.01 and for a dispersion dominated signal regime of 1.09 was obtained in this experiment.

At first glance, the 1986 paper of **Zizak, Lanauze and Winefordner** (*"Cross-beam polarization in flames with a pulsed dye laser"*)[38] paper repeats many of the experimental results of the paper of Lanauze and Winefordner[0] which shares two of the authors of this paper. **However several very important conceptual advances are made in this paper which dramatically advance the concept of polarisation spectroscopy laser diagnostics.** The most important of these was **to consider polarisation spectroscopic detection of combustion, rather than seeded, species for measurement of both species concentration and temperature.**

Noting the recent measurement of OH concentration in flames via saturated absorption spectroscopy using a UV cw dye laser probe beam and a UV pulsed dye laser pump beam by Kychakoff, Howe and Hanson (1984)[39], **Zizak, Lanauze and Winefordner attempted to detect OH in a premixed air-acetylene capillary burner using polarisation spectroscopy.**

Applying the concept of a finite beam intersection angle to allow spatial resolution of the sample volume, the authors focussed a pump beam into the air-acetylene flame to intersect the probe beam at intersection angles of $\chi = 7^o$ to 45^o to find a $\cot^2(\chi)$ dependence of signal strength on beam intersection angle. The remainder of the experiments were undertaken for a beam intersection angle of $\chi = 7^o$. The spatial resolution for this configuration was ~ 0.7 mm^3 with a pump/probe beam interaction length of ~ 1.5 mm. In an extension of the experiment described in paper of Lanauze and Winefordner[36], their previous paper[0], Zizak, Lanauze and Winefordner obtained the first 1-D profile of the (NaCl seeded at 300 µg/ml) sodium profile in an acetylene/air slot burner flame. The profile, each point representing a single shot measurement, was obtained by

traversing the slot burner across the intersection volume of pump and probe beams. This experiment was improved by the removal of interpolariser optical elements leading to an experimentally determined polariser extinction ratio of 1.7×10^{-4} and **resultant detection limit of 10 μg/ml**. It is not stated if this is and averaged or single-shot result. Both pump and probe beams were focussed into the flame to improve spatial resolution.

In their conclusion, Zizak, Lanauze and Winefordner point out the difficulty in direct interpretation of the measured induced dichroism, $\Delta\alpha$, in terms of the absolute number density of the target species due to collisional perturbation of the population of the Zeeman sublevels and suggest that *"the influence of gas composition in the signal strength must be investigated for quantitative measurements of the total number densities in the combustion gases."*

The development of polarisation as a combustion diagnostic technique can be traced from this 1986 paper of Zizak, Lanauze and Winefordner. Experimental investigations of polarisation spectroscopy detection of combustion and flow species were extensive from 1993-1996.

- **OH:** (Nyholm, Maier, Aminoff and Kaivola, *"Detection of OH in flames using polarization spectroscopy"* (1993)[40], Nyholm, Fritzon and Alden, *"Two-dimensional imaging of OH in flames by use of polarization spectroscopy"* (1993)[3], Nyholm, *"Measurements of OH rotational temperatures in flames by using polarization spectroscopy"* (1994)[32], Nyholm, Fritzon and Alden, *"Single-pulse two-dimensional temperature imaging in flames by degenerate four-wave mixing and polarization spectroscopy"* (1994)[41].
- **NH and OH:** Suvenev, Dreizler, Dreier and Wolfrum, *"Polarisation-spectroscopic measurement and spectral simulation of OH ($A^2\Sigma$-$X^2\Pi$) and NH ($A^3\Pi$-$X^3\Sigma$) transitions in atmospheric pressure flames"* (1995)[42].
- **NH_3 and CO:** Nyholm, Fritzon, Georgiev and Alden, *"Two-photon induced polarization spectroscopy applied to the detection of NH_3 and CO molecules in cold flows and flames."* (1995)[43].
- **C_2 :** Nyholm, Kaivola and Aminoff, *"Polarization spectroscopy applied to C_2 detection in a flame"* (1995)[44], which was foreshadowed by a much earlier investigation by Aminoff, Kaivola and Nyholm, (First Europ. Conf. on Quantum Electronics. Hanover, Germany, Digest of Technical Papers (University Hanover, Hanover, 1988), Paper MoCD4))[45].
- **N_2 :** Kaminski, Lofstedt, Fritzon and Alden, *"Two-photon polarization spectroscopy and (2+3)-photon laser induced fluorescence of N_2"* (1996)[46].
- **NO:** Lofstedt, Fritzon and Alden, *"Investigation of NO detection in flames by the use of polarization spectroscopy"* (1996)[30].
- **NO and OH:** Lofstedt and Alden, *"Simultaneous detection of OH and NO in a flame using polarization spectroscopy"* (1996)[47].

These experiments were largely interpreted on the basis of the simple rate equation theory of Teets, Kowalski, Hill, Carlson and Hansch[1] which includes very little analysis of collisional processes. Notwithstanding this, the theory appears to be remarkably applicable to these atmospheric pressure and high collision rate experiments. However, the authors of the papers listed above continually call for investigation of the effect of collisional population transfer on the polarisation spectroscopy signal to allow truly quantitative experiments:

> ***"An important problem in the use of polarization spectroscopy in flame studies of a more quantitative nature is collisional relaxation. Measurements of absolute concentrations of radicals would require knowledge of the collisional depolarization of the magnetic sublevels."***
>
> Nyholm, Maier, Aminoff and Kaivola
> *"Detection of OH in flames using polarization spectroscopy"*[40]

Despite the need to quantify LPS via realistic population models, very few experimental investigations of the quantitative dependence of polarisation spectroscopy on saturation or collisional processes in combustion exist in the literature. **Reichardt, Giancola and Lucht** (*"Experimental Investigation of saturated polarization spectroscopy for quantitative concentration measurements"*, 2000))[48] and **Reichardt, Di Teodoro and Farrow** (*"Collisional dependence of polarization spectroscopy with a picosecond laser"*, 2000)[49] represent the most significant papers in investigating this aspect of polarisation spectroscopy.

Reichardt, Giancola and Lucht[48] used a Hencken burner which produced a well-characterised H_2/air flame to measure line-centre and line-integrated OH LPS signal as a function of equivalence ratio for $P_1(2)$ and $Q_1(8)$ transitions for both focussed and unfocussed beams. The pump and the probe beams intersected at 4.7° and were tuned to transitions in the A $^2\Sigma^+$-X $^2\Pi(0,0)$ band of OH near 306 nm. A circularly polarised pump beam was used to probe the $P_1(2)$ transition and a linearly polarised pump beam for the $Q_1(8)$ experiments. A 2.6 cm unfocussed beam intersection length was used for unsaturated measurements to produce sufficient signal, while the saturated signal[c] was collected with focussed beams for a beam intersection length of 3 mm. The probed volume was ~ 2.5 cm above the surface of the Hencken burner.

[c] Saturation measurements indicated the LPS signal was linearly dependent on the laser intensity for pump intensities greater than ~ 60 MW/cm^2.

The number density predicted by the experimental LPS signal was compared that calculated using a NASA Lewis equilibrium code. Correction for absorption were considered in the LPS determination of number density, with a maximum correction of 45% in OH concentration. The linecentre absorptivity measurements were also checked against the equilibrium number densities confirming that the OH concentrations produced in the flame showed a similar dependence on flame equivalence ratio to the equilibrium calculations for fuel-lean flames. However, the OH concentrations calculated from the absorptivity measurements predicted higher OH concentrations than the equilibrium calculations for fuel-rich flames. The authors attributed this to edge effects due to diffusion in the fuel-rich flames.

The (absorption corrected) number densities predicted by the linecentre and line-integrated LPS signal were very similar in their dependence on flame equivalence ratio for both unfocussed and focussed beams. The experimentally determined number densities closely matched the equilibrium calculation number densities for fuel-lean flames, but underestimated the number densities for near-stoichiometric flames for the case of unfocussed beams for the $P_1(2)$ experiment and for both focussed and unfocussed beams for the $Q_1(8)$ experiment. The underestimation was least obvious for the $Q_1(8)$ experiment for the case of focussed beams. The best fit to the equilibrium number densities was obtained for the $P_1(2)$ experiment for focussed beams. The linecentre absorptivity was least for the $P_1(2)$ experiment. Due to the lower sensitivity to absorption in the saturated (focussed beam) experiments, **Reichardt, Giancola and Lucht's equivalence ratio experiment demonstrated that low absorption, saturated regime LPS produced quantitative predictions of OH number density in an atmospheric pressure H_2/air flame for nanosecond laser pulse lengths.**

Reichardt, Di Teodoro and Farrow[49] followed the paper of Reichardt, Giancola and Lucht[48] with an investigation of the collisional dependence of LPS for picosecond laser systems. OH LPS signal was monitored as a function of buffer gas (argon) pressure in a flow-cell. The frequency doubled output of a distributed feedback dye laser was used to pump the $A\ ^2\Sigma^+$-$X\ ^2\Pi(0,0)\ P_1(2)$ transition of OH. The laser pulse length was 120 ps. The laser was circularly polarised and the two beams intersected at an angle of 0.6° for a beam intersection length of 25 cm. The OH was produced by photolysis of H_2O_2 produced by bubbling argon through 85% wt. % H_2O_2.

OH LIF and OH LPS line-centre signal was monitored for the saturation measurements. The OH LIF signal showed a typical saturation curve with saturation for pump irradiances above 10MW/cm^2. The OH LPS curve showed an unusual double structure with increasing pump beam intensity. The LPS signal showed a cubic dependence on signal strength for pump intensities below ~ 2 MW/cm^2 and appeared to enter a saturated regime for pump intensities above 40 MW/cm^2. However, the

LPS signal exhibits a plateau between these two regimes at ~ 10MW/cm^2. The authors noted that similar plateaux in the short-pulse theoretical studies of DFWM were attributable to Rabi beating.

The pressure dependence of LPS signal was investigated for unsaturated (~ 1 MW/cm^2) and saturated (~ 500 MW/cm^2) pump beam intensities for cell pressures from 10 – 500 Torr. The authors calculated that this pressure range corresponds to a dephasing rate of ~ 2 x 10^8 - 10^{10} s^{-1}. The unsaturated LPS signal drops by a factor of 18 as the pressure increases from 10 to 500 Torr. In comparison, the saturated LPS signal drops by a factor of 3 over the same pressure range. The unsaturated LPS signal was corrected for absorption, but the saturated LPS signal was not corrected for absorption.

The experimental LPS signals were collected for a laser pulse length of ~ 120 ps. Reichardt, Di Teodoro and Farrow derived an analytic expression for the (unsaturated) LPS signal strength using a perturbative theory which assumes an exponentially decaying laser pulses. In this theory, the line-centre (unsaturated) LPS signal is given by

$$\frac{I_{PS}(\omega=\omega_0)}{N^2} \propto \frac{\left(10+5\left(\frac{\gamma_{eg}}{\gamma_{pulse}}\right)+\left(\frac{\gamma_{eg}}{\gamma_{pulse}}\right)^2\right)}{\gamma_{eg}\cdot\left(1+\left(\frac{\gamma_{eg}}{\gamma_{pulse}}\right)\right)\cdot\left(2+\left(\frac{\gamma_{eg}}{\gamma_{pulse}}\right)\right)\cdot\left(3+\left(\frac{\gamma_{eg}}{\gamma_{pulse}}\right)\right)} \qquad \text{Equation 3}$$

where

I_{PS} is the line-centre (unsaturated) LPS signal,

N is the molecular concentration,

γ_{eg} is the "coherence dephasing rate between any two Zeeman states in levels g and e"[49] in s^{-1}, and

γ_{pulse} is the pulse decay rate in s^{-1}.

Using this theory, Reichardt, Di Teodoro and Farrow predicted a fall in unsaturated LPS signal of close to 10^3 for the pressure range 10 - 100 Torr for a 10 ns laser pulse length. The analytic expression closely matches the experimental unsaturated LPS signal dependence on cell pressure if a pulse-length of 85 ps is assumed. A density matrix numerical analysis by the authors also predicted the experimental saturated LPS signal dependence on cell pressure. **The experimental results of this paper indicate that the saturated LPS signal is less affected by collision rate than the unsaturated LPS signal. The additional theoretical investigations suggest that saturated LPS signal due to a picosecond laser system will be less susceptible to collision rate than that due to a nanosecond laser system.**

Infrared LPS

The following investigations are worth mentioning in passing as they involve recent developments which increase the applicability of polarisation spectroscopy to combustion.

A major limitation on the application of polarisation spectroscopy to combustion is in the number of accessible transitions in the visible and UV for the most important combustion species. There has been an increasing effort to extend laser combustion diagnostics to the infra-red wavelength range to take advantage of the large range of vibrational transitions available for combustion species and accessible to existing laser systems[50] [51] This investigation has also been intensified by the development of IR cameras for imaging applications. An advantage of the infrared LPS technique over infrared fluorescence techniques is the lack of spectral filtering required to discriminate against the strong background for combustion systems in the infrared region.

In 2002, **Roy, Lucht and Mcilroy**[52] presented LPS of CO_2 where both pump and probe beams were in the mid-infrared (~ 2.7 μm). The authors claimed that the experiment was one of the first mid-infrared LPS experiment reported in the literature.

The experiment pumped the *"P(13) and P(14) resonances of the (0 0^0 0) → (0 0^1 0) transition of CO_2"*[52]. Experiments were taken at sub-atmospheric pressure (in a low-pressure cell) and in an atmospheric pressure CO_2 jet. The experiments were supported by a time-dependent density matrix computation which modelled the Zeeman state populations of the upper and lower levels of the pumped transition[d].

The mid-infrared beams were produced by a frequency doubled Nd:YAG pumped optical parametric generator (OPG). The infra-red pulse length for this system is ~ 4 ns and the linewidth < 0.016 cm^{-1}. The 2.7 μm beam had pulse length ~ 5 ns and an energy of ~ 4 mJ. The experiment used a near-collinear pump/probe beam geometry with a beam intersection angle of ~ 7°. The pump beam was circularly polarised. The 1 mJ pump and 30 mJ probe beams were focussed to ~ 100 μm diameter with a beam interaction distance of ~ 2 μm. The polarisers were made from TiO_2 with an crossed extinction ratio of 2.5 x 10^{-5} for the atmospheric pressure experiments. The pressure induced birefringence of the cell windows increased the achievable crossed polariser extinction ratio to 8 x 10^{-5} for the low-pressure cell experiments. The infrared LPS signal was detected (after passing through a bandpass filter[e]) by a liquid nitrogen cooled InSb detector

[d] To model the P(14) transition, Roy, Lucht and Mcilroy used 58 Zeeman states and two bath states.

[e] The bandpass filter used was not specified in the paper.

(Judson, EG&G) and amplified by a 1.6 MHz bandwidth amplifier produced by the same manufacturer.

The experiment was conducted in the saturated regime. The density matrix calculated lineshapes[f] closely matched experimental lineshapes for the P(13) and P(14) transitions for the atmospheric pressure CO_2 jet flows and reasonably matched the dispersive lineshape obtained for the P(14) transition in a CO_2 low pressure cell (120 Torr). A linear dependence of the infrared LPS signal (for the P(14) transition) on the square of the number density of CO_2 in a CO_2/Ar flow at atmospheric pressure was noted experimentally, although this dependence predicted a non-zero LPS signal intercept at zero CO_2 concentration. Roy, Lucht and McIlroy suggested either flow-meter uncertainty at low flow rates or *"differing collisional rates and processes that occur for different ratios of CO_2 to argon concentration in the jet"*[52] could explain the non-zero intercept[g]. This claim was supported by a slightly narrower lineshape found for a low concentration CO_2 flow (CO_2:Ar = 0.31) in comparison with a high concentration CO_2 flow (CO_2:Ar = 14).

The density matrix calculations of Roy, Lucht and McIlroy produced matches of 3-5:1 between experimental and theoretical lineshape signal to noise ratios for the atmospheric pressure flows. The lineshape for the low-pressure cell was complicated by incomplete modelling of the stress birefringence of the cell windows. The high level of equivalence between the density matrix calculations and the experimental results indicates that mid-infrared LPS may be developed for quantitative number density determination.

The two papers of **Settersen, Farrow and Gray**, *"Coherent infrared-ultraviolet double-resonance spectroscopy of CH_3"*[53] and *"Infrared-ultraviolet double-resonance spectroscopy of OH in a flame"*[54], describe double-resonance LPS experiments which avoid the requirement for infra-red detection by pumping in the infrared and probing in the UV. The papers investigated a range of double-resonance techniques; two-colour polarisation spectroscopy (TC-PS) and two-colour resonant four-wave mixing spectroscopy (TC-RFWM) to detect photolytically produced CH_3, and TC-PS, TC-RFWM and two-colour laser induced fluorescence (TC-LIF) to detect OH in a flame.

[f] The density matrix calculations assumed a pulse with Fourier-transform limited frequency spectrum and pulse length of 2 ns in comparison with the experimental pulse length of ~4-5 ns and linewidth of < 0.016 cm^{-1}.

[g] Roy, Lucht and McIlroy calculated spontaneous emission rates of 7.789 s^{-1} for P(13) and 7.848 s^{-1} for P(14). The kinetic theory of gases was used to calculate a dephasing rate of 9.3 x 10^9 s^{-1} for CO_2/CO_2 collisions and 8.6 x 10^9 s^{-1} for CO_2/Ar collisions. Roy *et al.* note *"that vibrational transfer cross-sections are probably much larger for CO_2-CO_2 collisions"*

For OH, Settersen, Farrow and Gray tuned the pump transition to the infra-red $X^2\Pi$- $X^2\Pi$ (1,0) ro-vibrational band of OH, and the probed transition to the UV $A^2\Sigma^+$- $X^2\Pi$ (1,1) electronic transition from the upper state of the pumped transition. In the case of TC-LIF, the fluorescence was monitored via the $A^2\Sigma^+$- $X^2\Pi$ (1,0) band of OH.

Spectra and saturation curves[h] were obtained for the three techniques. TC-PS and TC-RFWM spectra obtained by scanning the pump beam near 3366.6 cm^{-1} with the probe beam tuned to the UV $A^2\Sigma^+$- $X^2\Pi$ (1,1) Q11(4f) transition of OH showed high signal to background ratios ($>10^3$ for TC-PS) in comparison to the TC-LIF experiment which demonstrated a signal to background ratio of 2[i] due to the thermal background for the lean, premixed (atmospheric pressure) methane/air flame. Based on these spectra, Settersen, Farrow and Gray estimated OH detection limits in the ground state of 5×10^{12} cm^{-3} per quantum state for TC-PS. Rotationally populated populations were noted in these TC-PS, TC-RFWM and TC-LIF spectra. The authors estimated that >90% of the pumped population is redistributed among the rotational states of the pump transition during the ~ 1.5 ns laser pulse[j]. The rotationally populated lines were strongest for the TC-LIF experiments, followed by the TC-RWFM and TC-PS experiments. **Settersen *et al.* suggest that the relative strength of the rotationally populated lines implies that *"polarisation is not strongly preserved in RET"*[54].**

Setterson, Farrow and Gray[53] also used TC-PS used to detect the important combustion intermediate CH_3. This species is difficult to detect due to the rapidly predissocciation of its electronically excited states and spectral interferences. The CH_3 radical was produced by flash photolysis of acetone or CH_3I. The IR pump beam was tuned to transitions from the $\tilde{X}\,^2A_2"$, $v_3 = 0$ band to the $\tilde{X}\,^2A_2"$, $v_3 = 1$ band of CH3, while the UV probe beam was tuned to transitions from the shared lower state in the $\tilde{X}\,^2A_2"$, $v_3 = 0$ band to the upper state $\tilde{B}\,^2A_1'$, $v_3 = 0$ band. Setterson *et al.* noted a CH_3 detection limit of 2×10^{13} cm^{-3} per quantum state.

The development of IR/IR and IR/UV polarisation spectroscopy extends the range its range of application as a combustion diagnostic where spectral interferences prevent the equivalent use of

[h] Saturation of the pump transition was shown to follow a $1/(1+I/I_{sat})$ dependence for TC-LIF and a $I^2/(1+4I/I_{sat})^3$ dependence on the pump beam intensity. IR saturation intensities of 100 MW/cm^2 and UV saturation intensities of 1 MW/cm^2 were reported.

[i] The TC-LIF signal was detected after spectral filtering by a 1/8 m-monochromator.

[j] The probe beam was delayed by 0.25 ns with respect to the pump beam.

fluorescent techniques. However, as in the case of UV/UV PS, quantitative number density and temperature determination will require extensive knowledge and modelling of collisional population transfer.

Simultaneous PLIF and PLPS in Natural Gas/O_2 and Natural Gas/Air flames

The current chapter describes two experiments in which LIF and LPS signals are simultaneously collected. The first experiment presents simultaneously collected (average) PLIF and PLPS images due to the OH distribution in a small fuel-lean natural gas/O_2 flame. The PLIF and PLPS signals may be collected simultaneously as the PLIF image is the fluorescence due to the laser sheet and the PLPS signal is produced by passage of the probe beam through the same sheet. The two images thus relate to the same distribution of the target species within the pump sheet volume and can be compared directly to compare the imaging capability of both techniques.

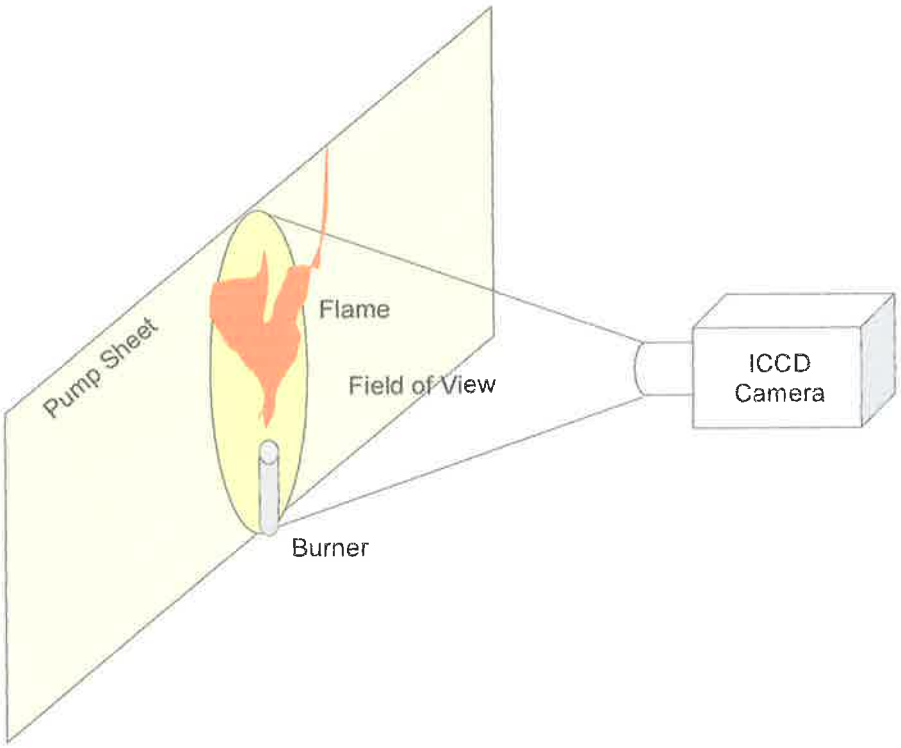

Figure 1: Configuration for collection of a PLIF image. The fluorescence by target species molecules pumped by the laser sheet is imaged by the ICCD camera. The resulting image indicates the spatial distribution of the target species in the plane of the laser sheet.

The second experiment presents LIF and LPS signal as a function of fuel equivalence ratio in a natural gas/air flame from a rectangular mixing burner. The LIF and LPS signal (after correction to represent the number density of the target species contributing to the signal) is compared with the OH number density calculated by the equilibrium module of the CHEMKIN (combustion modelling) library. The results of this experiment indicate that the species number densities predicted by (saturated) LPS and (linear regime) LIF signal for nanosecond pulse length laser systems show similar dependence on equivalence ratio in an atmospheric pressure natural gas/air flame.

Introduction to Planar Laser Induced Fluorescence (PLIF)

Planar Laser Induced Fluorescence images the fluorescence due to the spatial distribution of the pumped target species population in the plane of the pump sheet. An ICCD camera is placed orthogonal to the pump sheet to collect the fluorescence (Figure 1).

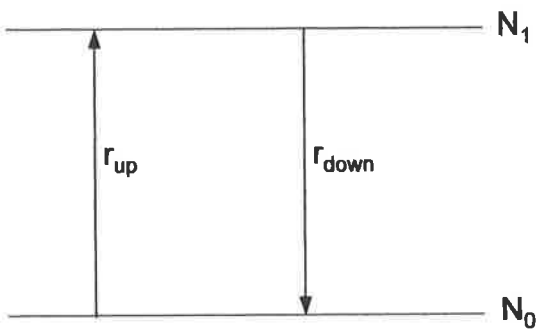

Figure 2: Closed two-level system.

The LIF signal, I_{LIF}, due to fluorescence induced by optical pumping of the transition from the lower state, 0, to the upper state, 1, is given by[28]

$$I_{LIF} = h\upsilon \cdot N_1 \cdot A_{10} \cdot \frac{\Omega}{4\pi} \cdot dv \qquad \text{Equation 4}$$

where

h_υ is the energy of the emitted photon,

N_1 is the population density of the upper state of the pumped transition,

A_{10} is the Einstein coefficient for spontaneous emission from the upper to the lower state of the pumped transition[k],

Ω is the solid angle from which the imaging optics collect the signal, and

dv is the pumped volume from which the fluorescence is collected.

The LIF signal is then proportional to the population of the *upper* state of the pumped transition.

Consider the two-level rate equation model for a closed two-level system discussed in Appendix II (and shown in Figure 2) with lower state population number density, N_0, and upper state population number density, N_1. The total population density is

$N_1(t) + N_0(t) = N$ Equation 5

[k] The fluorescent transition need not be the same as the pumped transition, but is assumed to be so in this chapter for simplicity of the discussion.

The transition rate from the lower to the upper state may include both stimulated absorption and collisional transition rates and is denoted by the term, r_{up}. The transition rate from the upper to the lower state includes spontaneous and stimulated emission as well as collisional transition rates (which may include quenching terms) and is denoted by the term, r_{down}. The total transition rate, r, is defined as

$r = r_{up} + r_{down}$. Equation 6

The time dependence of the population density of the upper state, $N(t)_0$, assuming an initially unpopulated upper state is given by

$$N_1(t) = N \cdot \frac{r_{up}}{r} \cdot \left(1 - e^{-rt}\right)$$ Equation 7

For later reference, the number density difference between the upper and the lower state of the pumped transition is

$$N_0(t) - N_1(t) = N \cdot \left(1 - 2 \cdot \frac{r_{up}}{r} \cdot \left(1 - e^{-rt}\right)\right)$$ Equation 8

The expressions for the number densities for this simple model contain transient exponential terms and converge to steady-state solutions for times, $t > 3/r$, where r has been defined in equation [5]. Characteristic rates and timescales for the significant collisional and optical population transfer processes are required to allow the timescale, 1/r, to be determined. Table 1 shows typical timescales for the significant collisional and optical processes for the $A^2\Sigma$-$X^2\Pi$ (0-0) band of the OH radical in atmospheric pressure flames.

If, for the sake of simplicity, we ignore all collisional processes other than the quenching rate, Q_{10}, (from the upper state, 1, to the lower state, 0) and write the stimulated emission rates from the lower state to the upper state and from the upper state to the lower state as $B_{01}W$ and $B_{10}W$ respectively the term, r, may be written as

$r = B_{01}W + B_{10}W + Q_{10} + A_{10}$ Equation 9

where

B_{01} is the Einstein coefficient for stimulated absorption from state, 0, to state, 1,

B_{10} is the Einstein coefficient for stimulated emission from state, 1, to state, 0,

A_{10} is the Einstein coefficient for spontaneous emission from state, 1, to state, 0, and

W is the spectral energy density of the pump beam, i.e. I_ν/c where I_ν is the spectral irradiance (the irradiance per unit frequency interval)

Population Transfer Process	Rate (s^{-1})	Characteristic Timescale (ns)	Comments
Spontaneous Emission	1.4×10^{6} s^{-1}	714 ns	(Eckbreth[28])
Quenching from the $A^2\Sigma$ state (v' = 0)	5.6×10^{8} s^{-1}	1.79 ns	(Eckbreth[28] quoting Bergano *et al.*[55]. Flame measurement 760 Torr)
	0.6×10^{9} s^{-1}	1.7 ns	(Tobai *et al.*[56] quoting Daily and Rothe[57]. Six-level model of a CH_4/air flame)
RET in the $A^2\Sigma$ state (v' = 0)	1.1×10^{9} s^{-1}	0.9 ns	(Tobai *et al.*[56] quoting Daily and Rothe[57]. Six-level model of a CH_4/air flame)
RET in the $X^2\Pi$ state (v" = 0)	2.2×10^{9} s^{-1}	0.45 ns	(Tobai *et al.*[56] quoting Daily and Rothe[57]. Six-level model of a CH_4/air flame)
VET in the $A^2\Sigma$ state (v' = 0 to v' = 1)	4.6×10^{8} s^{-1}	2.2 ns	(Tobai *et al* [56] quoting [58] for 10^5 Pa)
Total removal rate in the $A^2\Sigma$ state (v' = 0)	0.8×10^{9} s^{-1}	1.25 ns	(Tobai *et al.*[56] quoting Daily and Rothe[57]. Six-level model of a CH_4/air flame at 2000 K)
Total repopulation rate in the $X^2\Pi$ state (v" = 0)	1.8×10^{9} s^{-1}	0.56 ns	(Tobai *et al.*[56])

Table 1: Characteristic rates and timescales for the significant collisional and optical processes for the for the $A^2\Sigma$-$X^2\Pi$ (0-0) band of the OH radical in atmospheric pressure CH_4/air flames.

It can be seen from Table 1 that the rate of spontaneous emission is negligible for the OH radical in atmospheric flames in comparison with collisional population transfer. The timescale associated with collisional quenching is ~ 1.8 ns so that, even disregarding the contribution of optical pumping, the transient exponential terms in equations [6] and [7] die out on a timescale of the order of 5.4 ns. It is clear that if the stimulated emission and absorption rates are much less than the quenching rate, there will be significant population variation over the 5 ns length of the laser pulse. However, if the stimulated emission and absorption rates are much greater than the quenching rate, the pumped populations will be approximately constant over much of the laser pulse length.

Consider the steady-state solutions to equations [4] and[5]

$$(N_1)_{\text{steady-state}} = N \cdot \frac{r_{up}}{r} = N \cdot \frac{B_{01}W}{B_{01}W + B_{10}W + Q_{10} + A_{10}} = N \cdot \left(\frac{B_{01}}{B_{01} + B_{10}}\right) \cdot \frac{1}{1 + \left(\frac{Q_{10} + A_{10}}{B_{01}W + B_{10}W}\right)}$$

Equation 10

and

$$(N_0 - N_1)_{steady-state} = N \cdot \left(1 - 2 \cdot \left(\frac{B_{01}}{B_{01} + B_{10}}\right) \cdot \frac{1}{1 + \left(\frac{Q_{10} + A_{10}}{B_{01}W + B_{10}W}\right)}\right)$$ Equation 11

There are two regimes where these steady-state expressions may be approximated. For a quenching dominated steady-state regime, $Q_{10} >> B_{10}W$, $B_{01}W$, A_{10}, these expressions reduce to

$$(N_1)_{\substack{steady-state \\ quenching\_dominated}} = N \cdot \left(\frac{B_{01}}{B_{01} + B_{10}}\right) \cdot \left(\frac{B_{01}W + B_{10}W}{Q_{10} + A_{10}}\right) = N \cdot \left(\frac{B_{01}W}{Q_{10} + A_{10}}\right)$$ Equation 12

and

$$(N_0 - N_1)_{\substack{steady-state \\ quenching\_dominated}} = N \cdot \left(1 - 2 \cdot \left(\frac{B_{01}W}{Q_{10} + A_{10}}\right)\right)$$ Equation 13

For a stimulated emission dominated steady-state regime, $B_{10}W$, $B_{01}W >> Q_{10}$, A_{10}, equations [9] and [10] approach

$$(N_1)_{\substack{steady-state \\ stimulated\_emission\_dominated}} = N \cdot \left(\frac{B_{01}}{B_{01} + B_{10}}\right)$$ Equation 14

and

$$(N_0 - N_1)_{\substack{steady-state \\ stimulated\_emission\_dominated}} = N \cdot \left(1 - 2 \cdot \left(\frac{B_{01}}{B_{01} + B_{10}}\right)\right)$$ Equation 15

Equation [9] indicates that, *assuming that the pumped populations have reached steady-state*, the upper state population (and hence the induced fluorescence) in a quenching dominated regime is linearly proportional to the pump beam intensity via the term, W. In the saturated, steady-state regime, as shown in equation [11], the upper-state population is independent of pump beam intensity.

A corollary of the above is that, for the quenching rate of 5.6 x 10^8 s^{-1} for the $A^2\Sigma$ state of OH, operation in the saturated (steady-state) regime implies that transient exponential terms in equations [7] and [8] are associated with a much shorter timescale than the 5 ns laser pulse length. In this case, the pumped populations can be assumed to be constant over much of the laser pulse. [Note that this simple model does not include more complex collisional population transfer processes such as rotational and vibrational energy transfer and is only indicative of the general behaviour of the pumped populations.]

(1) Simultaneous PLIF and PLPS Imaging in a Premixed Natural Gas/O_2 Flame from a Modified Glass-Blowing Torch

The following imaging experiment was performed in

- the saturated (steady-state) regime of PLPS, and
- near-linear regime of PLIF.

The PLIF and PLPS imaging techniques may be applied simultaneously as the PLIF signal is the fluorescence due to absorption from the pump sheet while the PLPS signal results from the transmission of the weak probe beam through the pump sheet. The fluorescence due to the probe beam is normally negligible in comparison with that due to the laser sheet due to the large difference in irradiance of each beam.

The simultaneous collection of PLIF and PLPS images allowed investigation of the relative distribution and saturation of the OH signal for the two techniques as a preliminary to quantitative experiments described later in this chapter to compare LIF and LPS in a natural gas/air flame from a rectangular mixing burner as a function of equivalence ratio. Typically, PLIF images appear free from the thermal gradient and beamsteering effects that plague coherent laser diagnostic techniques in combustion and are apparent in the PLPS images presented in this thesis. The PLIF images collected in this experiment were free of thermal beamsteering structures. However the spatial resolution of the PLIF images was not sufficient to conclusively state independence from such effects when compared with the scale of the thermal gradient structures in the simultaneously collected PLPS images .

The PLIF and PLPS imaging experiment compares simultaneously collected average images representing the same OH distribution in a stable premixed natural gas/O_2 flame. The LPS signal was highly saturated at 8.9 MW/cm^2 and the LIF signal was collected in the near-linear regime of optical pumping. Since the two signals are related to the intensity of the laser sheet, this result indicates that the saturation of the LPS signal occurs at a much lower intensity than the LIF signal. Note that this result disagrees with the LIF and LPS saturation curves presented by Reichardt, Di Teodoro and Farrow, where the linear behaviour of the LIF signal and the cubic behaviour of the LPS signal (for a picosecond laser pulse-length) occur for pump irradiances of less than 1MW/cm^2 with a plateau region occurring in the LPS saturation curve at ~ 10 MW/cm^2.

A major problem with the imaging experiments described in this thesis was in the signal strength of the polarisation spectroscopy images. It was necessary to select the flame with highest OH PLPS signal in order to obtain high quality images and to operate at the highest laser energy available. For example, a natural gas/O_2 flame produced much better signal than a natural gas/air or H_2/O_2 flame, as would be expected from the equilibrium OH concentrations for each flame and the quadratic

dependence of the signal on target species number density. It was for this reason that the LPS imaging experiments were not conducted in the linear regime of optical pumping.

Most of the images in this thesis were collected for a natural gas/O_2 flame from the modified glass-blowing torch described in Chapter III with best signal obtained for a small fuel-lean flame close to blowoff. For comparison with the images due to the premixed flame, Figure 3 shows an example of a (100 shot) average $A^2\Sigma$–$X^2\Pi$ (0-0) $P_2(8)$ OH PLPS image for a methane diffusion flame (minus the probe beam extinction background). The image had a maximum average signal above the probe extinction background of 40 counts at a gain of 9.0 for a beam intersection angle of 13.6° and a circularly polarised pump beam. The diffusion flame was very small to enable it to be imaged in the small sample region above the burner, with the methane flow reduced to practically nothing to create a nearly spherical, barely visible flame sitting over the burner tip. An equivalent stretched image is shown in Figure 4 to demonstrate again the distortion of the imaged region in the collected image. A second average image was taken with the laser wavelength slightly detuned to confirm the image corresponded to OH PLPS signal and not to flame emissions.

The simultaneous PLIF and PLPS imaging experiment described below used a horizontally polarised pump beam and a 13.6° pump/probe beam intersection angle to probe the OH distribution in a fuel-lean premixed natural gas/O_2 flame from a modified glass-blowing torch. The experimental arrangement is shown in Figure 5. The PLPS geometry and optics were largely unchanged from the imaging experiment described in Chapters III, V and VI. The exceptions to this were the exception of the absence of the ½–wave or ¼-wave rhomb previously used to rotate the plane of polarisation of the pump beam to vertical or to produce a circularly polarised pump beam and an additional horizontal aperture used to truncate the pump sheet to allow direct scaling of the two images.

The PLIF ICCD was positioned normal to the pump beam sheet and triggered with a 10 ns gate to collect the fluorescence and scattered signal. The strong PLIF signal was collected at a gain of 1.0, while the weaker PLPS signal was collected at a gain of 9.0. The timing was an extension of the previous PLPS experiments (see Figure 6). The primary trigger for the PLPS timing (which controlled the laser and PLPS ICCD) was allowed to trigger an additional ICCD which collected the PLIF signal. Due to timing jitter with respect to triggering of the PLPS ICCD, the PLPS signal was collected with a gate of 200 ns. However, checks confirmed that flame emissions[1] collected by the PLPS imaging system were insignificant for the fuel lean natural gas/O_2 flames from the modified glass-blowing torch imaged with this gate.

[1] Flame emissions for the fuel lean natural gas/O_2 flame from the modified glass-blowing torch were typically less than one count on a 50 shot average at gain 8.0 for this gate.

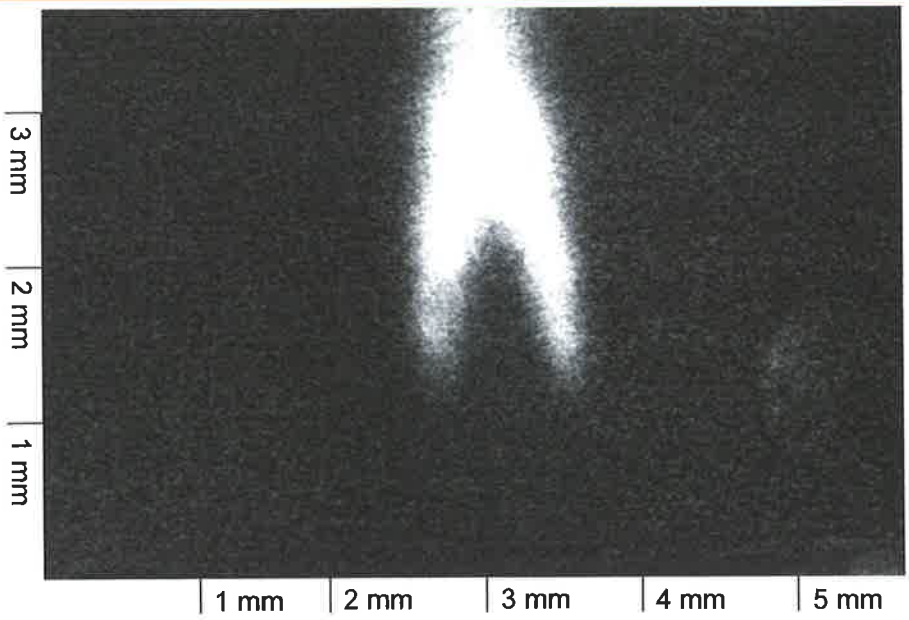

Figure 3: OH PLPS image collected for a natural gas diffusion flame and corrected for the probe beam extinction background for a circularly polarised pump beam and a beam intersection angle of 13.6°. The probed transition was $A^2\Sigma$–$X^2\Pi$ (0-0) $P_2(8)$. The tip of the modified glass blowing torch is at the very base of the image.

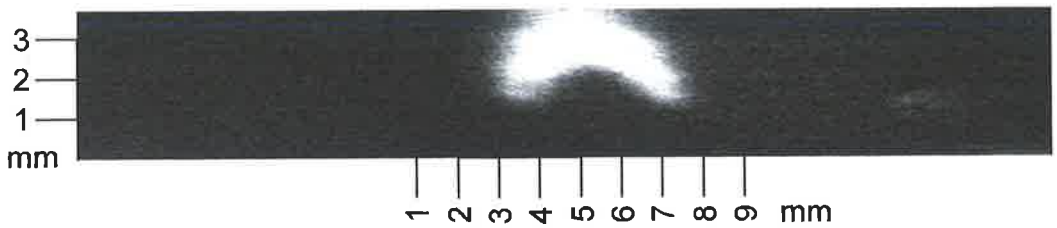

Figure 4: Stretched OH PLPS image shown in Figure 3 indicating the dimensions of the probed OH distribution in the elliptical pump/probe interaction region for the beam intersection angle of 13.6°. The tip of the modified glass blowing torch is at the very base of the image.

The PLIF ICCD was positioned 965 mm from the premixed flame. The resultant PLIF images collected with an f2 lens took up only 27 x 18 pixels of the 576 x 384 pixel array as shown in Figure 7. Figure 8 shows the equivalent OH PLPS image, which utilises much of the available 576

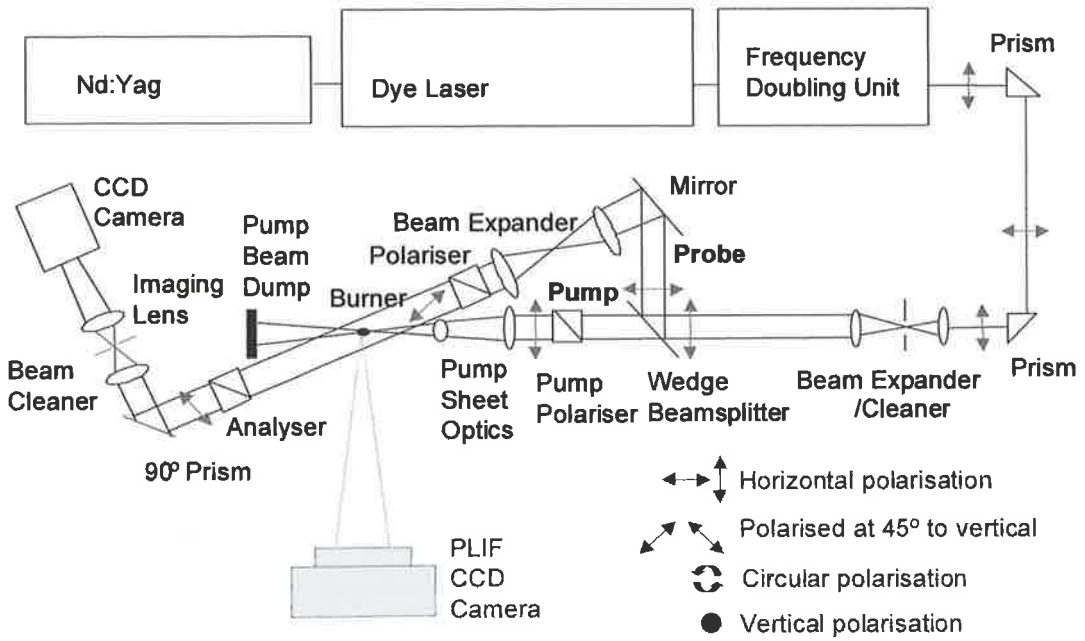

Figure 5: Experimental arrangement for simultaneous PLIF and PLPS imaging. The pump beam is horizontally polarised and the probe beam is polarised at $\pi/4$ to the vertical. The pump and probe beams intersect at 15° in the horizontal plane.

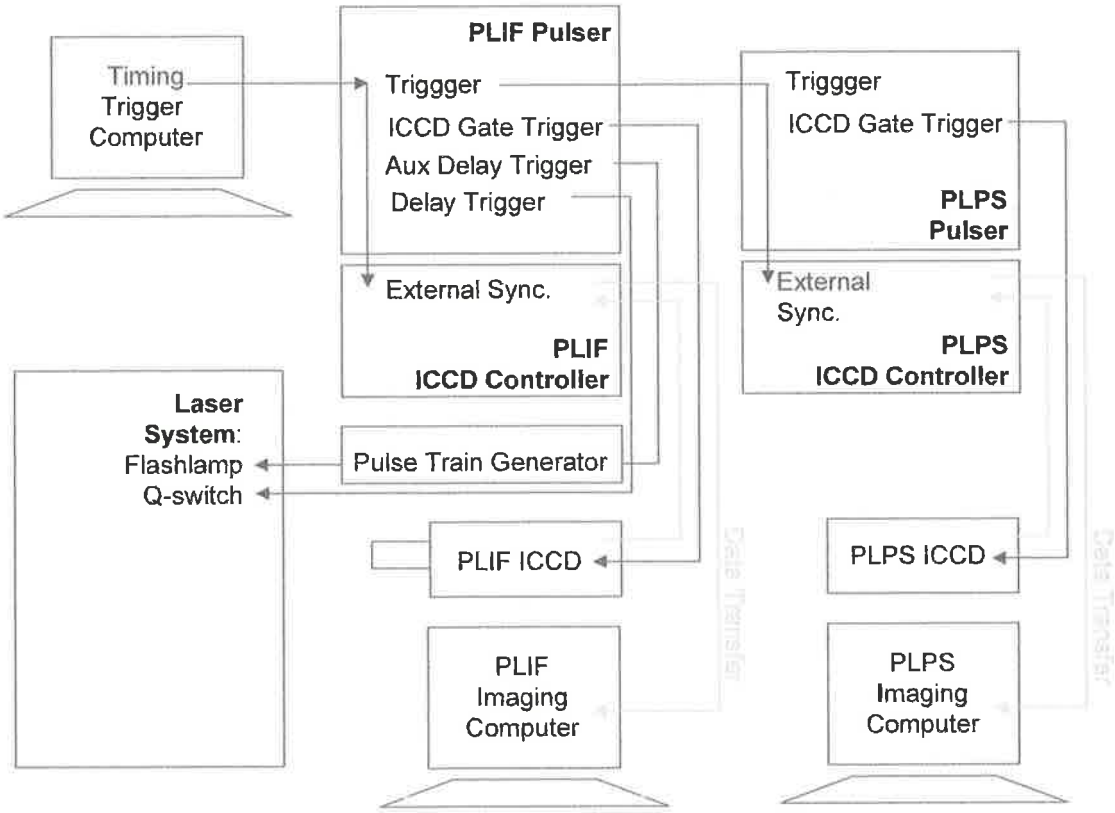

Figure 6: Timing control for simultaneous PLIF and PLPS imaging.

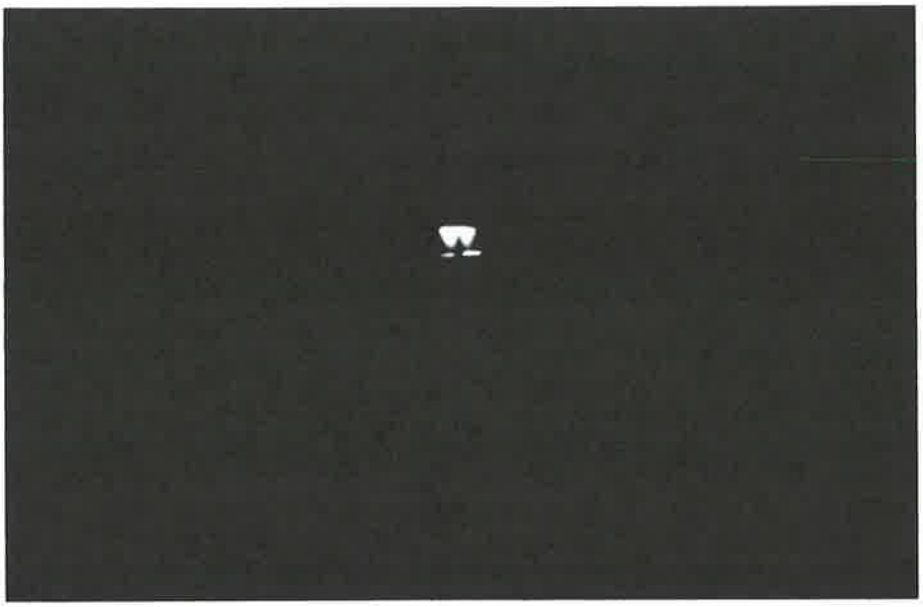

Figure 7: Uncorrected (50 shot average) OH PLIF image indicating the small fraction of the ICCD array utilised to image the approximately 3 mm high sheet/flame interaction region at a distance of 965 mm. Two flat regions of signal due laser scatter are visible at the base of the small flame OH distribution. The pump sheet height producing the PLIF signal and the scattering from the tip of the burner was < 3 mm and the region of OH signal approximately 4 - 5 mm wide. The minimum focus distance for the PLIF ICCD camera was ~ 800 mm without additional lens systems.

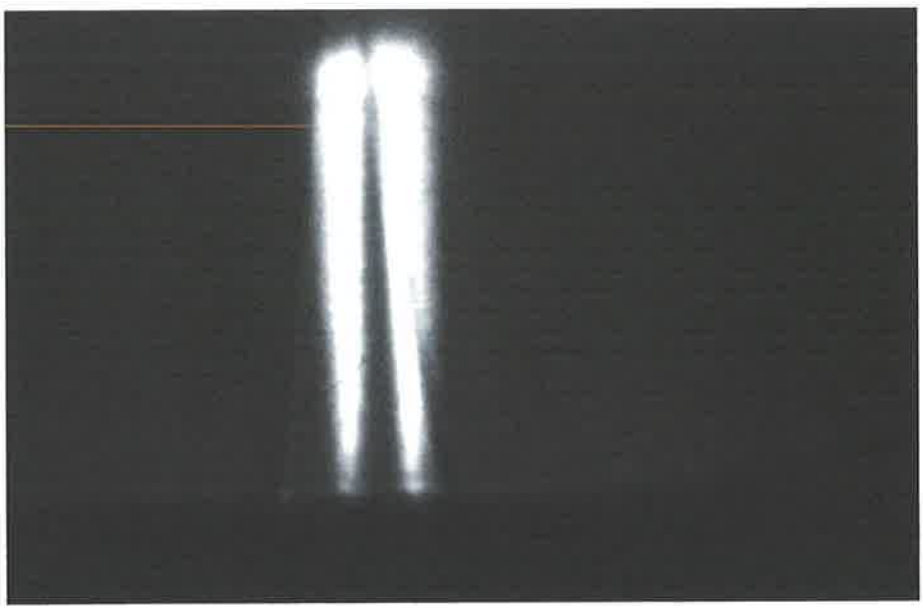

Figure 8: Uncorrected (50 shot average) Mode 1 OH PLPS image collected simultaneously with the PLIF image in Figure 7. The relative scale of the two flame images (the images in Figures 7 and 8 represent the full 378 x 576 array of the ICCD detector) indicates the relative resolution for the given experimental arrangement.

x 384 pixel array of the PLPS ICCD, imaged approximately 1.3 m beyond the flame. The difference in spatial resolution is obvious from the two images. Although additional lenses could be used to magnify the PLIF image, the clear advantage to be inferred from the two images is the high spatial direct resolution available to PLPS when applied as a remote visualisation technique.

The PLIF signal strength decreases as the square of the object/image distance, r, as does the level of detected flame emissions. The background emissions are then typically minimised by the use of spectral filters. The PLPS signal is carried on the probe beam cross-section and signal strength will be strong as far as probe beam can be propagated. Background flame emissions may be minimised by both spatial and spectral filters, and additionally reduce due to the r^2 variation with distance. In this experiment, the PLPS ICCD camera was placed approximately 1.3 m from the flame. However, the ICCD camera could as easily been placed at a greater distance from the flame limited only by the degree of divergence of the probe beam. Note however, that the imaging optics would be reselected to minimise thermal density gradient structures in the collected images as discussed in Chapter VI.

PLIF and PLPS images for the $A^2\Sigma$–$X^2\Pi$ (0-0) $Q_2(8)$ transition were simultaneously collected representing 17 parallel planes as the pump beam was spatially scanned across the base of the flame. The PLPS image set is similar to those obtained in Chapters III, V and VI. Checks were made that the depth of field of the PLIF ICCD lens system included the full 6 mm width of the tip of the small burner and flame used in the experiment so that the PLIF images are in focus for all 17 images of the PLIF image set.

The PLIF images required no background correction, flame emissions being undetectable and signal levels on the level of ~ 1000 counts at a gain of 0.1. A 310nm (FWHM 10 nm) narrowband filter and a 10 ns gate was used to minimise flame background emissions in the PLIF images. OH PLIF signal due to the unfocussed probe beam was not detected in the PLIF images when the pump sheet was blocked at this low gain.

The background flame emissions in the case of the collected PLPS images were on the order of 1 count at a gain of 8.0 for the fuel lean natural gas/O_2 flames imaged below. Detectable background flame emissions were noted in PLPS images collected for more luminous and sooty flames. It should be noted however, that the PLPS imaging system included no spectral filtering elements for all images presented in this thesis. The PLPS imaging system minimised PLIF contributions to the PLPS signal by using an lens/iris system to spatially filter the PLPS signal (no PLIF contributions to the LPS signal were noted throughout the experiments in this thesis).

In order to compare the signal due to each technique, it is necessary to interpret the images in terms of the number density of the target species. The theory of Teets, Kowalski, Hill, Carlson and Hansch predicts that the PLPS signal is proportional to the square of the induced dichroism experienced by the probe beam, $\Delta\alpha^{i,i'}_{J,J''}$, according to the equation

$$I_{PLPS} = I_{probe\_0} \cdot \left(\xi + K \cdot \left(\Delta\alpha^{i,i'}_{J,J''}\right)^2\right) \qquad \text{Equation 16}$$

where

I_{PLPS} is the PLPS signal,

I_{probe_0} is the probe beam intensity incident on the primary probe beam polariser,

ξ is the extinction ratio of the probe beam polarisers, and

K is a constant which includes geometrical factors.

The induced dichroism is proportional to the sum (defined in Chapter I)

$$\Delta\alpha^{i,i'}_{J,J''} = \sum_{M}\left(N_{J,M} \cdot (\sigma^{i}_{J,J'',M,M''} - \sigma^{i'}_{J,J'',M,M''}) \cdot C_{JJ''}\right) \qquad \text{Equation 17}$$

where

$\Delta\alpha^{i,i'}_{J,J''}$, is the induced dichroism experienced by the probe beam for the transition (J,M) to (J",M"), and is defined as the difference in absorption coefficients for the two orthogonal polarisation states, i and i', of the probe beam,

$N_{J,M}$ is the number density of the lower state (J,M),

$\sigma^{probe}_{J,J'',M,M''}$ is the rotational/Zeeman component of the absorption cross-section for the probe transition (J,M) to (J",M"), and

$C_{J,J''}$ is the non-rotational (e.g. electronic/vibrational) component of the absorption cross-section for the probe transition (J,M) to (J",M").

For the case of a shared pump and probe beam transition, the contribution to the dichroism by the population of the upper state of the transition must be considered and the expression for the induced dichroism becomes

$$\Delta\alpha^{i,i'}_{J,J''} = \sum_{M}\left((N_{J,M} - N_{J',M'}) \cdot (\sigma^{i}_{J,J'',M,M''} - \sigma^{i'}_{J,J'',M,M''}) \cdot C_{JJ''}\right) \qquad \text{Equation 18}$$

In comparison, the PLIF signal is proportional to the number density, $N_{J',M'}$, of the upper state of the pumped transition which, for the case of a shared pump and probe beam transition, corresponds to the number density of the upper state of the probed transition, $N_{J''}$.

$$I_{PLIF} \propto N_{J''} \qquad \text{Equation 19}$$

The steady-state dependence of the upper state population on the pump sheet intensity, I_{pump}, given earlier in the chapter in equation [10], may be rewritten as

$$\left(N_{J'',M''}\right)_{steady-state} \propto \frac{1}{1+\left(\frac{I_{sat}}{I_{pump}}\right)} \qquad \text{Equation 20}$$

so that the saturation behaviour of the PLIF signal is described by the equation

$$I_{\substack{PLIF \\ steady-state}} = \frac{d}{1+\left(\frac{I_{sat}}{I_{pump}}\right)} \qquad \text{Equation 21}$$

where I_{sat} is the saturation intensity and d is a constant.

If the saturation is small, so that $I_{pump} << I_{sat}$, the steady-state behaviour of the PLIF signal becomes

$$I_{\substack{PLIF \\ steady-state \\ low\_pump\_intensity}} = d \cdot \frac{I_{pump}}{I_{sat}} \qquad \text{Equation 22}$$

If the saturation is large, i.e. $I_{pump} >> I_{sat}$, the steady-state PLIF signal approaches independence of the pump sheet intensity

$$I_{\substack{PLIF \\ steady-state \\ high\_pump\_intensity}} = d \cdot \left(1-\left(\frac{I_{sat}}{I_{pump}}\right)\right) \approx d \qquad \text{Equation 23}$$

The saturation behaviour of the PLPS signal may also be described in two regimes. The theory of Teets, Kowalski, Hill, Carlson and Hansh[1] predicts that the induced dichroism is linearly dependent on the pump beam intensity for low beam intensities. It is reasonable to assume the induced dichroism approaches a constant value for large beam intensities, i.e.

$$I_{\substack{PLPS \\ low\_pump\_intensity}} = I_{probe\_0} \cdot \left(\xi + G \cdot \left(I_{pump}\right)^2\right) \qquad \text{Equation 24}$$

$$I_{\substack{PLPS \\ high\_pump\_intensity}} = I_{probe\_0} \cdot \left(\xi + H\right) \qquad \text{Equation 25}$$

where G and H are constants dependent on the induced dichroism.

For a single laser system with shared pump and probe transitions, the PLPS signal demonstrates the following dependence on laser intensity, I.

$$I_{\substack{PLPS \\ low\_pump\_intensity \\ shared\_pump/probe\_transitions}} = k \cdot I + g \cdot I^3 \qquad \text{Equation 26}$$

$$I_{\substack{PLPS \\ high\_pump\_intensity \\ shared\_pump/probe\_transitions}} = (k+h) \cdot I \qquad \text{Equation 27}$$

where g, h and k are constants.

If the LPS signal is corrected for linearity with the probe beam profile, for the probe beam extinction background and the square root taken to represent the induced dichroism, the dependence on laser intensity becomes

$$\Delta\alpha_{\substack{PLPS \\ low\_pump\_intensity \\ shared\_pump/probe\_transitions}} = \sqrt{g}\cdot I \qquad \text{Equation 28}$$

$$\Delta\alpha_{\substack{PLPS \\ high\_pump\_intensity \\ shared\_pump/probe\_transitions}} = \sqrt{h} \qquad \text{Equation 29}$$

The simultaneously collected $A^2\Sigma$–$X^2\Pi$ (0-0) $Q_2(8)$ OH PLPS and PLIF images of this experiment are presented in Figures 9 and 10 respectively. The two image sets represent simultaneously collected images for a series of vertically oriented cross-sections through the flame as the pump sheet is spatially scanned across the tip of the burner. The images in each set are 50 shot averages, uncorrected for laser intensity fluctuations. The images have been corrected as described below to represent terms proportional to the number density of the target species.

Figure 9 shows images of the square root of the (50 shot) average PLPS Mode 2 signal. The images are also stretched along the horizontal axis by the factor 3.86 for allow direct comparison with the distribution of signal in the PLIF images. The PLPS images are corrected for the extinction background due to the crossed probe beam polarisers, the ratio, S/B, calculated and the square root of each pixel signal taken to produce an image proportional to the induced dichroism.

The PLPS images are presented in inverse grey-scale, with the darkest colour corresponding to lowest signal and the lightest colour to highest signal. The speckled region at the base and right-hand edge of each image corresponds to regions outside the probe beam profile where the image correction technique produces anomalous count levels. The full range of the colour map has been selected to map the 5-95% range of the corrected signal in each image to avoid bleaching of the image by random high count levels in the non-probe profile region. It will also be noted that the flame appears to be tilted in the stretched PLPS images. This highlights the accentuation of misalignment to the axis normal to the pump/probe beam intersection plane in stretched PLPS images for small beam intersection angles.

Figure 10 shows the uncorrected PLIF images, presented in a false colour map where lighter colours represent high signal levels and darker colours low signal levels. A 71 x 51 pixel region of the full image collected by the PLIF ICCD has been selected for these expanded images. The images required no correction for dark counts (~0 counts for this ICCD) and, as discussed above, effectively no correction for flame emissions or PLIF contributions due to the unfocussed probe beam. The horizontal band of signal at the base of each PLIF image is laser scattering from the tip of the burner. The lack of flame emission is clear in the images where the pump beam is close to the edge of the flame and there the OH PLIF signal due to the pump beam is close to zero.

Neither the PLPS nor the PLIF images in Figures 9 and 10 have been corrected for the pump sheet intensity profile.

Figures 9 and 10: (Pages following) Set of simultaneous OH PLPS and PLIF images of a fuel/lean premixed natural gas/O_2 flame for a horizontally polarised pump beam (with a probe beam polarised at $\pi/4$ to the vertical axis) and a pump/probe intersection angle of 13.6°. The image set was obtained by translating the pump sheet across the tip of glass-blowing torch to image a series of parallel, vertically oriented cross-sections through the flame. The two sets of images represent corresponding PLPS (Figure 9) and PLIF (Figure 10) images. The pixelation of the PLIF images (71 x 51 pixels) is due to the relatively small fraction of the CCD array occupied by the flame image. The PLIF images are uncorrected. The PLPS images have been corrected for the probe extinction background, the factor, S/B, calculated and the square root taken to represent the induced dichroism. The last image in the PLIF image set has been omitted as it is effectively blank.

Figure 9: PLPS images as described in the caption above. The PLPS images are plotted on a greyscale based on the 5 to 95% signal strength of each image with black representing the lowest signal.

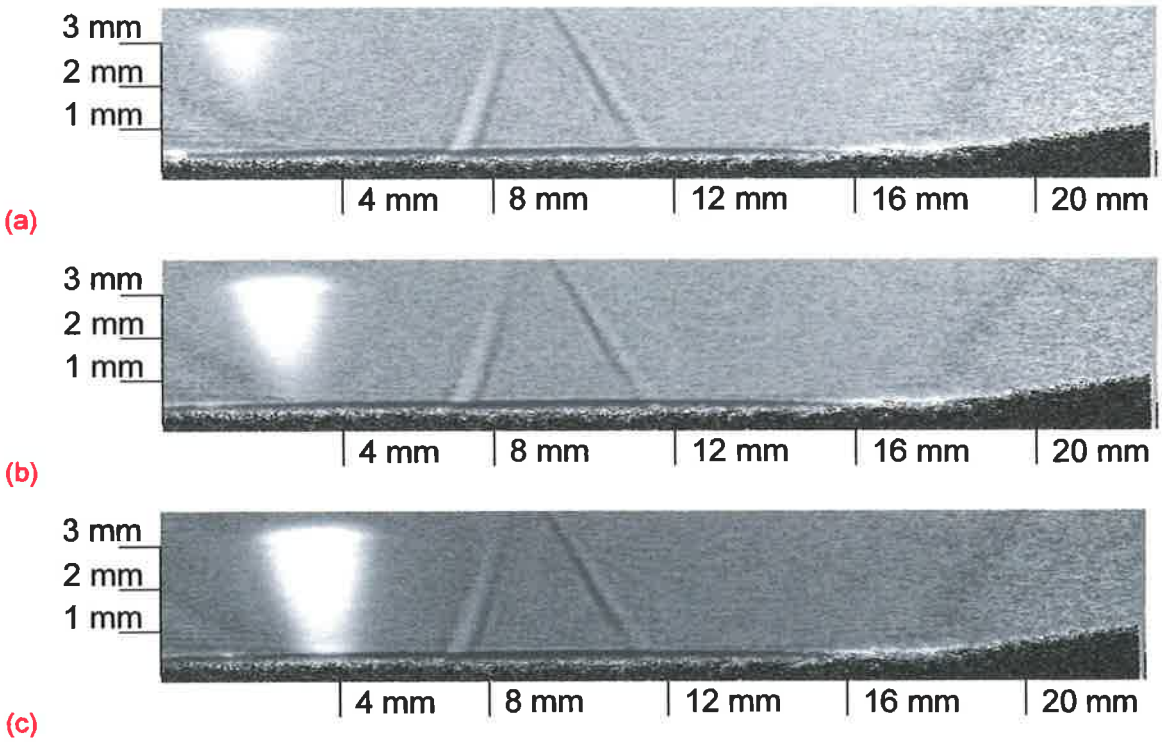

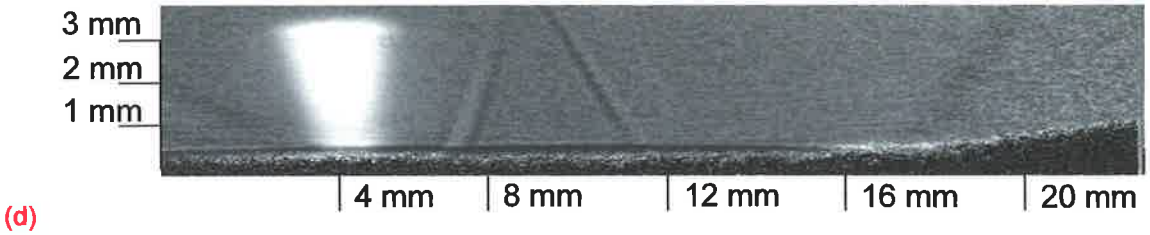
3 mm
2 mm
1 mm
4 mm
8 mm
12 mm
16 mm
20 mm

(d)

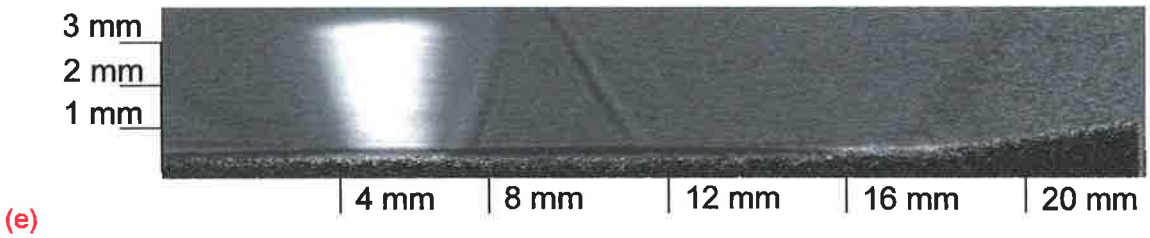
3 mm
2 mm
1 mm
4 mm
8 mm
12 mm
16 mm
20 mm

(e)

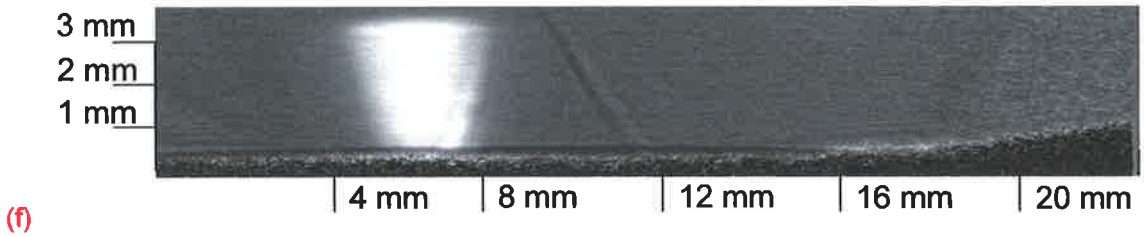
3 mm
2 mm
1 mm
4 mm
8 mm
12 mm
16 mm
20 mm

(f)

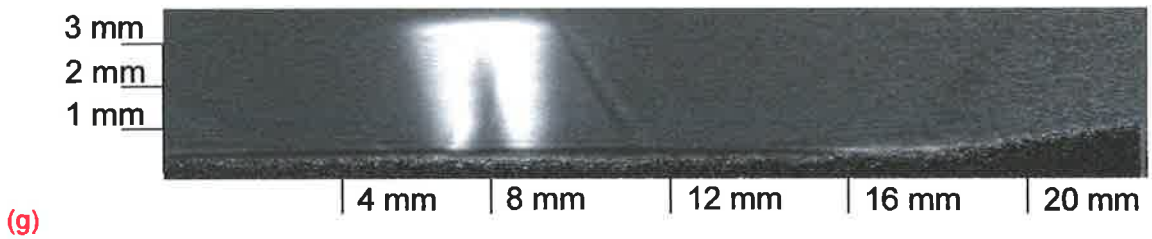
3 mm
2 mm
1 mm
4 mm
8 mm
12 mm
16 mm
20 mm

(g)

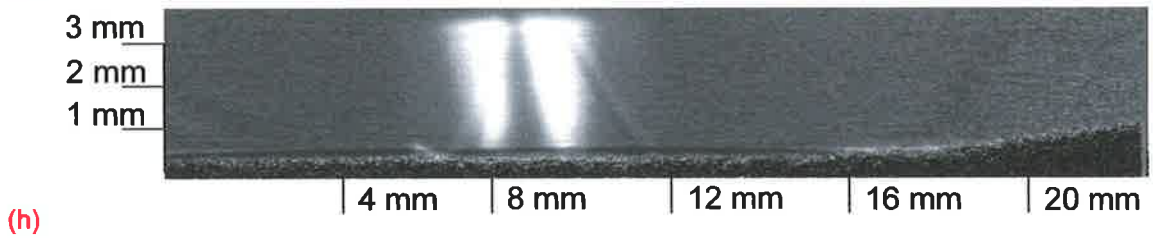
3 mm
2 mm
1 mm
4 mm
8 mm
12 mm
16 mm
20 mm

(h)

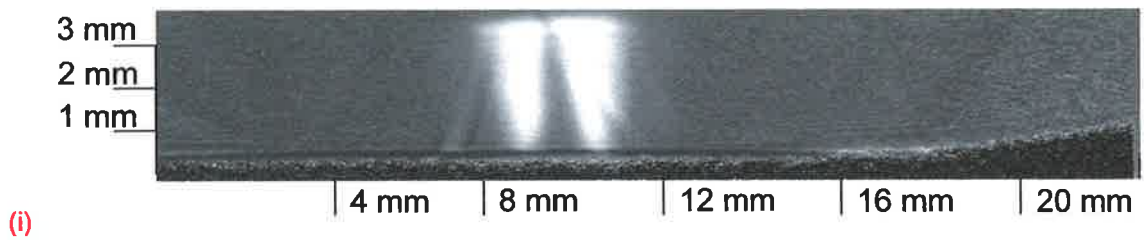
3 mm
2 mm
1 mm
4 mm
8 mm
12 mm
16 mm
20 mm

(i)

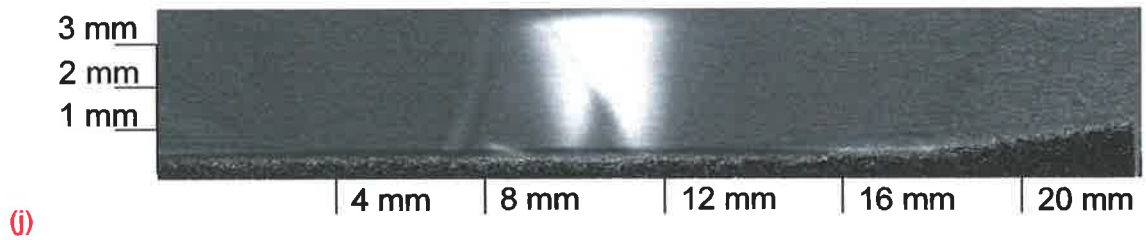
3 mm
2 mm
1 mm
4 mm
8 mm
12 mm
16 mm
20 mm

(j)

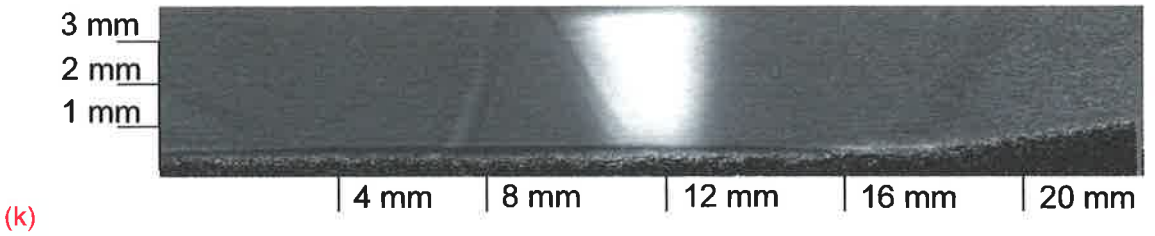
3 mm
2 mm
1 mm
4 mm
8 mm
12 mm
16 mm
20 mm

(k)

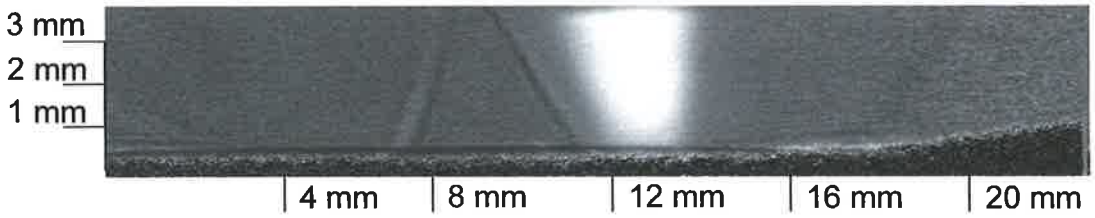
3 mm
2 mm
1 mm
4 mm
8 mm
12 mm
16 mm
20 mm

(l)

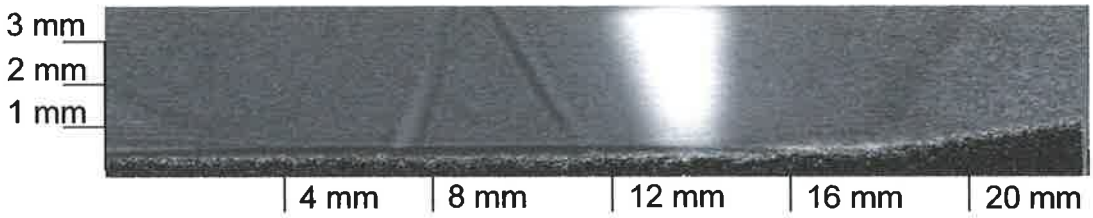
3 mm
2 mm
1 mm
4 mm
8 mm
12 mm
16 mm
20 mm

(m)

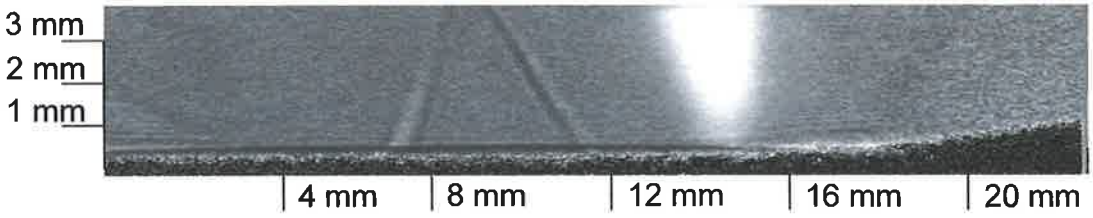
3 mm
2 mm
1 mm
4 mm
8 mm
12 mm
16 mm
20 mm

(n)

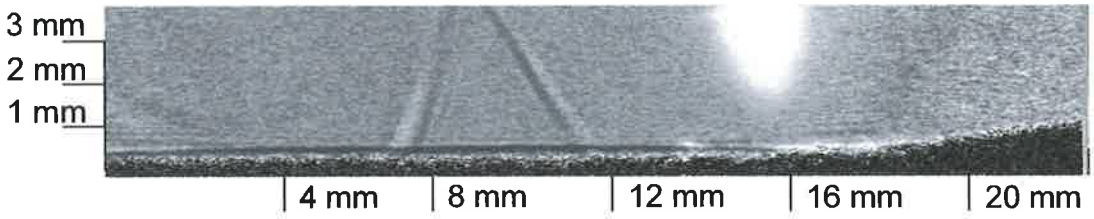
3 mm
2 mm
1 mm
4 mm
8 mm
12 mm
16 mm
20 mm

(o)

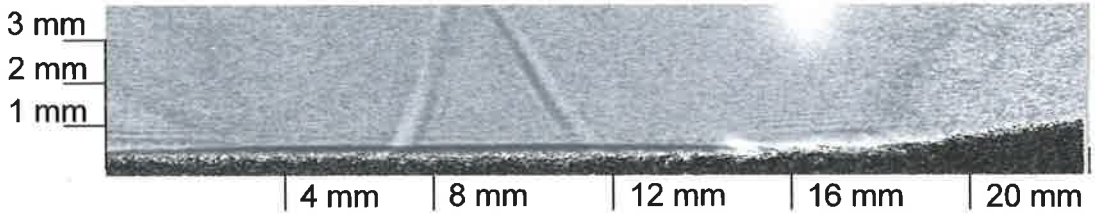
3 mm
2 mm
1 mm
4 mm
8 mm
12 mm
16 mm
20 mm

(p)

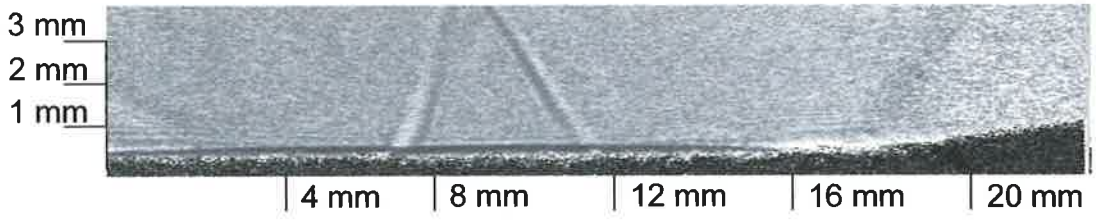
3 mm
2 mm
1 mm
4 mm
8 mm
12 mm
16 mm
20 mm

(q)

Figure 10: PLIF images as described in the caption above. The PLIF images are plotted on a false colour map based on the 0 to 100% signal strength of each image with black representing the lowest signal and lightest colours maximum signal.

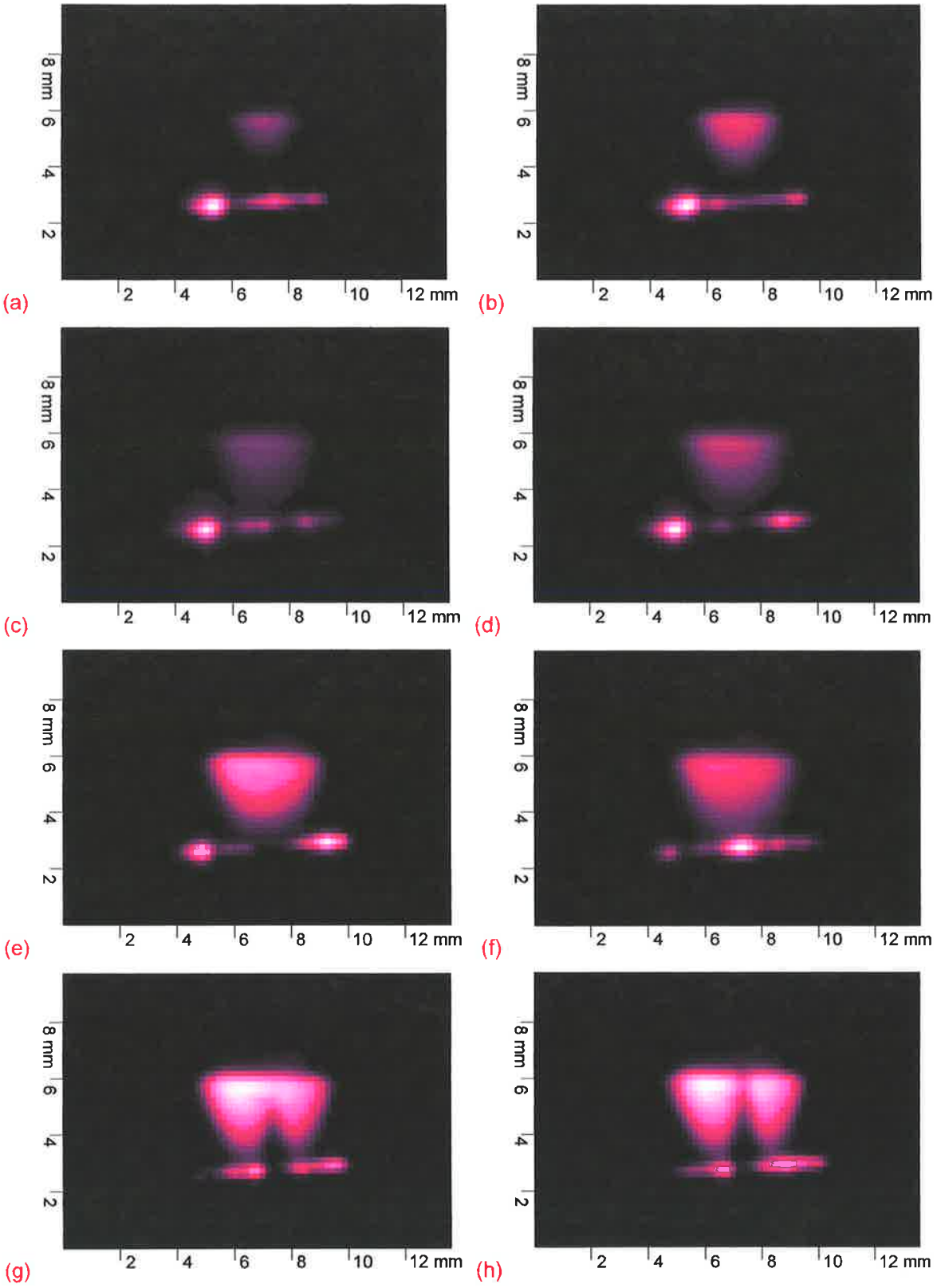

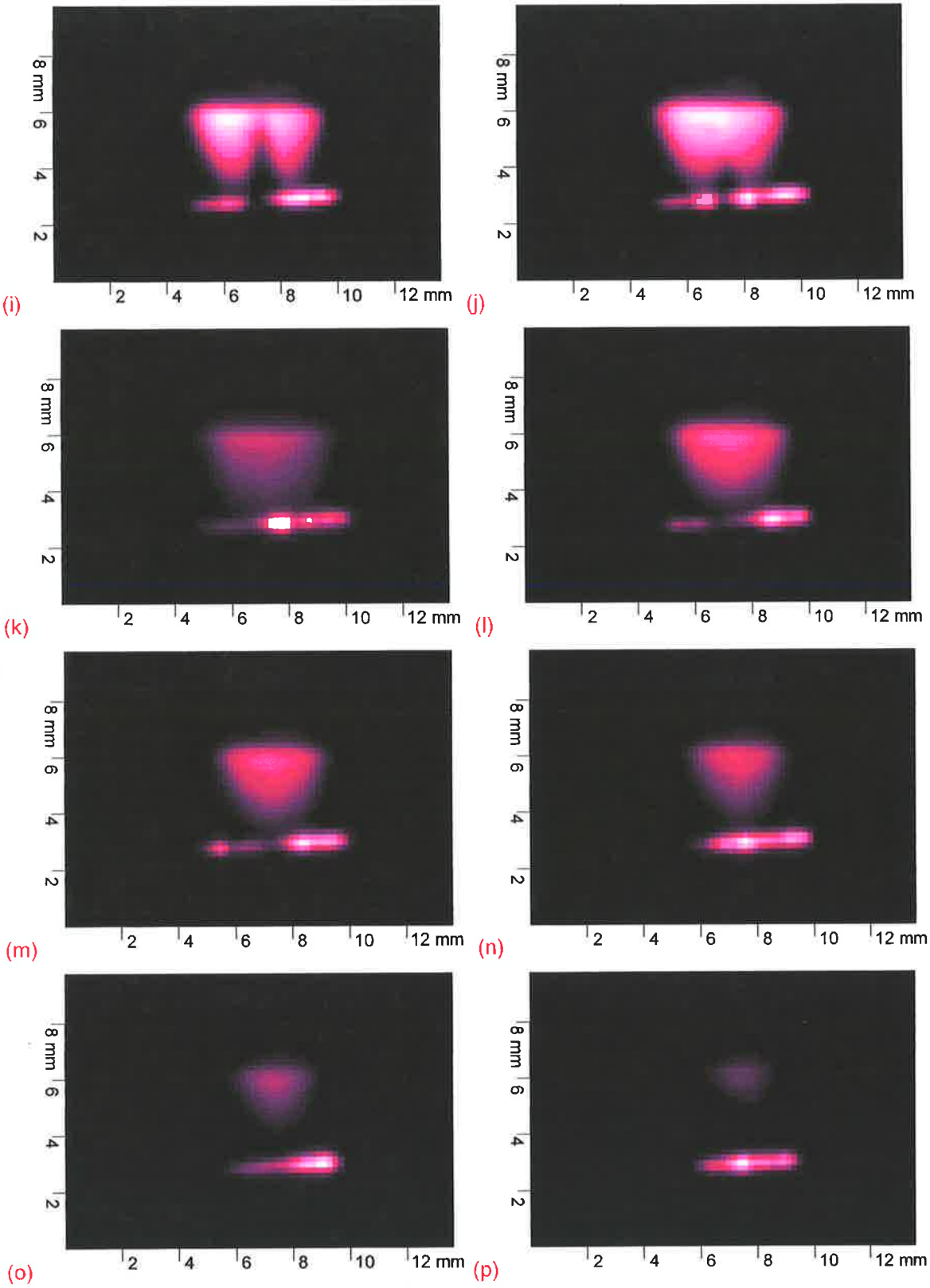
8 mm
6
4
2
2
4
6
8
10
12 mm
(i)
(j)
(k)
(l)
(m)
(n)
(o)
(p)

Significant differences between the images produced with each technique are immediately obvious. The saturation of collected images was investigated to determine the regime for which each set of images was collected before the images could be interpreted.

To allow direct comparison of the saturation of the signal distribution for the PLIF and PLPS images, a pump beam position in the flame was chosen so the major OH signal did not overlap any thermal density gradient features (approximately case (k) in Figures 9 and 10 above) which could introduce errors in estimating signal strength. Figures 11 and 12 show (a) vertical and (b) horizontal cross-sections of the signal strength in the collected (50 shot average) PLIF and PLPS images for case (k) respectively. The series of curves on each figure represent the signal as the laser energy (both pump and probe beams) is reduced by UV ND filters from that at which the images of Figures 11 and 12 were collected. The differing signal behaviour between the two techniques noted in the images of Figure 11 and 12 is emphasised by the dramatic difference between the PLIF and PLPS vertical cross-sections.

There is little difference in the trends of the horizontal cross-sections between the two techniques aside from an apparent difference in the width of the OH distribution for the two techniques after accounting for the required elongation of the collected PLPS image to represent the elliptical pump/probe intersection volume. The horizontal width of the stretched OH PLPS cross-section, even when corrected to represent number density, is smaller that that for the OH PLIF cross-section. (Note that the probe beam was much larger than the area of the flame, so that the PLPS images are not truncated by the probe beam profile.)

It should be remembered that for the small beam intersection angles, (as discussed in Chapter III) the stretched PLPS image represents the elliptical interaction region as seen from an angle of incidence of $\pi/2 - \chi$ where χ is the beam intersection angle. The PLPS signal intensity is the integrated signal along the probe beam path as it passes through the pump sheet. For a pump beam thickness of ~ 0.2 mm and a beam intersection angle of 13.6°, the signal is integrated along a pump/probe path length of 0.85 mm. However, even in a small flame such as that used in this experiment (about 4 mm extent of horizontal OH distribution for detectable signal), averaging over this path length would not account for the difference in apparent horizontal extent of the OH distribution in the PLIF and the stretched PLPS images due to the relatively slow horizontal variation of the OH number density across the flame.

The horizontal cross-sections have been included to indicate the level of absorption for passage of the pump sheet through the flame, which would complicate the interpretation of the saturation curves later in this section. However, these cross-sections are relatively symmetric around the central axis of the flame with any existing asymmetries equally ascribable to the slight vertical

misalignment of the flame. Consequently, absorption is not considered in the following discussion of the vertical cross-sections.

Figures 11 and 12 show the uncorrected (aside from a background level correction in the case of the PLPS images) PLIF and PLPS signal cross-sections respectively. Figure 13 shows vertical cross-sections calculated from the OH PLPS vertical cross-sections in Figure 12 to represent the square root of the Mode 2 probe corrected signal.

The vertical cross-sections of Figures 11 and 13 should be relatively comparable with respect to the distribution of signal if the two techniques share the same dependence on target species number density and pump sheet intensity. However, the PLIF signal drops linearly from a maximum signal at the top of the pump sheet, to zero just above the tip of the burner, while the square root of the corrected PLPS signal remains high for all heights above the burner tip where the pump beam was present[m].

The saturation of the uncorrected PLIF, uncorrected (aside from the background) PLPS and square root Mode 2 PLPS signals as a function of fractional laser intensity is shown in Figures 15 to 18. The range of curves in each figure represents the sampled signal at different heights above the tip of the burner. The saturation of the collected images was investigated by placing ND filters in the laser beam, cutting both pump and probe beam simultaneously. The images of Figures 9 and 10 were collected at the 100 % level of laser intensity.

The sample region was placed at the midpoint of the pump beam path through the flame. For the PLIF images, the sample region is 1 pixel x 1 pixel corresponding to a sample area of 0.206 mm x 0.206 mm. For the PLPS images, which have a greater spatial resolution, the sample region is 19 pixels x 19 pixels corresponding to approximately the same sample area as for the PLIF images.

The ND filter transmission for each (average) PLPS/PLIF image pair was determined by measuring the probe beam transmission in a region of the collected PLPS image with no apparent OH signal. Figure 14 shows the measured ND filter transmittivity in comparison with the nominal transmission factor. The X-axis represents the nominal UV ND filter rating.

Figures 15 and 16 show the saturation of the uncorrected PLIF signal. A fit to the saturation dependence of equation [21] for the data collected at a height of 2.47 mm above the tip of the burner (where the signal level is highest) indicates that the images of Figure 10 were collected in

[m] The pump sheet was truncated at top and base to limit the height of the sheet in order to provide a sense of scale between the PLIF and PLPS images.

the linear (or near-linear) regime of optical pumping. The PLIF signal is then linearly dependent on the pump sheet intensity and must be corrected for the pump sheet profile intensity to represent the spatial distribution of the population in the upper state of the pumped transition[n].

Figure 17 shows the saturation of the uncorrected (aside from the background correction) PLPS signal for a range of heights above the burner tip. Figure 18 shows the saturation of the equivalent square root of the corrected PLPS signal, representing the magnitude of the induced dichroism. Fits for the data sampled 2.5 mm above the burner tip to the roughly cubic and linear saturation dependence of the uncorrected PLPS signal of equations [26] and [27] are shown on Figure 17. Fits for the same dataset to the linear and constant saturation dependence of the induced dichroism of equations [28] and [29] are shown on Figure 18.

It is clear that the PLPS images of Figure 9 were taken in a highly saturated regime. Figure 18, which shows the saturation dependence of the induced dichroism, indicates that the PLPS signal in Figure 9 is independent of changes of up to 50% in the pump sheet intensity. If the pump profile is reasonably constant, the images of Figure 9 require no correction for the pump beam intensity. Correction for the pump profile is only required if the pump intensity drops to less than 50% of the pump intensity at a height of 2.5 mm above the tip of the burner.

An average pump sheet profile was measured at the end of the simultaneous PLIF and PLPS experiment by imaging the fluorescence from a fused silica cuvette containing Rhodamine 101 in the pump path at the position where the flame was located. The concentration of the dye was reduced until the collected fluorescence was linear with the dye concentration. The resultant vertical pump beam intensity profile is shown in Figure 19. The intensity of the sheet reduces significantly from a maximum at the top of the sheet to the base of the sheet at the tip of the burner in a similar manner to the reduction of PLIF signal with decreasing height above the burner.

Figure 20 shows the PLIF saturation vertical cross-sections corrected for the vertical intensity of the pump sheet[o]. It is clear that the distribution of the corrected PLIF signal cross-sections differs significantly from the square root of the Mode 2 PLPS cross-section shown in Figure 13. Figure 21 compares the corrected PLIF and the square root Mode 2 PLPS cross-sections from Figures 20 and 13 respectively collected at 100% laser energy. The square root Mode 2 PLPS cross-section (representing the induced dichroism) is approximately constant between 0.5 and 2.5 mm above the

[n] Assuming the quenching rate is constant over the imaged region.

[o] Each column of the 50 shot average uncorrected PLIF image was divided by the equivalent pump sheet profile of Figure 22 (normalised to the intensity at the arbitrary height of 2.47 mm above the burner tip).

tip of the burner. However, the sheet corrected PLIF signal rises near-linearly with distance from the burner tip.

The difference cannot be attributed to the width of the laser sheet as both the corrected PLIF signal and induced dichroism are linearly dependent on the sheet width. The sheet profile shown in Figure 19 is constant enough that the PLPS images need not be corrected for heights greater than 0.8 mm above the tip of the burner. Both cross-sections have been corrected for their dependence on pump intensity cross-section and probe beam profile as required given the relative saturation of each technique.

The collection efficiency of the PLIF lens was considered as a possible source of the near-linear reduction in PLIF signal strength near the burner tip if the tip blocked an increasing fraction of the PLIF fluorescence from reaching the collection lens close to the burner tip. However, the PLIF grid scaling images show a constant whitescale intensity in the imaged region, and consideration of the geometry refutes this argument.

The difference between the corrected PLIF and PLPS cross-sections cannot be attributed to either saturation as described by equations [22] to [29] above or to optical factors. The PLPS signal is in the highly saturated regime and should be independent of transient exponential changes in population. However, the PLIF signal was collected in the linear regime of optical pumping where transient effects may still contribute to the population number density during the length of the laser pulse. The models used to analyse the above data are very simple and include minimal discussion of collisional population transfer other than quenching. Collisional processes such as rotational energy transfer (RET), vibrational energy transfer (VET) and dephasing (change of Zeeman state on collision) have been ignored. It can be concluded from the differences in corrected signal distribution that comparison of PLIF and PLPS signal in atmospheric pressure flames must consider reasonably complex models of collision processes for quantitative analysis.

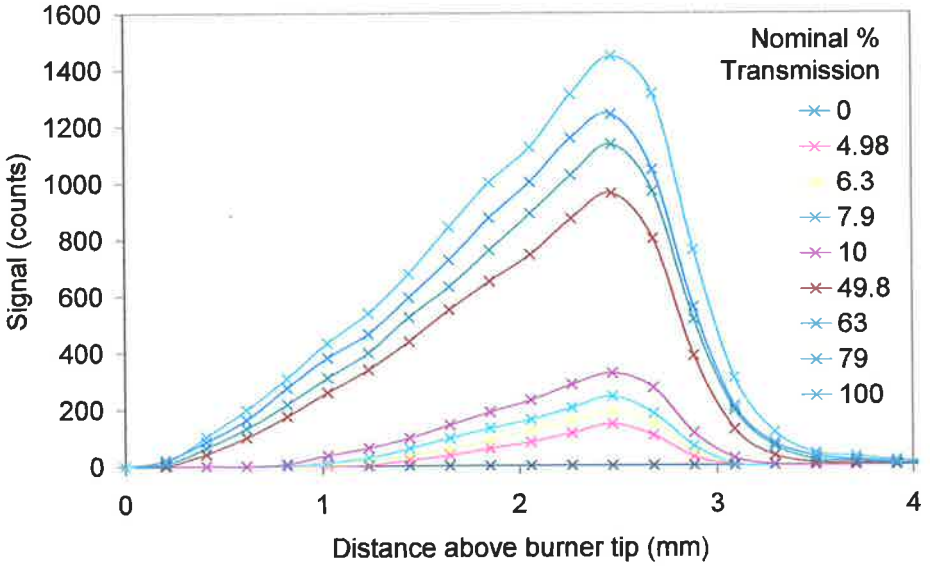

(a)

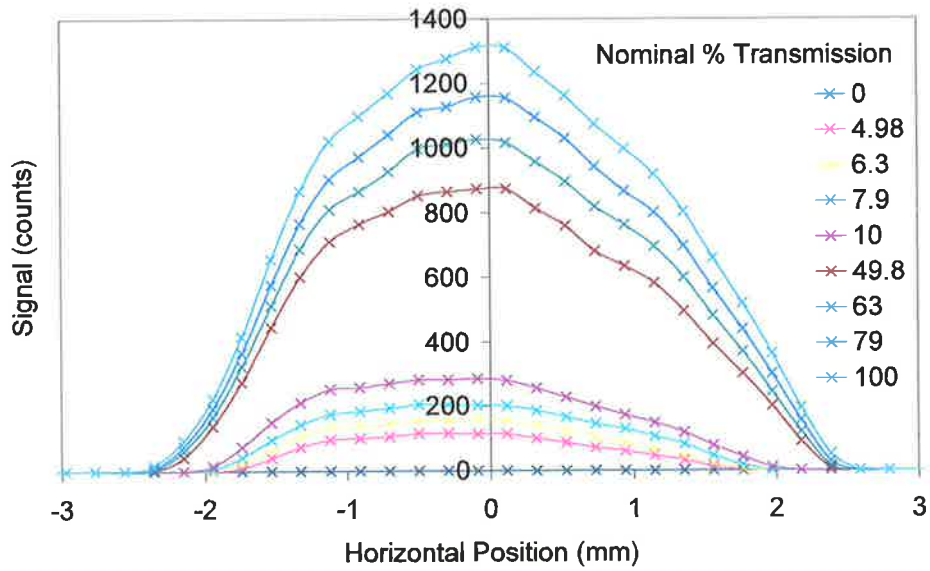

(b)

Figure 11: (50 shot average) PLIF image (a) vertical and (b) horizontal cross-sections for approximately case (k) in Figures 9 and 10 above. The vertical cross-sections were taken at the midpoint of the pump sheet path through the flame and the horizontal cross-sections at a height of 1.85 mm above the tip of the burner. The data consists of either a single column or a single row of the 50 shot average uncorrected PLIF image. 1 pixel in the PLIF images corresponds to a sample area of 0.206 mm X 0.206 mm. The range of curves on each figure represent the signal strength as the laser energy (both pump and probe beams) is reduced by UV ND filters (the curves are labelled with the nominal ND filter transmission) from the laser intensity at which the images in Figures 9 and 10 were collected.

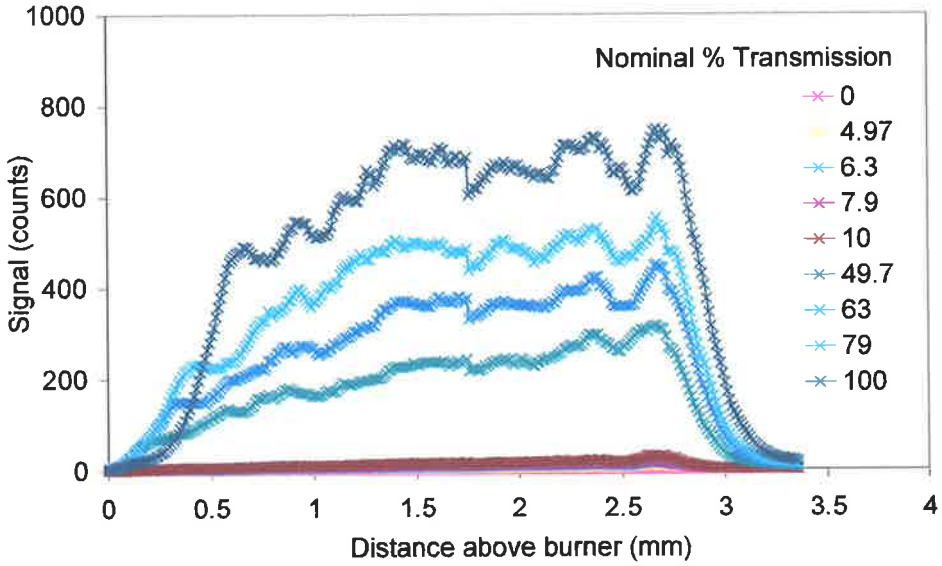

(a)

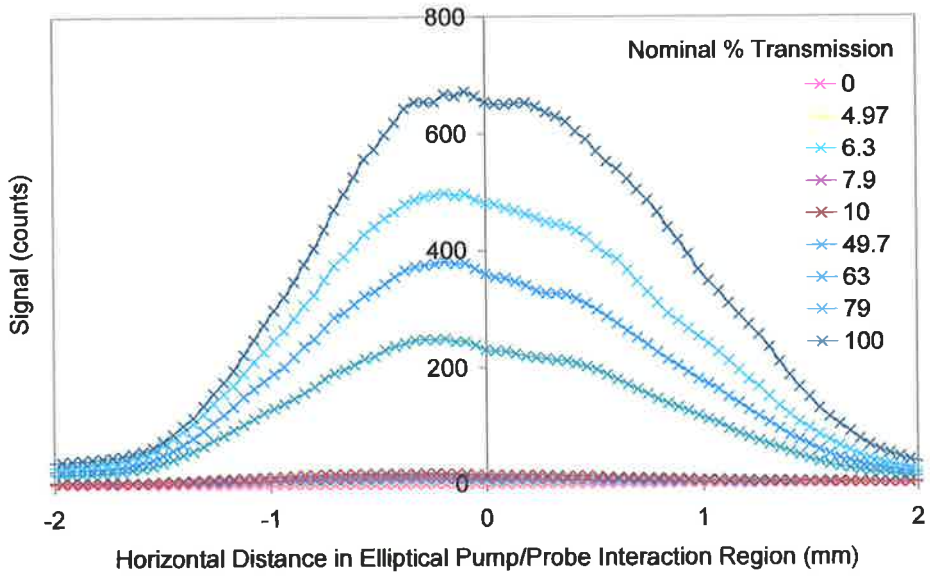

(b)

Figure 12: (50 shot average) PLPS image (a) vertical and (b) horizontal cross-sections for approximately case (k) in Figures 9 and 10 above. The vertical cross-sections were taken at the midpoint of the pump sheet path through the flame and the horizontal cross-sections at a height of 1.85 mm above the tip of the burner. The data consists of either the average of 19 columns or 19 rows of the 50 shot average uncorrected (aside from a zero background correction) PLPS image. The sample size was chosen to match that of the PLIF cross-sections in Figure 11. The range of curves on each figure represent the uncorrected PLPS signal strength as the laser energy (both pump and probe beams) is reduced by UV ND filters (the curves are labelled with the nominal ND filter transmission) from the laser intensity at which the images in Figures 9 and 10 were collected.

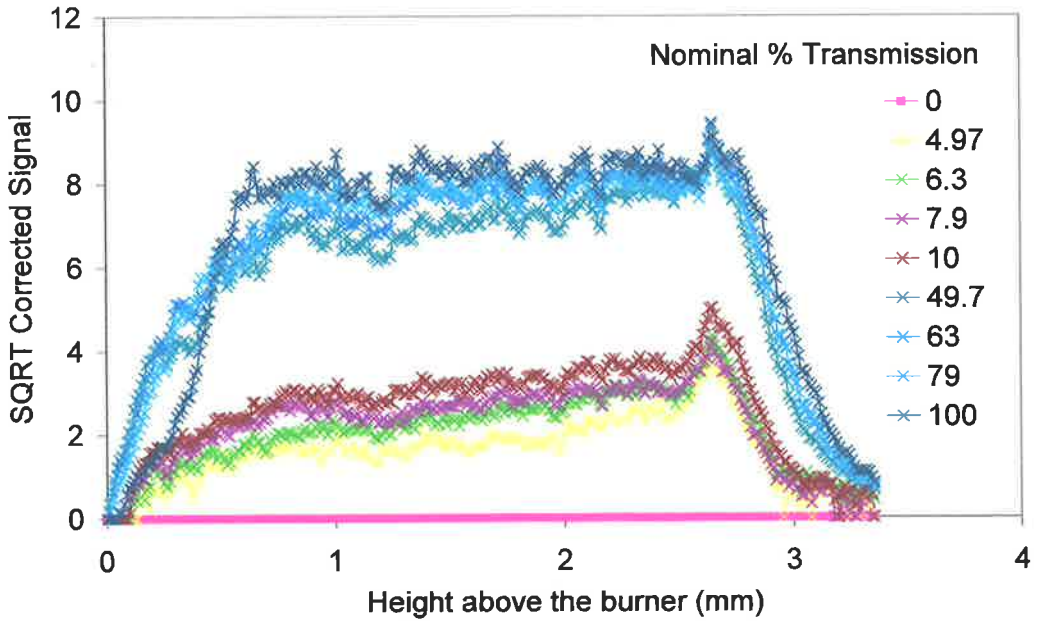

Figure 13: (50 shot average) corrected PLPS image cross-sections for approximately case (k) in Figures 9 and 10 above. The vertical cross-sections were taken at the midpoint of the pump sheet path through the flame. The data consists of the average of 19 columns of the 50 shot average uncorrected (aside from a zero background correction) PLPS image corrected to represent a cross-section equivalent to the induced dichroism, i.e. to the square root of a Mode 2 corrected PLPS image. The sample size was chosen to match that of the PLIF cross-sections in Figure 11. The range of curves on each figure represent the signal strength as the laser energy (both pump and probe beams) is reduced by UV ND filters (with nominal transmission as labelled) from the laser intensity at which the images in Figures 9 and 10 were collected.

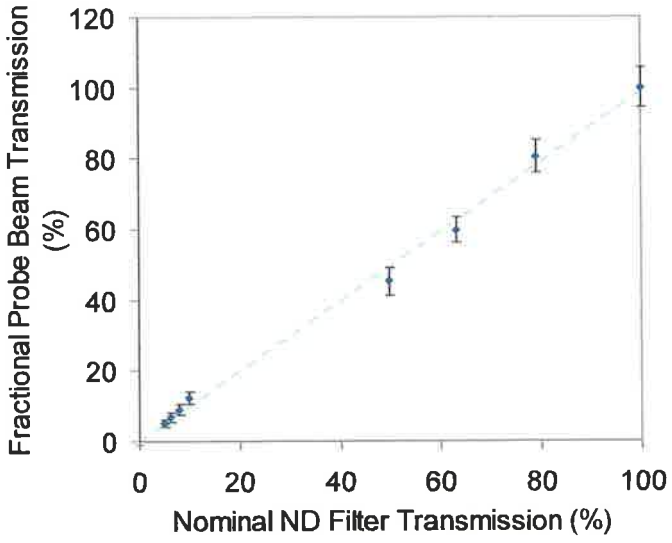

Figure 14: ND filter transmission estimation using the fractional transmission of a PLPS-free section of the probe beam in the (50 shot average) PLPS images.

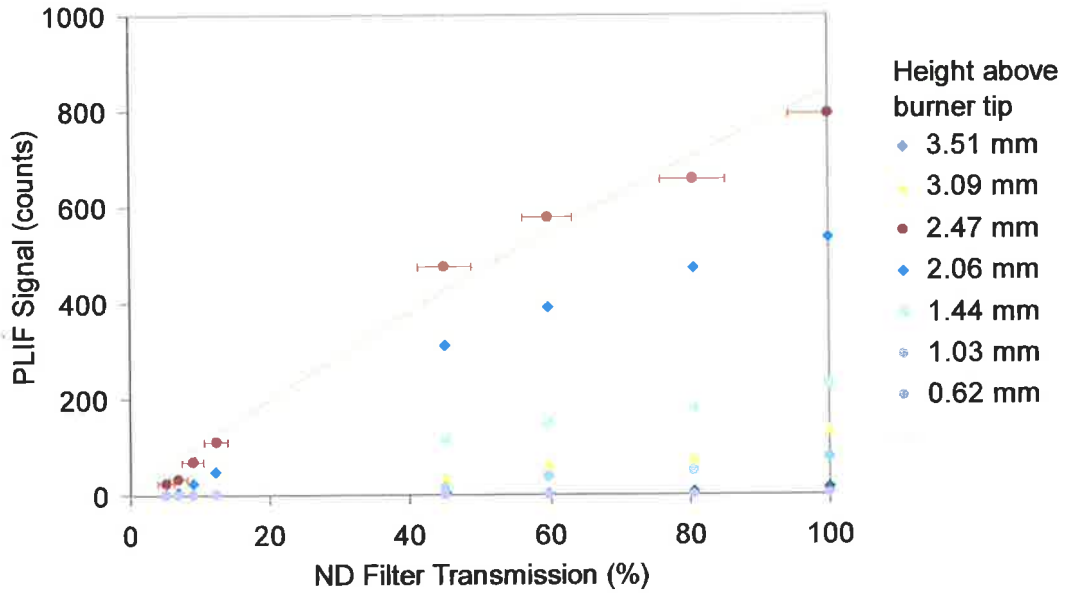

Figure 15: PLIF saturation curves for a range of distances above the burner tip as a function of ND filter transmission percentage. The PLIF images of Figure 10 were taken at 100% transmission on this scale. X axis error bars are included for the data set for a distance of 2.47 mm above the burner tip. As the PLIF data originate from a single averaged pixel, there are no Y axis error bars. The orange line is a fit to the h = 2.47 mm data according to equation [21]. The 100% transmission level corresponds to a pump sheet intensity of 8.9 MW/cm^2.

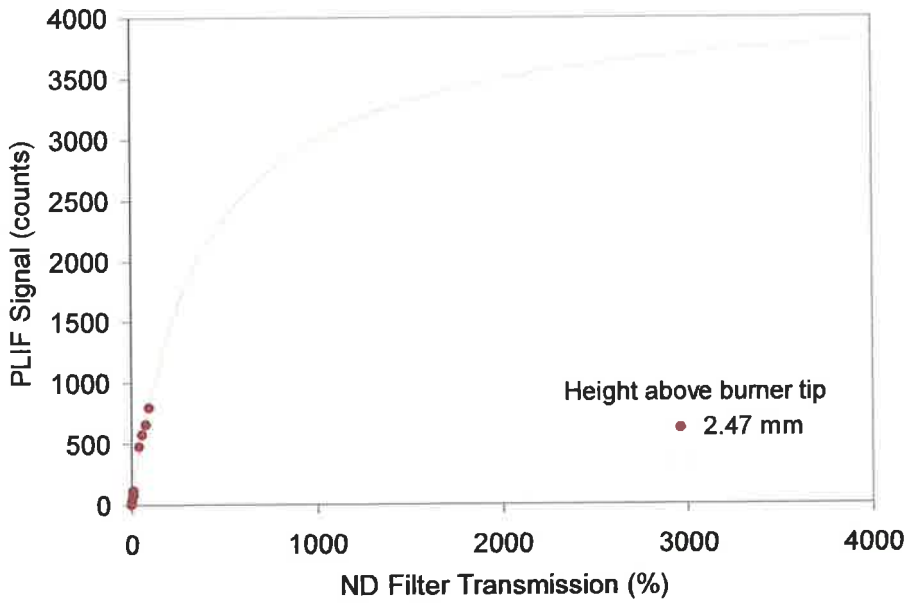

Figure 16: Fit of the h = 2.47 mm data from the figure above to the saturation curve (orange) defined in equation [21] indicating the PLIF signal was collected in the near-linear regime of optical pumping.

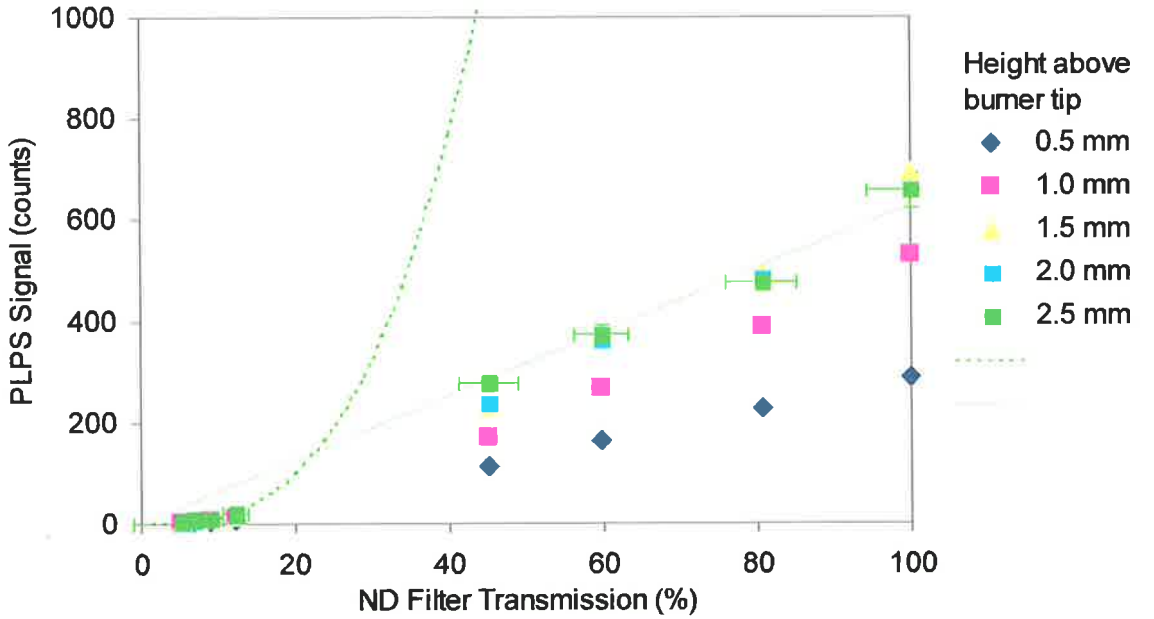

Figure 17: PLPS saturation curves for a range of distances above the burner tip as a function of ND filter transmission percentage. The PLPS images of Figure 9 were taken at 100% transmission on this scale. X and Y axis error bars are included for the data set for a distance of 2.5 mm above the burner tip. The dashed green line is the fit of the h = 2.5 mm data to the saturation dependence of equation [26] and the solid green line is the fit to equation [27].

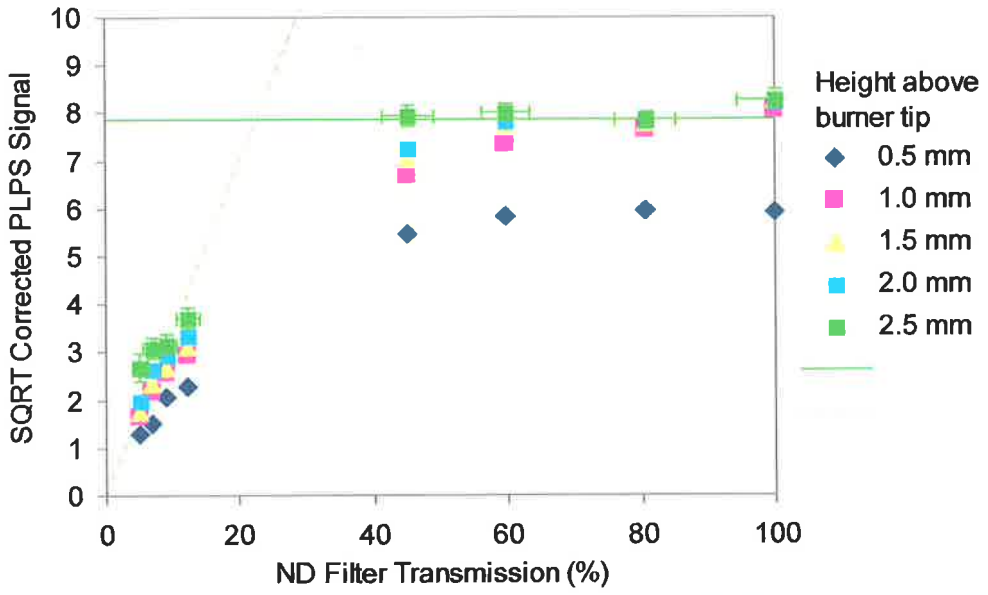

Figure 18: Saturation curves for the square root of the corrected PLPS signal shown in the figure above. The dashed and the solid green line are the fits of the h = 2.5 mm data to the saturation dependence described by equations [28] and [29] respectively. The 100% transmission level corresponds to a pump sheet intensity of 8.9 MW/cm^2.

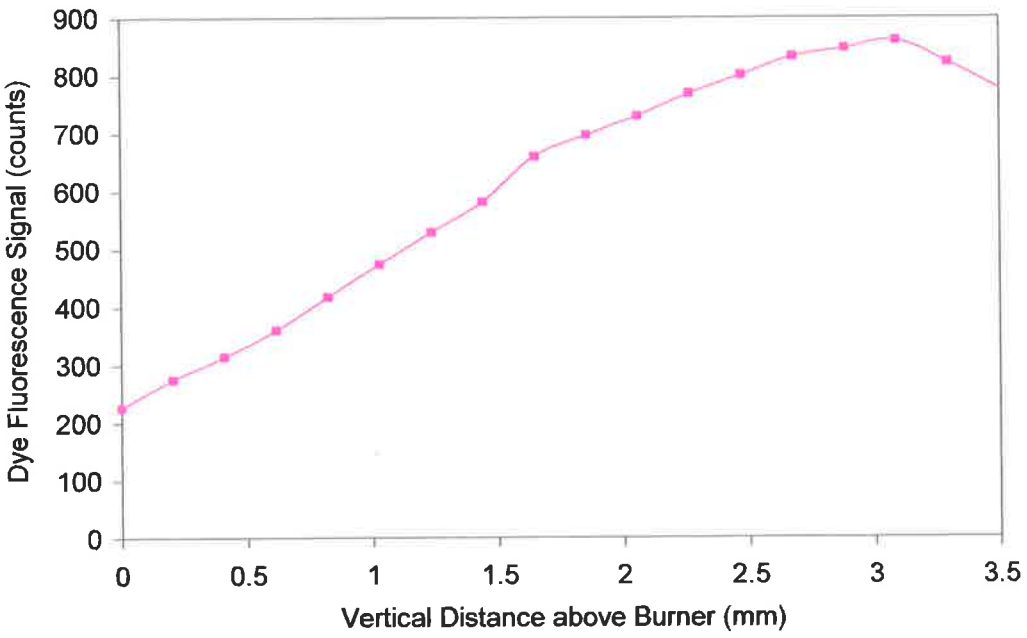

Figure 19: Vertical pump sheet profile for the simultaneous PLIF and PLPS experiment.

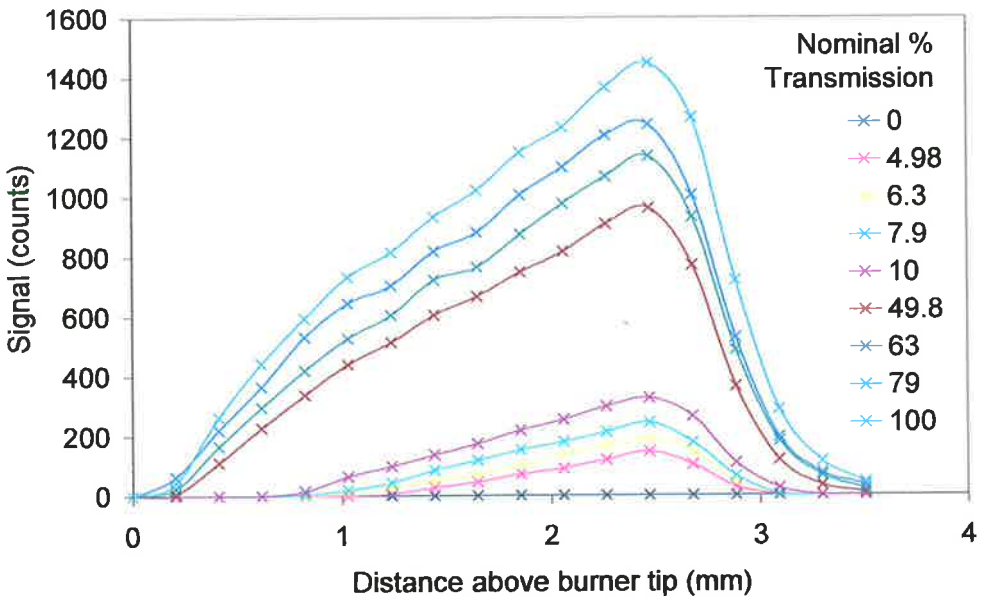

Figure 20: (50 shot average) PLIF image vertical cross-sections of Figure 11 corrected for the pump sheet profile. The range of curves on each figure represent the signal strength as the pump energy is reduced by UV ND filters (the curves are labelled with the nominal ND filter transmission) from the laser intensity at which the images in Figures 9 and 10 were collected.

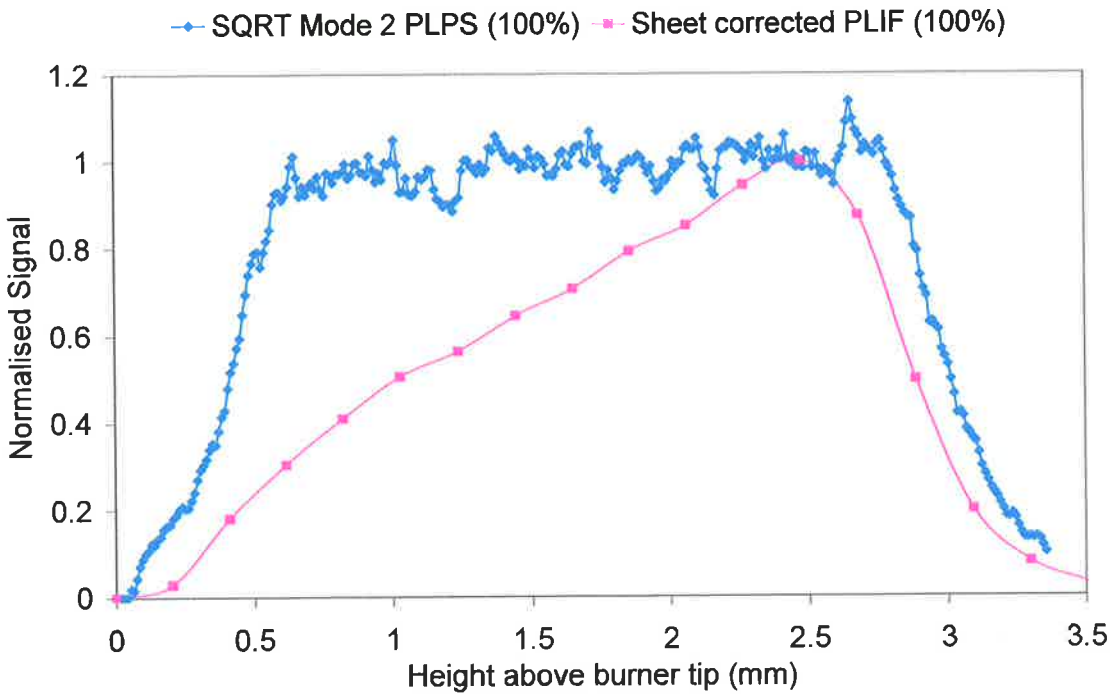

Figure 21: Comparison of the corrected PLIF vertical cross-section and the square root Mode 2 PLPS vertical cross-section collected at the same laser energy as the images of Figures 11 and 12. The cross-sections have been normalised for comparison to the signal strength at the arbitrary height of 2.47 mm above the tip of the burner.

(2) Simultaneous LIF and LPS signal vs. Equivalence Ratio in a Natural Gas/Air Flame from a Rectangular Mixing Burner

This experiment was essentially the same experiment as in the case of simultaneous PLIF and PLPS imaging. The two CCD cameras were once-again used for data collection. However, the modified glass-glowing torch was replaced by a standard rectangular burner built in the School of Chemical Engineering by Idzham Fauzi Mohd Ariff and Muzhar [p].

An internal structure consisting of a honeycomb of 0.6 mm internal diameter tubes supplied the natural gas and air flows (see Figure 22). The honeycomb was made up of bundles of 7 tubes, each consisting of a central natural gas tube surrounded by 6 air tubes. The disparate number of fuel/oxidiser tubes was designed to closely match the relative flows of fuel and oxidiser required to produce an stoichiometric natural gas/air flame. The internal tube structure was encased in a brass case and surrounded by a 18 mm wide nitrogen shroud.

[p] *"Design and Testing of a Flat Flame Calibration Burner"*, School of Chemical Engineering 4th Year Research Project Report, 2000.

Figure 22: Fuel and oxidiser tube structure in the interior of the mixing burner. The shorter (0.6 mm internal diameter) tubes supply the air flow and surround the longer tubes supplying the natural gas. The internal tube structure was encased in a brass case and surrounded by a 18 mm wide nitrogen shroud.

The fuel and oxidiser mixed above the surface of the burner and the flows were adjusted until the flame base was lifted ~ 2-3 mm as shown in Figure 23. Figure 24 shows the burner in operation. The nitrogen shroud is supplied through the ~ 18 mm gap surrounding the central burner casing. The outer casing which contains the nitrogen flow can just be seen in the figure.

The flowrates of the fuel, oxidiser and nitrogen lines were monitored via Fischer and Porter 1/2" and 1/4" flowmeters. Pressure gauges were attached to each flowmeter to determine the operating pressure.

The mixing burner was designed to produce a uniform flow distribution. Figure 25 shows OH ($A^2\Sigma$–$X^2\Pi$ (0-0) $Q_2(8)$) PLIF images of natural gas/air flames produced by the mixing burner for a range of flame equivalence ratios. The images are presented in a false colour map with black representing zero signal and lightest colours representing the highest signal. The images were collected at a gain of 1.76 and background contributions (which were mainly due to fluorescence induced by the probe beam rather than to flame emissions) were corrected for.

Figure 23: Near-stoichiometric natural gas/air flame lifted ~ 2-3 mm above the surface of the rectangular mixing burner.

Figure 24: Rectangular mixing burner in operation. The nitrogen flow surrounds the CH_4/air flame and isolates the combustion process from the ambient air.

The pump sheet was less than 5 mm high and passed through the flame ~ 20 mm above the surface of the burner. The distribution of PLIF signal indicates the path of the pump sheet through the flame. The PLIF images are 200 shot unweighted averages and were collected in the linear regime of optical pumping. The signal is then proportional to the product of the laser intensity at the selected point in the flame and the local number density of the target species. The vertical variation of the signal is largely due to the pump sheet intensity profile. However, the flame chemistry should be uniform at a given height above the surface of the burner for a perfectly flat

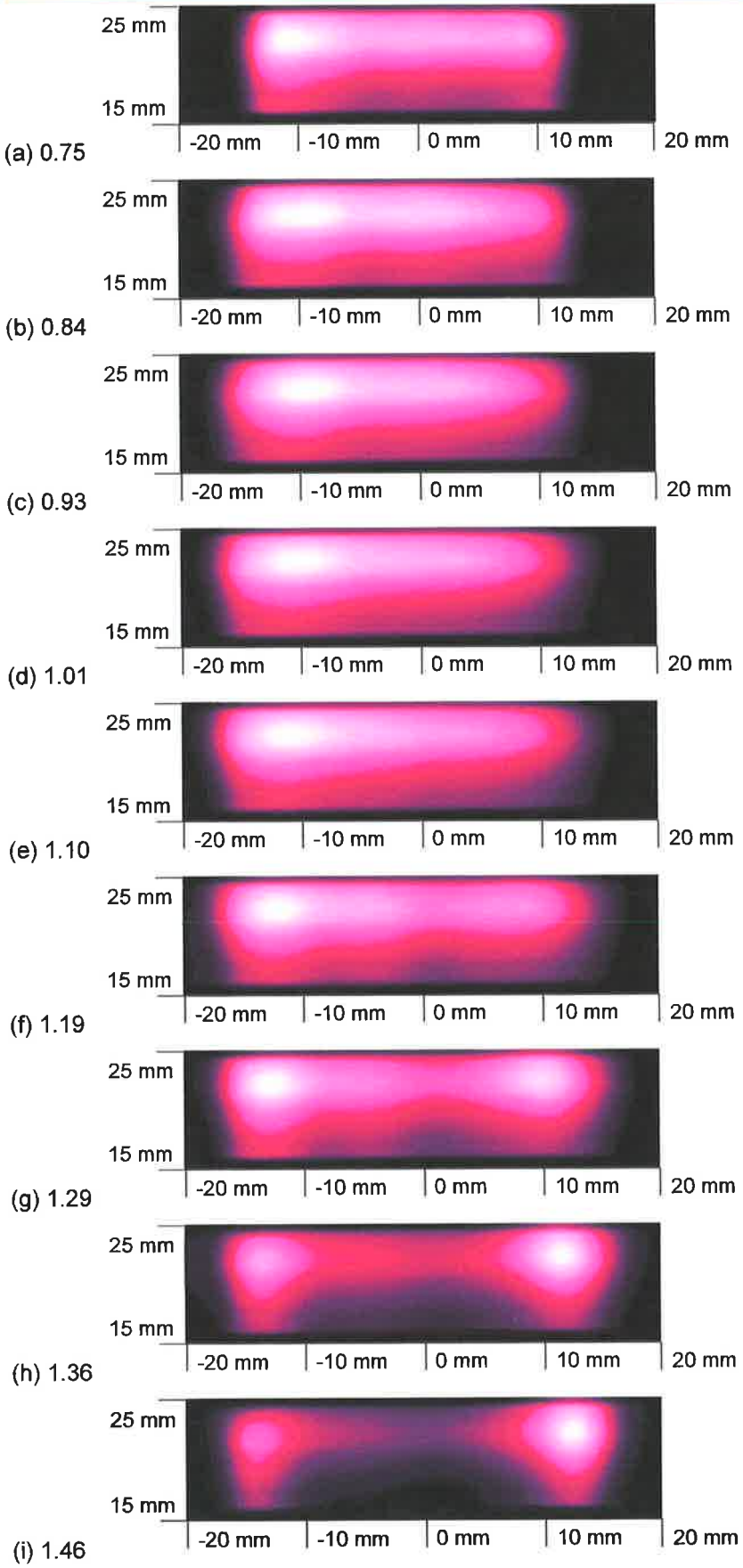

Figure 25: (200 shot) average OH PLIF images for the natural gas/air flame produced by a (rectangular) premixed burner for a range of equivalence ratios. The nitrogen shroud surrounding the burner was insufficient to prevent edge effects due to diffusion forming in the three fuel-rich flames with highest fuel concentration. The increase in OH concentration at the edge of these flames is apparent in images (g), (h) and (i). The colour map of the images are scaled from 0 to 100% of the signal range in each images. and a false colour map applied to highlight the spatial variations in the OH signal. Black indicates zero signal and highest signal is indicated by the lightest colours. The sheet propagates from left to right in the images. The absorption of the sheet as it passes through the flame can be clearly noted. The equivalence ratio for which each image was taken is listed beside each image.

Figure 26: Horizontal cross-sections of (200 shot average) OH signal in Figure 25 at a height of 20 mm above the surface of the burner. Each datapoint corresponds to an sample area of 0.206 mm x 0.206 mm. The equivalence ratio for which each image was taken is listed on each image.

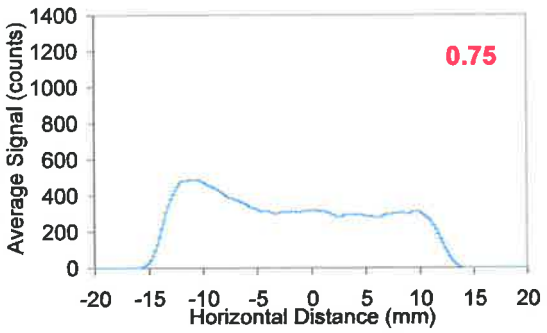

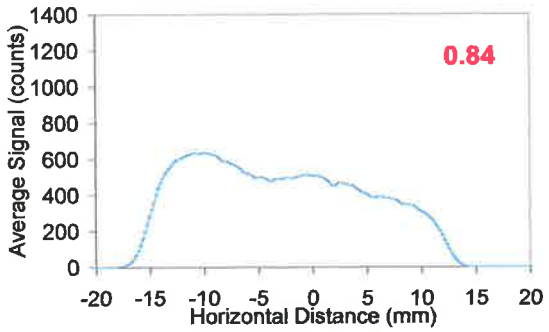

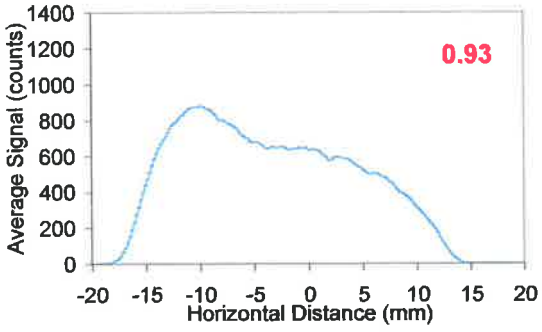

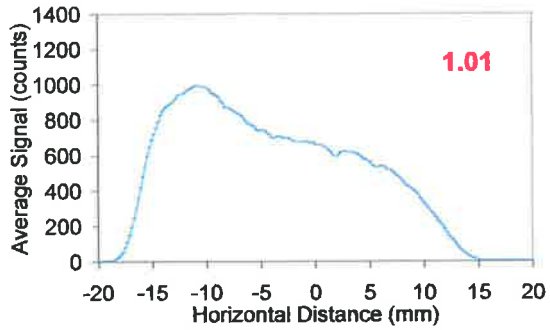

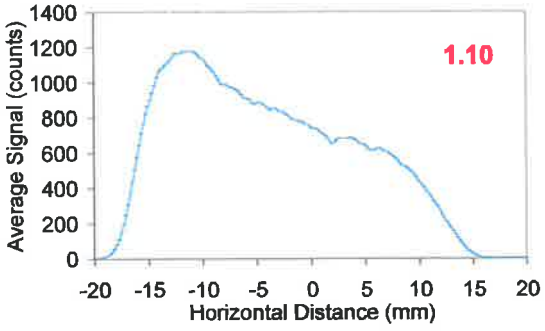

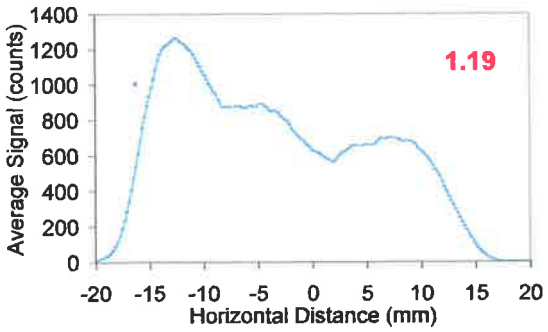

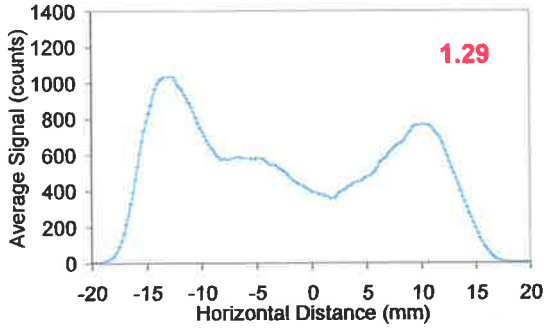

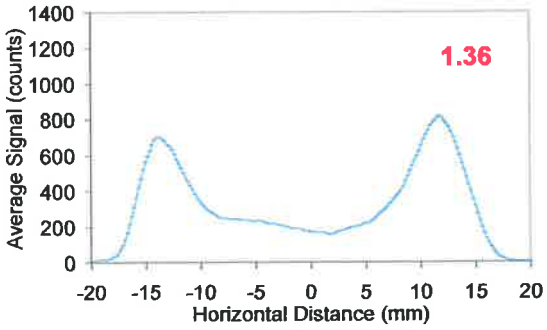

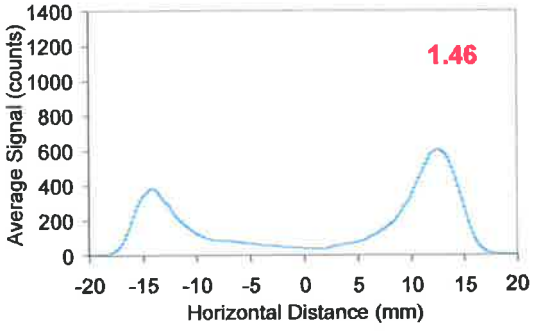

flame. The horizontal variations in the signal are due to the combined effects of non-uniform fuel/oxidiser mixing, imperfect shielding from the ambient air by the nitrogen shroud and absorption of the pump sheet.

Figure 26 shows horizontal cross-sections of the uncorrected PLIF signal at a height of 20 mm above the surface of the burner. The absorption of the pump sheet as it passes from left to right through the flame is apparent. It is also clear that the nitrogen shroud surrounding the burner was insufficient to prevent edge effects due to diffusion in the three fuel-rich flames with highest fuel concentration. The increase in OH concentration at the edge of these flames is apparent in the images and cross-sections (g), (h) and (i) of Figures 25 and 26. These edge effects give an estimate of the extent to which the ambient air diffuses through the nitrogen shroud. The centre of the flame is minimally affected by air diffusion and we can assume that the central flame OH concentration is close to that which would be calculated based on the equivalence ratio of the fuel/oxidiser mix.

Simultaneous PLIF and PLPS images were collected as sets of 100 images **for a range of flame equivalence ratios**. The PLPS images were collected using a region of interest on the CCD array of 50 rows of 576 pixels each[q]. Due to the limited image area, it was not possible to simultaneously collect a section of the probe beam which was signal free to correct the PLPS signal for the probe beam profile on a shot-to-shot basis.

An average probe beam profile was used to correct the PLPS signal. Flame emissions for the PLPS images were less than 1 count for all flames in this experiment. PLIF image backgrounds of flame emissions and fluorescence from the probe beam were taken as a function of equivalence ratio to correct the PLIF images. A number of PLIF and PLPS images in each dataset were null images, missing the signal due to jitter largely introduced by the improvised timing system. These images were not used in the averaged results. The first 10 shots in each dataset were discarded after it was noted that the laser energy took approximately 10 shots to stabilise.

Saturation curves for the LIF and LPS signal with pump sheet intensity were collected simultaneously for a near-stoichiometric flame The saturation of the LIF signal (corrected for the probe extinction background) is shown in Figure 27 as a function of percentage of the pump sheet intensity at which the simultaneous PLIF/PLPS experiment was undertaken. The 100% sheet intensity was estimated to be ~ 4.4 MW/cm^2. The nominal

[q] The timing program became erratic during the experiment due to a heatwave. The improvised timing of the experiment was controlled by the readout time of the PLPS ICCD, which was itself a function of the number of rows of the CCD selected in the region of interest for the set of images.

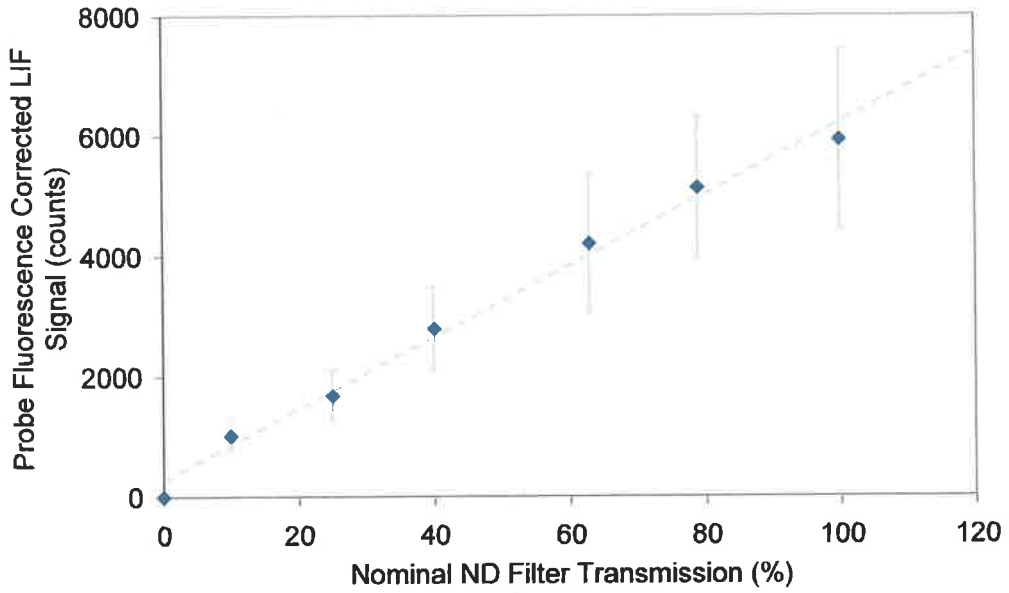

Figure 27: (200 shot average) LIF signal (corrected for the probe beam fluorescence background) collected for a near-stoichiometric natural gas/air flame from the rectangular mixing burner as a function of percentage of pump sheet irradiance at which the simultaneous LPS and LIF experiment was conducted(4.4 MW/cm^2). The signal was collected in the centre of the burner, 20 mm above the burner surface.

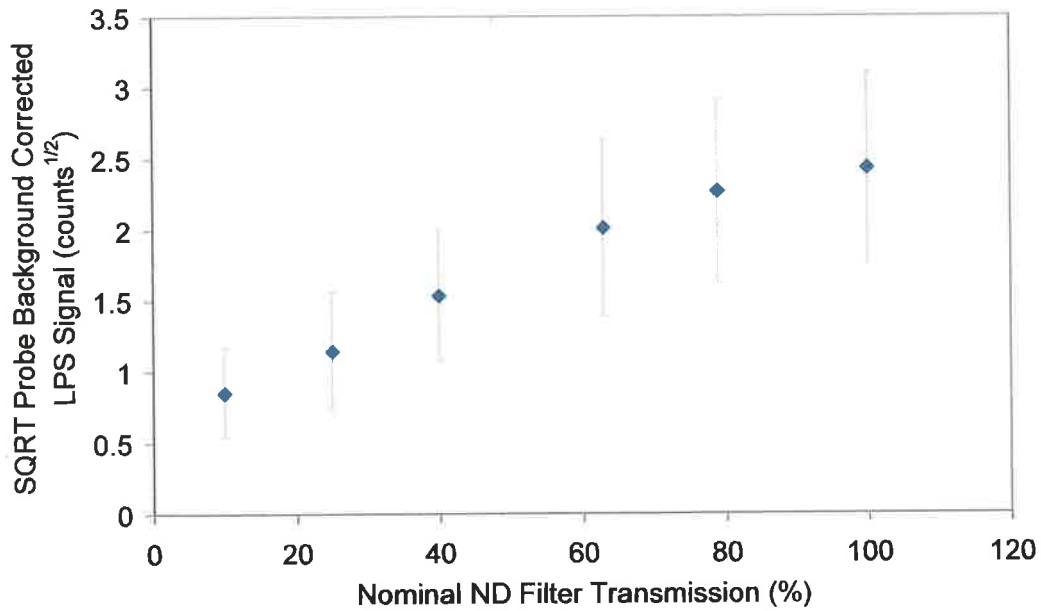

Figure 28: Square root of the (200 shot average) LPS signal (corrected for the probe beam extinction background) collected for a near-stoichiometric natural gas/air flame from the rectangular mixing burner as a function of percentage of the pump sheet irradiance at which the simultaneous LPS and LIF experiment was conducted (4.4 MW/cm^2). The signal was collected in the centre of the burner, 20 mm above the burner surface.

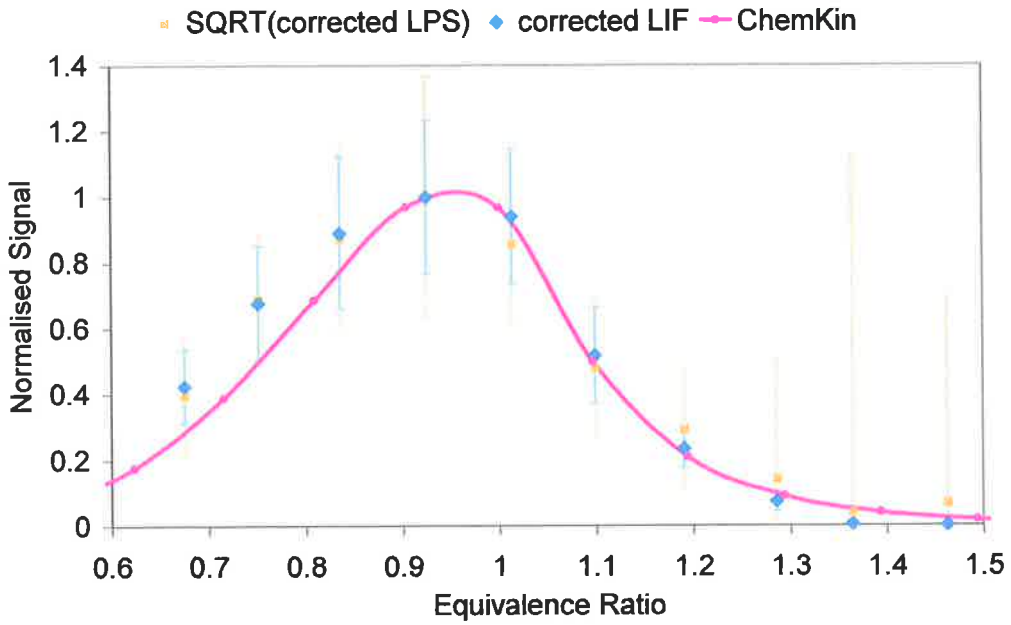

Figure 29: The square root of the corrected (highly saturated)LPS signal (corrected for the probe beam extinction background), the (linear regime) LIF signal (corrected for the probe beam fluorescence) and the OH number density predicted by the equilibrium module of the CHEMKIN library plotted as a function of flame equivalence ratio for the natural gas/air flame from the rectangular mixing burner. A CH_4/air flame is assumed for the CHEMKIN calculations.

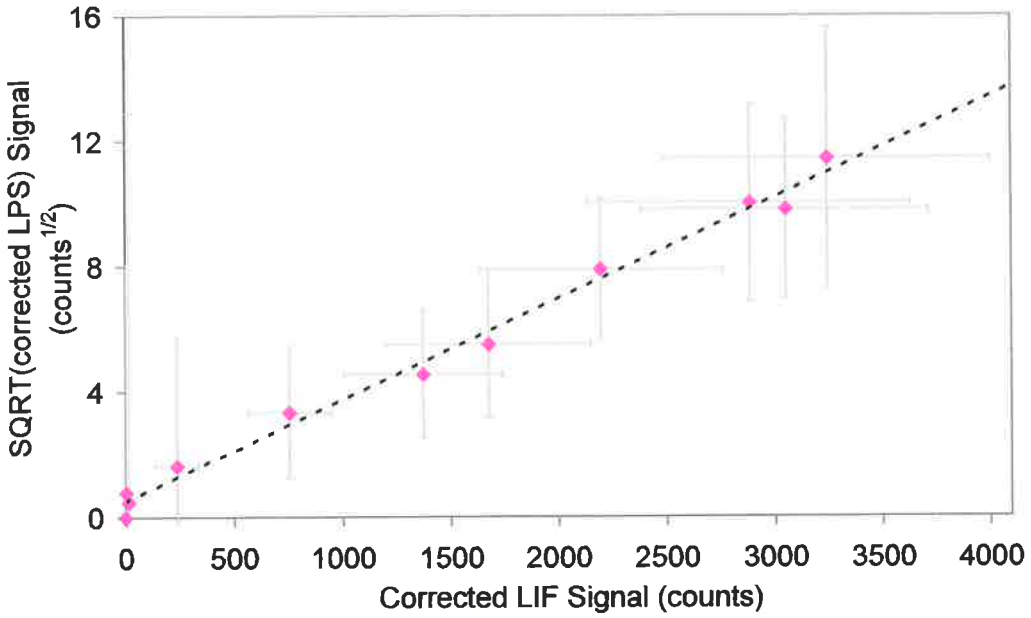

Figure 30: The square root of the (highly saturated) LPS signal (corrected for the probe beam extinction background) collected as a function of equivalence ratio and shown in Figure 29 is linearly related to the linear regime LIF signal (corrected for the probe beam fluorescence) shown in the same figure.

transmission of the ND filters used to attenuate the laser energy (pump beam only) was used to plot this data. The LIF signal is obviously collected *in the linear saturation regime*. The saturation curve for the LPS signal (corrected for the probe beam extinction background) shown in Figure 28 shows that the LPS signal is *close to saturation* at the maximum pump sheet irradiance of ~ 4.4MW/cm^2. This agrees with the onset of saturation of the PLPS images as shown in Figure 18 for the simultaneous PLIF and PLPS imaging experiment. The non-zero intercept in the case of the LIF signal is unlikely to be due to Rayleigh scattering as this would be proportional to the pump sheet intensity. The flame emissions for the PLIF images of this flame were undetectable at the experiment gain of 6 and the average fluorescence contribution due to the probe sheet (at this high gain) has been corrected for.

The simultaneously collected (linear regime) LIF and square root of the (saturated) LPS signal is shown in Figure 29 as a function of flame equivalence ratio[r]. The LIF and LPS signal was collected for the same sample area of 0.2 x 0.2 mm in the centre of the flame from the rectangular mixing burner at a height of 20 mm above the burner surface. The LIF signal was collected at a ICCD gain of 5 and is corrected for a background largely consisting of fluorescence due to the pump sheet. The LPS signal is corrected for a probe beam extinction background (which is assumed to be independent of the equivalence ratio) and the square root of the signal taken to represent the number density of the target species.

There has been no attempt to correct for absorption of the pump sheet or the probe beam. Preliminary experiments indicated absorption of up to 26% of the probe beam for near-stoichiometric flames. This corresponds to a maximum deviation of 14% in the pump sheet intensity in the centre of the flame assuming a symmetric OH distribution along the beam path through the flame. The (linear regime) LIF signal is linearly dependent on the pump sheet intensity in the target region. It can be expected that the LIF signal for near-stoichiometric flames has been underestimated by ~ 14% due to this absorption. The (saturated) LPS signal is dependent on the collected probe beam intensity, but independent of variations of the pump sheet intensity. The square root of the (saturated) LPS signal (after correction for, i.e. subtraction of, the probe beam extinction background) is then proportional to the square root of the absorption of the probe beam as it passed through the flame. Due to the central position of the sample region in the flame, the square root of the absorption of the probe beam as it passes through the flame is equivalent to the

[r] The experimental equivalence ratios calculated from the relative flows of the natural gas and air was found to be underestimated (when the experimental LIF signal was compared with the OH number density dependence on equivalence ratio) due to miscalibration of the ¼" natural gas flowmeter. The experimental natural gas flows were corrected by a constant factor to allow the LIF signal to best match the equilibrium OH number density dependence on equivalence ratio.

absorption of the probe beam at a point half-way through the flame (i.e. at the sample point). As the pump and probe beam path length through the flame vary only by ~ 3%, the (background corrected) PLIF and the square root of the (probe background corrected) saturated PLPS signals will demonstrate the same dependence on absorption as a function of flame equivalence ratio. Assuming a symmetric flame, the linear regime LIF signal and square root of the saturated LPS signal in Figure 29 should be underestimated by the same factor of ~ 14% for near-stoichiometric flames with the highest OH number densities.

Note that a definite advantage of the saturated LPS technique is that the absorption dependent intensity parameter is the probe beam profile which is measured at the ICCD, while the (linear regime) LIF technique requires that the pump sheet intensity within the flame at the target volume be known for correction. The pump sheet intensity at the sample point may be estimated for steady, symmetric flames, but is otherwise a source of error in data correction. The saturated LPS technique requires only absorption dependent beam intensities which may be measured directly outside the combustion region.

The absorption factor common to both the (background corrected) linear regime LIF signal and the square root of the (probe extinction background corrected) saturated LPS signal may be eliminated if the square root of the LPS signal is plotted against the LIF signal (Figure 30). This plotting method eliminates both the effects of absorption and average variations in laser energy due to the linear dependence of both techniques on laser energy.

There is a clear linear relationship between the number densities predicted by the two techniques. The data was taken for a range of flame equivalence ratios for an atmospheric natural gas/air flame. The linearity between the square root of the (probe background corrected) saturated LPS signal and the simultaneously (background corrected) linear regime LIF does not appear to affected by the large range in flame conditions and flame temperatures (~ 1540 to 2230 K based on estimated equilibrium flame temperatures[s] for the range of flame equivalence ratios) in this experiment.

Figure 29 shows the (probe fluorescence corrected) LIF signal and square root of the (probe extinction background corrected) LPS signal in comparison with the calculated equilibrium OH

[s] Temperatures provided by Dr Bassam Dally of the School of Mechanical Engineering, The University of Adelaide, using the equilibrium module of the CHEMKIN library assuming a CH_4/air flame.

number density for a CH_4/air flame (solid pink line)[t] as a function of flame equivalence ratio. The number densities were calculated using the equilibrium module of the combustion modelling CHEMKIN library. The data and the calculated OH number densities in Figure 29 were normalised by an arbitrary scaling factor to allow direct comparison. (The equilibrium OH number density for a stoichiometric CH_4/air flame is ~ 1 x 10^{16} cm^{-3}). The population of the J = 8 line is very stable with respect to the range of temperatures of the flame in this experiment, showing a maximum deviation of ~ 3 % for an extremely fuel lean flame from that for a stoichiometric flame, and characteristically < 1% deviation from the stoichiometric J = 8 flame population for most of the flame conditions studied. The effects of both temperature and chemical composition (equilibrium calculations were also undertaken for compressed natural gas as well as assuming pure CH_4) were undetectable with respect to the plot of calculated equilibrium OH number density as a function of equivalence ratio.

In Figure 29, the (probe fluorescence corrected) LIF signal and square root of the (probe extinction background corrected) LPS signal have nearly the same dependence on flame equivalence ratio and closely follow the calculated equilibrium OH number density curve. However, the LIF and LPS signal for fuel-lean flames similarly lie above the calculated OH number density curve, even if the underestimation of the near-stoichiometric LIF and LPS signal due to absorption is considered. There is no obvious explanation of the variation of the LIF and square root of the LPS signal from the calculated equilibrium number densities for fuel-lean flames in this experiment. However, the similarities of the dependence of the LIF and square root of the LPS signal on fuel equivalence ratio strongly suggests a relationship between the number densities predicted by the two techniques for this flame. **Figure 30 demonstrates a clear linearity between the number densities predicted by the (background corrected) linear LIF signal and the square root of the (probe extinction background corrected) saturated LPS signal in a graphical form where absorptive effects are common to the two techniques and are cancelled by the plotting method.**

Ignoring the effects of absorption, the corrected (linear regime) LIF and corrected square root (highly saturated) LPS signal should both be linearly proportional to the number density of the OH radical in the target region. The linear regime LIF signal is proportional to the number density of the upper state, $N_{J"}$,

$$I_{PLIF\_linear\_regime} \propto N_{J"} \qquad \text{Equation 30}$$

The square root of the highly saturated (probe background corrected) LPS signal is proportional to the saturated induced dichroism

[t] OH concentrations also provided by Dr Bassam Dally of the School of Mechanical Engineering, The University of Adelaide, using the equilibrium module of the CHEMKIN library assuming a CH_4/air flame, and also for a CNG/air flame..

$$\Delta\alpha_{highly\_saturated} \propto \sqrt{I_{PLPS}_{highly\_saturated} - I_{probe\_0} \cdot \xi}$$ Equation 31

where (assuming a shared pump and probe beam transition)

$$\left(\Delta\alpha^{i,i'}_{J,J''}\right)_{highly\_saturated} = \sum_{M}\left(\left(N_{J,M} - N_{J'',M''}\right)_{high\_saturated} \cdot \left(\sigma^{i}_{J,J'',M,M''} - \sigma^{i'}_{J,J'',M,M''}\right) \cdot C_{JJ''}\right)$$ Equation 32

Looking at equations [27] to [29], it is not difficult to believe that the linear regime LIF and the highly saturated (probe background corrected) LPS signals are proportional to the total number density of the target species. However, the linear regime LIF signal is inversely proportional to the quenching rate via the dependence on the number density of the upper state of the pumped transition, $N_{J''}$. The quenching rate is a function of the flame chemistry and hence of equivalence ratio. The linearity between the linear LIF and square root of the (probe background corrected) saturated LPS signal, i.e. the (saturated) induced dichroism, suggests that the induced dichroism is also somehow inversely proportional to the number density of the upper state of the pumped transition.

Remember that for the simple two-level model (including collisional quenching as the only collisional population transfer rate) assuming a linear regime of optical pumping, the population of the upper state of the pumped transition is given by

$$\left(N_1\right)_{\substack{steady-state \\ quenching\_dominated}} = N \cdot \left(\frac{B_{01}W}{Q_{10} + A_{10}}\right)$$ Equation 33

The difference in population between the lower and upper states of the pumped transition is

$$\left(N_0 - N_1\right)_{\substack{steady-state \\ quenching\_dominated}} = N \cdot \left(1 - 2 \cdot \left(\frac{B_{01}W}{Q_{10} + A_{10}}\right)\right)$$ Equation 34

Writing the Zeeman state dependence of these factors explicitly, the induced dichroism may be written as

$$\left(\Delta\alpha^{i,i'}_{J,J''}\right)_{\substack{saturated \\ (steady-state \\ quenching\_dominated)}} = N \cdot \sum_{M}\left(\left(1 - 2 \cdot \left(\frac{B_{01\_M}W}{Q_{10\_M} + A_{10\_M}}\right)\right) \cdot \left(\sigma^{i}_{J,J'',M,M''} - \sigma^{i'}_{J,J'',M,M''}\right) \cdot C_{JJ''}\right)$$

Equation 35

The appearance of the difference in the squares of the Clebsch-Gordon coefficients for the characteristic modes of propagation of the probe beam in the sum in equation [35] means that constant terms in the (blue coloured) coefficient term in the equation disappear under summation to leave

$$\left(\Delta\alpha^{i,i'}_{J,J''}\right)_{\substack{saturated \\ (steady-state \\ quenching\_dominated)}} = 2 \cdot N \cdot \sum_{M}\left(\left(\frac{B_{01\_j}W}{Q_{10\_j} + A_{10\_j}}\right) \cdot \left(\sigma^{i}_{J,J'',M,M''} - \sigma^{i'}_{J,J'',M,M''}\right) \cdot C_{JJ''}\right)$$ Equation 36

If the spontaneous emission rate is insignificant with respect to the quenching rate, which is assumed to be independent of the M, equations [30] and [33] may be rewritten as

$$\left(N_1\right)_{\substack{\text{steady-state}\\ \text{quenching\_dominated}}} = \left(\frac{N}{Q_{10}}\right)\cdot B_{01}W \qquad \text{Equation 37}$$

$$\left(\Delta\alpha^{i,i'}_{J,J''}\right)_{\substack{\text{saturated}\\ \text{(steady-state}\\ \text{quenching\_dominated)}}} = 2\cdot\left(\frac{N}{Q_{10}}\right)\cdot\sum_{M}\left(B_{01\_j}W\cdot\left(\sigma^{i}_{J,J'',M,M''}-\sigma^{i'}_{J,J'',M,M''}\right)\cdot C_{JJ''}\right) \qquad \text{Equation 38}$$

This **simple** model indicates that **for this simple, two-level, linear (quenching-dominated) saturation regime model of population**

- ignoring all collisional population transfer rates other than quenching directly into the lower state of the pumped transition (assumed to be independent of M), and
- for an insignificant spontaneous emission rate in comparison with the quenching rate,

the LIF signal and the square root of the (probe background corrected) LPS signal are similarly inversely proportional to the quenching rate.[u] Note however, that this simple models requires that the LIF and square root of the LPS signal are both in the linear (steady-state) regime. This, however, does not agree with the saturation of the square root of the LPS signal shown in Figure 28. However, the model is very simple, and does not predict the difference in saturation intensities for LIF and LPS signals shown in Figures 15 and 18, and 27 and 28 above.

This chapter has shown that saturated LPS and linear regime LIF (for the A $^2\Sigma$-X $^2\Pi$(0,0) $P_2(8)$ transition) predict a similar dependence of OH number density as a function of flame equivalence ratio for an atmospheric pressure natural gas/air flame from a rectangular mixing burner. The similarity between the predicted number densities due to the two techniques is highlighted by the plotting method which, due to the simultaneous collection of linear regime LIF and saturated LPS signal from the central region of rectangular mixing burner, allows absorption factors to be cancelled. The predicted number density dependence on equivalence ratio closely follows the OH number density predicted by the equilibrium module of the CHEMKIN library for fuel-rich flames, but overestimates the OH number density for fuel-lean flames. Reichardt, Giancola and Lucht[48] similarly showed a strong correspondence between saturated LPS signal for a H_2/air flame and number density calculated by a NASA Lewis equilibrium code for the A $^2\Sigma$-X $^2\Pi$(0,0) $P_1(2)$ and $Q_1(8)$ transitions of OH. Saturation curves collected for a near-stoichiometric flame indicated that the LPS signal in the experiments described in this chapter (for a nanosecond pulsed laser system) saturates at a much lower pump sheet intensity that the LIF signal. This result is supported by

[u] Note that the analysis in this chapter ignores any transient or exponential decay contributions to the LIF signal.

saturation measurements (Figures 15 and 18) obtained for a premixed natural gas/O_2 flame from a modified glass-blowing torch.

However, simultaneously collected highly saturated PLPS and linear regime PLIF images in the first section of this chapter predict dramatically different OH number density distributions as a function of height in a natural gas/O_2 flame from the modified glass-blowing torch. The saturated LPS images predict near constant OH concentration over the base 3 mm of the natural gas/O_2 flame. The LPS images were corrected for and divided by the probe beam background and the square root taken to represent OH number density. The linear regime LIF images however, even after correction for the intensity profile of the pump sheet, predict a near linear drop of OH concentration close to the tip of the burner. The difference between the two sets of images cannot be understood in terms of field of view of the PLIF ICCD. It is possible that the method for collecting the pump sheet intensity profile was flawed and the experiment should be repeated.

The agreement between the simultaneous linear regime LIF and saturated LPS predictions of number density (for a nanosecond pulse length laser system) as a function of flame equivalence ratio show great promise for comparative use of the fluorescence and the coherent techniques in combustion environments where there is a strong fluorescence or radiant background. The LPS technique may be applied to detection of resonant transitions and requires little spectral filtering, although for imaging applications, care must be taken to minimise thermal density gradient structures in the collected image. In this thesis, we have demonstrated that the range of beam geometries has been extended to allow PLPS images to be collected for all beam intersection angles. PLIF and PLPS images may be collected simultaneously as the PLPS image results from the transmission of the probe beam through the pump sheet and the PLIF image from the fluorescence from that sheet.

The experiments in this chapter were limited by the weak LPS signal, especially in the natural gas/air flame form the rectangular mixing burner. The number density dependence on the flame equivalence ratios is promising. However, further simultaneous linear LIF and saturated LPS experiments should be undertaken in an range of well characterised flames to confirm this result. If imaging experiments are undertaken, accurate correction for the probe beam background in the case of the saturated LPS signal and for the pump sheet profile in the case of the linear regime LIF signal must be applied. Flames from standard burners should be well isolated from ambient air by nitrogen shrouds to avoid the appearance of edge effects due to diffusion which complicate the interpretation of the experimental results.

An investigation of saturation of the LPS signal as a function of probe beam intensity should also be undertaken as increased probe beam intensity will increase the delectability of the LPS images. The

probe beam intensity must be very much less than the saturation intensity due to the pump beam in order to not perturb the pumped population densities.

It has been suggested[49 59] that the future of LPS as a laser diagnostic technique lies in picosecond pulse length laser systems where the signal is less susceptible to the effects of collisional population transfer. However, at this stage of quantification of polarisation spectroscopy in combustion, parallel investigations of nanosecond and picosecond LPS will provide valuable information about trace combustion species, as collisional information is as important as absolute number densities in combustion modelling.

The next two chapters integrate the results of Chapters II and IV into a Jones matrix format suitable for the calculation of the realistic LPS experiments including misalignment of imperfect optical elements. Chapter VIII describes the general dependence of the LPS signal due to passage of the probe beams through the region of induced birefringence and dichroism as a function of beam intersection angle and polarisation directions of the pump and probe beams in matrix format. These matrices may be combined with general Jones matrices representing polarisers, rhombi, and birefringent inter-probe beam-polariser cell windows to easily calculate the LPS signal strength for specific experimental arrangements. Chapter IX defines the behaviour of imperfect optical elements important to the behaviour of polarisation spectroscopy. Combined Jones matrices for the most common experimental configurations are derived. Similarities and significant differences from the equations derived by Teets, Kowalski, Hill, Carlson and Hansch[1] are noted in the resultant calculations of LPS signal strength.

Chapter VIII: Jones Matrix Description of the Induced Dichroism and Birefringence

The calculation of the LPS signal in Chapters II and IV may be simplified and applied to a wide variety of experimental configurations by the application of Jones matrix calculus[60]. This chapter adapts the standard Jones matrices for birefringent and dichroic materials to describe the results of Chapters II and IV. This allows the LPS signal in more general experiments including imperfect and misaligned optical elements to be calculated rapidly. The following chapter, Chapter IX , summarises combinations of Jones matrices representing the most common experimental configurations.

R. Clark Jones[60] developed the Jones calculus to describe the effect of a series of optical elements in the path of a collimated, polarised beam in terms of 2X2 matrices. Clark Jones considered polarisers, retarding beamplates, birefringent and dichroic materials as the basic optical elements. As the elements do not include lensing elements, the calculus does not require 3X3 matrices to describe the transmitted electric field.

In the Jones calculus, the polarisation state of a collimated beam is defined by a two element vector, termed the Jones vector, representing the electric field of the beam in the plane normal to the direction of propagation. The polarisation state of the beam is defined aside from an arbitrary phase factor so the Jones vector, $\underline{E}$, is equivalent to the Jones vector, $\underline{E}e^{i\phi}$.

The action of optical elements in the probe beam path is described by 2 X 2 matrixes, the Jones matrices. The optical elements act on the Jones vector via a matrix calculus with the order dependent proviso that the progressive transmission of a beam, with Jones vector, $\underline{E}$, through the optical elements represented by the matrices, $\underline{A}$, $\underline{B}$ and $\underline{C}$, is described by the equation

$$\underline{E}_{transmitted\_through\_A,B,C} = \underline{C}\cdot(\underline{B}\cdot(\underline{A}\cdot\underline{E})) = (\underline{C}\cdot\underline{B}\cdot\underline{A})\cdot\underline{E} \qquad \text{Equation 1}$$

The combined matrix, $\underline{C}\cdot\underline{B}\cdot\underline{A}$, may thus be used to describe the ordered action of the set of optical elements, A, B and C.

The standard description of the behaviour of an imperfect polariser may be used to illustrate the Jones calculus and to clarify its usage for those not familiar with it.

Standard Jones Matrix Description of the Behaviour of Imperfect Polarisers

A perfect polariser is assumed to completely absorb or deflect from the beam path one polarisation component of an input beam. An imperfect polariser will transmit a fraction, t_1, of the input beam electric field polarised parallel to the polariser's transmission axis, and a fraction, t_2, of the input beam electric field polarised parallel to the extinction axis of the polariser. The extinction and transmission axes are typically orthogonal. The extinction ratio, ξ, of the polariser is defined as

$$\xi = \frac{t_2^2}{t_1^2} \qquad \text{Equation 2}$$

and represents the ratio of the transmitted intensities for light polarised parallel and perpendicular to the extinction axis of the polariser.

Consider a polariser placed in the path of the probe beam in the coordinate system of Chapter II. The probe beam propagates along the Z axis and is polarised at the angle, γ, to the vertical X axis. The electric vector of the probe beam may be written as

$$\frac{\underline{E}_{probe}}{E_0} = \begin{pmatrix} \cos(\gamma) \\ \sin(\gamma) \\ 0 \end{pmatrix} \qquad \text{Equation 3}$$

where $\underline{E}_{probe}$ represents the electric field of the incident probe beam, and E_0 is the magnitude of the electric field of the incident probe beam.

The transmission axis of a polariser in the probe beam path and aligned at an angle, η, to the vertical X axis, may be represented by the unit vector, $\hat{\underline{v}}$, where

$$\hat{\underline{v}} = \begin{pmatrix} \cos(\eta) \\ \sin(\eta) \\ 0 \end{pmatrix} \qquad \text{Equation 4}$$

The extinction axis of the polariser is represented by the unit vector, $\hat{\underline{u}}$.

$$\hat{\underline{u}} = \begin{pmatrix} -\sin(\eta) \\ \cos(\eta) \\ 0 \end{pmatrix} \qquad \text{Equation 5}$$

The component of the electric vector of the probe beam which is transmitted through the polariser is given by the vector equation

$$\frac{\underline{E}_{probe\_transmitted\ polariser\_at\_\eta}}{E_0} = t_1\left(\frac{\underline{E}_{probe}}{E_0}.\hat{\underline{u}}\right)\hat{\underline{u}} + t_2\left(\frac{\underline{E}_{probe}}{E_0}.\hat{\underline{v}}\right)\hat{\underline{v}} \qquad \text{Equation 6}$$

where the order dependent convention for complex vectors of Appendix III has been preserved with the inner or dot product of two vectors providing the projection of the first vector onto the second.

This equation simplifies to

$$\frac{\underline{E}_{probe\_transmitted\ polariser\_at\_\eta}}{E_0} = \begin{pmatrix} \cos(\gamma)\cdot\left(\frac{(t_1-t_2)}{2}\cos(2\eta)+\frac{(t_1+t_2)}{2}\right)+\sin(\gamma)\cdot\frac{(t_1-t_2)}{2}\sin(2\eta) \\ \cos(\gamma)\cdot\frac{(t_1-t_2)}{2}\sin(2\eta)+\sin(\gamma)\cdot\left(\frac{(t_1+t_2)}{2}-\frac{(t_1-t_2)}{2}\cos(2\eta)\right) \\ 0 \end{pmatrix} \qquad \text{Equation 7}$$

where the right hand side of the equation may be rewritten as a function of the probe beam polarisation as

$$\frac{\underline{E}_{probe\_transmitted\ polariser\_at\_\eta}}{E_0} = \begin{pmatrix} \frac{(t_1-t_2)}{2}\cos(2\eta)+\frac{(t_1+t_2)}{2} & \frac{(t_1-t_2)}{2}\sin(2\eta) & P_{13} \\ \frac{(t_1-t_2)}{2}\sin(2\eta) & -\frac{(t_1-t_2)}{2}\cos(2\eta)+\frac{(t_1+t_2)}{2} & P_{23} \\ P_{31} & P_{32} & P_{33} \end{pmatrix} \cdot \begin{pmatrix} \cos(\gamma) \\ \sin(\gamma) \\ 0 \end{pmatrix}$$

Equation 8

This equation isolates the original probe beam polarisation vector to the right of the equation. The matrix on the left of this vector represents the action of the polariser on the incident probe beam electric field. The unknown components of the 3X3 polariser matrix do not participate in the calculation of the transmitted polarisation state of the probe beam. The Jones calculus was developed as a 2X2 matrix system to utilise this property.

For the probe beam described above, the representative 2X2 Jones vector is

$$\underline{E} = E_0 \cdot \begin{pmatrix} \cos(\gamma) \\ \sin(\gamma) \end{pmatrix} \qquad \text{Equation 9}$$

The Jones matrix describing the action of the imperfect polariser, $P(\eta)$, aligned with transmission axis at the angle, η, to the vertical X axis of the probe beam with polarisation axis lying at the angle, γ, to the X axis is given by

$$P(\eta)=\begin{pmatrix}\frac{(t_1-t_2)}{2}\cos(2\eta)+\frac{(t_1+t_2)}{2} & \frac{(t_1-t_2)}{2}\sin(2\eta)\\ \frac{(t_1-t_2)}{2}\sin(2\eta) & -\frac{(t_1-t_2)}{2}\cos(2\eta)+\frac{(t_1+t_2)}{2}\end{pmatrix}$$ Equation 10

Jones calculus characteristically simplifies matrices defining optical elements, such as P(η) above, by defining each matrix in terms of rotation matrices and a simplified action matrix which expresses the characteristic behaviour of the optical element in its simplest form. In the case of the polariser considered above, the angle between the frame of the probe beam and the frame based on the transmission and extinction axes of the polariser is η. The rotation matrix associated with a rotation of a vector through this angle is

$$R(\eta)=\begin{pmatrix}\cos(\eta) & -\sin(\eta)\\ \sin(\eta) & \cos(\eta)\end{pmatrix}$$ Equation 11

and for a reverse rotation

$$R(-\eta)=\begin{pmatrix}\cos(-\eta) & -\sin(-\eta)\\ \sin(-\eta) & \cos(-\eta)\end{pmatrix}=\begin{pmatrix}\cos(\eta) & \sin(\eta)\\ -\sin(\eta) & \cos(\eta)\end{pmatrix}$$ Equation 12

The effect of these two matrices applied in series is to return a vector to its original state via the action of unit matrix as

$$R(\eta)R(-\eta)=\begin{pmatrix}1 & 0\\ 0 & 1\end{pmatrix}$$ Equation 13

To define the action of an imperfect polariser on the linearly polarised electric field of a collimated beam, the rotation vector, R(-η), is first applied to rewrite the polarisation state of the probe beam in the frame of the transmission and extinction axes of the polariser. The simplified polariser matrix in this frame reduces to

$$P_{simplified}=\begin{pmatrix}t_1 & 0\\ 0 & t_2\end{pmatrix}$$ Equation 14

and is independent of the angular position. Equation [14] is the standard Jones matrix for an imperfect polariser assuming no phase differences are introduced between probe beam components parallel and perpendicular to the polariser transmission axis. The probe beam is returned to the original frame by application of the rotation vector, R(η). The combined operation is represented by the matrix series

$$P(\eta)=R(\eta)\cdot P_{simplified}\cdot R(-\eta)=\begin{pmatrix}\cos(\eta) & -\sin(\eta)\\ \sin(\eta) & \cos(\eta)\end{pmatrix}\cdot\begin{pmatrix}t_1 & 0\\ 0 & t_2\end{pmatrix}\cdot\begin{pmatrix}\cos(\eta) & \sin(\eta)\\ -\sin(\eta) & \cos(\eta)\end{pmatrix}$$ Equation 15

which is equivalent to the matrix of equation [10].

Jones calculus describes the transmission of a polarised input beam. The calculus does not describe the behaviour of unpolarised light. In addition, care must be taken in definition of the matrix description of the action of optical elements.

Consider the action of two imperfect polarisers with action matrix defined by equation [14]. If perfectly crossed, the combined polariser matrix is given by

$$P_{\substack{\text{simplified}\\ \text{perfectly\_crossed}}} \cdot P_{\text{simplified}} = \begin{pmatrix} t_2 & 0 \\ 0 & t_1 \end{pmatrix} \cdot \begin{pmatrix} t_1 & 0 \\ 0 & t_2 \end{pmatrix} = \begin{pmatrix} t_1 \cdot t_2 & 0 \\ 0 & t_1 \cdot t_2 \end{pmatrix} = t_1 \cdot t_2 \cdot \begin{pmatrix} 1 & 0 \\ 0 & 1 \end{pmatrix} \qquad \text{Equation 16}$$

as would be expected, and if perfectly aligned, the combined polariser matrix is

$$P_{\substack{\text{simplified}\\ \text{perfectly\_aligned}}} \cdot P_{\text{simplified}} = \begin{pmatrix} t_1 & 0 \\ 0 & t_2 \end{pmatrix} \cdot \begin{pmatrix} t_1 & 0 \\ 0 & t_2 \end{pmatrix} = \begin{pmatrix} t_1^2 & 0 \\ 0 & t_2^2 \end{pmatrix} \qquad \text{Equation 17}$$

Equation [17] describes a combined matrix which defines a polariser with extinction ratio

$$\xi_{\text{combined}} = \left(\frac{t_2^2}{t_1^2} \right)^2 \qquad \text{Equation 18}$$

This implies that two polarisers each with an extinction ratio of 10^{-6} may be used in series to act as polariser with extinction ratio of 10^{-12}. This may be true for polarisers where the transmission/extinction mechanism is based on reflection (where repeated reflections may be used to increase the purity of polarisation of a transmitted beam). However, where the extinction ratio is a function of optical imperfections, such as flaws in a calcite crystal polariser, the action matrix does not accurately define the behaviour of the polariser and predicts erroneous results in equations [16] and [17]. The Jones matrix representing the action of an imperfect polariser is reconsidered in Chapter IX.

We continue now from this introduction to Jones calculus to derive matrices representing the effects of the induced dichroism and birefringence on the transmitted probe beam electric field.

Matrix descriptions of the induced linear dichroism and birefringence due to a linearly polarised pump beam

Conventionally, the Jones matrix representing transmission a distance, Λ, though a linearly birefringent and dichroic material is written

$$B = \begin{pmatrix} e^{-\frac{\alpha_o}{2}\cdot\Lambda}\cdot e^{-i\cdot k_o\cdot\Lambda} & 0 \\ 0 & e^{-\frac{\alpha_e}{2}\cdot\Lambda}\cdot e^{-i\cdot k_e\cdot\Lambda} \end{pmatrix} \qquad \text{Equation 19}$$

or,

$$B = e^{-\frac{\alpha_{av}}{2}\cdot\Lambda}\cdot e^{-i\cdot k_{av}\cdot\Lambda}\cdot\begin{pmatrix} e^{-\frac{\Delta\alpha_{lin}}{4}\cdot\Lambda}\cdot e^{-i\cdot\frac{\Delta k_{lin}}{2}\cdot\Lambda} & 0 \\ 0 & e^{\frac{\Delta\alpha_{lin}}{4}\cdot\Lambda}\cdot e^{i\cdot\frac{\Delta k_{lin}}{2}\cdot\Lambda} \end{pmatrix} \qquad \text{Equation 20}$$

where k_o and k_e are the wavenumbers for ordinary and extraordinary polarisation modes of propagation, and α_o and α_e are the equivalent absorption coefficients, and we have defined

$$k_{av} = \frac{k_o + k_e}{2} \qquad \text{Equation 21}$$

$$\alpha_{av} = \frac{\alpha_o + \alpha_e}{2} \qquad \text{Equation 22}$$

and

$$\Delta k_{lin} = k_o - k_e \qquad \text{Equation 23}$$

$$\Delta\alpha_{lin} = \alpha_o - \alpha_e \qquad \text{Equation 24}$$

In this matrix format, it is assumed that the ordinary polarisation mode of propagation corresponds to the first component of the electric field of the Jones vector, and that the extraordinary polarisation mode of propagation corresponds to the second component of the vector. Identification of the angular directions of the two induced polarisation mode components of the probe beam in the experimental geometry will allow the results obtained in Chapter II to be applied in a matrix format.

Consider the set of system axes based on the probe beam path described in Chapter II, and termed the probe beam frame in this chapter with axes X, Y and Z. The Z axis corresponds to the direction of propagation of the probe beam. The X axis is vertical. The pump and probe beams intersect in the horizontal YZ plane. The probe beam polarisation direction lies at the angle, γ, to the vertical X axis in the usual sense of rotation with respect to the XYZ axes. The electric field of the probe beam is

$$\underline{E}_{probe} = E_{probe\_0}\cdot\begin{pmatrix}\cos(\gamma)\\ \sin(\gamma)\\ 0\end{pmatrix} \qquad \text{Equation 25}$$

The linearly polarised pump beam propagates at an angle, χ, from the Z axis, with the sense of the rotation towards the positive Y axis. The frame of the pump beam is described by the right-handed set of axes, X', Y' and Z'. These axes are defined as X' = the vertical X axis, Y' = the component of the pump beam polarisation direction lying in the XY plane and Z' is the direction of propagation of the pump beam. The polarisation direction lies at the angle, κ, to the vertical X' axis in the usual sense of rotation for a right-handed set of axes. The pump beam electric field which represents the induced optic axis of the uniaxial medium is parallel to the unit vector,

$$\hat{\underline{E}}_{optic\_axis} = \begin{pmatrix} \cos(\kappa) \\ \sin(\kappa)\cdot\cos(\chi) \\ -\sin(\kappa)\cdot\sin(\chi) \end{pmatrix} \qquad \text{Equation 26}$$

As shown in equations [54] and [55] of Chapter II, the unit vectors representing the ordinary and extraordinary polarisation modes may be written

$$\hat{\underline{E}}_{ordinary} = \frac{\begin{pmatrix} -\sin(\kappa)\cdot\cos(\chi) \\ \cos(\kappa) \\ 0 \end{pmatrix}}{\sqrt{\cos^2(\kappa)+\sin^2(\kappa)\cdot\cos^2(\chi)}} \qquad \text{Equation 27}$$

and

$$\hat{\underline{E}}_{extraordinary} = \frac{\begin{pmatrix} \cos(\kappa) \\ \sin(\kappa)\cdot\cos(\chi) \\ 0 \end{pmatrix}}{\sqrt{\cos^2(\kappa)+\sin^2(\kappa)\cdot\cos^2(\chi)}} \qquad \text{Equation 28}$$

These vectors lies at the angles of inclination, γ_o and γ_e, of the ordinary and extraordinary polarisation directions from the vertical X axis in the electric field plane of the probe beam given by

$$\gamma_o = -\text{a tan}\left(\frac{\cot(\kappa)}{\cos(\chi)}\right) \qquad \text{Equation 29}$$

and

$$\gamma_e = \text{a tan}\left(\tan(\kappa)\cdot\cos(\chi)\right) \qquad \text{Equation 30}$$

Note that the two polarisation modes are orthogonal. We may then define the simplified Jones vector X_s axis, $X_{Jones\_linear\_pump}$, to lie at the angle, γ_o, to the vertical X axis of the pump/probe beam geometry. The simplified Jones vector Y_s axis, $Y_{Jones\_linear\_pump}$, lies at the angle, $\gamma_e = \gamma_o + {}^{\pi}/_{2}$, to the vertical X axis.

The simplified Jones matrix for a dichroic and birefringent medium written in equation [20] describes the behaviour of the optically pumped system with respect to the simplified axes, X_s and Y_s. The additional rotation matrixes, $R(\gamma_o)$ and $R(-\gamma_o)$, combine with the simplified Jones matrix for a dichroic and birefringent medium to **define the action of the dichroic and birefringent medium for a linearly polarised pump beam in the frame of the probe beam** with vertical X axis as

$$B_{\substack{linear\_pump \\ probe\_frame}} = R(\gamma_0) \cdot B_{linear\_pump} \cdot R(-\gamma_0) \qquad \text{Equation 31}$$

where

$$B_{linear\_pump} = e^{-\frac{\alpha_{av}}{2}\cdot\Lambda} \cdot e^{-i\cdot k_{av}\cdot\Lambda} \cdot \begin{pmatrix} e^{-\frac{\Delta\alpha_{lin}}{4}\cdot\Lambda} \cdot e^{-i\cdot\frac{\Delta k_{lin}}{2}\cdot\Lambda} & 0 \\ 0 & e^{\frac{\Delta\alpha_{lin}}{4}\cdot\Lambda} \cdot e^{i\cdot\frac{\Delta k_{lin}}{2}\cdot\Lambda} \end{pmatrix} \qquad \text{Equation 32}$$

and

$$\gamma_o = -a\tan\left(\frac{\cot(\kappa)}{\cos(\chi)}\right) \qquad \text{Equation 33}$$

The terms, Δk_{lin} and $\Delta\alpha_{lin}$, required for calculation of the birefringent and dichroic Jones matrix in equation [32] are functions of the angle of intersection of pump and probe beams and are obtained from the linearly polarised pump beam induced birefringence, $\Delta n_{lin}(\chi)$,

$$\Delta n_{lin}(\chi) = n_o - n_e(\chi) = (1 - \sin^2(\kappa)\cdot\sin^2(\chi))\cdot(n_o - n_e) \qquad \text{Equation 34}$$

Matrix descriptions of the induced linear and circular dichroism and birefringence due to a circularly polarised pump beam

There are two regimes for which the characteristic polarisation modes of propagation of the probe beam due to a circularly polarised pump beam may be approximated easily:

- for $\cos^2(\chi) << \sigma^2, \Delta$, and
- for $\cos^2(\chi) << \sigma^2, \Delta$,

where $^{\Delta}/_{2}$ has been identified as the fractional induced linear birefringence due to the circularly polarised pump beam and σ the equivalent circular fractional birefringence.

The pump/probe beam geometry used in this chapter for the case of a linearly polarised pump beam is adjusted slightly for the case of a circularly polarised pump beam as was done in Chapter IV. It is assumed that the pump beam propagates along the Z' axis and the probe beam, polarised at the angle, γ, to the vertical X' axis, propagates at the angle, χ, to the Z' axis. The pump beam polarisation axis representing the induced optic axis lies along the direction of pump beam propagation.

Case 1: $\cos^2(\chi) >> \sigma^2, \Delta$

The polarisation modes of propagation induced by a circularly polarised pump beam for $\cos^2(\chi) >> \sigma^2, \Delta$ are given in equation [26] of Chapter IV.

$$\left(\underline{E}_{0\_approx}\right)_{\iota} = \cos(\chi)\cdot\begin{pmatrix} i\cdot\sigma\cdot\cos(\chi) \\ \cos(\chi)\cdot s_{\iota} \\ -\sin(\chi)\cdot s_{\iota}\end{pmatrix} \qquad \iota = \alpha, \beta \qquad \text{Equation 35}$$

where the term, s_{ι}, is defined as

$$\left(\frac{n_i}{n_o}\right)^2 = 1 + s_{\iota} \qquad \iota = \alpha, \beta \qquad \text{Equation 36}$$

Remembering that the general unit electric vector for a beam propagating at the angle, χ, to the Z' axis and with axis of polarisation lying at the angle, η, to the vertical X' axis is written

$$\hat{\underline{E}}_{plane\_of\_polarisation} = \begin{pmatrix} \cos(\eta) \\ \sin(\eta)\cdot\cos(\chi) \\ -\sin(\eta)\cdot\sin(\chi)\end{pmatrix} \qquad \text{Equation 37}$$

It can be seen that the angles of inclination of the polarisation vectors to the vertical X' axis, γ_i, defined in equation [35], are

$$\gamma_{\iota} = a\tan\left(\frac{s_{\iota}}{\sigma\cdot\cos(\chi)}\right) \qquad \iota = \alpha, \beta \qquad \text{Equation 38}$$

To second order, the terms, s_{ι}, of equation [36] are defined in equations [11] and [12] of Chapter IV.

$$\left(s_{\alpha}\right)_{0\_approx} = \left(\frac{\Delta-\sigma^2}{2}\right)\cdot\sin^2(\chi) + \sqrt{\sin^4(\chi)\cdot\left(\frac{\Delta+\sigma^2}{2}\right)^2 + \cos^2(\chi)\cdot\sigma^2} \qquad \text{Equation 39}$$

and

$$\left(s_{\beta}\right)_{0\_approx} = \left(\frac{\Delta-\sigma^2}{2}\right)\cdot\sin^2(\chi) - \sqrt{\sin^4(\chi)\cdot\left(\frac{\Delta+\sigma^2}{2}\right)^2 + \cos^2(\chi)\cdot\sigma^2} \qquad \text{Equation 40}$$

For small intersection angles, $\chi \sim 0$, of pump and probe beams, these two equations reduce to

$$\left(s_{\alpha}\right)_{\substack{0\_approx \\ \chi\approx 0}} = \sigma \cdot \cos(\chi) \qquad \text{Equation 41}$$

and

$$\left(s_{\beta}\right)_{\substack{0\_approx \\ \chi\approx 0}} = -\sigma \cdot \cos(\chi) \qquad \text{Equation 42}$$

while the angles of inclination of the polarisation vectors, γ_i, may be approximated by

$$\gamma_{\alpha} = -\gamma_{\beta} \qquad \text{Equation 43}$$

This indicates that the two resulting polarisation modes are not orthogonal, even in this near-collinear approximation, so that the application of the standard birefringent and dichroic matrix is not possible in this regime. However, it is possible to express the action of the induced birefringence and dichroism in this case in matrix form. The XY frame of the probe beam electric field frame is used with the X axis vertical in orientation and XY and Z (the direction of propagation of the probe beam) making a right-handed axial system..

For simplicity, equations [39] and [40] are rewritten as

$$\left(s_{\alpha}\right)_{0\_approx} = a + b \qquad \text{Equation 44}$$

and

$$\left(s_{\beta}\right)_{0\_approx} = a - b \qquad \text{Equation 45}$$

where

$$a = \left(\frac{\Delta - \sigma^2}{2}\right) \cdot \sin^2(\chi) \qquad \text{Equation 46}$$

and

$$b = \sqrt{\sin^4(\chi) \cdot \left(\frac{\Delta + \sigma^2}{2}\right)^2 + \cos^2(\chi) \cdot \sigma^2} \qquad \text{Equation 47}$$

The rewritten electric field modes of propagation are

$$\left(\underline{E}_{0\_approx}\right)_{\alpha} = \cos(\chi) \cdot \begin{pmatrix} i \cdot \sigma \cdot \cos(\chi) \\ \cos(\chi) \cdot (a+b) \\ -\sin(\chi) \cdot (a+b) \end{pmatrix} \qquad \text{Equation 48}$$

and

$$\left(\underline{E}_{0\_approx}\right)_{\beta} = \cos(\chi) \cdot \begin{pmatrix} i \cdot \sigma \cdot \cos(\chi) \\ \cos(\chi) \cdot (a-b) \\ -\sin(\chi) \cdot (a-b) \end{pmatrix} \qquad \text{Equation 49}$$

or, in the XY polarisation frame of the probe beam, as

$$\left(\underline{E}_{0\_approx}\right)_{\substack{\alpha \\ probe\_beam\_frame}} = \cos(\chi)\cdot\begin{pmatrix} i\cdot\sigma\cdot\cos(\chi) \\ a+b \end{pmatrix} \qquad \text{Equation 50}$$

and

$$\left(\underline{E}_{0\_approx}\right)_{\substack{\beta \\ probe\_beam\_frame}} = \cos(\chi)\cdot\begin{pmatrix} i\cdot\sigma\cdot\cos(\chi) \\ a-b \end{pmatrix} \qquad \text{Equation 51}$$

We now express the probe beam electric field,

$$\frac{\underline{E}_{probe}}{E_0} = \begin{pmatrix} E_{probe\_x} \\ E_{probe\_y} \end{pmatrix} \qquad \text{Equation 52}$$

as a linear combination of the two polarisation modes, ignoring the common cos(χ) factor.

$$\frac{\underline{E}_{probe}}{E_0} = \begin{pmatrix} E_{probe\_x} \\ E_{probe\_y} \end{pmatrix} = A\cdot\begin{pmatrix} i\cdot\sigma\cdot\cos(\chi) \\ a+b \end{pmatrix} + B\cdot\begin{pmatrix} i\cdot\sigma\cdot\cos(\chi) \\ a-b \end{pmatrix} \qquad \text{Equation 53}$$

leading to two simultaneous equations with solutions

$$A = \frac{1}{2\cdot b}\cdot\left(E_{probe\_y} + i\cdot\frac{(a-b)}{\sigma\cdot\cos(\chi)}\cdot E_{probe\_x}\right) \qquad \text{Equation 54}$$

$$B = -\frac{1}{2\cdot b}\cdot\left(E_{probe\_y} + i\cdot\frac{(a+b)}{\sigma\cdot\cos(\chi)}\cdot E_{probe\_x}\right) \qquad \text{Equation 55}$$

After transmission a distance, Λ, through the birefringent and dichroic region, the electric field of the probe beam is written

$$\frac{\underline{E}_{\substack{probe \\ transmitted\_\Lambda}}}{E_0} = A\cdot e^{-\frac{\alpha_\alpha}{2}\cdot\Lambda}\cdot e^{i\cdot k_\alpha\cdot\Lambda}\cdot\begin{pmatrix} i\cdot\sigma\cdot\cos(\chi) \\ a+b \end{pmatrix} + B\cdot e^{-\frac{\alpha_\beta}{2}\cdot\Lambda}\cdot e^{i\cdot k_\beta\cdot\Lambda}\cdot\begin{pmatrix} i\cdot\sigma\cdot\cos(\chi) \\ a-b \end{pmatrix} \qquad \text{Equation 56}$$

or

$$\frac{\underline{E}_{\substack{probe \\ transmitted\_\Lambda}}}{E_0\cdot e^{-\frac{\alpha_{av}}{2}\cdot\Lambda}\cdot e^{-i\cdot k_{av}\cdot\Lambda}} = A\cdot e^{-\frac{\Delta\alpha_{circ}}{4}\cdot\Lambda}\cdot e^{-i\cdot\frac{\Delta k_{circ}}{2}\cdot\Lambda}\cdot\begin{pmatrix} i\cdot\sigma\cdot\cos(\chi) \\ a+b \end{pmatrix} + B\cdot e^{\frac{\Delta\alpha_{circ}}{4}\cdot\Lambda}\cdot e^{i\cdot\frac{\Delta k_{circ}}{2}\cdot\Lambda}\cdot\begin{pmatrix} i\cdot\sigma\cdot\cos(\chi) \\ a-b \end{pmatrix}$$

Equation 57

Substitution of equations [54] and [55] and introduction of the term, ϕ, defined as

$$\phi = \left(\frac{\Delta k_{circ}}{2} - i\cdot\frac{\Delta\alpha_{circ}}{4}\right)\cdot\Lambda \qquad \text{Equation 58}$$

into equation [57] (see Appendix VIII) gives

$$\frac{\underline{E}_{\substack{probe \\ transmitted\_\Lambda}}}{E_0\cdot e^{-\frac{\alpha_{av}}{2}\cdot\Lambda}\cdot e^{-i\cdot k_{av}\cdot\Lambda}} = \frac{1}{2\cdot b}\begin{pmatrix} e^{-i\cdot\phi}\cdot\left(E_{probe\_y} + i\cdot\frac{(a-b)}{\sigma\cdot\cos(\chi)}\cdot E_{probe\_x}\right)\cdot\begin{pmatrix} i\cdot\sigma\cdot\cos(\chi) \\ a+b \end{pmatrix} \\ -e^{i\cdot\phi}\cdot\left(E_{probe\_y} + i\cdot\frac{(a+b)}{\sigma\cdot\cos(\chi)}\cdot E_{probe\_x}\right)\cdot\begin{pmatrix} i\cdot\sigma\cdot\cos(\chi) \\ a-b \end{pmatrix} \end{pmatrix} \qquad \text{Equation 59}$$

which may be rewritten in terms of the input probe beam polarisation

$$\frac{E_{probe\_transmitted\_\Lambda}}{E_0 \cdot e^{-\frac{\alpha_{av}}{2}\Lambda} \cdot e^{-i\cdot k_{av}\cdot\Lambda}} = \frac{1}{b}\cdot\begin{pmatrix} b\cdot\cos(\phi)+i\cdot a\cdot\sin(\phi) & \sigma\cdot\sin(\phi)\cdot\cos(\chi) \\ \dfrac{\sin(\phi)\cdot(a^2-b^2)}{\sigma\cdot\cos(\chi)} & b\cdot\cos(\phi)-i\cdot a\cdot\sin(\phi) \end{pmatrix}\cdot\begin{pmatrix} E_{probe\_x} \\ E_{probe\_y} \end{pmatrix} \quad \text{Equation 60}$$

The Jones matrix for the action of the dichroism and birefringence induced by a circularly polarised pump beam for $\cos^2(\chi) >> \sigma^2, \Delta$ in the XY frame of the probe beam is then given by

$$B_{\substack{circ\_pump \\ \cos^2(\chi)>>\sigma^2,\Delta \\ probe\_frame}} = \frac{e^{-\frac{\alpha_{av}}{2}\Lambda}\cdot e^{-i\cdot k_{av}\cdot\Lambda}}{b}\cdot\begin{pmatrix} b\cdot\cos(\phi)+i\cdot a\cdot\sin(\phi) & \sigma\cdot\sin(\phi)\cdot\cos(\chi) \\ \dfrac{\sin(\phi)\cdot(a^2-b^2)}{\sigma\cdot\cos(\chi)} & b\cdot\cos(\phi)-i\cdot a\cdot\sin(\phi) \end{pmatrix} \quad \text{Equation 61}$$

Note that this matrix is written in terms of the XY polarisation frame of the probe beam with the X axis vertical (normal to the beam intersection plane). A combined matrix including rotation matrices, as in equation [31], is not required to represent the action of the region of induced dichroism and birefringence due to the derivation method used to avoid difficulties with the non-orthogonal polarisation modes of the probe beam.

For small beam intersection angles, $\chi \sim 0$, substitution of the terms, a and b, obtained from the approximate refractive index solutions of equations [41] and [42] into the Jones matrix of equation [60] gives

$$B_{\substack{circ\_pump \\ \chi\sim 0 \\ probe\_frame}} = e^{-\frac{\alpha_{av}}{2}\Lambda}\cdot e^{-i\cdot k_{av}\cdot\Lambda}\cdot\begin{pmatrix} \cos(\phi) & \sin(\phi) \\ -\sin(\phi) & \cos(\phi) \end{pmatrix} \quad \text{Equation 62}$$

Note that this matrix is independent of rotation with respect to the XY plane, as would be expected for two purely circular characteristic modes of propagation for the case of a near-collinear pump/probe geometry and no clearly defined beam intersection plane.

The induced birefringence, $\Delta n_{circ}(\chi)$, required for calculation of the term, ϕ, for a circularly polarised pump beam for the general range of pump/probe beam intersection angles, $\cos^2(\chi) >> \sigma^2, \Delta$, is given to second order by the equation

$$\frac{\Delta n_{circ}(\chi)}{n_0} = \frac{n_\alpha - n_\beta}{n_0} = \sqrt{\sin^4(\chi)\cdot\left(\frac{\Delta+\sigma^2}{2}\right)^2 + \cos^2(\chi)\cdot\sigma^2} \quad \text{Equation 63}$$

where n_0 is the unperturbed refractive index.

Case 2: $\cos^2(\chi) << \sigma^2, \Delta$

This regime of pump/probe intersection angles was modelled in Chapter IV by considering the propagation of purely linearly polarised probe beam components through the region of dichroism and birefringence. The probe beam components were subjected to the action of the α and β induced birefringence and dichroism. The two linearly polarised probe beam components are approximately orthogonal for $\cos^2(\chi) << \sigma^2, \Delta$.

For large pump/probe intersection angles, the X component of the probe beam is identified as the β polarisation mode. The remaining YZ components of the probe beam in the plane of intersection of pump and probe beams are assumed to represent the α polarisation mode. The frame of the probe beam must be rotated through $\pm{}^{\pi}/_{2}$ for application of the dichroic and birefringent Jones matrix defined in equation [20]. In this case, the simplified Jones vector X_s axis lies at the angle, ${}^{\pi}/_{2}$, to the vertical X axis of the pump beam frame, while the simplified Jones vector Y_s axis lies at the angle, $\gamma_e = \gamma_o + {}^{\pi}/_{2} = \pi$, to the vertical X axis.

The simplified Jones matrix of equation [20] is combined in the usual manner with the rotation matrices of angle of rotation, $\eta = {}^{\pi}/_{2}$, giving the combined probe frame matrix in the frame of the probe beam

$$B_{\substack{circ\_pump \\ \cos^2(\chi)<<\sigma^2,\Delta \\ probe\_frame}} = e^{-\frac{\alpha_{av}}{2}\Delta}\cdot e^{-ik_{av}\Delta}\cdot\begin{pmatrix} e^{\frac{\Delta\alpha_{circ\_linear\_approx}}{4}\Delta}\cdot e^{i\frac{\Delta k_{circ\_linear\_approx}}{2}\Delta} & 0 \\ 0 & e^{\frac{\Delta\alpha_{circ\_linear\_approx}}{4}\Delta}\cdot e^{-i\frac{\Delta k_{circ\_linear\_approx}}{2}\Delta} \end{pmatrix}$$

Equation 64

The induced birefringence, $\Delta n_{circ\_linear\_approx}(\chi)$, used to calculate the terms, $\Delta k_{circ\_linear\_approx}$ and $\Delta\alpha_{circ\_linear\_approx}$, for the combined Jones matrix of equation [64] for a circularly polarised pump beam and $\cos^2(\chi) << \sigma^2, \Delta$ is given, to second order, by

$$\frac{\Delta n_{circ\_linear\_approx}(\chi)}{n_0} = \frac{n_\alpha - n_\beta}{n_0} \approx \sin^2(\chi)\cdot\frac{(\Delta+\sigma^2)}{2}$$

Equation 65

where n_0 is the unperturbed refractive index.

In Summary:

The Jones matrices representing the action of the region of induced birefringence and dichroism **in the frame of a probe beam** [a] (propagating at χ to the pump beam and polarised at γ to the beam intersection plane) and applicable for all beam intersection angles, χ, are given by

For a linearly polarised pump beam: polarised at κ to the beam intersection plane:

$$B_{\substack{linear\_pump \\ probe\_frame}} = R(\gamma_0)\cdot B_{linear\_pump}\cdot R(-\gamma_0) \qquad \text{Equation 66}$$

where

$$B_{linear\_pump} = e^{-\frac{\alpha_{av}\cdot\Lambda}{2}}\cdot e^{-i\cdot k_{av}\cdot\Lambda}\cdot\begin{pmatrix} e^{-\frac{\Delta\alpha_{lin}\cdot\Lambda}{4}}\cdot e^{-i\cdot\frac{\Delta k_{lin}}{2}\cdot\Lambda} & 0 \\ 0 & e^{\frac{\Delta\alpha_{lin}\cdot\Lambda}{4}}\cdot e^{i\cdot\frac{\Delta k_{lin}}{2}\cdot\Lambda}\end{pmatrix} \qquad \text{Equation 67}$$

$$\gamma_o = -a\tan\left(\frac{\cot(\kappa)}{\cos(\chi)}\right) \qquad \text{Equation 68}$$

and the terms, Δk_{lin} and $\Delta\alpha_{lin}$, are obtained from the induced birefringence, $\Delta n_{lin}(\chi)$, given by

$$\Delta n_{lin}(\chi) = n_o - n_e(\chi) = (1-\sin^2(\kappa)\cdot\sin^2(\chi))\cdot(n_o - n_e) \qquad \text{Equation 69}$$

For a circularly polarised pump beam:

Case 2: $\cos^2(\chi) << \sigma^2, \Delta$

$$B_{\substack{circ\_pump \\ \cos^2(\chi)>>\sigma^2,\Delta \\ probe\_frame}} = \frac{e^{-\frac{\alpha_{av}\cdot\Lambda}{2}}\cdot e^{-i\cdot k_{av}\cdot\Lambda}}{b}\cdot\begin{pmatrix} b\cdot\cos(\phi)+i\cdot a\cdot\sin(\phi) & \sigma\cdot\sin(\phi)\cdot\cos(\chi) \\ \frac{\sin(\phi)\cdot(a^2-b^2)}{\sigma\cdot\cos(\chi)} & b\cdot\cos(\phi)-i\cdot a\cdot\sin(\phi)\end{pmatrix} \qquad \text{Equation 70}$$

where

$$\phi = \left(\frac{\Delta k_{circ}}{2} - i\cdot\frac{\Delta\alpha_{circ}}{4}\right)\cdot\Lambda \qquad \text{Equation 71}$$

$$a = \left(\frac{\Delta-\sigma^2}{2}\right)\cdot\sin^2(\chi) \qquad \text{Equation 72}$$

[a] X = the normal to the beam intersection plane, Y = lies in the beam intersection and normal to the direction of propagation of the probe beam and Z = the direction of propagation of the probe beam.

$$b = \sqrt{\sin^4(\chi)\cdot\left(\frac{\Delta+\sigma^2}{2}\right)^2 + \cos^2(\chi)\cdot\sigma^2} \qquad \text{Equation 73}$$

and the induced birefringence, $\Delta n_{circ}(\chi)$, required for calculation of the term, ϕ, is given by

$$\frac{\Delta n_{circ}(\chi)}{n_0} = \frac{n_\alpha - n_\beta}{n_0} = \sqrt{\sin^4(\chi)\cdot\left(\frac{\Delta+\sigma^2}{2}\right)^2 + \cos^2(\chi)\cdot\sigma^2} \qquad \text{Equation 74}$$

where n_0 is the unperturbed refractive index, σ is the fractional induced circular birefringence and $\Delta/2$ the fractional induced linear birefringence due to the circularly polarised pump beam.

Note that for near-collinear beam intersection, $\chi \sim 0$, equation [70] reduces to

$$B_{\substack{circ\_pump \\ \chi\sim 0 \\ probe\_frame}} = e^{-\frac{\alpha_{av}}{2}\Lambda}\cdot e^{-i k_{av}\Lambda}\cdot\begin{pmatrix}\cos(\phi) & \sin(\phi)\\ -\sin(\phi) & \cos(\phi)\end{pmatrix} \qquad \text{Equation 75}$$

Case 2: $\cos^2(\chi) << \sigma^2, \Delta$

$$B_{\substack{circ\_pump \\ \cos^2(\chi)<<\sigma^2,\Delta \\ probe\_frame}} = e^{-\frac{\alpha_{av}}{2}\Lambda}\cdot e^{-i k_{av}\Lambda}\cdot\begin{pmatrix} e^{\frac{\Delta\alpha_{circ\_linear\_approx}}{4}\Lambda}\cdot e^{-i\frac{\Delta k_{circ\_linear\_approx}}{2}\Lambda} & 0 \\ 0 & e^{\frac{\Delta\alpha_{circ\_linear\_approx}}{4}\Lambda}\cdot e^{-i\frac{\Delta k_{circ\_linear\_approx}}{2}\Lambda}\end{pmatrix} \qquad \text{Equation 76}$$

where the induced birefringence, $\Delta n_{circ\_linear\_approx}(\chi)$, used to calculate the terms, $\Delta k_{circ\_linear\_approx}$ and $\Delta\alpha_{circ\_linear\_approx}$, is given by

$$\frac{\Delta n_{circ\_linear\_approx}(\chi)}{n_0} = \frac{n_\alpha - n_\beta}{n_0} \approx \sin^2(\chi)\cdot\frac{(\Delta+\sigma^2)}{2} \qquad \text{Equation 77}$$

where n_0 is the unperturbed refractive index, σ is the fractional induced circular birefringence and $\Delta/2$ the fractional induced linear birefringence due to the circularly polarised pump beam.

This chapter has derived general Jones matrices written in the frame of the probe beam to describe the transmission of a polarised beam a distance, Λ, through a birefringent and dichroic medium. The derivation takes note of

- **decomposition of the probe beam into the characteristic polarisation modes of propagation in the pumped medium, and**
- **the geometrical dependence of the induced birefringence.**

These Jones matrices allow variations of the standard experimental geometry to be investigated easily for all beam intersection angles, χ, via standard Jones matrix methods. Chapter IX demonstrates the calculation of combined matrices

representing a series of optical components placed in the probe beam path to model a range of standard polarisation spectroscopy experiments.

Chapter IX: The Effect of Imperfect and Misaligned Optical Elements.

In polarisation spectroscopy, the primary limitation on the achievable signal to background ratio is the extinction ratio of the probe beam polarisers, ξ. Teets, Kowalski, Hill, Carlson and Hansch[1] noted that the intensity background is proportional to the term, $\xi + \theta^2 + b^2$,

where

ξ is the extinction ratio of the probe beam polariser pair,

θ is the angle of deviation from perfect crossing of the probe beam polarisers and

b represents the birefringence of any optical elements placed in the probe beam path between the probe beam polarisers.

Given that polarisers with extinction ratios ~10^{-6} are commonly available, this chapter will investigate experimental variables which will affect transmitted electric field on the order of magnitude of 10^{-3} to find the limiting factors on quantitative polarisation spectroscopy. The primary sources of such variations are imperfect and misaligned optical elements. This chapter uses Jones calculus to investigate the effects of each of these factors on the LPS signal strength.

This chapter begins with a revision of the matrix description of the principal optical elements in the probe beam path likely to contribute to the LPS signal and background. Once the optical characteristics of the elements are defined, the effects of

- input probe beam polarisation,
- misalignment of the optical elements, and
- imperfect optical elements

are investigated for their influence on the LPS signal.

Matrix Descriptions of Imperfect Optical Elements

In Chapter VIII, we noted that the conventional Jones matrix representing an imperfect polariser does not represent the behaviour of an imperfection-limited polariser. As the behaviour of the probe beam polarisers is of primary importance to polarisation spectroscopy, we consider the following description of imperfection-limited polariser matrices below. This section also describes the behaviour of rhombi, waveplates and birefringent optical elements applicable to polarisation spectroscopy.

(i) Imperfect Polariser Matrices

The conventional Jones matrix representing an imperfect polariser is

$$P_{conventional} = \begin{pmatrix} t_1 & 0 \\ 0 & t_2 \end{pmatrix} \qquad \text{Equation 1}$$

where t_1 is the transmittivity of the polariser along the transmission axis, and t_2 is the transmittivity of the polariser along the extinction axis. In this thesis, the extinction ratio of a polariser is defined as *the ratio*, for unpolarised input, *of transmittivities of electric field components polarised parallel to the extinction and to the transmission axes*, i.e.

$$\xi_{conventional} = \left(\frac{t_2}{t_1}\right)^2 \qquad \text{Equation 2}$$

As shown in Chapter VIII, for two such polarisers placed in series, the combined polariser matrix is given by

$$P_{\substack{conventional \\ perfectly\_crossed}} \cdot P_{conventional} = \begin{pmatrix} t_2 & 0 \\ 0 & t_1 \end{pmatrix} \cdot \begin{pmatrix} t_1 & 0 \\ 0 & t_2 \end{pmatrix} = t_1 \cdot t_2 \cdot \begin{pmatrix} 1 & 0 \\ 0 & 1 \end{pmatrix} \qquad \text{Equation 3}$$

for identical polarisers with crossed transmission axes, and

$$P_{\substack{conventional \\ perfectly\_aligned}} \cdot P_{conventional} = \begin{pmatrix} t_1 & 0 \\ 0 & t_2 \end{pmatrix} \cdot \begin{pmatrix} t_1 & 0 \\ 0 & t_2 \end{pmatrix} = \begin{pmatrix} t_1^2 & 0 \\ 0 & t_2^2 \end{pmatrix} \qquad \text{Equation 4}$$

for identical polarisers with aligned transmission axes. The two perfectly aligned polarisers combine to act as a polariser with extinction ratio given by the product of the extinction ratios of each.

$$\xi_{\substack{conventional\_combined \\ perfectly\_aligned}} = \left(\frac{t_2^2}{t_1^2}\right)^2 = \left(\frac{t_2}{t_1}\right)^4 \qquad \text{Equation 5}$$

This result implies that two such polarisers, each with an extinction ratio of 10^{-6}, could be used in aligned series to act as a polariser with extinction ratio of 10^{-12} (assuming the polarisers could be aligned with an accuracy of 10^{-12}). If the polariser extinction ratio is a function of optical imperfections, such as flaws in a calcite crystal, the conventional Jones matrix is not sufficient to

represent the behaviour of the imperfect polariser and predicts erroneous results in equations [4] and [5].

The Jones matrix representing the action of an imperfect polariser is reconsidered in the present chapter. A more realistic model of the polariser behaviour which includes the effects of imperfection scattering requires the

- transmission, t_1, of a fraction of the probe beam electric field polarised parallel to the transmission axis of the polariser
- transmission, t_2, of a fraction of the probe beam electric field polarised parallel to the extinction axis,
- scattering of a fraction, s_1, of the probe beam electric field polarised parallel to the transmission axis to be transmitted polarised parallel to the extinction axis, and
- scattering of a fraction, s_2, of the probe beam electric field polarised parallel to the extinction axis of the polariser to be transmitted polarised parallel to the transmission axis of the polariser.

The possibility of phase changes associated with the scattering[a] has not been considered in this chapter. **The polariser model attempts to obtain an order of magnitude estimate of the change in the LPS signal for a more accurate model of imperfect polariser behaviour.**

The Jones matrix representing these four attributes is written as

$$P_{imperfect} = \begin{pmatrix} t_1 & s_2 \\ s_1 & t_2 \end{pmatrix} \qquad \text{Equation 6}$$

with extinction ratio

$$\xi_{imperfect} = \left(\frac{t_2^2 + s_2^2}{t_1^2 + s_1^2} \right) \approx \left(\frac{t_2^2 + s_2^2}{t_1^2} \right) \qquad \text{Equation 7}$$

The standard Jones imperfect polariser matrix then represents imperfect polariser behaviour for regimes where the extinction axis transmission, t_2, is very much greater than the imperfection constants, s_1 and s_2, i.e. $t_2 >> s_1, s_2$. For a greater imperfection level, the imperfection-limited Jones matrix given above may be used to describe the polariser behaviour.

[a] Jones calculus is based on the assumption that individual electric field components retain a coherent phase relationship. This allows the electric field on transmission through each optical element to be obtained by adding corresponding electric field components rather than intensities. If this is not the case, the Mueller calculus is more applicable. In the following sections, it is assumed that the scattering centres within a high-quality cube polariser are small enough to impart a minimal phase change to the scattered radiation and hence that the use of Jones calculus is valid.

Two imperfection-limited polarisers acting in series, are represented by the combined matrices for identical polarisers with crossed transmission axes

$$P_{\substack{\text{imperfect}\\ \text{perfectly\_crossed}}} \cdot P_{\text{imperfect}} = \begin{pmatrix} t_2 & -s_1 \\ -s_2 & t_1 \end{pmatrix} \cdot \begin{pmatrix} t_1 & s_2 \\ s_1 & t_2 \end{pmatrix} = \begin{pmatrix} t_1 \cdot t_2 - s_1^{\,2} & (-s_1 + s_2) \cdot t_2 \\ (s_1 - s_2) \cdot t_1 & t_1 \cdot t_2 - s_2^{\,2} \end{pmatrix} \qquad \text{Equation 8}$$

and for identical polarisers with aligned transmission axes

$$P_{\substack{\text{imperfect}\\ \text{perfectly\_aligned}}} \cdot P_{\text{imperfect}} = \begin{pmatrix} t_1 & s_2 \\ s_1 & t_2 \end{pmatrix} \cdot \begin{pmatrix} t_1 & s_2 \\ s_1 & t_2 \end{pmatrix} = \begin{pmatrix} t_1^2 + s_1 \cdot s_2 & (t_1 + t_2) \cdot s_2 \\ (t_1 + t_2) \cdot s_1 & t_2^2 + s_1 \cdot s_2 \end{pmatrix}$$

Equation 9

These matrices take account of the rotation matrices required to write the analyser matrix in the frame of the primary polariser. The combined extinction ratio for two such perfectly aligned, imperfection-limited polarisers is

$$\xi_{\substack{\text{combined\_imperfection\_limited}\\ \text{perfectly\_aligned}}} = \left(\frac{\left(t_2^2 + s_1 \cdot s_2\right)^2 + (t_1 + t_2)^2 \cdot s_2^{\,2}}{\left(t_1^2 + s_1 \cdot s_2\right)^2 + (t_1 + t_2)^2 \cdot s_1^{\,2}} \right) \qquad \text{Equation 10}$$

For s_1, s_2 and t_2 of the same order of magnitude, and remembering that $1 > t_1 >> t_2, s_1, s_2$ for a good polariser, equations [8] to [10] reduce to

$$P_{\substack{\text{imperfect}\\ \text{perfectly\_crossed}\\ s \approx t_2}} \cdot P_{\text{imperfect}} = \begin{pmatrix} t_1 \cdot t_2 & 0 \\ 0 & t_1 \cdot t_2 \end{pmatrix} \qquad \text{Equation 11}$$

for identical polarisers with crossed transmission axes, and

$$\left(P_{\substack{\text{imperfect}\\ \text{perfectly\_aligned}}} \cdot P_{\text{imperfect}} \right)_{s \approx t_2} = \begin{pmatrix} t_1^2 & t_1 \cdot s_2 \\ t_1 \cdot s_1 & t_2^2 + s_1 \cdot s_2 \end{pmatrix} \qquad \text{Equation 12}$$

for identical polarisers with aligned transmission axes, with a combined extinction ratio of

$$\xi_{\substack{\text{combined\_imperfection\_limited}\\ \text{perfectly\_aligned}\\ s \approx t_1}} = \left(\frac{t_1^{\,2} \cdot s_2^{\,2}}{t_1^{\,4}} \right) = \left(\frac{s_2}{t_1} \right)^2 \qquad \text{Equation 13}$$

The resultant combined extinction ratio for two perfectly aligned imperfection-limited polarisers for imperfection levels satisfying the condition, $s_1, s_2 \approx t_2$, is of the same order of magnitude as the extinction ratio of a single imperfection-limited polariser. This is more representative of the experimental behaviour of such polarisers than the extinction ratio suggested by the conventional Jones polariser matrix calculation in equation [5]. **Note also that the matrix of equation [11] representing perfectly crossed imperfection-limited polarisers does not contain a significant contribution from the imperfection terms, s_1 and s_2, and is dependent on only the conventional Jones polariser coefficients, t_1 and t_2.**

Note:

The mathematical treatment above does not include phase differences introduced by the different optical path lengths experienced by the two transmitted polarisation components, which may be significant as shown below. For a calcite crystal, the ordinary and extraordinary refractive indices[61] are n_o = 1.72 and n_e = 1.51 at λ_o = 303 nm. Over a path length, L, the ordinary and extraordinary rays generate a phase difference, ϕ, of

$$\phi = 2 \cdot \pi \cdot \frac{L}{\lambda_0} \cdot (n_e - n_o) \qquad \text{Equation 14}$$

where λ_0 is the vacuum wavelength of the transmitted radiation. For a 10 mm calcite crystal, this represents a phase difference of 14 000π, or a free space path difference between the two components of 2.1 mm.

The flatness of the polariser surfaces is also an issue. A difference in path length, ΔL,

$$\Delta L = \frac{\lambda_0}{n_e - n_o} \qquad \text{Equation 15}$$

introduces a phase difference of 2π between the two transmitted polarisation components. In the case of the calcite crystal above, this corresponds to approximately a fifth of a free-space wavelength. This level of flatness is well within the tolerance of high quality manufacture and any phase difference may be included in the polariser matrix by including a complex phase factor, $e^{i\phi}$, in the extinction constant, t_2. The following results may be adjusted by replacing the factor, t_2, by $t_2 e^{i\phi}$. Equivalent terms may also be included in the imperfection factors, as long as the scattering does not dephase the scattered electric field component.

(ii) Imperfect Rhomb and Waveplate Matrices

Rhombi and waveplates may be used to create a circularly polarised pump beam or to rotate the plane of polarisation[b] of either pump or probe beam. In the first case, it is used after the pump beam polariser, in the second, it is used prior to the primary beam polariser.

A quarter-wave plate or rhomb is used to introduce a phase difference of $\pi/2$ between two equal and orthogonal, linearly polarised components of the incident pump beam to produce circularly polarised light. Alternatively, a half-wave plate or rhomb, introducing a phase difference of π between the two equal components, may be used to rotate the linear polarisation of incident beam by $\pi/2$.

A waveplate introduces the required phase difference via birefringence. A rhomb introduces the phase difference via reflection at internal (totally internally reflecting) surfaces. In both cases, the input beam must contain electric field components in each of the two polarisation modes of propagation in the rhomb or waveplate for a phase difference between the two components to be introduced.

The behaviour of a rhomb or waveplate may be imperfect in two respects

- **the introduced phase difference may differ from $\pi/2$, for a quarter-wave plate, or π for a half-wave plate, and**
- **the rhomb or waveplate may be misaligned to the input beam polarisation direction so that the two input probe beam components are not equal.**

The second effect may be dealt with using conventional Jones calculus and rotation matrices. The first must be explicitly stated in the relevant Jones matrix. We ignore the effects of imperfections in the crystal or waveplate material itself as the effects of these are likely to be much smaller in magnitude than the effects of misalignment or introduced phase difference[c]. For the sake of simplicity in the following section, we base the following paragraphs on the matrix description of a rhomb.

[b] A half-wave rhomb rotated through an angle, θ, with respect to the incident probe beam polarisation rotates the plane of polarisation of the transmitted beam through the angle, 2θ.

[c] In the case of a waveplate or rhomb, we deal with probe beam polarisation components of the same order of magnitude of intensity. In the case of a polariser, one polarisation component is many orders of magnitude less in intensity than the other and so may be significantly influenced by the contribution of a small scattered component from the other.

The Jones matrix for a perfect quarter-wave rhomb is

$$F_{perfect\_\frac{1}{4}\_wave\_rhomb} = \begin{pmatrix} e^{i\cdot\frac{\pi}{8}} & 0 \\ 0 & e^{-i\cdot\frac{\pi}{8}} \end{pmatrix} = \begin{pmatrix} 1 & 0 \\ 0 & e^{-i\cdot\frac{\pi}{4}} \end{pmatrix} \qquad \text{Equation 16}$$

where either of the two matrices is acceptable within the Jones algebra as the electric field is only required to be determined to within an arbitrary phase factor. The matrix is written with respect to the frame of the rhomb or waveplate, so that the X_{rhomb} and Y_{rhomb} axes refer to the probe beam components polarised parallel to the "ordinary" and "extraordinary" transmission axes of the rhomb. The equivalent Jones matrix for a half-wave rhomb is

$$F_{perfect\_\frac{1}{2}\_wave\_rhomb} = \begin{pmatrix} 1 & 0 \\ 0 & e^{-i\cdot\frac{\pi}{2}} \end{pmatrix} \qquad \text{Equation 17}$$

We describe an imperfect rhomb by allowing the phase factor in these matrices to differ from $\pi/4$ or $\pi/2$.

$$F_{imperfect\_rhomb} = \begin{pmatrix} 1 & 0 \\ 0 & e^{-i\upsilon} \end{pmatrix} \qquad \text{Equation 18}$$

Absorption along the optical path within a rhomb is the same for both polarisation components as the induced phase difference is due to total internal reflection rather than to birefringence. Due to total internal reflection (and assuming normal incidence onto the face of the rhomb), the fractional transmission is the same for both polarisation modes and is assumed to be unity in this chapter. The Jones matrix for a half- or quarter-wave plate may also include small polarisation dependent absorption factors caused by the birefringent nature of the optical element.

Typical Jones matrices in each case are of the form

$$F_{\substack{(non-dichroic)\\imperfect\_rhomb}} = e^{-\frac{\alpha_{rhomb}\cdot T}{2}} \cdot \begin{pmatrix} 1 & 0 \\ 0 & e^{-i\upsilon} \end{pmatrix} \qquad \text{Equation 19}$$

and

$$F_{\substack{dichroic\\imperfect\_wave-plate}} = \begin{pmatrix} e^{-\frac{\alpha_{wave\_plate\_o}\cdot T}{2}} & 0 \\ 0 & e^{-\frac{\alpha_{wave\_plate\_e}\cdot T}{2}} \cdot e^{-i\upsilon} \end{pmatrix} = e^{-\frac{\alpha_{wave\_plate\_o}\cdot T}{2}} \cdot \begin{pmatrix} 1 & 0 \\ 0 & e^{-\frac{\Delta\alpha_{wave\_plate}\cdot T}{2}} \cdot e^{-i\upsilon} \end{pmatrix} \qquad \text{Equation 20}$$

where

T is the path length through the waveplate or rhomb,

α_{rhomb} is the absorption coefficient for the rhomb, and

$\alpha_{wave\text{-}plate\_o}$ and $\alpha_{wave\text{-}plate\_e}$ are the ordinary and extraordinary absorption coefficients for the wave-plate with dichroism, $\Delta\alpha_{wave\text{-}plate} = \alpha_{wave\text{-}plate\_o} - \alpha_{wave\text{-}plate\_e}$.

(iii) Linearly and Circularly Birefringent Optical Element Matrices (representing birefringent optical components in the probe beam path between the probe beam polarisers)

As noted by Teets *et al.*, the LPS signal strength is strongly dependent on the birefringence of optical elements between the probe beam polarisers. Experimentally, the effects may be minimised in situ by applying pressure to the birefringent elements, inducing stress birefringence. In practice, non-birefringent optical materials should be chosen for inter-polariser usage.

We are primarily concerned with non-focussing optical elements, such as cell windows in the probe beam path, which may introduce ellipticity into the probe beam path due to intrinsic or stress birefringence. The optic axis of such an element may not be known. The birefringence of the element acts to introduce a phase difference between the two polarisation components of an input probe beam with respect to the frame of the optical element. In this regard, the birefringent element may be considered to be acting as a waveplate or rhomb.

The Jones matrix representing a linearly birefringent optical element may be written as

$$B_{linearly\_birefringent\_element} = \begin{pmatrix} 1 & 0 \\ 0 & e^{-ib} \end{pmatrix} \qquad \text{Equation 21}$$

where b is the phase difference introduced between the two incident polarisation states in the frame of the optical element introduced by dispersion. If dichroism is significant over the thickness, t, of the birefringent element, the Jones matrix may be modified to be written

$$B_{\substack{dichroic \\ linearly\_birefringent\_element}} = \begin{pmatrix} e^{-\frac{\alpha_{b\_o}}{2}t} & 0 \\ 0 & e^{-ib} \cdot e^{-\frac{\alpha_{b\_e}}{2}t} \end{pmatrix} = e^{-\frac{\alpha_{b\_o}}{2}t} \cdot \begin{pmatrix} 1 & 0 \\ 0 & e^{-ib} \cdot e^{-\frac{\Delta\alpha_{b\_lin}}{2}t} \end{pmatrix} \qquad \text{Equation 22}$$

where α_{b_o} and α_{b_e} are the ordinary and extraordinary absorption coefficients for the birefringent element and the factor, $\Delta\alpha_{b\_lin} = \alpha_{b\_o} - \alpha_{b\_e}$, is the linear dichroism of the optical element with respect to the direction of propagation of the probe beam within the medium.

Purely circularly birefringent optical elements must be represented by a matrix which is independent of rotation as the (purely) circular birefringence is not a function of the polarisation direction of the probe beam. To satisfy this condition, the matrix must be of the form

$$\begin{pmatrix} a & -b \\ b & a \end{pmatrix} \text{ or } \begin{pmatrix} a & b \\ -b & a \end{pmatrix} \qquad \text{Equation 23}$$

and may be written as

$$B_{circularly\_birefringent\_element} = \begin{pmatrix} \cos\left(\frac{b}{2}\right) & \sin\left(\frac{b}{2}\right) \\ -\sin\left(\frac{b}{2}\right) & \cos\left(\frac{b}{2}\right) \end{pmatrix}$$

Equation 24

where, once again, the introduced phase difference between the two probe beam components is b. The matrix is unchanged by application of rotation matrices.

The matrix representing the behaviour of a dichroic circularly birefringent element is written

$$B_{\substack{dichroic \\ circularly\_birefringent\_element}} = e^{-\left(\frac{\alpha_{b\_circ\_av} T}{2}\right)} \cdot \begin{pmatrix} \cos\left(\frac{b_{circ}}{2} + i \cdot \frac{\Delta\alpha_{b\_circ} \cdot T}{4}\right) & \sin\left(\frac{b_{circ}}{2} + i \cdot \frac{\Delta\alpha_{b\_circ} \cdot T}{4}\right) \\ -\sin\left(\frac{b_{circ}}{2} + i \cdot \frac{\Delta\alpha_{b\_circ} \cdot T}{4}\right) & \cos\left(\frac{b_{circ}}{2} + i \cdot \frac{\Delta\alpha_{b\_circ} \cdot T}{4}\right) \end{pmatrix}$$

Equation 25

where $\alpha_{b\_circ\_av}$ is the average of the α and β absorption coefficients for the birefringent element and the factor, $\Delta\alpha_{b\_circ} = \alpha_{b\_\alpha} - \alpha_{b\_\beta}$, is the circular dichroism of the optical element with respect to the direction of propagation of the probe beam within the medium.

The Jones wave-plate, rhomb and birefringent matrices described above are based on the conventional Jones matrices, but also include consideration of absorptive components and imperfections in the optical elements. The imperfection-limited polariser matrix has been developed to estimate the application of imperfection-limited polarisers, where the conventional Jones imperfect polariser matrix gives misleading results as described above.

Combined Polariser/Dichroic-Birefringent Medium/Polariser Matrices

Polarisation spectroscopy is based on the dichroism and birefringence experienced by a linearly polarised probe beam. The LPS signal is that fraction of the probe beam intensity which passes through crossed polarisers enclosing the dichroic and birefringent region. In some experimental configurations, additional optical elements may lie between the probe beam polarisers. **We can combine the matrices representing the effects of the probe beam polarisers, inter-polariser components and the birefringent and dichroic medium to describe the combined transmission of the probe beam electric field**. This approach is limited only by the increasingly unwieldiness of the resultant matrices in more complex experiments. The transmitted electric field may be calculated by applying the combined matrix to a Jones vector representing the input electric field of the probe beam.

This section calculates several of the most common combined polariser/optical medium combinations for the three induced birefringence/dichroism matrices derived in Chapter VIII. Imperfection-limited polariser matrices are assumed. The result obtained may then be applied to conventional Jones polariser matrices by setting the imperfection constants, s_1 and s_2, to zero.

(i) Polariser/ Induced Linearly Dichroic-Birefringent Medium/Polariser Matrix

Consider the case of a linearly polarised pump beam with no birefringent optical elements between the probe beam polarisers. We use the coordinate system of the previous chapters with the pump beam polarised at the angle, κ, to the vertical X axis. The probe beam is polarised at the angle, γ, to the X axis. The pump and probe beams intersect at the angle, χ, in the YZ plane.

Chapter VIII noted that the induced ordinary polarisation direction characteristic of propagation of the probe beam is aligned at the angle, γ_o, to the X axis where

$$\gamma_o = -\text{a tan}\left(\frac{\cot(\kappa)}{\cos(\chi)}\right) \qquad \text{Equation 26}$$

The ordinary and extraordinary ray polarisations are orthogonal, requiring an input beam polarisation (due to transmission through the primary probe beam polariser) lying at the angle, $\gamma_o + \pi/4$, to the vertical X axis for maximum LPS signal.

Assuming that the transmission axis of the primary probe beam polariser is to be aligned to this direction, we take into account the possibility of misalignment of the transmission axes of both probe beam polarisers. We allow the primary polariser to be misaligned to the angle, $\gamma_o + \pi/4$, to the vertical X axis by the angle, $\Delta\gamma$. The analyser is allowed to deviate from perfect crossing with the primary polariser by the angle, $\Delta\theta$. We define the transmission axis of the primary probe beam

polariser to lie at the angle, $\gamma_0 + \pi/4 + \Delta\gamma$, to the vertical X axis, and the nearly crossed analyser transmission axis to lie at the angle, $\pi/2 + \Delta\theta$, to the transmission axis of the primary polariser. Note this definition of the "uncrossing angle" of the probe beam polarisers, $\Delta\theta$, is opposite in sign to that used by Teets, Kowalski, Hill, Carlson and Hansch[1].

In the frame of the probe beam electric field axes, $X_{probe}Y_{probe}$ (with X_{probe} vertical and Y_{probe} lying in the beam intersection plane), the combined matrix describing the transmission of the probe beam through the two polarisers and the linearly dichroic/birefringent region is written

$$C_{linear} = R\left(\gamma_0 + \frac{3\pi}{4} + \Delta\gamma + \Delta\theta\right)\cdot P_{imperfect}\cdot R\left(-\left(\gamma_0 + \frac{3\pi}{4} + \Delta\gamma + \Delta\theta\right)\right) \cdot R(\gamma_0)\cdot B_{linear\_pump}\cdot R(-\gamma_0) \cdot R\left(\gamma_0 + \frac{\pi}{4} + \Delta\gamma\right)\cdot P_{imperfect}\cdot R\left(-\left(\gamma_0 + \frac{\pi}{4} + \Delta\gamma\right)\right) \quad \text{Equation 27}$$

[Note that, due to the length of the expression, the right-hand-side of the equation has been written on three lines]. The resultant matrix, C_{linear}, may be applied to a two-element probe beam input beam electric vector written in the $X_{probe}Y_{probe}$ frame of the probe beam electric field plane to evaluate the transmitted probe beam electric field and hence the LPS signal.

The rotation matrices may be rearranged to write the combined matrix as

$$C_{linear} = R(\gamma_0)\cdot R\left(\frac{3\pi}{4} + \Delta\gamma + \Delta\theta\right)\cdot P_{imperfect}\cdot R\left(-\left(\frac{3\pi}{4} + \Delta\gamma + \Delta\theta\right)\right) \cdot B_{linear\_pump} \cdot R\left(\frac{\pi}{4} + \Delta\gamma\right)\cdot P_{imperfect}\cdot R\left(-\left(\frac{\pi}{4} + \Delta\gamma\right)\right)\cdot R(-\gamma_0) \quad \text{Equation 28}$$

or, alternatively,

$$C_{linear} = R\left(\gamma_0 + \frac{\pi}{4}\right)\cdot R\left(\frac{\pi}{2} + \Delta\gamma + \Delta\theta\right)\cdot P_{imperfect}\cdot R\left(-\left(\frac{\pi}{2} + \Delta\gamma + \Delta\theta\right)\right) \cdot R\left(-\frac{\pi}{4}\right)\cdot B_{linear\_pump}\cdot R\left(\frac{\pi}{4}\right) \cdot R(\Delta\gamma)\cdot P_{imperfect}\cdot R(-\Delta\gamma)\cdot R\left(-(\gamma_0 + \frac{\pi}{4})\right) \quad \text{Equation 29}$$

$$C_{linear} = R\left(\gamma_0 + \frac{\pi}{4}\right)\cdot C_{linear\ partial}\cdot R\left(-(\gamma_0 + \frac{\pi}{4})\right) \quad \text{Equation 30}$$

where

$$B_{linear} = e^{-\frac{\alpha_{av}}{2}\cdot\Lambda}\cdot e^{-i\cdot k_{av}\cdot\Lambda}\cdot\begin{pmatrix} e^{-\frac{\Delta\alpha}{4}\cdot\Lambda}\cdot e^{-i\cdot\frac{\Delta k}{2}\cdot\Lambda} & 0 \\ 0 & e^{\frac{\Delta\alpha}{4}\cdot\Lambda}\cdot e^{i\cdot\frac{\Delta k}{2}\cdot\Lambda}\end{pmatrix} = e^{-\frac{\alpha_{av}}{2}\cdot\Lambda}\cdot e^{-i\cdot k_{av}\cdot\Lambda}\cdot\begin{pmatrix} e^{-i\cdot\phi} & 0 \\ 0 & e^{i\cdot\phi}\end{pmatrix} \quad \text{Equation 31}$$

and

$$\phi = \left(\frac{\Delta k}{2} - i \cdot \frac{\Delta \alpha}{4}\right) \cdot \Lambda$$ Equation 32

The partial matrix, $C_{\substack{linear \\ partial}}$, defined as

$$C_{\substack{linear \\ partial}} = R\left(\frac{\pi}{2} + \Delta\gamma + \Delta\theta\right) \cdot P_{imperfect} \cdot R\left(-\left(\frac{\pi}{2} + \Delta\gamma + \Delta\theta\right)\right) \cdot R\left(-\frac{\pi}{4}\right) \cdot B_{linear\_pump} \cdot R\left(\frac{\pi}{4}\right) \cdot R(\Delta\gamma) \cdot P_{imperfect} \cdot R(-\Delta\gamma)$$ Equation 33

represents the combined action of the polarisers and induced linearly dichroic-birefringent medium in a probe beam *polarisation frame* with X" and Y" axes lying at π/4 to the induced ordinary and extraordinary axes respectively, i.e. the frame of a primary polariser with transmission axis aligned at π/4 to the induced ordinary axis. **This frame is the frame which leads to maximum LPS signal.**

For reference (for the case of a linearly polarised pump beam), the X" axis lies at the angle, $\gamma_o + \pi/4$, to the vertical X axis and the Y" axis lies at the angle, $\gamma_o + 3\pi/4$, to the vertical X axis in the plane of the electric field of the probe beam.

The partial matrix for the polariser/induced linearly birefringent and dichroic medium/polariser combination is calculated in Appendix X and takes advantage of the matrix expansion derived in Appendix IX which expresses a matrix of the form, R(η)·M·R(-η), as an additive series of simple 2 x 2 matrices, i.e.

$$R(\eta) \cdot M \cdot R(-\eta) = R(\eta) \cdot \begin{pmatrix} a & b \\ c & d \end{pmatrix} \cdot R(-\eta) = \frac{\left(\begin{pmatrix} \cos(2\cdot\eta) & \sin(2\cdot\eta) \\ \sin(2\cdot\eta) & -\cos(2\cdot\eta) \end{pmatrix} \cdot (a-d) + \begin{pmatrix} 1 & 0 \\ 0 & 1 \end{pmatrix} \cdot (a+d) + \begin{pmatrix} -\sin(2\cdot\eta) & \cos(2\cdot\eta) \\ \cos(2\cdot\eta) & \sin(2\cdot\eta) \end{pmatrix} \cdot (c+d) + \begin{pmatrix} 0 & -1 \\ 1 & 0 \end{pmatrix} \cdot (c-b)\right)}{2}$$

Equation 34

or, in the case of $\eta = \Delta\eta << 1$, to

$$R(\Delta\eta) \cdot M \cdot R(-\Delta\eta) = R(\Delta\eta) \cdot \begin{pmatrix} a & b \\ c & d \end{pmatrix} \cdot R(-\Delta\eta) = \begin{pmatrix} a & b \\ c & d \end{pmatrix} + \begin{pmatrix} -(c+b) & a-d \\ a-d & (c+b) \end{pmatrix} \cdot \Delta\eta$$ Equation 35

The derivation assumes identical probe beam polarisers with imperfection constants, $s_1 \sim s_2 \sim s << 1$, and expresses the partial matrix to first order expansion in the small variables by

$$\frac{C_{\substack{linear \\ partial}}}{t_1^2 \cdot e^{-\frac{\alpha_{av}}{2}\cdot\Lambda} \cdot e^{-i\cdot k_{av}\cdot\Lambda}} = \begin{pmatrix} \zeta & 0 \\ -\Delta\theta + i\cdot\phi & \zeta \end{pmatrix}$$ Equation 36

where

$$\zeta = \frac{t_2}{t_1} = \sqrt{\xi}$$ Equation 37

Note that polariser imperfection term,

$$\sigma = \frac{s}{t_1}$$ Equation 38

appears only to second order in the matrix and so does not occur in equation [36].

Writing the ϕ dependence explicitly, equation [36] becomes

$$\frac{C_{\substack{linear\\partial}}}{t_1^2 \cdot e^{-\frac{\alpha_{xy}\cdot\Lambda}{2}} \cdot e^{-i k_{xy}\cdot\Lambda}} = \begin{pmatrix} \zeta & 0 \\ \left(\frac{\Delta\alpha\cdot\Lambda}{4} - \Delta\theta + i\cdot\frac{\Delta k\cdot\Lambda}{2}\right) & \zeta \end{pmatrix}$$ Equation 39

where the induced linear dichroism, $\Delta\alpha$, and the difference in wavenumber, Δk, for the two polarisation modes of propagation of the probe beam are functions of the beam intersection angle and are shown in equations [68] and [65] of Chapter II respectively to be proportional to the induced birefringence, $\Delta n_{lin}(\chi)$,

$$\frac{\Delta n_{lin}(\chi)}{\Delta n_{0\_lin}} = (1 - \sin^2(\kappa)\cdot\sin^2(\chi))$$ Equation 40

Here, the term, Δn_{0_lin}, is the induced linear dichroism for collinear pump and probe beams.

The partial matrix of equation [36] takes account of possible misalignment of the primary polariser, $\Delta\gamma$, and mis-crossing of the analyser with the primary polariser, $\Delta\theta$, with respect to the X"Y" axes. Equations [36] and [39] show that the partial matrix is independent to first order of misalignment of the primary polariser with the angle, $\gamma_o + \pi/4$, to the vertical X axis. The angle, γ_o, is the angle of the ordinary polarisation axis from the vertical X axis and is related to the direction of the optic axis induced by the pump beam. Consequently, the partial matrix of equation [36] is independent to first order of misalignment of the probe beam with respect to the ordinary and extraordinary axes induced by the pump beam. This is reassuring, as experimentally, it is reasonably difficult to align the pump and probe beams polarisation directions to the same accuracy with which the probe beam polarisers are crossed.

The partial matrices of equations [36] and [39] are the same as those obtained with the conventional Jones polariser matrix definition. The matrices have been calculated using the assumption that all angle deviations, $\Delta\gamma$ etc, the induced birefringent/dichroic term, $\Delta\phi$, and polariser constants, σ and ζ, are of the same order of magnitude, with the consequent condition that $\zeta >> \sigma^2$.

A probe beam with input polarisation direction misaligned by a small angle, $\pi/4 + \Delta\psi$, to the induced ordinary axis, close to the transmission axis of the primary probe beam polariser, and represented by the electric field vector

$$\underline{E} = E_0 \cdot \begin{pmatrix} \cos(\Delta\psi) \\ \sin(\Delta\psi) \end{pmatrix} \approx E_0 \cdot \begin{pmatrix} 1 \\ \Delta\psi \end{pmatrix} \qquad \text{Equation 41}$$

will be transmitted through the analyser with electric field (to first order in the small coefficients) given by

$$\frac{\underline{E}_{out}}{E_0} = C_{\substack{linear \\ partial}} \cdot \begin{pmatrix} 1 \\ \Delta\psi \end{pmatrix} = t_1^2 \cdot e^{-\frac{\alpha_{av}}{2}\cdot\Lambda} \cdot e^{-i\cdot k_{av}\cdot\Lambda} \cdot \begin{pmatrix} \zeta & 0 \\ \frac{\Delta\alpha\cdot\Lambda}{4} - \Delta\theta + i\cdot\frac{\Delta k\cdot\Lambda}{2} & \zeta \end{pmatrix} \cdot \begin{pmatrix} 1 \\ \Delta\psi \end{pmatrix}$$

$$= t_1^2 \cdot e^{-\frac{\alpha_{av}}{2}\cdot\Lambda} \cdot e^{-i\cdot k_{av}\cdot\Lambda} \cdot \begin{pmatrix} \zeta \\ \frac{\Delta\alpha\cdot\Lambda}{4} - \Delta\theta + \zeta\cdot\Delta\psi + i\cdot\frac{\Delta k\cdot\Lambda}{2} \end{pmatrix} \qquad \text{Equation 42}$$

$$\approx t_1^2 \cdot e^{-\frac{\alpha_{av}}{2}\cdot\Lambda} \cdot e^{-i\cdot k_{av}\cdot\Lambda} \cdot \begin{pmatrix} \zeta \\ \frac{\Delta\alpha\cdot\Lambda}{4} - \Delta\theta + i\cdot\frac{\Delta k\cdot\Lambda}{2} \end{pmatrix} = C_{\substack{linear \\ partial}} \cdot \begin{pmatrix} 1 \\ 0 \end{pmatrix}$$

Equation [42] indicates that the transmitted electric field is, to first order, *independent* of small misalignments of the input probe beam polarisation with respect to the primary probe beam polariser. The same *independence* is noted if the Y" component, $\Delta\Psi$, is complex, denoting a small ellipticity of the input probe beam polarisation.

The transmitted intensity for a probe beam aligned close to the primary probe beam polariser transmission axis and transmitted through the analyser/induced linearly dichroic-birefringent region/polariser combination is then

$$\left(\frac{I_{out}}{I_0}\right)_{\substack{linear\_pump \\ probe\text{-}aligned\_to\_primary\_polariser}} \approx t_1^4 \cdot e^{-\alpha_{av}\cdot\Lambda} \cdot \left(\xi + \Delta\theta^2 + \frac{(\Delta\alpha\Lambda)^2}{16} + \frac{(\Delta k\Lambda)^2}{4} - \Delta\theta\cdot\frac{(\Delta\alpha\Lambda)}{2}\right) \qquad \text{Equation 43}$$

This expression is equivalent to that of Teets *et al.* given their opposite definition of the direction of $\Delta\theta$. However, the term, $i\cdot\Delta k\cdot\Lambda/2$, appears with opposite sign in the partial matrix above when compared to Teets *et al.*'s expression for the transmitted probe beam electric field for the case of a linearly polarised pump beam.

Note once again that, to first order, the polariser imperfection term, σ, representing scattering from one polarisation mode to the other does not contribute to the transmitted signal strength.

A probe beam polarisation input at $\pi/4$ to the transmission axis of the primary polariser (used as an element to select one component of the probe beam rather than using a Fresnel rhomb to rotate the input plane of polarisation) produces an transmitted electric field (to first order) given by

$$\frac{\underline{E}_{out}}{E_0} = \frac{C_{\substack{linear \\ partial}}}{\sqrt{2}} \cdot \begin{pmatrix} 1 \\ 1 \end{pmatrix} = t_1^2 \cdot \frac{e^{-\frac{\alpha_{av}}{2}\cdot\Lambda} \cdot e^{-i\cdot k_{av}\cdot\Lambda}}{\sqrt{2}} \cdot \begin{pmatrix} \zeta \\ \frac{\Delta\alpha\cdot\Lambda}{4} - \Delta\theta + \zeta + i\cdot\frac{\Delta k\cdot\Lambda}{2} \end{pmatrix} \qquad \text{Equation 44}$$

with transmitted intensity

$$\left(\frac{I_{out}}{I_0}\right)_{\substack{linear\_pump\\probe\_at\_\pi/4\_to\_primary\_polariser}} \approx \frac{t_1^4}{2}\cdot e^{-\alpha_{av}\cdot\Lambda}\cdot\left(\xi+(\zeta-\Delta\theta)^2+\frac{(\Delta\alpha\Lambda)^2}{16}+\frac{(\Delta k\Lambda)^2}{4}+(\zeta-\Delta\theta)\cdot\frac{(\Delta\alpha\Lambda)}{2}\right)$$

Equation 45

Aside from the obvious reduction in transmitted intensity by a factor of 2, the effect of using the primary polariser as a polarisation component selector is to add an extra term to the background and to change the coefficient of the term which is linear with the induced dichroism, $\Delta\alpha$.

(ii) Polariser/ Induced Circularly Dichroic-Birefringent Medium/Polariser Matrix for $\cos^2(\chi) >> \sigma^2, \Delta$

Consider the case of a circularly polarised pump beam with no birefringent optical elements between the probe beam polarisers. The pump and probe beams intersect in the YZ plane. Equations describing the action of the region of induced birefringence and dichroism in the $X_{probe}Y_{probe}$ frame of the probe beam were derived in Chapter VIII. The equivalent matrix representing this behaviour and written in the $X_{probe}Y_{probe}$ probe beam frame is

$$B_{\substack{circ\_pump\\ \cos^2(\chi)>>\sigma^2,\Delta\\ probe\_frame}} = \frac{e^{-\frac{\alpha_{av}\cdot\Lambda}{2}}\cdot e^{-i\cdot k_{av}\cdot\Lambda}}{b}\cdot\begin{pmatrix}(b\cdot\cos(\chi)+i\cdot a\cdot\sin(\chi)) & \sigma\cdot\sin(\chi)\cdot\cos(\chi)\\ \dfrac{\sin(\chi)\cdot(a^2-b^2)}{\sigma\cdot\cos(\chi)} & b\cdot\cos(\chi)-i\cdot a\cdot\sin(\chi)\end{pmatrix}$$

Equation 46

where

$$a=\left(\frac{\Delta-\sigma^2}{2}\right)\cdot\sin^2(\chi)$$

Equation 47

$$b=\sqrt{\sin^4(\chi)\cdot\left(\frac{\Delta+\sigma^2}{2}\right)^2+\cos^2(\chi)\cdot\sigma^2}$$

Equation 48

and the terms, $\Delta/2$ and σ, represent the fractional linear and circular dichroism induced by the circularly polarised pump beam respectively.

The characteristic modes of probe beam propagation for the case of a circularly polarised pump beam are elliptically polarised. For near-collinear pump and probe beams, the polarisation modes are purely circularly polarised *and the direction of polarisation of the probe beam does not affect the LPS signal*. The characteristic polarisation modes progressively tend towards linear polarisation as the angle between pump and probe beams approaches $\pi/2$. The ordinary polarisation axis for this beam intersection angle lies in the horizontal plane, $\gamma_0 = \pi/2$, and a probe beam polarisation of $3\pi/4$ to the vertical X axis is required for maximum signal.

In Chapter IV, it was shown that a probe beam polarised at $\pi/4$ (or $3\pi/4$) to the vertical X axis leads to non-zero LPS signal for all beam intersection angles and is the probe beam polarisation which produces maximum signal for orthogonal beam intersection. In order to be consistent with the probe beam polarisation required as the beam intersection angle approaches $\pi/2$, we select an optimal probe beam polarisation direction of $3\pi/4$ from the X axis for the following discussion.

We define the primary probe beam polariser transmission axis to lie at the angle, $3\pi/4 + \Delta\gamma$, to the vertical X axis, and the nearly crossed analyser transmission axis to lie at the angle, $\pi/2 + \Delta\theta$, to the transmission axis of the primary polariser. In the frame of the probe beam polarisation axes, $X_{probe}Y_{probe}$, the combined matrix describing the transmission of the probe beam through the two polarisers and the dichroic/birefringent region is written

$$C_{circ\_pump} = R\left(\frac{5\pi}{4} + \Delta\gamma + \Delta\theta\right)\cdot P_{imperfect}\cdot R\left(-\left(\frac{5\pi}{4} + \Delta\gamma + \Delta\theta\right)\right) \cdot B_{circ\_pump} \cdot R\left(\frac{3\pi}{4} + \Delta\gamma\right)\cdot P_{imperfect}\cdot R\left(-\left(3\frac{\pi}{4} + \Delta\gamma\right)\right) \quad \text{Equation 49}$$

or, as rewritten in the previous section

$$C_{circ\_pump} = R\left(\frac{3\pi}{4}\right)\cdot R\left(\frac{\pi}{2} + \Delta\gamma + \Delta\theta\right)\cdot P_{imperfect}\cdot R\left(-\left(\frac{\pi}{2} + \Delta\gamma + \Delta\theta\right)\right) \cdot R\left(-\frac{3\pi}{4}\right)\cdot B_{circ\_pump}\cdot R\left(3\frac{\pi}{4}\right) \cdot R(\Delta\gamma)\cdot P_{imperfect}\cdot R(-\Delta\gamma)\cdot R\left(-\frac{3\pi}{4}\right) \quad \text{Equation 50}$$

$$C_{circ\_pump} = R\left(\frac{3\pi}{4}\right)\cdot C_{\substack{circ\\partial}}\cdot R\left(-\frac{3\pi}{4}\right) \quad \text{Equation 51}$$

The partial matrix,

$$C_{\substack{circ\\partial}} = R\left(\frac{\pi}{2} + \Delta\gamma + \Delta\theta\right)\cdot P_{imperfect}\cdot R\left(-\left(\frac{\pi}{2} + \Delta\gamma + \Delta\theta\right)\right) \cdot R\left(-\frac{3\pi}{4}\right)\cdot B_{circ\_pump}\cdot R\left(\frac{3\pi}{4}\right)\cdot R(\Delta\gamma)\cdot P_{imperfect}\cdot R(-\Delta\gamma) \quad \text{Equation 52}$$

represents the combined action of the polarisers and induced circularly dichroic-birefringent medium in a probe beam polarisation frame with X" and Y" axes lying at $3\pi/4$ and $5\pi/4$ to the vertical X axis respectively. Once again, the partial matrix takes account of possible misalignment of the primary polariser with respect to the induced optic axis frame, $\Delta\gamma$, and mis-crossing of the analyser with the primary polariser, $\Delta\theta$.

The partial combined matrix is derived in Appendix XI under the same assumptions as for the case of a linearly polarised pump beam and is given by

$$\frac{C_{\substack{circ\\partial}}}{t_1^2 \cdot e^{-\frac{\alpha_{av}}{2}\cdot\Lambda} \cdot e^{-i\cdot k_{av}\cdot\Lambda}} = \begin{pmatrix} \zeta & 0 \\ -\Delta\theta + \phi\cdot\left(\frac{a^2-b^2}{2\cdot b\cdot\sigma\cdot\cos(\chi)} - \frac{\sigma\cdot\cos(\chi)}{2\cdot b}\right) + i\cdot\frac{a}{b}\cdot\phi & \zeta \end{pmatrix} \quad \text{Equation 53}$$

where

$$\zeta = \frac{t_2}{t_1} = \sqrt{\xi} \quad \text{Equation 54}$$

and where the term representing the scattering imperfections in an imperfection-limited polariser, which has been written as

$$\Sigma = \frac{s}{t_1} \quad \text{Equation 55}$$

to avoid confusion with the induced circular dichroism term, σ, for the case of a circularly polarised pump beam, does not occur in the first order matrix of equation [53].

Writing

$$m = \frac{a^2 - b^2 - \sigma^2\cdot\cos^2(\chi)}{2\cdot b\cdot\sigma\cdot\cos(\chi)} \quad \text{Equation 56}$$

and

$$n = \frac{a}{b} \quad \text{Equation 57}$$

so that

$$\frac{C_{\substack{circ\\partial}}}{t_1^2 \cdot e^{-\frac{\alpha_{av}}{2}\cdot\Lambda} \cdot e^{-i\cdot k_{av}\cdot\Lambda}} = \begin{pmatrix} \zeta & 0 \\ -\Delta\theta + \phi\cdot(m + i\cdot n) & \zeta \end{pmatrix} \quad \text{Equation 58}$$

or

$$\frac{C_{\substack{circ\\partial}}}{t_1^2 \cdot e^{-\frac{\alpha_{av}}{2}\cdot\Lambda} \cdot e^{-i\cdot k_{av}\cdot\Lambda}} = \begin{pmatrix} \zeta & 0 \\ -\Delta\theta + \left(\frac{\Delta k\Lambda}{2} - i\cdot\frac{\Delta\alpha\Lambda}{4}\right)\cdot(m + i\cdot n) & \zeta \end{pmatrix} \quad \text{Equation 59}$$

$$= \begin{pmatrix} \zeta & 0 \\ \left(-\Delta\theta + m\cdot\frac{\Delta k\Lambda}{2} + n\cdot\frac{\Delta\alpha\Lambda}{4}\right) + i\cdot\left(n\cdot\frac{\Delta k\Lambda}{2} - m\cdot\frac{\Delta\alpha\Lambda}{4}\right) & \zeta \end{pmatrix}$$

the LPS signal for a probe beam closely aligned to the transmission axis of the primary probe beam polariser is

$$\left(\frac{I_{out}}{I_0}\right)_{\substack{circular\_pump\\ \cos^2(\chi)>>\Delta,\sigma^2\\ probe-aligned\_to\_primary\_polariser}} \approx t_1^4\cdot e^{-\alpha_{av}\cdot\Lambda}\cdot\begin{pmatrix} \xi + \Delta\theta^2 + \left(m^2+n^2\right)\cdot\left(\left(\frac{\Delta k\Lambda}{2}\right)^2 + \left(\frac{\Delta\alpha\Lambda}{4}\right)^2\right) \\ -2\cdot\Delta\theta\cdot\left(m\cdot\frac{\Delta k\Lambda}{2} + n\cdot\frac{\Delta\alpha\Lambda}{4}\right) \end{pmatrix} \quad \text{Equation 60}$$

For near collinear angles, χ, of pump and probe beams, where $\sin^2(\chi) << 1$, the terms, a and b, reduce to

$$a = 0 \qquad \text{Equation 61}$$

$$b = \sigma \cdot \cos(\chi) \qquad \text{Equation 62}$$

and the terms, m and n, to

$$m = -1 \qquad \text{Equation 63}$$

$$n = 0 \qquad \text{Equation 64}$$

The partial combined matrix may then be written as

$$\frac{C_{\substack{\text{circ}\\ \text{near\_collinear}\\ \text{partial}}}}{t_1^2 \cdot e^{-\frac{\alpha_{av}}{2}\cdot\Lambda} \cdot e^{-i\cdot k_{av}\cdot\Lambda}} = \begin{pmatrix} \zeta & 0 \\ -\Delta\theta - \phi & \zeta \end{pmatrix} \qquad \text{Equation 65}$$

or

$$\frac{C_{\substack{\text{circ}\\ \text{near\_collinear}\\ \text{partial}}}}{t_1^2 \cdot e^{-\frac{\alpha_{av}}{2}\cdot\Lambda} \cdot e^{-i\cdot k_{av}\cdot\Lambda}} = \begin{pmatrix} \zeta & 0 \\ \left(-\Delta\theta - \frac{\Delta k}{2}\Lambda\right) + i\cdot\frac{\Delta\alpha}{4}\cdot\Lambda & \zeta \end{pmatrix} \qquad \text{Equation 66}$$

The linear and circular partial combined matrices given in equations [39] and [66] are very similar in form and produce the same first order *independence* of misalignment of the input probe beam polarisation with respect to the transmission axis of the primary polariser, $\Delta\Psi$, and of the primary probe beam polariser with respect to the induced optic axis frame, $\Delta\gamma$.

For the analyser/induced circular dichroism-birefringence/polariser combination matrix described by equation [66] assuming a near-collinear geometry and with a probe beam closely aligned to the primary probe beam polariser, the transmitted intensity is given by

$$\left(\frac{I_{out}}{I_0}\right)_{\substack{\text{circular\_pump}\\ \text{approx\_collinear}\\ \text{probe\sim aligned\_to\_primary\_polariser}}} \approx t_1^4 \cdot e^{-\alpha_{av}\cdot\Lambda} \cdot \left(\xi + \Delta\theta^2 + \frac{(\Delta\alpha\Lambda)^2}{16} + \frac{(\Delta k\Lambda)^2}{4} + \Delta\theta\cdot\Delta k\Lambda\right) \qquad \text{Equation 67}$$

This expression is once again equivalent to that of Teets *et al.* allowing for the opposite definition convention in direction of $\Delta\theta$ with the exception, once again, that the term, $i\cdot\Delta k\cdot\Lambda/2$, appears with opposite sign in the partial matrix above when compared to Teets *et al.*'s expression for the transmitted electric field for a circularly polarised pump beam. The more general transmitted intensity of equation [60] reduces to this expression in the case of near-collinear beam intersection.

The geometric dependence of the induced dichroism, $\Delta\alpha$, and difference in wavenumbers, Δk, for the two probe beam polarisation components for a circularly polarised pump beam required for calculation of equation [67] and the more generally valid expression of equation [60] is that of the

induced birefringence, Δn_{circ}. This dependence was shown in Chapter IV to have the general form (for $\cos^2(\chi) >> \sigma^2, \Delta$)

$$\left(\frac{\Delta n_{circ}(\chi)}{n_o}\right)_{0\_approx} = \sqrt{\sin^4(\chi)\cdot\left(\frac{\Delta+\sigma^2}{2}\right)^2 + \cos^2(\chi)\cdot\sigma^2} \qquad \text{Equation 68}$$

For near-collinear beams, this reduces to

$$\left(\frac{\Delta n_{circ}(\chi)}{n_0}\right)_{\substack{0\_approx \\ \chi\approx 0}} \approx \cos(\chi)\cdot\sigma \qquad \text{Equation 69}$$

(iii) Polariser/Induced Circular Dichroic-Birefringent Medium/Polariser Matrix for $\cos^2(\chi) << \sigma^2, \Delta$

As described in Chapter IV, the characteristic induced modes of propagation approach linear polarisation for near-normal intersection of pump and probe beams. The ordinary ray is polarised at $\gamma_0 = \pi/2$ to the vertical X axis, with the orthogonal extraordinary ray polarisation lying parallel to the X axis. This requires a probe beam input with polarisation lying at $3\pi/4$ to the vertical X axis to maintain a right-handed axial system with the propagation direction of the probe beam representing the Z axis.

As such, the combined matrix and partial combined matrices in this case are special cases of Case (i) for a linearly polarised pump beam with ordinary ray polarisation lying at $\gamma_0 = \pi/2$ to the vertical X axis. In the frame of the $X_{probe}Y_{probe}$ probe beam, the combined matrix is given by

$$C_{circ\_linear\_approx} = R\left(\gamma_0 + \frac{3\pi}{4}\right)\cdot C_{\substack{circ\_linear\_approx \\ partial}}\cdot R\left(-(\gamma_0 + \frac{3\pi}{4})\right) \qquad \text{Equation 70}$$

with partial combined matrix written in a probe beam *polarisation frame* with X" and Y" axes lying at $3\pi/4$ and $5\pi/4$ to the vertical X axis as

$$\frac{C_{\substack{circ\_linear\_approx \\ partial}}}{t_1^2\cdot e^{-\frac{\alpha_{av}}{2}\cdot\Lambda}\cdot e^{-ik_{av}\cdot\Lambda}} = \begin{pmatrix} \zeta & 0 \\ -\Delta\theta + i\cdot\phi & \zeta \end{pmatrix} \qquad \text{Equation 71}$$

or

$$\frac{C_{\substack{circ\_linear\_approx \\ partial}}}{t_1^2\cdot e^{-\frac{\alpha_{av}}{2}\cdot\Lambda}\cdot e^{-ik_{av}\cdot\Lambda}} = \begin{pmatrix} \zeta & 0 \\ \left(-\Delta\theta + \frac{\Delta\alpha}{4}\Lambda\right) + i\cdot\frac{\Delta k}{2}\cdot\Lambda & \zeta \end{pmatrix} \qquad \text{Equation 72}$$

Note that due to the similarity between the partial combined matrices for the cases of a linearly polarised pump beam and a (near-orthogonal intersection) circularly polarised pump beam, the LPS signal follows the form based on an induced linear dichroism

$$\left(\frac{I_{out}}{I_0}\right)_{\substack{circular\_pump \\ near\_orthogonal\_linear\_approx \\ probe\text{-}aligned\_to\_primary\_polariser}} \approx t_1^4 \cdot e^{-\alpha_{av}\Lambda} \cdot \left(\xi + \Delta\theta^2 + \frac{(\Delta\alpha\Lambda)^2}{16} + \frac{(\Delta k\Lambda)^2}{4} - \Delta\theta \cdot \frac{(\Delta\alpha\Lambda)}{2}\right) \quad \text{Equation 73}$$

rather than the form (equation [67]) associated by Teets *et al.* with a circularly polarised pump beam and near-collinear pump/probe beam intersection.

The induced birefringence, $\Delta n_{circ\_linear\_approx}$, required to calculate the geometric dependence of the induced dichroism, $\Delta\alpha$, and difference in wavenumbers, Δk, for a circularly polarised pump beam (for $\cos^2(\chi) << \sigma^2, \Delta$) was shown in Chapter IV to be

$$\frac{\Delta n_{circ\_linear\_approx}(\chi)}{n_0} \approx \sin^2(\chi) \cdot \frac{(\Delta + \sigma^2)}{2} \quad \text{Equation 74}$$

where $\Delta/2$ and σ, represent the fractional linear and circular dichroism induced by the circularly polarised pump beam respectively.

It has been shown in the previous three sections, that the matrices derived in Chapter VIII to describe the behaviour of the induced birefringence and dichroism may be combined with matrices representing imperfect probe beam polarisers to produce relatively simple combined matrices summarising the action of the combined system.

The near-collinear expression for the transmitted probe beam intensity derived by Teets *et al.* for a linearly polarised pump beam may be applied directly for all beam intersection angles. However, the LPS signal for the case of a circularly polarised pump beam follows the form derived by Teets *et al.* only for near-collinear beam intersection. For near-orthogonal beam intersection, the LPS signal for a circularly polarised pump beam follows the form characteristic of the LPS signal for a linearly polarised pump beam due to the dominance of an induced linear dichroism in both cases. For intermediate beam intersection angles, and a circularly polarised pump beam, the LPS signal follows the form of equation [60], where the geometric dependence of the induced birefringence of equation [68] must be used to determine the induced dichroism, $\Delta\alpha$, and the wavenumber difference, Δk.

The LPS signal is sensitive to misalignment from perfect crossing of primary probe beam polariser and analyser, $\Delta\theta$. The LPS signal is, however, *independent* to first order of misalignment, $\Delta\gamma$, of the primary polariser from an angle of $\pi/4$ to the induced ordinary polarisation axis, i.e. misalignment from the condition which provides maximum LPS signal strength. The detected signal is also insensitive to slight misalignment or small ellipticity of

the incident probe beam polarisation with respect to the transmission axis of the primary polariser.

The matrix representing the action of an imperfection-limited polariser has produced combined matrices equivalent to those which would be produced by the conventional Jones matrix for an imperfect polariser. The imperfection constants, s_1 and s_2, do not appear in the first order forms of the combined matrices. For imperfection levels such that the approximation, $s_1, s_2 \sim t_2$, is valid, the LPS signal is independent of the scattering terms in the imperfection-limited polariser matrix and the standard Jones matrix representing an imperfect polariser may be applied.

(iv) Polariser/Linear Induced Dichroic-Birefringent Medium/Polariser Matrix with Linearly Birefringent Inter-Polariser Optical Elements

Often the experimental arrangement demands that cell windows and optical elements are placed between the probe beam polarisers enclosing the region of induced birefringence and dichroism. If the optical elements exhibit birefringent or dichroic behaviour, either intrinsic or induced by a pressure difference on the two surfaces of the optical element, additional terms are contributed to the form of the transmitted LPS signal.

Teets *et al.* described both additional background and signal contributing terms dependent on the optical element birefringence term, b, in the LPS signal strength. However, if the optical element birefringence is linear, the orientation of the ordinary and extraordinary axes of the element with respect to the probe beam polarisation should affect the LPS signal strength. A birefringent optical element with ordinary or extraordinary axis roughly aligned to the probe beam polarisation direction will see minimal contributions due to the element birefringence as the probe beam will be transmitted primarily along one characteristic polarisation mode. Birefringent contributions are maximised if the probe beam polarisation direction lies equally between the ordinary and extraordinary polarisation axes. This dependence is not noted in the theory of Teets *et al.*

Appendix XII derives a combined matrix for an analyser/birefringent element/induced linearly dichroic and birefringent medium/birefringent element/polariser. The ordinary axes of the two birefringent elements, initial, i, and final, f, are defined to lie at the angles, $\pi/4 + a_j$,(j = i, f), to the induced ordinary polarisation axis.

The combined matrix is written in the X"Y" frame of the probe beam as

$$C_{linear+linearly\_birefringent\_optical\_elements} = R\left(\gamma_0 + \frac{3\pi}{4} + \Delta\gamma + \Delta\theta\right) \cdot P_{imperfect} \cdot R\left(-\left(\gamma_0 + \frac{3\pi}{4} + \Delta\gamma + \Delta\theta\right)\right)$$
$$\cdot R\left(\gamma_0 + \frac{\pi}{4} + a_f\right) \cdot B_f \cdot R\left(-\left(\gamma_0 + \frac{\pi}{4} + a_f\right)\right)$$
$$\cdot R(\gamma_0) \cdot B_{linear\_pump} \cdot R(-\gamma_0)$$
$$\cdot R\left(\gamma_0 + \frac{\pi}{4} + a_i\right) \cdot B_i \cdot R\left(-\left(\gamma_0 + \frac{\pi}{4} + a_i\right)\right)$$
$$\cdot R\left(\gamma_0 + \frac{\pi}{4} + \Delta\gamma\right) \cdot P_{imperfect} \cdot R\left(-\left(\gamma_0 + \frac{\pi}{4} + \Delta\gamma\right)\right)$$

Equation 75

Rearranging the rotation matrices, this becomes

$$C_{linear+linearly\_birefringent\_optical\_elements} = R\left(\gamma_0 + \frac{3\pi}{4} + \Delta\gamma + \Delta\theta\right) \cdot P_{imperfect} \cdot R\left(-\left(\frac{3\pi}{4} + \Delta\gamma + \Delta\theta\right)\right)$$
$$\cdot R\left(\frac{\pi}{4} + a_f\right) \cdot B_f \cdot R\left(-\left(\frac{\pi}{4} + a_f\right)\right)$$
$$\cdot B_{linear\_pump}$$
$$\cdot R\left(\frac{\pi}{4} + a_i\right) \cdot B_i \cdot R\left(-\left(\frac{\pi}{4} + a_i\right)\right)$$
$$\cdot R\left(\frac{\pi}{4} + \Delta\gamma\right) \cdot P_{imperfect} \cdot R\left(-\left(\gamma_0 + \frac{\pi}{4} + \Delta\gamma\right)\right)$$

Equation 76

or, finally,

$$C_{linear+linearly\_birefringent\_optical\_elements} = R\left(\gamma_0 + \frac{\pi}{4}\right) \cdot \left[R\left(\frac{\pi}{2} + \Delta\gamma + \Delta\theta\right) \cdot P_{imperfect} \cdot R\left(-\left(\frac{\pi}{2} + \Delta\gamma + \Delta\theta\right)\right)\right]$$
$$\cdot \left[R(a_f) \cdot B_f \cdot R(-a_f)\right] \cdot \left[R\left(-\frac{\pi}{4_i}\right) \cdot B_{linear\_pump} \cdot R\left(\frac{\pi}{4_i}\right)\right] \cdot \left[R(a_i) \cdot B_i \cdot R(-a_i)\right]$$
$$\cdot \left[R(\Delta\gamma) \cdot P_{imperfect} \cdot R(-\Delta\gamma)\right] \cdot R\left(-\left(\gamma_0 + \frac{\pi}{4}\right)\right)$$
$$= R\left(\gamma_0 + \frac{\pi}{4}\right) \cdot C_{\substack{linear+linearly\_birefringent\_optical\_elements \\ partial}} \cdot R\left(-(\gamma_0 + \frac{\pi}{4})\right)$$

Equation 77

For convenience, the standard form of the linearly birefringent matrix is expanded in a linear approximation as

$$B_j = B0_j \cdot \begin{pmatrix} e^{ib_j} & 0 \\ 0 & e^{-ib_j} \end{pmatrix} = B0_j \cdot \begin{pmatrix} 1+ib_j & 0 \\ 0 & 1-ib_j \end{pmatrix}$$
$$= B0_j \cdot \left(\begin{pmatrix} 1 & 0 \\ 0 & 1 \end{pmatrix} - \begin{pmatrix} -1 & 0 \\ 0 & 1 \end{pmatrix} \cdot ib_j\right)$$

Equation 78

where it is assumed that the birefringent term, b_j, is small. **Note that, as defined, the phase difference introduced between the two probe beam components is $2 \cdot b_j$.**

The combined partial matrix, $C_{\substack{linear+linearly\_birefringent\_optical\_elements \\ partial}}$, is derived in Appendix XII and written

$$\frac{C_{\substack{linear+linearly\_birefringent\_optical\_elements \\ partial}}}{t_1^2 \cdot B0_i \cdot B0_f \cdot e^{-\frac{\alpha_{av}}{2}\cdot\Lambda} \cdot e^{-i\cdot k_{av}\cdot\Lambda}} = \begin{pmatrix} \zeta & 0 \\ \frac{\Delta\alpha\cdot\Lambda}{4} - \Delta\theta + i\cdot\left(\frac{\Delta k\cdot\Lambda}{2} + b_f\cdot\sin(2a_f) + b_i\cdot\sin(2a_i)\right) & \zeta \end{pmatrix}$$

Equation 79

This form consists of the partial matrix for the case of no birefringent elements between the polarisers with an additional term for each birefringent element. Each additional term is the product of the birefringence term, b_j, and the sine of twice the angle, a_j, of deviation of the birefringent element's ordinary polarisation direction from $\gamma_0 = \pi/4$, where γ_0 is the alignment of the induced ordinary polarisation axis of the region of induced dichroism and birefringence from the vertical X axis. **The matrix indicates that a linearly birefringent inter-polariser optical element may be rotated to minimise the birefringent contribution to the transmitted intensity.**

(v) Polariser/Circular Induced Dichroic-Birefringent Medium/Polariser Matrix with Linearly Birefringent Inter-Polariser Optical Elements

It is reasonable to expect that the combined matrix in the case of a circular induced birefringence and dichroism should have a similar dependence on inter-polariser linearly birefringent optical elements to that noted in the case of a linear pump beam.

The ordinary and extraordinary modes of propagation, in case of a circularly polarised pump beam, are elliptically polarised. As described in Chapter IV, the transmitted intensity is maximised for an input probe beam polarisation alignment of $\pi/4$, $3\pi/4$ ... to the vertical X axis. For convenience in derivation, the ordinary axes of the birefringent inter-polariser elements are defined to lie at the angles, $\pi/4 + a_j$, (j = i,f) to the vertical X axis in the combined matrix. The result is then interpreted in terms of axes lying at the angle, $3\pi/4 + a_j$, (j = i,f) to the vertical X axis by replacing the term, a_j, by the term, $a\_para_j = \pi/2 + a_j$. The combined matrix is written as

$$C_{circ+linearly\_birefringent\_optical\_elements} = R\left(\frac{5\pi}{4} + \Delta\gamma + \Delta\theta\right) \cdot P_{imperfect} \cdot R\left(-\left(\frac{5\pi}{4} + \Delta\gamma + \Delta\theta\right)\right)$$
$$\cdot R\left(\frac{\pi}{4} + a_f\right) \cdot B_f \cdot R\left(-\left(\frac{\pi}{4} + a_f\right)\right)$$
$$\cdot B_{circ\_pump} \cdot \qquad \text{Equation 80}$$
$$\cdot R\left(\frac{\pi}{4} + a_i\right) \cdot B_i \cdot R\left(-\left(\frac{\pi}{4} + a_i\right)\right)$$
$$\cdot R\left(\frac{3\pi}{4} + \Delta\gamma\right) \cdot P_{imperfect} \cdot R\left(-\left(3\frac{\pi}{4} + \Delta\gamma\right)\right)$$

or,

$$C_{circ+linearly\_birefringent\_optical\_elements} = R\left(3\frac{\pi}{4}\right) \cdot R\left(\frac{\pi}{2} + \Delta\gamma + \Delta\theta\right) \cdot P_{imperfect} \cdot R\left(-\left(\frac{\pi}{2} + \Delta\gamma + \Delta\theta\right)\right)$$
$$\cdot R\left(3\frac{\pi}{4}\right) \cdot \left[R\left(\frac{\pi}{4} + a_f\right) \cdot B_f \cdot R\left(-\left(\frac{\pi}{4} + a_f\right)\right)\right]$$
$$\cdot B_{circ\_pump} \cdot$$
$$\cdot \left[R\left(\frac{\pi}{4} + a_i\right) \cdot B_i \cdot R\left(-\left(\frac{\pi}{4} + a_i\right)\right)\right] \cdot R\left(-3\frac{\pi}{4}\right) \qquad \text{Equation 81}$$
$$\cdot R(\Delta\gamma) \cdot P_{imperfect} \cdot R(-\Delta\gamma) \cdot R\left(-3\frac{\pi}{4}\right)$$
$$= R\left(3\frac{\pi}{4}\right) \cdot C_{\substack{circ+linearly\_birefringent\_optical\_elements \\ partial}} \cdot R\left(-3\frac{\pi}{4}\right)$$

The partial matrix is written in the X"Y" polarisation frame with the ordinary, or X", axis lying at $3\pi/4$ to the vertical X axis and is derived in Appendix XIII as

$$\frac{C_{\substack{circ+linearly\_birefringent\_optical\_elements\\partial}}}{t_1^2 \cdot B0_i \cdot B0_f \cdot e^{-\frac{\alpha_{av}}{2}\cdot\Lambda} \cdot e^{-i\cdot k_{av}\cdot\Lambda}} = \frac{C_{\substack{circ\\partial}}}{t_1^2 \cdot B0_i \cdot B0_f \cdot e^{-\frac{\alpha_{av}}{2}\cdot\Lambda} \cdot e^{-i\cdot k_{av}\cdot\Lambda}} - \begin{pmatrix} 0 & 0 \\ i\cdot(b_f\cdot\sin(2a_f)+b_i\cdot\sin(2a_i)) & 0 \end{pmatrix}$$

Equation 82

or in terms of the angle, a_para_j,

$$\frac{C_{\substack{circ+linearly\_birefringent\_optical\_elements\\partial}}}{t_1^2 \cdot B0_i \cdot B0_f \cdot e^{-\frac{\alpha_{av}}{2}\cdot\Lambda} \cdot e^{-i\cdot k_{av}\cdot\Lambda}} = \frac{C_{\substack{circ\\partial}}}{t_1^2 \cdot B0_i \cdot B0_f \cdot e^{-\frac{\alpha_{av}}{2}\cdot\Lambda} \cdot e^{-i\cdot k_{av}\cdot\Lambda}} + \begin{pmatrix} 0 & 0 \\ i\cdot(b_f\cdot\sin(2a\_para_f)+b_i\cdot\sin(2a\_para_i)) & 0 \end{pmatrix}$$

Equation 83

The second matrix of the right-hand-side of equation [83] can be seen in the equivalent linear pump beam equation, and represents the contribution of the inter-polariser birefringent elements. Once again, it is apparent that the birefringent terms may be minimised by rotation of the inter-polariser elements so that the probe beam polarisation lies approximately along the ordinary or extraordinary axes of the birefringent element.

(vi) Polariser/Linear or Circular Induced Dichroic-Birefringent Medium/Polariser Matrix with Circularly Birefringent Inter-Polariser Optical Elements

The matrix component representing the linearly birefringent optical elements in sections (iv) and (v) show a dependence on the angular alignment of the ordinary and extraordinary axes of the element. It is fairly obvious that there will be no such angular dependence for circularly birefringent optical elements. The derivations of the partial combined matrices in this section follow those of cases (iv) and (v) with the birefringent optical element matrix being independent of rotation matrices, which hence are not required in the combined matrices.

The matrix describing the circularly birefringent optical elements is written as

$$B_{circ} = B0_{circ}\cdot\begin{pmatrix}\cos(b) & \sin(b)\\ -\sin(b) & \cos(b)\end{pmatrix} \approx B0_{circ}\cdot\left(\begin{pmatrix}1 & 0\\ 0 & 1\end{pmatrix} + b\cdot\begin{pmatrix}0 & 1\\ -1 & 0\end{pmatrix}\right)$$

Equation 84

where, once again, the introduced phase difference between the probe beam components is 2b.

Appendices XIV and XV calculate the combined matrices for circularly birefringent inter-polariser optical elements enclosing the region of induced birefringence and dichroism in the probe beam path. The partial combined matrices are

$$\frac{C_{\substack{linear+circularly\_birefringent\_optical\_elements \\ partial}}}{t_1^2 \cdot B0_i \cdot B0_f \cdot e^{-\frac{\alpha_{av}}{2}\Lambda} \cdot e^{-ik_{av}\cdot\Lambda}} = \frac{C_{\substack{linear \\ partial}}}{t_1^2 \cdot B0_i \cdot B0_f \cdot e^{-\frac{\alpha_{av}}{2}\Lambda} \cdot e^{-ik_{av}\cdot\Lambda}} + \begin{pmatrix} 0 & 0 \\ (b_f + b_i) & 0 \end{pmatrix} \qquad \text{Equation 85}$$

for the case of a linearly polarised pump beam, and

$$\frac{C_{\substack{circ+circularly\_birefringent\_optical\_elements \\ partial}}}{t_1^2 \cdot B0_i \cdot B0_f \cdot e^{-\frac{\alpha_{av}}{2}\Lambda} \cdot e^{-ik_{av}\cdot\Lambda}} = \frac{C_{\substack{circ \\ partial}}}{t_1^2 \cdot B0_i \cdot B0_f \cdot e^{-\frac{\alpha_{av}}{2}\Lambda} \cdot e^{-ik_{av}\cdot\Lambda}} + \begin{pmatrix} 0 & 0 \\ (b_f + b_i) & 0 \end{pmatrix} \qquad \text{Equation 86}$$

for the case of a circularly polarised pump beam. It can be seen that the contribution of the circularly birefringent inter-polariser optical elements is represented by the second matrix on the right-hand sides of equations [69] and [70]. As expected, the birefringent terms may not be minimised by rotation of the optical elements.

We have developed combined matrices representing the action of an analyser/region of induced birefringence and dichroism/polariser in the probe beam path. The matrices are simple and may be used to easily investigate the dependence of the LPS signal on input probe beam polarisation states.

It has been shown that the transmitted intensities calculated using these matrices reduce to those of Teets *et al.* (aside from the sign associated with the term, $i\Delta k\Lambda/2$) for near-collinear beam intersection and input probe beam polarisations closely aligned to the transmission axis of the primary probe beam polariser. The LPS signal calculated by Teets *et al.* for the case of a linearly polarised pump beam is applicable for all beam intersection angles. However, the LPS signal in the case of a circularly polarised pump beam takes the more general form shown in equation [60] for intermediate beam intersection angles ($\cos^2(\chi) >> \sigma^2, \Delta$) and has the form conventionally associated with a linearly polarised pump beam for orthogonal beam intersection.

The intensity contributions to the LPS signal strength due to linearly birefringent inter-polariser optical elements may be minimised by rotation of the optical elements around the axis defined by the direction of propagation of the probe beam. The birefringent intensity terms produced by circularly birefringent inter-polariser optical elements cannot be minimised by rotation.

It should also be noted that the polariser model above predicts that the polarisation of the extinction background term, ξ, of the LPS signal is normal to the polarisation of the primary LPS signal components. The extinction background term is polarised

parallel to the extinction axis of the analyser, while the LPS signal terms are polarised parallel to the transmission axis of the analyser. This indicates that, for the case of a significant probe beam extinction background, a second polariser placed after and aligned with transmission axis parallel to the probe beam analyser will further decrease the extinction background level with respect to the LPS signal components. The preferred configuration to decrease a probe beam extinction background would then be a single polariser used to polarise the probe beam, and two polarisers in series with aligned transmission axes to act as probe beam analyser. It is also optimal to use a rhomb to rotate the input probe beam polarisation so that its polarisation direction lies parallel to the transmission axis of the primary polariser.

The polarisation signal is most sensitive to mis-crossing of the probe beam polarisers, $\Delta\theta$. The combined matrices are independent, to first order, of slight misalignment of the input probe beam polarisation with respect to the transmission axis of the primary polariser. In addition, the matrices are independent of misalignment of the primary probe beam polariser from an angle of $\pi/4$ to the induced ordinary axis, an orientation which produces maximum LPS signal.

Nomenclature

Chapter I: Introduction to Polarisation Spectroscopy.

Conventions:

Complex numbers are written as x + i y.

Subscripts:

circ with respect to circular polarisation.

corr refers to a correction which accounts for the contributions of the pumped upper state population to the induced dichroism in the linear regime of optical pumping.

crossed_polarisers for the case of perfectly crossed polarisers.

lin with respect to linear polarisation.

lower with respect to the lower state of the transition.

probe with respect to the probe beam.

pump with respect to the pump beam.

unconfined_combustion for the case of unconfined combustion where no birefringent inter-polariser optical elements are required in the probe beam path.

upper with respect to the lower state of the transition.

x with respect to the X-axis, which lies in the horizontal intersection plane of pump and probe beams.

y with respect to the Y-axis, which correspond to the axis along which the pump and probe beams propagate.

z with respect to the Z-axis, which is vertical.

- with respect to right circular polarisation.

+ with respect to left circular polarisation.

Variables and Constants:

Roman Alphabet

b birefringence of optical elements in the probe beam path between the probe beam polariser pair.

c speed of light.

$C_{J,J''}$ non-rotational (e.g. electronic/vibrational) component of the absorption cross-section for the probe transition (J,M) to (J",M").

D(x) dispersive lineshape.

E_0 probe beam electric field strength incident on the input polariser of the probe beam polariser pair.

$E_{probe\_transmitted}$ probe beam electric field strength transmitted through the nearly crossed probe beam polarisers.

$\hbar$ Planck's constant divided by 2π.

i_{probe} polarisation state of the probe beam component.

i_{pump} polarisation state of the pump beam.

$I_{probe\_transmitted}$ intensity of the probe beam transmitted through the probe beam analyser.

J rotational quantum number of the shared lower state of the pump and probe transitions.

J' rotational quantum number of the upper state of the pump transition.

J" rotational quantum number of the upper state of the probe transition.

L interaction length of pump and probe beams measured along the probe beam path.

L(x) Lorentzian lineshape.

M Zeeman quantum number for the state J.

M' Zeeman quantum number for the state J'.

M" Zeeman quantum number for the state J".

n refractive index. If a subscript is used, it denotes the appropriate polarisation state.

N_J Boltzmann equilibrium population of the lower state, J, shared by both pump and probe transitions.

N_{JM} number density of the lower state, (J,M), shared by both pump and probe transition.

$N_{J'M'}$ number density of the upper state, (J',M'), of the pump transitions.

N_{JM_lower} number density of the lower state, (J,M), of the pumped transition.

N_{JM_upper} number density of the upper state, (J',M'), of the pumped transition.

P transition $J_{upper} = J_{lower} - 1$ ($\Delta J = -1$)

Q transition $J_{upper} = J_{lower}$ ($\Delta J = 0$)

R transition $J_{upper} = J_{lower} + 1$ ($\Delta J = +1$)

$r_{Teets\ et\ al}$ relaxation ratio ranging in value between -1 and 1, defined as

$$r_{Teets\_et\_al} = \frac{\gamma - \gamma'}{\gamma + \gamma'}.$$

S_{pulsed} saturation parameter for a pulsed laser system.

S_{cw} saturation parameter for a cw laser system.

t laser pulse length.

x relative detuning of the probe beam from linecentre for the probed transition (J,M).

Greek Alphabet

α absorption coefficient. If a subscript is used, it denotes the appropriate polarisation state.

$\alpha^{i_{probe}}_{J,J'',M,M''}$ absorption coefficient for the probe transition (J,M) to (J",M") for the probe beam polarisation component, i_{probe}.

$\alpha^{i_{probe}}_{J,J''}$ total absorption coefficient for the probed transition from the lower state, J, to the upper state, J", for the probe polarisation component, i_{probe}.

χ pump/probe beam intersection angle.

$\Delta\alpha$ optically induced dichroism at the probe beam angular frequency.

$\Delta\alpha_0$ linecentre induced dichroism for the probe beam.

$\Delta\alpha^{i,i'}_{J,J''}$ induced dichroism for the probed transition from the lower state, J, to the upper state, J", for the two orthogonal polarisation states, i and i', of the probe beam.

Δn optically induced birefringence at the probe beam angular frequency.

γ linewidth of a Lorentzian dichroism, $\Delta\alpha$.

γ lifetime of the lower, J, state of the pump transition.

γ' lifetime of the upper, J', state of the pump transition.

θ a small angle of deviation from perfectly crossed probe beam polarisers. Teets *et al* use the direction convention that the angle between primary probe beam polariser and analyser is $\pi/2 - \theta$.

$\sigma_{J,J''}$ total absorption cross-section for the probe transition divided by the factor 2J +1.

$\sigma_{J,J'}$ total absorption cross-section for the pump transition divided by the factor 2J +1.

$\sigma^{i_{probe}}_{J,J'',M,M''}$ rotational/Zeeman component of the absorption cross-section for the probe transition (J,M) to (J",M"), for the probe polarisation component, i_{probe}.

$\sigma^{i_{pump}}_{J,J',M,M'}$ rotational/Zeeman component of the absorption cross-section for the pump transition (J,M) to (J',M'), for the probe polarisation component, i_{pump}.

ω angular frequency of the probe beam.

ω_0 angular frequency of the probe beam at linecentre.

ω_{pump} angular frequency of the pump radiation.

ξ the finite extinction ratio of the probe beam polarisers.

$\zeta_{J,J',J''}$ factor a function of only the rotational quantum numbers for the pump and probe transitions defined by Teets, Kowalski, Hill, Carlson and Hansch as

$$\zeta_{J,J',J''} = (2J+1) \cdot \frac{\sum_{M} \sigma^{i_{pump}}_{J,J',M,M'} \cdot (\sigma^{i}_{J,J'',M,M''} - \sigma^{i'}_{J,J'',M,M''})}{\sum_{M} \sigma^{i_{pump}}_{J,J',M,M'} \cdot \sum_{M} \sigma^{i_{probe}}_{J,J'',M,M''}}$$

$\zeta_{J,J',J''\_general}$ factor — a $\zeta_{J,J',J''}$ factor defined by Teets, Kowalski, Hill, Carlson and Hansch and stated to be applicable to cw or pulsed laser application.

ζ_{J,J',J''_corr} factor — a $\zeta_{J,J',J''}$ factor valid in the linear regime of optical pumping in an experiment where spontaneous emissions and collisional population transfer between the Zeeman states or the upper and lower states of the pump/probe transitions is negligible. The corr subscript refers to a correction which accounts for the contributions of the pumped upper state population to the induced dichroism.

$Z_{J,J',J''}$ factor — a function of only the rotational quantum numbers for the pump and probe transitions which combines all rotational dependence of the induced dichroism aside from the rotational dependence of the Boltzmann equilibrium populations and defined in this thesis as

$$Z_{J,J',J''} = \frac{\sigma_{J,J'} \cdot \sigma_{J,J''} \cdot \zeta_{J,J',J''}}{C_{J,J'} \cdot C_{J,J''}}$$

$Z_{J,J',J''\_general}$ factor — $Z_{J,J',J''}$ factors relating to the $\zeta_{J,J',J''\_general}$ factors which are stated to be applicable to cw or pulsed laser application.

Z_{J,J',J''_corr} factor — $Z_{J,J',J''}$ factors relating to the ζ_{J,J',J''_corr} factors valid in the linear regime of optical pumping in an experiment where spontaneous emissions and collisional population transfer between the Zeeman states or the upper and lower states of the pump/probe transitions is negligible. The corr subscript refers to a correction which accounts for the contributions of the pumped upper state population to the induced dichroism.

Chapter II: Uniaxial Gas Model of Polarisation Spectroscopy: Linearly Polarised Pump Beam

Conventions:

In notation, an underline has been used to represent a vector and an overscore a unit vector.

Complex numbers are written as x + i y.

Subscripts:

e with respect to the extraordinary polarisation mode.

lin with respect to a linearly polarised pump beam.

o with respect to the ordinary polarisation mode.

probe with respect to the probe beam.

pump with respect to the pump beam.

x with respect to the x axis of the principal axis system of the gas.

y with respect to the y axis of the principal axis system of the gas.

z with respect to the z axis of the principal axis system of the gas.

|| with respect to the polarisation component of the probe beam which is parallel to the pump beam polarisation direction.

⊥ with respect to the polarisation component of the probe beam which is perpendicular to the pump beam polarisation direction.

Variables and Constants:

Roman Alphabet

B magnetic flux density.

c speed of light.

C_1 ratio of the elements of the third-order tensor of non-linear susceptibility, used in the expression for LPS signal strength obtained by Lavrinenko and Gancheryonok, and defined as

$$C_1 = \frac{\chi_{1122}}{\chi_{1221}}$$

C_2 ratio of the elements of the third-order tensor of non-linear susceptibility, used in the expression for LPS signal strength obtained by Lavrinenko and Gancheryonok, and defined as

$$C_2 = \frac{\chi_{1212}}{\chi_{1221}}$$

D magnitude of the displacement vector.

E electric field strength.

E_0 magnitude of the electric field of the probe beam incident on the primary probe beam polariser.

$\hat{\underline{E}}_{extraordinary}$ unit vector of the probe beam component normal to the ordinary axis.

$\hat{\underline{E}}_{extraordinary\_approx}$

unit vector electric field for extraordinary probe beam component based on the assumption the induced birefringence is small, $n_e \sim n_o$.

$\hat{\underline{E}}_{optic\_axis}$ unit vector of the pump beam electric field which represents the direction of the optic axis.

$\hat{\underline{E}}_{ordinary}$ unit vector of the probe beam component lying parallel to the ordinary axis.

$\underline{E}_{probe}$ electric vector of the probe beam incident on the primary probe beam polariser and assumed to be aligned to the transmission axis of the primary polariser. The polariser is assumed to be perfect.

$\underline{E}_{\substack{probe \\ transmitted}}(\Lambda)$

electric vector of the probe beam after transmission a distance, $\Lambda(\chi)$, through the region of induced dichroism and birefringence.

$\underline{E}_{\substack{probe \\ transmitted\_through\_analyser}}(\Lambda)$

electric vector of the probe beam transmitted through the probe beam analyser after passing after passing a distance, $\Lambda(\chi)$, through the region of induced dichroism and birefringence.

$\hat{\underline{E}}_{pump}$ unit electric vector for the pump beam.

$\hat{\underline{E}}_{pump\_\perp}$ unit pump vector in the electric field plane of the pump beam and perpendicular to the pump beam electric vector.

f function of the projection of the probe beam electric vector onto the ordinary and extraordinary unit vectors, defined as

$$f = \left(\underline{E}_{probe} \cdot \hat{\underline{E}}_{ordinary}\right) \cdot \left(\hat{\underline{E}}_{ordinary} \cdot \hat{\underline{R}}_{analyser}\right)$$

$F_{lin}(\gamma,\kappa,\chi)$ geometric dependence (aside from that implicit in the induced birefringence) of the LPS signal strength for perfectly crossed polarisers and a linearly polarised pump beam.

$$F_{lin}(\gamma,\kappa,\chi) = \frac{\left(\sin(2\gamma)\cdot\left(\cos^2(\kappa) - \sin^2(\kappa)\cdot\cos^2(\chi)\right) - \cos(2\gamma)\cdot\sin(2\kappa)\cdot\cos(\chi)\right)^2}{\sin^2(\chi)\cdot\left(1-\sin^2(\kappa)\cdot\sin^2(\chi)\right)^2}$$

g function of the projection of the probe beam electric vector onto the ordinary and extraordinary unit vectors, defined as

$$g = \left(\underline{E}_{probe} \cdot \hat{\underline{E}}_{extraordinary}\right) \cdot \left(\hat{\underline{E}}_{extraordinary} \cdot \hat{\underline{R}}_{analyser}\right)$$

$G_{lin}(\kappa,\chi)$ function representing the geometric dependence of the induced birefringence.

$$G_{lin}(\kappa,\chi) = 1 - \sin^2(\kappa) \cdot \sin^2(\chi)$$

$H_{lin}(\gamma,\kappa,\chi)$ function representing the combined geometric dependence of the factors, $F_{lin}(\gamma,\kappa,\chi)$ and $G_{lin}(\kappa,\chi)^2$ in the LPS signal strength for perfectly crossed polarisers and a linearly polarised pump beam.

$$H_{lin}(\gamma,\kappa,\chi) = F_{lin}(\gamma,\kappa,\chi) \cdot G_{lin}(\kappa,\chi)^2 = \frac{\left(\sin(2\gamma) \cdot \left(\cos^2(\kappa) - \sin^2(\kappa) \cdot \cos^2(\chi)\right) - \cos(2\gamma) \cdot \sin(2\kappa) \cdot \cos(\chi)\right)^2}{\sin^2(\chi) \cdot (1 - \sin^2(\kappa) \cdot \sin^2(\chi))}$$

H magnetic field strength.

I_0 intensity of the probe beam incident on the primary probe beam polariser.

$I_{L\&G}$ expression for the LPS signal strength derived by Lavrinenko and Gancheryonok.

$I_{probe\ transmitted\_through\_analyser}(\Lambda)$

intensity of the probe beam transmitted through the probe beam analyser after passing a distance, $\Lambda(\chi)$, through the region of induced dichroism and birefringence.

j current density.

k magnitude of the wavevector.

k_0 magnitude of the free space wavevector for the probe beam.

k_{av} average of the magnitudes of the ordinary and extraordinary wavevectors.

k_e magnitude of the wavevector for the probe beam component polarised parallel to the extraordinary axis.

k_o magnitude of the wavevector for the probe beam component polarised parallel to the ordinary axis.

$k_{\parallel}$ magnitude of the wavevector for the probe beam component polarised parallel to the pump beam polarisation.

$k_{\perp}$ magnitude of the wavevector for the probe beam component polarised perpendicular to the pump beam polarisation.

$\underline{k}$ wavevector.

$\hat{\underline{k}}_{probe}$ unit vector of the wavevector for the probe beam.

K constant used in the expression for LPS signal strength obtained by Lavrinenko and Gancheryonok, and defined as

$$K = \frac{9}{16}\left(\frac{\omega_{probe}}{c \cdot n_{probe}}\right)^2 |\chi_{1221}|^2 |E_{probe}|^2 |E_{pump}|^4$$

l width of the pumping beam, used in the expression for LPS signal strength obtained by Lavrinenko and Gancheryonok.

$L(\chi)$ probe beam path length in the region of induced dichroism and birefringence, given by

$$L(\chi) = \frac{W}{|\sin(\chi)|}$$

n refractive index.

n_{av} average of ordinary and extraordinary refractive indices.

n_e extraordinary refractive index.

n_o ordinary refractive index.

n_{probe} refractive index of the medium at the probe frequency, ω_{probe}, used in the expression for LPS signal strength obtained by Lavrinenko and Gancheryonok.

$\underline{P}_{\parallel}(\chi,\gamma,\kappa)$ component of the probe beam electric field which is parallel to the pump beam polarisation.

$\underline{P}_{ordinary}$ component of the probe beam electric field which is parallel to the ordinary axis, (i.e. the component polarised parallel to the Y' principal axis).

$\underline{Q}_{\perp}(\chi,\gamma,\kappa)$ component of the probe beam electric field which is perpendicular to the pump beam polarisation.

$\underline{Q}_{extraordinary}$ component of the probe beam electric field which is parallel to the extraordinary axis, (i.e. lying in the X'Z' principal plane).

r position.

$\hat{\underline{R}}_{analyser}$ unit vector parallel to the transmission axis of the probe beam analyser.

t time.

W thickness of the pump beam.

x relative detuning of the probe beam from linecentre for the probed transition.

X x axis of the probe beam axis system, which is normal to the beam intersection plane.

X' x axis of the principal axis system.

Y y axis of the probe beam axis system, which lies in the beam intersection plane and normal to the direction of propagation of the probe beam.

Y' x axis of the principal axis system.

Z z axis of the probe beam axis system, which corresponds to the direction of propagation of the probe beam.

Z' z axis of the principal axis system, which corresponds to the direction of the optic axis.

Greek Alphabet:

α_{av} average of ordinary and extraordinary absorption coefficients.

α_e absorption coefficient for the probe beam component polarised parallel to the extraordinary axis.

α_o absorption coefficient for the probe beam component polarised parallel to the ordinary axis.

$\alpha_{||}$ absorption coefficient for the probe beam component polarised parallel to the pump beam polarisation.

$\alpha_{\perp}$ absorption coefficient for the probe beam component polarised perpendicular to the pump beam polarisation.

χ pump/probe beam angle of intersection measured from the direction of travel of the probe beam.

χ_{ijkl} elements of the third-order tensor of non-linear susceptibility, used in the expression for LPS signal strength obtained by Lavrinenko and Gancheryonok.

Δk small difference in the magnitudes of the ordinary and extraordinary wavevectors.

Δn small induced birefringence.

Δn_0 linecentre induced birefringence.

$\Delta\alpha$ small induced dichroism.

$\Delta\alpha_0$ linecentre induced dichroism.

ε susceptibility tensor relating the electric vector to the displacement vector.

γ angle of the probe beam polarisation from the normal to the pump/probe beam intersection plane.

η angle of the ordinary axis direction from the normal to the beam intersection plane.

φ angle of the probe beam propagation with respect to the induced optic axis.

κ angle of the pump beam polarisation axis from the normal to the pump/probe beam intersection plane.

Λ path length of the probe beam through the region of induced birefringence and dichroism.

μ magnetic susceptibility.

ρ charge density.

ω angular frequency.

ω_0 linecentre angular frequency.

ω_{probe} probe beam angular frequency, used in the expression for LPS signal strength obtained by Lavrinenko and Gancheryonok.

Chapter III: Orthogonal Imaging for a Linearly Polarised Pump Beam.

Conventions:

Complex numbers are written as x + i y.

Subscripts:

i and i' orthogonal polarisation states of the two probe beam components which experience the pump induced dichroism.

Variables and Constants:

Roman Alphabet

B probe beam extinction background due to the finite extinction ratio of the probe beam polarisers.

d distance which represents the increase in the distance measured along the axis lying in the beam intersection plane in the elliptical beam intersection volume which is imaged by each pixel, and defined as

$$d = \frac{W}{|\tan(\chi)|}$$

$f_{detector}$ collection efficiency of the detection system.

H probe beam path length through the combustion region excluding the interaction volume of pump and probe beams.

$H_{lin}(\gamma,\kappa,\chi)$ function representing the combined geometric dependence of the LPS signal strength for perfectly crossed polarisers and a linearly polarised pump beam and defined in Chapter II.

I_0 probe beam intensity incident on the primary probe beam polariser.

I_{probe} LPS signal (including probe extinction background).

$I_{probe\_blocked\_pump}$ probe extinction background (obtained by blocking to the pump beam).

$I_{\substack{probe\_transmitted \\ circ/linear\_pump \\ crossed\_polarisers \\ unconfined\_combustion}}$

LPS signal (including the probe beam extinction background) obtained for either a circularly or linearly polarised pump beam for the case of crossed polarisers and unconfined combustion where there are no birefringent optical elements in the probe beam path between the probe beam polarisers.

J shared lower rotational state of the pump and probe transitions.

J' upper rotational state of the pumped transition.

J" upper rotational state of the probe transition.

L interaction length of pump and probe beams measured along the probe beam path.

Mode 1 a largely uncorrected image (corrected for the non-zero background of the ICCD alone).

Mode 2 image representing the ratio, S/B, of the pure signal, S, (free of probe beam extinction components) to the background (with flame), B. The ratio is proportional to the square of the induced dichroism.

p pixel resolution of the stretched image with respect to the axis lying in the beam intersection plane, and ignoring any magnification factors due to imaging systems placed after the probe beam analyser, defined as

$$p = \frac{p_{90°}}{|\sin(\chi)|}$$

$p_{90°}$ pixel resolution in an orthogonal beam intersection geometry, with respect to the axis lying in the beam intersection plane.

q pump sheet thickness resolution measured along the direction of propagation of the probe beam, given by

$$q = \frac{W}{|\sin(\chi)|}$$

R_{signal} ratio of the LPS signal (including probe extinction background), I_{probe}, to the probe extinction background (obtained by blocking to the pump beam), $I_{probe\_blocked\_pump}$, and related to the pure LPS signal, S, to probe extinction background, B, ratio, S/B, via the equation

$$R_{signal} = \frac{I_{probe}}{I_{probe\_blocked\_pump}} = \frac{B + S}{B} = 1 + \frac{S}{B}$$

S signal component of the collected probe beam intensity, above the probe beam extinction background.

$T_{analyser}$ transmission axis transmittivity of the probe beam primary analyser.

$T_{polariser}$ transmission axis transmittivity of the probe beam primary polariser.

W thickness of the laser sheet.

x fractional detuning of the probe beam transition from line-centre.

Greek Alphabet

$A^2\Sigma$–$X^2\Pi$ (0-0) transition of OH transition from the v = 0 vibrational band of the ground electronic state $X^2\Pi$ to the v = 0 vibrational band of the first electronic state $A^2\Sigma$ of the hydroxyl radical, OH.

α_{av} average induced absorption coefficient for the two probe beam polarisation modes of propagation in the pump/probe beam interaction region.

$\alpha_{unperturbed}$ absorption coefficient for the probe beam within the combustion region, but outside the interaction volume of pump and probe beams.

χ intersection angle of pump and probe beams.

$\Delta\alpha_0$ line-centre induced dichroism experienced by the probe beam, and defined in equation [32] of Chapter I as

$$\Delta\alpha^{i,i'}_{J,J''} = -N_J \cdot \frac{I_{pump}\, t}{\hbar\omega_{pump}} \cdot Z_{J,J',J''} \cdot C_{J,J'} \cdot C_{J,J''}$$

where the pump transition is from the shared lower rotational state, J, to the upper rotational state, J', the upper rotational state of the probe beam transition is J" and the terms, i and i', refer to the polarisation states of the two probe beam components which experience the induced dichroism.

γ angle of the probe beam polarisation from the normal to the pump/probe beam intersection plane.

κ angle of the pump beam polarisation axis from the normal to the pump/probe beam intersection plane.

ξ finite extinction ratio of the probe beam polarisers.

Chapter IV: Uniaxial Gas Model of Polarisation Spectroscopy: Circularly Polarised Pump Beam.

Conventions:

Complex numbers are written x + i y.

Subscripts:

0_approx approximation assuming characteristic circular or elliptical polarisation modes of propagation for the probe beam components for near-collinear and intermediate beam intersection. Defined by the condition, $\cos^2(\chi) >> \sigma^2, \Delta$.

α with respect to the α characteristic polarisation mode of propagation of the probe beam.

β with respect to the β characteristic polarisation mode of propagation of the probe beam.

linear_approx approximation assuming characteristic linear polarisation modes of propagation for the probe beam components for near-orthogonal beam intersection. Defined by the condition, $\cos^2(\chi) << \sigma^2, \Delta$.

x with respect to the X axis (which is normal to the beam intersection plane).

y with respect to the Y axis (which lies in the beam intersection plane).

z with respect to the Z axis (which represents either the direction of propagation of the pump or probe beam).

Variables and Constants:

Roman Alphabet

a constant, may be complex.

b constant, may be complex.

c speed of light.

C_1 ratio of the elements of the third-order tensor of non-linear susceptibility, used in the expression for LPS signal strength obtained by Lavrinenko and Gancheryonok, and defined as

$$C_1 = \frac{\chi_{1122}}{\chi_{1221}}$$

C_2 ratio of the elements of the third-order tensor of non-linear susceptibility, used in the expression for LPS signal strength obtained by Lavrinenko and Gancheryonok, and defined as

$$C_2 = \frac{\chi_{1212}}{\chi_{1221}}$$

$\underline{D}$ displacement vector.

$\underline{E}$ electric field vector.

$\underline{E}_{probe}$ electric field of the probe beam incident on the primary probe beam polariser.

E_{probe_0} magnitude of the probe beam electric field incident on the probe beam primary polariser.

$\underline{E}_{probe}(\Lambda)$ electric field of the probe beam after transmission a distance, Λ, through the region of induced birefringence and dichroism.

$E_{plane\_of\_polarisation}$ general form of the electric field of the probe beam.

$\underline{E}_{probe\_transmitted\_through\_analyser}(\Lambda)$ probe beam electric field after transmission a distance, Λ, through the region of induced birefringence and dichroism and the probe beam analyser.

$F_{circ}(\gamma,\chi)$ geometric dependence of the LPS signal for the case of perfectly crossed polarisers and no inter-polariser birefringent optical elements in the probe beam path aside from that implicit in the induced birefringence.

f complex coefficient of the α polarisation mode electric field vector in the vector decomposition of the probe beam electric field in terms of the unnormalised polarisation modes, α and β.

g complex coefficient of the β polarisation mode electric field vector in the vector decomposition of the probe beam electric field in terms of the unnormalised polarisation modes, α and β.

$I_{L\&G}$ expression for the LPS signal strength derived by Lavrinenko and Gancheryonok.

I_{probe_0} intensity of the probe beam incident on the probe beam primary polariser.

$I_{probe\_transmitted\_through\_analyser}(\Lambda)$ probe beam intensity after transmission a distance, Λ, through the region of induced birefringence and dichroism and the probe beam analyser.

$J_{circ}(\gamma,\chi)$ function representing the combined geometric dependence of the factors, $F_{circ}(\gamma,\chi)$ and the induced dichroism due to the circularly polarised pump beam in the LPS signal strength for perfectly crossed polarisers and a linearly polarised pump beam and written for the two approximation regimes

For $\cos^2(\chi) >> \sigma^2, \Delta$: collinear and intermediate beam intersection angles

$$J_{circ}(\gamma,\chi)_{0\_approx} = \frac{\left(\left(\cos^2(\gamma)\cdot\sin^4(\chi)\cdot\Delta+\cos^2(\chi)\right)\cdot\sigma\right)^2 + \left(\cos(\chi)\cdot\sin^2(\chi)\cdot\cos(\gamma)\cdot\sin(\gamma)\cdot\left(\Delta-\sigma^2\right)\right)^2}{\left(\cos(\chi)\cdot\sin(\chi)\right)^2}$$

For $\cos^2(\chi) << \sigma^2, \Delta$: near orthogonal imaging

$$J_{circ}(\gamma,\chi)_{linear\_approx} = \sin^2(2\cdot\gamma)\cdot\sin^2(\chi)\cdot\left(\frac{\Delta+\sigma^2}{2}\right)^2$$

k magnitude of the wavevector.

k_0 magnitude of the free space wavevector for the probe beam.

k_α magnitude of the wavevector associated with the α polarisation mode of propagation of the probe beam.

k_β magnitude of the wavevector associated with the β polarisation mode of propagation of the probe beam.

l width of the pumping beam, used in the expression for LPS signal strength obtained by Lavrinenko and Gancheryonok.

n_α refractive index associated with the α polarisation mode of propagation of the probe beam.

n_β refractive index associated with the β polarisation mode of propagation of the probe beam.

n_e extraordinary refractive index.

n_o ordinary refractive index.

n_0 unpumped refractive index for the probe beam transition.

n_{probe} refractive index of the medium at the probe frequency, ω_{probe}, used in the expression for LPS signal strength obtained by Lavrinenko and Gancheryonok.

$\underline{\hat{R}}_{analyser}$ unit vector representing the transmission axis of the probe beam analyser.

s_ι $\iota = \alpha, \beta$ s function related to the α and β refractive index solution via the equation

$$\left(\frac{n_\iota}{n_o}\right)^2 = 1 + s_\iota$$

W thickness of the pump beam.

x fractional detuning from linecentre, ω_0.

Greek Alphabet

α_{av} average of α and β absorption coefficients for the probe beam.

α_α absorption coefficient associated with the α polarisation mode of propagation of the probe beam.

α_β absorption coefficient associated with the β polarisation mode of propagation of the probe beam.

χ pump/probe beam intersection angle.

χ_{ijkl} elements of the third-order tensor of non-linear susceptibility, used in the expression for LPS signal strength obtained by Lavrinenko and Gancheryonok.

δ complex off-diagonal elements in the electric susceptibility tensor representing the optical activity.

$\underline{\delta}$ vector containing the complex off-diagonal elements in the electric susceptibility tensor representing the optical activity.

Δ twice the induced *fractional* linear birefringence due to a circularly polarised pump beam defined via the equation $n_e^2 = n_o^2 \cdot (1 + \Delta)$ such that $\Delta << 1$, and hence approximated by $n_e = n_o \cdot (1 + \Delta/2)$ so that $\Delta n_{lin}/no = \Delta/2$.

$\Delta\alpha^{i,i'}_{J,J''}$ induced dichroism for the probed transition from the lower state, J, to the upper state, J", for the two orthogonal polarisation states, i and i', of the probe beam.

ε electric susceptibility tensor.

γ angle of the probe beam polarisation direction from the normal to the beam intersection plane.

φ angle of propagation of the probe beam with respect to the induced optic axis.

Λ path length of the probe beam through the region of induced birefringence and dichroism.

μ magnetic susceptibility.

σ *fractional* induced circular birefringence for a circularly polarised pump beam. defined via the equations $\sigma = \delta/n_o^2$ and $\Delta n_{circ} = \sigma \cdot n_o$.

$\sigma^{i_{pump}}_{J,J',M,M'}$ square of the Clebsch-Gordon coefficient for a pump beam with polarisation, i_{pump}, for the transition from state (J,M) to (J',M').

$\sigma^{i}_{J,J'',M,M''}$ square of the Clebsch-Gordon coefficient for a probe beam with polarisation, i, for the transition from state (J,M) to (J",M").

$\sigma_{J,J''}$ total absorption cross-section for the probe transition divided by the factor 2J +1.

$\sigma_{J,J'}$ total absorption cross-section for the pump transition divided by the factor 2J +1.

ω angular frequency.

ω_0 linecentre angular frequency.

ω_{probe} probe beam angular frequency, used in the expression for LPS signal strength obtained by Lavrinenko and Gancheryonok.

$\zeta_{J,J',J''}$ factor a function of only the rotational quantum numbers for the pump and probe transitions defined by Teets, Kowalski, Hill, Carlson and Hansch and described in Chapter I.

ζ_{J,J',J''_corr} factor a $\zeta_{J,J',J''}$ factor valid in the linear regime of optical pumping in an experiment where spontaneous emissions and collisional population transfer between the Zeeman states or the upper and lower states of the pump/probe transitions is negligible. The corr subscript refers to a correction which accounts for the contributions of the pumped upper state population to the induced dichroism.

$\zeta_{J,J',J''\_add\_corr}$ factor additional ζ_{J,J',J''_corr} factor related to the linear dichroism induced by a circularly polarised pump beam.

$Z_{J,J',J''}$ factor a function of only the rotational quantum numbers for the pump and probe transitions which combines all rotational dependence of the induced dichroism aside from the rotational dependence of the Boltzmann equilibrium populations and defined in Chapter I.

Z_{J,J',J''_corr} factor $Z_{J,J',J''}$ factors relating to the ζ_{J,J',J''_corr} factors valid in the linear regime of optical pumping in an experiment where spontaneous emissions and collisional population

transfer between the Zeeman states or the upper and lower states of the pump/probe transitions is negligible. The corr subscript refers to a correction which accounts for the contributions of the pumped upper state population to the induced dichroism.

Z_{J,J',J''_add_corr} factor additional Z_{J,J',J''_corr} factor related to the linear dichroism induced by a circularly polarised pump beam.

Chapter V: Orthogonal Imaging for a Circularly Polarised Pump Beam.

Subscripts:

0_approx with respect the near-collinear and intermediate beam intersection angle approximation regime defined by the condition, $\cos^2(\chi) >> \sigma^2, \Delta$.

add with respect to the additional calculated linear dichroism due to a circularly polarised pump beam.

circ with respect to circular polarisation.

corr refers to a correction which accounts for the contributions of the pumped upper state population to the induced dichroism in the linear regime of optical pumping.

lin with respect to linear polarisation.

linear_approx with respect to the near-orthogonal beam intersection angle approximation regime defined by the condition, $\cos^2(\chi) << \sigma^2, \Delta$, where the characteristic polarisation modes of propagation of the probe beam are assumed to be linearly polarised.

Variables and Constants:

Roman Alphabet

B probe beam extinction background due to the finite extinction ratio of the probe beam polarisers.

$F_{lin}(\chi)$ dependence of the LPS signal strength due to a linearly polarised pump beam on pump/probe beam intersection angle, χ, and defined in Chapter II.

J shared lower rotational state of the pump and probe transitions.

$J_{circ}(\gamma,\chi)$ dependence of the LPS signal strength due to a circularly polarised pump beam on pump/probe beam intersection angle, χ, the polarisation direction of the probe beam polarisation direction from the vertical, γ, and the induced linear, $\Delta/2$, and circular, σ, induced dichroism due to the circularly polarised pump beam, and defined in Chapter IV.

$J_{circ}(\gamma,\chi)_{0\_approx}$ function representing the J dependence of the LPS signal strength due to a circularly polarised pump beam for the near-collinear and intermediate beam intersection angle approximation regime defined by the condition, $\cos^2(\chi) >> \sigma^2, \Delta.$, and defined in Chapter IV.

$J_{circ}(\gamma,\chi)_{linear\_approx}$

function representing the J dependence of the LPS signal strength due to a circularly polarised pump beam for near-orthogonal beam intersection angle approximation regime defined by the condition, $\cos^2(\chi) << \sigma^2$, and defined in Chapter IV.

I_{probe} LPS signal (including probe extinction background).

$I_{probe\_blocked\_pump}$ probe extinction background (obtained by blocking to the pump beam).

Re Reynolds number.

R_{signal} ratio of the LPS signal (including probe extinction background), I_{probe}, to the probe extinction background (obtained by blocking to the pump beam), $I_{probe\_blocked\_pump}$, and related to the pure LPS signal, S, to probe extinction background, B, ratio, S/B, via the equation

$$R_{signal} = \frac{I_{probe}}{I_{probe\_blocked\_pump}} = \frac{B + S}{B} = 1 + \frac{S}{B}$$

S signal component of the collected LPS signal, above the probe beam extinction background.

Greek Alphabet

χ pump/probe beam intersection angle.

Δ (twice) the maximum fractional induced linear dichroism due to a circularly polarised pump beam.

γ angle of the probe beam polarisation direction from the normal to the beam intersection plane.

σ maximum fractional induced circular dichroism due to a circularly polarised pump beam.

$Z_{J,J',J''}$ factor a function of only the rotational quantum numbers for the pump and probe transitions which combines all rotational dependence of the induced dichroism aside from the rotational dependence of the Boltzmann equilibrium population defined in Chapter I.

Z_{J,J',J''_add_corr} factor additional Z_{J,J',J''_corr} factor representing the J dependence (aside from the rotational dependence of the Boltzmann equilibrium population) of the induced linear dichroism due to a circularly polarised pump beam defined in Chapter IV.

Z_{J,J',J''_corr} factor $Z_{J,J',J''}$ factor accounting for the contribution of the upper state of a shared pump/probe transition to the induced dichroism. Valid in the linear regime of optical pumping in an experiment where spontaneous emissions and collisional population transfer between the Zeeman states or the upper and lower states of the pump/probe transitions is negligible.

Chapter VI: Near Collinear Polarisation Spectroscopy Imaging in Combustion

Variables and Constants:

Roman Alphabet

B probe beam extinction background due to the finite extinction ratio of the probe beam polarisers.

I_{probe} LPS signal (including probe extinction background).

$I_{probe\_blocked\_pump}$ probe extinction background (obtained by blocking to the pump beam).

r radius of the flame.

R_{signal} ratio of the LPS signal (including probe extinction background), I_{probe}, to the probe extinction background (obtained by blocking to the pump beam), $I_{probe\_blocked\_pump}$, and related to the pure LPS signal, S, to probe extinction background, B, ratio, S/B, via the equation

$$R_{signal} = \frac{I_{probe}}{I_{probe\_blocked\_pump}} = \frac{B + S}{B} = 1 + \frac{S}{B}$$

Re Reynolds number.

S signal component of the collected LPS signal, above the probe beam extinction background.

W thickness of the pump sheet.

Greek Alphabet

χ pump/probe beam intersection angle.

γ angle of the probe beam polarisation direction from the normal to the beam intersection plane.

κ angle of the pump beam polarisation axis from the normal to the pump/probe beam intersection plane.

Chapter VII: Simultaneous PLIF and PLPS in Combustion

Subscripts:

high_pump_intensity with respect to large steady-state saturation, $I_{pump} >> I_{sat}$.

highly_saturated with respect to a steady-state regime which is highly saturated.

linear_regime with respect to a steady-state regime which is linear with the specified beam intensity.

low_pump_intensity with respect to small steady-state saturation, $I_{pump} << I_{sat}$.

quenching_dominated steady-state regime where $Q_{10} >> B_{10}W$, $B_{01}W$, A_{10}.

saturated with respect to a steady-sate regime which is independent of the specified beam intensity.

shared_pump/probe_transitions with respect to the case of shared pump and probe beam transitions.

steady-state with respect to the steady-state solutions of the target species populations.

stimulated_emission_dominated steady-state regime where $B_{10}W$, $B_{01}W >> Q_{10}$, A_{10}.

Variables and Constants:

Roman Alphabet

A_{10} Einstein coefficient for spontaneous emission from the upper state, 1, to the lower state, 0, of the pumped transition.

B probe beam extinction background due to the finite extinction ratio of the probe beam polarisers.

B_{01} Einstein coefficient for stimulated absorption from the lower state, 0, to the upper state, 1.

B_{10} Einstein coefficient for stimulated emission from the upper state, 1, to the lower state, 0.

$C_{J,J''}$ non-rotational (e.g. electronic/vibrational) component of the absorption cross-section for the probe transition (J,M) to (J",M").

d a constant.

dv pumped volume from which the LIF signal fluorescence is collected.

g a constant dependent on the induced dichroism.

G a constant dependent on the induced dichroism.

h a constant dependent on the induced dichroism.

H a constant dependent on the induced dichroism.

h_v energy of a photon.

I_{LIF} LIF signal intensity.

I_{PLIF} PLIF signal.

I_{PLPS} PLPS signal.

I_{probe_0} probe beam intensity incident on the primary probe beam polariser.

I_{PS} (analytic) line-centre (unsaturated) LPS signal of Reichardt, Di Teodoro and Farrow.

I_{pump} intensity of the pump beam.

K a constant in an expression for the LPS signal which includes geometrical factors.

k a constant.

L absorption length.

M Zeeman quantum number.

Mode 1 a largely uncorrected image (corrected for the non-zero background of the ICCD alone).

Mode 2 image representing the ratio, S/B, of the pure signal, S, (free of probe beam extinction components) to the background (with flame), B. The ratio is proportional to the square of the induced dichroism.

N molecular concentration or total population density of the target species population.

N_1 population density of the upper state, 1, of the pumped transition.

N_0 population density of the lower state, 0, of the pumped transition.

N_{JM} number density of the lower state of the shared pump and probe transitions, (J,M).

$N_{J'M'}$ number density of the upper state of the pump transition, (J',M').

$N_{J''}$ number density of the upper state of the pumped transition with rotational quantum number, J".

Q_{10} quenching rate from the upper state, 1, to the lower state, 0.

r_{up} combined transition rate from the lower state, 0, to the upper state, 1, of the pumped transition.

r_{down} combined transition rate from the upper state, 1, to the lower state, 0, of the pumped transition.

r total transition rate between the lower state, 0, and the upper state, 1, of the pumped transition, defined as $r = r_{up} + r_{down}$.

t time.

s term related to the induced dichroism and defined by Wieman and Hansch.

S signal component of the collected LPS signal, above the probe beam extinction background.

W spectral energy density of the pump beam (i.e. I_ν/c where I_ν is the spectral irradiance (the irradiance per unit frequency interval and c is the speed of light).

x detuning.

Greek Alphabet

α_o linecentre absorption coefficient.

χ pump/probe beam intersection angle.

$\Delta\alpha$ induced dichroism.

$\Delta\alpha^{i,i'}_{J,J''}$ induced dichroism experienced by the probe beam, defined by Teets, Kowalski, Hill, Carlson and Hansch.

$\Delta\alpha_{PLPS}$ induced dichroism which produces the PLPS signal.

γ_{eg} "coherence dephasing rate between any two Zeeman states in levels g and e", defined in the derivation of Reichardt, Di Teodoro and Farrow's analytic expression for LPS signal strength.

γ_{pulse} laser pulse decay rate defined in the derivation of Reichardt, Di Teodoro and Farrow's analytic expression for LPS signal strength.

θ polariser uncrossing angle.

$\sigma^{probe}_{J,J'',M,M''}$ rotational/Zeeman component of the absorption cross-section for the probe transition (J,M) to (J",M").

Ω solid angle from which the LIF imaging optics collect fluorescence.

ξ extinction ratio of the probe beam polarisers.

Chapter VIII: Jones Matrix Description for the Geometrically Dependent Induced Dichroism and Birefringence

Conventions:

Complex numbers are written x + i y.

Subscripts:

0_approx for the case of a circularly polarised pump beam, with respect the near-collinear and intermediate beam intersection angle approximation regime defined by the condition, $\cos^2(\chi) >> \sigma^2, \Delta$.

α one of the characteristic polarisation modes of propagation of the probe beam induced by a circularly polarised pump beam.

av an average with respect to the ordinary and extraordinary polarisation modes of propagation of the probe beam.

β one of the characteristic polarisation modes of propagation of the probe beam induced by a circularly polarised pump beam.

circ with respect to the induced circular birefringence due to a circularly polarised pump beam.

circular_pump with respect to a circularly polarised pump beam.

e with respect to the extraordinary polarisation mode of propagation of the probe beam.

extraordinary with respect to the extraordinary polarisation mode of propagation of the probe beam.

lin with respect to the induced linear birefringence due to a linearly polarised pump beam.

linear_approx for the case of a circularly polarised pump beam, with respect to the near-orthogonal beam intersection angle approximation regime defined by the condition, $\cos^2(\chi) << \sigma^2, \Delta$, where the characteristic polarisation modes of propagation of the probe beam are assumed to be linearly polarised.

linear_pump with respect to a linearly polarised pump beam.

o with respect to the ordinary polarisation mode of propagation of the probe beam.

optic axis with respect to the induced optic axis.

ordinary with respect to the ordinary polarisation mode of propagation of the probe beam.

perfectly_aligned with respect to polarisers with perfectly aligned transmission axes.

perfectly_crossed with respect to perfectly crossed polarisers.

probe with respect to the probe beam.

probe_0 with respect to the probe beam incident on the primary probe beam polariser.

probe _frame with respect to the probe frame.

simplified with respect to the frame of the optical element which reduces the Jones matrix for that element to its simplest form.

Variables and Constants:

Roman Alphabet

a term related to the induced linear birefringence, $\Delta/2$, and the induced circular birefringence, σ, due to a circularly polarised pump beam according to the equation

$$a = \left(\frac{\Delta - \sigma^2}{2}\right) \cdot \sin^2(\chi)$$

b term related to the induced linear birefringence, $\Delta/2$, and the induced circular birefringence, σ, due to a circularly polarised pump beam according to the equation

$$b = \sqrt{\sin^4(\chi) \cdot \left(\frac{\Delta + \sigma^2}{2}\right)^2 + \cos^2(\chi) \cdot \sigma^2}$$

B Jones matrix representing transmission a distance, Λ, though a linearly birefringent and dichroic material.

B_{linear_pump} simplified Jones matrix representing transmission a distance, Λ, though a linearly birefringent and dichroic material due to a linearly polarised pump beam in the X_sY_s frame of the simplified matrix.

$B_{\substack{linear\_pump \\ probe\_frame}}$

Jones matrix representing transmission a distance, Λ, though a linearly birefringent and dichroic material due to a linearly polarised pump beam in the XYZ frame of the probe beam.

$B_{\substack{circ\_pump \\ \cos^2(\chi)>>\sigma^2,\Delta \\ probe\_frame}}$

Jones matrix for the action of the dichroism and birefringence induced by a circularly polarised pump beam in the frame of the probe beam for $\cos^2(\chi) >> \sigma^2, \Delta$.

$B_{\substack{circ\_pump \\ probe\_frame \\ \chi\sim 0}}$

Jones matrix for the action of the dichroism and birefringence induced by a circularly polarised pump beam in the frame of the probe beam for $\chi \sim 0$.

$B_{\substack{circ\_pump \\ \cos^2(\chi)<<\sigma^2,\Delta \\ probe\_frame}}$

Jones matrix for the action of the dichroism and birefringence induced by a circularly polarised pump beam in the frame of the probe beam for $\cos^2(\square) << \sigma^2, \Delta$.

$\underline{E}$ electric field of the probe beam.

E_0 magnitude of the probe beam electric field incident on the primary probe beam polariser.

$\left(\underline{E}_{0\_approx}\right)_\iota$, $\iota = \alpha, \beta$ vectors representing the polarisation modes of propagation induced by a circularly polarised pump beam for $\cos^2(\chi) >> \sigma^2, \Delta$.

$\hat{\underline{E}}_{extraordinary}$ unit vector representing the extraordinary polarisation mode of the probe beam for a linearly polarised pump beam.

$\hat{\underline{E}}_{optic\_axis}$ unit electric vector which represents the induced optic axis of the uniaxial medium for a linearly polarised pump.

$\hat{\underline{E}}_{ordinary}$ unit vector representing the ordinary polarisation mode of the probe beam for a linearly polarised pump beam.

$\hat{\underline{E}}_{plane\_of\_polarisation}$ general electric vector for a beam propagating at the angle, χ, to the Z' axis and with axis of polarisation lying at the angle, η, to the vertical X' axis.

$\underline{E}_{probe}$ electric field of the probe beam incident on the primary probe beam polariser.

E_{probe_0} magnitude of the electric field of the probe beam incident on the primary probe beam polariser.

$\underline{E}_{probe\_transmitted\_\Lambda}$ electric vector of the probe beam transmitted a distance through the region of induced birefringence and dichroism.

$\underline{E}_{\substack{probe\_transmitted \\ polariser\_at\_\eta}}$ component of the electric vector of the probe beam transmitted through a polariser with transmission axis aligned at the angle, η, to the X axis.

E_{probe_x} X component of the unit probe electric field vector in the frame of the probe beam.

E_{probe_y} Y component of the unit probe electric field vector in the frame of the probe beam.

k_a wavenumber for the α polarisation mode of propagation of the probe beam due to a circularly polarised pump beam.

k_b wavenumber for the β polarisation mode of propagation of the probe beam due to a circularly polarised pump beam.

k_e wavenumber for the extraordinary polarisation mode of propagation of the probe beam due to a linearly polarised pump beam.

k_o wavenumber for the ordinary polarisation mode of propagation of the probe beam due to a linearly polarised pump beam.

k_{av} average of the two characteristic polarisation modes of propagation of the probe beam.

$P(\eta)$ Jones matrix describing the action of the imperfect polariser (aligned with transmission axis at the angle, η, to the vertical X axis) in the frame of the probe beam.

$P_{simplified}$ simplified polariser matrix.

$P_{simplified\ perfectly\_aligned}$

simplified polariser matrix for an analyser with transmission axis perfectly aligned with a primary polariser.

$P_{simplified\ perfectly\_crossed}$

simplified polariser matrix for an analyser with transmission axis perfectly crossed with a primary polariser.

$R(\eta)$ rotation matrix associated with a rotation of a vector through the angle, η.

s_{ι} term related to the a and b induced refractive indices induced by a circularly polarised pump beam via the equation

$$\left(\frac{n_\iota}{n_o}\right)^2 = 1 + s_\iota \qquad \iota = \alpha, \beta$$

t_1 fraction of the input beam electric field transmitted polarised parallel to a polariser's transmission axis.

t_2 fraction of the input beam electric field transmitted polarised parallel to the extinction axis of a polariser.

$\underline{\hat{v}}$ unit vector representing the transmission axis of a polariser aligned at the angle, η, to the X axis in the frame of the probe beam.

$\underline{\hat{u}}$ unit vector representing the extinction axis of a polariser with transmission axis aligned at the angle, η, to the X axis in the frame of the probe beam.

X X axis of the probe beam frame (vertical).

X' X axis of the pump beam frame (vertical).

$X_{Jones\_linear\_pump}$ simplified Jones matrix X_s axis characteristic of the propagation of the probe beam through the region of induced birefringence and dichroism due to a linearly polarised pump beam.

X_s X axis in the frame of the simplified Jones vector.

Y Y axis of the probe beam frame (lying in the beam intersection plane and normal to the probe direction of propagation).

Y' Y axis of the pump beam frame (lying in the beam intersection plane and normal to the pump direction of propagation).

$Y_{Jones\_linear\_pump}$ simplified Jones matrix Y_s axis characteristic of the propagation of the probe beam through the region of induced birefringence and dichroism due to a linearly polarised pump beam.

Y_s Y axis in the frame of the simplified Jones vector.

Z Y axis of the probe beam frame (parallel to the probe direction of propagation).

Z' Y axis of the pump beam frame (parallel to the pump direction of propagation).

Greek Alphabet

α_a absorption coefficient for the α polarisation mode of propagation of the probe beam.

α_b absorption coefficient for the β polarisation mode of propagation of the probe beam.

α_e absorption coefficient for the extraordinary polarisation mode of propagation of the probe beam.

α_o absorption coefficient for the ordinary polarisation mode of propagation of the probe beam.

α_{av} average of the absorption coefficients for the two characteristic polarisation modes of propagation of the probe beam.

A coefficient of the α polarisation mode vector in the linear decomposition of the probe beam unit vector into the two polarisation modes due to a circularly polarised pump beam.

B coefficient of the β polarisation mode vector in the linear decomposition of the probe beam unit vector into the two polarisation modes due to a circularly polarised pump beam.

χ pump/probe beam intersection angle.

Δ (twice) the fractional induced linear birefringence due to a circularly polarised pump beam.

$\Delta\alpha_{lin}$ induced dichroism due to a linearly polarised pump beam.

$\Delta\alpha_{circ}$ induced dichroism due to a circularly polarised pump beam for $\cos^2(\chi) >> \sigma^2, \Delta$.

$\Delta\alpha_{linear\_approx}$ induced dichroism due to a circularly polarised pump beam for $\cos^2(\chi) << \sigma^2, \Delta$.

Δk_{lin} difference in wavenumbers for the ordinary and extraordinary modes of propagation of the probe beam for the case of a linearly polarised pump beam.

Δk_{circ} difference in wavenumbers for the α and β modes of propagation of the probe beam for the case of a circularly polarised pump beam for $\cos^2(\chi) >> \sigma^2, \Delta$.

Δk_{linear_approx} difference in wavenumbers for the α and β modes of propagation of the probe beam for the case of a circularly polarised pump beam for $\cos^2(\chi) << \sigma^2, \Delta$.

$\Delta n_{lin}(\chi)$ induced birefringence due to a linearly polarised pump beam, derived in Chapter II.

$\Delta n_{circ}(\chi)$ induced birefringence due to a circularly polarised pump beam for $\cos^2(\chi) >> \sigma^2, \Delta$, derived in Chapter IV.

$\Delta n_{linear\_approx}(\chi)$ induced birefringence due to a circularly polarised pump beam for $\cos^2(\chi) << \sigma^2, \Delta$, derived in Chapter IV.

ϕ term including the induced dichroism and the difference between α and β wavenumbers due to a circularly polarised pump beam and defined as

$$\phi = \left(\frac{\Delta k_{circ}}{2} - i \cdot \frac{\Delta \alpha_{circ}}{4} \right) \cdot \Lambda$$

γ polarisation direction of the probe beam with respect to the vertical X axis.

γ_a angle of inclination of the α polarisation direction from the vertical X axis in the electric field plane of the probe beam.

γ_b angle of inclination of the β polarisation direction from the vertical X axis in the electric field plane of the probe beam.

γ_e angle of inclination of the extraordinary polarisation direction from the vertical X axis in the electric field plane of the probe beam.

γ_o angle of inclination of the ordinary polarisation direction from the vertical X axis in the electric field plane of the probe beam.

η angle of the transmission axis of a polariser in the probe beam path from the X axis.

κ polarisation direction of the pump beam with respect to the vertical X' axis.

Λ pump/probe beam interaction length, measured along the probe beam path.

σ fractional induced circular birefringence due to a circularly polarised pump beam.

ξ polariser extinction ratio.

$\xi_{combined}$ combined extinction ratio for two polarisers with perfectly aligned transmission axes.

Chapter IX: The Effect of Imperfect and Misaligned Optical Elements.

Conventions:

Complex numbers are written x + i y.

Subscripts:

0_approx
: with respect to the collinear and intermediate beam intersection angle approximation discussed in Chapter IV for a circularly polarised pump beam for $\cos^2(\chi) >> \sigma^2, \Delta$.

approx_collinear
: with respect to approximately collinear pump and probe beams.

$\cos^2(\chi) >> \sigma^2, \Delta$
: with respect to the collinear and intermediate beam intersection angle approximation described in Chapter IV for a circularly polarised pump beam.

$\cos^2(\chi) << \sigma^2, \Delta$
: with respect to the near-orthogonal beam intersection angle approximation described in Chapter IV for a circularly polarised pump beam.

circ
: with respect to a circularly polarised pump beam or a circularly birefringent optical element.

circular_pump
: with respect to a circularly polarised pump beam.

j = i, f
: i = initial, f = final birefringent optical element in the probe beam path between the probe beam polarisers.

lin
: with respect to a linearly polarised pump beam.

linear_approx
: with respect to the linear approximation derived for near orthogonal beam intersection for a circularly polarised pump beam in Chapter IV such that $\cos^2(\chi) << \sigma^2, \Delta$.

linear_pump
: with respect to a linearly polarised pump beam.

perfectly _aligned
: with respect to an analyser with transmission axis perfectly aligned with that of a primary polariser.

probe_aligned_at_π/4_to_primary_polariser
: with respect to a probe beam with polarisation direction aligned at $\pi/4$ to the transmission axis of the primary probe beam polariser.

probe_aligned_to_primary_polariser
: with respect to a probe beam with polarisation direction aligned to the transmission axis of the primary probe beam polariser.

perfectly _crossed
: with respect to an analyser with transmission axis perfectly crossed with that of a primary polariser.

Variables and Constants:

Roman Alphabet

a
: term related to the birefringence due to a circularly polarised pump beam and defined in Chapter IV as

$$a = \left(\frac{\Delta - \sigma^2}{2}\right) \cdot \sin^2(\chi)$$

a_j angle defining the orientation of the ordinary axis of a linearly birefringent optical element, such that the ordinary axis of the element lies at the angle, $\pi/4 + a_j$ (j = i, f), to the induced ordinary axis of the region of induced dichroism and birefringence due to the pump beam.

a_para_j angle related to a_j and defined as $a\_para_j = \pi/2 + a_j$.

b term related to the birefringence due to a circularly polarised pump beam and defined in Chapter IV as

$$b = \sqrt{\sin^4(\chi)\cdot\left(\frac{\Delta+\sigma^2}{2}\right)^2 + \cos^2(\chi)\cdot\sigma^2}$$

Use context to differentiate between this usage and the term, b, used to represent the birefringence due to birefringent optical elements in the probe beam path between the probe beam polarisers.

b birefringence term due any optical elements placed in the probe beam path between the probe beam polarisers as used by Teets, Kowalski, Hill, Carlson and Hansch,

or

phase difference introduced between the two orthogonal incident probe beam polarisation states by dispersion.

b_j (half the) phase difference introduced between the two probe beam components by each birefringent optical element in the probe beam path.

B_j matrix representing each linearly birefringent optical element (j = i, f) in the probe beam path.

B_{circ} matrix representing each circularly birefringent optical element in the probe beam path.

$B0_j$ coefficient of the matrix in the linear expansion of the linearly birefringent optical element matrix.

$B_{linearly\_birefringent\_element}$ Jones matrix representing a linearly birefringent optical element.

$B_{\substack{dichroic\\linearly\_birefringent\_element}}$ Jones matrix representing a dichroic linearly birefringent optical element.

$B_{circularly\_birefringent\_element}$ Jones matrix representing a circularly birefringent optical element.

$B_{\substack{dichroic\\circularly\_birefringent\_element}}$ Jones matrix representing a dichroic circularly birefringent optical element.

B_{linear_pump} matrix derived in Chapter VIII to describe the general geometric behaviour of the region of induced linear dichroism and birefringence due to a linearly polarised pump beam.

$B_{\substack{circ\_pump\\ \cos^2(\chi)>>\sigma^2,\Delta\\probe\_frame}}$

matrix derived in Chapter VIII to describe the general geometric behaviour of the region of induced dichroism and birefringence due to a circularly polarised pump beam for $\cos^2(\chi) >> \sigma^2, \Delta$.

C_{circ_pump} combined matrix describing the transmission of the probe beam through the two probe beam polarisers and a region of induced dichroism and birefringence region due to a circularly polarised pump beam in the $X_{probe}Y_{probe}$ axis frame for $\cos^2(\chi) >> \sigma^2, \Delta$.

$C_{\substack{circ \\ partial}}$

combined matrix representing the action of the probe beam polarisers and region of induced dichroism and birefringence due to a circularly polarised pump beam in a probe beam polarisation frame with X" and Y" axes lying at $3\pi/4$ and $5\pi/4$ to the vertical X axis respectively for $\cos^2(\chi) >> \sigma^2, \Delta$.

$C_{\substack{circ+circularly\_birefringent\_optical\_elements \\ partial}}$

partial matrix representing the action of the probe beam polarisers, circularly birefringent inter-probe beam polariser-optical elements and region of induced dichroism and birefringence due to a circularly polarised pump beam in a probe beam polarisation frame with X" and Y" axes lying at $3\pi/4$ and $5\pi/4$ to the vertical X axis respectively for $\cos^2(\chi) >> \sigma^2, \Delta$.

$C_{circ+linearly\_birefringent\_optical\_elements}$ combined matrix describing the transmission of the probe beam through the two probe beam polarisers, linearly birefringent inter-probe beam polariser-optical elements and a region of induced dichroism and birefringence region due to a circularly polarised pump beam in the $X_{probe}Y_{probe}$ axis frame for $\cos^2(\chi) >> \sigma^2, \Delta$.

$C_{\substack{circ+linearly\_birefringent\_optical\_elements \\ partial}}$

partial matrix representing the action of the probe beam polarisers, linearly birefringent inter-probe beam polariser-optical elements and region of induced dichroism and birefringence due to a circularly polarised pump beam in a probe beam polarisation frame with X" and Y" axes lying at $3\pi/4$ and $5\pi/4$ to the vertical X axis respectively for $\cos^2(\chi) >> \sigma^2, \Delta$.

$C_{circ\_linear\_approx}$ combined matrix describing the transmission of the probe beam through the two probe beam polarisers and a region of induced dichroism and birefringence due to a circularly polarised pump beam in a near-collinear pump/probe beam geometry (for $\cos^2(\chi) << \sigma^2, \Delta$) in the $X_{probe}Y_{probe}$ axis frame.

$C_{\substack{circ\_linear\_approx \\ partial}}$

combined matrix representing the action of the probe beam polarisers and region of induced dichroism and birefringence due to a circularly polarised pump beam in a probe beam polarisation frame with X" and Y" axes lying at $3\pi/4$ and $5\pi/4$ to the vertical X axis respectively for near-orthogonal beam intersection (for $\cos^2(\chi) << \sigma^2, \Delta$).

C_{linear} combined matrix describing the transmission of the probe beam through the two probe beam polarisers and a region of induced linear dichroism and birefringence in the $X_{probe}Y_{probe}$ axis frame.

$C_{linear\ partial}$

partial matrix representing the combined action of the probe beam polarisers and induced linearly dichroic-birefringent medium in a probe beam *polarisation frame* with X" and Y" axes lying at $\pi/4$ to the induced ordinary and extraordinary axes respectively. This frame is the frame which leads to maximum LPS signal.

$C_{linear+circularly\_birefringent\_optical\_elements\ partial}$

partial matrix representing the action of the probe beam polarisers, circularly birefringent inter-probe beam polariser-optical elements and the region of induced linear dichroism and birefringence in a probe beam *polarisation frame* with X" and Y" axes lying at $\pi/4$ to the induced ordinary and extraordinary axes respectively.

$C_{linear+linearly\_birefringent\_optical\_elements}$

combined matrix representing the action of the probe beam polarisers, linearly birefringent inter-probe beam polariser-optical elements and the region of induced linear dichroism and birefringence in the $X_{probe}Y_{probe}$ axis frame.

$C_{linear+linearly\_birefringent\_optical\_elements\ partial}$

partial matrix representing the action of the probe beam polarisers, linearly birefringent inter-probe beam polariser-optical elements and the region of induced linear dichroism and birefringence in a probe beam *polarisation frame* with X" and Y" axes lying at /4 to the induced ordinary and extraordinary axes respectively.

$\underline{E}$ electric field of the probe beam incident on the primary probe beam polariser.

E_0 magnitude of the probe beam electric field incident on the primary probe beam polariser.

$\underline{E}_{out}$ electric field of the probe beam transmitted through the probe beam analyser after passing the primary probe beam polariser and the region of induced birefringence and dichroism.

$F_{perfect\_\frac{1}{4}\_wave\_rhomb}$ Jones matrix for a perfect quarter-wave rhomb.

$F_{perfect\_\frac{1}{2}\_wave\_rhomb}$ Jones matrix for a perfect half-wave rhomb.

$F_{imperfect\_rhomb}$ Jones matrix for an imperfect rhomb.

$F_{(non-dichroic)\ imperfect\_rhomb}$

Jones matrix for an imperfect rhomb including the effects of absorption over the path length through the rhomb.

$F_{dichroic\ imperfect\_wave-plate}$

Jones matrix for an imperfect waveplate including the effects of absorption and dichroism over the path length through the rhomb.

I_{out} probe beam intensity transmitted through the probe beam analyser after passing the primary probe beam polariser and a region of induced birefringence and dichroism.

I_0 probe beam intensity incident on the primary probe beam polariser.

k_{av} average of the wavenumbers experienced by the two characteristic probe beam polarisation modes of propagation due to the pump beam.

L path length.

m term related to the birefringence due to a circularly polarised pump beam and defined in terms of the factors, a and b (defined in Chapter IV), as

$$m = \frac{a^2 - b^2 - \sigma^2 \cdot \cos^2(\chi)}{2 \cdot b \cdot \sigma \cdot \cos(\chi)}$$

n term related to the birefringence due to a circularly polarised pump beam and defined in terms of the factors, a and b (defined in Chapter IV) as

$$n = \frac{a}{b}$$

n_0 unperturbed refractive index in the absence of a pump beam.

n_e extraordinary refractive index.

n_o ordinary refractive index.

$P_{conventional}$ conventional Jones matrix representing an imperfect polariser.

$P_{imperfect}$ Jones matrix representing the behaviour of an imperfection-limited polariser.

$R(\eta)$ rotation matrix representing rotation through the angle, η.

s_1 fraction of the probe beam electric field polarised parallel to the transmission axis scattered and transmitted polarised parallel to the extinction axis in the description of an imperfection-limited polariser.

s_2 fraction of the probe beam electric field polarised parallel to the extinction axis of the polariser scattered and transmitted polarised parallel to the transmission axis in the description of an imperfection-limited polariser.

t thickness of an optical element.

t_1 transmittivity (with respect to the electric field) of an conventional imperfect polariser along the transmission axis.

t_2 transmittivity (with respect to the electric field) of an conventional imperfect polariser along the extinction axis.

T path length.

X_{probe} (vertical) X axis in the probe beam electric field axis system.

X_{rhomb} X axis corresponding to the ordinary transmission axis of a rhomb.

X'' axis lying at the angle, $\gamma_o + \pi/4$, to the vertical X axis in the plane of the electric field of the probe beam.

Y_{probe} Y axis in the probe beam electric field axis system. Parallel to the probe beam electric field component lying in the beam intersection plane.

Y_{rhomb} Y axis corresponding to the extraordinary transmission axis of a rhomb.

Y'' axis lying at the angle, $\gamma_o + 3\pi/4$, to the vertical X axis in the plane of the electric field of the probe beam.

Greek Alphabet

α_{av} average of the absorption coefficients experienced by the two characteristic probe beam polarisation modes of propagation due to the pump beam.

α_{b_α} α absorption coefficient for a circularly birefringent optical element.

α_{b_β} β absorption coefficient for a circularly birefringent optical element.

$\alpha_{b\_circ\_av}$ average of the α and β absorption coefficients for a circularly birefringent optical element.

α_{b_e} extraordinary absorption coefficient for a linearly birefringent optical element.

α_{b_o} ordinary absorption coefficient for a linearly birefringent optical element.

α_{rhomb} rhomb absorption coefficient.

$\alpha_{wave\text{-}plate\_o}$ waveplate ordinary absorption coefficient.

$\alpha_{wave\text{-}plate\_e}$ waveplate extraordinary absorption coefficient.

$B0_{circ}$ coefficient of the matrix in the linear expansion of the circularly birefringent optical element matrix.

χ angle of pump/probe beam intersection in the YZ plane.

Δ (twice the) fractional linear dichroism induced by a circularly polarised pump beam.

$\Delta\alpha$ induced dichroism experienced by the two characteristic probe beam polarisation modes of propagation due to the pump beam.

$\Delta\alpha_{b\_circ}$ circular dichroism of a circularly birefringent optical element with respect to the direction of propagation of the probe beam within the element.

$\Delta\alpha_{b\_lin}$ linear dichroism of a birefringent optical element with respect to the direction of propagation of the probe beam within the element.

$\Delta\alpha_{wave\text{-}plate}$ waveplate dichroism.

$\Delta\gamma$ deviation of the primary polariser from the angle, $\gamma_o + \pi/4$, to the vertical X axis.

$\Delta\eta$ angle of rotation around the axis representing the direction of propagation of the probe beam.

Δk difference in wavenumbers experienced by the two characteristic probe beam polarisation modes of propagation due to the pump beam.

ΔL difference in path length.

Δn_{0_lin} induced linear birefringence for collinear pump and probe beams.

$\Delta n_{lin}(\chi)$ induced linear birefringence experienced by the probe beam for a pump/probe beam intersection angle of χ.

$\Delta n_{circ}(\chi)$ induced birefringence experienced by the probe beam for a pump/probe beam intersection angle of χ and a circularly polarised pump beam for $\cos^2(\chi) >> \sigma^2, \Delta$ and derived in Chapter IV.

$\Delta n_{circ\_linear\_approx}(\chi)$ induced birefringence due to a circularly polarised pump beam calculated in Chapter IV in the linear approximation derived for near orthogonal beam intersection such that $\cos^2(\chi) << \sigma^2, \Delta$.

$\Delta\theta$ deviation of the analyser from perfect crossing with the probe beam primary polariser.

$\Delta\psi$ misalignment of the input probe beam polarisation direction from the angle, $\pi/4$, to the induced ordinary axis.

ϕ phase .

γ angle of the probe beam polarisation direction from the vertical X axis.

γ_o angle of the induced ordinary polarisation direction from the vertical X axis.

η angle of rotation around the axis representing the direction of propagation of the probe beam.

κ angle of the pump beam polarisation direction from the vertical X axis.

λ_0 vacuum wavelength.

θ angle of deviation from perfect crossing of the probe beam polarisers.

σ fractional circular dichroism induced by a circularly polarised pump beam

or

the polariser imperfection term, defined as

$$\sigma = \frac{s}{t_1}$$

and used in the case of a linearly polarised pump beam where there is no possibility of confusion with the induced circular dichroism term, σ, due to a circularly polarised pump beam.

Σ polariser imperfection term, defined as

$$\Sigma = \frac{s}{t_1}$$

and used in the case of a circularly polarised pump beam to avoid confusion with the induced circular dichroism term, σ.

ξ polariser extinction ratio. In this thesis, the extinction ratio of a polariser is defined as *the ratio*, for unpolarised input, *of transmittivities of electric field components polarised parallel to the extinction and to the transmission axes.*

$\xi_{conventional}$ extinction ratio for a polariser described by the conventional Jones matrix for imperfect polarisers.

$\xi_{conventional\_combined\ perfectly\_aligned}$ combined extinction ratio for two polarisers with perfectly aligned transmission axes described by the conventional Jones matrices for imperfect polarisers.

$\xi_{imperfect}$ extinction ratio associated with an imperfection-limited polariser.

$\xi_{combined\_imperfection\_limited\ perfectly\_aligned}$ combined extinction ratio for two imperfection-limited polarisers with perfectly aligned transmission axes.

ζ polarisation extinction term, defined as

$$\zeta = \frac{t_2}{t_1} = \sqrt{\xi}$$